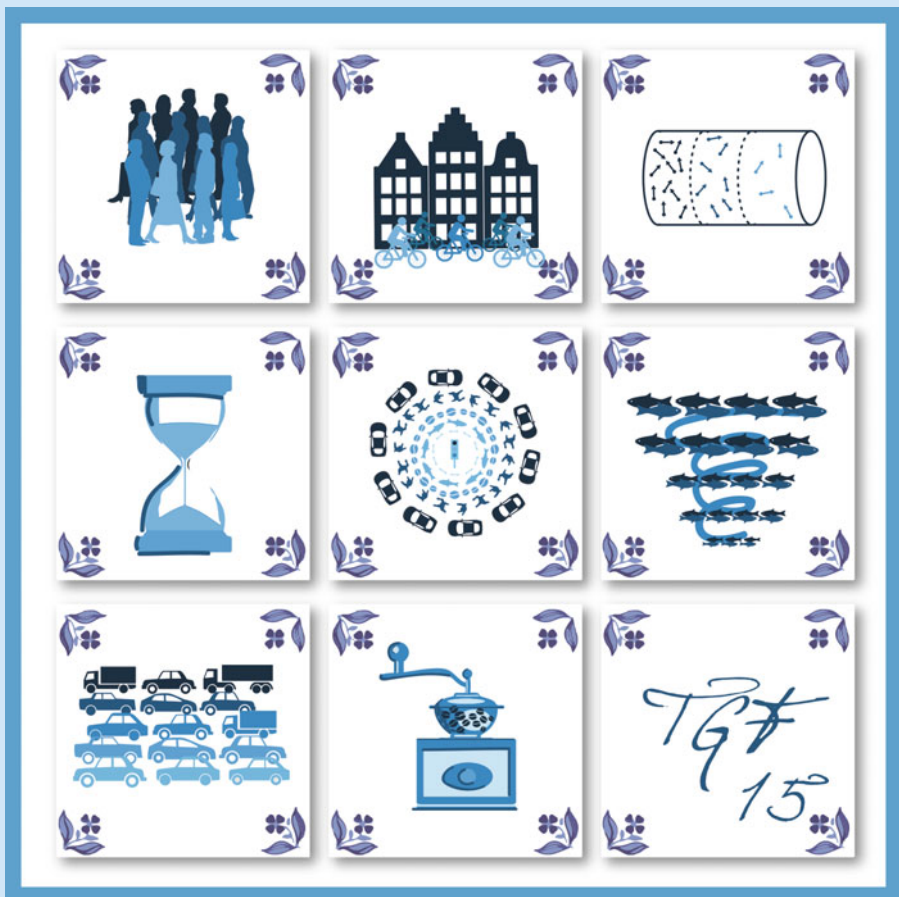Victor L. Knoop

Winnie Daamen

Editors

Traffic and
Granular Flow '15

Springer

Traffic and Granular Flow '15

Victor L. Knoop · Winnie Daamen
Editors

Traffic and Granular Flow '15

Editors
Victor L. Knoop
Transport & Planning
Delft University of Technology
Delft
The Netherlands

Winnie Daamen
Transport & Planning
Delft University of Technology
Delft
The Netherlands

International Scientific Committee

- Cécile Appert-Rolland, Paris-Sud University Orsay, France
- Jean-Michel Auberlet, IFSTTAR, France
- Stefania Bandini, University of Milano-Bicocca, Italy
- Robert Bertini, Calpoly, USA
- Nicolai Bode, University of Essex, England
- Christine Buisson, IFSTTAR, France
- Michael Cassidy, University of California at Berkeley, USA
- Mohcine Chraibi, Forschungszentrum Jülich, Germany
- Maria Davidich, Siemens AG, Germany
- Bart De Schutter, Delft University of Technology, The Netherlands
- Vikash Gayah, Penn State University, USA
- Samer Hamdar, George Washington University, USA
- Serge Hoogendoorn, Delft University of Technology, The Netherlands
- Timon Idema, Leiden University, The Netherlands
- Anders Johansson, University of Bristol, UK
- Boris Kerner, Daimler AG, Germany
- Tobias Kretz, PTV Group, Germany
- Gerta Köster, University of Applied Sciences Munich, Germany
- Sylvain Lassare, IFSTTAR, France
- Jean-Patrick Lebacque, IFSTTAR, France
- Sueng Jae Lee, University of Illinois, USA
- Hani Mahmassani, Northwestern University, USA
- Reinhart Kühne, German Aerospace Center, Germany
- Kai Nagel, Berlin University of Technology, Germany
- Katsuhiro Nishinari, University of Tokyo, Japan
- Vincenzo Punzo, Ispra, Italy
- Michel Rascle, University of Nice, France
- Meead Saberi, Monash University, Australia
- Ludger Santen, University of Saarland, Germany
- Majid Sarvi, Monash University, Australia
- Andreas Schadschneider, University of Cologne, Germany

Preface

These are the proceedings of the eleventh edition of the Traffic and Granular Flow conference, held from 28 to 30 October 2015 in the Netherlands. This edition of this worldwide biannual conference is organised by the Delft University of Technology, where it returns after 12 years. What started as a one-time event in 1995 has grown in 20 years to a conference series with a very good scientific reputation.

The conference is known for facilitating links between various disciplines. In this edition, we had among other things contributions on pedestrian flow, vehicular flow, granular flow, and biological flow. The proceedings provide a concise overview of the most important developments in this field over the past two years. It consists of 79 high-quality papers; contributions come from over 30 countries, spread over all continents. We believe this book presents recent innovative insights and provides a long-term reference for scientific work.

We are grateful for the financial support given by the Transport Institute of the Delft University of Technology. Moreover, organising this conference would not have been possible without the help of many colleagues. For help in preparing the conference, we would like to mention Nicole Fontein, Priscilla Hanselaar, Jeanette van Leeuwen, Julia Barelds, Ilse Galama and Fieke Beemster. In the preparation of the proceedings, we value the help of Tjeerd Oudkerk. Also, the help of the international scientific committee in assessing the abstracts is highly acknowledged, as well as the assistance of the previous organisers.

Shortly before the conference, Matthias Craesmeyer has deceased. This is a great loss for the field, which has lost a talented young scholar.

We are happy to contribute to the tradition of Springer proceedings of the Traffic and Granular Flow conference, and are looking forward to the next edition, organised in 2017 by Samer Hamdar in Washington DC.

Delft   Victor L. Knoop
February 2016   Winnie Daamen

Contents

Part I
Pedestrians

Methodology for Generating Individualised Trajectories from Experiments

Wolfgang Mehner, Maik Boltes and Armin Seyfried

Abstract Traffic research has reached a point where trajectories are available for microscopic analysis. The next step will be trajectories which are connected to human factors, i.e. information about the agent. The first step in pedestrian dynamics has been done using video recordings to generate precise trajectories. We go one step further and present two experiments for which ID markers are used to produce individualised trajectories: a large-scale experiment on pedestrian dynamics and an experiment on single-file bicycle traffic. The camera set-up has to be carefully chosen when using ID markers. It has to facilitate reading out the markers, while at the same time being able to capture the whole experiment. We propose two set-ups to address this problem and report on experiments conducted with these set-ups.

1 Introduction

Laboratory experiments are a valuable tool when conducting research into traffic or pedestrian dynamics. The data can be analysed to uncover effects which are important for modelling, and it can be used to validate simulations.

When conducting such experiments, one always has at least two conflicting requirements. On the one hand, the observed subjects have to be detected reliably, which requires a large focal length, i.e. a larger zoom factor, of the used camera. On the other hand, one wants to observe as much of the experiment as possible, which requires a small focal length. When using ID markers, this situation gets worse, since the required resolution is most likely higher than with other markers, e.g. coloured

W. Mehner (✉)
Visual Computing Institute, RWTH Aachen University, Aachen, Germany
e-mail: mehner@vision.rwth-aachen.de

M. Boltes · A. Seyfried
Jülich Supercomputing Centre, Forschungszentrum Jülich GmbH,
52428 Jülich, Germany
e-mail: m.boltes@fz-juelich.de

A. Seyfried
e-mail: a.seyfried@fz-juelich.de

3

caps. Employing multiple cameras may be the only viable solution when using ID markers, which will make it more difficult to calibrate the cameras. As a result, camera set-ups for such experiments have to be carefully engineered.

In the following, we present two experiments using ID markers and the solutions we have chosen in order to address the above mentioned problems. In detail, those consist of: (1) A large-scale experiment with pedestrians, where the markers are read out everywhere, which however requires a complex camera system (Sect. 3). (2) An experiment on single-file bicycle traffic, where the markers are only read out in one camera view. Using overlapping fields of view, the IDs can still be transferred to trajectories generated from detections in other views (Sect. 4).

2   Related Work

Characteristics of pedestrians have been the subject of experiments before. A motion capture system was used by Jelić et al. [5], while otherwise video recordings seem to be a common choice for data acquisition. Boltes et al. [1] use colour-coded markers to associate detected trajectories to the pedestrians' heights, which is important for a precise localisation on the ground plane. Daamen et al. [3] investigate the influence of different classes of pedestrians (children, elderly, disabled) on the capacity of a door, and to that end equipped participants with caps of different colour, indicating their class. Individualised trajectories are used by Bukáček et al. [2] to link the behaviour of the participants across different runs of an experiment. Stuart et al. [11] use ID markers in experiments with individuals with disabilities, to investigate their impact on pedestrian dynamics. However, the ID markers used in both these experiments have the undesirable property that they protrude over the participants' heads, which makes experimentation at high densities more difficult.

Bicycle traffic has been investigated before by Navin [9], who used video to analyse single-file bicycle traffic on an oval track. Experiments similar to ours were performed by Rui et al. [10], who to the best of your knowledge do not produce individualised trajectories. Zhang et al. [15] used video recordings to obtain fundamental diagrams, and also focus on properties of bicycles and electric bicycles. The dynamics during bicycle races were investigated by Trenchard et al. [13]. Single-lane experiments for cars, in the same spirit as our bicycle experiments, were performed by Nakayama et al. [8] and Tadaki et al. [12].

3   Pedestrian Experiments

The pedestrian experiments were performed as part of the project BaSiGo in Düsseldorf, Germany, in 2013. The aim was to investigate pedestrian flows in various geometries, such as corridors and different intersections, especially at very high den-
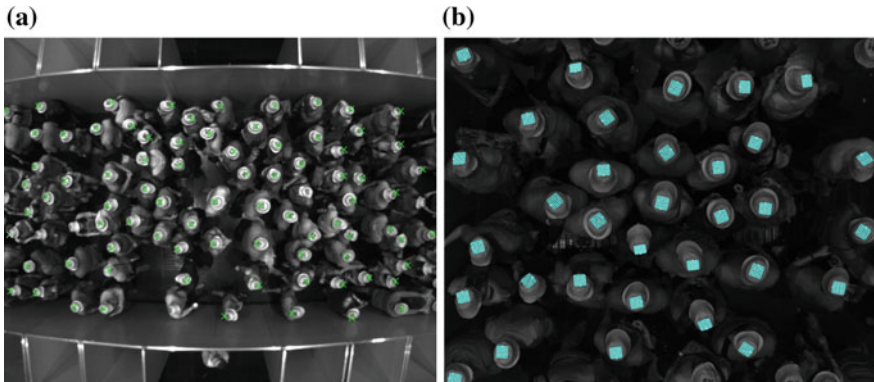
Fig. 1 Camera views of the pedestrian experiment with detected markers: overview camera (**a**); the view of a grid camera (**b**)

sities. For example, corridors of 4 and 5 m width and a length of over 10 m were set up (see Fig. 1a). Therefore a huge number of participants is required to reach a steady state at high densities in such large geometries.

This requires a very large number of ID markers and powerful detection and tracking algorithms, already presented in [7]. However, to guarantee success a carefully engineered camera set-up and calibration procedure is equally important. The cameras used to record the experiments have to be able to read out the markers, while at the same time covering the 10 m × 10 m area used for the experiments. The ID markers also provide information on the head rotation, therefore the markers are read out in the entry area, to get the full information (position and rotation) everywhere. While the universal availability of the IDs simplifies the task of linking the trajectories across the different camera views, this set-up makes the calibration of the camera grid more difficult.

3.1 Camera Grid

The experiments were recorded with a grid of 6 × 4 overhead cameras (see Fig. 1a), mounted 7.5 m above the floor. Each camera covered an area of a little over 2.5 m $(=\frac{10\,\text{m}}{4}) \times 1.67$ m $(=\frac{10\,\text{m}}{6})$ measured at 2 m above the floor, the maximum presumed height of the participants. With this set-up, the markers can be read out everywhere in the observed area. A little overlap between the views of neighbouring cameras makes it possible to "hand over" trajectories without losing them in blind spots. Given the resulting small opening angles of the cameras, an image resolution of 1280 × 1024 pixels turned out to be sufficient to read out the markers. The markers had a size of 8.5 cm × 8.5 cm and fitted comfortably on a normal hat, making them usable at high densities of up to 10 persons per square metre.

Since the set-up uses monocular cameras, the height of a person is needed to compute the location on the ground plane from the marker detected on the head

(compare the discussion in [1]). The camera grid included an additional camera for computing the height of the participant. This camera's field of view overlapped with other cameras entirely. If a marker is detected in this camera and an overlapping view, then the height can be computed via triangulation. The computed heights can be saved in a list and retrieved via the marker ID, and can thus be used everywhere in the grid to compute the exact locations of the participants.

The intrinsic calibration of the cameras (focal length, lens distortion, …) is done using a standard technique [16]. Bundle adjustment [4] is used to obtain the external calibration (positions and rotations of the cameras) of the grid. To estimate these parameters, a minimisation problem is set up. The positions of identifiable objects in the scene are projected into the view of each camera which can see the objects. For each object, this yields the image position of the projection, which is compared with the known image position for this object, which must be obtained by a different method, e.g. manual annotation. The difference in these two positions is called the reprojection error. The average reprojection error for all objects and cameras is minimised. This yields the camera calibration parameters, because these parameters influence the projection process.

One challenge with this approach based on reprojection errors is that the estimation of the parameters is unreliable in some regards. For example, the camera can be moved along the optical axis (which in our set-up corresponds to a varying height of the overhead cameras above ground) without much change to the reprojection error. This is a bad property, given that measurement errors (imprecise annotations of the image positions) also figure into the minimisation problem. Other properties of the set-up, the small opening angles of the cameras and the small overlaps, further complicate the calibration.

3.2 Discussion

The described set-up is able to deliver detailed and precise individualised trajectories, including the rotation of the heads, provided for the entire area used for experimentation. While this is ideal with regards to the type of data one would want for investigating pedestrian dynamics, this set-up requires a lot of effort to design and use correctly. This effort stems from the amount and the processing of the produced image data, as well as the calibration and synchronisation of the large number of cameras. All these problems have to be addressed in the design of the recording system, which requires expertise in a number of computer vision topics. On the other hand, given the size of the experiments, over 2000 participants in 4 days of experimentation, this effort seems justified. The only limitation of a design like this is that it can probably not be extended to cover a larger area at reasonable cost.

In conclusion, this set-up puts its focus on the utility of the produced data without much regard for the resulting effort. For experiments with a lower number of participants, easier and faster solutions would be preferable.

4 Bicycle Experiments

The bicycle experiments were performed in Wuppertal, Germany, in 2012. The single-file set-up allows to compare the behaviour of the cyclists to pedestrians and cars [14], for which such experiments have been performed before.

One camera ('top view', see Fig. 2a) was set up to observe the entire experiment from above. However a top–down perspective could not be achieved easily given the surroundings. The bicycles were equipped with markers, which could however not be read in the top view. Therefore, an additional camera ('side view', see Fig. 2b) was set up to identify the drivers. They additionally wore yellow helmets, which can be detected in both views, and thus be used to associate the trajectories generated from both views. Additionally, the drivers are visible in the second row of the side view, which could be used for further measurements.

4.1 Detection and Tracking

The helmets in the top view are detected by finding local extrema in the Laplacian scale-space, followed by suppressing low-texture areas (compare [6]), and colour filtering. The helmets in the front of the side view are found by thresholding the HSV colour-value of each pixel and then performing connected component labelling. The marker boxes are found by detecting the red dots using the same technique as for the helmets in the top view. Three red dots can be associated to yield the position of the marker grid, which is then binarised and read out. The tracking procedure uses Kalman filtering to deal with missing detections, but is otherwise very simple because of the relatively reliable detections.
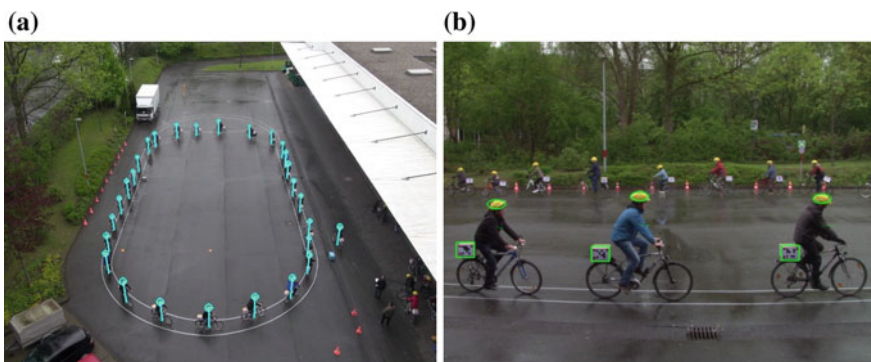
Fig. 2 Camera views of the bicycle experiment with detected helmets and markers: top view with trajectories and heights (**a**); side view for marker read out (**b**)

It is not possible to read out the markers in the top view, or in the back of the side view. Therefore, only the trajectories in the front of the side view have IDs attached to them, while the others are 'anonymous'.

4.2 Associating Anonymous Trajectories

In the pedestrian experiment, we could associate trajectories across different views using their IDs. Here, this is not possible anymore, since only the trajectories in the front of the side view have IDs attached to them. We need a more advanced technique for associating the remaining 'anonymous' trajectories with the ones in the front view. This will then allow us to transfer the IDs to them, and thereby other information, such as the height of the helmets above the ground.

We make use of the fundamental matrix [4]. Given points P_i in world coordinates and their projection into two different camera views, $p_i^{(1)} = (x_i^{(1)}, y_i^{(1)}) = project^{(1)}(P_i)$ and $p_i^{(2)} = (x_i^{(2)}, y_i^{(2)}) = project^{(2)}(P_i)$, we can find a fundamental matrix F, such that:

$$(x_i^{(1)}, y_i^{(1)}, 1) \cdot F \cdot (x_i^{(2)}, y_i^{(2)}, 1)^T = 0, \ \text{for all } i \tag{1}$$

Given eight pairs of corresponding points, this matrix is unique up to scale. More points can be used to estimate it in a least-squares fashion. For more details see [4]. Note that we only need corresponding pixel coordinates in both camera views. The 3D geometry of the scene can thus be bypassed.

Given a point in the first camera view, with unknown world coordinates, we are still able to constrain its position in the second view, given F:

$$(x_i^{(1)}, y_i^{(1)}, 1) \cdot F = (a, b, c) \ \text{and} \ (a, b, c) \cdot (x_i^{(2)}, y_i^{(2)}, 1)^T = 0 \tag{2}$$

It can be seen that a point in the first view parametrises a line in the second view in implicit notation, via the fundamental matrix.

The relationship given by the fundamental matrix can be used to associate trajectories tracking the same physical object in two views. Given trajectories in two views $P^{(v)}(t) = (x^{(v)}(t), y^{(v)}(t))$ and a number of overlapping frames T, we can compute an average distance between the lines $(a(t), b(t), c(t)) = (x^{(1)}(t), y^{(1)}(t), 1) \cdot F$ and the points $(x^{(2)}(t), y^{(2)}(t))$. In each step, the line parametrisation has to be normalised in order to compute meaningful distances across different frames:

$$(a_i(t), b_i(t), c_i(t)) = \left(x_i^{(1)}(t), y_i^{(1)}(t), 1\right) \cdot F \tag{3}$$

$$D_{i,j} = \frac{1}{|T|} \sum_{t \in T} \left| \left(a_i(t)^2 + b_i(t)^2\right)^{-\frac{1}{2}} \cdot (a_i(t), b_i(t), c_i(t)) \cdot \left(x_j^{(2)}(t), y_j^{(2)}(t), 1\right)^T \right| \tag{4}$$

This yields a distance $D_{i,j}$ between every pair $P_i^{(1)}(t)$ and $P_j^{(2)}(t)$ of trajectories. We only associate them if:

$$j = \mathrm{argmin}_h D_{i,h} \text{ and } i = \mathrm{argmin}_h D_{h,j} \tag{5}$$

This is preferable to a greedy strategy of simply picking the closest match for one trajectory and then moving on to the next. Our strategy leads to a unique solution, and helps to suppress associations with meaningless trajectories resulting from false-positive detections. More advanced approaches, such as the Hungarian algorithm, are possible as well.

4.3 Evaluation

We provide some numbers to give an impression of the performance of the auto-mated trajectory generation for the bicycle experiments. We manually cleaned up the trajectories in the top view for one of the experiments and compared them to the trajectories reported by the detection and tracking algorithm. There were 33 partici-pants in the experiment. In 9400 frames, 228888 positions needed to be reported. The algorithm only failed to report 254 (false negatives), but missed no trajectory com-pletely. There were 2082 additional detections reported, belonging to 19 trajectories made up of false-positive detections. While these numbers show that the system does not produce perfect results, the performance is high enough that a manual clean up of the results can be done with very little effort.

4.4 Discussion

The linking of the cameras is much easier to do with this approach, since the esti-mation of the fundamental matrix takes less effort than the full 3D calibration in the pedestrian experiments. Additionally, the required precision is easier to achieve. The external calibration of the camera which actually reports the measurements is still required, of course. Overall, this set-up, with one camera to view the entire experiment and one camera to read the ID markers, seems better suited for smaller experiments. A few prerequisites have to be met, however. For example all participants have to pass in front of the camera reading out the IDs at least once per experimental run. The density in the field of view of this camera should also not be too high, or the association of the trajectories will get more difficult.

5 Conclusion

We have presented two experiments we conducted, and discussed the requirements and the resulting solutions for the data capturing. Both experiments included infor-mation that was obtained from one camera in the grid and then transferred to the

trajectories of the entire experiment. We showed two techniques to accomplish this, once using the marker IDs themselves, once by exploiting the interaction of trajectories and the camera geometry.

References

1. Boltes, M., Seyfried, A.: Collecting pedestrian trajectories. Neurocomputing **100**, 127–133 (2013)
2. Bukáček, M., Hrabák, P., Krbálek, M.: Experimental study of phase transition in pedestrian flow. Transp. Res. Procedia **2**, 105–113 (2014)
3. Daamen, W., Hoogendoorn, S.: Capacity of doors during evacuation conditions. Procedia Eng. **3**, 53–66 (2010)
4. Hartley, R., Zisserman, A.: Multiple View Geometry in Computer Vision. Cambridge University Press (2003)
5. Jelić, A., Appert-Rolland, C., Lemercier, S., Pettré, J.: Properties of pedestrians walking in line: fundamental diagrams. Phys. Rev. E **85**(3), 036111 (2012)
6. Lowe, D.G.: Distinctive image features from scale-invariant keypoints. Int. J. Comput. Vision **60**(2), 91–110 (2004)
7. Mehner, W., Boltes, M., Mathias, M., Leibe, B.: Robust marker-based tracking for measuring crowd dynamics. In: Proceedings of the 10th International Conference on Computer Vision Systems, pp. 445–455 (2015)
8. Nakayama, A., Fukui, M., Kikuchi, M., Hasebe, K., Nishinari, K., Sugiyama, Y., Tadaki, S., Yukawa, S.: Metastability in the formation of an experimental traffic jam. New J. Phys. **11**(8), 083025 (2009)
9. Navin, F.P.: Bicycle traffic flow characteristics: experimental results and comparisons. ITE J. **64**(3), 31–37 (1994)
10. Rui, J., Mao-Bin, H., Qing-Song, W., Song, S.W.G.: Experimental feature of bicycle flow and its modeling. arXiv:1411.1136 (2014)
11. Stuart, D., Christensen, K., Chen, A., Kim, Y., Chen, Y.: Utilizing augmented reality technology for crowd pedestrian analysis involving individuals with disabilities. In: Proceedings of the ASME 2013 International Design Engineering Technical Conferences and Computers and Information in Engineering Conference (2013)
12. Tadaki, S., Kikuchi, M., Fukui, M., Nakayama, A., Nishinari, K., Shibata, A., Sugiyama, Y., Yosida, T., Yukawa, S.: Phase transition in traffic jam experiment on a circuit. New J. Phys. **15**(10), 103034 (2013)
13. Trenchard, H., Richardson, A., Ratamero, E., Perc, M.: Collective behavior and the identification of phases in bicycle pelotons. Physica A: Stat. Mech. Appl. **405**, 92–103 (2014)
14. Zhang, J., Mehner, W., Holl, S., Boltes, M., Andresen, E., Schadschneider, A., Seyfried, A.: Universal flow-density relation of single-file bicycle, pedestrian and car motion. Phys. Lett. A **378**(44), 3274–3277 (2014)
15. Zhang, S., Ren, G., Yang, R.: Simulation model of speed-density characteristics for mixed bicycle flow—comparison between cellular automata model and gas dynamics model. Physica A: Stat. Mech. Appl. **392**(20), 5110–5118 (2013)
16. Zhang, Z.: A flexible new technique for camera calibration. IEEE Trans. Pattern Anal. Mach. Intell. **22**(11), 1330–1334 (2000)

Advances in Measuring Pedestrians at Dutch Train Stations Using Bluetooth, WiFi and Infrared Technology

Jeroen van den Heuvel, Danique Ton and Kim Hermansen

Abstract As of 2014, three Dutch train stations have been equipped with automated pedestrian traffic sensors, as part of the SMART Station initiative of NS Stations. These stations are Utrecht Central station, Amsterdam Airport Schiphol train station and Leiden Central station. SMART Station consists of hybrid Bluetooth/WiFi sensors for tracking and infrared sensors for counting. Combining data from both sensor types results in useful insights into the pedestrian dynamics. In this paper, four SMART Station cases are presented. Firstly, an estimation of escalator capacity will be presented. Secondly, we will show the temporal and spatial flow characteristics of a very large bike parking facility. Thirdly, the use of train stations by non-train passengers will be explored. Fourthly and finally, the occupancy of a station hall will be explored.

1 Introduction

In recent history, train ridership in The Netherlands has increased significantly. A relatively limited number of large train stations has 'absorbed' a relatively large share of the total growth. The concentration of rail passenger traffic at specific train stations poses significant challenges on the pedestrian infrastructure of these stations. To get a better insight into the crowd challenges at its train stations, NS Stations—the stations and real estate division of Netherlands Railways (NS)—has initiated a program to measure pedestrian behaviour in a systematic and automated way.

J. van den Heuvel (✉)
Faculty of Civil Engineering and Geosciences, Department of Transport and Planning,
Delft University of Technology, Stevinweg 1, 2628 CN Delft, The Netherlands
e-mail: j.p.a.vandenheuvel@tudelft.nl

J. van den Heuvel · D. Ton
NS Stations (Netherlands Railways), Stationshal 17, 3511 CE Utrecht, The Netherlands
e-mail: danique.ton@nsstations.nl

K. Hermansen
BLIP Systems, Hækken 2, Vester Hassing, 9310 Vodskov, Denmark
e-mail: kim.hermansen@blipsystems.com

In 2013, we have presented our first paper on measurements of pedestrian flows at train stations using Bluetooth in The Netherlands [1]. The paper contains the main findings of our study into the route choice behaviour of passengers regarding vertical infrastructure at Utrecht Central station. Data of an experimental set-up of eight Bluetooth-only sensors at Utrecht Central station has been used.

In this paper, four cases are presented using data from permanent sensor set-ups with combined Bluetooth, WiFi and infrared sensors, which have been installed at three large train stations in The Netherlands. This paper is structured as follows. Section 2 describes SMART Station and—briefly—the logic behind it. Sections 3–6 cover the cases, with one case in each section. Section 7 concludes this paper.

2 SMART Station

The main objective of SMART Station is to measure pedestrian flows, route choice, activity choice, dwell times and occupancy of pedestrian infrastructure at Dutch train stations with an automated data collection system. The solution has to be competitive with traditional data collection methods on the more complex stations regarding costs and benefits. Moreover, data collection has to be performed in a way that the privacy of all station users is respected. Therefore, SMART Station has been following the guidelines for privacy-by-design [2]. Since the successful pilot in 2012, three of the largest train stations in the Netherlands have been equipped with sensors: Utrecht Central station, Amsterdam Airport Schiphol station and Leiden Central station, with respectively 250,000, 83,000 and 85,000 train passengers per average workday.

The basic concept of SMART Station is to combine multiple sensor and data processing technologies to measure pedestrian flows. Several experiments in 2011 and 2012 with various state-of-the-art technologies have shown that combining global and local measurements by different types of sensors delivers the best results regarding cost effectiveness and data quality [3]. This strategy enabled us to prevent compromises regarding measurement capabilities of individual technologies, but allowed to deploy the best of all available technology.

In the current configuration, Bluetooth/WiFi sensors from BLIP Systems are used for tracking, and infrared sensors from Irisys are used for counting. The Bluetooth/WiFi sensors track global movements and dwell times of mobile devices (i.e., smartphones, tablets and laptops). The infrared sensors count local passenger traffic at strategic points inside the station. Combining global and local data results in a detailed picture of pedestrian dynamics [3].

For many reasons, not all pedestrians are detected by the tracking sensors. To overcome this limitation, a penetration ratio is calculated by combining tracking and counting data. This ratio describes the ratio between the number of counts and the number of tracks at a specific site at the station. Similar to other studies, we have found a Bluetooth ratio of 5–10 %. For the WiFi penetration rate, we have found a ratio of 20–25 % [3].

3 Case 1: Upward Escalator Capacity at Utrecht Central Station

The first case consists of the estimation of the practical escalator capacity at Utrecht Central station. At this station, each platform is connected to the station hall by two pairs of escalators and one fixed stairway. Counting sensors have been installed at the escalators of platform 11/12. This platform is used by various train types—intercity and regional trains—, and therefore is found to have a representative passenger population for the whole station [4]. The sensors have been installed at the inflow and outflow section of the downward and upward escalator respectively (red line in photo in Fig. 1). This location is chosen to avoid incorrect measurements due to congestion in front of the escalator. Congestion or congested flow frequently occurs at the platform after the arrival of a train, and measurements at these sites should be avoided due to a known limitation of Irisys infrared sensors.

The counting sensor data is available from a 1-min aggregation level for both the upward and the downward direction. For the capacity estimation, a data set with measurements from 7.00 to 19.00 h from 1 January to 17 September 2014 has been created. Only the flow in upward direction from platform to station hall has been included as congestion only tends to occur in this direction. Arriving passengers (upward direction) are brought to the station in bulk due to train arrivals, while the arrival time of departing passengers (downward direction) is distributed over time between train departures. Filtering out incomplete measurements due to off-line sensors resulted in a data set with 74,700 min with counts in the upward direction.

All observations in the data set have been ordered to find the time frames in which the escalator was potentially used at capacity. In 1-min aggregated data, capacity traffic conditions have been found by selecting the pairs of subsequent minutes in
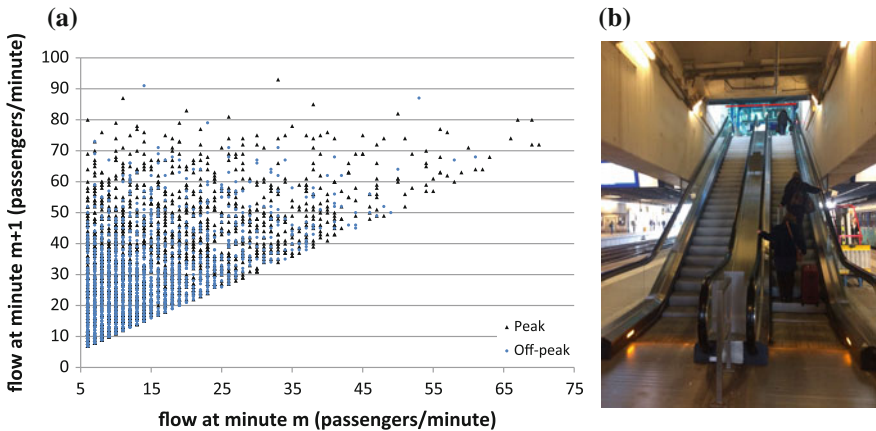
Fig. 1 From platform 11/12 to station hall (upward) escalator flows at Utrecht Central station: flows (**a**); situation (**b**)

which a number of pedestrians (>5) have been counted during the first (m) and second minute ($m + 1$). These pairs represent the traffic dynamic that an escalator gets congested shortly after the arrival of a crowded train. The queue at the platform starts to work as a buffer of pedestrians, which allows the flow at the escalator to reach capacity. The higher the counts during both minutes, the more likely it has been that the escalator has been used at capacity.

The data set consisted of 3,389 pairs of minutes (9.1 % of the total data set) which both—m and $m + 1$—had counts larger than five. Figure 1 is a graphical representation of the data. In the graph, the pairs have been classified into off-peak and peak hours (7.00–9.00 h and 17.00–19.00 h). An estimation of the capacity of an escalator can be found by looking at the observations with the highest flow at minute $m + 1$s. Based on the data, a capacity estimation of 75 persons per minute ($+/-5$) seems reasonable for peak hours, and 70 persons per minute ($+/-5$) for off-peak hours.

4   Case 2: The Use of a Large Bike Parking Facility at Utrecht Central Station

The second case covers the in- and outflow of a very large bike parking facility at Utrecht Central station, which has been in operation since July 2014. The facility is located right under the main station entrance at the non-city centre side (Jaarbeurs Square, at Jaarbeurs Convention Centre) and has a capacity for 4,200 bikes. For this analysis, a combined data set with tracking and counting data has been used.

For relating the flows to and from the bike parking facility to the train station, a tracking sensor has been installed at the entrance of the bike parking facility where people arrive and leave while wheeling their bikes. The pedestrian-only entry/exit on the other side of the bike parking facility is closely situated to the main entrance of the train station. This is one of the two main entrances which has been equipped with both a tracking and counting sensors. Therefore, the hourly penetration ratio of this entrance could be used to calculate the total flows from the tracking data.

The data set covered 15 days, from 2 to 16 September 2014. In this time frame, a total number of 165,927 complete routes has been generated based on the tracking data, which were related to this entrance of the station hall. During the same time frame, the counting sensors recorded a flow of 691,006 pedestrians, which is an average of slightly over 46,000 pedestrians per day. The busiest day was 9 September, with a total, bi-directional flow of 50,235. The average penetration ratio was 24 %, varying between 20 and 27 %, depending on the day of the week.

A total of 15,951 routes (9 %) has been identified to fit the condition of a detection at both the Jaarbeurs entrance of the station hall and the bike parking facility. Using the penetration ratio, the total flow is estimated at approximately 66,500, or a daily average of about 4,400. On the busiest day, the total flow reached over 5,700. As a typical passenger arrives with his bike at the station in the morning and leaves again

(a)   **(b)**
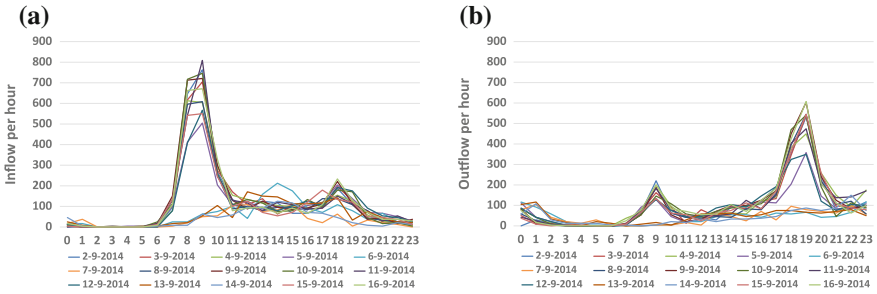
Fig. 2 Hourly inflow (**a**) and outflow (**b**) of the Jaarbeurs Square Bike Parking facility at Utrecht Central station

in the evening, this number is equivalent to approximately 2,850 bikes that have been parked in the facility during the day. So the occupancy ratio is estimated on 67 %, assuming that no one other than train passengers use this facility. Figure 2 shows the hourly inflows and outflows of the facility.

5 Case 3: Intra-city (Non-passenger) Flows in Utrecht Central Station and Leiden Central Station

Historically, many train stations have been built at the outer perimeter of cities. In the subsequent decades or even centuries after the establishment of the central train stations, many cities have grown towards the train station, as these provided main transportation links to other cities. Because the land on the city centre side of the train stations became scarce, cities started to grow at the other side of the station. Because railway tracks, particularly the railway yards, became a barrier between both city sides, many train stations also started to function as links between both city sides. This has resulted in intra-city, non-passenger, pedestrian flows of significant volumes. Because these pedestrians do not use trains, their movements are hardly captured in any data set that describes the primary function of the train station. The automated measurements at Utrecht Central station and Leiden Central station created the possibility to analyse these intra-city pedestrian flows over a longer time frame. For this case, two data sets have been used.

The first consists of combined tracking and counting data of Utrecht Central station, from 11 January until 24 April 2014. After removing the days with incomplete data, a total 84 days have been included in the data set, covering 753,859 complete routes (average of 8,975 per day). These routes represented pedestrian movements that fitted the condition that the pedestrian has been detected at both entrances at the train station with 30 min without being detected at any platform, but has been detected inside the station hall (non-passenger). From the counting data, the penetration rate has been derived. For this segment, the penetration rate varies between 17 and 25 %,

(a)

(b)
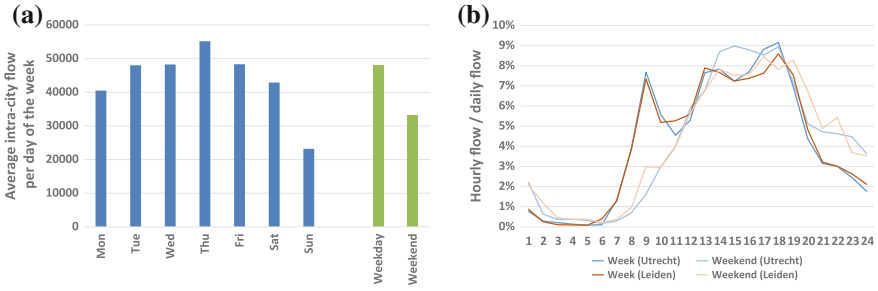
Fig. 3 Flows at the station. Total flows at Utrecht Central station per day and day type (**a**). Temporal distribution of intra-city flows at Utrecht Central station and Leiden Central station (**b**)

averaging at 21 %. The second data set consists of tracking data of Utrecht Central station and Leiden Central station of 1 to 29 April 2015. For Utrecht Central station and Leiden Central station, a total number of 219,223 and 39,604 routes has been included respectively, covering the intra-city flows during 24 h per day.

Figure 3 shows the results of the analysis. It shows that the station hall of Utrecht Central station is used by approximately 50,000 non-passengers on an average weekday. On weekend days, the intra-city flow is significantly lower, particularly on Sundays (20,000). Comparing the temporal distribution of the intra-city flows at Utrecht Central station and Leiden Central station, it becomes clear that the daily patterns are similar, both for week days and for weekend days. The evening peak of both week and weekend days occurs between 17.00 and 18.00 h and has a share of 9 % of the total daily flow.

6 Case 4: Occupancy at Utrecht Central Station

For estimation of the size of station halls, which usually combine the function of walking and waiting, both the number of pedestrians (flow) and the duration of their stay (dwell) are important factors. Therefore, station occupancy will be explored in this fourth and final case. The data is from tracking sensors in the station hall of Utrecht Central station.

Before the morning peak hour at Monday 2 March 2015, an overhead wire at one of the station tracks got damaged and caused total shut down of all train traffic to and from Utrecht during peak hour, due to the extremely inconvenient location of the incident [5]. This situation prevented departing passengers to leave the station by train. As most sources of train traffic information are situated in the central hall, many passengers decided to wait there. This caused an overload of the station hall.

The orange graph of Fig. 4 shows the occupancy of the station hall after the incident. The maximum occupancy was reached around 8.00 h, with approximately 3,000 mobile devices detected. This number was derived from determining the number of non-finished routes for each minute of the day. A non-finished route indicates that a
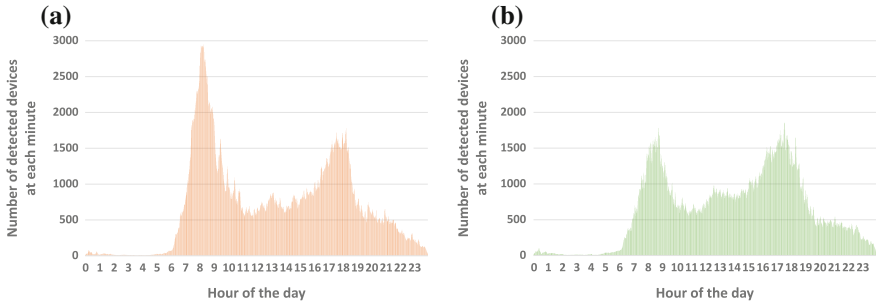
Fig. 4 Occupancy pattern at Utrecht Central station: major service disruption (Monday, 2 March 2015) (**a**); normal day (Tuesday, 3 March 2015) (**b**)

passenger did not finish his/her route (i.e. from entrance to platform) at that particular minute yet, but will do so at a later moment in time. Note that applying a penetration ratio of 20–25 % on this number of mobile devices results in an estimated occupancy of 12,000–15,000 passengers in the station hall. In contrast, the green graph of Fig. 4 shows the occupancy distribution during the next day (3 March 2015), when no service disruptions occurred. During that day, a peak of 1,800 mobile devices (7,000–9,200 pedestrians) is detected in the station hall.

A critical remark about this comparison has to be made. It is based on the assumption that pedestrians have not enabled or disabled Bluetooth or WiFi on their mobile device when they are in the station hall. The service disruption of 2 March could have triggered passengers who were waiting in the station to enable WiFi in their search for additional information. However, no counting sensors have been installed in this area, since they were located at the station entrance and at some escalators to the platforms. Therefore, we have no data to assess the validity of this assumption.

7   Conclusions and Future Developments

This paper has presented a broad selection of our recent insights from measurements of pedestrians at three large train stations in The Netherlands using Bluetooth, WiFi and infrared technology. These insights are extremely valuable for the design and operation of train stations.

The first case has shown that the escalator capacity is estimated to be 70–75 (+/−5) persons per minute for peak and off-peak hours respectively. The second case has shown the inflow and outflow of a very large bike parking facility with 4,200 places. The intra-city, non-passenger flows through train stations have been the central topic of the third example. It has shown that these flows through train stations consist of tens of thousands movements per day. The fourth case consisted of an example of station occupancy, which is the product of flow and dwell times. It has been shown that a major service disruption can cause a two thirds increase in the peak load of the pedestrian space of a train station.

Currently, NS Stations is working on the expansion of SMART Station at Amsterdam Airport Schiphol by installing counting sensors at stairs and escalators. These sensors will generate the data which is required to calculate the penetration ratio. This will proof to which extent Schiphol train station is different from other large train stations in city centres, due to the location at the airport. Moreover, SMART Station sensors are being installed at Amsterdam Central station in January 2016. This station is mainly used for very large intra-city flows. Therefore, measurements at this station will reveal whether the observed pattern of Utrecht Central station and Leiden Central station can be considered as generalised. And finally, a current discussion with stakeholders might result in a SMART Station at Amsterdam South station, which is located at the Central Business District of Amsterdam. This station is amongst the fastest growing stations in the country and is expected to be faced with pedestrian congestion within a couple of years.

References

1. Van den Heuvel, J., Voskamp, A., Daamen, W., Hoogendoorn, S.: Using Bluetooth to estimate the impact of congestion on pedestrian route choice at train stations. In: Traffic and Granular Flow '13 (2015)
2. van den Heuvel, J., Thiellier, E., van Gerwen, N.: Privacy by design bij reizigersmetingen op stations. Priv. Compliance **3**, 17–21 (2013)
3. Daamen, W., Van den Heuvel, J., Ton, D., Hoogendoorn, S.: Using Bluetooth and WiFi to unravel real-world slow mode activity travel behaviour. In: Presented at the 14th International Conference on Travel Behaviour Research. Windsor, United Kingdom, 19–25 July 2015
4. Ton, D., Van den Heuvel, J., Daamen, W., Hoogendoorn, S.: Route and activity location choice behaviour of departing passengers in train stations. In: Presented at the hEART (European Association for Research in Transportation) 2015 Conference. Copenhagen, Denmark, 9–11 Sept 2015
5. RTLNieuws: Geen treinen rond Utrecht: dit zijn de gevolgen (2015). http://www.rtlnieuws.nl/nieuws/binnenland/geen-treinen-rond-utrecht-dit-zijn-de-gevolgen

Avoiding Walls: What Distance Do Pedestrians Keep from Walls and Obstacles?

Ernst Bosina, Mark Meeder, Beda Büchel and Ulrich Weidmann

Abstract To avoid colliding with walls and obstacles, pedestrians keep a certain distance to them. This so-called separation distance or wall clearance distance was documented in early literature on pedestrian transport. For modelling purposes, it can be subtracted from a walkway's width to obtain an effective width. Literature on this topic is scarce and the values that can be found are often contradictory, largely due to a lack of data. This work aims at contributing to the knowledge about the pedestrian wall distance by applying several high-resolution measurement techniques. Measurements were carried out using ultrasonic transducers and laser scanners at locations where high numbers of pedestrians move in a unidirectional flow. The results confirm that pedestrians keep a minimum distance to walls and that the effect of obstacles is noticeable several metres downstream of the cross section in which they occur. Furthermore, it was found that the kept distance depends on the pedestrian density. Lastly, this paper suggests a method for determining the effective width of walkways that can be used in pedestrian facility design.

1 Introduction

An important aspect of pedestrian movement is the avoidance of obstacles. When moving around, pedestrians actively avoid colliding with walls and obstacles, and aim to keep a certain distance to them. In pedestrian facilities, like an underpass in a railway station, the spaces adjacent to walls and obstacles are therefore not utilised by

E. Bosina (✉) · M. Meeder · B. Büchel · U. Weidmann
Institute for Transport Planning and Systems, ETH Zürich, Zürich, Switzerland
e-mail: ebosina@ethz.ch

M. Meeder
e-mail: mark.meeder@ivt.baug.ethz.ch

B. Büchel
e-mail: bbuechel@student.ethz.ch

U. Weidmann
e-mail: weidmann@ivt.baug.ethz.ch

pedestrians, thus reducing the flow rate. That reduction is expressed as a separation distance that determines the effective width of walkways.

In pedestrian simulations [1] as well as in analytical approaches to pedestrian flow characteristics [2] this behaviour needs to be taken into account. However, accurate literature on these distances is scarce. Only few attempts to quantify the separation distance can be found in literature [3–10].

2 Theory

Models of pedestrian flows can either describe the behaviour of individual pedestrians, or the characteristics of the flow as a whole. The latter type are so-called aggregated flow models that are usually analytical (as opposed to the numerical nature of simulations) and can be used to calculate pedestrian flow rates and densities. In doing so, the quality of pedestrian facilities can be assessed by determining the pedestrian level-of-service [4].

In practice, one might have pedestrian counting data, for example in a certain cross section of a corridor or underpass and is interested in the level-of-service. Dividing the counting data over suited time intervals, one can calculate the specific flow using the width of the corridor:

$$F_s = \frac{N}{T \cdot W_e} \tag{1}$$

where N is the number of counted pedestrians in time interval T and W_e is the effective width. Using the pedestrian fundamental diagram [10], the density and by extension the level-of-service can be determined.

To calculate the effective width, a separation distance is usually subtracted from the actual width of the walkway to reflect the influence of walls and obstacles. For example, for a corridor with straight walls and no further obstacles in the vicinity, the effective width w_e becomes:

$$W_e = W - 2 \cdot d_w \tag{2}$$

where d_w is the separation distance or wall distance.

Similarly, certain values are subtracted for objects like pillars, vending machines, and so forth. The exact amount to be subtracted depends on the characteristics of the object in question. Furthermore, objects in the middle of the stream can impact the flow beyond their actual position. The aforementioned principles are illustrated in Fig. 1.

Knowledge about the precise mechanisms of the separation distance does not exist. Usually, it is considered as a constant distance next to the wall or obstacle,

Fig. 1 Example of a straight corridor where areas around walls, a vending point and a pillar are not used by pedestrians, illustrating the principle of separation distance [11]
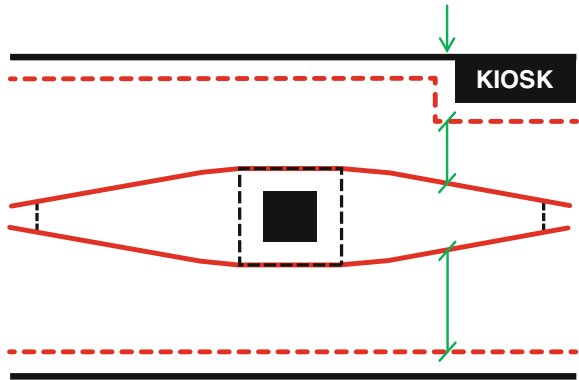
where pedestrians do not walk. In literature, only few values for these distances were found, as mentioned in Sect. 1. This is corroborated by the lack of data in the field. Furthermore, in some cases the values found are contradictory [6, 7].

3 Measurement Method

This work aims to further knowledge about the pedestrian wall distance by applying observations techniques with high spatial resolutions. The measurements were done in real-life situations and therefore the measurement device had to suit the corresponding requirements. For the determination of the distances kept from walls, small ultrasonic sensors were used which were attached to the wall. They measure the distance to the nearest object in front of the sensor, for example the nearest point of a passing pedestrian. Compared to video recordings and similar observation techniques this approach enables a more accurate and direct measurement of the separation distance. The small size of the sensors allows attaching them a wall without strongly influencing the behaviour of passing pedestrians. The sensors were mounted at 95 cm above floor level which was determined to be the approximate height of the nearest point of an average pedestrian. The sensors recorded distance values every 0.05 s. Based on these values, automated data extraction was used to retrieve the nearest point of pedestrians passing the sensor. The data obtained are used to determine the distribution of wall clearance distances and to find a suitable method for calculating the minimum separation distance.

For researching the influence of obstacles in pedestrian flows, a laser scanner was used. The device measures the distance to all nearest objects in a 180° field of view with a resolution of 0.5° and a frequency of 20 Hz. Using this method the trajectories of pedestrians in a horizontal plane can be obtained.

4   Results

Measurements of wall clearance distances were done along a smooth granite wall on a ramp (Fig. 3) as well as at a 1.33 m wide bottleneck (Fig. 2). The nearest point of each pedestrian was recorded and subsequently used to evaluate the distance pedestrians keep from the wall. Figure 4 shows the number of pedestrians passing the wall in fixed distance intervals. It has to be noted that due to occlusion by others, pedestrians further away from the wall are not always recorded by the sensor.

Based on the data, three zones can be distinguished. Closest to the wall, at distances under 10 cm, almost no pedestrians were recorded. This could be considered the absolute wall clearance distance, closer than which pedestrians do not pass under
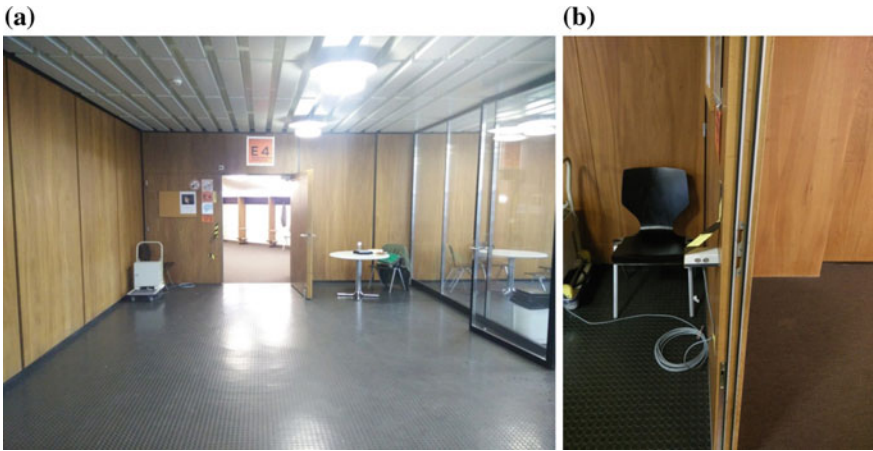
Fig. 2 Location of wall clearance measurements at a bottleneck: view of the bottleneck (**a**) and the sensor (**b**)

Fig. 3 Location of wall clearance measurements at a smooth granite wall next to a ramp
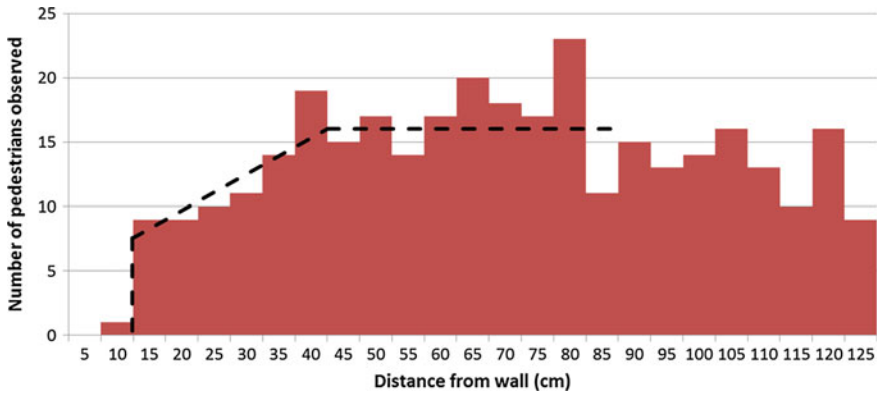
Fig. 4 Frequency of pedestrians observed at different wall distances for the ramp location, divided in 5 cm intervals

normal circumstances. At distances over 40 cm, no influence of the wall can be perceived: pedestrians are equally distributed across this part of the ramp. In the distance range between 10 and 40 cm, a constant increase in the amount of pedestrians walking at a certain distance from the wall was observed. Within this zone the pedestrian flow is reduced compared to the flow unaffected by the wall. This indicates that the wall clearance distance is not a single value expressing an absolute distance, but rather a value describing the reduction of the pedestrian flow in the proximity of walls. Assuming a linear increase of the flow in the aforementioned transition range, this principle can be expressed by

$$d_w = d_1 + (d_2 - d_1) \cdot \left(\frac{1 - a}{2} \right) \tag{3}$$

where d_1 and d_2 are the lower and higher boundary of the transition range and a is the ratio between the flows at the lower and upper boundary of the transition range. Inserting the values mentioned above, a wall clearance distance of 18 cm was calculated. This value corresponds to 10 cm in the first zone and 8 cm representing the reduction in flow in the second zone.

The same measurements were done for a bottleneck serving as an access to a big lecture hall in a university building at ETH Zürich (Fig. 5). In contrast to the previous measurement no wall clearance distance is observed. Pedestrians pass at very short distances, even right at the edge of the bottleneck, and therefore the effective width equals the physical width of the bottleneck. In addition to the ultrasonic sensor measurements a manual pedestrian count was conducted, allowing the comparison of the measured wall distances with the pedestrian flow rates (Fig. 6). The wall distance clearly decreases with increasing pedestrian flow, indicating that the distance not only depends on the characteristics of the wall itself but also on the pedestrian density.
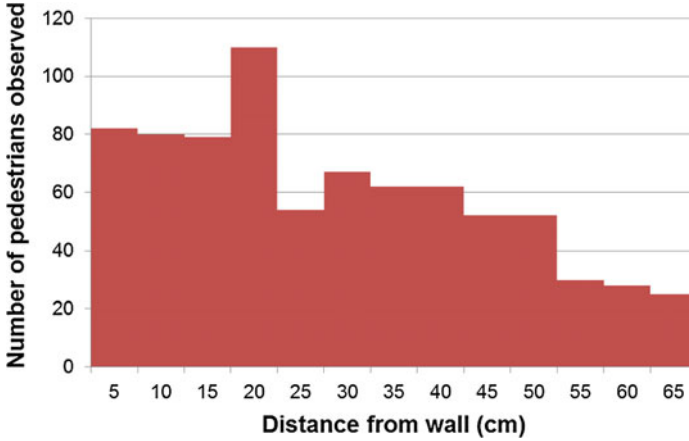
Fig. 5 Frequency of pedestrians observed at different wall distances for the bottleneck location, divided in 5 cm intervals
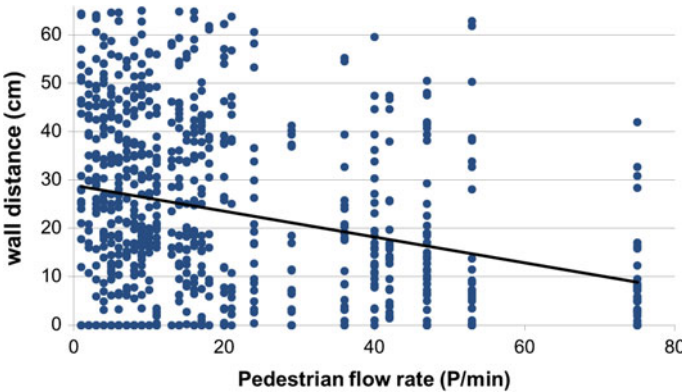
Fig. 6 Wall distances measured at different pedestrian flow rates for the bottleneck location

To determine the influence of obstacles on pedestrian flows, laser scanner measurements were done by placing an artificial obstacle in a corridor (Fig. 7). Trajectories of the nearest point of pedestrians were extracted from the data (Fig. 8). As expected, the influence of an obstacle can be observed both up- and downstream of the object as pedestrians start to change their walking direction a few metres in advance. Compared to values from literature, indicating an effective width reduction of 0.31 m measured 3 m upstream from a 0.60 m wide obstacle [5], the influence measured is slightly lower. For the situation with the obstacle in the middle of the corridor, the influence length of the obstacle can be estimated at 2–2.5 m. The difference could be explained by the fact that the obstacle in the experiment is not sufficiently high to obstruct the view of pedestrians, which might cause different behaviour than around ceiling-high obstacles. The observed shape of the pedestrian flow around the
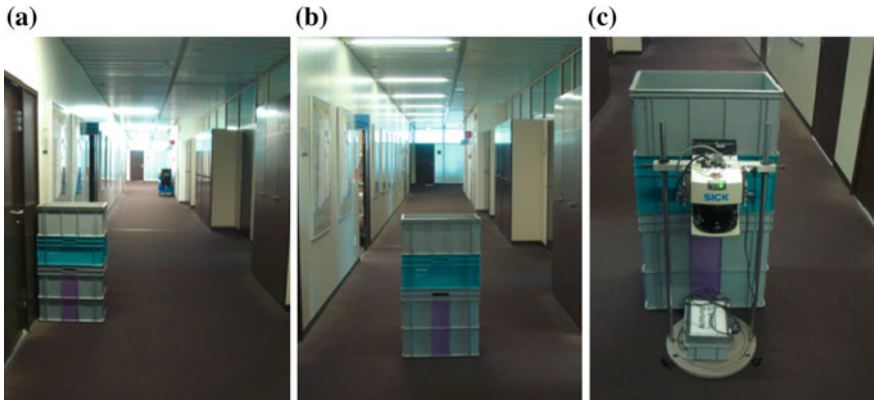
Fig. 7 Location of the laser scanner measurements for the obstacle on the side (**a**) and in the middle of the corridor (**b, c**)
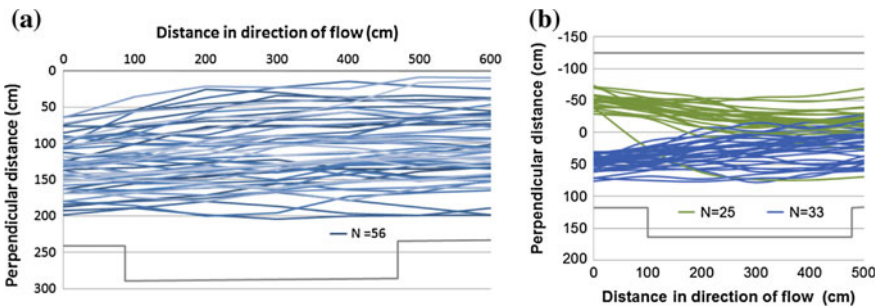
Fig. 8 Pedestrian trajectories around an obstacle on the side (**a**) and in the middle (**b**) of a hallway. Trajectories describe the movement of the nearest point of each person. The *light blue lines* are upstream of the obstacle, the *dark blue lines* downstream

obstacles (Fig. 8) corresponds with the literature (Fig. 1). The flow width reduction is noticeable a certain distance in front of the obstacle to nearly its full extent.

5 Conclusion

The conducted measurements show that the pedestrian wall clearance distance can be reliably measured. Furthermore, ultrasonic transducers present a cheap and quick method to count pedestrians and measure key characteristics of pedestrian flows.

The results confirm existing knowledge that pedestrians keep a certain minimum distance from walls and obstacles. However, this distance should not be considered an absolute value, as the distance kept to walls varies between pedestrians. Rather, the flow in the proximity of walls can be divided in three sections: a section where the flow is zero closest to the wall, a section with undisturbed conditions furthest from

the wall, and a section with reduced pedestrian flow in between. In addition, it was found that the distance kept to obstacles is dependent on the pedestrian density. To study this effect, more data linking distance measurements to flow rates is needed.

In situations where the pedestrian flow utilises the entire flow capacity, which typically occurs in bottlenecks like entrances to train platforms, the measurement results indicate that a wall distance of zero should be assumed. To clarify what causes this phenomenon, and whether it only occurs at narrow bottlenecks like the one researched, further measurements at wider bottlenecks should be carried out.

As expected, the effect of obstacles on pedestrian flows is not limited to the cross section in which the obstacle occurs and can also be observed upstream. However, the data indicates that the influences of walls and obstacles are slightly overestimated in literature, especially at higher pedestrians flows and narrower flow cross sections. It is therefore suggested to focus on these aspects in future research.

References

1. Helbing, D., Molnár, P.: Social force model for pedestrian dynamics. Phys. Rev. E **51**(5), 4282–4286 (1995)
2. Weidmann, U., Kirsch, U., Puffe, E., Jacobs, D., Pestalozzi, C., Conrad, V.: Verkehrsqualität und Leistungsfähigkeit von Anlagen des leichten Zweirad- und des Fussgängerverkehrs. Forschungsauftrag VSS 2007/306, ETH Zürich, Zürich (2013)
3. Annesley, T., Dix, M., Beswick, A., Buchanan, P.: Development and application of pedestrian assignment models in London railway station studies. Traffic Eng. Control **30**, 345–352 (1989)
4. Fruin, J.J.: Pedestrian planning and design. In: Metropolitan Association of Urban Designers and Environmental Planner. New York (1971)
5. Habicht, T.A., Braaksma, J.P.: Effective width of pedestrian corridors. J. Transp. Eng. **110**(1), 80–93 (1984). doi:10.1061/(ASCE)0733-947X(1984)110:1(80)
6. de Neufville, R., Grillot, M.: Design of pedestrian space in airport terminals. Transp. Eng. J. ASCE **108**(1), 87–102 (1982)
7. Pauls, J.L.: Building evacuation: research findings and recommendations. In: Canter, D. (ed.) Fires and Human Behaviour, pp. 251–275. Wiley, Chichester, New York (1980)
8. Schopf, J.M.: Bewegungsabläufe, Dimensionierung und Qualitätsstandards für Fussgänger, Radfahrer und Kraftfahrzeugverkehr. Dissertation, Technische Universität Wien, Wien (1985)
9. Transportation Research Board: Highway Capacity Manual. No. 209 in Transportation Research Board Special Report. Transportation Research Board, Washington (1985)
10. Weidmann, U.: Transporttechnik der Fussgänger—Transporttechnische Eigenschaften des Fussgängerverkehrs (Literaturauswertung), zweite ergänzte Auflage edn. No. 90 in Schriftenreihe des IVT. Institut für Verkehrsplanung, Transporttechnik, Strassen- und Eisenbahnbau, ETH Zürich, Zürich (1993)
11. Buchmüller, S., Weidmann, U.: Handbuch zur Anordnung und Dimensionierung von Fussgängeranlagen in Bahnhöfen. Technical report, Institut für Verkehrsplanung und Transportsysteme (IVT), ETH Zürich, Zürich (2008)

Estimation of Density Levels in the Holy Mosque from a Network of Cameras

Yasir S. Ali, Basim Zafar and Mohammed Simsim

Abstract In this work we developed a system for estimating the density levels in the holy mosque of Makkah using video cameras installed in the mosque. This set-up relies on dividing the image into smaller segments and counting the number of people in each segment to infer the density. This algorithm used texture and SIFT interest point features to get an accurate count of the number of people at each segment using support vector regression. Having segments at different sizes helped to account for objects with different size in the image. In addition, the use of overlapping segment smooth the estimated density maps as each pixel receive a contribution from different patches. Our methodology has been tested extensively with different cameras during the Fasting season of 2015 with images from very crowded areas in the mosque.

1 Introduction

Al-Masjid Al-Haram is the prayer direction for all Muslims around the world and Muslims travel to Al-Haram mosque for Hajj and Umrah rituals. With the new expansion completed, the mosque will be a huge complex and thus indoor navigation and route planning techniques will be highly in need. People tend to stay close to the gate they entered from, which causes congestion to build near the gates and gives a false indication of the mosque being fully occupied while some places inside remain vacant [3]. Density estimation from image has captured good attention in the published literature. Xiaohua et al. [11] employed support vector machines with wavelet descriptors for classifying crowd density into four groups. Their work achieved

---

Y.S. Ali (✉)
Science and Technology Unit, Umm Al-Qura University, Mecca, Saudi Arabia
e-mail: ysali@uqu.edu.sa

B. Zafar
Electrical Engineering Department, Umm Al-Qura University, Mecca, Saudi Arabia
e-mail: bjzafar@uqu.edu.sa

M. Simsim
Ministry of Hajj, Mecca, Saudi Arabia
e-mail: mohsimsim@gmail.com

Fig. 1 Snap shots from the holy mosque in Makkah showing different density levels. Even though the mosque is mostly crowded, it can sometimes be almost empty as in the *top left* image

classification accuracy of 95 % for moderate density crowds. Ma et al. [11] calculated texture features for small images blocks for computing crowd density. Davies et al. [4] have used the ratio of foreground pixels/edges to the total image size as indication of the image density. Velastin et al. [10] employed both background removal followed by edge detection to estimate the crowd area in the image. Reisman et al. [7] presented a new method for crowd detection by detecting the inward motion via Hough transform analysis. Marana et al. [5, 6] used texture analysis to estimate the crowd density. They have noted high texture frequencies are associated with fine textures which correspond to high density crowds (Fig. 1).

2   Density Estimation

In this paper, we addressed the problem of measuring the status of crowd distribution in Al-Haram in a manner that helps authorities to better manage the mosque occupancy and control the gates based on accurate and real time information. We developed a system that informs the authorities as well as the public about the crowd distribution in different sections of the mosque. This helps the authorities decide when to divert the crowds and which part is fully occupied or vacant. This system generates a density map for the covered area of the mosque which is then transmitted to the public via VMS (variable-message sign), smartphone apps as well as websites that provide regular updates and the crowd status and advice the public when is the best time to visit the mosque.
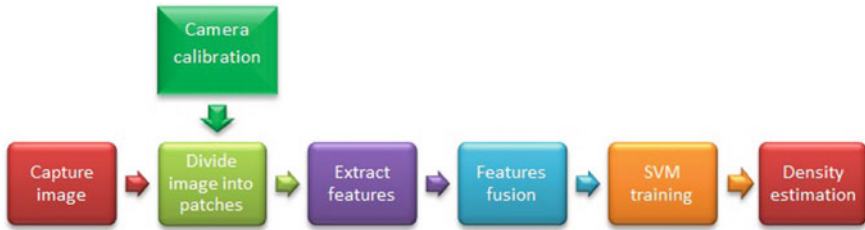
Fig. 2 Process flow for density estimation for small image segments or patches

Figure 2 shows the process flow for our methodology to compute the density of crowds in an image. Firstly, an image is captured from a camera, which has to be known and calibrated a priori [9]. Thus, it is not advisable to take prerecorded videos from an unknown camera, because the calibration settings will not be available for computing the coverage area of the camera which leads to incorrect density estimation. After that, a set of features are extracted from the image and processed to get the count and density.

The image is divided into smaller overlapping blocks or patches. The patches have different sizes to allow a multi-scale processing of the image data [1]. Smaller patches have consistent densities but they have repeated features and they can easily be affected with low frequency noise [2]. On the other hands, larger patches contain more features and thus better relevant to irrelevant frequency ratio. At the features extraction step, a confidence weight is given to each patch which weight the importance of features in the given patches with respect to those at upper and lower scales [2, 8].

Texture and SIFT (Scale-Invariant Features Transform) features have been employed to estimate the count of people in image patches and thus computing the density of the patch. Texture features can give good indication of the number of people inside the block size the crowd head can be viewed as repeated texture pattern.To extract texture, the image gradient is computed and transformed into Fourier domain where high frequency and weak signals and suppressed. The retain frequency and reconstructed back to spatial domain and peak points are extracted followed with non-maxima suppression. Finally, statistical moments and entropy are extracted to represent the patch features [2].

The SIFT algorithm extracts prominent local features in the image by applying sequence of image transformation and extracting minima and maxima of the transformed image [2]. SIFT features are extracted from the image patch and clustered into codebook of a defined size. Also, these features are used to impose confidence weight on the count of the patches at different scales.

At patch level, the previous three features are concatenated together to form one vector and these feature and individually normalised to be used for support vector regression [8]. The individual normalisation of each bin is because they represent different entities. In order to ensure that the counts from different patches are smooth, they resultant density computed for these patches are normalised for each pixel. The
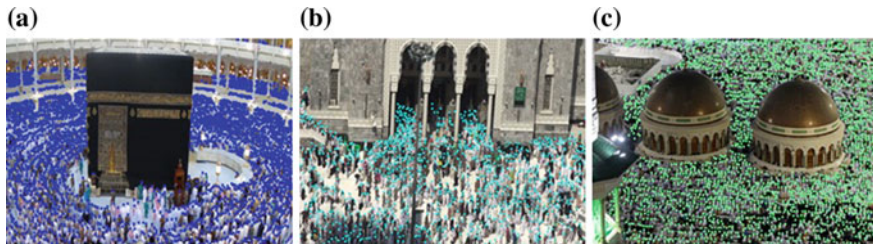
Fig. 3 Sample of images using during the training phase with their ground-truth labels

support vector machine engine has been trained using 70 manually labelled images representing a wide range of crowds for image from Al-Haram. Figure 3 shows sample of the training images using with their manual labels.

3   Results and Discussions

To validate the accuracy of our system we firstly installed cameras at known locations in Al-Masjid Al-Haram where the coverage area of the camera is approximately computed. The camera set-up parametres has been recorded (camera height and angle) which can be used later to compute the actual area of image patches. We used HD camera with overall resolution of 1280×720 pixels. We have set the smallest image patch to be 160×120 pixels and we also extracted patches with large size (320×120, 160×240 and 320×240). During the processing more than 200 patches are extracted from each image and for each patch we computed the texture features and stored the first four statistical movements and the entropy (5-D vector). For SIFT features, during the training, a dictionary of 512 words is created. For each new SIFT point extracted for a new image patch, its descriptor is approximated to the nearest word in the dictionary be means of k-nearest neighbour search [2].

Patch level features are fed into support vector regression (SVR) which was trained previous using the 50 annotated images described in the previous section. The SVR will return the count of people within the given patch. Here, we assumed that these patches represent a coherent regions and thus they should have an equal density distribution. Therefore, the patch density value is computed as the count of people divided by the patch area which is obtained from the calibration stage. Since the count and thus the density estimation is computed for an overlapping and variable size patches, the overall density level of each pixel is computed using Eq. 1 by weighting the density of the patch d_K which contains pixel with the patch weight w and summing this for all patches that contains pixel i.

$$d(i) = \frac{\sum_k d_k(i) * w_k(i)}{\sum_k w_k(i)} \tag{1}$$

Figure 4 shows an example for density estimation from one image using the proposed method. Left is an image from Al-Masjid Al-Haram while the right side is the density map. The blue colour indicates low density, while the red colour indicates highest density and the green ones are comfortable density levels. The density image has been smoothed out to eliminate blocking effects. Ideally, the densities should be computed for very small patches. However, such patches will not contain sufficient information to infer the count of people or density levels.

The results presented in Fig. 4 lacks a reference scale upon which the density is defined. In these figure auto scaling on figures is applied which assigns the lowest density to blue and the largest to dark red in all figures. Instead of this we adopted Fruin level of services (LoS) to represent the density with 6 standard levels which represent a meaningful status for the crowd level. However, the density indicated here is not the standard density defined in Fruin LoS because the density levels in Al-Haram is much more than they places where these LoS are defined and having more than 2 person per square meter is very common in Al-Haram, whereas elsewhere this is considered as dangerous level. Table 1 shows the reference levels of service for the density levels, the actual density for each level and how this can affect the crowd flow.

Figure 5 presents more results for our density estimation method. We have conducted various video recordings during the fasting month at which the mosque will be fully occupied. Even though we used 6 density levels when generating the density

(a)   **(b)**
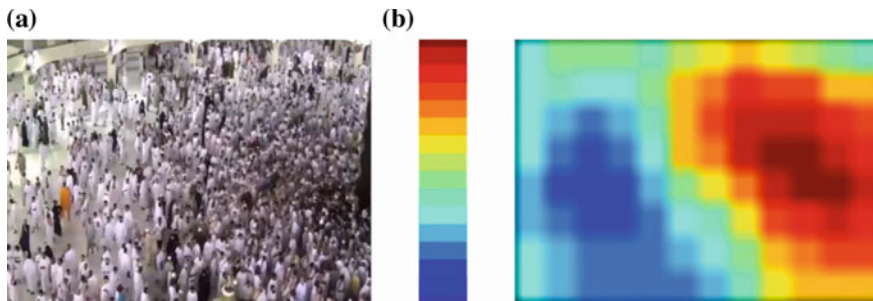
Fig. 4 Al-Masjid Al-Haram: image (**a**); computed densities (**b**)

Table 1 Representation of 6 levels of service and their actual density values

LoS (Level of Service)	Danger level	Density (P/m^2)
LoS A	Safe and comfortable	Less than 0.5
LoS B	Safe	0.5–1.0
LoS C	Safe, not comfortable	1.0–2.0
LoS D	Not safe	2.0–2.5
LoS E	Highly dangerous	2.5–3.0
LoS F	Collision	Above 3.0
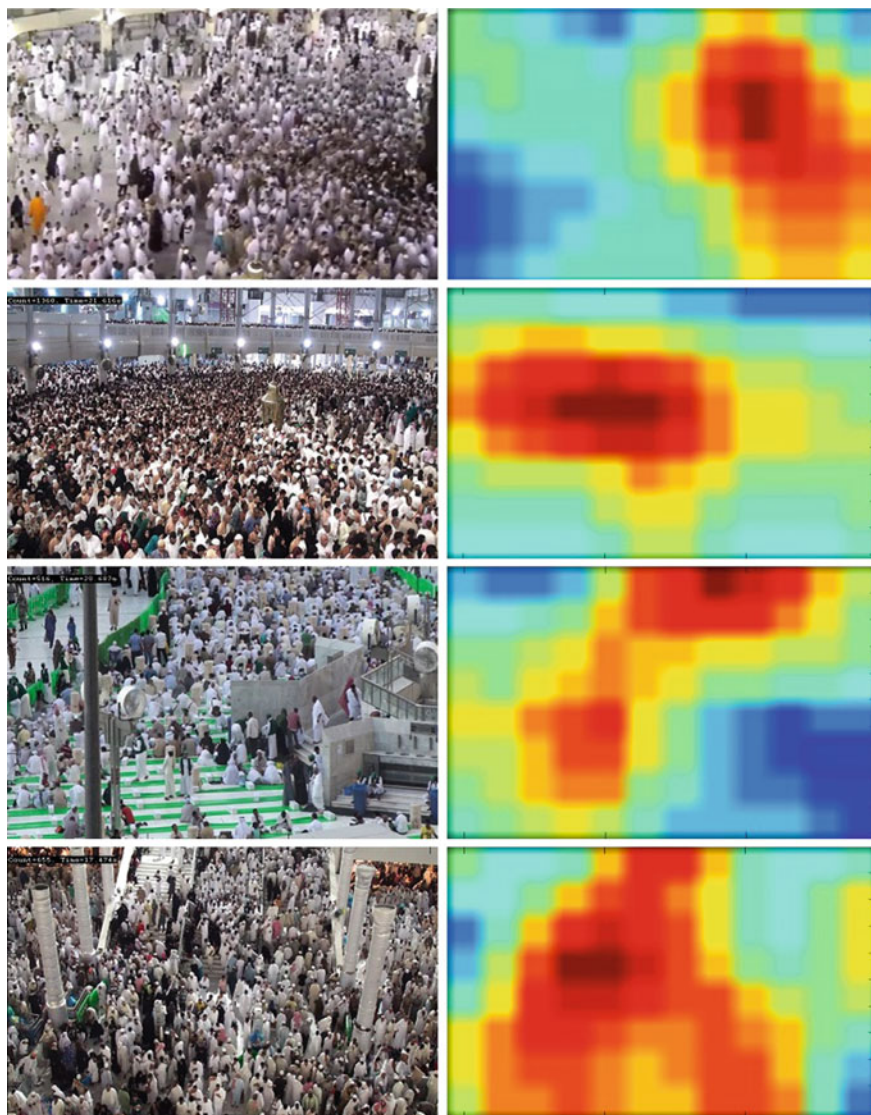
Fig. 5 Sample images from Al-Masjid Al-Haram (*left*) and their corresponding density maps (*right*)

maps. there are more values in between these levels since this density map has been smoothed with an averaging filter to remove blocking effects. In the second image, even though the image shows high density crowds, our algorithm gives the high density label only to the parts far away from the camera as high density, while the closer parts are labelled as moderate density even though the density is very high. This is because the area of the patches are not correctly estimated due to errors in camera calibration. The third and fourth row show that the density has been correctly computed and the vacant part in the third row has been labelled as dark blue.

4 Conclusion

In this paper we represented a methodology for computing crowd density in Al-Masjid Al-Haram. The proposed methodology relies on dividing the image into smaller patches with known area and counting the number of people in each patch using texture and interest point features. to account for crowds with different size, an overlapping patches with different size have been used. This allows computing a smooth density map by averaging the per pixel density across all patches that contains it. This algorithm relies on good camera extrinsic calibration, so that correct patch area can be assigned to near and far patches. The computational complexity of this algorithm is not high and it can further be reduced by parallel implementation since the patches can be processed independently.

References

1. Guo, J., Wu, X., Cao, T., Yu, S., Xu, Y.: Crowd density estimation via markov random field (MRF). In: 2010 8th World Congress on Intelligent Control and Automation (WCICA), pp. 258–263. IEEE (2010)
2. Idrees, H., Saleemi, I., Seibert, C., Shah, M.: Multi-source multi-scale counting in extremely dense crowd images. In: Proceedings of the IEEE Conference on Computer Vision and Pattern Recognition, pp. 2547–2554 (2013)
3. Khozium, M.: A hybrid intelligent information system for the administration of massive mass of Hajjis. Life Sci. J. **9**(4), 171–180 (2012)
4. Ma, W., Huang, L., Liu, C.: Advanced local binary pattern descriptors for crowd estimation. In: Pacific-Asia Workshop on Computational Intelligence and Industrial Application, 2008. PACIIA'08, vol. 2, pp. 958–962. IEEE (2008)
5. Marana, A., Costa, L.D.F., Lotufo, R., Velastin, S.: On the efficacy of texture analysis for crowd monitoring. In: International Symposium on Computer Graphics, Image Processing, and Vision, 1998. Proceedings. SIBGRAPI'98, pp. 354–361. IEEE (1998)

6. Marana, A., Velastin, S., Costa, L., Lotufo, R.: Estimation of crowd density using image processing. In: IEE Colloquium on Image Processing for Security Applications (Digest No.: 1997/074), pp. 1–11. IET (1997)
7. Reisman, P., Mano, O., Avidan, S., Shashua, A.: Crowd detection in video sequences. In: 2004 IEEE Intelligent Vehicles Symposium, pp. 66–71. IEEE (2004)
8. Roqueiro, D., Petrushin, V.A.: Counting people using video cameras. Int. J. Parallel, Emergent Distrib. Syst. **22**(3), 193–209 (2007)
9. Salih, Y., Malik, A.S.: Depth and geometry from a single 2D image using triangulation. In: 2012 IEEE International Conference on Multimedia and Expo Workshops (ICMEW), pp. 511–515. IEEE (2012)
10. Velastin, S., Yin, J., Davies, A., Vicencio-Silva, M., Allsop, R., Penn, A.: Analysis of crowd movements and densities in built-up environments using image processing. In: IEE Colloquium on Image Processing for Transport Applications, pp. 1–8. IET (1993)
11. Xiaohua, L., Lansun, S., Huanqin, L.: Estimation of crowd density based on wavelet and support vector machine. Trans. Inst. Meas. Control **28**(3), 299–308 (2006)

Is Slowing Down Enough to Model Movement on Stairs?

Gerta Köster, Daniel Lehmberg and Felix Dietrich

Abstract There are many well validated models of pedestrian movement on a flat surface. This is not the case for movement on stairs. Experiments show that pedestrians slow down when climbing or descending stairs. Hence, it is tempting to model movement on stairs by simply slowing down by a factor. But this would imply that, other than being slower, motion on stairs mirrors motion in the plane. Is that assumption justified? We conduct field observations that reveal similarities but also significant differences. Thus, we argue that modelling movement on stairs by slowing down free-flow velocities may be an acceptable first shot. True microscopic behaviour, however, like treading from step to step and keeping to a straight line instead of trying to overtake can only be captured by a dedicated model. We present an extension to the Optimal Steps Model that achieves this.

1 Introduction

There is a long tradition of modelling pedestrian motion in the plane. For discussions and overviews see for example [3, 7]. Model development has been complemented by a range of controlled experiments and field observations that make validation possible, at least to a certain extent. One focus is on fundamental diagrams that epitomise the dependency of speed or flow on the density of a crowd (e.g. [2, 19, 24]). Bottlenecks are also intensively studied (e.g. [11, 12, 18]). State-of-the-art models are able to calibrate model parameters to a scenario using one data set, such as a fundamental diagram, and to then reproduce other observed effects in the same scenario, such as the density in front of a bottleneck. We refer to [2, 16, 21] for more in-depth discussions. Competing models can be checked against each other

G. Köster (✉) · D. Lehmberg
Munich University of Applied Sciences, 80335 Munich, Germany
e-mail: koester@hm.edu

F. Dietrich
Munich University of Applied Sciences and TU München, 85747 Garching, Germany
e-mail: felix.dietrich@hm.edu

and against empirical observations for at least a minimum of characteristic scenarios that are compiled by standardisation bodies such as RiMEA or NIST (e.g. [8, 14]).

Models for movement on stairs are far less developed. Experiments show that pedestrians slow down when climbing or descending stairs [5, 6, 10, 13]. Noren et al. [13] give a summary of the state of the art on ascending stairs with a focus on long stairs. But how much do they slow down? And under which conditions? Are there, perhaps, other fundamental characteristics for movement on stairs? Fujiyama and Tyler [6] measure a strong correlation between walking speed on a flat surface and on stairs. Given free-flow velocities it is thus tempting to model movement on stairs by simply slowing down by a factor. In fact, to our knowledge, this is what modellers tend to do as a first shot. But this implies that, other than being slower, motion on stairs mirrors motion in the plane. Can we simply assume this? In the plane there is a clear linear dependency of the walking speed on the step length in the range of normal walking [9, 15, 16]. This means that, at least in that range, the influence of frequency adds variation but does not dominate. On a staircase the opposite may well be true: the depth of a tread limits the stride length; in addition pedestrians usually do not take more than one stair at a time [15]. In line with this argument, [6] claim that the step frequency may be the dominant factor on stairs. The length of the stairway, too, influences speed [10]. Finally speed and flow seem to depend on the density with fundamental diagrams similar to those for flat surfaces [1, 20] but with a difference between upstairs and downstairs flow. This in line with findings that the speed, too, differs in ascent and descent [17].

All in all, literature on the subject still seems scarce and inconclusive, especially if one wants to build an all-purpose model. Within the frame of this paper we therefore focus on one simple but important question: Can we model movement on stairs by simply slowing down by a factor? To tackle this question, we conducted a field observation at the Munich University of Applied Sciences. Trajectories of students on stairs, walking to and from a lecture hall, were captured and analysed. In the results Sect. 2 we first present the observational data and derive a list of requirements from the observations. From that we build a model by extending the Optimal Steps Model. We validate the model by re-enacting the scenario in the field observation. Finally we discuss our results, open issues and future work in Sect. 3.

2   Results

The experiment was set-up in fall 2014. A camera was installed to observe the flow on two identically constructed staircases to and from a lecture hall at the Lothstraße 64 campus of Munich University of Applied Sciences as seen in Fig. 1. The experiment was not controlled. From the video material and, given the set-up in an engineering and computer science building, it seems nonetheless safe to assume that the participants were between 18 and 25 years old, predominantly male and had a free-flow speed well above the 1.34 m/s used in Weidmann's benchmark data [23]. The stairways at Lothstraße 64 have 24 stairs in total, where the seventh stair is a small plateau

Fig. 1 Modelling and simulation project 2014: Entrance hall, Lothstrae 64, Participants are students aged 18–25. Experiment 1 on 23-10-2014, 15:00, only downstairs, 56 pedestrians (**a**). Experiment 2 on 04-11-2014, 09:45, upstairs 90 pedestrians, downstairs 34 pedestrians (**b**)
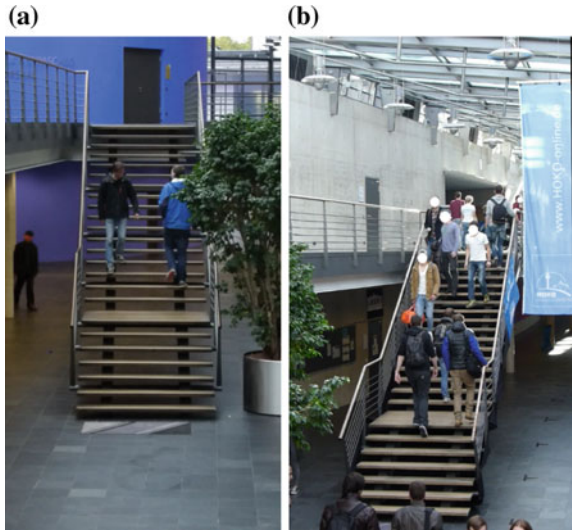
(1.52 m deep). Each normal stair is 0.3 m deep. The difference in height between each stair is 0.165 m, so that the total height difference is 3.96 m. The total horizontal length is 8.4 m (Fig. 1). Trajectories and pedestrian positions were extracted from the video using the open source tracker tool 'Tracker v. 4.86' under the GPL-3.0 licence (https://www.cabrillo.edu/dbrown/tracker/) and projected on the plane.

Table 1 shows the horizontal speed component averaged over the whole staircase. The results are in accordance with our own earlier results from a controlled experiment [15] and former observations [10]. Clearly pedestrians slow down on stairs. The factor is roughly 1/2. The linear regression in Fig. 5 shows the measured walking speed downstairs in dependency on the density. The slope is small and, more importantly, the coefficient of determination is close to zero. Table 2 gives more statistical information. Due to the many data points, the p-values are extremely small. That is, while there clearly is a statistically significant dependency, it explains very little of the variation in the data. Thus, we hesitate to accord to the density-speed relationship on staircases the same importance that we give it in the plane. Instead, we argue that one must look closer to see what characterises movement on stairs.

Table 1 Average speed on stairs measured at MUAS in November 2014

	Horizontal[a] speed upstairs (m/s)	Horizontal[a] speed downstairs (m/s)
Experiment 1	–	0.64
Experiment 2	0.59	0.69

[a]The horizontal speed is the projection of the velocity vector on the plane

Table 2 Statistical analysis of the speed-density relationship in the downstairs experiment

	Experiment 1 down	Experiment 2 up	Experiment 2 down
Slope	**−0.0705**	**−0.1192**	**−0.1416**
Intercept	0.6815	0.6314	0.6959
p-value	1E-22	1E-68	1E-17
Coefficient of determination r^2	**0.06678**	**0.1160**	**0.08547**
Std-error	0.007149	0.006635	0.01618
Data points	1361	2462	821

In an experiment in 2012 single participants in a controlled experiment kept to a straight line in the middle of the staircase [17]. This preference was observed again in the new experiment even when the students could have cut a diagonal towards their target, e.g. toilets positioned to the side of the staircase. More importantly, and surprisingly, they hardly deviated from the straight line when other pedestrians were present. Deviation would be necessary for evasion manoeuvres. Also pedestrians stepped from tread to tread rarely taking two steps at a time. They did not use a tread twice. With this, the stride length is fixed by the depth of a tread.

We wish to devise a simple model that captures our observations. The outcome from simulation experiments should be that the

Requirement 1   Agents step from tread to tread.
Requirement 2   There is little deviation from narrow paths perpendicular to the orientation of the treads.
Requirement 3   Agents decelerate on stairs.
Requirement 4   Measured speed-density relation is reproduced after calibration.

Our locomotion model for stairs is inspired by the Optimal Steps Model in the plane that was published and validated in [16, 17, 21, 22]. The Optimal Steps Model advances pedestrians step by step with their natural stride length. At each stepping event, the position of the next step is found by optimising utility on a disc around the pedestrian with the pedestrian's free-flow stride length as the radius. The shorter the travel time to the target the higher the utility. Pedestrians avoid collisions and slow down in a dense crowd because other pedestrians locally decrease utility. Then the local utility optimum is no longer on the circle's rim but inside the disc. As a consequence, agents make smaller steps and may even skip steps if the old position is better than any other position.

For the Optimal Steps Model on stairs we change the area where the utility maximum is searched. We limit it to the intersection of the disc with a line that represents a tread, thus restricting free movement just like the real stairs do. Figure 2 illustrates the concept. In addition we demand that, if several locations on that line are of almost identical utility (difference smaller than 10^{-4}), the one closest to the last position is chosen. This gives straight paths a little edge over deviations. We believe that this
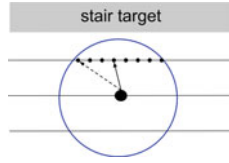
Fig. 2 Optimal Step Model for stairs: the reachable next positions are all points along the edge located on the next tread. We use the point with the shortest distance if utilities do not differ significantly

is plausible, because straight down is where gravity pulls the pedestrian. It is also necessary from an algorithmic point of view, because a wide target at the end of the staircase would lead to equal utility along each tread line. Note that this is a model of the projection of the true three dimensional motion onto the plane. At the end of the staircase the agents are one floor up or down.

To test our model we re-enact the scenario in the second observation. This means that, over a period of about 500 s we create virtual pedestrians at the head and the foot of the stairs heading down and up respectively just as was observed during the experiment. In this way we get the same number of pedestrians over time in the experiment and the simulation. For simplicity in the simulation, we do not treat the resting place in the middle of the stairs differently from the rest. We find this justified because it is unclear whether pedestrians on a short landing immediately switch back to motion in the plane or whether they stick to the rhythm they acquired on the stairs. Our agents do the latter. Figure 3 depicts the speed on the stairs over time both for the empirical observation and the computer experiment. The average speeds are very close and exhibit a similar pattern. Note that the average free-flow velocity in the simulation is 1.52 m/s so that the deceleration is caused by the stepping mechanism not by reducing preferred speeds. The comparison of the path widths in Fig. 4 again shows a similar pattern. The agents in the simulation stick even closer to a narrow path than in reality. We conclude that the Optimal Step Model on stairs meets our first three requirements. The last requirement remains: reproduction of the fundamental diagram.

We compare the density-speed relationship of the observed data with the simple deceleration model where the free-flow velocities in the Optimal Steps Model for the plane are divided by 2 and the simulation results for the Optimal Steps Model for stairs. Note that, for the Optimal Steps Model for stairs, the free-flow velocities are unaltered so that all deceleration is caused by the different stepping mechanism on stairs. All other parameters are chosen to be identical: The free-flow velocities are normally distributed about 1.52 m/s with a standard deviation of 0.11 m/s which matches preferred speeds for predominantly male and young students taken from controlled experiments at MUAS in 2012. The personal distance function, a smooth function on compact support [4, 21], that decreases utility when pedestrians get too close, and thus keeps the simulation collision free, is calibrated, so that the Optimal Steps Model on stairs reproduces the fundamental diagram. Figure 5 shows
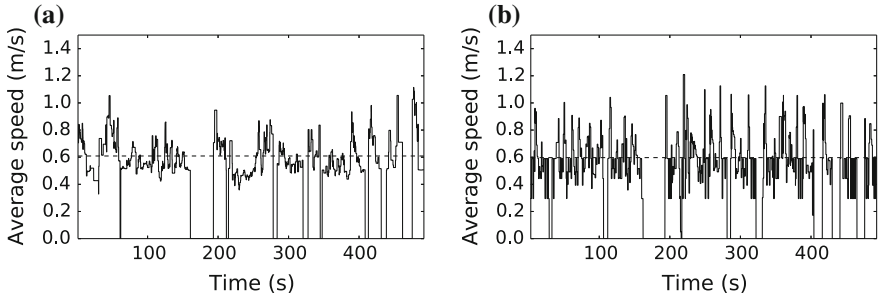
Fig. 3 Average speed over time. Experiment 2. The *line* indicates the overall average speed of 0.61 m/s (**a**). Re-enactment with the Optimal Steps Model for stairs with overall average speed of 0.60 m/s (**b**)
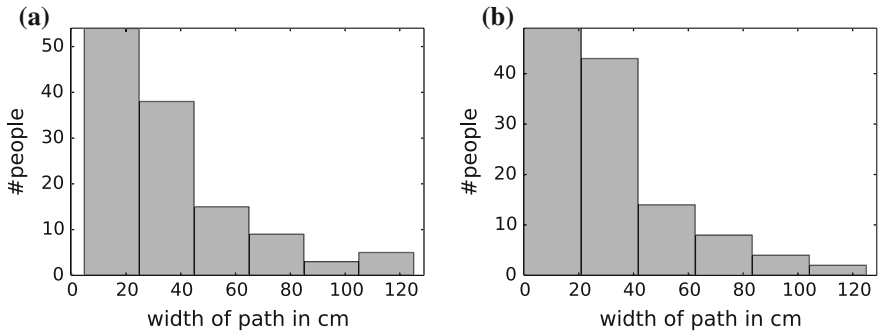
Fig. 4 Path width. Histogram of maximum path width in experiment (**a**). Path width in re-enactment with the Optimal Step Model for stairs (**b**)
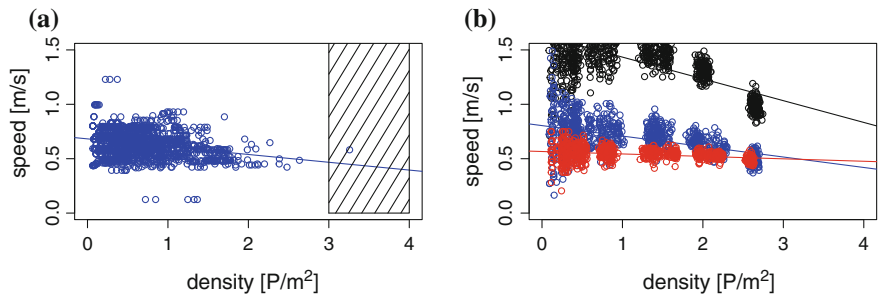
Fig. 5 Speed density relation. Experiment. Slope -0.0705, $r^2 = 0.067$, p-value $p = 0$ (**a**). Simulations with normally distributed free-flow velocities ($\mu = 1.52$, $\sigma = 0.11$). OSM for the plane (*black*); OSM for the plane slowed down by factor 0.5 (*blue*); OSM stair model (*red*) (**b**)

the downstairs case. While the standard Optimal Steps Model yields too fast speeds, both, the simple deceleration model and the Optimal Steps Model for stairs, show speed-density relationships that are close to the one in the observation. In that sense, the deceleration ansatz seems a good first shot. However, when we look at stride lengths and movement of agents in the diagonal direction, the deceleration model no longer fits our observations.

3   Discussion

In this contribution we addressed the following research question: Can one model movement on stairs by reducing the free-flow velocity in a model designed for motion in the plane? To answer this question we presented empirical results from an observation of students climbing and descending a staircase to a lecture hall. We also presented simulation results for a deceleration model and for a model that was designed to match the empirical observations.

We found that both, the dedicated model and the simple deceleration model well matched the measured speed-density relationship on the stairs. At a first glance this seems good news. By simply fixing the preferred speeds, which can be done by changing one input parameter in most tools, we get acceptable fundamental diagrams. At a second glance we realise that fundamental diagrams may not play an important role at all, when looking at movement on stairs. A linear regression of the observed data revealed a small slope in the dependency and a small coefficient of determination. That is, other than in the plane, the effect of density on the flow is small. In addition, pedestrians moved with a quasi-fixed step length set by the depth of the tread, they hardly overtook each other and they headed up or down with very little deviation from a straight line perpendicular to the treads. None of this holds in the plane.

In view of these results it seems questionable whether simple deceleration adequately models movement on stairs. The Optimal Steps Model for stairs, also a very simple model, was able to reproduce all observed behaviours and also the fundamental diagram. While questions, like the effect of fatigue, the differences between upstairs and downstairs movement, the transition phase between plane and stairs, and many more remain open, we argue that the Optimal Steps Model for stairs is at least one step closer to a biomechanically correct model. This may open the door for more detailed investigations of motion, like stumbling.

References

1. Burghardt, S., Seyfried, A., Klingsch, W.: Performance of stairs-fundamental diagram and topographical measurements. Transp. Res. Part C: Emerg. Technol. **37**, 268–278 (2013)
2. Davidich, M., Köster, G.: Predicting pedestrian flow: a methodology and a proof of concept based on real-life data. PloS one **8**(12), e83355 (2013)
3. Dietrich, F., Köster, G.: Gradient navigation model for pedestrian dynamics. Phys. Rev. E **89**(6), 062801 (2014)
4. Dietrich, F., Köster, G., Seitz, M., von Sivers, I.: Bridging the gap: from cellular automata to differential equation models for pedestrian dynamics. J. Comput. Sci. **5**(5), 841–846 (2014)
5. Frantzich, H.: Study of movement on stairs during evacuation using video analysing techniques. LUTVDG/TVBB–3079–SE (1996)
6. Fujiyama, T., Tyler, N.: Pedestrian speeds on stairs: an initial step for a simulation model (2004)
7. Hamacher, H.W., Tjandra, S.A.: Mathematical modelling of evacuation problems: a state of art. Fraunhofer-Institut für Techno-und Wirtschaftsmathematik, Fraunhofer (ITWM) (2001)
8. Isenhour, M.L., Löhner, R.: Verification of a pedestrian simulation tool using the NIST recommended test cases. Transp. Res. Procedia **2**, 237–245 (2014)
9. Kirtley, C., Whittle, M.W., Jefferson, R.: Influence of walking speed on gait parameters. J. Biomed. Eng. **7**(4), 282–288 (1985)
10. Kretz, T., Grünebohm, A., Kessel, A., Klüpfel, H., Meyer-König, T., Schreckenberg, M.: Upstairs walking speed distributions on a long stairway. Saf. Sci. **46**(1), 72–78 (2008)
11. Kretz, T., Grünebohm, A., Schreckenberg, M.: Experimental study of pedestrian flow through a bottleneck. J. Stat. Mech. Theory Exp. **2006**(10), P10014 (2006)
12. Liddle, J., Seyfried, A., Steffen, B.: Analysis of bottleneck motion using voronoi diagrams. In: Pedestrian and Evacuation Dynamics, pp. 833–836. Springer (2011)
13. Norén, J., Delin, M., Fridolf, K.: Ascending stair evacuation: what do we know? Transp. Res. Procedia **2**, 774–782 (2014)
14. RiMEA e.V., .e.: Rimea: Richtlinie für mikroskopische entfluchtungsanalysen (2009). http://www.rimea.de/
15. Seitz, M.J., Dietrich, F., Köster, G.: A study of pedestrian stepping behaviour for crowd simulation. Transp. Res. Procedia **2**, 282–290 (2014)
16. Seitz, M.J., Köster, G.: Natural discretization of pedestrian movement in continuous space. Phys. Rev. E **86**(4), 046108 (2012)
17. Seitz, M.J., Köster, G.: How update schemes influence crowd simulations. J. Stat. Mech. Theory Exp. **2014**(7), P07002 (2014)
18. Seyfried, A., Passon, O., Steffen, B., Boltes, M., Rupprecht, T., Klingsch, W.: New insights into pedestrian flow through bottlenecks. Transp. Sci. **43**(3), 395–406 (2009)
19. Seyfried, A., Steffen, B., Klingsch, W., Boltes, M.: The fundamental diagram of pedestrian movement revisited. J. Stat. Mech. Theory Exp. **2005**(10), P10002 (2005)
20. Shah, J., Joshi, G., Parida, P.: Behavioral characteristics of pedestrian flow on stairway at railway station. Procedia-Soc. Behav. Sci. **104**, 688–697 (2013)
21. von Sivers, I., Köster, G.: Dynamic stride length adaptation according to utility and personal space. Transp. Res. Part B: Methodological **74**, 104–117 (2015)
22. von Sivers, I., Köster, G.: Realistic stride length adaptation in the optimal steps model. In: Traffic and Granular Flow'13, pp. 171–178. Springer (2015)
23. Weidmann, U.: Transporttechnik der fussgänger (1992)
24. Zhang, J., Seyfried, A.: Comparison of intersecting pedestrian flows based on experiments. Phys. A: Stat. Mech. Appl. **405**, 316–325 (2014)

Data-Driven Characterisation
of Multidirectional Pedestrian Traffic

Marija Nikolić, Michel Bierlaire and Flurin Hänseler

Abstract We propose the framework for pedestrian traffic characterisation that is derived by extending Edie's definitions through a data-driven discretisation. The discretisation framework is based on three-dimensional Voronoi diagrams in order for the characterisation to be as independent as possible from an arbitrarily chosen aggregation. It can be designed through the utilisation of pedestrian trajectories described either analytically or as a sample of points.

1 Introduction and Background

Congestion is a phenomenon which negatively affects pedestrian dynamics and represents an increasing issue in numerous public spaces. In order to provide convenience and safety for pedestrians, understanding and predicting of pedestrian traffic is essential. Indicators such as velocity, density and flow have been used for this purpose. Different approaches to the definitions of these indicators exist in the literature. They are mostly based on an arbitrarily chosen discretisation (in both, space and time) that may (i) generate noise in data and lead to unreliable results, (ii) lead to the loss of heterogeneity across space and pedestrians and (iii) result in undesired outcomes if the pedestrians do not all walk in the same direction.

We propose a novel approach to pedestrian traffic characterisation by adapting widely used definitions proposed by [1] through a data-driven discretisation. The

M. Nikolić (✉) · M. Bierlaire · F. Hänseler
Transport and Mobility Laboratory, School of Architecture,
Civil and Environmental Engineering, École Polytechnique Fédérale de Lausanne,
Lausanne, Switzerland
e-mail: marija.nikolic@epfl.ch

M. Bierlaire
e-mail: michel.bierlaire@epfl.ch

F. Hänseler
e-mail: flurin.haenseler@epfl.ch

discretisation framework is based on three-dimensional (3D) Voronoi diagrams [3]. It is designed through the utilisation of pedestrian trajectories described either analytically or as a sample of points.

2 Related Literature

Edie's definitions [1] were first introduced to characterise the vehicular traffic, and later extended to pedestrian traffic by [5]. The definitions are derived based on pedestrian trajectories in a three-dimensional time-space region V (Fig. 1) of length dx, with dy and duration dt. The volume of the region V is given as $Vol(V) = dx \times dy \times dt$, with the unit in squared metres times seconds.

The density (k) is defined as the total time pedestrians spend in V, divided by its volume

$$k(V) = \frac{\sum_{n=1}^{N} t_n}{Vol(V)}, \tag{1}$$

where N corresponds to the number of pedestrians present in V.

The flow (q) is defined as the total distance travelled by pedestrians in $x(d^x)$ and $y(d^y)$ directions in V, divided by its volume

$$\mathbf{q}(V) = \begin{pmatrix} q^x(V) \\ q^y(V) \end{pmatrix} = \begin{pmatrix} \frac{\sum_{n=1}^{N} d_n^x}{Vol(V)} \\ \frac{\sum_{n=1}^{N} d_n^y}{Vol(V)} \end{pmatrix}, \tag{2}$$

where N corresponds to the number of pedestrians present in V.

The speed is defined as the ratio between flow and density

$$\mathbf{v}(V) = \begin{pmatrix} \frac{q^x(V)}{k(V)} \\ \frac{q^y(V)}{k(V)} \end{pmatrix}. \tag{3}$$

Fig. 1 Pedestrian trajectories in three-dimensional time-space diagram
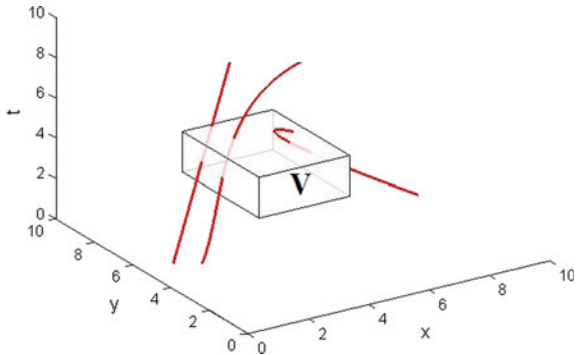
In the limit $dt \rightarrow 0$ density reduces to the number of pedestrians present in $[dx \times dy]$ at a specific moment in time. In the limit $dx \rightarrow 0$ $(dy \rightarrow 0)$ flow is interpreted as the number of pedestrians per unit of time and per unit of length. In order to be as independent as possible from an arbitrary selection of dx, dy and dt we introduce a discretisation framework that is established in accordance with 3D Voronoi diagrams. Note that two-dimensional Voronoi diagrams have been investigated in the literature to derive pedestrian flow indicators [4].

3 Space-Time Partitioning

We consider space-time representation where the triplet (x, y, t) represents a physical position (x, y) in space at a specific time t (the distance along each of the two spatial axes is expressed in metres, and the unit for time is seconds). The trajectory of pedestrian i is a curve in space and time. It is a set of points

$$\Gamma_i : \{p_i(t) | p_i(t) = (x_i(t), y_i(t), t)\}, \tag{4}$$

indexed by time t, such that a given pedestrian is at position (x_i, y_i) at time t. In practice, the analytical description of a trajectory is seldom available. Instead, the pedestrian trajectory data is collected through an appropriate tracking technology. In this case time is discretised and the trajectory is described as a finite collection of triplets

$$\Gamma_i : \{p_{is} | p_{is} = (x_{is}, y_{is}, t_s)\}, \tag{5}$$

where $s = [1, 2, \ldots, T]$ and $t_s = [t_1, t_2, \ldots, t_T]$ corresponds to the available sample.

We consider 3D Voronoi diagrams associated with pedestrian trajectories for the assignment rule d_* that has both spatial and temporal component. A point $p = (x, y, t)$ is assigned to pedestrian i if it is closer to a given pedestrian than to any other for the assignment rule d_*. As a result, the discretisation assigns 3D Voronoi 'tubes'/sequences of 3D Voronoi cells (V_i) to each pedestrian trajectory/sequence of points for each pedestrian.

The assignment rules d_* considered in this study are the Naive distance (d_N), Time-Transform distance (d_{TT}), Mahalanobis distance (d_M) and Distance To Interaction (d_{DTI}). d_N represents the standard Euclidean distance in $\mathbb{R}^2$ when the points have the same time flag, otherwise it goes to infinity. d_{TT} uses a conversion constant expressed in metres per second to convert the temporal difference between points into the spatial one. d_M is employed in order to favour points that are in the movement direction of a pedestrian. d_{DTI} is used so as to anticipate a possible interaction between the points when performing the assignment.

We define the set of all points in V_i corresponding to a specific time t, that is

$$V_i(t) = \{(x(t), y(t), t) \in V_i\}. \tag{6}$$
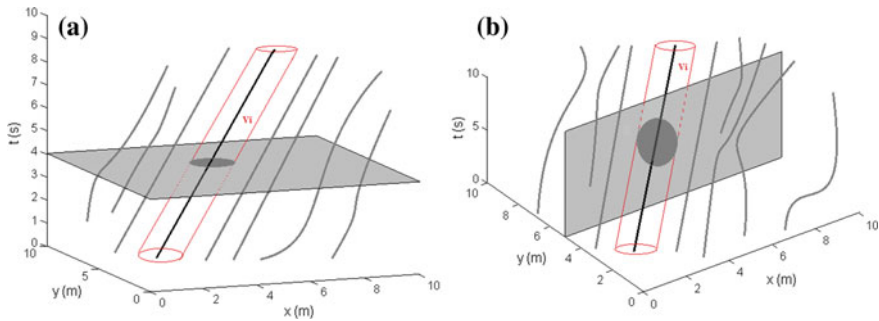
Fig. 2 3D Voronoi-based discretisation. Set in V_i for a specific time t (**a**) and a specific location y (**b**)

It represents the set of dimension 2 or a physical area on the floor (illustrated in Fig. 2a). The area of this cell is denoted by $|V_i(t)|$, with the unit in m^2.

Similarly, we define the set of all points in V_i corresponding to a specific locations x and y, that is

$$V_i(x) = \{(x, y, t) \in V_i\}, \; V_i(y) = \{(x, y, t) \in V_i\}. \tag{7}$$

They represents the set of dimension 2 or a segment perpendicular to x, respectively y, that is occupied by pedestrian i and a time interval that pedestrian i occupies that segment (illustrated in Fig. 2b). The areas of these cells are denoted by $|V_i(x)|$ and $|V_i(y)|$, with the unit in ms.

4 Definitions of Pedestrian Traffic Indicators

The definitions proposed by [1] are revised according to the discretisation framework described in Sect. 3. The density of the cell $V_i(t)$ is defined as

$$k_i^t = \frac{1}{|V_i(t)|}, \tag{8}$$

where $|V_i(t)|$ is the area of the set given by Eq. 6. The flow through the segments perpendicular to x and y for pedestrian i is defined as

$$\mathbf{q}_i = \begin{pmatrix} q_i^x \\ q_i^y \end{pmatrix} = \begin{pmatrix} \frac{1}{|V_i(x)|} \\ \frac{1}{|V_i(y)|} \end{pmatrix}, \tag{9}$$

where $|V_i(x)|$ and $|V_i(y)|$ are the areas of the sets given by Eq. 7. The velocity is defined as the ratio between the flow and density

$$\mathbf{v}_i = \begin{pmatrix} \frac{q_i^x}{k_i^t} \\ \frac{q_i^y}{k_i^t} \end{pmatrix}. \tag{10}$$

Here, we consider $\mathbf{q}_i$ and $\mathbf{v}_i$ in x and y directions only. The framework, however, allows for the specification and measurement of the indicators in any other direction of interest.

5 Conclusion and Future Work

We propose the approach to data-driven pedestrian traffic characterisation. It can be applied to pedestrian trajectory data available either in a form of an analytical description or as a finite collection of points. The approach is expected to (i) reflect the heterogeneity across pedestrians and space; (ii) lead to smooth transitions in measured traffic characteristics and (iii) reproduce the settings with different movement conditions.

In our future research we will consider trajectories that are generated in a simulated environment to evaluate the performance of the approach for different assignment rules. In particular, the focus will be on the ability of the approach to produce realistic indicators and its robustness with respect to the sampling rate. Additionally, the framework will be applied on the data from the real-world scenes. The future research will also aim to examine the effectiveness of additional assignment rules (e.g. probabilistic assignment based on behavioural rules). We plan to further extend the approach through a stream-based framework [2] for the cases when more aggregated measures are of interest.

References

1. Edie, L.C.: Discussion of traffic stream measurements and definitions. Port of New York Authority (1963)
2. Nikolić, M., Bierlaire, M.: Pedestrian-oriented flow characterization. Transp. Res. Procedia **2**, 359–366 (2014)
3. Okabe, A., Boots, B., Sugihara, K., Chiu, S.N.: Spatial Tessellations: Concepts and Applications of Voronoi Diagrams, vol. 501. Wiley (2009)
4. Steffen, B., Seyfried, A.: Methods for measuring pedestrian density, flow, speed and direction with minimal scatter. Phys. A Stat. Mech. Appl. **389**(9), 1902–1910 (2010)
5. van Wageningen-Kessels, F., Hoogendoorn, S.P., Daamen, W.: Extension of Edie's definitions for pedestrian dynamics. Transp. Res. Procedia **2**, 507–512 (2014)

Asymmetric Pedestrian Dynamics on a Staircase Landing from Continuous Measurements

Alessandro Corbetta, Chung-Min Lee, Adrian Muntean and Federico Toschi

Abstract We investigate via extensive experimental data the dynamics of pedestrians walking in a corridor-shaped landing in a building at Eindhoven University of Technology. With year-long automatic measurements employing a Microsoft Kinect™ 3D-range sensor and *ad hoc* tracking techniques, we acquired few hundreds of thousands pedestrian trajectories in real-life conditions. Here, we discuss the asymmetric features of the dynamics in the two walking directions with respect to the flights of stairs (i.e. ascending or descending). We provide a detailed analysis of position and speed fields for the cases of pedestrians walking alone undisturbed and for couple of pedestrians in counter-flow. Then, we show average walking velocities exploring all the observed combinations in terms of numbers of pedestrians and walking directions.

1 Introduction

During the last two decades experimental investigations of pedestrians dynamics flourished, fostering a transition from qualitative to quantitative analyses. Several geometric configurations and flow scenarios have been studied in controlled laboratory conditions, such as corridors, bottlenecks, intersections and T-junctions

_____

A. Corbetta (✉) · F. Toschi
Eindhoven University of Technology, Eindhoven, The Netherlands
e-mail: a.corbetta@tue.nl

A. Corbetta
Politecnico di Torino, Turin, Italy

C.-M. Lee
California State University Long Beach, Long Beach, CA, USA
e-mail: chung-min.lee@csulb.edu

A. Muntean
Karlstad University, Karlstad, Sweden
e-mail: adrian.muntean@kau.se

F. Toschi
CNR-IAC, Rome, Italy
e-mail: f.toschi@tue.nl

[1, 15, 16]. More recently, 3D-range cameras and wireless sensors enabled reliable measurements in real-life conditions [3, 4, 9, 11], allowing for data collection with reduced (potential) influences of laboratory environments. Notably, these technologies are privacy-safe, as recorded pedestrians are not identifiable, thus, unlimited data collections, e.g., via long term measurement campaigns [4] are possible.

In this paper, we analyse the dynamics of pedestrians on a landing (intermediate planar area between flights of stairs) which has a corridor-like geometry. Few experimental data have been collected in these scenarios, typically in the context of evacuation [7, 10]. Driven by fundamental curiosity, we recorded the landing on a 24/7 basis and acquired trajectories of walking pedestrians in a year-long experimental campaign. Our data include multiple natural traffic scenarios, such as uni- or bi-directional flows with one or several pedestrians. After categorising the measurements based on walking directions and number of pedestrians involved, we compare pedestrian positions and velocities among different flow conditions. We note that individuals walking on a landing are either ascending or descending the neighbouring stair flights. This aspect induces asymmetries in the dynamics, likely related to the different physical fatigue of pedestrians. These asymmetries, that we observe here and discuss, appear on side of cultural preferences, for instance for walking side [8].

This paper is organised as follows: in Sect. 2 we provide a description of our measurement set-up and a primer of the recording technique. In Sect. 3 we give a detailed overview of the dynamics of pedestrians walking alone and in avoidance of one other individual via position and velocity fields. Moreover, we comment on the average velocities considering all possible flow conditions and addressing all direction combinations. A concluding discussion is reported in Sect. 4.

2 Measurement Site

We measured the pedestrian traffic on a landing within the Metaforum building at Eindhoven University of Technology. The landing connects the two staircases in the configuration presented in Fig. 1a, c, where individuals ascend in a clockwise direction from the ground to the first floor of the building. The landing is 5.2 m long and 1.2 m wide, and the steps have the same width. Individuals at the ground floor reach the landing after 18 steps, then they climb 4 further steps arriving at the first floor. Pedestrian traffic mainly comes from students walking between the canteen of the building (ground floor) to the dining area (first floor) and *vice versa*. Considering the reference system in Fig. 1c, we indicate the walking direction that leads to the first floor as *left to right* (2R, for brevity) and as *right to left* (2L) the opposite case. On average, 2,200 pedestrians cross the facility every working day, and occupancy peaks at around 12 PM (lunch time) and at around 3 PM (afternoon break). At peak hours, typically there are multiple pedestrians walking in the facility (up to six pedestrians have been recorded in our observation window at once) in co-flow (uni-directional dynamics) or counter-flow (bi-directional dynamics). Conversely, off-peak traffic is mostly due to individuals walking alone, *undisturbed* by other pedestrians. We refer
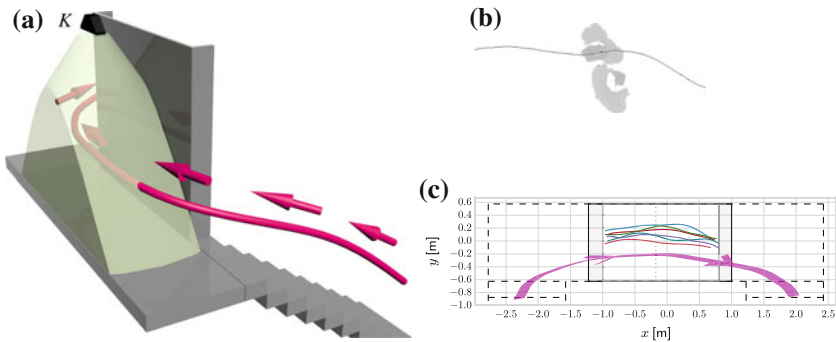
Fig. 1 Sketch of the landing including the view cone of the Kinect™ sensor (marked with a letter 'K') (**a**). A frame taken in the landing by the Kinect™ sensor; two pedestrians walking in opposite directions are present. The depth field (z) is represented via the grey scale. Brighter pixels are farther from the camera plane (**b**). Planar view of the landing with dimensions and the xy reference system considered. The walking direction from the ground to the first floor (from left to right) is depicted (**c**). Examples of trajectories collected are reported

to our previous work [4] for time histories and statistics about daily traffic. In this work, we discuss pedestrian dynamics data acquired during 108 working days in the period October 2013–October 2014. In this campaign we collected *ca.* 230,000 time-resolved high-resolution trajectories.

We measured trajectories of pedestrians via an automatic head tracking procedure that allows non-intrusive and privacy respecting data acquisition in real-life condition. Such procedure is based on the 3D-depth data delivered by an overhead and downward looking Microsoft Kinect™ 3D-range sensor. 3D-depth frames represent a filmed scene as a three dimensional (x, y, z) pixel *cloud* (cf. Fig. 1b). Pedestrian identification (segmentation) can be operated by identifying and isolating pixel *clusters* within such a cloud. Heads, that we track as particles, are the topmost portions of each cluster (cf. [2, 11]).

We filmed at 15 frames per second in the central, 1.8 m long (cf. Fig. 1c), section of the landing, by placing a Kinect™ sensor at a height of *ca.* 4 m (cf. Fig. 1a). Technical aspects of our detection approach, inspired by [11], are discussed in the appendix of [6]. Furthermore, we employed the OpenPTV library [12], developed by the Particle Tracking Velocimetry [13] community in fluid mechanics, to perform heads tracking and to retrieve trajectories (cf. Fig. 1c).

3 Pedestrian Dynamics

The U-shape of the landing influences the dynamics of pedestrians that follow curved trajectories to reach the staircase at the opposite end of the walkway. Hence, contrarily from what is expected in a rectilinear corridor of similar size, pedestrian positions and velocities are asymmetric in space. These aspects depend on the flow conditions (undisturbed pedestrian vs. multiple pedestrians) as well as on the walking directions (ascending vs. descending).

Fig. 2 Positions and velocities of pedestrians walking undisturbed. Positions concentrate mostly in thin curved layers following the U-shaped geometry (**a**). To evaluate these layers we address separately pedestrians going from left to right (2R, for brevity) and from right to left (2L). For each 'horizontal' location x in the observation window ($x \in (-1, 0.8)$ m), we consider the distribution y_x of pedestrian positions in 'vertical' direction. We report the 15th and the 85th percentiles of y_x as a function of x (thus the vertical interval $(y_{x,15}, y_{x,85})$). Layers for pedestrians going to the left and to the right are identical but a roughly 20 cm vertical offset. Fields of average walking speed in space (**b**, **c**). Respectively for pedestrians going to the *left* (**b**) and to the *right* (**c**). In both cases the maximum velocity (higher for pedestrians going to the *left*, that have already descended a ramp of stairs) are reached after the central part of the corridor. Thus, pedestrians decelerate to approach the next ramp
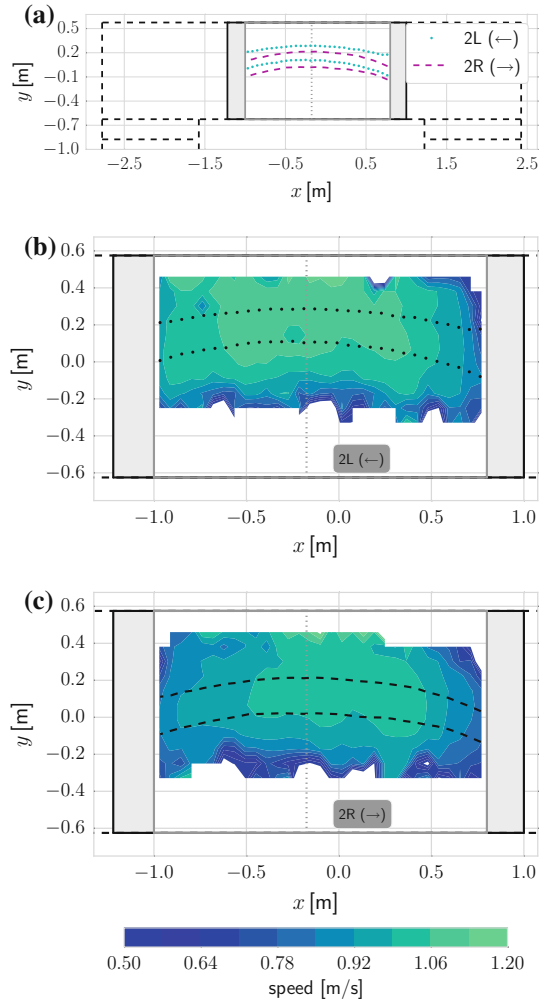
Direction-dependent differences can be observed for pedestrians walking undisturbed. Pedestrian trajectories concentrate within thin curved layers that are located at the *relative* right hand side of the facility (cf. Fig. 2a, the relative right hand side is at the absolute top for people going to the left and at the absolute bottom for people going to the right. See the caption and cf. [4] for the layer estimation idea). These layers reflect a preferred walking path, ideally located along their axes, that acts as 'guiding centre' of trajectories fluctuations (cf. [5] for analysis and modelling of such stochastic fluctuations). Although the relative position of the layers conforms with the cultural habit of keeping the driving side (cf. e.g., [8]), an influence of the landing geometry cannot be excluded. In fact, the shape of the landing limits the sight on the staircases, hence, right hand side positions may be kept to ease potential collisions (cf. Fig. 3). Walking speed is affected by the walking direction too: pedestrians descending from the stairs walk faster (cf. Fig. 4). The walking speed varies

Fig. 3 Positions and velocities of pedestrians walking in presence of a peer having an opposite velocity (counter-flowing). Examples of trajectories in counter-flow (**a**). Simultaneous detections are connected via *grey* segments. The pedestrian going to the right enters first (**a**). When the pedestrian going to the left appears, he or she modifies the trajectories moving to the relative right to avoid collision. In avoidance regime, pedestrians positions concentrate on the relative right (**b**). The layer of preferred positions is calculated as in Fig. 2a. Notably, the symmetry with respect to the corridor 'vertical' axis ($x \approx -0.1$ m. Cf. *Dotted grey line*) is lost. Average speed fields for pedestrians going from right to left (**c**) and from left to right (**d**) in presence of a second pedestrians going in opposite direction. The preferred positions layer is reported and compared with the preferred positions layer in case of undisturbed pedestrians (cf. Fig. 2). Pedestrians going to the left and to the right have smaller walking speed than in the undisturbed case. Notably, pedestrians going to the right walk significantly more slowly
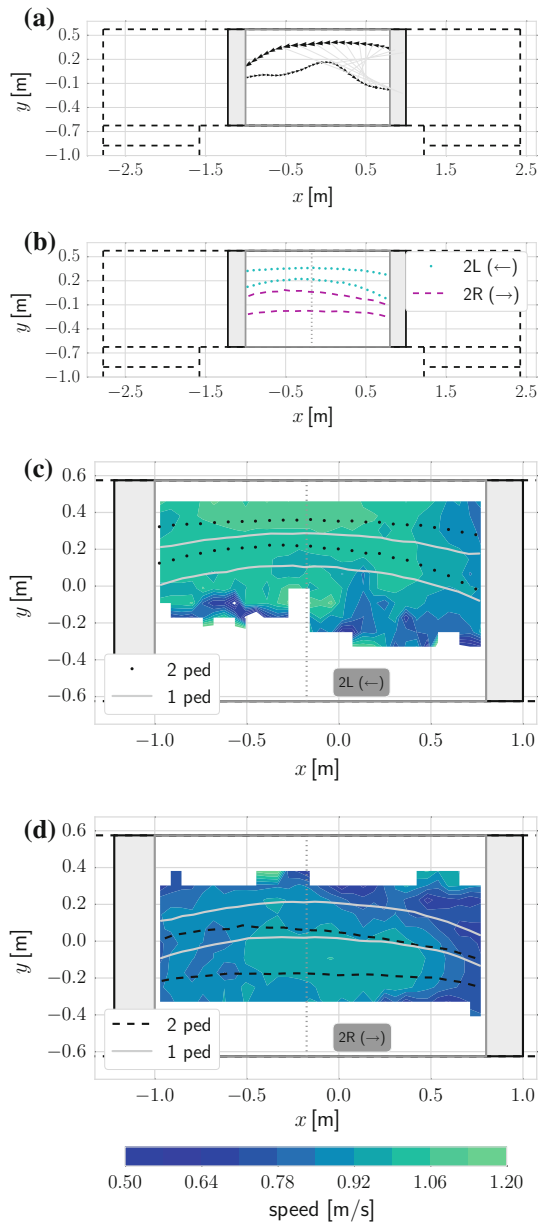
in space and its contours are roughly transversal with respect to the position layers. The speed peaks around the central section of the corridor, and remains high in the second half of the walkway. Individuals walk slower near the staircases to adapt their velocity to the ascent/descent of the stairs (a speed drop of about 30 % is measured in our observation window, cf. Fig. 2b, c).
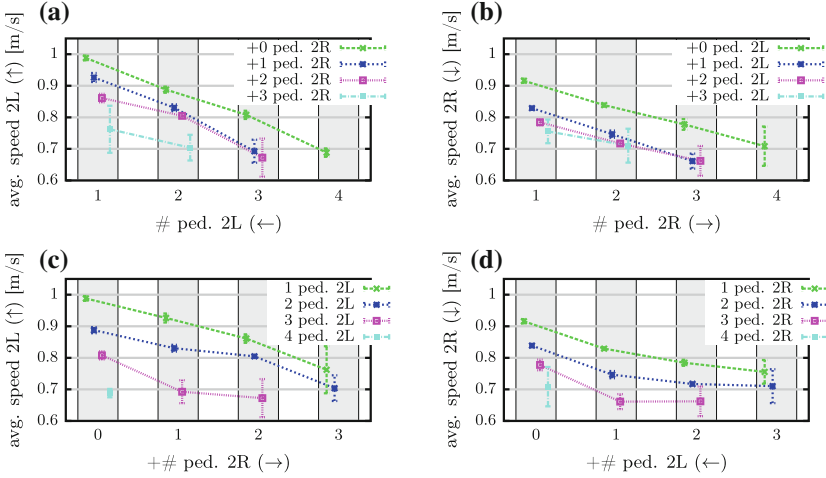
Fig. 4 Fundamental diagrams of different system state variable pairs (cf. Eq. (1)). We report on the vertical axis average walking speeds for pedestrians going to the left (descending) in (**a**, **c**) and for pedestrians going to the right (ascending) in (**b**, **d**). Average speeds are considered in dependence on the number of pedestrians in co-flow and counter-flow: in (**a**, **b**), the number of co-flowing pedestrians is on the horizontal axis, while the number of counter-flowing pedestrians is accounted via the different curves (for example, in (**a**) '+2 ped. 2R' means that there are two pedestrians going to the right in addition to a number of pedestrians going left). Diagrams (**c**, **d**) contain a 'transposed' information, as the number of counter-flowing pedestrians is on the horizontal axis while the number of co-flowing pedestrians changes across the curves. We consider just system states for which there are at least 100 frames. The size of the error bars (possibly underestimated) is $\max(s) - \min(s)$, where $s = \{s_1, s_2, s_3, s_4\}$, and the s_i are average values computed on a random even partition in four sets of the speed data at a given (# ped. 2L, # ped. 2R) state

Direction-dependent differences increase when the presence of other pedestrians triggers avoidance mechanisms. The simplest avoidance scenario involves exactly two pedestrians walking in opposite direction (i.e., counter-flowing, cf. Fig. 3a). In this condition, the path layers are shifted to the relative right to avoid collision. Contrary to the single pedestrian case, these layers have no overlap (cf. Fig. 2a vs. Fig. 3b). Furthermore, they are not symmetric with respect to the central corridor vertical axis ($x \approx -0.1$ m). In both 2L and 2R cases, layers are wider near the entrance side with similar distribution to the undisturbed pedestrian case. Moving across the landing, the layers constrict and shift toward the relative right hand side. We observe a drop in the walking speed in comparison with the undisturbed pedestrians, especially around the central horizontal axis ($y \approx 0$ m) where collisions may potentially occur. Higher walking speeds are reached at the relative right hand side of the pedestrians, where collisions are mostly avoided. Comparing the counter-flow dynamics in pedestrian pairs with the undisturbed dynamics, we observe further direction-related asymmetries: (i) position shift to the relative right from the undisturbed case is larger for pedestrians ascending (2R); (ii) the speed drop in counter-flow is larger for pedestrians ascending (2R).

When more than two pedestrians are present, different walking configurations are possible. Moreover, pedestrians may have social interactions (e.g. conversations) and move in groups (cf., e.g., [14]), that may influence the walking behaviour (we ignore here such possible influences). We address the walking dynamics considering average walking speeds in all possible uni- and bi-directional flow configurations. We refrain from spatial analyses and we take here velocity averages over the observation window (cf. Figs. 2b, c and 3c, d). We identify configurations considering the number of pedestrians going to the left (*# ped. 2L*) and the number of pedestrians going to the right (*# ped. 2R*). After grouping pedestrians that in each frame walk in the same direction, we evaluate their average speed (respectively, *avg. speed 2L* and *avg. speed 2R*). In other words, we give a simplified description of the system state through a tuple:

$$(\text{\# ped. 2L}, \text{\# ped. 2R}, \text{ avg. speed 2L}, \text{ avg. speed 2R}). \tag{1}$$

Considering average speed versus the number of pedestrians yields fundamental diagram plots, that we report in Fig. 4. We observe a twofold monotonic behaviour (within error bar) with directional dependence. First, the average speed of pedestrians decreases as the number of pedestrians increases either in co-flow or in counter-flow situations. Second, average speeds of ascending pedestrians are lower than those of descending pedestrians for any given combination of co-flowing and counter-flowing pedestrians. However, while an increase of co-flowing pedestrians (for fixed number of counter-flowing individuals) yields nearly linear reductions of the average speed (cf. Fig. 4a, b), the trend for increasing the number of pedestrians in counter-flow is not linear (cf. Fig. 4c, d). We observe the following features: (i) the velocity response to the number of counter-flowing pedestrians is different in the cases of individuals going to the left and going to the right, and (ii) specifically for the population going to the right, significant speed drops occur as soon as one counter-flowing pedestrian is present; the exact number of counter-flowing individuals seems to play a minor role.

4 Discussion

We acquired experimentally and in real-life conditions a large set of trajectories of pedestrians walking on a landing. The trajectories span over multiple flow conditions involving a variable number of pedestrians walking in different direction configurations; in particular, both co-flows and counter-flows occur and are recorded. The U-shape of the landing as well as the previous ascent/descent of the stairs induce asymmetries in the dynamics that add up with cultural walking side preferences. Pedestrians walking undisturbed keep the relative right side, even if no avoidance is necessary. This cultural preference is likely enhanced because of the limited vision near the staircases, which yields a choice of positions preventing possible inbound collisions. We considered average walking speed for all possible combinations of occupancy and walking directions. Pedestrians that have climbed the stair case (going to the right) appear to move slower than those who just descended for all flow config-

urations. Interestingly, the increment of co-flowing pedestrians yields nearly linear speed reductions, while this is not true when the number of counter-flowing pedestrians increases.

References

1. Boltes, M., Seyfried, A.: Collecting pedestrian trajectories. Neurocomputing **100**, 127–133 (2013)
2. Brščić, D., Kanda, T., Ikeda, T., Miyashita, T.: Person tracking in large public spaces using 3-D range sensors. IEEE Trans. Hum. Mach. Syst. **43**(6), 522–534 (2013)
3. Brščić, D., Zanlungo, F., Kanda, T.: Density and velocity patterns during one year of pedestrian tracking. Transp. Res. Procedia **2**, 77–86 (2014)
4. Corbetta, A., Bruno, L., Muntean, A., Toschi, F.: High statistics measurements of pedestrian dynamics. Transp. Res. Procedia **2**, 96–104 (2014)
5. Corbetta, A., Lee, C., Benzi, R., Muntean, A., Toschi, F.: Fluctuations and mean behaviours in diluted pedestrian flows (2015). Manuscript
6. Corbetta, A., Muntean, A., Vafayi, K.: Parameter estimation of social forces in pedestrian dynamics models via a probabilistic method. Math. Biosci. Eng. MBE **12**(2), 337–356 (2015)
7. Hoskins, B.L., Milke, J.A.: Differences in measurement methods for travel distance and area for estimates of occupant speed on stairs. Fire Saf. J. **48**, 49–57 (2012)
8. Moussaïd, M., Helbing, D., Garnier, S., Johansson, A., Combe, M., Theraulaz, G.: Experimental study of the behavioural mechanisms underlying self-organization in human crowds. Proc. Roy. Soc. Lond. B Biol. Sci. **276**, 2755–2762 (2009)
9. Roggen, D., Wirz, M., Tröster, G., Helbing, D.: Recognition of crowd behavior from mobile sensors with pattern analysis and graph clustering methods. Netw. Heterogen. Media **6**(3), 521–544 (2011)
10. Ronchi, E., Reneke, P.A., Kuligowski, E.D., Peacock, R.D.: An analysis of evacuation travel paths on stair landings by means of conditional probabilities. Fire Saf. J. **65**, 30–40 (2014)
11. Seer, S., Brändle, N., Ratti, C.: Kinects and human kinetics: a new approach for studying pedestrian behavior. Transp. Res. Part C Emerg. Technol. **48**, 212–228 (2014)
12. The OpenPTV Consortium: OpenPTV: Open source particle tracking velocimetry. http://www.openptv.net/ (2012)
13. Willneff, J.: A spatio-temporal matching algorithm for 3D particle tracking velocimetry. Ph.D. thesis, ETH Zürich (2003)
14. Zanlungo, F., Ikeda, T., Kanda, T.: Potential for the dynamics of pedestrians in a socially interacting group. Phys. Rev. E **89**, 012811 (2014)
15. Zhang, J., Klingsch, W., Schadschneider, A., Seyfried, A.: Transitions in pedestrian fundamental diagrams of straight corridors and T-junctions. J. Stat. Mech. Theory Exp. **2011**(6), P06004 (2011)
16. Zhang, J., Seyfried, A.: Comparison of intersecting pedestrian flows based on experiments. Phys. A **405**, 316–325 (2014)

Experimental Study of High-Density Pedestrian Flow Field Characteristics at a Crossing

Liping Lian, Weiguo Song, Yuen Kwok Kit Richard and Chunlin Wu

Abstract This paper presents an experimental study on four-directional intersecting pedestrian flows to give insight into collective movement characteristics of pedestrians at a crossing. The experiments were performed in a university and up to 364 students took part in. Pedestrian trajectories are extracted by means of automatic image processing. From trajectories, we get positions of each person in each frame and find pedestrian gap at high densities. Velocity field and its corresponding streamlines and contour lines are constructed and analysed. An efficient rotary traffic pattern occurs when people walk on their right hand side along the corridors. Moreover, turbulence intensities in different scenarios are compared and the results imply that putting an obstacle in the centre of cross area and pedestrians walking on the right hand side along the corridors will improve traffic stability in the cross area. These findings can be used to calibrate pedestrian simulation models and help us understand the mechanism of collective movement better.

1 Introduction

In recent years, crowd disasters have attracted worldwide attention. High density and the meeting of two or more directional flows are the main causes of serious casualties. The study of pedestrian dynamics is urgent and of great importance.

L. Lian (✉) · W. Song · C. Wu
State Key Laboratory of Fire Science, University of Science
and Technology of China, Hefei 230026, People's Republic of China
e-mail: lplian@mail.ustc.edu.cn

W. Song
e-mail: wgsong@ustc.edu.cn

C. Wu
e-mail: chunlin@mail.ustc.edu.cn

Y.K.K. Richard
Department of Civil and Architectural Engineering, City University of Hong Kong,
Hong Kong, China
e-mail: Richard.Yuen@cityu.edu.hk

By now, the experimental studies of high-density pedestrian flows focus on crowd disaster investigation. Helbing et al. [3] analysed Mina Stampede happened in 2006, and defined local density and local velocity measurement to describe microscopic characteristics. Wang et al. [10] also investigated Mina Stampede and used proper orthogonal decomposition method and parameters in fluid mechanic to describe pedestrian movement characteristics. Other crowd disasters, for example Love Parade Disaster [4, 5] happened in 2010, Duisburg, are also widely investigated. However, the resource of empirical data is limited and often not well recorded. Helbing et al. [2] simulated different pedestrian traffic designs at a crossing by using social force model. They found when pedestrians walk in one-way regulation and an obstacle was put in the centre of cross area, stripes can form in the cross area. If the four pedestrian streams met in right order, rotary traffic can be formed. Zhang et al. [11] investigated fundamental diagrams in T-junctions and found pedestrians velocities after merging are bigger than those before merging at the same density. The collective behaviours of two ant streams at a crossing under high-density and panic conditions were studied [1]; researchers found alternate moving and clogging states in each ant stream. However, controlled experimental study for entering pedestrian flows is still rare, especially under high-density conditions.

In this paper, we design controlled experiments for four-directional intersecting pedestrian flows at a crossing and aim to investigate high-density pedestrian movement characteristics. The experiment will be introduced in Sect. 2. Results and discussion are given in Sect. 3. The last section is summary and perspectives.

2   Experiment

The sketch of the experimental set-up is shown in Fig. 1.

The experimental scene was composed by two perpendicular corridors and the corridors were made by some partitions. Each corridor had a length of 8 m and a width of 3.2 m. Besides, in some experimental scenes, there was an obstacle putting in the centre of cross area. The obstacle was a desk whose length is 1.0 m and width is 0.8 m. The participants were 364 male students with average age of 20 years old and average height 1.70 m. They were asked to wear red and yellow hats and divided into four-directional pedestrian flows standing orderly in the waiting area. There were four high-density experimental scenarios and they were separately named OO-WS, OO-WR, WOH-WR and WOV-WR according to whether putting an obstacle or not and the walking instruction. OO means without an obstacle, WOH means with an obstacle putting in horizontal direction, WOV means with an obstacle putting in vertical direction, WS means pedestrians were asked to walk straight in the corridors, WR means pedestrians were asked to walk on their right hand side in the corridors.

The whole experimental process was recorded by a camera located on the top floor of a 15-m-high building. By using mean-shift algorithm [7], each pedestrians coordinates in each frame of video recordings can be automatically detected. Then, we adopted direct linear transformation method to transform image coordinates to real space coordinates [9].

Fig. 1 Sketch of the experimental set-up [6]
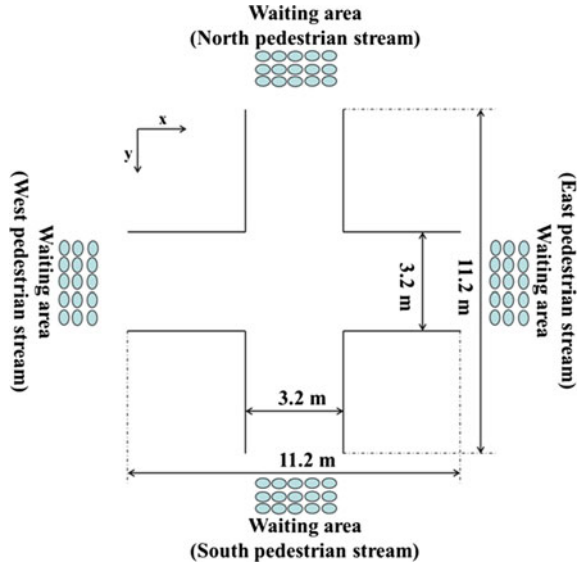
3 Result and Discussion

Figure 2a shows a snapshot of instantaneous velocity filed in experiment OO-WR. The red arrows represent the velocities of pedestrians walking from west to east. The magenta arrows represent the velocities of pedestrians walking from east to west. The green arrows represent the velocities of pedestrians walking from north to south. The blue arrows represent the velocities of pedestrians walking from south to north. An approximate rotary traffic in the cross area can be seen in Fig. 2a. Moreover, we can observe some pedestrians change their expected walking paths in the cross area, which indicate the complex movement in the cross area. For the convenience to represent the flow direction, we constructed the local velocity field based on each pedestrians velocity and its corresponding stream lines, as shown in Fig. 2b. The method of local velocity we adopt is proposed by Helbing et al. [3], here we give a simple introduction. The local velocity at position $\mathbf{r}$ and at time t is defined as $\mathbf{V}(\mathbf{r}, t) = \frac{\sum_i \mathbf{v}_i f(\mathbf{r}_i(t) - \mathbf{r})}{\sum_i f(\mathbf{r}_i(t) - \mathbf{r})}$. In which $f(\mathbf{r}_i(t) - \mathbf{r}) = \frac{1}{\pi R^2} exp(- \parallel \mathbf{r}_i(t) - \mathbf{r} \parallel^2 / R^2)$, $\mathbf{r}_i(t)$ represents the instantaneous velocity of pedestrian i at time t, $\mathbf{r}_i(t)$ represents the position of pedestrian i at time t, R is a measurement parameter, here $R = 0.6$. To avoid boundary effect, we study central area 4 m × 4 m, so the scopes of coordinates in Fig. 2a, b are different. Figure 2b shows a rotary traffic in the intersecting area and the overall flow direction agrees with Fig. 2a.

Furthermore, the contour lines of local velocity field are also constructed in order to investigate velocity distribution at a crossing, as shown in Fig. 3. Note the scopes of the coordinates are also different in left and right figures. Figure 3a shows when pedestrians walk straight in the corridors, the velocity in the cross area will quickly
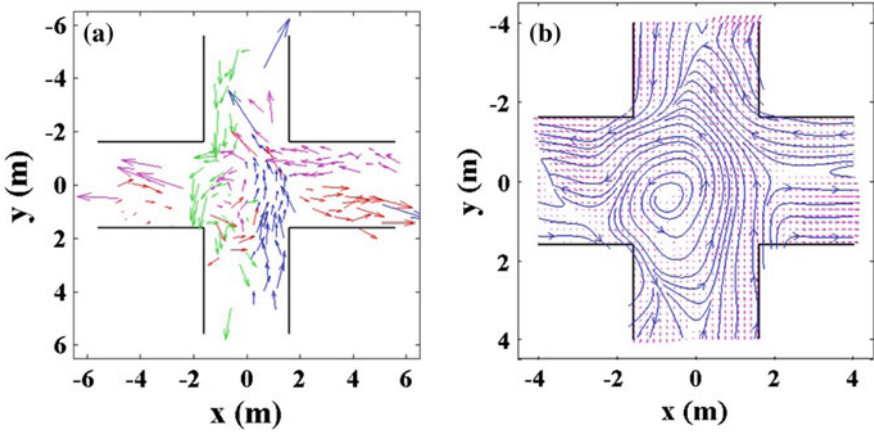
Fig. 2 Scenario OO-WR: velocity field (**a**); stream lines (**b**)
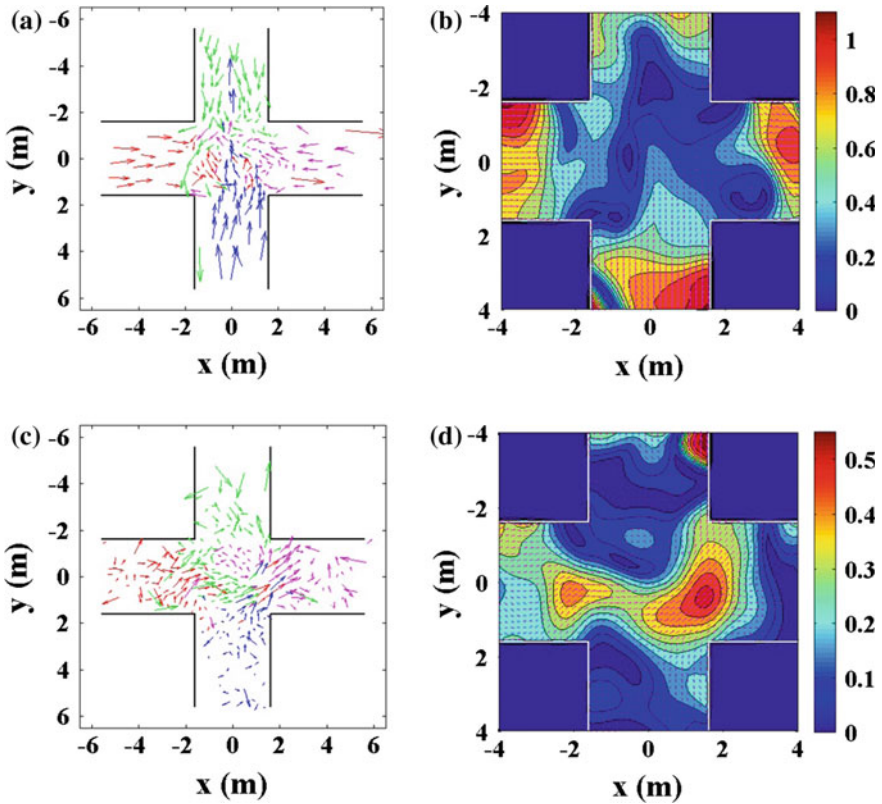
Fig. 3 Scenario OO-WS at the time of 6.4 s and the density in the cross area is 8.1 ped/m^2 *top*; scenario OO-WS at the time of 20 s and the density in the cross area is 9.5 ped/m^2 *bottom*. Instantaneous velocity field (**a**, **c**); contour lines (**b**, **d**)
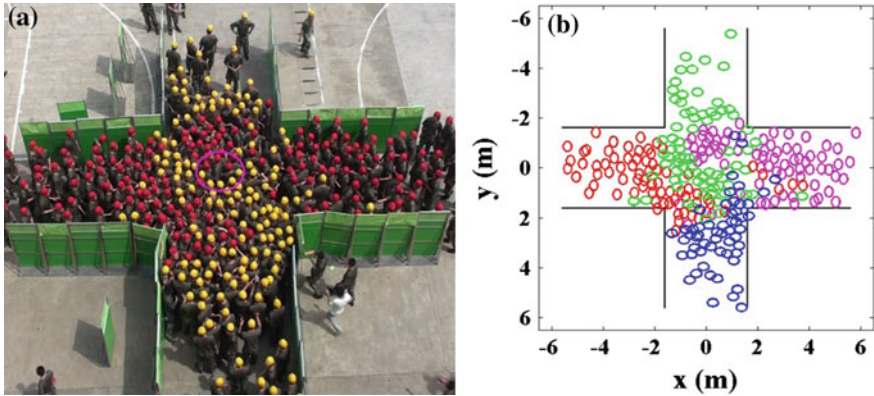
Fig. 4 Scenario OO-WS when the density in the cross area is 9.08 ped/m^2: snapshot (**a**); sketch (**b**)

become small, while pedestrians in the corridors still keep going. At this moment, the cross area is jamming. As the density in the cross area becomes larger, pedestrians in the cross area will have strong interaction with each other, the velocity in the cross area increases and pedestrians in the corridor will stop or slow down, as shown in Fig. 3b.

To get insight into high-density period in scenario OO-WS, we find pedestrian gaps as marked in a magenta ellipse in Fig. 4a. When we use circles to represent pedestrians, it is unexpected that pedestrian gaps can be seen more clearly, as shown in Fig. 4b, which calibrates the simulation results of Majian [8]. Moreover, in Fig. 4b different colours represent different pedestrian flows and it shows pedestrians in the same direction cooperate together and move on as a whole at this moment.

In the experiment, the movement in the cross area is chaotic, the local density in the centre of cross area can exceed 10 ped/m^2 [6]. We further investigate the movement characteristics in the cross area. Figure 5 shows the average local velocity field over time and its corresponding stream lines in each scenario. We choose time interval when the motion state in the cross area is relatively stable and the density is not very low, in this paper we take time interval that satisfies the average velocity over space is less than 1 m/s and the density in the cross area is greater than 2 ped/m^2. Figure 5 shows the average local velocity field is like rotary traffic. It is no doubt that when asking pedestrian to walk on their right hand side along the corridors, rotary traffic will occur in the cross area, which agrees with the simulation results [2]. However, it is unexpected that the average velocity field is like rotary traffic in scenario OO-WS, where pedestrians are instructed to walk straight, which may be because pedestrians in China have right hand side preference.

Moreover, turbulence intensity I, a parameter in fluid mechanics, is used to quantitative characterise movement in the cross area. Figure 6 shows time evolution of space-averaged turbulence intensity I. Turbulence intensity I in scenario OO-WS is biggest and fluctuates strongly, which indicates chaotic movement when pedestrian walked straight in the corridors. The red dashed line, where pedestrians walk on
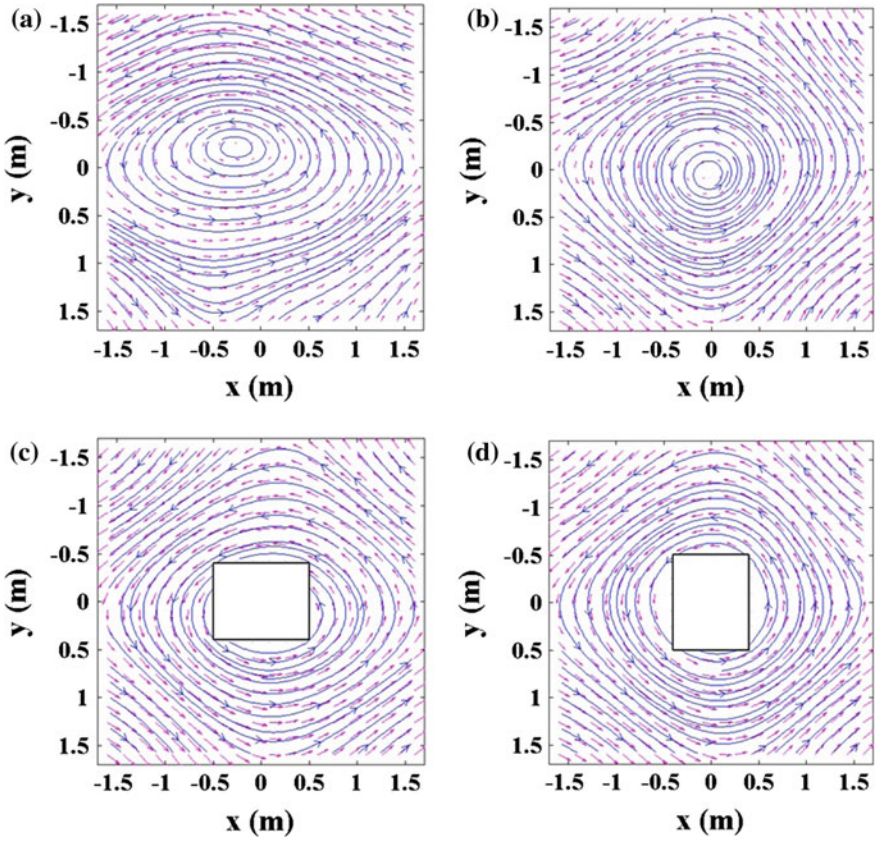
Fig. 5 Time-averaged local velocity field; scenario OO-WS (**a**); scenario OO-WR (**b**); scenario WOH-WR (**c**); scenario WOV-WR (**d**)

Fig. 6 Time evolution of space-averaged turbulence intensity I
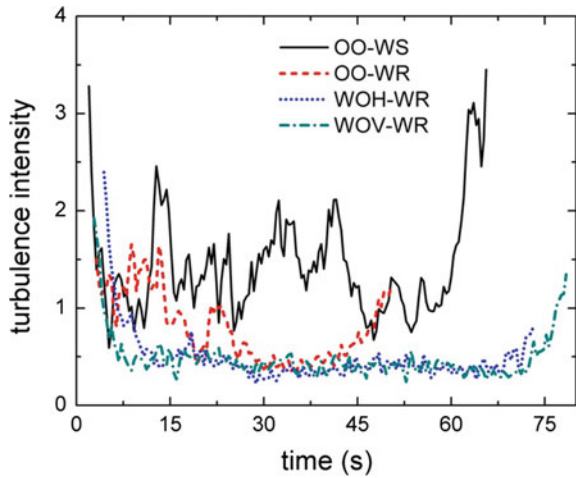
their right hand side in the corridors, at first is not stable and then become relatively stable. That may be due to at the beginning of the experiment one of the pedestrian streams walked fast to avoid possible conflicts in the cross area. When putting an obstacle in the centre of the cross area and pedestrians walk on the right hand side in the corridor, namely in scenarios WOH-WR and WOV-WR, the turbulence intensity will be smaller and become relatively stable.

4   Summary and Perspectives

Experiments of high-density pedestrian flows at a crossing are conducted. When pedestrians walk straight in the corridors, the cross area soon become crowded and pedestrians have strong interaction with each other. During the interaction, pedestrian gap forms. By using local velocity measurement, local velocity streamlines and contour at a crossing are obtained. An appropriate rotary traffic is formed when pedestrians walk on their right hand side along the corridors. When pedestrians walk straight, the cross area will soon become jammed. After significant interaction, the velocity in the cross area increases. In addition, we find turbulence intensity in the cross area is smaller and the traffic in the cross area is relatively stable if putting an obstacle in the centre of cross area and pedestrians walk on their right hand side along the corridors. It is hoped that more experiments in complex configurations will be conducted and analysed in future work.

References

1. Dias, C., Sarvi, M., Shiwakoti, N., Ejtemai, O., Burd, M.: Investigating collective escape behaviours in complex situations. Saf. Sci. **60**, 87–94 (2013)
2. Helbing, D., Buzna, L., Johansson, A., Werner, T.: Self-organized pedestrian crowd dynamics: experiments, simulations, and design solutions. Transp. Sci. **39**(1), 1–24 (2005)
3. Helbing, D., Johansson, A., Al-Abideen, H.Z.: Dynamics of crowd disasters: an empirical study. Phys. Rev. E **75**(4), 046109 (2007)
4. Helbing, D., Mukerji, P.: Crowd disasters as systemic failures: analysis of the love parade disaster. EPJ Data Sci. **1**(1), 1–40 (2012)
5. Krausz, B., Bauckhage, C.: Loveparade 2010: automatic video analysis of a crowd disaster. Comput. Vis. Image Underst. **116**(3), 307–319 (2012)
6. Lian, L., Mai, X., Song, W., Richard, Y.K.K., Wei, X., Ma, J.: An experimental study on four-directional intersecting pedestrian flows. J. Stat. Mech. Theory Exp. **2015**(8), P08024 (2015)

7. Liu, X., Song, W., Zhang, J.: Extraction and quantitative analysis of microscopic evacuation characteristics based on digital image processing. Phys. A Stat. Mech. Appl. **388**(13), 2717–2726 (2009)
8. Ma, J., Song, W., Lo, S.: Simulation of Crowd-Quakes with Heterogeneous Contact Model. In: Traffic and Granular Flow, pp. 103–110, Springer, (2013)
9. Tian, W., Song, W., Ma, J., Fang, Z., Seyfried, A., Liddle, J.: Experimental study of pedestrian behaviors in a corridor based on digital image processing. Fire Saf. J. **47**, 8–15 (2012)
10. Wang, J., Weng, W., Zhang, X.: New insights into the crowd characteristics in Mina. J. Stat. Mech. Theory Exp. **2014**(11), P11003 (2014)
11. Zhang, J., Klingsch, W., Rupprecht, T., Schadschneider, A., Seyfried, A.: Empirical study of turning and merging of pedestrian streams in T-junction (2011). arXiv:1112.5299

Empirical Study of the Influence of Social Groups in Evacuation Scenarios

Cornelia von Krüchten, Frank Müller, Anton Svachiy, Oliver Wohak and Andreas Schadschneider

Abstract The effects of social groups on pedestrian dynamics, especially in evacuation scenarios, have attracted some interest recently. However, due to the lack of reliable empirical data, most of the studies focussed on modelling aspects. It was shown that social groups can have a considerable effect, e.g. on evacuation times. In order to test the model predictions we have performed laboratory experiments of evacuations with different types and sizes of the social groups. The experiments have been performed with pupils of different ages. Parameters that have been considered are (1) group size, (2) strength of intra-group interactions, and (3) composition of the groups (young adults, children, and mixtures). For all the experiments high-quality trajectories for all participants have been obtained using the `PeTrack` software. This allows for a detailed analysis of the group effects. One surprising observation is a decrease of the evacuation time with increasing group size.

1 Introduction

The influence of social groups in pedestrian dynamics, especially in evacuation scenarios, is an area of recent interest, see e.g. [3, 4] and other contributions in these proceedings. The situations that are considered are widespread and well-known in everyday life. For example, many people visit concerts or soccer matches not alone, but together with family and friends in so-called social groups. In case of emergency, these groups will try to stay together during an evacuation. The strength

C. von Krüchten (✉) · F. Müller · A. Svachiy · O. Wohak
Institut für Theoretische Physik, Universität zu Köln, 50937 Köln, Germany
e-mail: cvk@thp.uni-koeln.de

A. Schadschneider
Institut für Physik und ihre Didaktik and Institut für Theoretische Physik,
Universität zu Köln, 50937 Köln, Germany
e-mail: as@thp.uni-koeln.de

of this cohesion depends on the composition of the social group. Several adult friends would form a loose group that is mainly connected via eye contact, whereas a mother would take her child's hand and form a strong or even fixed bond. In addition, even the size of the social groups could have an effect on the evacuation behaviour.

In order to consider these phenomena in a more detailed way, a cooperation of researchers of the universities of Cologne and Wuppertal and the Forschungszentrum Jülich has performed several experiments aiming at the determination of the general influence of inhomogeneities on pedestrian dynamics. They contained two series of experiments with pupils of different ages in two schools in Wuppertal. The first series focussed on the determination of the fundamental diagram of inhomogeneous groups, i.e. pedestrians of different size. The second series of experiments considered evacuation scenarios. In several runs the parameters of the crowd of evacuating pupils were varied, i.e. the size of the social group and its structure and the interaction between the group members. Here, we present first results for these evacuation experiments.

2   Teaching Units

The experiments were accompanied by teaching units for all involved students providing an introduction into the topic of traffic and pedestrian dynamics.

In classes of fifth and sixth grade, the focus of the classes was on the important quantities of pedestrian dynamics, especially density, time and bottleneck situations. This introduction to crowd effects and pedestrian behaviour was intended to raise awareness for their relevance for their everyday lives and safety issues. Therefore we arranged little experiments the students could perform themselves, e.g. the panic experiment according to Mintz [2] (see Fig. 1). In small groups the pupils had to pull several wooden wedges out of a bottle with a narrow neck as fast as possible and observe the blocking of the wedges when every students pulls at the same time. This experiment was supposed to indicate that coordination can lead to better results compared to selfish behaviour.

The older pupils of classes 10 and 11 participated in an introduction to cellular automata and the physics of traffic. They received several worksheets on the Game of Life and other cellular automata, especially the Nagel-Schreckenberg model [5]. The aim of these lessons was to obtain a first qualitative and quantitative understanding of the collective effects in traffic systems. This should help to increase the identification with the experiments they later participated in and raise awareness about the relevance of this kind of research for everyday life.

Fig. 1 Panic experiment according to Mintz. Every pupil is assigned a cord with a wedge on its end lying in a bottle with a narrow neck. If every student pulls at the same time and as fast as possible, the wedges block at the bottleneck. On the other hand, behaving in a coordinate way leads to a smooth process that is significantly faster (*Photo* V. Ziemer, U. Wuppertal)

3 Experimental Set-Up and Procedure

The experiments were performed in two schools in Wuppertal. Students of four classes participated as part of project work. The experimental room was built in the school's assembly hall.

3.1 Experimental Set-Up

The experimental area was a square room of 5×5 m^2 bounded by several small buckets. In the centre of this area there was a square starting area of 3×3 m^2 denoted by the white marks. The students stepped into the room through the entrance that is shown below in Fig. 2 and assembled in the starting area. During the evacuation they had to leave the room using the exit on the left side. The exit door was built by two upstanding platforms and had a variable width changing between 0.8 and 1.2 m. The area behind the door was connected to the waiting area before the entrance, so the students could walk on a closed path. For the collection of data all experiments were recorded by a camera system. This system was mounted on the hall's ceiling and contained customary digital cameras and GoPros.

All students wore caps of different colour. Each colour represented a certain interval of body heights. The body height of each pupil was measured before the

Fig. 2 The experimental area consists of a square room of 5×5 m^2, with a starting area in the middle. The pupils had to leave this room through the exit at the left. They wore colourful caps to distinguish the different body heights

experiments started. This information is needed to determine the position accurately, but the different colours can also be used to draw conclusions about the composition of the group of evacuating pupils later in the video. All caps showed also a black point at the middle of the head. That allows to recognise and track each person in the video.

3.2 Experimental Procedure

In general, the pupils had to perform several evacuation runs. For each run, a group of 32–46 persons assembled in the starting area, distributed nearly uniformly. During the evacuation, the students were allowed to use the whole experimental area.

After a starting signal, the participants had to leave the room using the exit door. They should walk briskly and evacuate the room as fast as possible. The pupils were told to imagine there would be a kind of danger, like fire or smoke. However, they were not allowed to run, scramble or push each other. After leaving the room they had to assemble again in the waiting area in front of the entrance and to wait for the next run.

The group of pupils that was placed into the experiment was compound in different ways to consider different parameters.

The first parameter that was varied in the experiment was the composition of the entire group. At all, there were two different age classes allowing for three different group compositions. The crowd could consist only of children aged 10–12 years, only of young adults aged 15–17, or a mixture of both groups whereby children and youths were equally represented.

The second parameter concerned the social group size. In several runs, the students had either to evacuate on their own without regarding the others around them, or to form pairs, or larger social groups. These groups could contain four, six or eight persons. Within one pair or social group the students had to try to stay together during the evacuation run.

As a third parameter we considered the interaction within the social group. The nature of the interaction can be specified by (i) its strength and (ii) the hierarchy of group members. Regarding the interaction strength, the group members could either be connected loosely, by just trying to stay together via eye contact, or they could have a fixed bond. A fixed bond was realised by holding each other's hand or some other physical contact. Furthermore, hierarchy of the group members could be different. In the first case, all partners were treated equally. Each group member had to leave the room and to stay together with their partners. In the other case, one student was declared as the 'leader', the other one as the 'follower'. The leader had to leave the room without regarding its partner or the other students, whereas the follower just had to follow the leader through the room.

This leads to four different ways to form pairs during the evacuation run. In the case of age-matched partners, the leader was chosen randomly. For the runs with the mixed crowd, the pairs were composed of one child and one teenager that took the part of the leader in the runs they were needed. All runs with larger social groups were done with loose bonds. In social groups of same age, there was no leader, but in mixed social groups one of the youths was declared as the leader.

To analyse the experiments the videos of the camera system that was mounted on the hall's ceiling was available. For each run of the experiment there is a video sequence. Using the `PeTrack` software [1], it is possible to extract the trajectories for each person and each run. The students were recognised via the black point in the middle of their coloured caps. The position of this point was tracked in each frame, generating the trajectory of each participant.

4 Analysis

First, we focus on the analysis of the data regarding the influence of group size on the evacuation scenario. Therefore, we use the data of one school and of the runs with larger groups. Most of these experiments were performed only with the older pupils with loose bonds and no leader-follower relationship, to which we restrict our analysis for now.

In different runs, the students formed groups of four, six and eight persons. In addition, one run with groups of six students and with an explicitly cooperative behaviour within the group was performed. They should concentrate a bit more on their group members and try to leave the room together. For comparison, we also consider the run with pairs and a loose bond that can be seen as a smaller group of two persons.
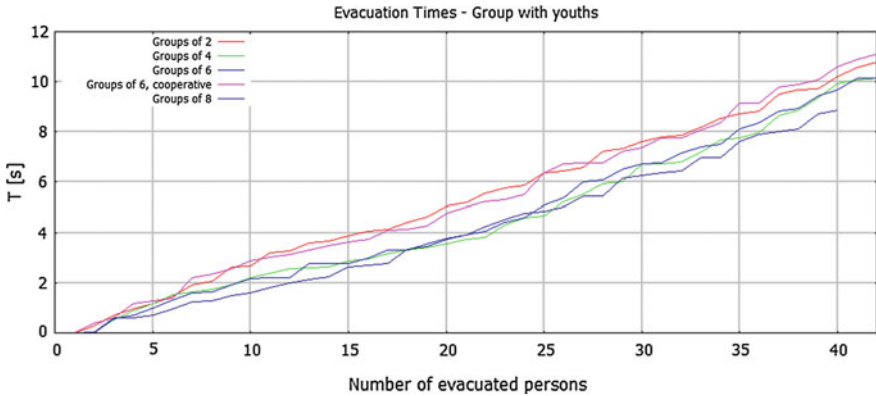
Fig. 3 Evacuation times for larger groups of one of the schools. The splitting of the curves into two groups is obvious. The shorter evacuation times belong to the runs with larger groups of four, six and eight persons, the longer ones to those with pairs and cooperative behaviour

4.1 Evacuation Times for Large Groups

First, we consider the evacuation time. In Fig. 3, we plot the number of evacuated persons against the time needed to leave the room. The results can be compared between the different runs.

The evacuation time for each person is defined as the time difference between the beginning of the evacuation and the moment when the person passes the door, exactly when he/she leaves the aisle that is formed by the two platforms. The beginning of the evacuation can be determined only approximately because the starting signal is not audible in the videos that are used for the extraction of the trajectories. For extracting the evacuation times we set the beginning on the moment of the first movement towards the door. However, for the analysis the influences of this inaccurate definition, the pre-movement time or other delays should be minimised. In doing so, we take the evacuation time of the very first person that left the room and subtract it from all the other times. Thereby, all plots start at zero for the first person and it is easier to compare different runs.

For the analysis of the runs with larger groups the evacuation times are shown in Fig. 3. All graphs show a nearly linear behaviour that could be expected. At the beginning of the evacuation all evacuation times are roughly the same. Between three and six evacuated persons the curves start to split into two groups. After increasing slightly, the difference between the two progresses remains nearly constant until the end of the evacuation. The main insight is that there are several runs that are clearly faster than other ones.

The upper two curves represent the evacuation in pairs and in groups of six with very cooperative behaviour. The lower graphs show the runs with larger groups of four, six and eight persons. Within the two groups of curves the differences are not large enough to separate the runs from each other. However, in the lower group,
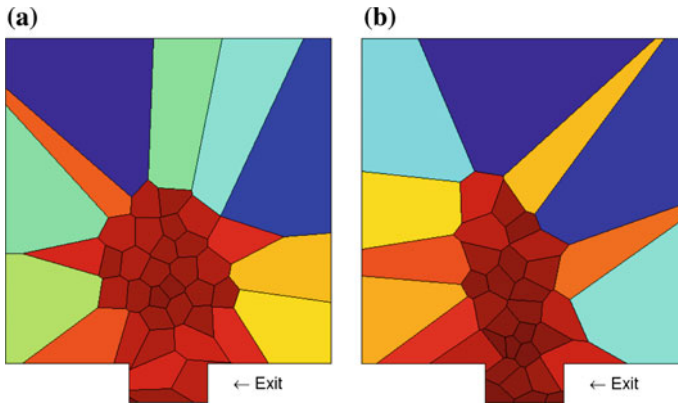
Fig. 4 Voronoi cells for each person in the room at time 4 s for the runs with pairs (**a**) and social groups of four persons (**b**). The colour of each cell depends on its size as a measure of density

the run with eight participants per group seems to be a bit faster at the end of the evacuation. The run with six participants per group and cooperative behaviour is clearly slower than the run with same group size but without this instruction. These results indicate that forming groups is advantageous for the evacuation, whereas behaving cooperatively inhibits this effect.

While looking for reasons for the differences in evacuation times, one first approach could be to determine the density distribution. Therefore, we determined the Voronoi cells [6, 7] within the experimental room for each person at different times. As a measure of density we coloured all cells dependent on their size: smaller cells are coloured in shades of red, larger ones in blue.

In Fig. 4 the density distributions for the run with pairs and with groups of four persons are shown. It is clearly seen that the distribution for the run in (b) is a bit narrower than the other one at the same time step. That means when forming groups, the children order rather behind each other than next to each other in front of the door. This behaviour seems to be advantageous for evacuating the room as it leads to a shorter evacuation time.

4.2 First Attempts to Interpretation

The results obtained so far suggest certain interpretations which, however, need to be substantiated by further experiments with better statistics. It is obvious from the plot of the evacuation times that increasing the group size leads to a decrease in evacuation times. The density distributions show the pupils ordered in different ways for forming groups than for pairs. A possible explanation is that the persons subordinate within the group and just follow the other group members. Because of that, there may be less conflicts between persons that meet at the door in competing for space. A person

is just in competition with persons of other groups, not with own group members. Increasing the group size reduces the number of possible competitors. This reduction of conflicts may have a positive influence on the evacuation time.

When the children have to show cooperative behaviour, the evacuation is slower than without this instruction. It is a possible explanation that here the effort to stay together is larger and reduces the effort to leave the room.

5 Summary and Outlook

We performed experiments under laboratory conditions to determine the influence of social groups on evacuations. A comparison of evacuation times between runs with different group sizes shows that increasing the group sizes lowers the evacuation time. The participants order in a different way for larger groups.

These first preliminary results have to be analysed in more detail. The statistics need to be improved by further experiments. However, with the help of the density distributions, photographs of the finish and the data of the second school we hope to get more information from the present experiments, e.g. about the microscopic mechanisms especially close to the exit. In addition, there are some few parameters that should also be analysed, e.g. the effect of body size and age.

References

1. Boltes, M., Seyfried, A., Steffen, B., Schadschneider, A.: Automatic extraction of pedestrian trajectories from video recordings. In: Pedestrian and Evacuation Dynamics 2008, pp. 43–54. Springer (2010)
2. Mintz, A.: Non-adaptive group behaviour. J. Abnorm. Soc. Psychol. **46**, 150–159 (1951)
3. Müller, F., Schadschneider, A.: Evacuation dynamics of asymmetrically coupled pedestrian pairs. In: Traffic and Granular Flow '15 (2016)
4. Müller, F., Wohak, O., Schadschneider, A.: Study of onfluence of groups on evacuation dynamics using a cellular automaton model. Transp. Res. Procedia **2**, 168–176 (2014)
5. Nagel, K., Schreckenberg, M.: A cellular automaton model for freeway traffic. J. Phys. **I**(2), 2221–2229 (1992)
6. Steffen, B., Seyfried, A.: Methods for measuring pedestrian density, flow, speed and direction with minimal scatter. Phys. A **389**, 1902–1910 (2010)
7. Voronoi, G.: Nouvelles applications des paramètres continus à la théorie des formes quadratiques. deuxième mémoire. recherches sur les parallélloèdres primitifs. Journal für die reine und angewandte Mathematik **134**, 198–287 (1908)

Detection of Steady State in Pedestrian Experiments

Weichen Liao, Antoine Tordeux, Armin Seyfried, Mohcine Chraibi, Xiaoping Zheng and Ying Zhao

Abstract Initial conditions could have strong influences on the dynamics of pedestrian experiments. Thus, a careful differentiation between transient state and steady state is important and necessary for a thorough study. In this contribution a modified CUSUM algorithm is proposed to automatically detect steady state from time series of pedestrian experiments. Major modifications on the statistics include introducing a step function to enhance the sensitivity, adding a boundary to limit the increase, and simplifying the calculation to improve the computational efficiency. Furthermore, the threshold of the detection parameter is calibrated using an autoregressive process. By testing the robustness, the modified CUSUM algorithm is able to reproduce identical steady state with different references. Its application well contributes to accurate analysis and reliable comparison of experimental results.

W. Liao (✉) · Y. Zhao
Beijing University of Chemical Technology, Beijing 100029, China
e-mail: w.liao@fz-juelich.de

Y. Zhao
e-mail: zhaoy@mail.buct.edu.cn

W. Liao · A. Tordeux · A. Seyfried · M. Chraibi
Forschungszentrum Jülich GmbH, 52428 Jülich, Germany
e-mail: a.tordeux@fz-juelich.de

A. Seyfried
e-mail: a.seyfried@fz-juelich.de

M. Chraibi
e-mail: m.chraibi@fz-juelich.de

A. Tordeux
Bergische Universität Wuppertal, 42119 Wuppertal, Germany

X. Zheng
Tsinghua University, Beijing 100084, China
e-mail: asean@mail.tsinghua.edu.cn

1 Introduction

In the past decades well-controlled laboratory experiments with pedestrians were per-
formed all around the world. Most of them were conducted in Europe, for instance
the recent works in Netherlands [5], France [11], Italy [20], Spain [8], Czech Repub-
lic [1], United Kingdom [6] and Germany [18]. Others were carried out mainly in
Japan [7], India [3], United States [4] and China [12]. During the analysis and com-
parison of these experiments, researchers focused on collective phenomena [9, 17]
and transport characteristics of pedestrian dynamics [13, 19]. However, few works
paid attention to how the quantities depend on the initial conditions and how the
characteristics change in time.

During a run of an experiment, the quantities to describe pedestrian dynamics
changes with time and space. Even in the same spatial area the quantities do not
remain constant. This variation is called transient state, which is caused by initial
conditions. Correspondingly, the state where the mean value, standard deviation
and autocorrelation are constant is called steady state, which is a good indicator to
show the independency of the system from the initial conditions. Thus, a careful
differentiation between transient state and steady state is a key point to the analysis
and comparison of pedestrian experiments. Nevertheless, few studies considered
the influence of the initial conditions by scrutinising the states. Rupprecht et al.
[16] investigated pedestrian flow with different segments of the time series. The
comparison shows these flows have different trends, which proves the change of state
has an influence on pedestrian dynamics. However, the difference between transient
state and steady state was not analysed. Cepolina [2] investigated the time series of
pedestrian flow. The flow changes obviously in transient state while keeps constant
in steady state. However, the method to detect steady state was not studied. Liao et
al. [13] proposed to select steady state manually from the time series of density and
speed. But this manual selection process is not uniquely reproducible. Krausz et al.
[10] proposed to use Cumulative Sum Control Chart (CUSUM) algorithm to detect
steady state automatically from the optical flow computations. However, the usage
of CUSUM algorithm is restricted to independent time series with a large amount of
observations, while the time series in pedestrian experiments are normally dependent
with limited observations. To our best knowledge, no uniform method is defined to
detect automatic and reproducible steady state in pedestrian dynamics.

To solve this problem we propose a modified CUSUM algorithm. The original
CUSUM algorithm is introduced in Sect. 2. The modification and the calibration are
described in Sects. 3 and 4, respectively. The robustness of the modified CUSUM
algorithm is verified in Sect. 5. Finally, the summary is made in Sect. 6.

2 CUSUM Algorithm

The CUSUM algorithm is a sequential analysis technique for monitoring transitions
[15]. The precondition is a time series covering the observations in all situations,
as well as a reference excluding the outliers. In pedestrian experiments let $(x_i)_{i=1}^n$
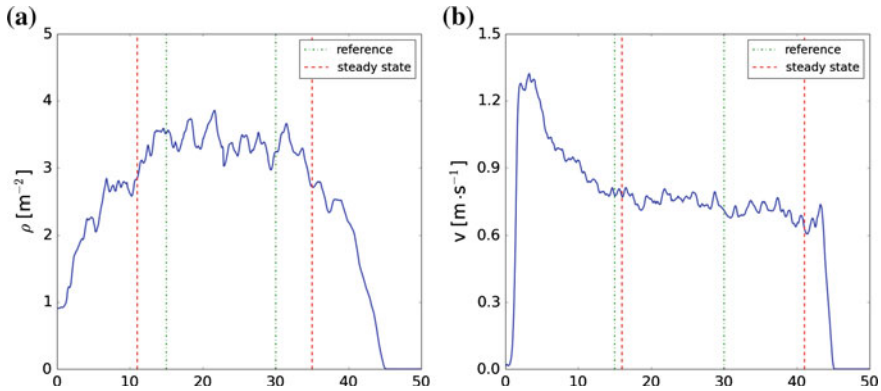
Fig. 1 The interval between the two *dash-dotted lines* is the manually selected steady state, which is regarded as the reference. The interval between the two *dashed lines* is the automatically detected steady state by the CUSUM algorithm. Density (**a**); speed (**b**)

denote the time series of density or speed (see the curve in Fig. 1). The manually selected steady state can be regarded as the reference $(x_i)_{i=j}^{m}$ ($j \geq 1$ and $m \leq n$) (see the interval between the two dash-dotted lines in Fig. 1).

The histogram for the distribution probability of the reference is plotted in Fig. 2. The curve shows the kernel estimation of the distribution, which is used to smooth the histogram. With the kernel estimation the upper percentile $Q(\alpha)$ and the lower percentile $Q(1 - \alpha)$ are better estimated.

Statistics s_i^+ and s_i^- are calculated as follows [15]:

$$s_i^+ = \max\{0, s_{i-1}^+ + x_i - Q(\alpha)\}, \quad s_0^+ = 0, \tag{1}$$

$$s_i^- = \max\{0, s_{i-1}^- + Q(1 - \alpha) - x_i\}, \quad s_0^- = 0. \tag{2}$$
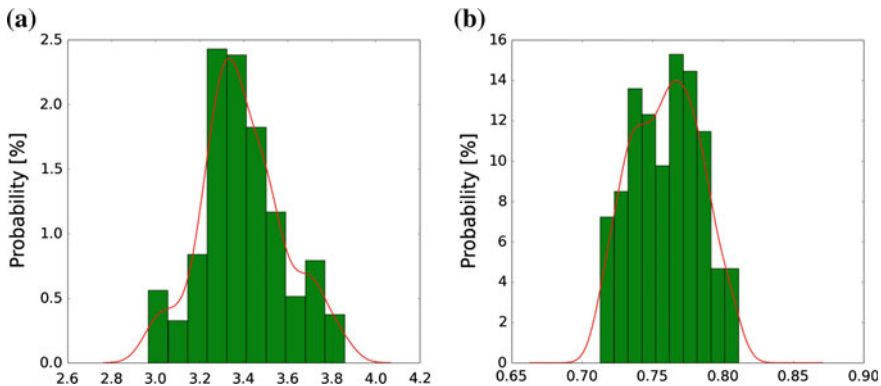
Fig. 2 Histogram for the distribution probability of the reference. The *curve* is the kernel estimation of the distribution. Density (**a**); speed (**b**)

(a)

(b)
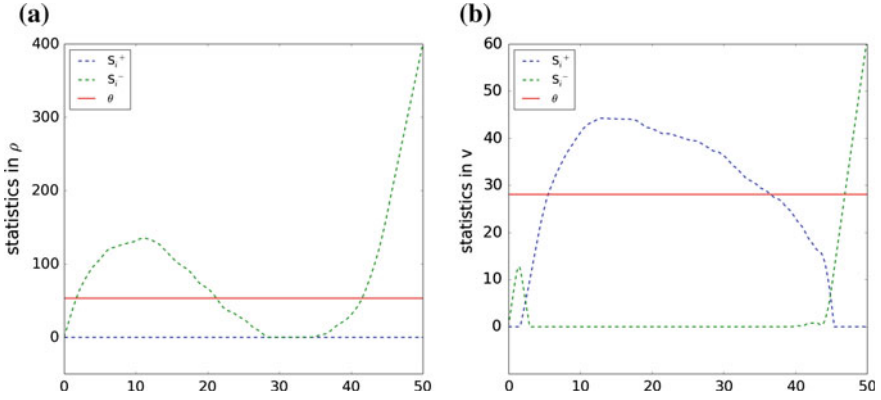
Fig. 3 Detection process by the original CUSUM algorithm: density (**a**); speed (**b**)

The statistics of the time series $(x_i)_{i=1}^{n}$ reflect the fluctuation degree. Higher statistics represent larger fluctuations, which might indicate a transition (see Fig. 3). The statistics of the reference $(x_i)_{i=j}^{m}$ are used to estimate the threshold of the detection parameter θ by the upper percentile.

Combining the statistics of the time series and the threshold, the intersections in Fig. 3 represent the detected transitions. One should note that these detected transitions are not the real ones in the time series. The detection process itself has a reaction time when reaching and leaving the transition:

$$t_{\text{reaching}} = (\max\{s_i\} - \theta)/f, \tag{3}$$

$$t_{\text{leaving}} = \theta/f, \tag{4}$$

where f is the frame number per second in the time series. Thus the real transition is the detected transition minus the corresponding reaction time. In Fig. 3 the interval where the statistics below the threshold is the steady state. The corresponding illustration is shown by the interval between the two dashed lines in Fig. 1.

3 Modification

The original CUSUM algorithm is able to detect steady state, but the detection process has deficiencies. The major one is that the statistics are not sensitive to the fluctuations (see Fig. 3). To overcome this point a step function is introduced to enhance the sensitivity:

$$F(\tilde{x}_i) = 1 \quad \text{if} \quad |\tilde{x}_i| > q(\alpha), \tag{5}$$

$$F(\tilde{x}_i) = -1 \quad \text{if} \quad |\tilde{x}_i| \leq q(\alpha), \tag{6}$$
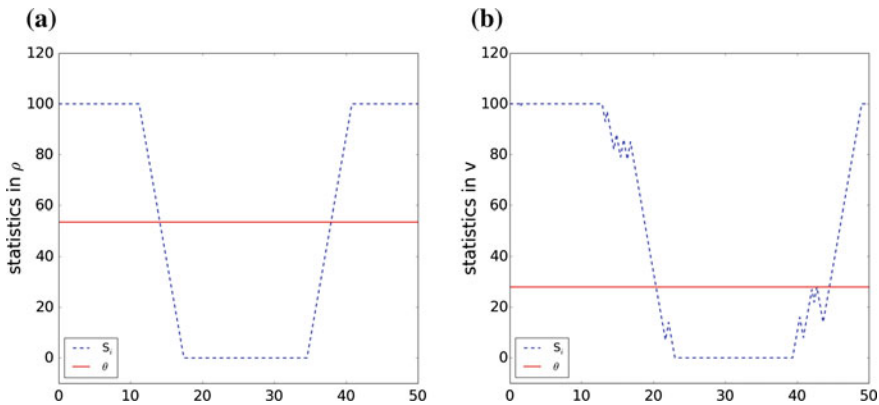
Fig. 4 Detection process by the modified CUSUM algorithm: density (**a**); speed (**b**)

where $q(\alpha)$ is the upper percentile of a standard normal distribution $N(0, 1)$. $\tilde{x}_i$ is the standard score transformation of the time series $(x_i)_{i=1}^n$:

$$\tilde{x}_i = (x_i - \mu)/\sigma, \tag{7}$$

where μ and σ are the mean value and standard deviation of $(x_i)_{i=j}^m$, respectively. Another deficiency is the non-limitation for the statistics, which might lead to an overlong transition. To avoid this situation a boundary $s_{\max} = 100$ is added to limit the increase of the statistics. Moreover, the statistics s_i^+ and s_i^- are calculated separately but then combined to detect steady state. To improve the redundant calculation new statistics $(s_i)_{i=1}^n$ are introduced:

$$s_i = \min\{\max\{0, s_{i-1} + F(\tilde{x}_i)\}, s_{\max}\}, \quad s_0 = s_{\max}. \tag{8}$$

After the modification, the statistics show clear and sensitive response to the fluctuations (see Fig. 4).

4 Calibration

Different methods can be used to calibrate the threshold of the detection parameter θ. The regular way is taking the reference $(x_i)_{i=j}^m$ directly, which requires enough observations in the reference. Since the duration of pedestrian experiments is relatively short, this way is not suitable for our work. Another way is using bootstrap method to extend the number of the observations. However, this method requires observations independent of each other, which is not realistic in our work. Thus we propose an autoregressive process $(y_i)_{i=1}^T$ to model the standard score of the reference $(x_i)_{i=j}^m$:

Fig. 5 Verification of the
robustness for the modified
CUSUM algorithm. The
detection process with three
different references gives
similar steady state
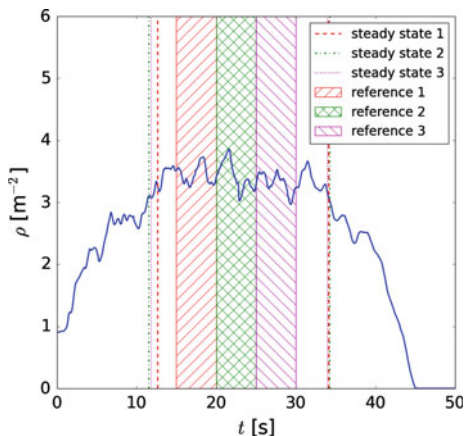
$$y_i = c \cdot y_{i-1} + \sqrt{1 - c^2} \cdot \varepsilon_i, \quad y_0 = 0. \qquad (9)$$

where c is the first autocorrelation of the reference, and $(\varepsilon_i)_{i=1}^T$ are independent
normal random variables. The modelling process can be achieved by both simulations
and analytics (see [14]).

5 Robustness

To test the robustness of the modified CUSUM algorithm, three different references
are selected from the same time series (see Fig. 5). Then, the detection process is
repeated under the same conditions. Figure 5 shows the detected steady state based
on different references is almost identical. This illustrates the modified CUSUM
algorithm is able to reproduce the same result between different researchers.

6 Summary

In the analysis of pedestrian experiments, finite size in time, space and events could
influence the system. Thus, it is necessary and important to carefully distinguish
between transient state and steady state. For this reason we propose a modified
CUSUM algorithm to automatically detect steady state from time series of pedes-
trian experiments. Major modifications on the statistics include introducing a step
function to enhance the sensitivity as well as adding a boundary to limit the increase.
In addition, the calculation is simplified to raise the computational efficiency. Further-
more, the threshold of the detection parameter is calibrated. Considering the fact that
the time series in pedestrian experiments are normally with limited and dependent
observations, an autoregressive process is employed to accomplish the calibration.

Verifying the robustness by using the same time series with different references, the modified CUSUM algorithm is proved to reproduce identical steady state. The application of the modified CUSUM algorithm well contributes to accurate analysis and reliable comparison of experimental results.

References

1. Bukáček, M., Hrabák, P., Krbálek, M.: Experimental analysis of two-dimensional pedestrian flow in front of the bottleneck. In: Traffic and Granular Flow'13, pp. 93–101. Springer (2015)
2. Cepolina, E.M.: Phased evacuation: an optimisation model which takes into account the capacity drop phenomenon in pedestrian flows. Fire Saf. J. **44**(4), 532–544 (2009)
3. Chattaraj, U., Seyfried, A., Chakroborty, P.: Comparison of pedestrian fundamental diagram across cultures. Adv. Complex Syst. **12**(03), 393–405 (2009)
4. Christensen, K., Sharifi, M.S., Stuart, D., Chen, A., Kim, Y.S., Chen, Y.: Overview of a large-scale controlled experiment on pedestrian walking behavior involving individual with disabilities. In: The 93rd Annual Meeting of the Transportation Research Board. Washington D.C., Jan 2014
5. Duives, D., Daamen, W., Hoogendoorn, S.: Anticipation behavior upstream of a bottleneck. Transp. Res. Procedia **2**, 43–50 (2014)
6. Fernández, R., Valencia, A., Seriani, S.: On passenger saturation flow in public transport doors. Transp. Res. Part A: Policy Pract. **78**, 102–112 (2015)
7. Fujii, K., Sano, T.: Experimental study on crowd flow passing through ticket gates in railway stations. Transp. Res. Procedia **2**, 630–635 (2014)
8. Garcimartín, A., Pastor, J., Ferrer, L., Ramos, J., Martín-Gómez, C., Zuriguel, I.: Flow and clogging of a sheep herd passing through a bottleneck. Phys. Rev. E **91**(2), 022808 (2015)
9. Helbing, D., Farkas, I., Vicsek, T.: Simulating dynamical features of escape panic. Nature **407**(6803), 487–490 (2000)
10. Krausz, B., Bauckhage, C.: Loveparade 2010: automatic video analysis of a crowd disaster. Comput. Vis. Image Underst. **116**(3), 307–319 (2012)
11. Lemercier, S., Moreau, M., Moussaïd, M., Theraulaz, G., Donikian, S., Pettré, J.: Reconstructing motion capture data for human crowd study. In: Motion in Games, pp. 365–376. Springer (2011)
12. Lian, L., Mai, X., Song, W., Richard, Y.K.K., Wei, X., Ma, J.: An experimental study on four-directional intersecting pedestrian flows. J. Stat. Mech. Theory Exp. **2015**(8), P08024 (2015)
13. Liao, W., Seyfried, A., Zhang, J., Boltes, M., Zheng, X., Zhao, Y.: Experimental study on pedestrian flow through wide bottleneck. Transp. Res. Procedia **2**, 26–33 (2014)
14. Liao, W., Tordeux, A., Seyfried, A., Chraibi, M., Drzycimski, K., Zheng, X., Zhao, Y.: Measuring the steady state of pedestrian flow in bottleneck experiments. Phys. A: Stat. Mech. Appl. (2016 in press). doi:10.1016/j.physa.2016.05.051
15. Page, E.: Continuous inspection schemes. Biometrika **41**(1/2), 100–115 (1954)
16. Rupprecht, T., Klingsch, W., Seyfried, A.: Influence of geometry parameters on pedestrian flow through bottleneck. In: Pedestrian and Evacuation Dynamics, pp. 71–80. Springer (2011)
17. Schadschneider, A., Klingsch, W., Klüpfel, H., Kretz, T., Rogsch, C., Seyfried, A.: Evacuation dynamics: empirical results, modeling and applications. In: Meyers, R.A. (ed.) Extreme Environmental Events, pp. 517–550. Springer (2011)
18. Seitz, M.J., Dietrich, F., Köster, G.: The effect of stepping on pedestrian trajectories. Phys. A: Stat. Mech. Appl. **421**, 594–604 (2015)
19. Seyfried, A., Passon, O., Steffen, B., Boltes, M., Rupprecht, T., Klingsch, W.: New insights into pedestrian flow through bottlenecks. Transp. Sci. **43**(3), 395–406 (2009)
20. Shimura, K., Ohtsuka, K., Vizzari, G., Nishinari, K., Bandini, S.: Mobility analysis of the aged pedestrians by experiment and simulation. Pattern Recogn. Lett. **44**, 58–63 (2014)

Statistical Models for Pedestrian Behaviour in Front of Bottlenecks

Nikolai W.F. Bode and Edward A. Codling

Abstract Understanding the movement of human crowds is important for our general understanding of collective behaviour and for applications in building design and event planning. Here, we focus on the flow of a crowd through a narrow bottleneck. We develop statistical models that describe how pedestrian behaviour immediately in front of a bottleneck affects the time lapse between consecutive pedestrians passing through the bottleneck. With this approach, we isolate the most important aspects of pedestrian behaviour from a number of candidate models. We fit our models to experimental data and find that pedestrian interactions immediately in front of the bottleneck appear to be less important for the observed time lapses than interactions further away from the bottleneck. Furthermore, we demonstrate how our approach can be used to rigorously compare microscopic pedestrian behaviours across different contexts by fitting the same statistical models to three separate datasets. We suggest that our approach is a promising tool to establish similarities and differences between simulated and real pedestrian behaviour.

1 Introduction

The movement of human crowds is an important example of collective behaviour and an understanding of such systems is important for applications in building design and event planning [9]. The general consensus is that interactions between individuals are crucial to the observed dynamics at the level of the crowd. This immediately leads to two questions. First, how do individuals interact? Second, do these interactions differ across contexts? Here, we present a framework to address both of these questions.

N.W.F. Bode (✉)
Department of Engineering Mathematics, University of Bristol,
Merchant Venturers Building, Woodland Road, Bristol BS8 1UB, UK
e-mail: nikolai.bode@bristol.ac.uk

E.A. Codling
Department of Mathematical Sciences, University of Essex, Wivenhoe Park,
Colchester CO4 3SQ, UK
e-mail: ecodling@essex.ac.uk

We focus on the paradigmatic and well-studied example of pedestrian crowds passing through narrow bottlenecks, such as exit doors. It is possible to address the aforementioned questions indirectly. For example, the average relationship between the speed of individuals and the density of crowds or the distribution of crowds in front of and inside bottlenecks provide insights into how pedestrians use the available space, whether they maintain a personal space around them and to what extent the presence of others obstructs their movement [8, 10]. Egress times can be used to investigate how different contexts (e.g. motivation of individuals) can affect the movement of a crowd [6]. Computer simulations are another well-accepted approach to explore the movement dynamics produced by different hypothesised models for interactions between individuals [9]. In contrast to such indirect approaches, our framework uses experimental, observational or simulated data to directly infer the most likely model for interactions between individuals from a set of candidate models.

For narrow bottlenecks, a conveniently measured quantity is the time lapse (or headway) between consecutive pedestrians passing through the exit. The distribution of these time lapses provides important insights: the mean is related to the pedestrian flow and the frequency of large values indicates the likelihood of jams, time-points when the flow of pedestrians slows down temporarily. Previous work has investigated properties of the distribution of time lapses. For example, it has been suggested that the distributions have a power law tail [6]. Investigating the exponent of this power law tail provides fundamental insights into the properties of the system. Exponents below a value of 2 suggest that the mean of the distribution does not converge, but grows without an upper bound as sample sizes increase—a profound issue for the prediction of bottleneck blockages. However, this scenario does not seem to apply to the pedestrian data investigated to date [6]. To study wide bottlenecks, Hoogendoorn and Daamen [8] suggest a dedicated definition of time lapses that takes the distance orthogonal to the movement direction between pedestrians into account. The authors then used a model which assumes that time lapse distributions are composed of the contribution of freely walking pedestrians and constrained pedestrians (who walk behind others) to estimate for bottlenecks of different widths the proportion of constrained and unconstrained pedestrians, as well as the average time lapse between consecutive pedestrians and the bottleneck capacity [8]. Our work presents a departure from this previous work. We develop statistical models that describe how pedestrian behaviour immediately in front of the bottleneck affects the time lapse between consecutive pedestrians passing through the bottleneck. With this framework we isolate the most likely model for pedestrian behaviour from a number of candidate models. Furthermore, we demonstrate how our approach can be used to compare microscopic pedestrian behaviours across different contexts by fitting the same statistical models to three separate datasets.

2   Methods

Let t_p and t_{p-1} be the time points at which two consecutive pedestrians cross a line that marks a physical bottleneck (e.g. an exit). We assume that the bottleneck is narrow, so that only one pedestrian at a time can exit. We define $\Delta t_p = t_p - t_{p-1}$ to be

the time lapse between two consecutive pedestrians passing through this bottleneck. We propose statistical models that describe the random variable T_p which takes values Δt_p. We assume that Δt_p are distributed according to gamma distributions and the models take the general form $T_p \sim \Gamma(\mu_{p-1}, \sigma)$, where Γ denotes the gamma distribution with mean μ_{p-1} and variance σ. While we treat σ as a constant model parameter, we propose a number of models in which μ_{p-1} depends on the relative positions of pedestrians in front of the bottleneck. A different way of describing our approach is that we perform a gamma regression on the values of Δt_p using pedestrian positions in front of the bottleneck as predictors. Specifically, we use pedestrian positions at time $p - 1$, i.e. at the time point when the previous pedestrian has just entered the bottleneck to predict Δt_p. The rationale behind our models is that relative pedestrian positions could affect the length of time it will take the next pedestrian to enter the bottleneck. For example, if two pedestrians are close to the bottleneck and equidistant from it, deciding who gets to exit next may take longer than if one pedestrian is much closer to the exit than the other. We propose five explanatory factors for the mean of T_p.

The first explanatory factor is a constant: $m_0 = \alpha_1$, where α_1 is a model parameter. It represents an intercept for μ_{p-1} and thus an expected baseline for Δt_p regardless of the relative positions of pedestrians.

The second explanatory factor, m_1, captures the effect on Δt_p of how densely pedestrians are clustered around the bottleneck. Let $< d >_k$ be the average distance to the exit of the k pedestrians nearest to the bottleneck (at time t_{p-1}; $k = 2, \ldots, 5$). Here and in the following, distances to the bottleneck are measured from the pedestrian position to the centre of the line pedestrians cross when entering the bottleneck. Then we define $m_1 = (\alpha_2 < d >_k - \alpha_3)^2$, where k, α_2 and α_3 are model parameters. For example, very low values of $< d >_k$ indicate that many pedestrians are very close to the bottleneck which may lead to higher expected Δt_p (pedestrians may compete against each other to exit as quickly as possible).

The third and fourth explanatory factors investigate effects of the relative positions of the two pedestrians nearest to the bottleneck. We define d_{ij} to be the difference in distance and θ_{ij} to be the angle between the two pedestrians i and j closest to the bottleneck entrance. θ_{ij} is defined as the angle between the vectors pointing from the position of pedestrians i and j to the centre of the bottleneck entrance. The third and fourth explanatory factors are defined as $m_2 = (\alpha_4 d_{ij} - \alpha_5)^2$ and $m_3 = (\alpha_6 \theta_{ij} - \alpha_7)^2$, where $\alpha_4 \ldots \alpha_7$ are model parameters.

The fifth explanatory factor takes the distance of the pedestrian nearest to the bottleneck, d_i, into account: $m_4 = (\alpha_8 d_i - \alpha_9)^2$ (where α_8 and α_9 are model parameters). This explanatory factor is motivated by the observation that in the absence of interactions with other pedestrians, the distance to the bottleneck of the closest pedestrian is likely to be the determining factor for Δt_p.

We use the five explanatory factors defined above to formulate 16 models for the mean of Δt_p by considering all possible combinations of m_1, m_2, m_3 and m_4 whilst including m_0 into all models. The predicted mean for a given model is the sum over all explanatory factors included in the model. For example, the model that includes m_1 and m_3 has predicted mean $\mu_{p-1} = m_0 + m_1 + m_3$ (m_0 is included in all models). We will refer to the different models by the formula for their predicted mean

(e.g. "$m_0 + m_1 + m_3$"). By comparing the extent to which these different models are supported by our data, we can establish which out of our explanatory factors best predicts Δt_p.

We use a maximum likelihood approach to fit our models. Let $f_\Gamma(\Delta t_p; \mu_{p-1}, \sigma)$ be the probability density function of a gamma distribution with mean μ_{p-1} and variance σ evaluated at Δt_p. Then we define the likelihood, L, of a given model as:

$$L = \prod_p f_\Gamma(\Delta t_p; \mu_{p-1}, \sigma), \tag{1}$$

where the product runs over all observed data points, Δt_p (i.e. time lapses). In Eq. 1, we assume that separate time lapses are conditionally independent given our models or that our models explain any relationships between the probability densities for separate time lapses. We describe below how we assess the validity of this assumption. For each model, we find the parameter values that maximise the likelihood (requiring $\alpha_1, \alpha_2, \alpha_4, \alpha_6, \alpha_8, \sigma$ to be positive). From the maximum likelihood, L_{max}, we compute the Akaike Information Criterion (AIC), $AIC = 2n - 2\log(L_{max})$, where n is the number of model parameters. We then use the AIC for model selection: models with lower AIC are better supported by the data than models with higher AIC.

We use scaled deviance residuals to assess the fit of our models to the data [5]. We plot these residuals against the predicted values, μ_{p-1}. This allows us to check if individual data points have particularly large residuals and should thus be treated as outliers. Theory predicts that the mean of the residuals should be approximately zero and systematic changes in this mean for increasing fitted values are indicative of poor model fit, suggesting that model assumptions do not hold [5]. We also plot the residuals as time series to test for correlations in our data over time that are not explained by the models. If models fit the data well, we expect that there are no systematic trends in the residuals over time.

We apply this analysis to three separate datasets. The first dataset is obtained from experiments conducted on 1 October 2014 at the DANA centre of the Science Museum in London with a crowd of 51 and a crowd of 71 visitors. Participants were asked to walk at a normal speed through a 0.6 m wide bottleneck (1.5 m long) at the end of a 2 m wide corridor. At the start of the experiment, the crowd was lined up in the corridor 3 m away from the bottleneck. Experiments were filmed from above at a rate of 10 frames per second and the camera (Microsoft LifeCam HD-3000 webcam™) was positioned directly above the centre of the start of the bottleneck (see Fig. 1a). For each frame, the position of all visible pedestrians was obtained manually by determining the position of the centre of participants' heads. Pedestrian positions were obtained in pixels and not converted to metres, as for the purpose of our analysis only relative differences in distances matter. Time is given in seconds throughout. To reduce the sensitivity of our analysis to errors in tracked positions resulting from camera distortion, we focussed our analysis on the relative pedestrian positions directly in front of the bottleneck (e.g. low values of parameter k) where such errors are small due to the positioning of our camera. This dataset contained 325
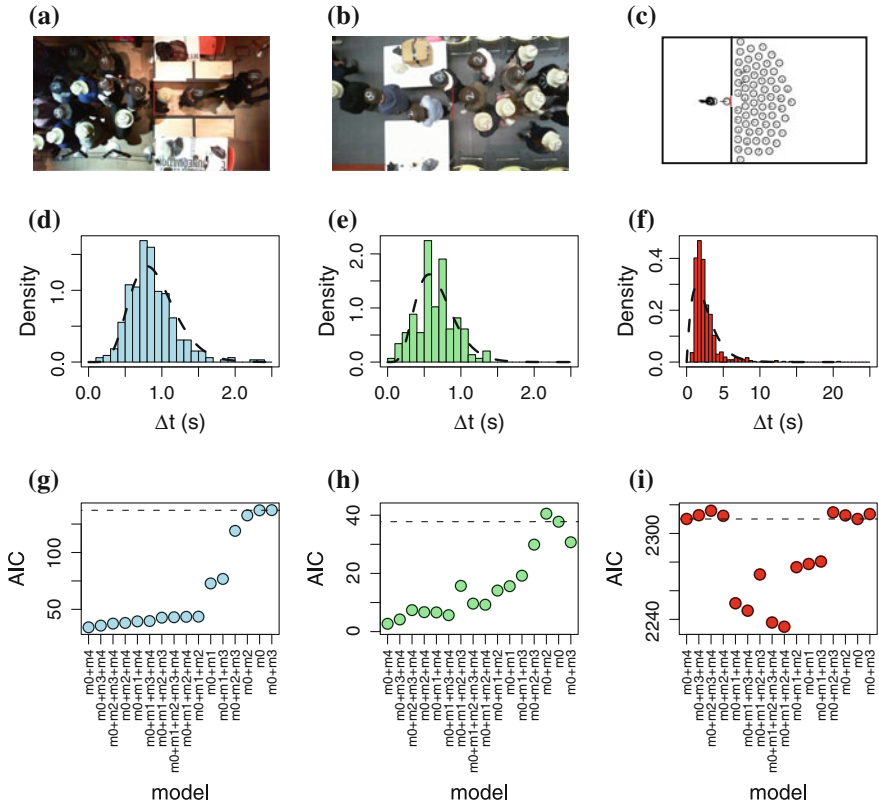
Fig. 1 Still images of experimental set-up in London (**a**), Bristol (**b**) and model simulations (**c**). *Red line* segments indicate the bottleneck location used in the analysis. time lapse distributions for the datasets presented in still images above (**d**–**f**). *Dashed lines* show gamma distribution fit corresponding to model m_0. AICs for all models analysed for the three datasets (**g**–**i**). Models are shown in the same order in all panels. *Dashed horizontal lines* indicate the AIC of the baseline model (m_0)

data points (1 run with 51 participants, 4 runs with 71 participants; we only consider time lapses when at least two pedestrians are still in front of the bottleneck).

The second dataset is obtained by repeating the same experiment with a group of 39 students at the University of Bristol on 11 March 2015. We used the same camera, but recorded at a rate of 15 frames per second (see Fig. 1b for a snapshot). This dataset contained 147 data points (4 runs with 39 participants; in one trial, the exit time of the last participant was not recorded).

The third dataset is obtained from simulations of a previously published model for pedestrian movement [1]. Briefly, pedestrians move in continuous two-dimensional space. The environment (e.g. walls), as well as preferred movement directions, are encoded in a discrete floor field [4] and interactions between pedestrians and the environment (e.g. avoiding walls) are modelled via forces acting on point masses [7]. We simulate crowds of 80 pedestrians, each with 0.5 m diameter, exiting a room

through one 0.8 m wide door (see Fig. 1c). At the start of simulations, pedestrians are distributed randomly inside the room. All other model details and parameters are given in previous work [1]. Simulation parameters are not fitted to the experimental data. In our simulated dataset, we aggregate the data from the first 200 s for 10 separate simulations. This results in 717 data points.

3 Results and Discussion

Figure 1d–f show the time lapse distributions for the three datasets we analyse. We begin by discussing the results for the first dataset to show how our framework can be used to identify the most likely model for pedestrian behaviour from our candidate models. Figure 1g shows the AICs for each model obtained from our maximum likelihood fits. We can see that most models are better supported by the data (i.e. have lower AICs) than the baseline model, m_0, which assumes time lapses are independent of the relative pedestrian positions in front of the bottleneck. It is also clear that our analysis does not simply favour more complex models. For example, the model with the most parameters, $m_0 + m_1 + m_2 + m_3 + m_4$, does not have the lowest AIC. Based on our results, the model that is best supported by the data is $m_0 + m_4$, in which time lapses depend on the distance of the pedestrian nearest to the bottleneck. At first glance this appears to be a trivial result: the closer individuals are to the exit, the less time it will take them to reach it. However, this model outperforms other models for interactions immediately in front of the bottleneck implying that such interactions are less predictive for the observed time lapses. This suggests that in this data the order in which pedestrians exit is already determined when individuals get close to the bottleneck meaning that interactions between pedestrians occur further away from the bottleneck. We caution that while this framework establishes the relative performance of different models, it should not be over-interpreted as determining the actual, true mechanism underlying pedestrian interactions: our approach is inherently probabilistic and only investigates a potentially incomplete set of candidate models.

Importantly, our analysis allows us to compare the relative performance of the different models across datasets (Fig. 1g–i). General trends in AICs indicate similarities or differences across contexts. The trends in AICs for our two experimental datasets are very similar (Fig. 1g, h), while the trend for the simulated dataset differs substantially from the others (Fig. 1i). For the simulated dataset, only models that include the contributing factor m_1 perform much better than the baseline model and the AIC of the model that is best supported in both experimental datasets, $m_0 + m_4$, does not even outperform the baseline model. The performance of models including m_1 for the simulated data suggests that the density of pedestrians in front of the bottleneck helps considerably to predict the time lapse between consecutive pedestrians. At this point we have to re-iterate that we have not fitted our simulations to the experimental data. Therefore, this result should not be interpreted to mean that our model or any similar model is based on fundamentally different interaction mechanisms than seen in experimental data. Rather, we show that our framework can be used to compare microscopic pedestrian behaviours across different contexts and datasets.
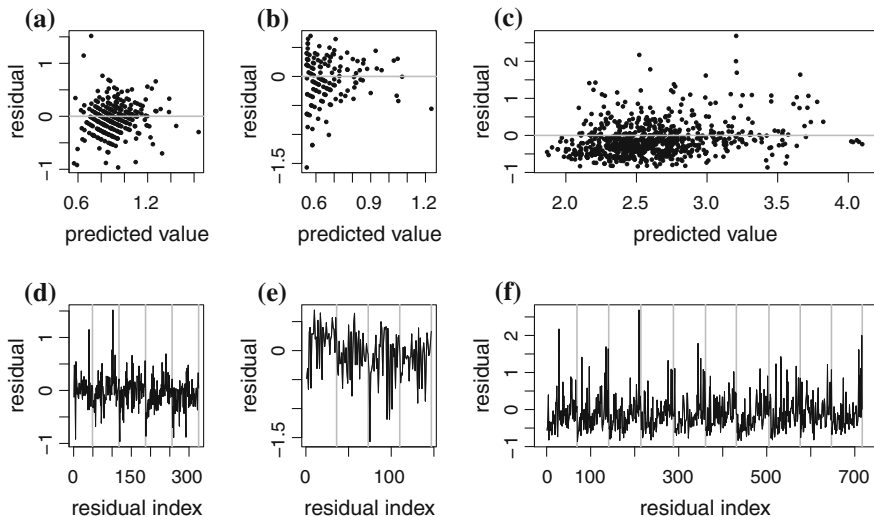
Fig. 2 Deviance residuals plotted against predicted mean time lapse for the model with the lowest AIC for the London (**a**), Bristol (**b**) and simulated (**c**) data. Plots of residuals ordered in time for the same data (**d**–**f**). *Vertical grey lines* separate data from different experimental or simulation runs

An additional advantage of our framework is that residuals provide a well-established approach to assess the fit of models to data. In Fig. 2 we show residual plots for the models with the lowest AIC for each dataset. There does not appear to be a systematic trend in residual means against predicted values (Fig. 2a–c). On close inspection, we find a consistent increase in residuals over time for each simulation run in the model data (Fig. 2f; multiple simulation runs are shown). In the experimental data, no such temporal correlations are immediately obvious (Fig. 2d, e). This suggests that our model does not capture aspects of the simulated data. One explanation for this result could be that our simulations implement forces between pedestrians: as the number of pedestrians in front of the bottleneck decreases, the pressure exerted on pedestrians by others behind them is decreased which results in longer time lapses. In this way, the analysis of residuals does not only highlight potential shortcomings of our statistical models, but it can also provide an additional way to highlight differences in interaction mechanisms between datasets.

4 Conclusions and Outlook

We have presented a framework of statistical models to analyse microscopic pedestrian behaviour in front of narrow bottlenecks. This approach allows us to isolate the most likely interaction mechanism from a list of possible mechanisms which can also be used to compare the behaviours underlying different simulations and datasets in a rigorous and quantitative way.

Our work presented here is a starting point and many extensions of our models to take different scenarios and behaviours into account are possible or even necessary depending on the context. For example, interactions within social groups, such as friends, could be considered [2]. Our framework could also be developed further to permit analysis of wider bottlenecks (an important topic, as wider bottleneck occur frequently and pedestrians appear to preferentially exit through wider bottlenecks [3]). Our models focus on interactions in front of bottlenecks but dynamics inside bottlenecks could have a strong influence on time lapses between consecutive pedestrians (e.g. consider a jammed bottleneck). If such dynamics are important, it is likely that our approach as presented here is not appropriate.

To test the usefulness of our framework, it will be necessary to apply our analysis to a wide variety of simulated, experimental and observational data. In particular, applying our analysis to experimental data in which the behaviour of individuals is controlled to some extent (e.g. motivation levels) would be very informative.

In conclusion, we suggest that our approach is a promising first step to directly establish mechanistic similarities and differences between simulated and real microscopic pedestrian behaviour.

References

1. Bode, N., Codling, E.: Human exit route choice in virtual crowd evacuations. Anim. Behav. **86**(2), 347–358 (2013)
2. Bode, N., Holl, S., Mehner, W., Seyfried, A.: Disentangling the impact of social groups on response times and movement dynamics in evacuations. PLoS ONE **10**(3), e0121227 (2015)
3. Bode, N., Kemloh Wagoum, A., Codling, E.: Information use by humans during dynamic route choice in virtual crowd evacuations. R. Soc. Open Sci. **2**, 140410 (2015)
4. Burstedde, C., Klauck, K., Schadschneider, A., Zittartz, J.: Simulation of pedestrian dynamics using a two-dimensional cellular automaton. Phys. A: Stat. Mech. Appl. **295**(3), 507–525 (2001)
5. Davison, A., Snell, E.: Residuals and diagnostics. In: Hinkley, D., Reid, N., EJ, S. (eds.) Statistical Theory and Modelling. Chapman and Hall, London (1991)
6. Garcimartín, A., Zuriguel, I., Pastor, J., Martín-Gómez, C., Parisi, D.: Experimental evidence of the faster is slower effect. Transp. Res. Procedia **2**, 760–767 (2014)
7. Helbing, D., Farkas, I., Vicsek, T.: Simulating dynamical features of escape panic. Nature **407**(6803), 487–490 (2000)
8. Hoogendoorn, S., Daamen, W.: Pedestrian behavior at bottlenecks. Transp. Sci. **39**(2), 147–159 (2005)
9. Schadschneider, A., Klingsch, W., Klüpfel, H., Kretz, T., Rogsch, C., Seyfried, A.: Evacuation dynamics: empirical results, modeling and applications. In: Encyclopedia of Complexity and Systems Science, pp. 3142–3176. Springer (2009)
10. Zhang, J., Seyfried, A.: Quantification of bottleneck effects for different types of facilities. Transp. Res. Procedia **2**, 51–59 (2014)

Congestion Dynamics in Pedestrian Single-File Motion

Verena Ziemer, Armin Seyfried and Andreas Schadschneider

Abstract This article considers execution and analysis of laboratory experiments of pedestrians moving in a quasi-one-dimensional system with periodic boundary conditions. To analyse characteristics of jams in the system we aim to use the whole experimental set-up as the measurement area. Thus, the trajectories are transformed to a new coordinate system. We show that the trajectory data from the straight and curved parts are comparable and assume that the distributions of the residuals come from the same continuous distribution. Regarding the trajectories of the entire set-up, the creation of stop-and-go waves in pedestrian traffic can be investigated and described.

1 Introduction

In recent years, many research groups have executed experiments with pedestrians, see e.g. [1, 4, 5, 10, 11]. One phenomenon which can be observed is a stop-and-go wave well-known from vehicular traffic, e.g., [2]. It is visible in the simplest system with a one-dimensional movement of pedestrians along a line with closed boundary conditions, e.g., for a ring [10] and for a circle [5].

In the following, we summarise previous work on one-dimensional pedestrian movements where stop-and-go waves were analysed. [10] executed the first one-dimensional experiments in 2005. For the first time high densities were examined in [7] and the existence of stop-and-go waves in pedestrian traffic was shown. In [7] also an adaptive velocity model with reaction time was proposed, which is able

V. Ziemer (✉)
Computer Simulation for Fire Safety and Pedestrian Traffic, Bergische
Universität Wuppertal, 42285 Wuppertal, Germany
e-mail: verena.ziemer@uni-wuppertal.de

A. Seyfried
Jülich Supercomputing Centre, Forschungszentrum Jülich GmbH,
52425 Jülich, Germany
e-mail: a.seyfried@fz-juelich.de

A. Schadschneider
Institut für Theoretische Physik, Universität zu Köln, 50937 Köln, Germany
e-mail: as@thp.uni-koeln.de

to reproduce qualitatively similar stop-and-go waves as they are observable in the experimental data, see [9]. A coexistence of two differing speed phases in this data was shown in [8] by analysing the fundamental diagram in specific density regions. A model that reproduces this coexistence was also proposed. The same experimental data was taken in [3] to test a stochastic headway dependent velocity model. [5] compared data from a circle with data from a straight line. Besides the free flow and congested regime of the fundamental diagram they found a third regime between both, named weakly constrained regime.

In [9], the measurement section of the nearly 27 m long corridor with closed boundary conditions covers 4 m only. This restriction makes it impossible to test models concerning number and dimension of a stop-and-go wave because of lack of data. A second restriction is the duration of an experiment run. In experiments, the duration may be too short to reach a stable state. That is why the lifetime of a stop-and-go wave, its length in space and the number of stop-and-go waves in the system cannot be observed.

In this article, we want to handle this problem. Experiments where the whole system was observed are analysed. Furthermore, we introduce a methodology to analyse characteristics of stop-and-go waves.

2 Experiments

Laboratory experiments were performed within the framework of the project BaSiGo in June 2013. The aim of those experiments is a better understanding of pedestrian dynamics in critical crowded states, e.g., in front of an entrance to a concert hall, thus in high densities. It included large-scale experiments in various scenarios with up to 1000 pedestrians per run during five days. The probands were mostly students (55 % male and 45 % female) at the age of 18–72 years, 25 years on average, with an average height of 1.71 m and received 50 € per day. 13 % of them were living in suburbs or rural areas and 68 % in cities or major cities.

2.1 Experimental Set-Up

One-dimensional laboratory experiments for pedestrians in a system with periodic boundary conditions were executed see Fig. 2a. The set-up is a ring corridor with a circumference about $C = 26.5$ m ($r_0 = 3$ m, $l = 4$ m). Six runs were performed with different numbers of participants ($N = 15, 30, 47, 55, 52, 59$) so that the global density ($\rho_g = N/C$) ranges from 0.57 to 2.27 ped/m. For each run, the pedestrians initially are arranged uniformly in the set-up. Then, there are two commands, the first to start walking with normal speed in the corridor and the second for stopping.

2.2 Data Collection

To enable the automatic tracking of the trajectories, the pedestrians wear hats with a marker. For each run the whole set-up was recorded from the top video camera
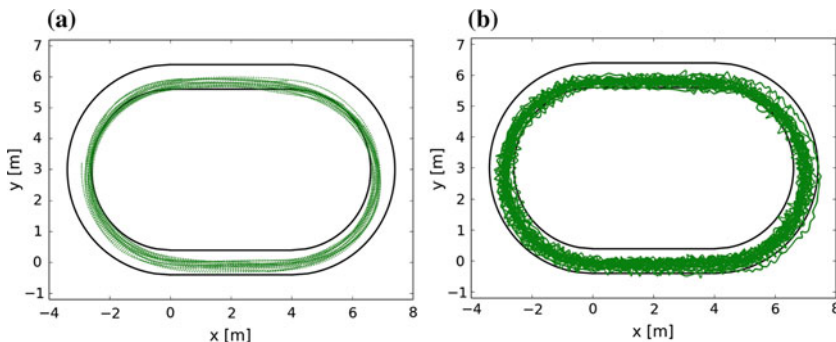
Fig. 1 Extracted trajectories for various values of N: $N = 15$ (**a**); $N = 59$ (**b**)

with a frame rate of 16 fps. From those video recordings pedestrian trajectories who are describing the movement of the heads of the pedestrians were extracted. For more details to this method we refer to [6] in these proceedings. Figure 1 shows the trajectories for the runs with $N = 15$ and $N = 59$ which leads to the global density 0.57 ped/m and 2.27 ped/m, respectively.

2.3 Data Preparation

We want to study one-dimensional characteristics of stop-and-go waves. Therefore, we introduce a coordinate $\hat{x}$ along the ring which corresponds to the distance from the origin measured along the middle line of the corridor. It corresponds to the walking distance of a person staying always in the middle. The coordinate $\hat{y}$ is always perpendicular to the $\hat{x}$-axis. It measures the deviation from the centre of the corridor, see Fig. 2. We call $\hat{x}$ the main position and $\hat{y}$ the orientated distance.

The transformation $\lambda : \mathbb{R}^2 \to \mathbb{R}^2$, $\begin{pmatrix} x \\ y \end{pmatrix} \mapsto \begin{pmatrix} \hat{x} \\ \hat{y} \end{pmatrix}$ is described by:

$$\hat{y} = \begin{cases} \sqrt{x^2 + (y - r_0)^2} - r_0 & x < 0, \\ \sqrt{(y - r_0)^2} - r_0 & 0 \leq x \leq l, \\ \sqrt{(x - l)^2 + (y - r_0)^2} - r_0 & x > l, \end{cases} \quad (1)$$

$$\hat{x} = \begin{cases} 2l + r_0\pi + r_0 \arccos(\frac{r_0 - y}{\sqrt{(x-l)^2 + (y-r_0)^2}}) & x < 0, \\ x & 0 \leq x \leq l, \ y < r_0, \\ 2l + r_0\pi - x & 0 \leq x \leq l, \ y \geq r_0, \\ l + r_0 \arccos(\frac{r_0 - y}{\sqrt{x^2 + (y-r_0)^2}}) & x > l. \end{cases} \quad (2)$$

Figure 3 shows the trajectories of adjusted data in the new coordinate system for two runs. The straight lines in the ring correlate to the intervals $[0, 4]$ m and $[14.42, 18.42]$ m of the main position. Just as well the two other intervals correlate
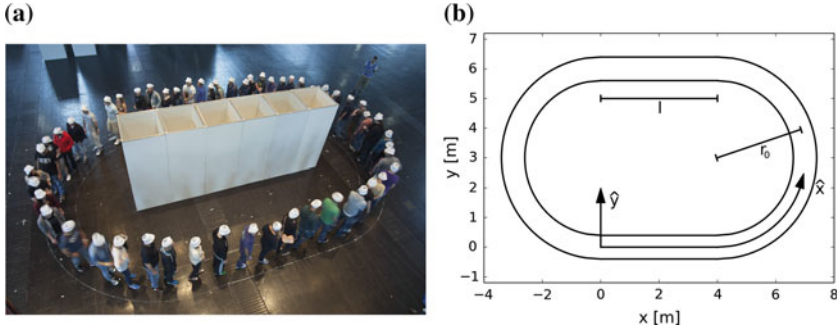
Fig. 2 The experiment. Photo by Marc Strunz (**a**). New coordinate system $\hat{x}$, $\hat{y}$ (**b**)
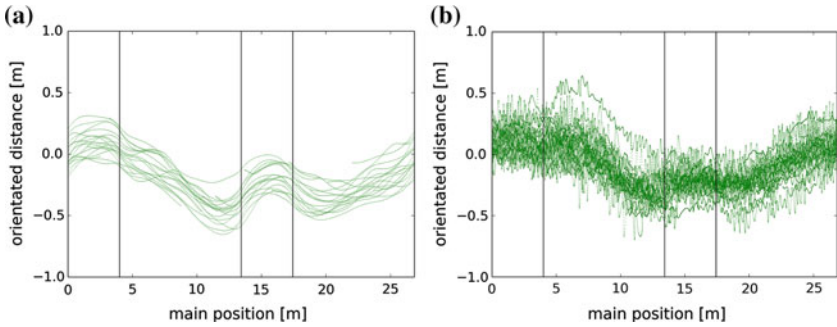
Fig. 3 Adjusted trajectories in the new coordinate system: $N = 15$ (**a**); $N = 59$ (**b**)

to the two curved parts. In the following, we will only examine the main position, described by Eq. 2 and omit the orientated distance. That means that all further calculations come from this one-dimensional main position.

3   Results

In this section we test whether the fundamental diagram has different properties in the straight and curved part of the corridor, i.e. whether it is influenced by the curvature.

3.1   Curvature-Dependence of the Fundamental Diagram

The ring corridor, our experimental set-up, has four parts, twice the straight line and twice the half circle. Figure 4 shows the Voronoi-based fundamental diagram for pedestrians moving in the straight line and in the curve. To distinguish between the six runs, each run has a separate symbol and colour.

The speed of pedestrian i at time t is calculated by the position difference over half a second divided by the time $v_i(t) = (\hat{x}_i(t + \Delta t) - \hat{x}_i(t - \Delta t))/(2\Delta t)$ with
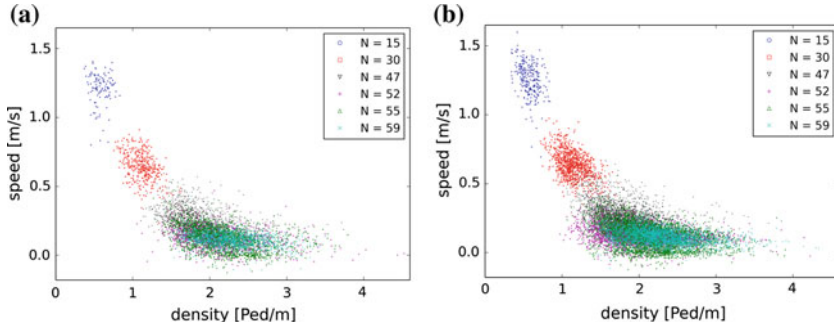
Fig. 4 The fundamental diagram of single-file pedestrian motion. Data from the straight part (**a**) and the curved part (**b**)

$\Delta t = 0.25$ s. The density is then $\rho_i(t) = d_i^{-1}$, where the Voronoi space d_i of pedestrian i is half the distance between the two neighbours $i - 1$ and $i + 1$, $d_i = (\hat{x}_{i-1} - \hat{x}_{i+1})/2$.

For analysing the characteristics of stop-and-go waves in the whole system we want to combine the data of both parts. First of all, we test the comparability of the fundamental diagram for the straight line and the curve. That means we study the distribution for both parts. The Kolmogorov–Smirnov test gives an indication whether two data clouds have the same distribution or not. A precondition for this test is that the data has to be independent, which can be shown with the autocorrelation.

We use two clouds with 3000 independent data points of each category, see Fig. 5 on the left side. The autocorrelation was tested for those data points to ensure that the observations are independent. An exponential function f for the shape of the speed according to the density is fitted by least square. The distributions of the residuals for the clouds are tested with the Kolmogorov–Smirnov test. The null hypothesis is H0: 'the distribution is the same for the two samples'. The frequency of residuals for both parts is shown in Fig. 5, right. With $p = 0.791$ we can clearly not reject the assumption that the distributions of the residuals come from the same continuous distribution.

With the Kolmogorov–Smirnov test we have shown that the density speed relation in the straight line is subject to the distribution of the density speed relation in
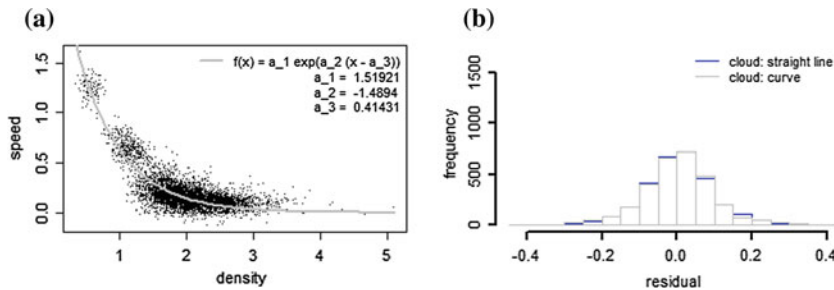
Fig. 5 Kolmogorov–Smirnov test. Fundamental diagram of single-file pedestrian motion for 6000 data points and its fitted exponential function (**a**); result (**b**)

the curve. That means that curvature effects on the fundamental diagram can be neglected.

3.2 Visualisation of Stop-and-Go Waves

To visualise stop-and-go waves, we use the knowledge that there is a coexistence of two separate speed phases. The fundamental diagram for the whole system for all six runs is shown in Fig. 6. By analysing the frequency of speeds in specific density regions the coexistence of two differing speed regimes can be identified, see Fig. 7. One peak is around the speed 0.12 m/s and the other one around 0 m/s. Negative speeds result from the swaying of heads of standing pedestrians.

In order to distinguish both phases, we introduce a stop speed v_{stop}. Standing pedestrians have a speed lower than this stop speed and moving pedestrians have a speed which is higher than the stop speed. We set the stop speed to $v_{stop} = 0.05$ m/s, which appears to be a reasonable value for our experiments. We have to note, that this value is not fixed and there might be better ones for other experiments.

Fig. 6 Fundamental diagram of single-file pedestrian motion
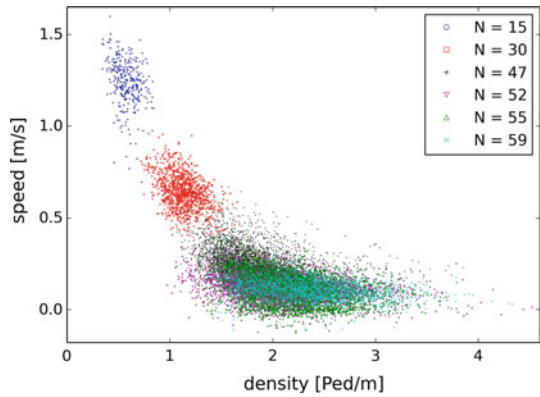
Fig. 7 Frequency of speed for certain density regions, $N = 55$
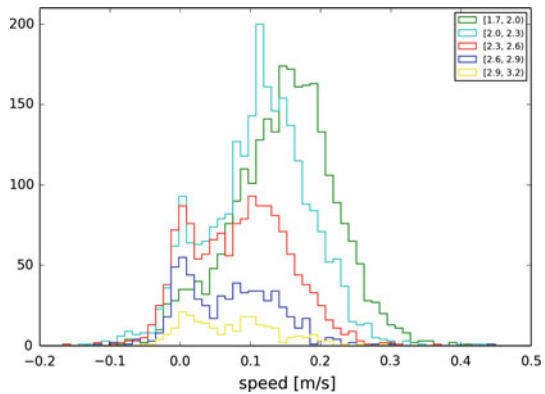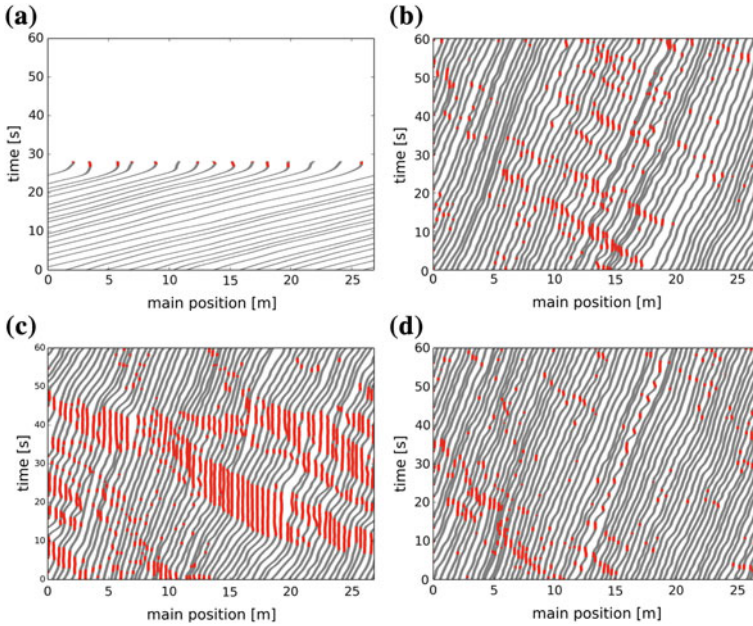
Fig. 8 Trajectories of the main positions. A *red dot* indicates a pedestrian in a congestion, that means he has a speed not higher than the stop speed. $N = 15$ (**a**). $N = 52$ (**b**). $N = 55$ (**c**). $N = 59$ (**d**)

3.3 Stop-and-Go Waves

We define a stop-and-go wave by a consecutive sequence of one or more standing pedestrians. Figure 8 shows the main positions of the pedestrians for 1 min for four different runs. The plotted positions have a length of 0.2 m to represent a body length. Pedestrians in a stop wave are marked in red. With 15 pedestrians in the system, no stopping occurs whereas 52, 55 or 59 pedestrians generate stop-and-go waves. Eye-catching is the run with 55 pedestrians. Long and big stop-and-go waves can be observed. The duration of the experiment run was too short to judge whether the regarded time interval represents a stable state.

A stop wave can be characterised by the number of pedestrians in this region at a certain time, by the length in space at a certain time and by the duration at a certain time and position. The length of a stop wave can be described by the number of standing pedestrians in a line or the distance between the first standing pedestrian and the last one. Higher densities lead to stop waves with more standing pedestrians than lower densities whereas the average length of a stop wave gets shorter. The duration of a stop wave can be described by the time while the first pedestrian in this stop wave is standing and the last standing pedestrian starts to move.

In the run $N = 52$, all stop waves have nearly the same speed around -0.5 m/s. The run $N = 59$ has lower speeds of stop waves around -0.32 m/s.

4   Conclusion

We extracted pedestrian trajectories from the whole set-up of a ring experiment. This data was transformed to a quasi-one-dimensional straight line. The resulting fundamental diagram for the straight and curved part have the same shape and are comparable, tested with the Kolmogorov–Smirnov test. The fundamental diagram of both parts shows a coexistence of two differing speed zones in specific density regions. A stop speed was introduced to distinguish between moving and standing pedestrians. Standing pedestrians define a stop wave that can be described by the characteristics length and duration. While the maximum number of pedestrians in a stop wave in our data is increasing with growing density, the average length decreases. In the future, we want to analyse those characteristics in a quantitative way.

References

1. Chattaraj, U., Seyfried, A., Chakroborty, P.: Comparison of pedestrian fundamental diagram across cultures. Adv. Complex Syst. **12**(3), 393–405 (2009)
2. Chowdhury, D., Santen, L., Schadschneider, A.: Statistical physics of vehicular traffic and some related systems. Phys. Rep. **329**(4–6), 199–329 (2000)
3. Eilhardt, C., Schadschneider, A.: Stochastic headway dependent velocity model for 1d pedestrian dynamics at high densities. Transp. Res. Procedia **2**, 400–405 (2014)
4. Hoogendoorn, S.P., Daamen, W., Bovy, P.H.L.: Microscopic pedestrian traffic data collection and analysis by walking experiments: behaviour at bottlenecks. In: Galea, E.R. (ed.) Pedestrian and Evacuation Dynamics 2003, pp. 89–100. CMS Press, London (2003)
5. Jelić, A., Appert-Rolland, C., Lemercier, S., Pettré, J.: Properties of pedestrians walking in line: fundamental diagrams. Phys. Rev. E **85**(3), 9 (2012)
6. Mehner, W., Boltes, M., Seyfried, A.: Methodology for generating individualized trajectories from experiments. In: Traffic and Granular Flow'15 (2016)
7. Portz, A., Seyfried, A.: Modeling stop-and-go waves in pedestrian dynamics. In: Wyrzykowski, R., Dongarra, J., Karczewski, K., Wasniewski, J. (eds.) PPAM 2009, Part II, pp. 561–568. Springer, Berlin, Heidelberg (2010)
8. Portz, A., Seyfried, A.: Analyzing stop-and-go waves by experiment and modeling. In: Peacock, R., Kuligowski, E., Averill, J. (eds.) Pedestrian and Evacuation Dynamics 2010, pp. 577–586. Springer (2011)
9. Seyfried, A., Boltes, M., Kähler, J., Klingsch, W., Portz, A., Rupprecht, T., Schadschneider, A., Steffen, B., Winkens, A.: Enhanced empirical data for the fundamental diagram and the flow through bottlenecks. In: Klingsch, W.W.F., Rogsch, C., Schadschneider, A., Schreckenberg, M. (eds.) Pedestrian and Evacuation Dynamics 2008, pp. 145–156. Springer, Berlin, Heidelberg (2010)
10. Seyfried, A., Steffen, B., Klingsch, W., Boltes, M.: The fundamental diagram of pedestrian movement revisited. J. Stat. Mech. **P10002** (2005)
11. Yanagisawa, D., Tomoeda, A., Nishinari, K.: Improvement of pedestrian flow by slow rhythm. Phys. Rev. E **85**, 016,111 (2012)

Determining the Density Experienced by Pedestrians in Unstable Flow Situations

Dorine C. Duives, Winnie Daamen and Serge P. Hoogendoorn

Abstract In recent years several methods have been proposed to compute the density of a crowd. Several studies have shown that the fundamental diagrams produced by means of these methods differ greatly depending on the chosen density computation method, especially in unstable flow situations where pedestrians are unequally distributed over the infrastructure. The results of these studies suggest that two density computation methods are to be preferred, namely the Voronoi and the XT-method. In light of these results, the question rises which of these two computation methods provides better results in more intricate flow situations that are unstable by nature. This study shows that when computing the density of pedestrian movements in confined spaces, the differences in the results generated by the two methods are limited. This study, furthermore, ascertains that the XT-method provides more realistic results for non-confined spaces.

1 Introduction

During the last decades numerous studies have attempted to understand, assess, predict and manage the movements of pedestrians. Understanding the dynamics which result from the interplay of the actions of a multitude of individuals is essential in order to manage pedestrian crowds and to design pedestrian infrastructure in which the safety of pedestrians can be guaranteed. With a thorough understanding of the dynamics of a pedestrian flow system, the predictive power of pedestrian traffic flow theory can be used to support the effective and efficient management of pedestrian facilities, which currently is mainly based on the experience and intuition of the crowd manager.

D.C. Duives (✉) · W. Daamen · S.P. Hoogendoorn
Delft University of Technology, Stevinweg 1, 2628 CN Delft, The Netherlands
e-mail: d.c.duives@tudelft.nl

W. Daamen
e-mail: w.daamen@tudelft.nl

S.P. Hoogendoorn
e-mail: s.p.hoogendoorn@tudelft.nl

One essential part of pedestrian traffic flow theory is the derivation of the fundamental diagram. Many researchers hypothesise that, similar to vehicular traffic, the general movement dynamics of pedestrians can be captured in a fundamental diagram. This diagram relates the density experienced by pedestrians and the walking speed these pedestrians adopt. Several realisations of this diagram have been presented over the years (e.g. [5, 6, 10, 11, 13]).

However, contrary to vehicular traffic, the existence and shape of the fundamental diagram is still debated. Many proposed fundamental diagrams have a similar parabolic shape, but the capacity point, jam density and free speed differ severely between diagrams. The culture (e.g. [8]), physical characteristics of the pedestrian (e.g. [13]), the interactions with the physical infrastructure (e.g. [10]) and the flow situation (e.g. [9]) have been mentioned as possible explanations for the differences.

Besides these characteristics of the situation, [2, 7, 14] have shown that also the method used to compute the density might introduce dissimilarities between the resulting fundamental diagrams. Johansson [7] transposed the available data sets to show the similarities in pedestrian movement behaviour captured by differently shaped fundamental diagrams. Zhang and Klingsch [14] illustrated that the resulting fundamental diagram varies with the location of the measurement area and the adopted density measures, namely the grid-based density measure, the area-wide density measure, a measure that averages the density within a certain area and a measure which uses a Voronoi diagram. Duives and Daamen [2] visualised the influence of seven distinct density measures on the resulting fundamental diagram. In the review of [2] two methods come out on top, namely the Voronoi [12] and the adapted XT-method (adapted version of [3]). Yet, whether these two methods produce similar results irrespective of the flow dynamics has not been determined.

This study scrutinises the differences in results produced by the Voronoi and adapted XT-method in case of unstable flow situations in comparison to the grid-based method proposed by [4]. In order to study the characteristics of these two methods, fundamental diagrams of several flow situations with an increasing level of complexity are compared. Underneath, first the methodology is elaborated upon in Sect. 2. Subsequently, the results are presented in Sect. 3. This paper finishes with conclusions regarding the (dis)advantages and applicability of both methods and some directions for further study.

2 Methodology for the Assessment of Density Measures

The following section elaborates on the set-up of the experiments. First, a formal description of the density measures is provided. Accordingly, the adopted flow situations and pedestrian simulation model are described.

2.1 Density Measures

In this study the results computed by means of three distinct density measures are investigated, namely the grid-based method proposed by [4], the Voronoi method proposed by [12] and an adapted version of the XT-method proposed by [3].

The *adapted XT-method* determines the total distance and total travel time by all pedestrians in a predetermined space-time region based on the trajectories. The density is afterwards computed as mentioned in Eq. 1. The global density computed for cell c at time t is assigned to the pedestrian p that resides at the centre of cell c at time t. If period T goes to zero, this measure will take on the form of the Grid-based formulation presented previously.

$$\rho(c,t) = \frac{\sum_p (t_{p,end} - t_{p,begin})}{A_c \cdot dt} \tag{1}$$

where $t_{p,begin}$ represents either the moment that pedestrian p enters cell c or the lower time boundary $t - 0.5dt$, $t_{q,end}$ either the moment that pedestrian p exits cell c or the upper time boundary $t + 0.5dt$. In Fig. 1 a visual representation of this method is provided. The thick part of each trajectory is being taken into account in the computation of the density of the pedestrian standing in the middle of the cell. The period dt is included to limit the time a pedestrian is accounted for during the computation. dt is set to 1 s in this paper.

The *Voronoi method* uses a more dynamic space-based measure to estimate the experienced density. In a Voronoi diagram a cell A_p consists of all points closer to the location of a pedestrian than to each other pedestrians. The inverse of the area A_p of the Voronoi cell corresponding to the location $\overrightarrow{x_p}(t)$ of pedestrian p at time t is allotted to pedestrian p (see Eq. 2). Eucledian distances are used to compute the Voronoi diagram.

Fig. 1 Visual representation of the adapted XT-method
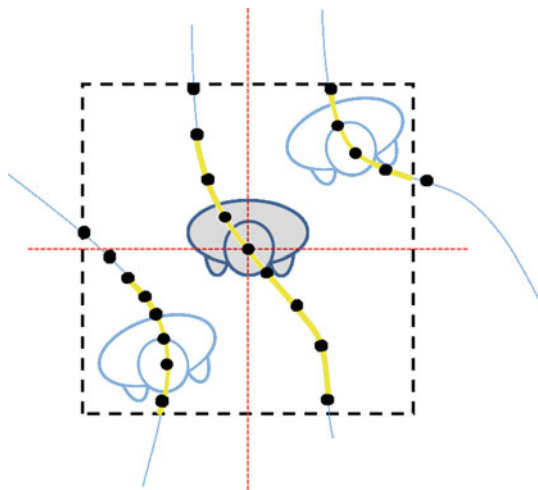
$$\rho(\vec{x_p}, t) = \frac{1}{A_p(t)} \tag{2}$$

The shape of the diagram needs to be computed for every time step since the shape of the Voronoi diagram changes over time. Besides that, boundary conditions are generally implemented in order to deal with pedestrians which are not enclosed on all sides by other pedestrians. The influence of this boundary conditions can be quite severe. Moreover, adopting the spatial boundary might incur errors of variable size in the estimation. Therefore, it has been chosen not to adopt a spatial boundary.

The *grid-based method* counts the number of pedestrians N_c within a cell c with area A_c in an orderly grid formation. Accordingly, one obtains an estimate for density within that specific cell. The estimate for the density in the cell is assigned to all pedestrians in that cell. This classic definition of density can mathematically be formulated as follows:

$$\rho(c, t) = \frac{N_c}{A_c} \tag{3}$$

In the remainder of this paper, this method is indicated as the $k = N/A$-method.

2.2 Flow Situations and Simulations

As mentioned before, this study investigates the influence of the density measures on the fundamental diagram depending on the flow situation. There has been chosen to increase the difficulty of the interaction behaviour in the flow situation, being a very simple one-dimensional flow situation in which only interactions along a line, a two-dimensional flow situation within a corridor, and a two-dimensional flow situation in an open space in which pedestrians are forced to interact. Consequently, the following three distinct flow situations are accounted for:

- *1D-Row*: This situation mimics the situation in which pedestrians walk in a straight line and cannot pass each other. By means of this scenario the influence of the metrics in the most simple flow situation possible is deduced.
- *2D-Row*: The pedestrians are walking through a 2 m wide straight corridor in one direction. There is the possibility to side step and overtake.
- *2D-Bottleneck*: In this situation pedestrians are walking towards a door. As such, the interactions between pedestrians are occurring under an angle.

For all three flow situations, several demand levels are taken into account in order to study the influence of the metrics under both free flow and congested conditions. In the 1D-row and 2D-row case the end of the corridor is temporarily jammed in order to create congestion. Each situation is modelled by means of Nomad. For the details of this microscopic pedestrian simulation model the reader is referred to [1] (Figs. 2 and 3).
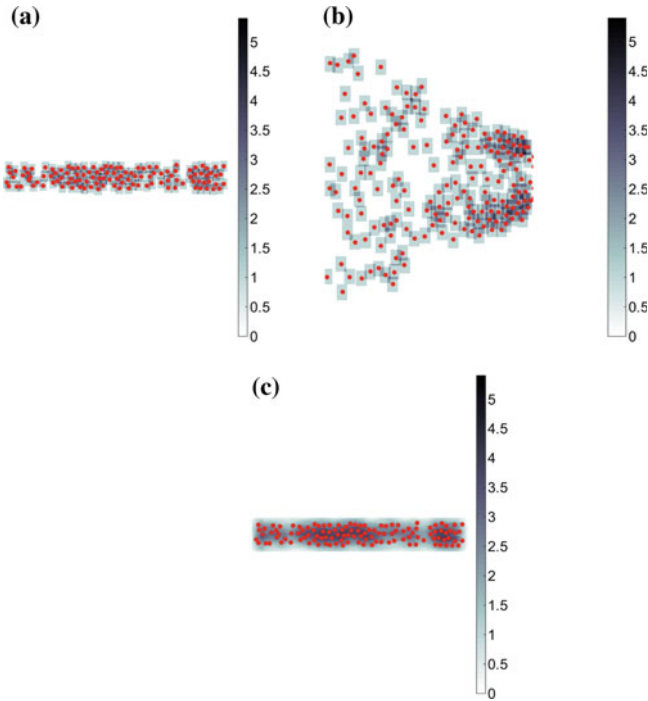
Fig. 2 Spatial distribution of the density resulting from three density computation methods for a uni-directional straight flow situation. $k = n/A$ (**a**). Edie (**b**). Voronoi (**c**)

3 Results

In order to understand how these differences arise, density plots have been made (see Fig. 4). The high and low density areas are located approximately at the same locations for all three density measures. In case of the 2D-bottleneck the two high density regions can be neatly distinguished by means of the all measures. However, especially at the boundaries of the flow, differences between the density measures arise.

In case of the Voronoi method the lateral space near the boundary is always assigned to the nearest pedestrian, even though this space might not be usable for their walking movements. Moreover, near these boundaries, the allotted space is highly dependent on the angle under which neighbours are standing. If pedestrians are not standing directly behind each other, one of the two is allotted a very low density, while the other is allotted a very high density, even though the amount of space they actually have is fairly similar. As a result, near the boundaries between traffic states and near walls, the Voronoi method can underestimate and overestimate the density. Moreover, due to the unequal assignment of space, an error is introduced of which the size is hard to establish which results in unstable outcomes.
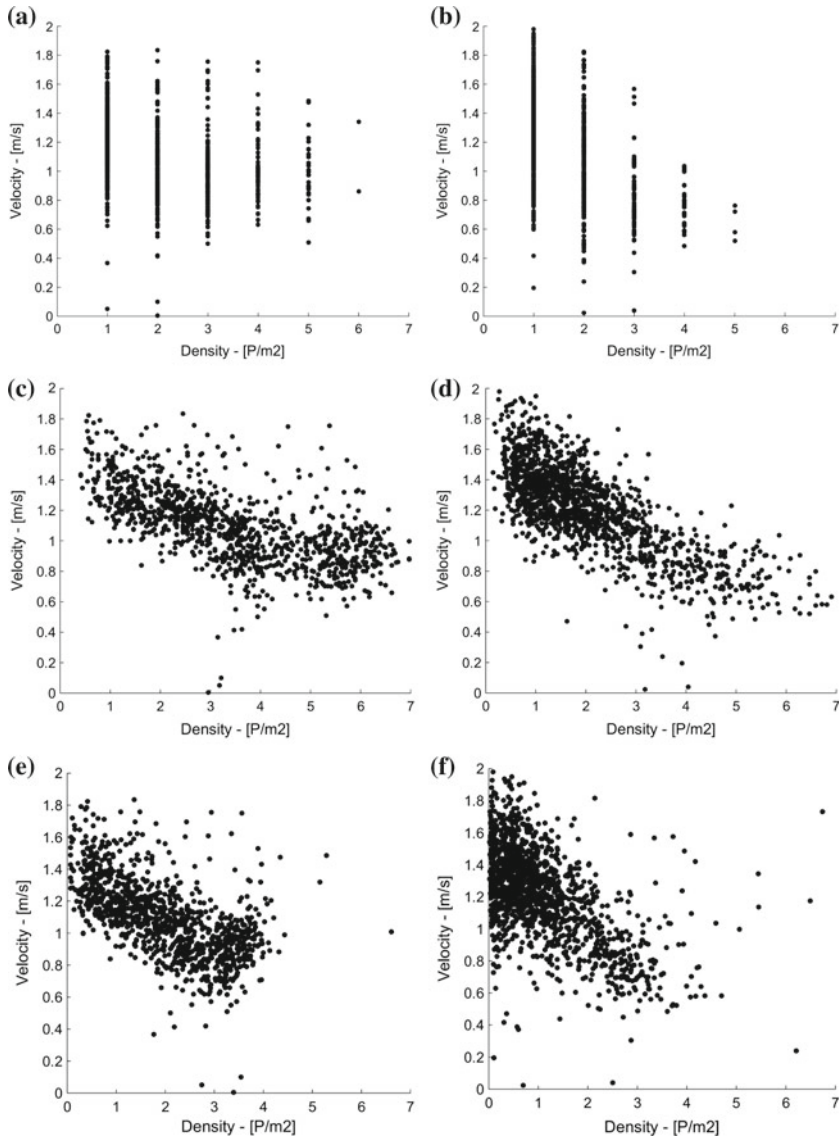
Fig. 3 Fundamental diagrams produced by the three methods for a 2D uni-directional straight flow situation (*left*) and a 2D uni-directional bottleneck flow situation (*right*). Row-2D: $k = n/A$ (**a**). Bottleneck-2D: $k = n/A$ (**b**). Row-2D: Edie (**c**). Bottleneck-2D: Edie (**d**). Row-2D: Voronoi (**e**). Bottleneck-2D: Voronoi (**f**)

By contrast, the XT-method accounts also for the relative presence of pedestrians which only enter the space-time box of a pedestrians for a fraction of time. As such, it takes more individuals into account than the grid-based and Voronoi method. Consequently, the XT-method generally finds higher densities than the $k = N/A$ and
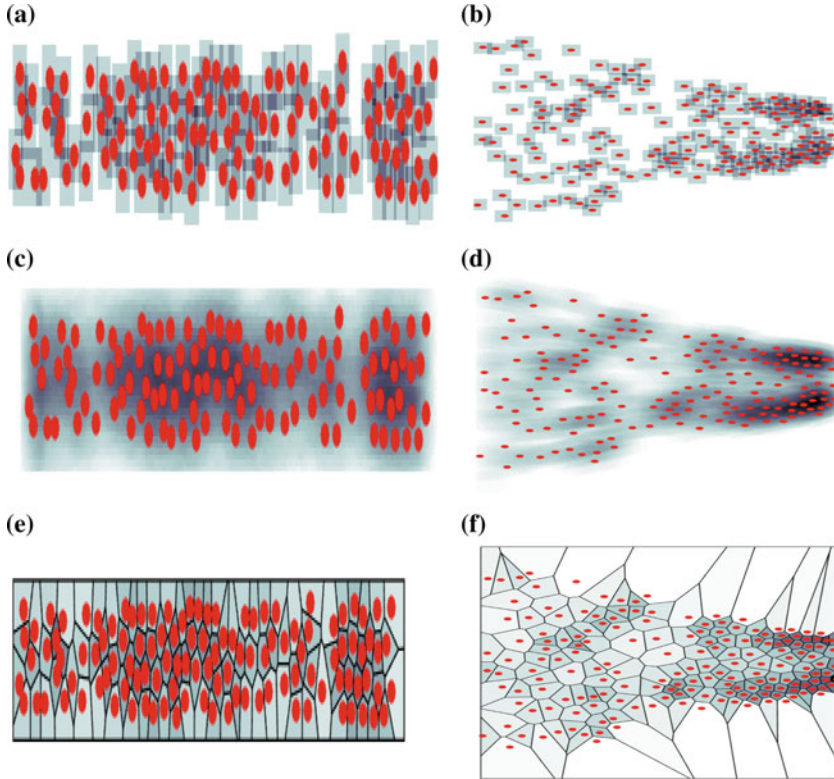
Fig. 4 Density plots for three methods and two flow situations, where the plots are computed based on the same data set and the same moment in time. The colour range represents the density, were high densities are *black* and low densities are *white*. Row-2D: $k = n/A$ (**a**). Bottleneck-2D: $k = n/A$ (**b**). Row-2D: Edie (**c**). Bottleneck-2D: Edie (**d**). Row-2D: Voronoi (**e**). Bottleneck-2D: Voronoi (**f**)

Voronoi methods. Besides that, the XT-method always takes the relative presence of pedestrians within a certain area into account, irrespective of the boundary conditions. As a results, space that is not used for the walking movement is also not assigned to a pedestrian, which reduces the noise in the computation.

4 Conclusions and Future Research

This paper provides an assessment of the applicability of the Voronoi method, the adapted version of Edie's XT-method and the $k = N/A$ method in more intricate and unstable flow situations. Each computation method is tested by means of three data sets considering three distinct scenarios, namely the movement of pedestrians along a line, in a wide corridor, and in a bottleneck flow situation. The data sets were generated using the microscopic pedestrian simulation model Nomad.

This study shows that if computing the density of pedestrian movements in confined spaces, the differences in the results generated by the two methods are limited. This study moreover concludes that particularly in the assessment of pedestrian movement dynamics in non-confined spaces and unstable flow situations both methods introduce noise. However, the XT-method introduces less noise than the Voronoi method in these unstable flow situations, and as such provides more realistic results for non-confined spaces and transitional situations in which density changes quickly over time and/or space.

Two suggestions for future research entail the assessment of the sensitivity of the results produced by these three measures with respect to these boundary conditions and the assessment of the other variables used to describe the walking behaviour of pedestrians quantitatively. In both directions of future research, understanding the behavioural implications of the assumptions is as important as determining the actual quantitative differences that arise.

References

1. Campanella, M., Hoogendoorn, S., Daamen, W.: The nomad model: theory, developments and applications. In: Daamen, W., Duives, D., Hoogendoorn, S. (eds.) The Conference on Pedestrian and Evacuation Dynamics 2014 (PED2014), Transportation Research Procedia, vol. 2, pp. 462–467 (2014)
2. Duives, D., Daamen, W., Hoogendoorn, S.: Quantification of the level of crowdedness for pedestrian movements. Phys. A: Stat. Mech. Appl. **427**, 162–180 (2015)
3. Edie, L.: Discussion of Traffic Stream Measurements and Definitions (1963)
4. Fruin, J.: Designing for pedestrians: a level-of-service concept. Highway Res. Rec. **355**, 1–15 (1971)
5. Hankin, B., Wright, R.: Passenger flow in subways. Oper. Res. **9**(2), 81–88 (1958)
6. Helbing, D., Johansson, A., Al-Abideen, H.: The dynamics of crowd disasters: an emperical study. Phys. Rev.—Part E **75**, 046109 (2007)
7. Johansson, A.: Constant net-time headway as key mechanism behind pedestrian flow dynamics. Phys. Rev. E **80** 026120 (2009)
8. Lam, W., Morrall, J., Ho, H.: Pedestrian flow characteristics in Hong Kong. Transp. Res. Rec. **1487**, 56–62 (1995)
9. Navin, F., Wheeler, R.: Pedestrian flow characteristics. Traffic Eng. **39**, 31–36 (1969)
10. Predtechenskii, V., Milinskii, A.: Planning for Foot Traffic Flow in Buildings. Amerind Publishing (1978)
11. Seyfried, A., Steffen, B., Klingsch, W., Boltes, M.: The fundamental diagram of pedestrian movement revisited. In: Traffic and Granular Flow 2005, p. P10002. Springer, Berlin (2005)
12. Steffen, B., Seyfried, A.: Methods for measuring pedestrian density, flow, speed and direction with minimal scatter. Phys. A: Stat. Mech. Appl. **389**(9), 1902–1910 (2010)
13. Weidmann, U.: Transporttechnik der Fussgänger. Technical report, Institut für Verkehrsplanung, Transporttechnik, Strassen- und Eisenbahnbau (1993)
14. Zhang, J., Klingsch, W., Schadschneider, A., Seyfried, A.: Transitions in pedestrian fundamental diagram of straight corridors and t-junctions. J. Stat. Mech.: Theory Exp. **6**, P06004 (2011)

Individual Microscopic Results of Bottleneck Experiments

Marek Bukáček, Pavel Hrabák and Milan Krbálek

Abstract This contribution provides a microscopic experimental study of pedestrian motion in front of the bottleneck, and explains the high variance of individual travel time by the statistical analysis of trajectories. The analysis shows that this heterogeneity increases with increasing occupancy. Some participants were able to reach lower travel times due to more efficient path selection and more aggressive behaviour within the crowd. Based on this observations, a linear model predicting travel time with respect to the aggressiveness of pedestrian is proposed.

1 Experiment

Various experiments have been conducted in order to verify crowd behaviour models and to enable fundamental research of pedestrians phenomena [6–9].

Advanced processing of video records provides microscopic analysis of individual behaviour [3, 4]. During critical situation, the individual behaviour plays an important role—less aggressive pedestrians spend more time in the monitored area, which may cause unexpected complications.

This article is based on an egress experiment organised at the Czech Technical University. A group of 75 students passes through an artificial room (Fig. 1), instructed to leave the area as fast as possible, to avoid running and pushing each other. The results supported phase transition studies as mentioned in [1, 2].

M. Bukáček (✉) · M. Krbálek
Faculty of Nuclear Sciences and Physical Engineering, Czech Technical University,
Trojanova 13, 120 00 Prague 2, Czech Republic
e-mail: bukacma2@fjfi.cvut.cz

M. Krbálek
e-mail: milan.krbalek@fjfi.cvut.cz

P. Hrabák
Institute of Information Theory and Automation, Czech Academy of Sciences,
Pod Vodarenskou vezi 4, 182 08 Prague 8, Czech Republic
e-mail: hrabak@utia.cas.cz

(a)

(b)
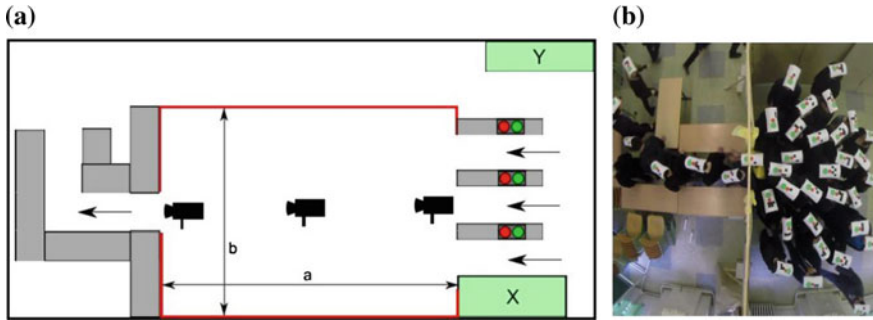
Fig. 1 Experiment organised. Schematic view (**a**): The distance from the entrance to the exit a = 7.2 m (considered for measuring of travel time), room width 4.5 m and exit width 0.6 m. Snapshot from exit (**b**)

Table 1 Summary of performed rounds

Round	J_{in} [ped/s]	J_{out} [ped/s]	$\overline{TT}$ [s]	$N(150)$ [ped]	# paths	Observation
# 2	0.99	0.99	5.67	3	158	Free flow
# 5	1.22	1.20	6.73	7	274	Free flow
# 4	1.37	1.30	16.59	24	294	Stable cluster
# 3	1.43	1.33	14.39	22	260	Stable cluster
# 6	1.39	1.31	20.40	33	270	Stable cluster
# 7	1.55	1.37	25.78	45	260	Transition
# 11	1.61	1.38	21.65	41	141	Transition
# 9	1.78	1.37	24.06	47*	148	Congestion
# 8	1.79	1.38	25.03	46*	144	Congestion
# 10	1.78	1.37	23.33	44*	214	Congestion

J_{in} and J_{out} refer to flow measured flow at the entrance, respectively at the exit, $\overline{TT}$ is mean travel time in given round. $N(150)$ specify the number of pedestrians in the room 150 s after initialisation and # paths denotes the number of passings in given round

Three entrances were controlled by traffic lights to get the demanded traffic mode inside the experimental area, see Table 1. To simulate random inflow conditions, green light was alternated by $k \cdot \Delta h$ seconds of red light, where k was generated from a geometric distribution and $\Delta h = 0.6$ s was the time step. Each round started with an empty room.

Unique codes on the hats of the participants enabled to detect and identify the trajectory of each participant. From this information, travel times (covering the period from entrance to exit) and Voronoi densities were extracted for further investigation.

2   Travel Time Analysis

As mentioned in [2], the recorded travel time significantly depends on the occupancy $N(t)$, defined as the number of pedestrians inside the room. Travel time increases linearly with occupancy and the variance is increasing as well, see Fig. 2. This phenomenon will be described by pedestrian's individual characteristics.

The term trajectory is understood to be the set of space-time coordinates assigned to one participant during one of his passings

$$\mathbf{x}_i = (x_i(t), y_i(t), t),$$

where $x_i(t)$ and $y_i(t)$ are coordinates of paths i in time t. Here, we note that the path identifier i does not refer to any specific participant, but to the recorded trajectory.

Travel time of trajectory i is defined as the time spent in the room, i.e.

$$TT(i) = T_{\text{out}}(i) - T_{\text{in}}(i),$$

where T_{in} and T_{out} are measured just behind entrances, resp. in front of the exit, see Fig. 1.

The occupancy in the room $N(t)$ was derived from paths; this quantity was used to determine the mean occupancy $\overline{N}(i)$ for each path i as

$$\overline{N}(i) = \frac{1}{TT(i)} \int_{T_{\text{in}}(i)}^{T_{\text{out}}(i)} N(t)\mathrm{d}t$$

2.1   Relative Travel Time

To compare the travel times measured under different conditions (stable state was not reached for the whole experiment), scaling based on mean occupancy was introduced. For each occupancy bin $(N - 1, N\rangle$ the mean travel time TT_N was defined as

Fig. 2 Travel time—occupancy dependency. Each *point* represents one passing, *lines* visualise mean and quantiles evaluated for given occupancy

(a)

(b)
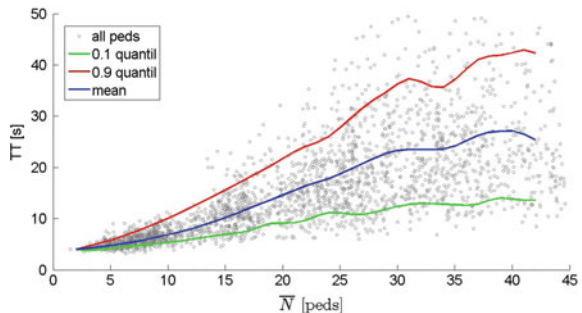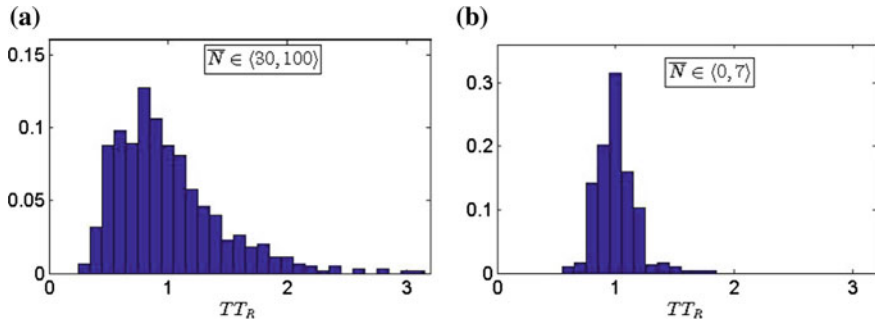
Fig. 3 Histograms of relative travel time. Data filtered for high density areas (**a**) and for low density areas **b**

$$TT_N = \operatorname*{mean}_{i} \left\{ TT(i) \mid \overline{N}(i) \in (N - 1, N] \right\}.$$

Then, the relative travel time for each path may be evaluated as

$$TT_R(i) = \frac{TT(i)}{TT_N}.$$

That enables to compare Travel time of paths reached under different conditions.

To underline the increase of variance in travel time, two histograms of relative travel time are plotted in Fig. 3. As one can see, the travel time of dominant majority of passings in free flow did not deviate more than 20 % from the mean value. On the other hand, the travel time in congested mode covered 50–200 % of TT_N.

2.2   Paths and Paths Density

Paths selection is one of the features, which affect reached travel time. The following study summarises the space usage described by paths density. The workload W of space element A_j is defined as

$$W(A_j) = \left| \left\{ i : \exists t \in \mathbf{x}_i : (x(t), y(t) \in A_j \right\} \right|,$$

where A_j is an area defined by rectangular grid, 0.2 m × 0.2 m.

Both trajectory and workload were evaluated in the area in front of the bottleneck, the visualisation is provided in Fig. 4. In the following, the terms slow and fast trajectories refer to set of 20 % higher, respectively lower travel time. These trajectories are compared under meta-stable and congested phase of the system. Several conclusions were drawn:

fast in metastable	slow in metastable	fast in crowd	slow in crowd
$\overline{N} \in [25, 35]$	$\overline{N} \in [25, 35]$	$\overline{N} \in [35, 50]$	$\overline{N} \in [35, 50]$
$TT \leq 10$	$TT \geq 21$	$TT \leq 15$	$TT \geq 35$
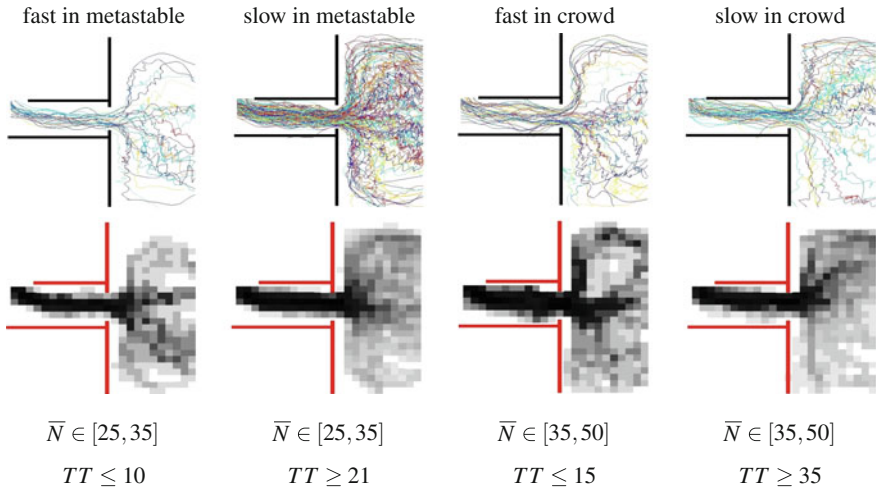
Fig. 4 Paths (*first row*) and path density (*second row*) evaluated for two different density areas: metastable cluster and congested crowd. For both traffic modes, trajectories of slow and fast pedestrians were compared. Here we note that the density was evaluated on a grid 0.2 m × 0.2 m, each trajectory contributed to any segment maximally ones. The darker the colour, the higher the workload

- the direct path to the exit was used more by fast trajectories,
- the area at the wall was used by fast paths,
- slow paths observed mainly along the angle 45° to the exit,
- observed asymmetry—fast on left, slow on right.

2.3 Individual Approach

More detail may be provided adding the pedestrian's identification. Here we use the Greek letters to denote identified participants.

While some participants reached similar travel times in free flow and congested mode, others were not able to pass through the dense crowd and spent incomparable more time in the room.

To compare participants, the individual relative travel time was defined as

$$\overline{TT}_\alpha = \underset{i}{\mathrm{mean}}\, \{TT_R(i) \mid i \in I_\alpha\},$$

where I_α is the set of paths assigned to pedestrian α.

The histograms of $\overline{TT}_\alpha$ for free flow and congested state are visualised in Fig. 5. As one can see, the heterogeneity among participants corresponds well to the variance of relative travel time introduced in Fig. 3.

(a)

(b)
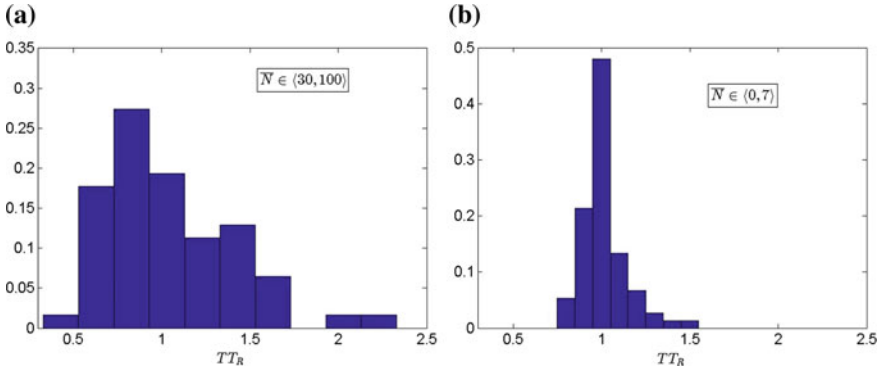
Fig. 5 Histograms of individual relative travel time: free flow mode (**a**); high occupancy periods (**b**)

Fig. 6 Individual travel time with respect to the mean occupancy. Data for three pedestrians with different strategies were highlighted and the piece-wise linear model is illustrated
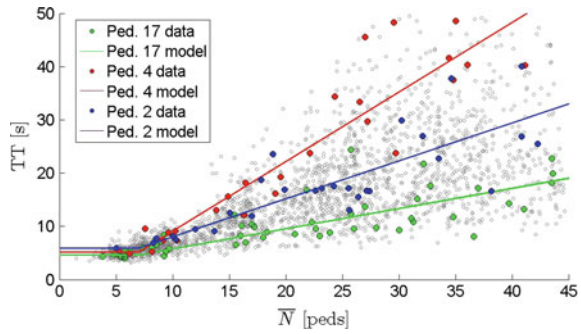
Thanks to participant identification, it is possible to highlight records corresponding to a given pedestrian in the travel time-occupancy diagram (Fig. 6). The observations show the same heterogeneity measured by individual relative travel time. While some participants were not affected much by the crowd, some were not able to reach the exit through the crowded area.

To compare the ability to push through the crowd, we define the pedestrian attribute 'aggressiveness' as the slope of piece-wise linear model

$$TT(i_\alpha) = \frac{S}{v_0} + \mathbf{1}_{\{\overline{N}(i_\alpha)>7\}}(\overline{N}(i_\alpha) - 7) \cdot \text{slope}(i_\alpha) + \text{noise}.$$

The factor $\overline{N} > 7$ specifies the mode, where pedestrians are affected by the motion of others. Until $\overline{N} < 7$, the free phase is observed and therefore the interactions may be neglected.

Compared to the classic linear model $TT(i_\alpha) = \frac{S}{v_0} + \overline{N}(i_\alpha).slope(i_\alpha)$, the piece-wise model fits the data much better, mainly in free flow area, where the travel time
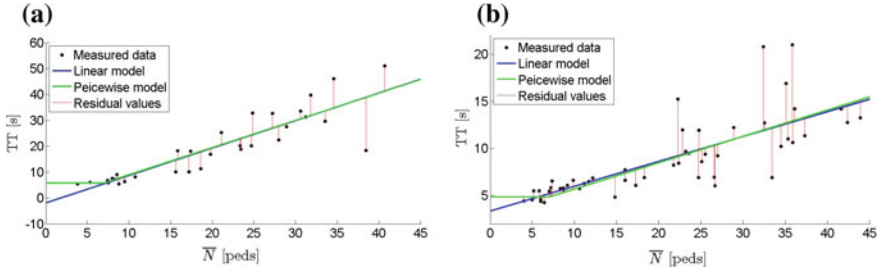
Fig. 7 Individual results of travel time linear model. For the selected participants, the standard and piece-wise linear model are compared. Slow participant (**a**). Fast participant (**b**)

Table 2 Table R^2 values for piece-wise and standard linear models evaluated for each pedestrian

Piece-wise model				Standard linear model			
mean	median	min	max	mean	median	min	max
0.688	0.691	0.386	0.936	0.679	0.676	0.362	0.938
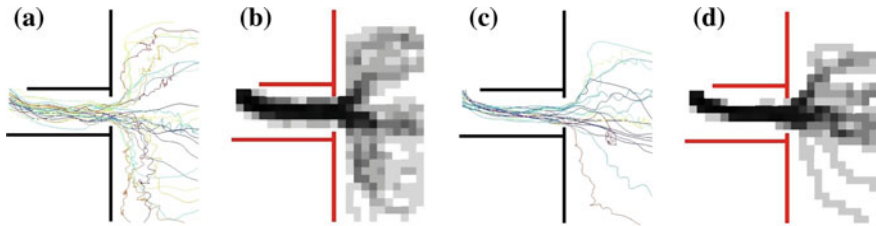
Fig. 8 Path densities. Path slow pedestrian (**a**). Path density slow pedestrian (**b**). Path fast pedestrian (**c**). Path density fast pedestrian (**d**)

obviously does not depend on occupancy. Vice versa, the area of constant TT trend does not affect the slope modelled in the crowded area, see Fig. 7.

Mean values of residuals in both models are similar (see Table 2), the lower value of mean R^2 for the piece-wise model corresponds to the facts mentioned above.

In the end, the path density was investigated with respect to individual behaviour, see Fig. 8. The observed trends are similar to the conclusions drafted from anonymous paths data.

To conclude this part, the observed variance is successfully explained by differences in individual behaviour. Pedestrians hold to their different strategies which leads to different performances.

3 Conclusions

Even when it was shown that lower travel time was reached by faster trajectories, the path selection itself would not imply fast passing. Fast paths were not shorter or

better curved to reach low travel time from physical point of view. However, these paths were more effective to get through the dense crowd.

To support this idea, we found out many tokens of aggressive behaviour from the camera records as pushing, rude overtaking or blocking each other. The concept of aggressiveness as a property of pedestrians fits this idea well. This is supported by the fact that some individuals reached low travel times under all conditions, while others were very sensitive to occupancy.

The effect of heterogeneity has a dramatic influence to the progress of evacuation. The time spent in dangerous area may be in mean value sufficiently low according to local guidelines, but there is a high probability that some part of the pedestrians would stay there much longer. This effect was implemented to the cellular automata model, see [5].

References

1. Bukáček, M., Hrabák, P.: Case study of phase transition in cellular models of pedestrian flow. Lec. Notes. In. comp.Sci. vol. 8751, pp. 508–517. Springer (2014)
2. Bukáček, M., Hrabák, P., Krbálek, M.: Experimental study of phase transition in pedestrian flow. Transp. Res. Procedia **2**, 105–113 (2014)
3. Bukáček, M., Hrabák, P., Krbálek, M.: Experimental analysis of two-dimensional pedestrian flow in front of the bottleneck. In: Traffic and Granular Flow'13, pp. 93–101. Springer (2015)
4. Duives, D., Daamen, W., Hoogendoorn, S.: Anticipation behavior upstream of a bottleneck. Transp. Res. Procedia **2**, 43–50 (2014)
5. Hrabák, P., Bukáček, M.: Conflict solution according to "aggressiveness" of agents in floor-field-based model. LNCS 9574, pp. 507–516. (2015)
6. Schadschneider, A., Chowdhury, D., Nishinari, K.: Stochastic Transport in Complex Systems: From Molecules to Vehicles. Elsevier (2010)
7. Seyfried, A., Portz, A., Schadschneider, A.: Phase coexistence in congested states of pedestrian dynamics. LNCS 6350, pp. 496–505. Springer (2010)
8. Steffen, B., Seyfried, A.: Methods for measuring pedestrian density, flow, speed and direction with minimal scatter. Phys. A: Stat. Mech. Appl. **389**(9), 1902–1910 (2010)
9. Zhang, J., Seyfried, A.: Quantification of bottleneck effects for different types of facilities. Transp. Res. Procedia **2**, 51–59 (2014)

Modelling Stride Length and Stepping Frequency

Isabella von Sivers, Gerta Köster and Benedikt Kleinmeier

Abstract A pedestrian motion model must be calibrated to measured data and validated against observations to achieve predictive power for the simulations. The relationship between the speed of pedestrians and the density of a crowd or the flow through bottlenecks are widely accepted as important characteristics of pedestrian movement. They are often used for calibration and validation. Other crucial characteristics of pedestrian movement have been discussed in recent studies. Two of these are the correlations between stride length and speed as well as between stepping frequency and speed. We show that one can reproduce these dependencies as measured in the experiments with the Optimal Steps Model (OSM), which captures stepping behaviour of pedestrians.

1 Introduction

Simulation of pedestrian movement helps to plan events, to ensure safety in case of an evacuation or to identify problems in the layout of buildings. For these applications, pedestrian motion models must have predictive power, that is, they must be calibrated and validated against observations and measured data. Widely accepted characteristics of pedestrian movement that are used for this are the correlations of density and speed or the flow through bottlenecks.

Other crucial characteristics of pedestrian movement have been discussed only recently. The correlations between stride length and speed as well as stride duration

I. von Sivers (✉) · G. Köster
Munich University of Applied Sciences, Lothstraße 34, 80335 Munich, Germany
e-mail: isabella.von_sivers@hm.edu

G. Köster
e-mail: gerta.koester@hm.edu

I. von Sivers
Technische Universität München, Arcisstrße 21, 80333 Munich, Germany

B. Kleinmeier
Munich University of Applied Sciences, Lothstraße 34, 80335 Munich, Germany
e-mail: benedikt.kleinmeier@gmail.com

and speed were investigated in several experiments [1–3, 5, 6, 9, 11, 13, 18]. In order to reproduce these correlations, a pedestrian locomotion model must capture true stepping behaviour. One such model is the Optimal Steps Model (OSM). We show that, with the OSM, one can reproduce the dependencies as measured in the experiments by [3, 5].

2 Materials and Methods

In this section, we outline findings about stride lengths and stepping frequencies of pedestrians that we use as a basis for our investigation. Furthermore, we describe a small modification in the stepping behaviour in our locomotion model, the Optimal Steps Model.

2.1 Stride Lengths and Stepping Frequencies of Pedestrians

The correlations between stride lengths and velocities or between stepping frequencies and velocities were observed and measured in several experiments [1–3, 5, 6, 9, 11, 13, 18]. The stride length l of walking humans correlates linearly with their velocity v. The parameters α and β of the linear function for the stride length

$$l = \alpha + \beta \cdot v \tag{1}$$

differ depending on the experiment or the observations. For example, the residual stride length α ranges from less than 10 cm [5] to more than 30 cm [9], the slope β from approximately 0.3 to 0.7.

Experiments and observations of the stepping frequency, that is, the inverse of the stride duration, show two main aspects [3, 5, 18]: When walking slowly (less than 1 m/s), the stride duration decreases with increasing speed; above a certain speed, the stride duration remains constant or decreases much more slowly than before. In this paper we focus on the walking in line experiment from [4, 5] where a full set of parameters is available for comparisons.

2.2 The Optimal Steps Model

The Optimal Steps Model (OSM) is a pedestrian locomotion model that was developed in 2012 at the Munich University of Applied Sciences [11]. Newer versions of the OSM [12, 15, 16] or combinations of the OSM with other social or navigational models [7, 17] were published in the following years. For this study, a slightly modified version of [16] is used.
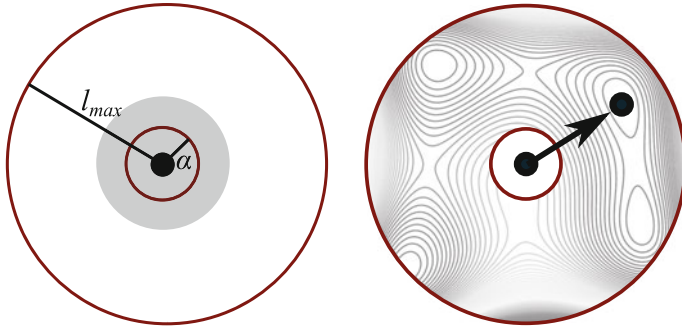
Fig. 1 Stride annulus in the OSM with maximum stride length l_{max} and minimum stride length α. The *grey* area depicts the torso of the pedestrian *Left*. Small scale navigation with the utility function in the OSM. Next step to the position with the highest utility value *Right*

The movement of the pedestrians in the OSM imitates to a certain degree the stepwise movement of humans [11]. Pedestrians in the OSM (version of [16]) make their next step within a circle of which the radius represents the maximum stride length. This stride length l_{max} of a pedestrian is determined from Eq. 1

$$l_{max} = \alpha + \beta \cdot v_{ff}, \tag{2}$$

using the pedestrian's free flow speed v_{ff}. Since pedestrians choose their next position on a whole disk, they can make very small steps. However, the linear correlations found in experiments imply a residual stride length α. Thus, we introduce a minimum stride length with the length α in the OSM. Now, the pedestrians search for their next position on an annulus. See Fig. 1.

Small scale navigation of the pedestrians in the OSM, that is the avoidance of other pedestrians and walls and the orientation to the next target, is modelled by a superposition of utility functions that reflect these behaviours [10, 11, 15, 16]. Hence, every place in the scenario has a specific utility value for each pedestrian at every time step. The position with the highest utility on the stride annulus becomes the next position of the pedestrian (see Fig. 1). Methods for solving this optimisation problem can be found in [11, 14–16].

For the results in this paper, we use the avoidance and orientation functions from [16]. The optimisation problem on the annulus is solved by the Nelder–Mead simplex method [8]. Positions are updated using an event driven scheme as described in [12].

We use the implementation of the Optimal Steps Model in the simulation framework VADERE at the Munich University of Applied Sciences. To allow reproduction we lay open the parameters after calibration to the fundamental diagram of [4].

3 Results

In this section, we describe our scenario which mimics the experiment in [4]. Then, we compare the correlations measured in the experiments with the correlations produced by the OSM.

3.1 Scenario and Calibration

We re-enact the walking-in-line experiment from [4, 5]. The scenario is shown in Fig. 2. Pedestrians walk along two circles. The number of pedestrians ranges from 8 to 28 pedestrians per circle. The radii of the circles are 2.4 and 4.1 m. The density on the circles is defined as the inverse of the distance between the centre of two pedestrians [5]. Thus, different densities and velocities can be observed.

We use α and β from [5] to parametrise the stepping mechanism in the Optimal Steps Model. We further calibrate the personal space parameters of the Optimal Steps Model to the fundamental diagram from [4], measured in the same series of experiments. The personal space parameters determine the distance agents try to keep from each other to preserve their personal space [16]. The simulation parameters are compiled in Table 1. In Fig. 3 the measured fundamental diagram is compared to the simulation output.

(a)   **(b)**
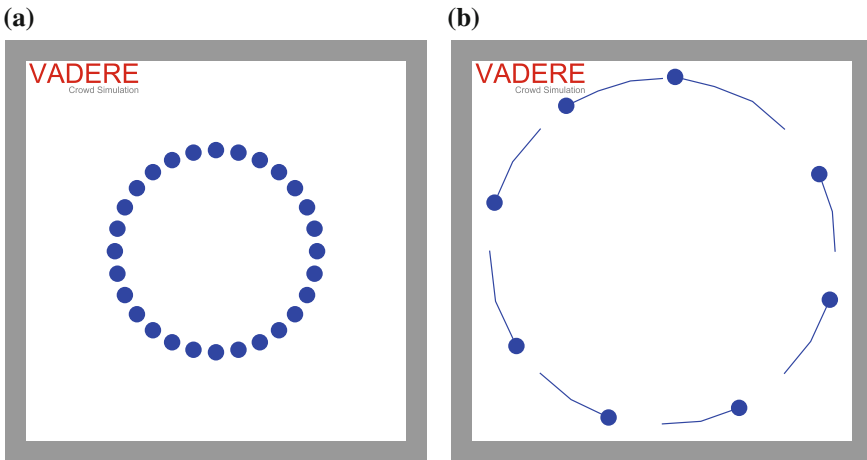
Fig. 2 Re-enactment of the experiment from [4, 5] with the OSM in the simulation framework VADERE. Highest density with 28 persons on the small circle (**a**). Snapshot before starting. Lowest density with 8 persons on the large circle (**b**). Snapshot shortly after starting. The trajectories of the first two to three strides are shown

Table 1 Parameters of the OSM after calibration to the experiment from [4, 5]

Param.	Description	Value
α	Residual stride length	0.065 m
β	Slope of the stride length function	0.724 m
r	Radius of a pedestrian's torso	0.2 m
δ_{int}	Intimate distance	0.45 m
δ_{pers}	Personal distance	1.20 m
δ_o	Distance kept from obstacles	0.8 m
μ_p	Strength of 'pedestrian avoidance'	55.0
a_p	Moderation between intimate and personal space	0.8
b_p	Intensity of intimate space	1
c_p	Intensity of personal space	3
μ_o	Strength of 'obstacle avoidance'	6.0
v_{mff}	Mean free-flow speed	1.4 m/s
σ_{mff}	Variance of the mean free-flow speed	0.2 m/s

Fig. 3 Fundamental diagram of the simulation output after calibration to the fundamental diagram from [4]
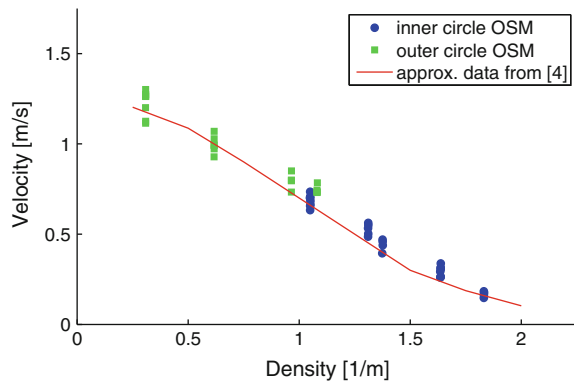
3.2 Stride Lengths and Stride Duration

Figure 4 shows the dependency of the pedestrians' stride lengths on their walking speeds in the simulation. The red line is the reference line from the controlled experiment [5]. The simulation results match the reference line quite well. Since only the minimum and maximum stride length in the free-flow case are fed into the Optimal Steps Model, this is an emergent model behaviour. The stepping mechanism adapts to changes in density.

For slow walking speeds the dependency of the stride duration on the walking speed in the simulation is almost identical to the dependency observed in the experiment from [5]. The stride duration decreases with increasing speed. However, there is a difference at higher velocities. In the experiment the stride duration remains approximately constant between 0.7 and 1.2 m/s. Then, it seems to increase again. In

Fig. 4 Correlation of stride lengths and velocities in the simulation compared to the reference line from the experiment [5]
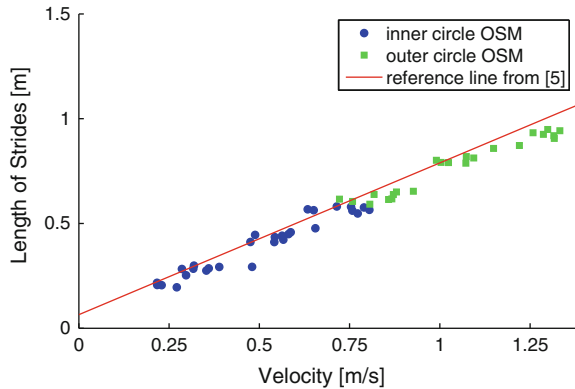
Fig. 5 Correlation of stride durations and velocities in the simulation compared to approximated data from [5] and reference curve from [3]
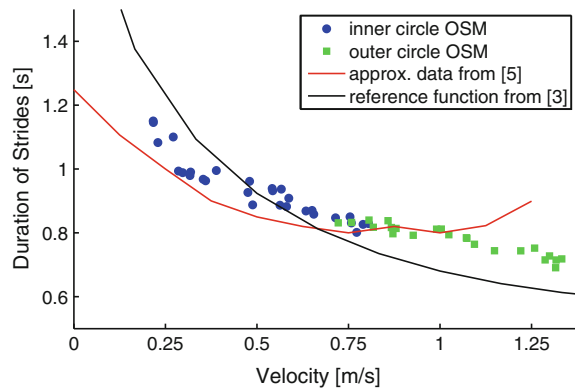
the simulation the stride duration keeps slowly decreasing beyond 0.7 m/s. In other experiments, this slow decrease when walking faster was also observed [3]. In Fig. 5 the simulation output of the Optimal Steps Model is compared to the data from [5] and [3]. Unfortunately, no error margins were reported for the experiments. In view of this, we argue that the general trend is well captured by the simulation.

4 Conclusions

In this paper, we focused on the reproduction of two characteristics of pedestrian movement that were measured in several recent experiments: stride length and stepping frequency. We used the Optimal Steps Model to simulate a scenario from an experiment where pedestrians walked on two circles with different radii and where the density was varied. The simulations reproduced the measured correlations between stride length and velocity as well as stride duration and velocity thus validation the Optimal Steps Model. We propose these correlations as suitable test cases for the validation of locomotion models that are able to capture stepwise movement.

References

1. Chattaraj, U., Seyfried, A., Chakroborty, P.: Comparison of pedestrian fundamental diagram across cultures. Adv. Complex Syst. **12**(3), 393–405 (2009)
2. Grieve, D.W., Gear, R.J.: The relationships between length of stride, step frequency, time of swing and speed of walking for children and adults. Ergonomics **9**(5), 379–399 (1966)
3. Hoogendoorn, S.P., Daamen, W.: Pedestrian behavior at bottlenecks. Transp. Sci. **39**(2), 147–159 (2005)
4. Jelić, A., Appert-Rolland, C., Lemercier, S., Pettré, J.: Properties of pedestrians walking in line: fundamental diagrams. Phys. Rev. E **85**(3), 036111 (2012)
5. Jelić, A., Appert-Rolland, C., Lemercier, S., Pettré, J.: Properties of pedestrians walking in line. II. Stepping behavior. Phys. Rev. E **86**(4), 046111 (2012)
6. Jezbera, D., Kordek, D., Kříž, J., Šeba, P., Šroll, P.: Walkers on the circle. J. Stat. Mech.: Theory Exp. **2010**(01), L01001 (2010)
7. Köster, G., Zönnchen, B.: Queuing at bottlenecks using a dynamic floor field for navigation. In: The Conference in Pedestrian and Evacuation Dynamics 2014. Transportation Research Procedia, pp. 344–352. Delft, The Netherlands (2014)
8. Nelder, J.A., Mead, R.: A simplex method for function minimization. Comput. J. **7**, 308–313 (1965)
9. Seitz, M.J., Dietrich, F., Köster, G.: A study of pedestrian stepping behaviour for crowd simulation. In: The Conference in Pedestrian and Evacuation Dynamics 2014. Transportation Research Procedia, pp. 282–290. Delft, The Netherlands (2014)
10. Seitz, M.J., Dietrich, F., Köster, G.: The effect of stepping on pedestrian trajectories. Phys. A: Stat. Mech. Appl. **421**, 594–604 (2015)
11. Seitz, M.J., Köster, G.: Natural discretization of pedestrian movement in continuous space. Phys. Rev. E **86**(4), 046108 (2012)
12. Seitz, M.J., Köster, G.: How update schemes influence crowd simulations. J. Stat. Mech.: Theory Exp. **7**, P07002 (2014)
13. Seyfried, A., Steffen, B., Klingsch, W., Boltes, M.: The fundamental diagram of pedestrian movement revisited. J. Stat. Mech.: Theory Exp. **2005**(10), P10002 (2005)
14. von Sivers, I.: Numerische Methoden zur Optimierung der Schrittrichtung und -weite in einem Modell der Personenstromsimulation. Master's thesis, Fernuniversität in Hagen (2013)
15. von Sivers, I., Köster, G.: Realistic stride length adaptation in the optimal steps model. In: Traffic and Granular Flow'13. Jülich, Germany (2013)
16. von Sivers, I., Köster, G.: Dynamic stride length adaptation according to utility and personal space. Transp. Res. Part B: Methodol. **74**, 104–117 (2015)
17. von Sivers, I., Templeton, A., Köster, G., Drury, J., Philippides, A.: Humans do not always act selfishly: Social identity and helping in emergency evacuation simulation. In: The Conference in Pedestrian and Evacuation Dynamics 2014. Transportation Research Procedia, pp. 585–593. Delft, The Netherlands (2014)
18. Weidmann, U.: Transporttechnik der Fussgänger, *Schriftenreihe des IVT*, vol. 90, 2 edn. Institut für Verkehrsplanung, Transporttechnik, Strassen- und Eisenbahnbau (IVT) ETH, Zürich (1992)

Experimental Study on the Influence of Step Phase in Pedestrian Movement

Chi Liu, Weiguo Song and Siuming Lo

Abstract There is a fundamental relationship between the headway and velocity in pedestrian dynamics; this is of great importance in building a pedestrian movement model. However, it is found that even if experiment conditions are strictly controlled, the velocity of pedestrians with the same headway varies considerably. This implies that states of pedestrians should be considered thoroughly, and its influence to macroscopic parameters needs to be quantified. A single-file pedestrian movement experiment is carried out to analyse the microscopic moving characteristics of pedestrians. The trajectories of participants in a straight passageway are extracted through an image processing method based on a mean-shift algorithm. The transverse swing of trajectories is correlated with the phase of pedestrians' steps period. The stride length and frequency of pedestrians are collected from the trajectories. Besides, the synchronisation of the lock-step group varies during the movement. The findings can give the stop-and-go phenomenon a new microscopic explanation. This study can be used to evaluate pedestrian microscopic movement and the development of evacuation models.

1 Introduction

Running a traffic system efficiently with limited resource is a great challenge for city coordinators and facility designers. Pedestrian movement plays an important role in traffic systems. Many measures have been adopted to improve efficiency and safety

C. Liu (✉) · W. Song
State Key Laboratory of Fire Science, University of Science and Technology of China,
Hefei 230026, People's Republic of China
e-mail: roygain@mail.ustc.edu.cn

W. Song
e-mail: wgsong@ustc.edu.cn

S. Lo
City University of Hong Kong, Tat Chee Avenue, Kowloon, Hong Kong
e-mail: bcsmli@cityu.edu.hk

of pedestrian traffic including route planning, density control, risk assessment, and evacuation. All of these approaches based on the researches of pedestrian dynamics.

Experiments and models are used to study pedestrian dynamics. Many models have been established to describe the movement and predict behaviour of pedestrian [1, 7]. Experiments do not only provide data for the simulation itself, but also impact significantly on model validation [3, 5–7]. One of the simplest forms of pedestrian movement, the one-dimensional pedestrian movement experiments have been carried out in the past few decades. For example, Seyfried et al. [6] organised a single-file pedestrian movement experiment. They observed pedestrians moving forward with the front neighbour at the same time-step in high density, which behaviour is called the lock-step. By analysing video recordings of a crowd disaster, Helbing et al. [2] found two sudden transitions leading from laminar to stop-and-go flows and from there to 'turbulent' crowd motion, which can trigger the trampling of people. Jelicet et al. [3] studied the phenomena of synchronisation and showed its dependence on flow densities by experimental analysis. Models containing stepping behaviour have also been built. Yanagisawa et al. [4] developed a simple model for pedestrians by dividing walking velocity into two parts, which are step size and pace of walking. They have discovered that a rhythm that is slower than the normal-walking pace in the free-flow situation increases the flow in congested situations.

In this paper, several single-file pedestrian movement experiments were performed. Based on a space coordinate tracking approach, the trajectories were obtained, containing information of stepping behaviour characteristics. By statistical analysis, we discuss basic elements of stepping behaviour, such as step length and step duration. We also make a comparison between the characteristics of synchronisation and anti-synchronisation movement.

2 Experiment

2.1 Experimental Set-Up

The experiment was conducted by the research group of Prof. Song, in Baoji China, in October, 2009. A sketch of the experimental set-up can be seen in Fig. 1. The experimental scene is like a stadium track which has a length of 21.94 m. There were 60 college students participating the experiment, of which 20 were male and 40 were female. The participants are between 19 and 22 years old and between 152 and 180 cm tall, on average 20 years old and 164 cm tall. There were 9 different experiment situations (5, 10, 15, 20, 25, 30, 40, 50, 60 pedestrians on the track) and the densities varied from 0.23 P/m (5 P/21.94 m) to 2.73 P/m (60 P/21.94 m). In order to reduce tracking error, the red area was selected to be analysed. The length and the width of the area are 3.6 m and 0.7 m, respectively.
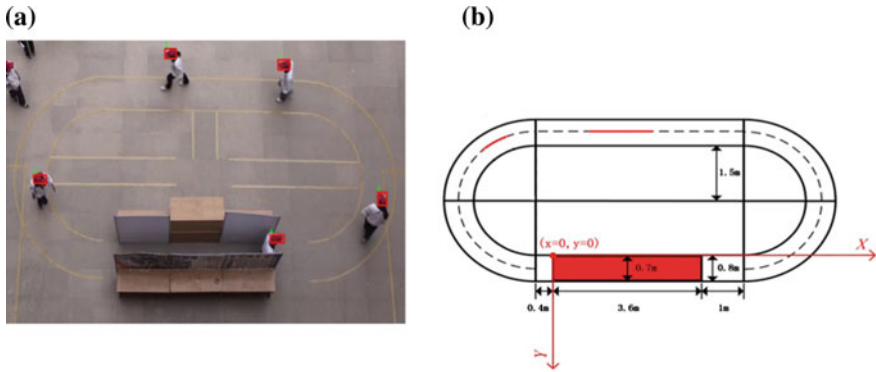
Fig. 1 The single-file experiment: picture (**a**) and its set-up (**b**)

2.2 Data Extraction

The experiment procedures were recorded by a video camera with a resolution of
1920×1080 pixels and a frame rate of 25 fps. The positions of the red hats from
each frame image were extracted by a mean-shift algorithm in Matlab. The Direct
Linear Transformation method was used to transform the trajectories which composed the image positions to the real space coordinates. Then, the time-space diagram
composed x-coordinates and y-coordinates of the trajectories, produced for further
analysis.

2.3 Statistical Method

When walking, humans alternate the feet their rest on. This causes the head of a
pedestrian to sway. The trajectories of participants sway more obviously when the
velocities get slower. Time-space diagrams of the head hence contain the information
of step length and step duration. The duration of a sway equals to the duration of a
single step, and the distance of the step can be derived from the wave length of the
sway (Fig. 2).

3 Results

3.1 Step Length and Step Duration

Step length and step duration are two basic variables of stepping behaviour. In previous researches, step length and step duration are investigated using experimental data

Fig. 2 Trajectories. Sway of the pedestrian trajectory (**a**). The time-space diagrams composed the information of step length and step duration (**b**). The *black* spots represent x-coordinate and the *red* spot represent y-coordinate of the pedestrian's position. When the velocity is lower, the swaying is more obvious
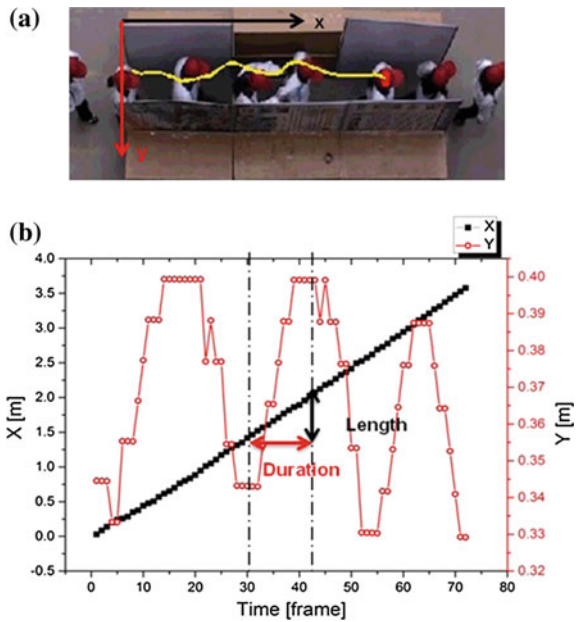
and simulation [3, 7]. In this paper, the variables are correlated with the headway, which can be directly obtained from the experiment data. The results are shown in Figs. 3 and 4.

From statistical results, we can observe that when the headway is larger than 1.1 m, the length and the duration of steps are almost steady. When the headway is smaller, both the length and the duration are linearly correlated with the headway. The stable length and duration are 0.59 m and 0.54 s. Compared with the results of previous research [3, 7], the step length and step duration of free walk in our experiments
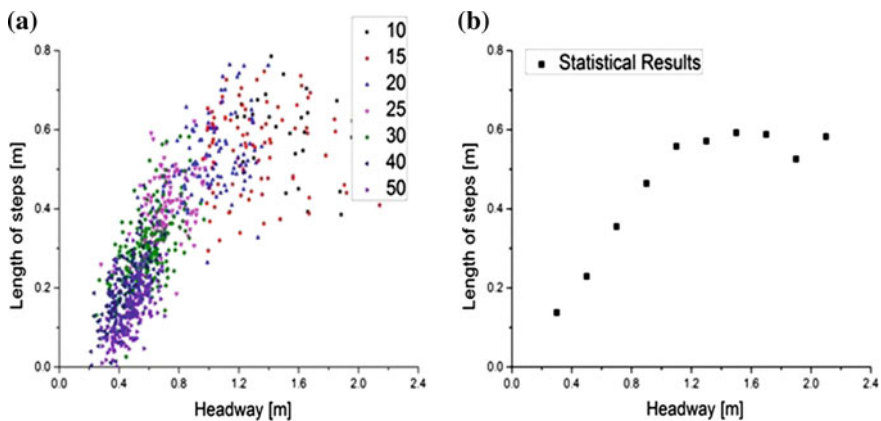
Fig. 3 Step length. All points (**a**). Means (**b**)
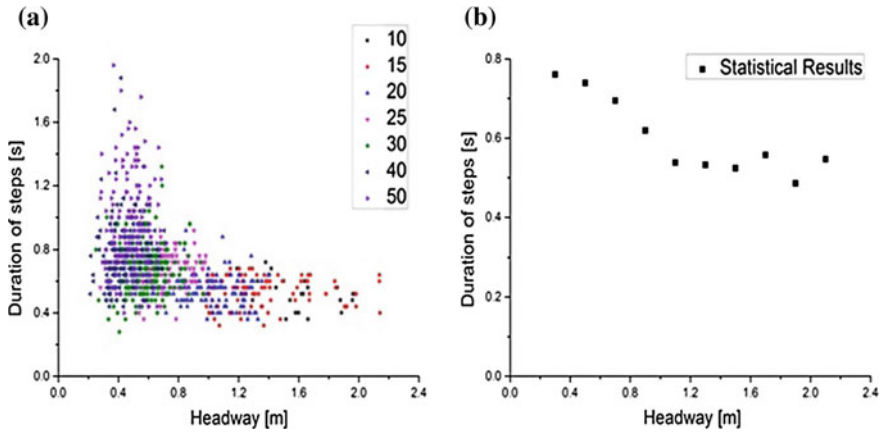
Fig. 4 Step duration. All points (**a**). Means (**b**)

correspond to the feature of Asian and low-velocity-movement. In Daichi's model [7], the step size is supposed to vary with the distance between two adjacent pedestrians, which means that the headway reduces the 'thickness' of pedestrians. The 'thickness' is about 0.35 m. By analysing the experimental data, we found the relation between the headway and the length of steps. This length is almost linearly correlated with the headway in congested situation. One possible explanation is the lock-step behaviour gives extra space to the following pedestrian to put a foot and move.

3.2 Stop-and-Go Behaviour

Helbing et al. [2] found that even with local densities up to 10 P/m^2, the motion of the crowd is not entirely stopped. The pedestrians will keep moving in a stop-and-go pattern. Stop-and-go waves start when the density is high and the flow drops below a critical value. In this single-file experiment, stop-and-go behaviour is particularly obvious in the situation of 50 pedestrians in the track. In the congested situation, the stop-and-go behaviour becomes an important factor that influences the velocities of pedestrian movement.

We suppose the following pedestrian will be reluctant to move when the headway between two adjacent pedestrians is smaller than a rather close distance and once a pedestrian stops, only if the headway is higher, the pedestrian will move on. By analysing the experimental data, we obtain 86 stops in a congested situation. The corresponding average stop-headway and move-on-headway are respectively 0.344 m and 0.487 m (Fig. 5).

3.3 Synchronisation and Anti-synchronisation Movement

According to previous researches, many scholars have studied macro features on the lock-step behaviour [3]. However, the microcosmic influence mechanism of

Fig. 5 An example of
stop-and-go phenomenon in
pedestrian movement. There
are 3 visible stops on this
time-space diagram
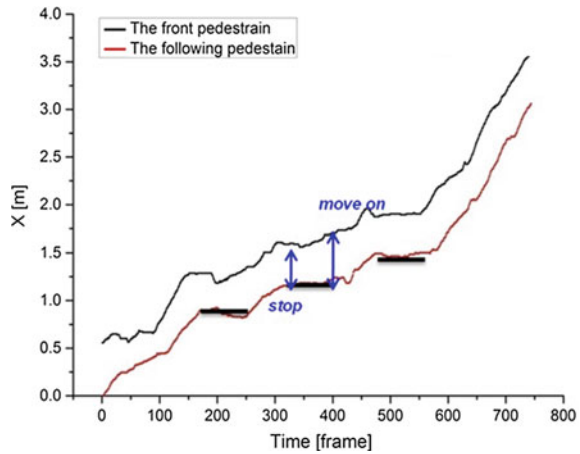
synchronisation lacks of experimental analysis. In our research, two modes are distinguished by time-space diagram. If the peak of the following pedestrian's step is closer to the peak of the leader pedestrian's step in time sequence, this step is considered as a synchronous step. This identification method might lack quantitative precision, but it can qualitatively distinguish synchronisation and anti-synchronisation movement.

From statistical results, we do not find visible difference of length and duration of steps between synchronous and anti-synchronous movement. One possible reason for the result is that the human body is stereoscopic. Once the leader pedestrian is moving, no matter whether the following pedestrian is synchronous or not, he or she will be able to find a space to put a foot and move on (Figs. 6, 7, 8 and 9).
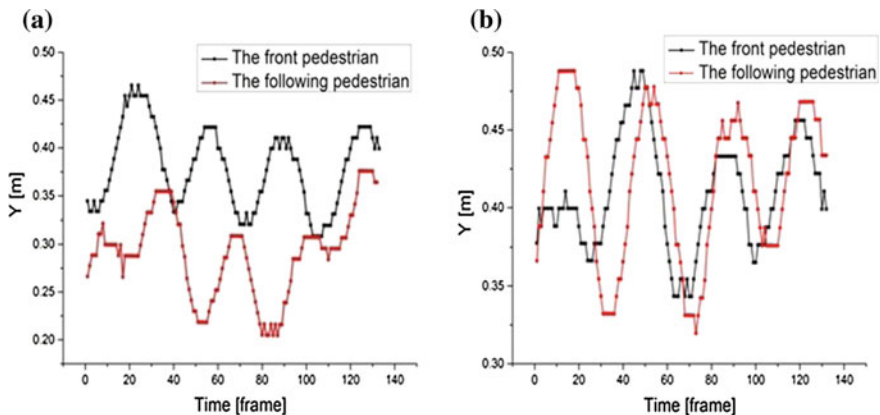
Fig. 6 Typical synchronous (**a**) and anti-synchronous (**b**) movements
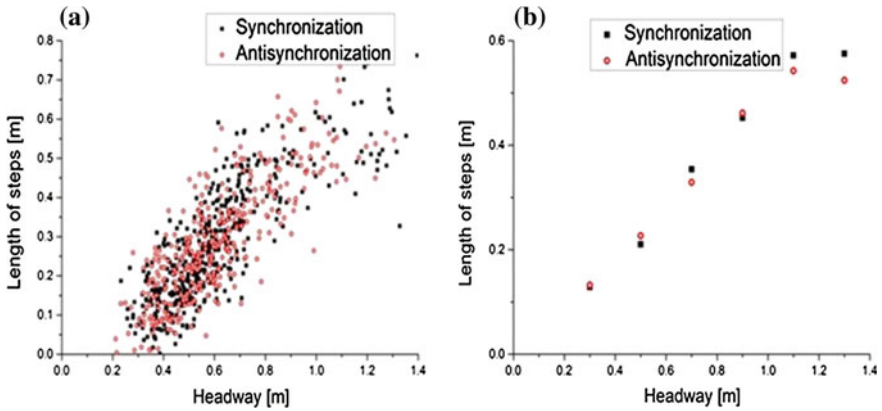
Fig. 7 Step length of two modes. All points (**a**). Means (**b**)
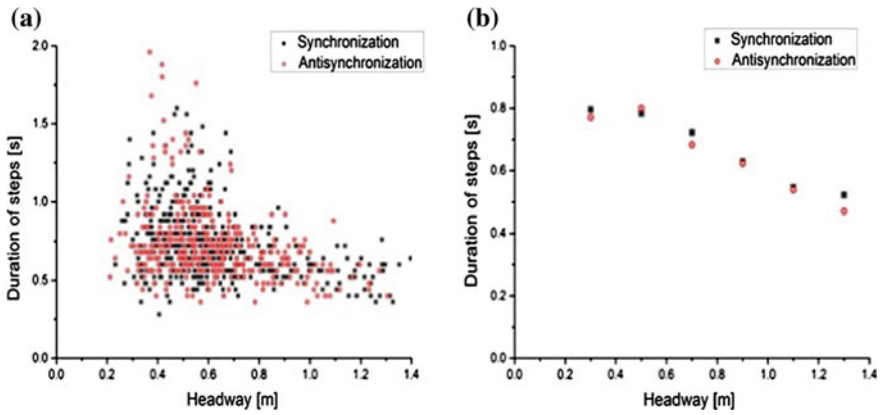
Fig. 8 Step duration of two modes. All points (scatter diagram) (**a**). Means (statistics) (**b**)

Fig. 9 Velocities of two modes
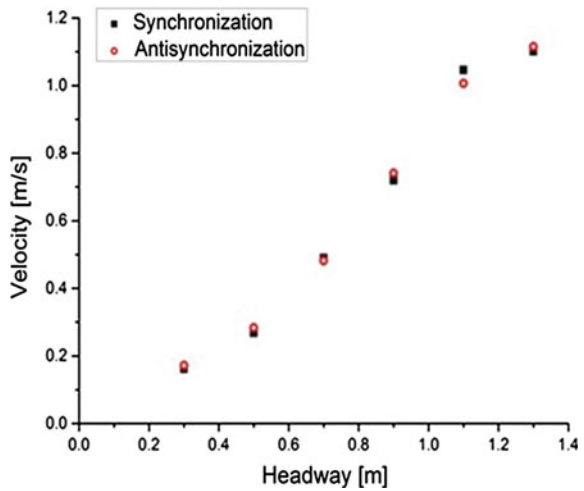
4 Summary

In this paper, we conducted a single-file experiment to study the stepping behaviour of pedestrian movement. By statistical analyses of the experiment, the relation between headway and movement characteristics is found, such as headway and step length, headway and step duration headway and stop-and-go behaviour. Those relations can be used in further model establishing. In addition, a quantitative comparison between the characteristics of synchronous and anti-synchronous movement is presented. From the data of our experiment, no visible difference between these two modes of movement is found.

Generally speaking, we thought synchronising pedestrians steps would improve the effect of movement. We proved such measure will be effective, because the duration of the steps will be controlled in high density. However, we found no evidence that shows spontaneous synchronisation will also improve the effect of the pedestrian movement. This fact should be considered in pedestrian intervention, which we plan to take on as future research.

References

1. Fu, Z., Zhou, X., Chen, Y., Gong, J., Peng, F., Yan, Z., Zhang, T., Yang, L.: The influence of random slowdown process and lock-step effect on the fundamental diagram of the nonlinear pedestrian dynamics: An estimating-correction cellular automaton. Commun. Nonlinear Sci. Numer. Simul. **20**(3), 832–845 (2015)
2. Helbing, D., Johansson, A., Al-Abideen, H.Z.: Dynamics of crowd disasters: an empirical study. Phys. Rev. E **75**(4), 046109 (2007)
3. Jelić, A., Appert-Rolland, C., Lemercier, S., Pettré, J.: Properties of pedestrians walking in line. II. Stepping behavior. Phys. Rev. E **86**(4), 046111 (2012)
4. Mai, X., Song, W., Ma, J.: New definition and analysis of spatial-headway in two-dimensional pedestrian flow. In: Traffic and Granular Flow'13, pp. 111–119. Springer (2015)
5. Porzycki, J., Lubaś, R., Mycek, M., Was, J.: Dynamic data–driven simulation of pedestrian movement with automatic validation. In: Traffic and Granular Flow'13, pp. 129–136. Springer (2015)
6. Seyfried, A., Steffen, B., Klingsch, W., Boltes, M.: The fundamental diagram of pedestrian movement revisited. J. Stat. Mech.: Theory Exp. **2005**(10), P10002 (2005)
7. Yanagisawa, D., Tomoeda, A., Nishinari, K.: Improvement of pedestrian flow by slow rhythm. Phys. Rev. E **85**(1), 016111 (2012)

The Influence of Moore and von-Neumann Neighbourhood on the Dynamics of Pedestrian Movement

Christian Rogsch

Abstract Developing models for pedestrian and evacuation dynamics using a cellular automata is based on the fundamental question of the neighbourhood pedestrians should use to move from one point to another point in a selected geometry. If a rectangular lattice is used for pedestrian movement and geometry representation, there are two possible types of neighbourhoods which can be chosen: the Moore-Neighbourhood or the von-Neumann-Neighbourhood. Both neighbourhoods are used in different kind of models. To show the effect the chosen neighbourhood has on the dynamics of pedestrian movement, different scenarios are investigated using both neighbourhoods by using the same evacuation model.

1 Introduction

Developing models for pedestrian and evacuation dynamics using a cellular automata is based on the fundamental question of the neighbourhood pedestrians should use to move from one point to another point in a selected geometry (see [5]). If a rectangular lattice is used for pedestrian movement and geometry representation, there are two possible types of neighbourhoods, which can be chosen:

- the Moore-Neighbourhood or
- the von-Neumann-Neighbourhood.

Both neighbourhoods (see Fig. 1) are used in different kind of models, e.g. the PedGo-Model [7] uses a Moore-Neighbourhood, the Dynamic Floor Field Model [4] uses a von-Neumann-Neighbourhood. To show the effect the chosen neighbourhood has on the dynamics of pedestrian movement, different scenarios are investigated using both neighbourhoods by using the same evacuation model. Contrary to [1, 6, 8–10], who show results in a more 'mathematical' way, in this paper more 'practical' results are shown, so some different kind of view to this problem is used.

C. Rogsch (✉)
Fire Protection Engineering, Bonhoefferstr. 16, 67435 Neustadt, Germany
e-mail: christian@rogsch.de

Fig. 1 von-Neumann-
Neighbourhood: pedestrian
(*black* cell in the centre) can
only move to *grey* cells by
moving over edge, by using a
Moore-Neighbourhood the
pedestrian can additionally
move to the *white* cells by
moving over corner
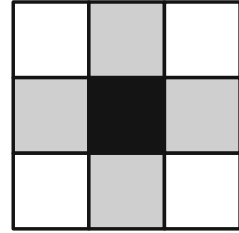
1.1 Wayfinding and Distance Map

As written above, cellular automata models for pedestrian movement are based
(if they use a square lattice) on the von-Neumann-Neighbourhood or the Moore-
Neighbourhood. This has an influence of the movement of pedestrians inside a cho-
sen geometry as well as an influence of the calculated map to find the exit. For this
kind of map several names are used, the most common names are distance map,
potential field or floor field. In Figs. 2 and 3 the difference of a distance map calcu-
lated by using the von-Neumann-Neighbourhood and the Moore-Neighbourhood is
shown. For additional calculation methods the paper of Kretz et al. [2] shows some
additional calculation methods for distance maps.

2 Scenarios

The scenarios presented in this paper are calculated with the 'Quo vadis?' soft-
ware tool developed by Joerg Meister [3], the software tool can be downloaded for
free of charge (December 2015) from http://quovadis-simulation.de/src/downloads.
php. The 'Quo vadis?' software has an 'enhanced' Floor Field Model implemented

(a)   **(b)**
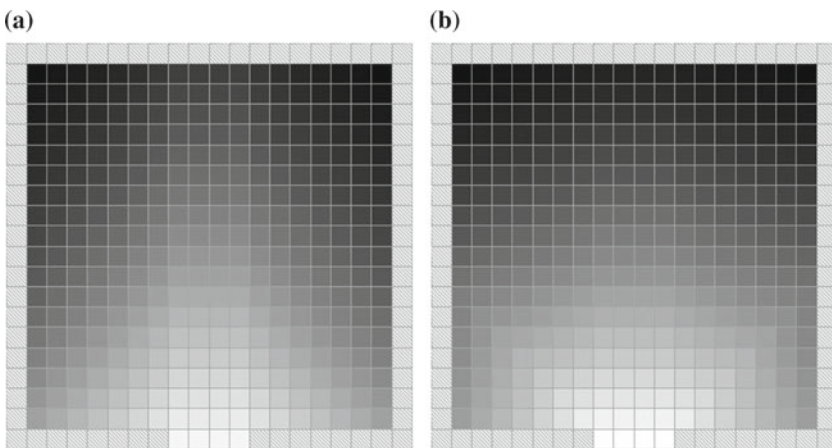
Fig. 2 Distance map calculated with a von-Neumann-Neighbourhood (**a**) and a Moore-
Neighbourhood (**b**)
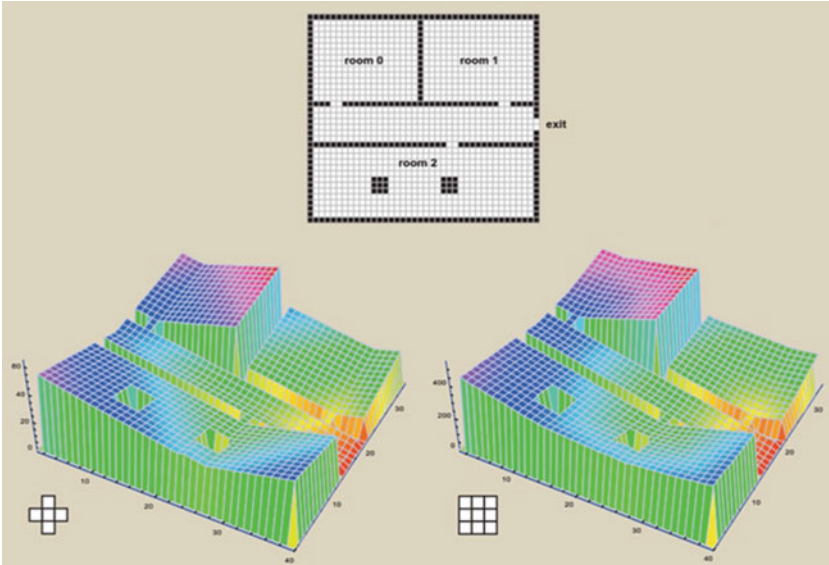
Fig. 3 3D Distance map visualisation calculated with a von-Neumann-Neighbourhood (*left*) and a Moore-Neighbourhood (*right*) for a simple corridor-room scenario [3]

[3, 4], which uses a dynamic floor field. If simulations are done without this dynamic floor field, the parameter k_S is set to 10 and the parameter k_D is set to 0, which means the dynamic floor field is not used in the simulation (only static floor field is used). If simulations are performed with both static and dynamic floor field, the corresponding parameters k_S and k_D are set to default values ($k_S = 3, k_D = 1$). As walking velocity a speed of 1 cell per time-step is used. The size of each lattice is 40×40 cm.

2.1 Simple Room

The first investigated scenario shows a simple room (see Fig. 4), where pedestrians are placed at one end. The exit is placed at the opposite side of the room. The simulation is done with an underlying von-Neumann and Moore floor field. Thus the results by doing a visual analysis seem to be very similar, the time-based results show some differences: by using the von-Neumann-Neighbourhood the simulation takes 51 time-steps to finish, by using a Moore-Neighbourhood it only takes 38 time-steps to finish.

2.2 Simple Corridor

Based on the results of the simple room scenario a very simple corridor is created (see Fig. 5), pedestrians also walk from top to bottom. Contrary to the results

Fig. 4 Simple room
scenario. Pedestrians walk
from *top* to *bottom* (exit is
signed with *pink* '00' at the
bottom)
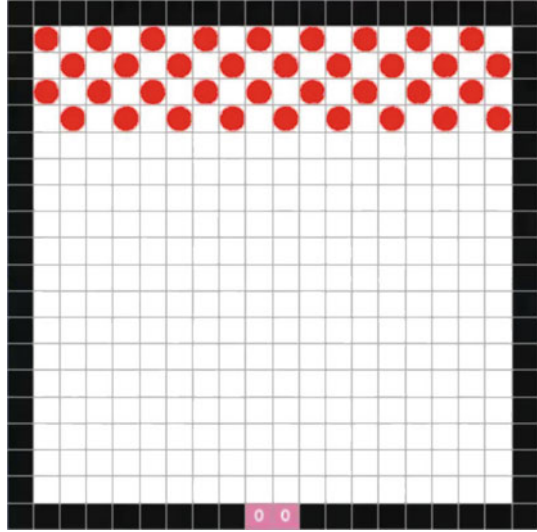
Fig. 5 Simple corridor
scenario. Pedestrians walk
from *top* to *bottom* (exit is
signed with *pink* '000' at the
bottom). Screenshot at half
of the simulation time.
von-Neumann *Left*, Moore
right
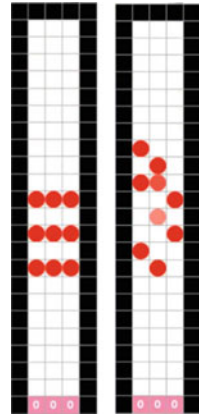
obtained from the simple room scenario, in this case the time-based results are simi-
lar, but the visual analysis shows differences. As shown in Fig. 5 the von-Neumann-
Neighbourhood simulation (left) shows a 'straight forward' movement to the exit
while the Moore-Neighbourhood simulation shows a 'line changing' behaviour of
the pedestrians, which means that the pedestrians do not tend to move straight for-
ward, they tend to move 'over corner' and change the lane they started. The distance
maps of both scenarios (von-Neumann and Moore) are the same, but at the Moore-
Neighbourhood pedestrian has always a chance to move forward 'over corner' with
the same possibility than moving 'straight forward'. In this simple scenario the effect
of this movement is clearly shown.
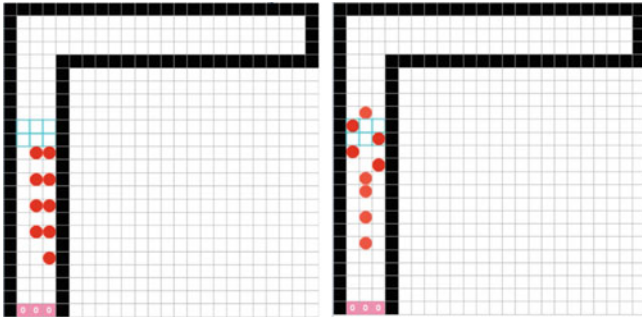
Fig. 6 Simple corner scenario. Pedestrians walk from *right* to *left* to *bottom* (exit is signed with *pink* '000' at the *bottom*). Screenshot at half of the simulation time. von-Neumann *Left*, Moore *right*

Fig. 7 Simple corner scenario. Pedestrian placement in the first simulations (*top*, see Fig. 6) and in the second simulations (*bottom*), where they behave visually in a von-Neumann simulation like a Moore simulation
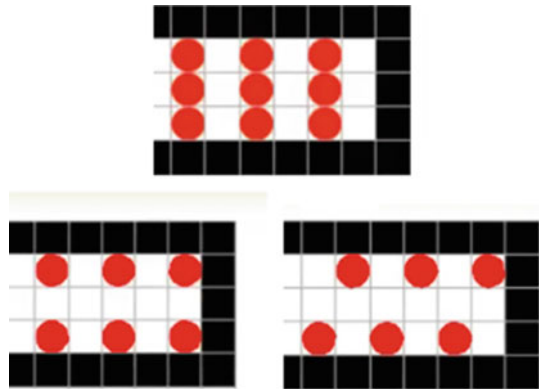
2.3 Simple Corner

Based on the results of the simple room and simple corridor scenario a simple corner is created (see Fig. 6), pedestrians walk from right to left to bottom. Thus, the two scenarios above have shown different results, the question was now, what result would predominate: the 'moving over corner' effect of the Moore-Neighbourhood, or the 'straight forward movement' effect of the von-Neumann-Neighbourhood. The results show, that the simulation does, what we expect. Both neighbourhoods show their effects clearly (von-Neumann: straight forward, Moore: moving over corner, to the inner wall), but the time-based results are nearly identical, so that in this case no 'neighbourhood-effect' shows us 'better' results. The same scenario calculated with other pedestrian placement (see Fig. 7) at the beginning of the simulation shows now (with the von-Neumann-Neighbourhood) that pedestrians are also trying to move to the inner wall as shown in the Moore-Neighbourhood simulation. So by dealing with simple scenarios it should be mentioned how pedestrians are placed at the beginning of a simulation, the influence of visual results can be large, while the time-depending influence can be neglected.

Fig. 8 Room-corridor
scenario. Pedestrians walk
from each room to the exit
on the *right* (exit is signed
with *pink* '000')
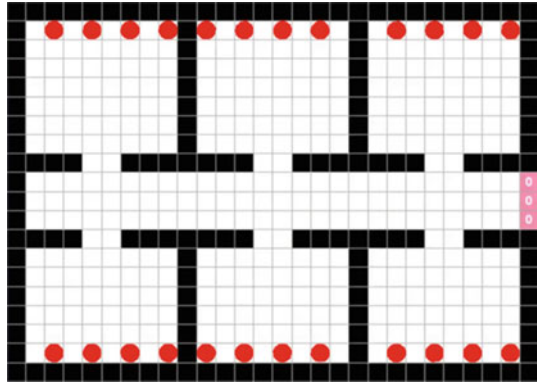
2.4 Rooms and Corridor

After the three simple scenarios based on room, corridor and corner movement, a
combination of the different scenarios will be shown. First, six rooms which lead
to a centred corridor are investigated (see Fig. 8). Each pedestrian has to move from
the end of a room through the door to the corridor and turn left or right towards
the exit. In each room four pedestrians are placed. This scenario has been investi-
gated with four possibilities: using the static floor field with a von-Neumann and
Moore-Neighbourhood and using a dynamic floor field also using the von-Neumann
and Moore-Neighbourhood. The visual results are as expected based on the pre-
vious simulation runs with a static floor field: if a Moore-Neighbourhood is used,
pedestrians tend to move more or less 'over corner' in the corridor and if a von-
Neumann-Neighbourhood is used they tend to move 'straight forward'. Also the
time-based results are similar, thus in this case it does not matter if a von-Neumann
or a Moore-Neighbourhood is used. But if a dynamic floor field is used, the visual
results are nearly identical. On both types of neighbourhoods (von-Neumann and
Moore) pedestrians tend not to move straight forward as seen by using the sta-
tic floor field in combination with the von-Neumann-Neighbourhood, they tend to
move like it can be seen by using a static floor field in combination with a Moore-
Neighbourhood. So, the visual results are different from the static floor field results
discussed above, and the time-based results are also differing. By using the dynamic
floor field, both simulation runs are slower as the static floor field is used. The type
of neighbourhood has no influence on the time-based results (static floor field and
von-Neumann or Moore-Neighbourhood: ca. 36 time-steps, dynamic floor field and
von-Neumann or Moore-Neighbourhood: ca. 50 time-steps).

2.5 Rooms, Corridor and Corners

The last scenario presented in this paper is a combination of rooms, corners and
a corridor (see Fig. 9). As in the previous simulation, also the four different com-

Fig. 9 Rooms, corners and corridor scenario. Pedestrians walk from each room to floor to exit on the *left* (exit is signed with *pink* '000')
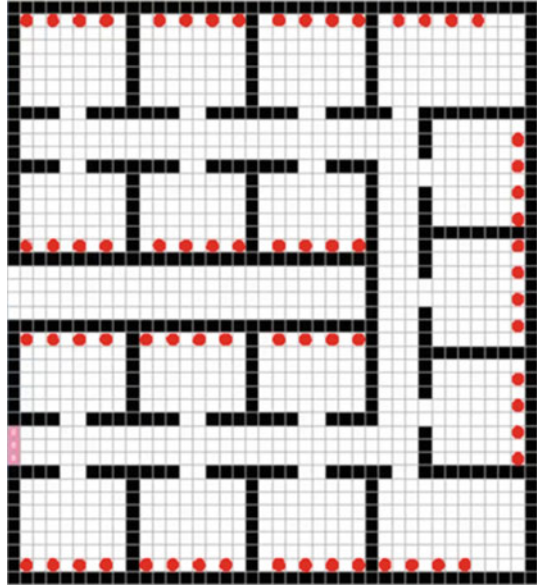
binations of floor field and neighbourhood are investigated. Here we can see, that the main parameter, which has an influence on our simulation results, is the corner movement. By using the static floor field the results clearly show that the pedestrian 'benefit' from the Moore-Neighbourhood. Based on this neighbourhood it is 'easier' for pedestrians to overtake an to use the full width of the corridor contrary to a von-Neumann-Neighbourhood, where a 'straight forward' movement dominates the simulation process, thus pedestrians do not use the full width of the corridor. This visual results is also clearly represented in the time-based results: with the von-Neumann-Neighbourhood, the simulation takes 120 time-steps, while using the Moore-Neighbourhood, it takes only 100 time-steps until all pedestrians have left the scenario. If now a dynamic floor field is used, the visual results are as different as in the static floor field observations. Pedestrians in simulations based on a von-Neumann-Neighbourhood still try to move 'straight forward' as expected. Sure, the effect is not as distinctive as in the static floor field simulation, but is still can be seen. If the time-based results are compared, the results are very different from the static floor field results: with dynamic floor field and von-Neumann-Neighbourhood 210 time-steps are necessary, by using the Moore-Neighbourhood only 150 time-steps are necessary.

3 Conclusions

In this paper several simple and complex scenarios for pedestrian movement using cellular automata software are investigated with the focus on the von-Neumann and Moore-Neighbourhood. For simple scenarios the neighbourhood does not have a very

big influence on the results, it is more the visual component, which is influenced by the neighbourhood. This is based on the fact, that on simple scenarios the effect of different simulation methods can not be seen clearly, because the scenario is to simple and short. To see the influence of different effect in a clear way, more complex scenarios have to be built, based on combinations of the simple scenarios. Only with these complex scenarios, like the scenario based on rooms, corners and corridor the simulation method (here: the neighbourhood and the static or dynamic floor field) could show how the results (visual and time-based) are influenced. Only on this investigation it is not possible to say, which is the right choice for pedestrian movement simulation. It is only possible to say what effects are 'created' by the different methods. If the results should fit to real scale and full scale evacuation trials or pedestrian movement, further research is necessary.

References

1. Davies, C.H.J.: The effect of neighbourhood on the kinetics of a cellular automaton recrystallisation model. Scripta Metallurgica et Materialia **33**, 1139–1143 (1995)
2. Kretz, T., Bönisch, C., Vortisch, P.: Comparison of various methods for the calculation of the distance potential field. In: Klingsch, W., Rogsch, C., Schadschneider, A., Schreckenberg, M. (eds.) Pedestrian an Evacuation Dynamics 2008, pp. 335–346 (2010)
3. Meister, J.: Simulation of crowd dynamics with special focus on building evacuations. Master's thesis, Fachhochschule Wedel, Germany (2007)
4. Nishinari, K., Kirchner, A., Namazi, A., Schadschneider, A.: Extended floor field CA model for evacuation dynamics (2003). arXiv:cond-mat/0306262
5. Schadschneider, A., Klingsch, W., Klüpfel, H., Kretz, T., Rogsch, C., Seyfried, A.: Evacuation dynamics: empirical results, modeling and applications. In: Meyers, R. (ed.) Encyclopedia of Complexity and Systems Science, vol. 5, p. 3142. Springer, New York (2009). ISBN: 978-0-387-75888-6
6. Seitz, M.J., Köster, G.: Natural discretization of pedestrian movement in continuous space. Phys. Rev. E **86**, 046108 (2012)
7. TraffGo-HT GmbH: PedGo Manual
8. Yamamoto, K., Kokubo, S., Nishinari, K.: Simulation for pedestrian dynamics by real-coded cellular automata (RCA). Phys. A: Stat. Mech. Appl. **379**(2), 654–660 (2007)
9. Zawidzki, M.: The influence of grid rotation in von Neumann and Moore neighborhoods on agent behavior in pedestrian simulation. Complex Syst. **23**, 343–354 (2014)
10. Zhang, P., Jian, X.X., Wong, S.C., Choi, K.: Potential field cellular automata model for pedestrian flow. Phys. Rev. E **85**, 021119 (2012)

Simulation of People Flow by a New Fuzzy Discrete Automata Model and an Ergonomic Approach

Henrique C. Braga, Gray F. Moita and Paulo E.M. Almeida

Abstract This work presents the computer program FUGA v. 1.0, developed to simulate the movement of people in constructed environments in normal situations and also during an evacuation in emergency situations. FUGA is based on a discrete automata model using pre-defined rules. This program uses an ergonomic approach associated with human movement and fuzzy logic as a computer intelligence tool to emulate the human decision-making process. The model incorporates mechanical and mental aspects, as well as their quantitative and qualitative nature. This work shows how selected ergonomic quantities are incorporated into a human decision-making process emulated by a fuzzy logic system. FUGA simulates environments with any internal or external geometry; with one or more floors; with or without staircases or ramps and with uni or multi directional flows. Some simulations are performed showing how the software FUGA can be used in the design of safer environments, in a way that could hardly be achieved by simply applying the existing regulations.

1 Introduction

This work presents the new computer program FUGA v. 1.0, developed to simulate the movement of people in constructed environments in normal situations and also during an evacuation in emergency situations. This program is based on a discrete automata model using pre-defined rules. There are several of evacuation models in the literature [5, 8], but FUGA introduces two paradigms still little used, but promisingly valuable. This program uses an ergonomic approach associated with

H.C. Braga (✉) · G.F. Moita · P.E.M. Almeida
Post-Graduate Program in Mathematical and Computational Modelling,
Centro Federal de Educação Tecnológica de Minas Gerais, CEFET-MG,
Av. Amazonas, 7675, Nova Gameleira, Belo Horizonte, MG CEP 30510-000, Brazil
e-mail: bragaseg@yahoo.com.br

G.F. Moita
e-mail: gray@dppg.cefetmg.br

P.E.M. Almeida
e-mail: pema@lsi.cefetmg.br

human movement and the fuzzy logic as a computer intelligence tool to emulate the human decision-making process.

The nuances involved in human movement are multidisciplinary, involving physical, environmental, organisational, physiological and mental aspects and an ergonomic approach allows for the incorporation of these different characteristics in the model. Thus, on top of those, there are several humans mental factors concurrently involved [4, 7]. Therefore, the modelling needs to incorporate all the mechanical and mental aspects, as well as their quantitative and qualitative nature. Fuzzy logic can encompass these features [6, 13].

This work shows how selected ergonomic quantities are incorporated into a human decision-taking process emulated by a fuzzy logic system. FUGA is capable of simulating environments with any internal or external geometry; with one or more floors; with or without staircases or ramps; with different kinds of floors and with uni or multi directional flows.

At the end, some simulations are shown to illustrate how the software can be used in the design of safer environments, in a way that could hardly be done by simply applying the existing safety regulations.

2 FUGA Background

2.1 Discretisation of the Constructed Environment

The first step is to discretise the constructed environment in the form of a bi-dimensional rectangle matrix named environment matrix (EM). Each element of the EM matrix has a specific meaning in the real world. Each element of the EM matrix represents a square with 9 cm of side (resolution of the simulation). Thus, the real constructed environment must be discretised so that all its elements are multiples squares with 9 cm sides.

Differently from the previous version [3], the current FUGA allows the simulation of movements in buildings with any quantities of floors, included staircases and ramps. The entire constructed environment must be represented in just one unique bi-dimensional rectangular matrix, independently of the size, geometry (both internal and external) and number of floors. For better understanding, Fig. 1 shows a two-floor environment connected by a staircase represented in just one single bi-dimensional matrix.

In Fig. 1, the empty area in the floors and in the staircase are show in white, the walls are in black, the exit in the first floor is in orange and the connections between the floors and the staircase are in dark blue. The part of the EM matrix which is not represented in the constructed environment (i.e., which is not included in the simulations) are in light blue surrounding the floors and the staircase. Finally, in grey are pointed the regions of the first and second floors which, in spite of not being obstructed by walls, does not allow human flow because the staircases cause restrictions in the movement.

Fig. 1 Two dimension representation of a constructed environment with two floors connected by a stair
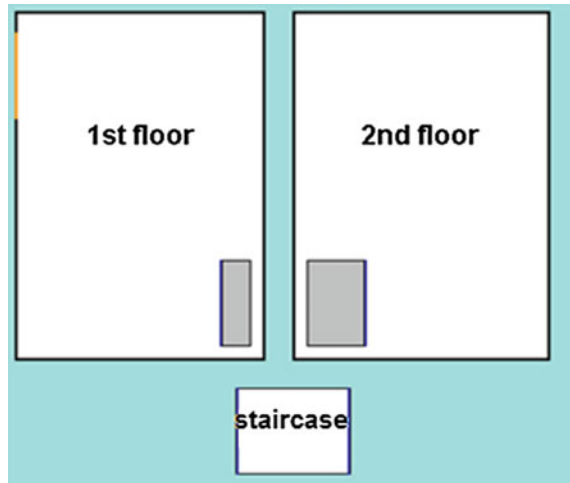
2.2 Ergonomics Variables

Anthropometric aspects A person's movement is a very sophisticated phenomenal in the three-dimensional space [9]. However, the current model is based on two dimensions, and, therefore, the persons will be represented by its vertical body representation. In this work, the human body will be represented by a square of 45 cm of side (25 elements with 81 cm^2 each).

Walking Velocity The walking velocity is an individual parameter that depends upon various others components [1], such as age, gender, physical condition, familiarity of the route; routing purpose; path length, route characteristics, visibility; mental and cultural aspects. In this model, as proposed by Thompson and Marchant [11], the walking velocity (v_w) will be considered as function of the distance between persons (d). When the movement happens in staircases, the walking velocities are reduced in 50%.

Input Variables The input variables are: PR (preferential route), AD (apparent distance), WE (wall effect), SL (stress level), IE (inertia effect) and AE (automata effect). Here, PR is an indication of ideal routes to the exits generated for a given artificial intelligence algorithm [2], AD is an empiric perception of the distance to the exits, WE is the effect of the restrictions on the neighbourhood of the walls, SL is the effect of the stress level of the people [10], IE is the tendency of keeping the same direction of movement and AE is the influence caused by the nearest people.

2.3 Decision-Making Process

The decision-making process is based on fuzzy logic, considering the above input variables and one output variable—RQ (route quality), which indicates the best

individual option of movement for each person in the location. The route to be chosen for each person will be the one that results in the higher RQ. Hence:

$$RQ_k = f_{Fuzzy}(input_k) \tag{1}$$

$$RQ_{ke} = max(RQ_k) \tag{2}$$

$$ke = k \ \forall \ RQ_{ke} = RQ_k \tag{3}$$

where f_{Fuzzy} is the function characteristic of fuzzy system; k is the option of the possible movements: L (left), U (up), D (down) and R (right); ke is the best movement option; RQ_k is each RQ for each possible movement calculated by the fuzzy system and RQ_{ke} is the RQ of the best route [3].

2.4 The Escape Time and the Possibilities of Internal Collision

The time for the effective escape of the environment is an important asset. The escape time is normally considered as the sum of three values: perception time, reaction time and effective movement time. With the software FUGA it is possible to consider, or not, the perception and the reaction time. Thus, in the start of the simulation, all people begin to move in the direction of the nearest available exit after the perception and reaction pre-set times.

Another important factor is the safety of the escape process. During the escape, different people behaviour can happen. The first two are the organised behaviour and the competitive behaviour [7]. In the organised behaviour one person does not touch another person. The social agreements are partially respected. This is the safest way. In the competitive behaviour, the people do not necessary respect the social agreements and large energy transfer can occur among the involved people.

A situation potentially dangerous is when the so-called critical jamming occurs. In the critical jamming, there are enormous energy transfers between different persons, which can potentially cause deaths or broken walls, and no free movement is possible.

The effective energy transfer between people cannot be directly determined by this version of the software FUGA, neither the possibilities of jamming. However, the software shows the parameter *Possibilities of Occurrence of Internal Collision* (POIC) among the people, which can be used as a qualitative indicator of the jamming possibilities.

There are four kinds of POIC. POIC 1 indicates how many times, during the escape up to the exit, the persons have the first best option of movement obtained by the fuzzy system (higher RQ option) blocked. POIC 2 indicate how many times, during the escape up to the exit, the persons have the first and the second best options of movement obtained by the fuzzy system blocked. According to the same rules, POIC 3 indicates how many times the first, the second and the third best options of movement are blocked. Finally, POIC 4 indicates how many times the persons have

all possibilities of movement blocked (the only option for the person in this situation is to remain in the same place, even if he/she wants to move).

Thus, a POIC 1 with low value indicates a low possibility of the occurrence of internal collisions or jamming, but a higher POIC 4 indicates a real possibility of jamming occurrence during the escape.

3 Results and Discussions

In order to better understand the influence of some parameter of the input of the fuzzy system, some examples are showed in Figs. 2, 3 and 4. Figure 2 shows the distance map [12] of the environment of Fig. 1. Each colourful band indicates a 1 m exit estrangement, beginning in the exit, passing the first floor, through the staircases and also covering all second floor. The distance map is produced by the algorithm used to obtain the values of PR and AD necessary for the input of the fuzzy system.

Figure 3 shows a simulation of an environment with two exits and one floor with various internals rooms. The persons are depicted in their initial positions, the exits are in orange and the routes used to get to the exits are in yellow. The blue ellipse highlights an area in the simulated environment that is zoomed in the right-hand side. In the enlarged image, an arrow identifies the route that a person used toward the passage of the room. From the PR e AD input variables, this person should have passed closer to the wall, but it did not happen due the effect of input variable WE.

Figure 4 shows the influence of input variable AE. In Fig. 4, 100 people positioned in the left of a large corridor are moving to the exit located at right end of it. The persons are showed placed in their initial position and the routes used to reach the exits are shown in yellow. At the beginning the persons occupied only the middle of the

Fig. 2 Distance map for Fig. 1 environment
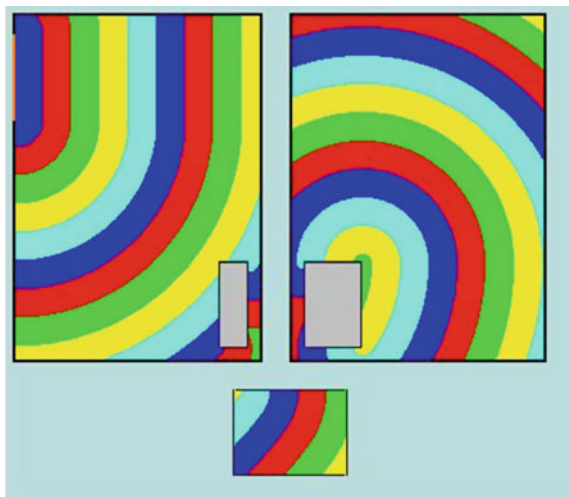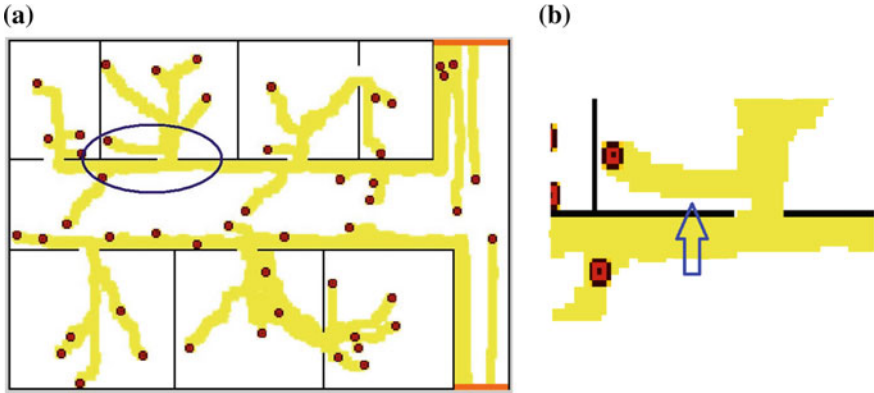
Fig. 3 Evacuation simulation of an environment (**a**), showing the influence of input variable WE on the route chosen by one person (**b**)

Fig. 4 Evacuation simulation in a corridor with 100 people, showing the influence of the input variable AE on the route choice (*yellow*) up to the exit

corridor. During the movement towards the exit the persons increased the occupied area of transversal section of the corridor due the effect of the input variable AE (an increase of the yellow range).

In order to better understand the potentiality of FUGA, some experiments are also made. Figure 5 shows a 400 m^2 square environment with 200, 500 or 1000 people
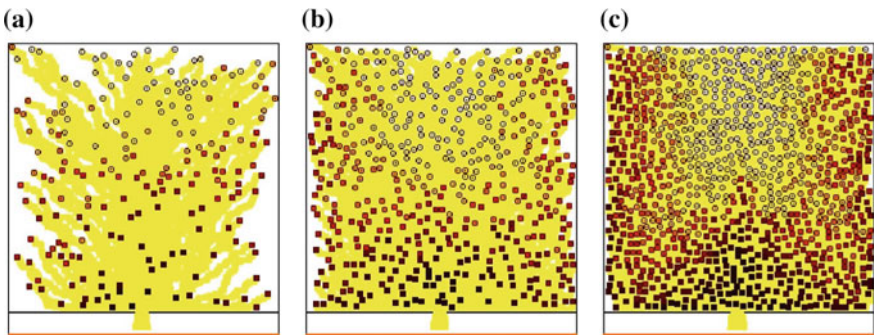
Fig. 5 Evacuation a 400 m^2 square environment with 200, 500 and 1000 persons (**a**, **b** and **c** respectively)
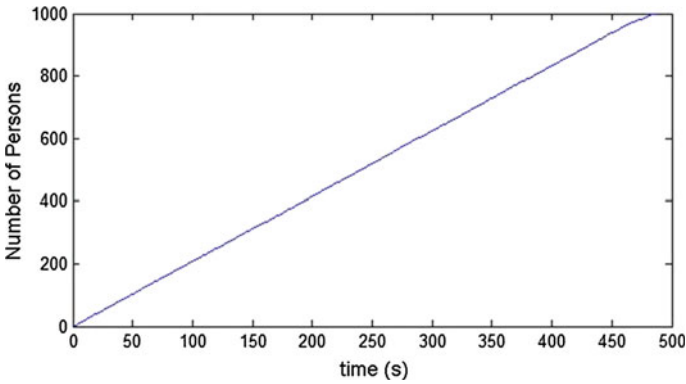
Fig. 6 Evolution of the total number of persons leaving the environment as a function of time
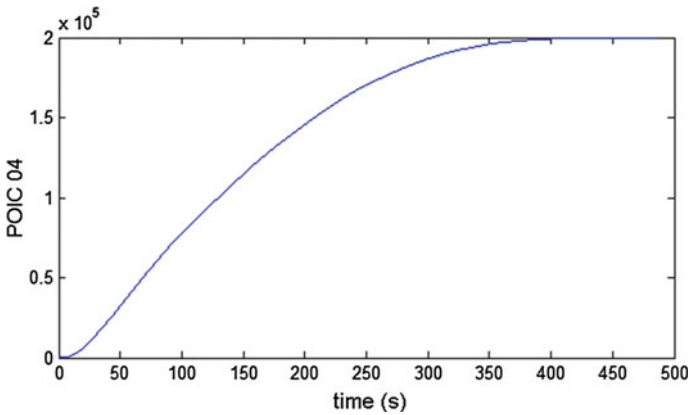
Fig. 7 Evolution of the values of POIC 4 as a function of time

in their initial position and the routes to get to the exits are in yellow. The results for the evacuation of 1000 people are showed in Figs. 6 and 7. Figure 6 shows the total number of persons leaving the environment as a function of time, considering the non-occurrence of a critical jamming. However, the values found for POIC as a function of time (Fig. 7) are very expressive and shows that this is a critical and potentially dangerous situation.

4 Final Considerations

The new software FUGA uses an ergonomic approach to incorporate the human behaviour and the fuzzy logic to emulate the decision-making process in people's movement. Important characteristics, such as the possibilities of simulating multi-

floor environments, performing multi directional movement and generating very precisely distance maps, for example, allow for a wide range of applications with good quality results. The utilisation of software FUGA can yield studies about safety of an environment during the project phase, which is very relevant as a complement to the legal codes application.

References

1. Abley, S.: Pedestrian Planning and Design Guide. LNTZ—Land Transport New Zealand, Wellington (2007)
2. Braga, H.C., Moita, G.F., Almeida, P.E.M.: Algorithm to generate the smallest discretized path to the exit of an environment. In: ABMEC (ed.) XXXVI CILAMCE—Ibero-Latin American Congress on Computational Methods in Engineering (2015)
3. Braga, H.C., Moita, G.F., Camargo, F., Almeida, P.E.M.: Simulation of the movement of people in emergency situations: ergonomic and computational aspects with fuzzy automata and its application in architectural design. Ambiente Construído **14**(2), 61–77 (2014)
4. Kuligowski, E.D.: Predicting human behavior during fires. Fire Technol. **49**(1), 101–120 (2013)
5. Kuligowski, E.D., Peacock, R.D., Hoskins, B.L.: A Review of Building Evacuation Models. National Institute of Standards and Technology (2005)
6. Nunes, I.L.: Handling human-centered systems uncertainty using fuzzy logics. Ergon. Open J. **3**, 38–48 (2010)
7. Pan, X., Han, C.S., Dauber, K., Law, K.H.: A multi-agent based framework for the simulation of human and social behaviors during emergency evacuations. AI Soc. **22**(2), 113–132 (2007)
8. Pelechano, N., Allbeck, J.M., Badler, N.I.: Virtual crowds: methods, simulation, and control. In: Synthesis Lectures on Computer Graphics and Animation, vol. 3. Morgan & Claypool Publishers (2008)
9. Schadschneider, A., Klüpfel, H., Kretz, T., Rogsch, C., Seyfried, A.: Fundamentals of pedestrian and evacuation dynamics. In: Multi-Agent Systems for Traffic and Transportation Engineering, pp. 124–154 (2009)
10. Staal, M.A.: Stress, Cognition, and Human Performance: A Literature Review and Conceptual Framework. NASA Technical Memorandum (2004)
11. Thompson, P.A., Marchant, E.W.: A computer model for the evacuation of large building populations. Fire Saf. J. **24**(2), 131–148 (1995)
12. Thompson, P.A., Marchant, E.W.: Testing and application of the computer model 'simulex'. Fire Saf. J. **24**(2), 149–166 (1995)
13. Yang, L., Zhao, T., Meng, F.: Ergonomic fuzzy evaluation of firefighting operation motion. J. Ind. Eng. **2013** (2013)

The Inflection Point of the Speed–Density Relation and the Social Force Model

Tobias Kretz, Jochen Lohmiller and Johannes Schlaich

Abstract It has been argued that the speed–density digram of pedestrian movement has an inflection point. This inflection point was found empirically in investigations of closed-loop single-file pedestrian movement. The reduced complexity of single-file movement does not only allow a higher precision for the evaluation of empirical data, but it occasionally also allows analytical considerations for microsimulation models. In this way it will be shown that certain (common) variants of the Social Force Model (SFM) do not produce an inflection point in the speed–density diagram if infinitely many pedestrians contribute to the force computed for one pedestrian. We propose a modified Social Force Model that produces the inflection point.

1 Introduction: Empirical Data on Pedestrians' Speed–Density Relation

In the course of recent years a number of experiments have been conducted in which pedestrians walk single-file in a closed loop [1, 9–12]. Having a different number of pedestrians in the loop, different densities are prepared. In a section of the loop line density and speed are measured. Figure 1 shows the experimental set-up from which most data stems. There were experiment runs in which the loop was larger and more pedestrians participated, but the principle was always the same.

The experiment has been conducted at various places around the world. Figure 2 shows the results for India and Germany. With the free speeds plotted in this diagram the existence of an inflection point is obvious. It is not quite clear, however, at which density curvature is maximally negative and also the density of the inflection point can only be estimated roughly.

T. Kretz (✉) · J. Lohmiller · J. Schlaich
PTV Group, Haid-und-Neu-Str. 15, 76131 Karlsruhe, Germany
e-mail: tobias.kretz@ptvgroup.com

J. Lohmiller
e-mail: jochen.lohmiller@ptvgroup.com

J. Schlaich
e-mail: johannes.schlaich@ptvgroup.com
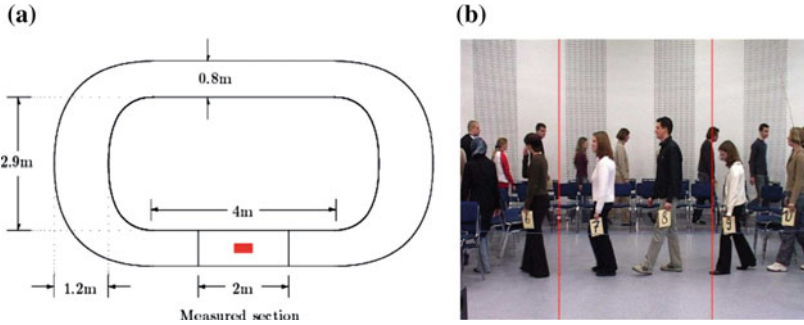
Fig. 1 Experimental set-up. *Source* Figs. 2 and 3 of [12]
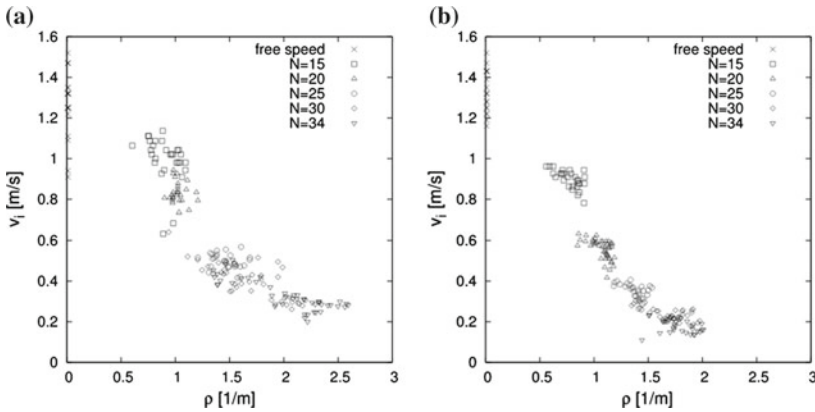
Fig. 2 Speed density diagram: India (**a**); Germany (**b**). *Source* Fig. 5 of [1]

Whereas Fig. 2 clearly shows that differences between India and Germany were found, the loop size (corridor length) and the profession of participants did not make a difference, at least not an obvious one. Compare Fig. 7 of [1] with Fig. 1 of [9].

The discussion[1] in [12] indicates that the existence of an inflection point is common sense and more so that for—at least moderately—high densities the curvature of the flow density relation is positive.

2 The Social Force Model for Steady States in Single-File Movement

The circular specification of the Social Force Model [2] is defined as[2]:

---

[1]Quote (p. 3): "*Domain I*: …*At low densities there is a small and increasing decline of the velocity* …*Domain III*: …*For growing density the velocity remains nearly constant*.".

[2]We neglect here forces from walls from the beginning since we are anyway working towards the one-dimensional case.

$$\ddot{\mathbf{x}}_\alpha(t) = \frac{\mathbf{v}_{0\alpha} - \dot{\mathbf{x}}_\alpha(t)}{\tau_\alpha} + \tilde{A}_\alpha \sum_\beta w(\mathbf{x}_\alpha(t), \mathbf{x}_\beta(t), \dot{\mathbf{x}}_\alpha(t), \lambda_\alpha) e^{-\frac{|\mathbf{x}_\beta(t) - \mathbf{x}_\alpha(t)| - R_\alpha - R_\beta}{B_\alpha}} \hat{e}_{\alpha\beta} \quad (1)$$

$$w(\mathbf{x}_\alpha(t), \mathbf{x}_\beta(t), \dot{\mathbf{x}}_\alpha(t), \lambda_\alpha) = \lambda_\alpha + (1 - \lambda_\alpha) \frac{1 + \cos(\theta_{\alpha\beta}(\mathbf{x}_\alpha(t), \mathbf{x}_\beta(t), \dot{\mathbf{x}}_\alpha(t)))}{2} \quad (2)$$

where $v_{0\alpha}$ is the desired speed of pedestrian α. $\tilde{A}_\alpha > 0$, $B_\alpha > 0$, $0 \le \lambda_\alpha \le 1$, and $\tau_\alpha > 0$ are parameters of the model. R denotes the body radius of a pedestrian. $\hat{e}_{\alpha\beta}$ points from pedestrian β on pedestrian α. $\mathbf{x}$ is the position of a pedestrian and dots mark time derivatives (i.e. speed and acceleration). The sum runs over all—potentially infinitely many—pedestrians in a simulation scenario. Function $w()$ is there to suppress forces acting from behind. In it $\theta_{\alpha\beta}$ is the angle between pedestrian α's velocity vector and the line connecting α and β.

From here on we assume that parameters $\tilde{A}$, B, λ, τ R, and v_0 have identical value for all pedestrians, so we omit the indices. This allows to combine $\tilde{A}$ and R into a new parameter $A = \tilde{A}e^{-2R}$.

Since it is obvious which properties are time dependent, we also omit the '(t)'. Then Eq. 1 reads for the one-dimensional case:

$$\ddot{x}_\alpha = \frac{v_0 - \dot{x}_\alpha}{\tau} + A \sum_\beta w(x_\alpha, x_\beta, \lambda) e^{-\frac{d_{\alpha\beta}}{B}} \quad (3)$$

$$d_{\alpha\beta} = |x_\beta - x_\alpha| \quad (4)$$

$$w(x_\alpha, x_\beta, \lambda) = \lambda \text{ if } x_\beta - x_\alpha < 0 \quad (5)$$

$$w(x_\alpha, x_\beta, \lambda) = -1 \text{ if } x_\beta - x_\alpha > 0 \quad (6)$$

with the additional assumption that for all pedestrians and times $\dot{x} > 0$. Thus we do not intend to model the loop from the experiment, but assume closed boundary conditions in 1d.

Elliptical specification II is a variant of the Social Force Model where the force between pedestrians—in addition to the mutual distance—also depends on the relative velocity of pedestrians α and β. The full definition is give in [3] and reduced to one dimension it can be found in [6]. If—as in the scenario discussed in this work—pedestrians α and β have the same velocity—vanishing relative velocity—elliptical specification II gives the same force for α as the circular specification. Therefore the further reasoning applies also to elliptical specification II (not elliptical specification I, though).

Now, we investigate the steady state of this—in fact both—model(s). Steady state means that the speeds and distances remain constant and consequently acceleration is zero for all pedestrians. With the left side of Eq. 3 being zero we can easily compute the steady state speed without having to solve a differential equation:

$$\dot{x}_\alpha = v_0 + \tau A \sum_\beta w(x_\alpha, x_\beta, \lambda) e^{-\frac{d_{\alpha\beta}}{B}} \quad (7)$$

As we chose that the parameters for all pedestrians are equal and the system has periodic boundary conditions or is infinitely large, all distances between neighbouring pedestrians are equal. Then necessarily the distance (centre point to centre point) from pedestrian α to the n next neighbour β_n can then be written as:

$$d_{\alpha\beta n} = nd_0 \tag{8}$$

If we resolve the $w()$ function into both directions—$w() = -1$ for all pedestrians ahead and $w() = \lambda$ for all pedestrians behind—we can rewrite Eq. 7 more explicitly with the sum running over natural numbers not pedestrians:

$$\dot{x}_\alpha = v_0 - (1 - \lambda)\tau A \sum_{n=1}^{\infty} e^{-\frac{nd_0}{B}} \tag{9}$$

Since d_0 and B both necessarily are positive it is $e^{-\frac{d_0}{B}} < 1$ and the sum is the geometric series with the well known result

$$\dot{x}_\alpha = v_0 - (1 - \lambda)\tau A \left(\frac{1}{1 - e^{-\frac{d_0}{B}}} - 1 \right) \tag{10}$$

$$= v_0 - (1 - \lambda)\tau A \frac{1}{e^{\frac{d_0}{B}} - 1} \tag{11}$$

$$= v_0 - (1 - \lambda)\tau A \frac{1}{e^{\frac{1}{B\rho}} - 1} \tag{12}$$

where ρ is the line density of pedestrians $\rho = 1/d_0$.

With appropriately chosen values for parameters v_0, λ, τ A, B Eq. 12 should be able to reproduce the empirical fundamental diagram as shown in Fig. 2—obviously not each single data point, but the general, average course. This includes that the speed density relation in Eq. 12 computed for/from the Social Force Model should also yield an inflection point. So for Eq. 12 we compute the second derivative of the speed function with regard to density:

$$v(\rho) = v_0 - (1 - \lambda)\tau A \frac{1}{e^{\frac{1}{B\rho}} - 1} \tag{13}$$

$$\frac{\partial v(\rho)}{\partial \rho} = -(1 - \lambda)\tau A \frac{e^{\frac{1}{B\rho}}}{B\rho^2 (e^{\frac{1}{B\rho}} - 1)^2} \tag{14}$$

$$\frac{\partial^2 v(\rho)}{\partial \rho^2} = (1 - \lambda)\tau A e^{\frac{1}{B\rho}} \frac{(2B\rho - 1)e^{\frac{1}{B\rho}} - (2B\rho + 1)}{B^2 \rho^4 (e^{\frac{1}{B\rho}} - 1)^3} \tag{15}$$

and test if it is zero for some density ρ_i:

$$(2B\rho_i - 1)e^{\frac{1}{B\rho_i}} - (2B\rho_i + 1) = 0 \tag{16}$$

This does not have a solution, but the left side of the equation is always negative and approaches zero only asymptotically for $\rho_i \to \infty$.

At this point, we could write down conclusions and title the paper "Requiem for the Social Force Model" (and a number of other models as well). However, experience teaches to first search for possibilities of resurrection. Still we note as first remarkable result of this work:

Result 1: *Neither the circular specification nor the elliptical specification II of the Social Force Model as originally defined produce an inflection point in the speed density relation for homogeneous steady-state one-dimensional movement.*

The next step does not follow as a consequence of what is written here so far, but it has to be justified a posteriori: we reconsider Eq. 7 and investigate a variant of the model where not all pedestrians, but only the nearest neighbours—the one in front and the one at the rear—exert a force on pedestrian α. This leads to

$$\dot{x}_\alpha = v_0 - (1 - \lambda)\tau A e^{-\frac{1}{B\rho}} \tag{17}$$

which we write seemingly unnecessarily complicated as

$$\dot{x}_\alpha = v_0 - (1 - \lambda)\tau A \frac{1}{e^{\frac{1}{B\rho}} - 0} \tag{18}$$

In this form we note that the only difference between Eqs. 12 and 18—so between the original formulation where infinitely many pedestrians exert a force on α and the nearest neighbour variant—is only that in the first case there is a '1' and in the second case a '0' in the denominator.

Having written the equations in this way the natural next question is "What if instead of the zero or one in Eqs. 12 and 18 we write there some $0 < k < 1$?":

$$\dot{x}_{k\alpha} = v_0 - (1 - \lambda)\tau A \frac{1}{e^{\frac{1}{B\rho}} - k} \tag{19}$$

respectively in dimensionless form:

$$f(x)_k(\rho) = 1 - \frac{e^a - k}{e^{\frac{a}{x}} - k} \tag{20}$$

This modifies the second derivative:

$$v_k(\rho) = v_0 - (1 - \lambda)\tau A \frac{1}{e^{\frac{1}{B\rho}} - k} \tag{21}$$

$$\frac{\partial v_k(\rho)}{\partial \rho} = -(1 - \lambda)\tau A \frac{e^{\frac{1}{B\rho}}}{B\rho^2 (e^{\frac{1}{B\rho}} - k)^2} \tag{22}$$

(a)

(b)
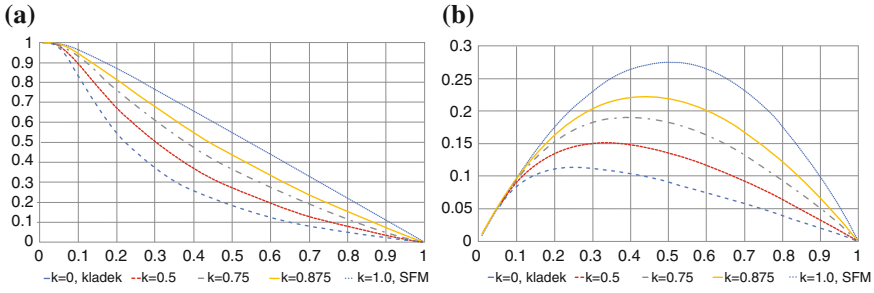
Fig. 3 Relations of the k-extended Social Force Model for various values of parameter k. The plots are based on the dimensionless variants of equations and it is $a = 0.2$. Speed density (**a**). Flow density (**b**)

$$\frac{\partial^2 v_k(\rho)}{\partial \rho^2} = (1 - \lambda)\tau A e^{\frac{1}{B\rho}} \frac{(2B\rho - 1)e^{\frac{1}{B\rho}} - k(2B\rho + 1)}{B^2 \rho^4 (e^{\frac{1}{B\rho}} - k)^3} \tag{23}$$

For $0 \leq k < 1$ the new equation to solve is

$$(2B\rho_i - 1)e^{\frac{1}{B\rho_i}} - k(2B\rho_i + 1) = 0 \tag{24}$$

and it has a solution. For $k = 0$ it is obviously $\rho_i = 1/(2B)$. For other values of k the solution needs to be computed numerically. Table 1 gives some values for $B\rho_i$.

The introduction of parameter k produces the desired inflection point in the fundamental diagram, see Fig. 3. To find an intuitively comprehensible interpretation for this extension, we write Eq. 21 in a slightly different manner

Table 1 Numerical solutions for the value ρ_i of the inflection point with regard to various values for parameter k. Values computed with [14]

k	$B\rho_i$	k	$B\rho_i$	k	$B\rho_i$
0.0	0.500	0.90	0.981	0.99	2.049
0.1	0.515	0.91	1.013	0.999	4.379
0.2	0.531	0.92	1.051	0.9999	9.416
0.3	0.551	0.93	1.096	0.99999	20.28
0.4	0.576	0.94	1.151	0.999999	43.68
0.5	0.606	0.95	1.219	0.9999999	94.10
0.6	0.646	0.96	1.309	0.99999999	202.7
0.7	0.703	0.97	1.435	0.999999999	436.8
0.8	0.793	0.98	1.635	0.9999999999	941.0

$$v_k(\rho) = v_0 - (1 - \lambda)\tau A \frac{1}{k} \frac{1}{\frac{e^{\frac{1}{B\rho}}}{k} - 1} \tag{25}$$

and undo the summation of the geometric series with k 'on the back' of the exponential function

$$v_k(\rho) = v_0 - (1 - \lambda)\tau A \frac{1}{k} \sum_{n=1}^{\infty} k^n e^{-\frac{n}{B\rho}} \tag{26}$$

$$= v_0 - (1 - \lambda)\tau A \sum_{n=1}^{\infty} k^{n-1} e^{-\frac{n}{B\rho}} \tag{27}$$

In terms of forces/acceleration this means:

$$\ddot{x} = \frac{v_0 - v}{\tau} - (1 - \lambda) A \sum_{n=1}^{\infty} k^{n-1} e^{-\frac{d_{\alpha\beta}}{B}} \tag{28}$$

This is easy to interpret: the next neighbours of α exert a force on α unmodified compared to the original SFM. The second next neighbours exert a force which is suppressed by a factor k (always compared to the original model without parameter k). The force from the next to next to next nearest neighbours is suppressed by a factor of k^2 and so on. This implies for example that if we take out each second pedestrian from a simulation and the next to next nearest neighbour becomes the next nearest neighbour the force from this new nearest neighbour is larger than before when s/he was just the next to next nearest neighbour although the distance to α is the same as before.

This can be comprehended intuitively. If two pedestrians approach 'me' independently and the first remote pedestrian overtakes and becomes the closest one 'my' *awareness* is shifted from the former to the new nearest neighbour and that would have an impact on my velocity changes, i.e. acceleration, i.e. forces. This intuitive comprehensibility of the model extension adds to the pleasure of having gained the desired inflection point. Thus:

Result 2: *Suppressing the force from each pedestrian in the sequence ordered by distance from the pedestrian for whom forces are calculated with an additional factor $0 < k < 1$ produces an inflection point in the resulting macroscopic speed–density relation and as a model extension can be motivated intuitively.*

We would like to emphasise that the introduction of parameter k as extension of the Social Force Model brings a major conceptual change. Without it forces of various pedestrians superpose without interfering. With parameter k on the contrary one has to know the local distribution of all pedestrians before one can compute the force of one pedestrian on another one. Forces do not superpose anymore. Instead the extended model—let us briefly call it 'SFMk'—is rather described by Sherif's famous description of social systems: "the properties of any part are determined by its membership in the total functional system." [13]. In this sense the SFMk structurally

bears some similarities to another extension of the Social Force Model—namely the dynamic potential [4, 5, 7, 8]—where the desired direction of pedestrians is computed such that they walk into the direction of earliest expected arrival, for this considering the distribution and movement state of all pedestrians in a holistic way. A difference, however, between SFMk and the dynamic potential is that in SFMk it is exactly known which pedestrian β_i contributes what to the effect on the movement of pedestrian α. This is not the case for the dynamic potential. We would therefore call the dynamic potential a mesoscopic or mean field or holistic modelling element while the SFMk is non-superposing but non-holistic and entirely microscopic.

3   Summary

In this contribution we have computed the macroscopic limit of the Social Force Model of pedestrian dynamics for single-file unidirectional movement. We found that the speed–density curve does not have an inflection point, but that with the introduction of one more parameter to the Social Force Model one can recover an inflection point. The new model intuitively makes sense considering that humans focus their awareness.

References

1. Chattaraj, U., Seyfried, A., Chakroborty, P.: Comparison of pedestrian fundamental diagram across cultures. ACS **12**(03), 393–405 (2009)
2. Helbing, D., Farkas, I., Vicsek, T.: Simulating dynamical features of escape panic. Nature **407**, 487–490 (2000)
3. Johansson, A., Helbing, D., Shukla, P.: Specification of the social force pedestrian model by evolutionary adjustment to video tracking data. ACS **10**(supp02), 271–288 (2007)
4. Kretz, T.: The effect of integrating travel time. In: Weidmann, et al. (ed.) Pedestrian and Evacuation Dynamics 2012, pp. 1013–1027 (2013)
5. Kretz, T.: Multi-directional flow as touch-stone to assess models of pedestrian dynamics. In: Annual Meeting of the TRB 2013 (2013)
6. Kretz, T.: On oscillations in the social force model. Phys. A (2015)
7. Kretz, T., Große, A.: From unbalanced initial occupant distribution to balanced exit usage in a simulation model of pedestrian dynamics. In: Shields, et al. (ed.) Human Behaviour in Fire Symposium, pp. 536–540 (2012)
8. Kretz, T., Große, A., Hengst, S., Kautzsch, L., Pohlmann, A., Vortisch, P.: Quickest paths in simulations of pedestrians. ACS **14**, 733–759 (2011)
9. Portz, A., Seyfried, A.: Analyzing stop-and-go waves by experiment and modeling. In: Peacock, et al. (ed.) Pedestrian and Evacuation Dynamics, pp. 577–586. Springer (2011)
10. Seyfried, A., Boltes, M., Kähler, J., Klingsch, W., Portz, A., Rupprecht, T., Schadschneider, A., Steffen, B., Winkens, A.: Enhanced empirical data for the fundamental diagram and the flow through bottlenecks. In: Klingsch, et al. (ed.) Pedestrian and Evacuation Dynamics 2008, pp. 145–156. Springer (2010)
11. Seyfried, A., Portz, A., Schadschneider, A.: Phase coexistence in congested states of pedestrian dynamics. In: Bandini, et al. (ed.) Cellular Automata. LNCS, vol. 6350, pp. 496–505. Springer (2010)
12. Seyfried, A., Steffen, B., Klingsch, W., Boltes, M.: The fundamental diagram of pedestrian movement revisited. JSTAT **2005**(10), P10002 (2005)
13. Sherif, M.: The Psychology of Social Norms. Harper (1936)
14. Wolfram Alpha: Publisher: Wolfram Alpha LLC (2015). Accessed 24 Mar 2015

Sensitivity Analysis of the Local Route Choice Parameters of the Continuum Model Regarding Pedestrian Movement Phenomena

Dorine C. Duives, Winnie Daamen and Serge P. Hoogendoorn

Abstract Numerous pedestrian simulation models have been proposed in the last decade, many of which simulate the movement behaviour of pedestrians microscopically. However, the numerous degrees of freedom of microscopic models complicate the calibration process severely. Moreover, the computation speed of many microscopic simulation models leaves much to be desired. Especially in cases where computation speed is essential and no microscopic data is available to calibrate the model, macroscopic models outperform microscopic models. This study provides a detailed assessment of the impact of the combination of delay and density within the formulation of the local route choice behaviour on the predicted movement dynamics of the crowd in a continuum model (Physica A 416:684–694, 2014 [9]; Transp Res Part C Emerg Technol 59:183–197, 2015 [10]). This study aims to understand how the parameters of the respective versions of the continuum model influence the development crowd movement phenomena. The impact of the parameter sets of the continuum model is assessed for a uni-directional bottleneck, uni-directional corner rounding, bidirectional straight walking and intersecting movements.

1 Introduction

In recent years, numerous (microscopic) pedestrian crowd simulation models have been proposed. The nature of these microscopic simulation models is very diverse, for instance Cellular Automata (e.g. [11]), Social Force models (e.g. [13]), and Collision Avoidance models (e.g. [12]). Generally, no exact solution exists, which complicates the use of predictions by these models for crowd management solutions. Moreover,

D.C. Duives (✉) · W. Daamen · S.P. Hoogendoorn
Delft University of Technology, Stevinweg 1, 2628 CN Delft, The Netherlands
e-mail: d.c.duives@tudelft.nl

W. Daamen
e-mail: w.daamen@tudelft.nl

S.P. Hoogendoorn
e-mail: s.p.hoogendoorn@tudelft.nl

given the high amount of detail in the description of the pedestrian movement behaviour, the computation speed of many microscopic simulation models leaves much to be desired.

As a consequence, especially in processes where computation speed is essential, such as for instance monitoring or management instructions, macroscopic simulation models outperform microscopic simulation models. This second type of models does not simulate individual behaviour, but estimates the aggregate characteristics of the crowd movement. Over the course of the last five years several continuum models have been presented (among others [2, 4, 14]).

Many of the recently proposed macroscopic models cannot simulate all relevant behavioural processes and characteristics of crowd movement, such as self-organisation and phase-transitions [9]. To the authors knowledge, the macroscopic models mentioned above cannot simulate the more sophisticated forms of self-organisation, such as stripe-formation or turbulence.

Studies [9] and [10] propose two versions of a multi-class continuum model that captures these two key dynamic features of pedestrian flow (i.e. self-organisation and phase-transitions). In both models, the global route choice (based on the distance to the exit) and local route choice (based on the interaction of pedestrians nearby dynamic changes in the traffic state) are balanced. The local route choice in the first version of the continuum model is based on only the gradient of the density, while in the second version a combination of the density and delay gradients is used.

This study provides a detailed assessment of the impact of the combination of delay and density within the formulation of the local route choice behaviour. It shows that the density and the delay gradients impact the walking behaviour in a similar manner in uni-directional movement base cases. Furthermore, this paper shows that the combination of delay and density gradients leads in most cases to either entirely similar (uni-directional flow situations) or undesirable behaviour (in bidirectional and intersecting flow situations).

This paper first describes the local route choice in both versions of the continuum model. The research methodology is presented in Sect. 3, the results in Sects. 4 and 5. Section 6 draws conclusions and shows avenues for future research.

2   Introduction of the Continuum Model

The continuum model presented in [9] describes the dynamics of the class-specific density $\rho_d(t, \mathbf{x})$ over time t and space $\mathbf{x}$, where d denotes the pedestrian class (i.e. a set of pedestrians that shares the same origin, destination and type of walking behaviour). In the following, the most important characteristics of the model are mentioned. For more specific details, we refer to the original papers [9, 10].

In the continuum model, the walking direction represents the results of the global choice behaviour of pedestrians, which is modelled by means of the value function proposed in [8]. Additionally, a local route choice component is introduced. It is

assumed that the local route choice can be expressed as a function of the class-specific densities ρ_d and density gradients $\nabla \rho_d$

$$\mathbf{q}_d = \boldsymbol{\gamma}_d(\rho_1, ..., \rho_D, \nabla \rho_1, ..., \nabla \rho_D) \cdot \rho_d \cdot U(\rho_1, ..., \rho_D) \tag{1}$$

where ρ_d represents the density resulting from the presences of class d, $\nabla \rho_d$ the gradient of the density of class d, U the absolute velocity, and $\boldsymbol{\gamma}_d$ the direction of the velocity. The local route costs for a pedestrian of class d aim to avoid high density areas, in particular when these areas are occupied by pedestrians from another class.

$$\boldsymbol{\gamma}_d^{density} = \sum_{d=1}^{D} \beta_d \cdot \rho_d \tag{2}$$

The values of β_d can be interpreted as weights that a pedestrian of class d attaches to densities of its own ($\delta = d$) and other classes ($\delta \neq d$).

In the second formulation of the model, both delay and density are accounted for [10]. The local delay caused by reduced walking speeds due to high densities is also incorporated in the local route choice decision.

$$\boldsymbol{\gamma}_d^{delay} = (\frac{1}{U(\rho_1, ..., \rho_D)} - \frac{1}{U(0)})dt \tag{3}$$

In this formulation, $U(0)$ represents the free flow speed and $U(\rho_d)$ the speed class d adopts under the influence of effective density ρ_d.

The influence of the density and delay are accordingly added, rendering the local route choice $\boldsymbol{\gamma}_d^{local}$ of pedestrians of class d.

$$\boldsymbol{\gamma}_d^{local} = -1 \cdot \frac{\beta_d^{density} \cdot \boldsymbol{\gamma}_d^{density} + \beta_d^{delay} \cdot \boldsymbol{\gamma}_d^{delay}}{\|\beta_d^{density} \cdot \boldsymbol{\gamma}_d^{density} + \beta_d^{delay} \cdot \boldsymbol{\gamma}_d^{delay}\|} \tag{4}$$

where $\beta_d^{density}$ and β_d^{delay} represent the weight of the influence of the delay and density components and $\boldsymbol{\gamma}_d^{density}$ and $\boldsymbol{\gamma}_d^{delay}$ represent the gradients of the density and delay.

This leads to the following route choice model

$$\boldsymbol{\gamma}_d = -\frac{\beta_d^{global} \cdot \boldsymbol{\gamma}_d^{global} + \beta_d^{local} \cdot \boldsymbol{\gamma}_d^{local}}{\|\beta_d^{global} \cdot \boldsymbol{\gamma}_d^{global} + \beta_d^{local} \cdot \boldsymbol{\gamma}_d^{local}\|} \tag{5}$$

where β_d^{global} and β_d^{local} are weights representing the influence of the global and local route choice components of pedestrians of class d. The global and local components of the route choice are first transformed into unit vectors before addition. As a consequence, the weight factors always have the same effect on the pedestrian flow, irrespective of the geometry and size of the infrastructure.

3 Methodology for the Assessment of the Sensitivity

As mentioned previously, this study aims to understand the impact of the addition of the delay component in the local route choice formulation on the predicted traffic state. Two distinct analyses are performed. Firstly, an analysis of the contribution of the delay to the traffic state is carried out, which does not take the interference of the density into account. Secondly, the influence of the interplay between density and delay on the traffic state is performed.

In total, six parameters of the continuum model influence the resulting crowd movement dynamics which can be separated into three pairs of antagonists. That is, the ratio $\beta_d^{local}/\beta_d^{global}$ manages the respective influences of the static and dynamic route choice, the ratio $\beta_d^{own}/\beta_d^{other}$ operates the influence of the density gradient of the own and other classes and the ratio $\beta_d^{delay}/\beta_d^{crowd}$ determines the influence of the delay and the density gradient. Table 1 displays the parameter settings which are tested in this study. These values have been chosen based on results of a previous study [6].

Given that crowd movement phenomena occur under different flow situations, this study studies the impact of the parameter sets with respect to the crowd movement dynamics that arise during several distinct flow situations. In total, four distinct flow situations are distinguished:

- *Uni-directional—Bottleneck*, where one class of pedestrians is generated on the left, walks through a bottleneck and exits on the right.
- *Uni-directional—Corner*, where one class of pedestrians is generated on the left and exits at the bottom after making a sharp 90° turn.
- *Bidirectional—Straight*, where two classes of pedestrians are generated, one from left to right and one from right to left.
- *Crossing flow scenario—90°*, where two classes of pedestrians are generated, one from left to right and one from bottom to top.

Over the years several crowd movement phenomena have been mentioned in research studies. In case of the four adopted flow situations a few specific ones apply. Namely, the funnelling upstream and dissipation downstream of bottlenecks [3] and corners [5], and the existence of self-organisation patterns such as lane formation in

Table 1 Parameter settings of the sensitivity test

	Math. def.	Influence of delay	Influence delay and crowd
Local versus global	$\dfrac{\beta_d^{local}}{\beta_d^{global}}$	0.2, 0.4, 0.6, 0.8, 1	0.7
Own versus other group	$\dfrac{\beta_d^{own}}{\beta_d^{other}}$	0.5	0.5
Delay versus density	$\dfrac{\beta_d^{delay}}{\beta_d^{crowd}}$	$\beta_d^{delay} = 1, \beta_{crowd} = 0$	$\beta_{delay} = 0.2 : 0.2 : 1,$ $\beta_d^{crowd} = 1 : -0.2 : 0.2$
Demand	q	1 P/m/s	1 P/m/s

corridors [7] and stripe-formation at intersections [1]. In the following, the continuum model can simulate crowd movements realistically when all these crowd movement phenomena can be predicted by means of the same parameter set.

4 Impact of Delay on the Movement Dynamics of the Crowds

In this section, the impact of the delay on the crowd movement dynamics is presented (i.e. $\beta_d^{crowd} = 0$). As a result, an increase of the impact of the local route choice behaviour on the movement behaviour via β_d^{local} is directly related to a similar increase of the impact of the delay on the movement behaviour. Underneath the resulting dynamics are discussed separately for the four distinct flow situations mentioned in Sect. 3.

The impact of delay on the movement dynamics of a flow around a corner is depicted in Fig. 1a–d. The dispersion of the flow upstream of the corner is increased by the increasing impact of the delay. An increase in the influence of the delay leads to an increase of the dispersion at and downstream of the corner. Due to the improved efficiency of the crowds' movements, the high density region just upstream of the bottleneck disappears.

For bottleneck flows, a similar analysis is presented in Fig. 1e–h. The results show that without local route choice, minor queues upstream of the bottleneck are found. A slight increase of the influence of the local route choice causes these minor queues to change into a full-fledged bottleneck. The simulation results, furthermore, clearly illustrate that an increase in the influence of the delay induces an increase in the dissipation of pedestrians downstream of the bottleneck. In some specific cases, a funnel shaped bottleneck flow arises. In most cases, however, the flow touches the upstream wall in which the bottleneck is located. Empirical research performed by e.g. [3], did not establish the formation of the latter shape.

Figure 1i–p depict the impact of delay on the movement dynamics of crowds in bidirectional and crossing situations. The graphs show that the impact of delay does not improve the traffic state. In both cases, the overall density of the flow situation does increase when the impact of the delay increases. Additionally, no formation of lanes is seen in any of the simulations. This is not surprising, since the crowd flow does not react differently on the own and other group based on the current formulation of the delay.

5 Impact of Combination of Delay and Density Gradients on the Movement Dynamics of the Crowds

The interplay between the influence of the density and delay gradients on the local route choice is analysed in this section. The same four case studies mentioned in Sect. 3 are used. Only this time, the ratio between β_d^{local} and β_d^{global} is kept stable at
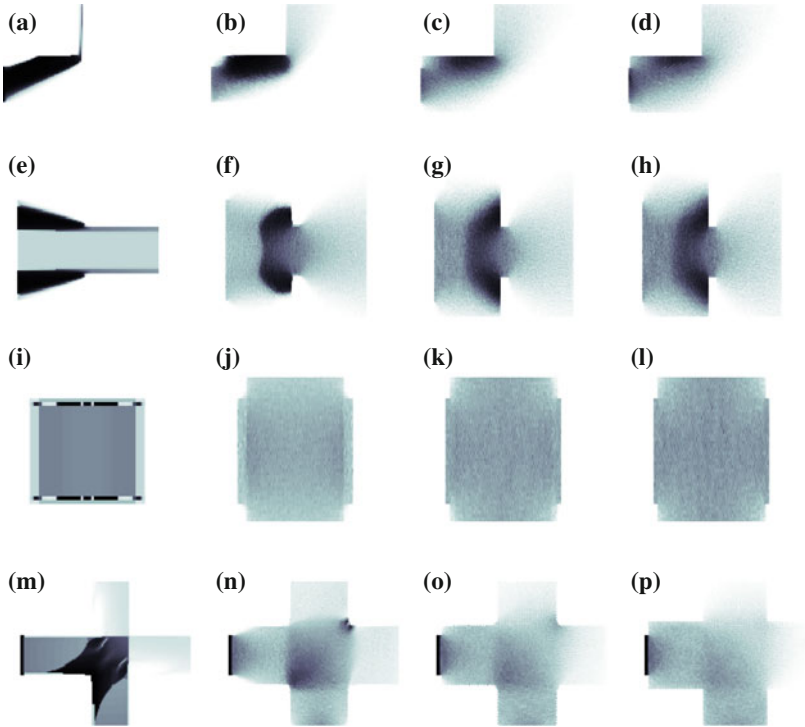
Fig. 1 Traffic state in four flow situations, where the influence of the local route choice consisting of only the delay component is varied. $\beta_d^{local} = 0$ represents situations in which only the global route choice is taken into account, and $\beta_d^{local} = 1$ represents situations in which the global and local route choice components carry equal weight. $\beta_d^{local} = 0$ (**a**); $\beta_d^{local} = 0.2$ (**b**); $\beta_d^{local} = 0.6$ (**c**); $\beta_d^{local} = 1.0$ (**d**); $\beta_d^{local} = 0$ (**e**); $\beta_d^{local} = 0.2$ (**f**); $\beta_d^{local} = 0.6$ (**g**); $\beta_d^{local} = 1.0$ (**h**); $\beta_d^{local} = 0$ (**i**); $\beta_d^{local} = 0.2$ (**j**); $\beta_d^{local} = 0.6$ (**k**); $\beta_d^{local} = 1.0$ (**l**); $\beta_d^{local} = 0$ (**m**); $\beta_d^{local} = 0.2$ (**n**); $\beta_d^{local} = 0.6$ (**o**); $\beta_d^{local} = 1.0$ (**p**)

0.7, while the ratio $\beta_d^{delay} / \beta_d^{crowd}$ ratio is varied. In all cases, only the distribution of the density for one of the pedestrian classes is displayed in order to illustrate the development of self-organisation behaviour.

The influence of the combination of delay and density on the movement dynamics of the crowd is visualised in Fig. 2a–f. As one can see, the traffic states do not differ between distinct realisations of a uni-directional flow situation while very distinct ratios of β_d^{delay} and β_d^{crowd} are used. The traffic state does not develop differently, since in both flow situations similar directional fields γ_d^{local} are found. That is, the local route choice does not change depending on the ratio $\beta_d^{delay} / \beta_d^{crowd}$.

In the bidirectional flow situation differences in the traffic state do arise, see Fig. 2g–i. Only in the cases where the influence of the delay gradient is less than the influence of the density gradient, lane formation remains visible after 90 s. Thus, it is concluded that especially the density gradient induces this type of self-organisation.
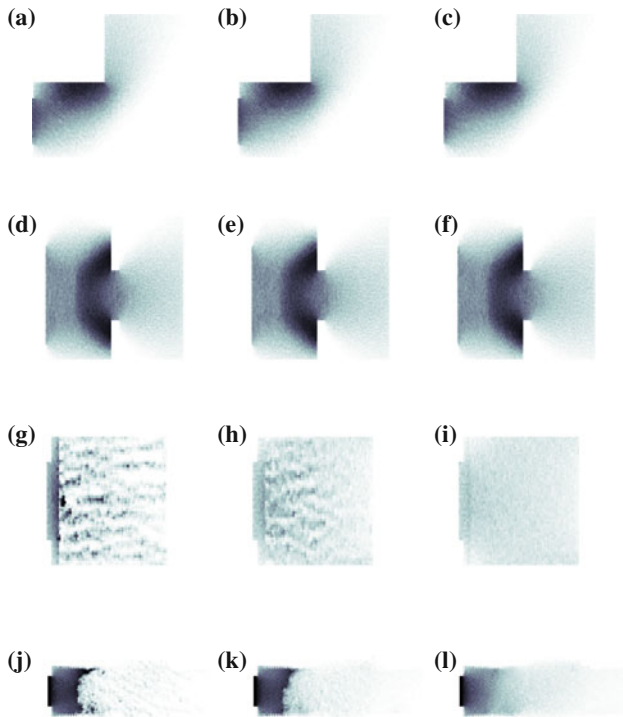
Fig. 2 Traffic state in four flow situations, where the relative weight of the density and delay components of the local route choice is varied. $\beta_d^{delay}/\beta_d^{crowd} = 0.2$ (**a**); $\beta_d^{delay}/\beta_d^{crowd} = 1$ (**b**); $\beta_d^{delay}/\beta_d^{crowd} = 5$ (**c**); $\beta_d^{delay}/\beta_d^{crowd} = 0.2$ (**d**); $\beta_d^{delay}/\beta_d^{crowd} = 1$ (**e**); $\beta_d^{delay}/\beta_d^{crowd} = 5$ (**f**); $\beta_d^{delay}/\beta_d^{crowd} = 0.2$ (**g**); $\beta_d^{delay}/\beta_d^{crowd} = 1$ (**h**); $\beta_d^{delay}/\beta_d^{crowd} = 5$ (**i**); $\beta_d^{delay}/\beta_d^{crowd} = 0.2$ (**j**); $\beta_d^{delay}/\beta_d^{crowd} = 1$ (**k**); $\beta_d^{delay}/\beta_d^{crowd} = 5$ (**l**)

Figure 2j–l display the effect of the combination of delay and density gradients on the movement dynamics in case of a crossing flow situation. When the density is dominant in the local route choice, stripe formation arises, while the combination of both effects results in blockage. When the impact of the delay is dominant within the local route choice, both groups are scattered over the entire infrastructure. As a result, blockage does not occur any more, nor does stripe formation.

6   Conclusions and Future Research

This study has provided a detailed assessment of the impact of the combination of delay and density gradient in the formulation of the local route choice behaviour of the continuum model proposed by [9, 10] on the predicted traffic state. By means of two distinct tests, the impact of these two types of gradients on the predicted traffic state has been analysed.

In the first test, for uni-directional flows the density and delay gradients were found to impact the walking behaviour in a similar manner. For bidirectional and intersecting flows no self-organisation was found in cases where only the delay, and not the density, was taken into account. The second test established that the traffic state in uni-directional flow situations is scarcely impacted by the $\beta_d^{delay}/\beta_d^{crowd}$ ratio, since the total local route choice gradient is barely impacted by the ratio.

Based on the results, it is concluded that especially the density component needs to be included in the local route choice in order to predict valid crowd movement behaviour. Since the influence of the delay component renders no different results, it is concluded that this component has no supplementary value.

References

1. Ando, K., Ota, H., Oki, T.: Forecasting the flow of people (in japanese). Railw. Res. Rev. **45**(8), 8–14 (1988)
2. Colombo, R., Garavello, M., Lecureau-Mercier, M.: Non-local crowd dynamics. C.R. Math **349**(13–14), 769–772 (2011)
3. Daamen, W., Hoogendoorn, S.: Emergency door capacity: Influence of door width, population composition and stress level. Fire Technol. **48**(1), 55–71 (2010)
4. Degond, P., Hua, J.: Self-organized hydrodynamics with congestion and path formation in crowds. J. Comp. Phys. (2013)
5. Dias, C., Ejtemai, O., Sarvi, M., Burd, M.: Exploring pedestrian walking through angled corridors. Transp. Res. Procedia **2**, 19–25 (2014)
6. Duives, D., Daamen, W., Hoogendoorn, S., Duives, D.C., Daamen, W., Hoogendoorn, S.P.: Continuum modelling of pedestrian flowspart 2: sensitivity analysis featuring crowd movement phenomena. Physica A **447**, 36–48 (2016)
7. Helbing, D., Molnar, P.: Self-organizing pedestrian movement. Environ. Plann. B Plann. Des. **28**, 361–383 (2001)
8. Hoogendoorn, S., Bovy, P.: Pedestrian route-choice and activity scheduling theory and models. Transp. Res. Part B: Methodol. **38**, 169–190 (2004)
9. Hoogendoorn, S., van Wageningen-Kessels, F., Daamen, W., Duives, D.: Continuum modelling of pedestrian flows: from microscopic principles to self-organised macroscopic phenomena. Physica A **416**, 684–694 (2014)
10. Hoogendoorn, S., van Wageningen-Kessels, F., Daamen, W., Sarvi, M., Duives, D.: Continuum theory for pedestrian traffic flow: local route choice modelling and its implications. Transp. Res. Part C Emerg. Technol. **59**, 183–197 (2015)
11. Hsu, J.J., Chu, J.: Long-term congestion anticipation and aversion in pedestrian simulation using floor field cellular automata. Transp. Res. Part C Emerg. Technol. **48**, 195–211 (2014)
12. Moussaid, M., Helbing, D., Theraulaz, G.: How simple rules determine pedestrian behavior and crowd disasters. PNAS **108**(17), 6884–6888 (2011)
13. Seer, S., Rudloff, C., Matyus, T., Brändle, N.: Validating social force based models with comprehensive real world motion data. Transp. Res. Procedia **2**, 724–732 (2014)
14. Treuille, A., Cooper, S., Popovic, Z.: Continuum crowds. ACM Transp. Graph. **25**, 1160–1168 (2006)

How to Get a Model in Pedestrian Dynamics to Produce Stop and Go Waves

Felix Dietrich, Stefan Disselnkötter and Gerta Köster

Abstract Stop and go waves in granular flow can often be described mathematically by a dynamical system with a Hopf bifurcation. We show that a certain class of microscopic, ordinary differential equation-based models in crowd dynamics fulfil certain conditions of Hopf bifurcations. The class is based on the Gradient Navigation Model. An interesting phenomenon arises: the number of pedestrians in the system must be greater than nine for a bifurcation—and hence for stop and go waves to be possible at all, independent of the density. Below this number, no parameter setting will cause the system to exhibit stable stop and go behaviour. The result is also interesting for car traffic, where similar models exist. Numerical experiments of several parameter settings are used to illustrate the mathematical results.

1 Introduction

Stop and go waves are a prominent feature of flows of both pedestrians in corridors and cars on highways. To investigate them experimentally, ring experiments have been conducted with cars [8], pedestrians [7], robots and even ants [5].

Even in almost homogeneous conditions, these waves can occur 'out of nowhere', meaning that a small error in the system can increase exponentially and change the flow from homogeneous to wavelike. Figure 1 shows the positions of 20 particles in a corridor with periodic boundary conditions—mathematically realised as a ring (see Fig. 2—in a computer simulation. Initially, the particles are all distributed with equal spacing. Numerical errors introduce inhomogeneities, which are amplified by the

F. Dietrich (✉)
Munich University of Applied Sciences, Technische Universität München, Munich, Germany
e-mail: felix.dietrich@tum.de

S. Disselnkötter
Johannes Gutenberg Universität Mainz, Mainz, Germany
e-mail: sdisseln@uni-mainz.de

G. Köster
Munich University of Applied Sciences, Munich, Germany
e-mail: koester@hm.edu
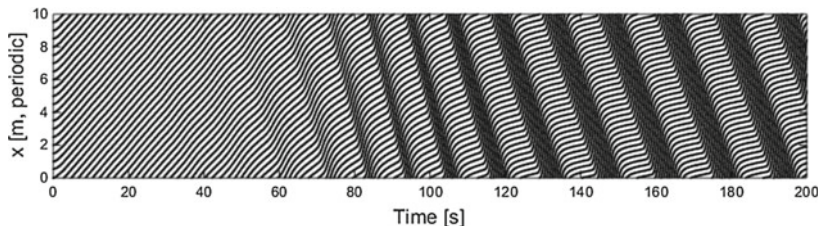
Fig. 1 Stop and go waves occur through a small (invisible here) perturbation in the initial positions of 20 pedestrians in a setting with periodic boundaries. The effect is visible after 60 s

Fig. 2 Circular scenario with ten pedestrians. The pedestrians at the *bottom* are closer together than the ones on *top*: a jam
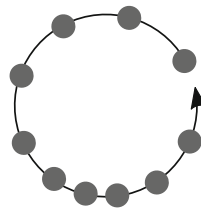
instability at the given parameter setting. The system moves away from the unstable steady state with equal spacing and enters the wavelike state. This behaviour is well known in mathematics as Hopf bifurcation of a dynamical system, where changing the value of a parameter changes the number of periodic orbits.

In car traffic, this phenomenon has been researched extensively [6, 9]. Models in crowd dynamics differ from models in car traffic in a number of ways. Most notably, they are two-dimensional focusing on path finding and navigation around other pedestrians and obstacles. In car traffic, most models are one-dimensional, producing so called single-file or single-lane flow.

In this paper, we present a mathematical and a numerical analysis for stop and go waves of a class of models in crowd dynamics. The original model formulation is two-dimensional. This is different from many previous analyses of pedestrian models, where only single-file movement models were used and often developed just for the purpose of stop and go analysis. Our model can also be used in a general two-dimensional setting [1]. We briefly outline the mathematical framework of dynamical systems and Hopf bifurcations. Then, we introduce the ring scenario, and outline the proof of a Hopf bifurcation in models similar to the Gradient Navigation Model. We discover an interesting phenomenon: with less than 10 pedestrians, no parameter value in the model leads to stop and go like movement. Numerical results illustrate the theoretical results.

2 Mathematical Framework

A dynamical system is a triplet of time T, space X and a continuous map f. This map advances states $x \in X$ in time. If time is continuous, for example $T = \mathbb{R}$, the advance is often described by a differential equation. Let $x(t)$ be the state at time t, then

$$\frac{dx}{dt} = \dot{x} = f(x(t)). \tag{1}$$

A steady state of a dynamical system is a state $x^* \in X$ where $f(x^*) = 0$. If a small perturbation ε to the steady state causes the system to return to x^* or stay close to it, the steady state is called stable. Otherwise, it is called unstable. Stability is more rigorously defined through the Jacobian of f:

Definition 1 Let f be the continuous right hand side of a differential equation with state space $X \subset \mathbb{R}^n$, such that

$$\dot{x} = f(x). \tag{2}$$

Furthermore, let $x^* \in X$ be a steady state such that $f(x^*) = 0$. We denote the Jacobian of f at x^* by J^*. The steady state x^* is called stable, if for all (possibly complex) eigenvalues λ of J^*,

$$\mathfrak{R}(\lambda) < 0. \tag{3}$$

Otherwise, x^* is called unstable.

Periodic solutions—including trivial ones—are present if J^* has pairs of conjugate eigenvalues on the imaginary axis, that means $\lambda_{1,2} = 0 \pm bi$, $b \in \mathbb{R}$, and no other eigenvalues with zero real part.

The map f may be dependent on several parameters $p = (p_1, \ldots, p_m)$ that influence the system behaviour. If the values are changed continuously, the number, position and stability of steady states can change. A doubling of the number of periodic steady states is called Hopf bifurcation. This is formalised in Definition 2 (adopted from [3, p.150ff]):

Definition 2 Consider a system with right hand side $f \in C^\infty(\mathbb{R}^n)$ where $f_\mu(x) = f(\mu, x)$, $\mu \in \mathbb{R}$ is a parameter, and $\dot{x} = f_\mu(x)$, $x \in \mathbb{R}^n$. Let (x_0, μ_0) be a steady state with the following properties:

1. Non-hyperbolicity: the Jacobian $D_x f_{\mu_0}(x_0)$ has exactly two distinct, complex conjugate eigenvalues with zero real part.
2. Transversality: the eigenvalues cross the imaginary axis when μ is varied at μ_0 with non-zero speed,

$$\left.\frac{\mathfrak{R}(\lambda(\mu))}{d\mu}\right|_{\mu=\mu_0} \neq 0.$$

3. Genericity: the first Lyapunov coefficient must not be zero.

The genericity condition determines whether the system is supercritical, subcritical, or degenerate.

Models for pedestrian dynamics are dynamical systems with parameters. We will show analytically that the first two conditions of Definition 2 hold, which is a strong indication that a Hopf bifurcation exists. These results mean a small change in the parameters can cause a periodic solution to arise: the stop and go waves.

3   Results

Consider the ring scenario shown in Fig. 2, where the arc length of the ring is $L > 0$. A number of $P \in \mathbb{N}$ pedestrians are placed equidistantly at positions x_i, and are all moving in the same direction on the ring. We ignore the shapes of the pedestrians and focus on their respective distances. The distance between pedestrian i and its successor $i + 1$ are called d_i, where $d_i = (x_{i+1} - x_i) \geq 0$.

Movement and interactions of pedestrians are described by the Gradient Navigation Model (GNM) which was introduced and validated in [1]. It is based on ordinary differential equations and has several parameters. Numerical simulations where stop and go waves occurred even in two-dimensional scenarios suggested the existence of Hopf bifurcations. Here, we look at the natural candidates among the model parameters to induce the bifurcations: the parameters for interaction strength between pedestrians.

To generalise the **theoretical results**, we use a more general interaction function than the one used in the Gradient Navigation Model. In this paper, the interactions are described with a generic non-negative, bounded and monotonically decreasing repulsion function $h(d_i, \mu)$, $h : \mathbb{R}_{\geq 0} \times \mathbb{R} \to [0, K]$, $K > 0$. This function depends on the distance d_i to the person in front and a shape parameter $\mu \in \mathbb{R}$. The function h is assumed to have compact support on $[0, \mu]$, such that

$$\mathrm{supp}(h) = \overline{\{d \in \mathbb{R}_{\geq 0} | h(d, \mu) \neq 0\}} = [0, \mu]. \tag{4}$$

Movement and interactions of pedestrians in the Gradient Navigation Model are governed by a navigation function N, which depends on the position of other pedestrians, other obstacles and the position of the target. The simplified scenario does not contain obstacles and all pedestrians are confined to the one-dimensional ring setting. This reduces the navigation function to

$$N(d, \mu) = K - h(d, \mu). \tag{5}$$

The position of pedestrian i is called x_i, and w_i is an auxiliary variable modelling the desired speed with max $w_i = K$ for all pedestrians. Also, the speed relaxation τ is set to 1 without loss of generality. The equations of motion of the GNM reduce to

$$\begin{aligned} \dot{x}_i &= w_i N(d_i, \mu) \\ \dot{w}_i &= \|N(d_i, \mu)\| - w_i. \end{aligned} \tag{6}$$

Initially, all pedestrians are distributed with equal spacing on the ring. This is a steady state of a reformulated dynamical system where the position of one pedestrian is fixed and all other positions are described relative to it. This is a achieved by a change of variables $z_i := x_i - x_1$. The corresponding system is

$$\dot{z}_i = w_i N(z_{i+1} - z_i, \mu) - w_1 N(z_2, \mu)$$
$$\dot{w}_i = \|N(z_{i+1} - z_i, \mu)\| - w_i. \tag{7}$$

The steady state of this system is given by

$$z_i^* = (i - 1)\frac{L}{P}$$
$$w_i^* = K N(\frac{L}{P}, \mu) \tag{8}$$

We formulate the main result of this paper as a theorem:

Theorem 1 *The system in Eq. 7 fulfils non-hyperbolicity and transversality conditions for a Hopf bifurcation at the steady state in Eq. 8 for the parameter μ.*

Proof See [2] for a detailed analysis. Define $F = F(\mu) := N(\frac{P}{L}, \mu)$ and $G = G(\mu) := \frac{\partial}{\partial d} N(\frac{P}{L}, \mu)$. Furthermore, define the vectors $Z = (z_2, z_3, \ldots, z_P)^T$ and $W = (w_2, w_3, \ldots, w_P)^T$. Let A, B, C and D be matrices in $\mathbb{R}^{(P-1) \times (P-1)}$, where

$$A = \begin{pmatrix} -2FG & FG & 0 & 0 \\ -FG & -FG & \cdots & 0 \\ \vdots & 0 & \ldots & FG \\ -FG & 0 & 0 & -FG \end{pmatrix}, \quad B = \begin{pmatrix} -F & F & 0 & 0 \\ \vdots & 0 & \ldots & 0 \\ -F & 0 & 0 & F \end{pmatrix},$$

$$C = \begin{pmatrix} G & 0 & 0 & 0 \\ -G & G & 0 & 0 \\ 0 & \ldots & \ldots & 0 \\ 0 & 0 & -G & G \end{pmatrix}, \quad D = -\mathbb{I} \tag{9}$$

The linearisation of the system in Eq. 7 at the steady state (Eq. 8) is given by

$$\begin{pmatrix} \dot{Z} \\ \dot{W} \end{pmatrix} = \underbrace{\begin{pmatrix} A & B \\ C & D \end{pmatrix}}_{=:J} \begin{pmatrix} Z \\ W \end{pmatrix}. \tag{10}$$

$\square$

A transformation of the original system yields a matrix with higher dimension, which by a similarity argument, allows for the calculation of the eigenvalues of J. We can proof that the eigenvalues have the form

$$\lambda_{1,2}(k) = \frac{1}{2}\left(\phi_k - 1 \pm \sqrt{1 + 6\phi_k + \phi_k^2}\right),$$
$$\phi_k := F(\mu) \cdot (-1 + \exp\frac{2\pi i k}{P}), \quad k \neq P. \tag{11}$$

We assume that the number of pedestrians on the ring is large, that means $P \gg 1$. We thus equate
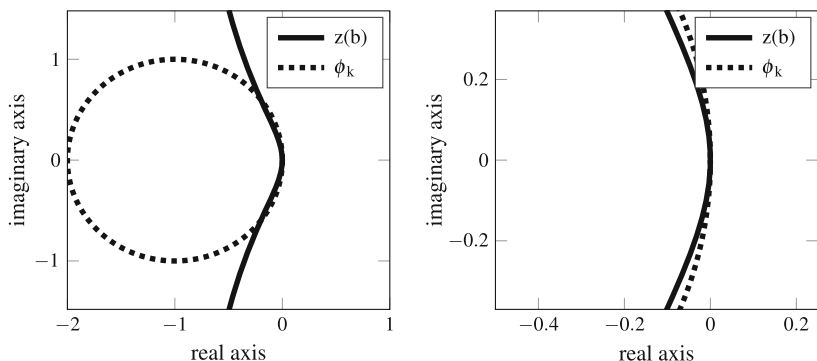
Fig. 3 Combination of the paired eigenvalues $z(b)$ and the matrix eigenvalues ϕ_k with $P = 100$. The *right* figure zooms into the *left* figure at $(0, 0)$

$$\frac{1}{2}\left(z - 1 \pm \sqrt{1 + 6z + z^2}\right) = ib, \ z \in \mathbb{C}, b \in \mathbb{R}/\{0\} \tag{12}$$

to find values $z_{1,2}(b) \in \mathbb{C}$ that might fulfil the non-hyperbolicity condition of a Hopf bifurcation–that is, two imaginary eigenvalues on the imaginary axis. We find

$$z(b) = \frac{-b^2 + 2bi}{8 + 2bi}, \tag{13}$$

which is depicted as black line in Fig. 3. For $F(\mu) \in [0, 1]$;, there exist ϕ_k and numbers b so that $\phi_k = z(b)$ (the crossings of the circle and the black line in Fig. 3). This can be shown by parametrising the curve $z(b)$, see [2]. Since we can find parameter values so that these crossing points exist, we can prove the non-hyperbolicity condition. To proof the transversality condition, we use Lemma 1.

Lemma 1 *Let $P(z, \mu)$ a polynomial in $z \in \mathbb{C}$ with parameter $\mu \in \mathbb{R}$. Let $\lambda(\mu) \in \mathbb{C}$ a differentiable curve of roots of P, which depends on μ. Then for all $\mu^* \in \mathbb{R}$ where $\frac{\partial P}{\partial z}\big|_{\mu=\mu^*} \neq 0$ it is*

$$\left.\frac{d\lambda}{d\mu}\right|_{\mu=\mu^*} = \left.\frac{-\frac{\partial P}{\partial \mu}}{\frac{\partial P}{\partial z}}\right|_{\mu=\mu^*}. \tag{14}$$

Proof Total differentiation of $P(\lambda, \mu)$ and the fact that $P(\lambda(\mu), \mu) = 0$ for all μ yields the result at $\mu = \mu^*$. □

Application of Lemma 1 on the characteristic polynomial of the higher-dimensional matrix described above, $P := \lambda^2 + \lambda - F(\mu) \cdot (1 - \exp(\frac{2\pi i}{P}))(\lambda + 2)$ yields the following:

$$\left.\frac{\lambda}{\partial F}\right|_{F=F(\mu_0)} = -\frac{b^2(b^2 - 2)}{(b^4 + 12b^2 + 4)F(\mu_0)} + i\frac{b(b^4 + 8b^2 + 4)}{(b^4 + 12b^2 + 4)F(\mu_0)}. \tag{15}$$

This can now be transformed to the final result, proving transversality:

$$\left.\frac{\Re(\lambda)}{\partial F}\right|_{F=F(\mu_0)} = -\frac{b^2(b^2-2)}{(b^4+12b^2+4)F(\mu_0)}. \tag{16}$$

The denominator in Eq. 16 is positive and the nominator is non-zero for $b \neq \sqrt{2}$, which is true for $P \gg 1$. Hence, the system fulfils the non-hyperbolicity and transversality conditions of a Hopf bifurcation. This completes the proof of Theorem 1.

The genericity condition in this case is quite complicated to proof. Since non-hyperbolicity and transversality is given, and the numerical results strongly indicate that stop and go waves occur, we simply assume genericity in this paper. The exact computations necessary for a proof are outlined in [2, 4].

For many pedestrians, it is very easy to find parameters for the interaction function h so that stop and go waves occur in **numerical simulations**. This can be seen in Fig. 1, where $P = 20$. For P close to 10, an interesting phenomenon occurs. As soon as there are less than ten pedestrians in the ring, no stop and go waves will occur for any value of the parameters. The size of the ring does not seem to matter, as confirmed by numerical experiments (see Fig. 4).
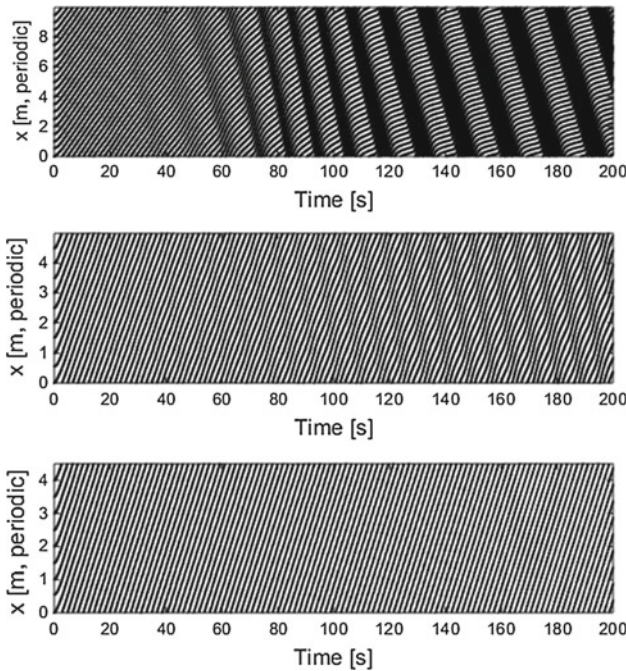
Fig. 4 Positions of 20, 10, and 9 pedestrians over time. In the last setting, the initial perturbation decreases and no stop and go waves occur. This is independent of the size of the ring, or the density, respectively

4   Conclusions and Discussion

We showed that Hopf bifurcations, which formally explain the existence of periodic steady state solutions in a dynamical system, can be found in a certain class of models in pedestrian dynamics. This helps to explain the phenomenon of stop and go waves. We also presented the mathematical analysis necessary to detect Hopf bifurcations so that it can be carried over to other models, such as force-based models. Numerical results for our system indicated that no stop and go waves may occur for any density or parameter value if the number of particles is below a threshold.

While our analysis is a step towards understanding periodic solutions in pedestrian dynamics, many open questions remain. It seems important that only the nearest neighbours are considered, and that the model incorporates a certain delay in the reaction to others. The results may also be interesting for car traffic, where there are similar models. It is particularly important for automatic distance control mechanisms that seek perfect alignment to the preceding car: If the settings are tuned incorrectly the alignment itself may cause the traffic system to enter a stop and go state.

References

1. Dietrich, F., Köster, G.: Gradient navigation model for pedestrian dynamics. Phys. Rev. E **89**(6), 062801 (2014)
2. Disselnkötter, S.: A bifurcation analysis for scenarios in the gradient navigation model. Master's thesis, Technische Universität München (2013)
3. Guckenheimer, J., Holmes, P.: Nonlinear oscillations, dynamical systems, and bifurcations of vector fields. Springer (1986)
4. Kuznetsov, Y.A.: Andronov-hopf bifurcation. Scholarpedia **1**(10), 1858 (2006)
5. Nishinari, K., Sugawara, K., Kazama, T., Schadschneider, A., Chowdhury, D.: Modelling of self-driven particles: Foraging ants and pedestrians. Physica A **372**(1), 132–141 (2006)
6. Orosz, G., Wilson, R.E., Stepan, G.: Traffic jams: dynamics and control. Philos. Trans. A: Math. Phys. Eng. Sci. **368**(1928), 4455–4479 (2010)
7. Portz, A., Seyfried, A.: Analyzing stop-and-go waves by experiment and modeling. In: Pedestrian and Evacuation Dynamics, vol. 1, pp. 577–586. Springer (2011)
8. Tadaki, S., Kikuchi, M., Fukui, M., Nakayama, A., Nishinari, K., Shibata, A., Sugiyama, Y., Yosida, T., Yukawa, S.: Phase transition in traffic jam experiment on a circuit. J. Phys. **15**(10), 103034 (2013)
9. Tordeux, A., Seyfried, A.: Collision-free nonuniform dynamics within continuous optimal velocity models. Phys. Rev. E **90**, 042812 (2014)

A Force-Based Model to Reproduce Stop-and-Go Waves in Pedestrian Dynamics

Mohcine Chraibi, Antoine Tordeux and Andreas Schadschneider

Abstract Stop-and-go waves in single-file movement are a phenomenon that is observed empirically in pedestrian dynamics. It manifests itself by the co-existence of two phases: moving and stopping pedestrians. We show analytically based on a simplified one-dimensional scenario that under some conditions the system can have unstable homogeneous solutions. Hence, oscillations in the trajectories and instabilities emerge during simulations. To our knowledge there exists no force-based model which is collision- and oscillation-free and meanwhile can reproduce phase separation. We develop a new force-based model for pedestrian dynamics able to reproduce qualitatively the phenomenon of phase separation. We investigate analytically the stability condition of the model and define regimes of parameter values where phase separation can be observed. We show by means of simulations that the predefined conditions lead in fact to the expected behaviour and validate our model with respect to empirical findings.

1 Introduction

In vehicular traffic, the formation of jams and the dynamics of traffic waves have been studied intensively [1, 2]. Particular car-following models including spacing and speed difference variables have been shown to reproduce realistic stop-and-go phenomena [3, Chap. 15]. In pedestrian dynamics this phenomenon has been observed empirically, especially when the density exceeds a critical value [4, 5]. Jams can be reproduced as a result of phase transitions from a stable homogeneous configuration to an unstable configuration. In the literature some space-continuous models [6–9]

M. Chraibi (✉) · A. Tordeux
Forschungszentrum Jülich GmbH, Jülich Supercomputing Centre, 52428 Jülich, Germany
e-mail: m.chraibi@fz-juelich.de

A. Tordeux
e-mail: a.tordeux@fz-juelich.de

A. Schadschneider
Institute for Theoretical Physics, Universität zu Köln, 50937 Köln, Germany
e-mail: as@thp.uni-koeln.de

reproduce partly this phenomenon. However, force-based models generally fail to describe pedestrian dynamics in jam situations correctly. Often uncontrollable oscillations in the direction of motion occur, which lead to unrealistic dynamics in form of collisions and overlappings [10].

In this work we present a force-based model that is able to reproduce stop-and-go waves for certain parameter values. By means of a linear stability analysis we derive conditions to define parameter regions, where the described system is unstable.

We study by numerical simulations if the system behaves realistically, i.e. jams emerge without any collisions in agreement with experimental results [4]. Furthermore, we validate the model by comparing the fundamental diagram with experiments. We conclude this paper with a discussion of the results and the limitations of the proposed model.

2 Model Definition

The phenomenon of stop-and-go waves in pedestrian dynamics was investigated experimentally in one-dimensional scenarios [4]. Therefore, we limit our analysis to 1D systems. Consider N pedestrians distributed uniformly in a narrow corridor with closed boundary conditions and neglect the effects of walls on pedestrians. Furthermore, for interactions among N pedestrians, we assume that pedestrian n is only influenced by the pedestrian right in front.

For the state variables position x_n and velocity $\dot{x}_n = \frac{dx_n}{dt}$ of pedestrian n we define the distance of the centres Δx_n and speed difference $\Delta \dot{x}_n$ of two successive pedestrians as

$$\Delta x_n = x_{n+1} - x_n, \qquad \Delta \dot{x}_n = \dot{x}_{n+1} - \dot{x}_n . \tag{1}$$

In general, pedestrians are modelled as simple geometric objects of constant size, e.g. a circle or ellipse. In one-dimensional space the size of pedestrians is characterised by a_n (Fig. 1), i.e. their length is $2a_n$. However, it is well-known that the space requirement of a pedestrian depends on its velocity and can be characterised by a linear function of the velocity [11–13]

$$a_n = a_0 + a_v \dot{x}_n , \tag{2}$$
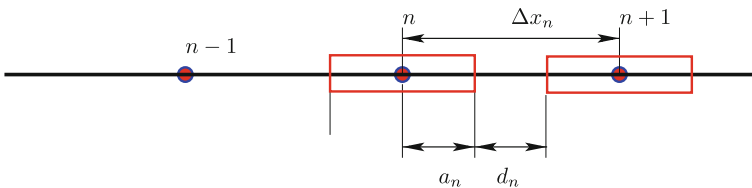
Fig. 1 Definition of the quantities characterising the single-file motion of pedestrians (represented by *rectangles*)

with a_0, characterising the space requirement of a standing person and $a_v \geq 0$ a parameter for the speed dependence with the dimension of time. The effective distance (distance gap) d_n of two consecutive pedestrians is then

$$d_n = \Delta x_n - a_n - a_{n+1} = \Delta x_n - a_v (\dot{x}_n + \dot{x}_{n+1}) - 2a_0. \tag{3}$$

At each time the change of state variables of pedestrian n is given by superposition of driving and repulsive terms. Thus, in general the equation of motion for pedestrian n described by a force-based model is given by

$$\ddot{x}_n = f\left(\dot{x}_n, \Delta \dot{x}_n, \Delta x_n\right) + \frac{v_0 - \dot{x}_n}{\tau}. \tag{4}$$

Typical values for the parameters are $\tau = 0.5\,\mathrm{s}$ for the relaxation time and $v_0 = 1.2\,\mathrm{m/s}$ for the desired speed.

For f we propose the following expression

$$f(\Delta x_n, \dot{x}_n, \dot{x}_{n+1}) = -\frac{v_0}{\tau} \ln\left(c \cdot R_n + 1\right), \tag{5}$$

with

$$R_n = r_\varepsilon\left(\frac{\Delta x_n}{a_n + a_{n+1}} - 1\right), \quad c = e - 1. \tag{6}$$

$r_\varepsilon(x)$ is an approximation of the non-differentiable ramp function

$$r_\varepsilon(x) = \varepsilon \ln(1 + e^{-x/\varepsilon}) \quad (0 < \varepsilon \ll 1). \tag{7}$$

Pedestrians anticipate collisions when their distance to their predecessors is smaller than a critical distance $a = a_n + a_{n+1}$. Therefore, a_n does not only model the body of pedestrian n but represents also a 'personal' safety distance. Assuming that $\dot{x}_n = 0$, for $\Delta x_n = 0$, i.e., $R_n = 1$, the repulsive force reaches the value $-v_0/\tau$ (at the limit $\varepsilon \to 0$) to nullify the effects of the driving term (Fig. 2).

Fig. 2 The absolute value of the repulsive force according to Eq. (5) (at the limit $\varepsilon \to 0$)
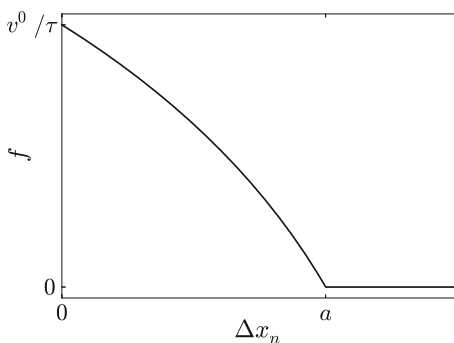
3   Linear Dynamics

In this section, we investigate the stability of the system (Eq. 4). The position of pedestrian n in the homogeneous steady state is given by

$$x_n = \frac{n}{\rho} + vt \, , \tag{8}$$

so that $x_{n+1} - x_n = \frac{1}{\rho} = \Delta x$, $\dot{x}_n = v$, being speed for the equilibrium of uniform solution. $\ddot{x}_n = 0$ for all n, where derivatives are taken with respect to t. For $\Delta y = \Delta x_n / a_0$ we consider small (dimensionless) perturbations ε_n of the steady state positions of the form

$$\varepsilon_n(t) = \alpha_n e^{zt}, \tag{9}$$

with $\alpha_n, z \in \mathbb{C}$. Replacing in (4) and expanding to first order yields a second-order equation for z. To obtain stability, one needs to ensure $\Re(z) < 0$ for the real part of all solutions z with the exception of the solution $z = 0$.

For the system (Eq. 4) with the repulsive force (Eq. 5) we obtain the following stability condition

$$\Phi := \left(\frac{1}{1 + 2\xi a_v' \Delta y} \right) \left(\frac{\xi}{1 + 2\xi a_v' \Delta y} + \xi a_v' \Delta y \right) - 1/2 < 0, \tag{10}$$

with $\xi = \frac{c}{d_0} \frac{v_0'}{a'}$, $a' = \frac{a}{a_0}$, $v_0' = v_0 \frac{\tau}{a_0}$ and $d_0 = 1 + c(1 - \Delta y / a')$.

Figure 3 shows the stability behaviour of the system with respect to the dimensionless parameters v_0' and $\tilde{a}_v = a_v / \tau$. The system becomes increasingly unstable with increasing v_0' (for a relatively small and constant $\tilde{a}_v$). Assuming that the free flow speed v_0 is constant, this means that increasing the reaction time τ or diminishing the safety space leads to unstable behaviour of the system. This results is well-known in traffic theory (see for instance [14]).

Fig. 3 Stability region in the $(\tilde{a}_v, v_0')$-space for $\Delta y = 1.5$. The *colours* are mapped to the values of Φ and $(\tilde{a}_v, v_0')$ are the dimensionless parameters in Eq. (10)
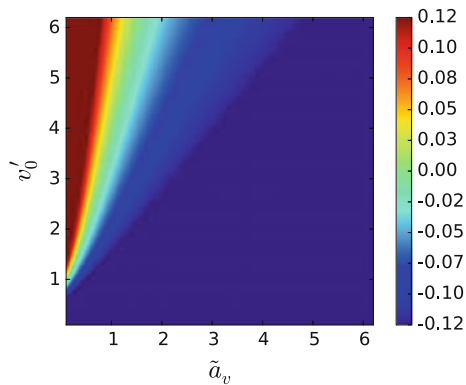
Fig. 4 Trajectories for $\Delta y_n = 1.5$ show stop-and-go waves
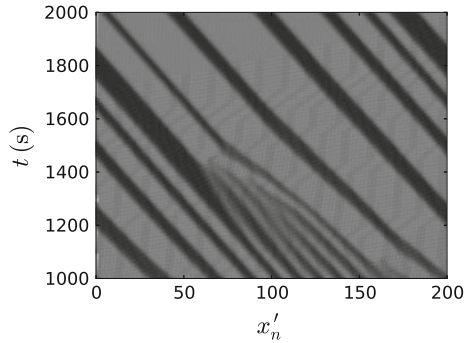
4 Simulations

We perform simulations with the introduced model to analyse the unstable dynamics. For $a_v = 0$, $v_0' = 1$ and $\Delta y_n = 1.5$ we calculate the solution for 3000 s. These parameters lay in the unstable regime of the model (Fig. 3). Thus, jam waves are expected to emerge. Figure 4 shows the trajectories of 133 pedestrians. ε in Eq. (7) is set to 0.01.

We observe jam waves propagating in the system. Note that the observed jam waves last for a long period of time (here 3000 s), which is a indication that they are not dependent on the initial conditions of the simulation and are 'stable' in time.

As shown in Fig. 5 the speed does not become negative, therefore backward movement is not observed. This condition favours the appearance of stable jams.

Having reproduced stop-and-go waves, the model will be further tested by comparing qualitatively the produced density-velocity relation (fundamental diagram). The same set-up as above is simulated several times. In order to scan a sufficiently large density interval, the number of pedestrians N is increased after each simulation. Figure 6 shows a comparison of the simulation results with experimental data
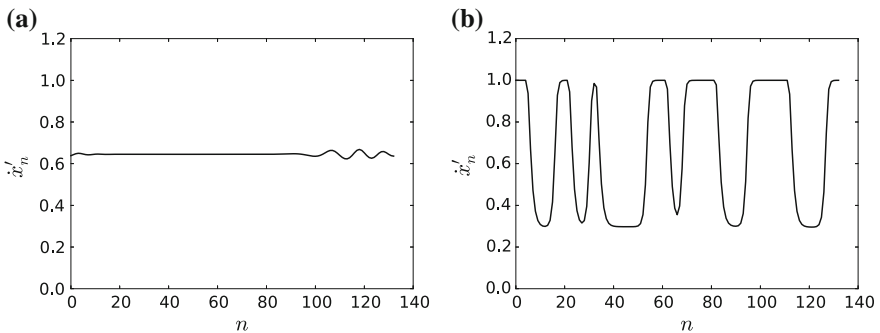
Fig. 5 Speed of pedestrians at different time steps: $t = 300$ s (**a**); $t = 2000$ s (**b**)

Fig. 6 Fundamental
diagram: comparison with
experiments from [5]
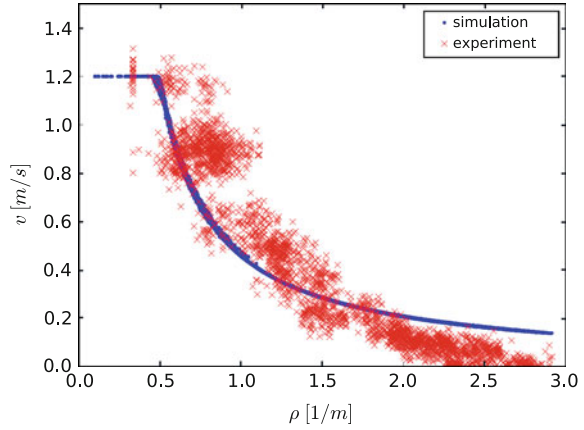
from [5]. The observed fundamental diagram is composed of two different regimes:
free flow regime, where the speed of pedestrians does not depend on the density
($\rho < 0.5\,\mathrm{m}^{-1}$), and a regime where the speed decreases with increasing density.
Here, we observe that the correct shape of the fundamental diagram is reproduced
quite well, although the velocity is slightly higher than the experimental velocities
for $\rho > 2\,\mathrm{m}^{-1}$.

5 Discussion

We have introduced a simple force-based model for which uniform solutions can be
unstable. By simulations we observe that the proposed model shows phase separation
in its unstable regime, in agreement with empirical results [4].

The linear stability condition of the models shows that we can find *realistic* para-
meter values in the unstable regime. However, depending on the chosen values for the
(rescaled) desired speed v_0', collisions *can* occur, as a result of backwards movement
and negative speeds.

Further investigations remain to be carried out to determine the set of parameter
values for which the model have unstable solutions with realistic (i.e. collision-free)
stop-and-go phenomena and meanwhile a better *quantitative* agreement with the
experimental data e.g. in form of the fundamental diagram.

References

1. Chowdhury, D., Santen, L., Schadschneider, A.: Statistical physics of vehicular traffic and some related systems. Phys. Rep. **329**(4–6), 199–329 (2000)
2. Orosz, G., Wilson, R.E., Stepan, G.: Traffic jams: dynamics and control. Philos. Trans. R. Soc. Lond. A: Math. Phys. Eng. Sci. **368**(1957), 4455–4479 (2010)
3. Treiber, M., Kesting, A.: Traffic Flow Dynamics. Springer, Berlin (2013). ISBN 978-3-642-32459-8
4. Portz, A., Seyfried, A.: Analyzing stop-and-go waves by experiment and modeling. In: Peacock, R., Kuligowski, E., Averill, J. (eds.) Pedestrian and Evacuation Dynamics 2010, pp. 577–586. Springer (2011)
5. Seyfried, A., Boltes, M., Kähler, J., Klingsch, W., Portz, A., Rupprecht, T., Schadschneider, A., Steffen, B., Winkens, A.: Enhanced empirical data for the fundamental diagram and the flow through bottlenecks. In: Klingsch, W.W.F., Rogsch, C., Schadschneider, A., Schreckenberg, M. (eds.) Pedestrian and Evacuation Dynamics 2008, pp. 145–156. Springer, Heidelberg (2010)
6. Eilhardt, C., Schadschneider, A.: Stochastic headway dependent velocity model for 1d pedestrian dynamics at high densities. Transp. Res. Procedia **2**, 400–405 (2014)
7. Lemercier, S., Jelic, A., Kulpa, R., Hua, J., Fehrenbach, J., Degond, P., Appert-Rolland, C., Donikian, S., Pettré, J.: Realistic following behaviors for crowd simulation. Comput. Graph. Forum **31**, 489–498 (2012)
8. Portz, A., Seyfried, A.: Modeling stop-and-go waves in pedestrian dynamics. In: Wyrzykowski, R., Dongarra, J., Karczewski, K., Wasniewski, J. (eds.) PPAM 2009, Part II, pp. 561–568. Springer, Berlin, Heidelberg (2010)
9. Seyfried, A., Portz, A., Schadschneider, A.: Phase coexistence in congested sates of pedestrian dynamics. In: Lecture Notes in Computer Science, vol. 6350, pp. 496–505 (2010)
10. Chraibi, M., Ezaki, T., Tordeux, A., Nishinari, K., Schadschneider, A., Seyfried, A.: Jamming transitions in force-based models for pedestrian dynamics. Phys. Rev. E **92**, 042809 (2015)
11. Jelić, A., Appert-Rolland, C., Lemercier, S., Pettré, J.: Properties of pedestrians walking in line. ii. stepping behavior. Phys. Rev. E **86**, 046111 (2012)
12. Seitz, M.J., Köster, G.: Natural discretization of pedestrian movement in continuous space. Phys. Rev. E **86**, 046108 (2012)
13. Weidmann, U.: Transporttechnik der Fussgänger. Technical Report Schriftenreihe des IVT Nr. 90, Institut für Verkehrsplanung,Transporttechnik, Strassen- und Eisenbahnbau, ETH Zürich, ETH Zürich, 2nd edn. (1993)
14. Bando, M., Hasebe, K., Nakayama, A., Shibata, A., Sugiyama, Y.: Dynamical model of traffic congestion and numerical simulation. Phys. Rev. E **51**(2), 1035–1042 (1995)

Impact of Impulse Stops on Pedestrian Flow

Jaeyoung Kwak, Hang-Hyun Jo, Tapio Luttinen and Iisakki Kosonen

Abstract We numerically study the impact of impulse stops on pedestrian flow for a straight corridor with multiple attractions. The impulse stop is simulated by the switching behaviour model, a function of the social influence strength and the number of attendees near the attraction. When the pedestrian influx is low, one can observe a stable flow where attendees make a complete stop at an attraction and then leave the attraction after a certain amount of time. When the pedestrian influx is high, an unstable flow is observed due to strong social influence. In the unstable flow, attendees near the attraction are crowded out from the clusters by others due to the interpersonal repulsion. The expelled pedestrians impede the pedestrian traffic between the left and right boundaries of the corridor. These collective patterns of pedestrian flow are summarised in a schematic phase diagram.

1 Introduction

Walking is a fundamental activity of human life, not only for moving between places, but also in interactions with surrounding environments. While walking to destinations, pedestrians may be influenced by attractive stimuli, such as artworks and shop displays. Some pedestrians may shift their attention to such attractions, opting to stop walking and making an impulse stop to join an attraction [2].

J. Kwak (✉) · T. Luttinen · I. Kosonen
Department of Built Environment, Aalto University, Espoo, Finland
e-mail: jaeyoung.kwak@aalto.fi

T. Luttinen
e-mail: tapio.luttinen@aalto.fi

I. Kosonen
e-mail: iisakki.kosonen@aalto.fi

H.-H. Jo
BK21plus Physics Division and Department of Physics, POSTECH,
Pohang, Republic of Korea
e-mail: johanghyun@postech.ac.kr

According to previous studies [3, 13], it has been reported that a growing number of attendees around an attraction are likely to attract more passers-by to the attraction, inferring that impulse stopping pedestrians can be affected by others' choices. It has been widely accepted that having more store visitors likely attracts more passer-by to the store in that a growing number of visitors increases the possibility of passers-by visiting the store. Therefore, marketing strategies have focused on increasing the number of the impulse stopping visitors [1].

By means of numerical simulations, we have investigated the impact of impulse stops on pedestrian flow for a straight corridor with multiple attractions. This study employs the switching behaviour model, as shown in the next section. In Sect. 3, we analyse the spatial distribution of the pedestrian flow, characterise the collective patterns, and then summarise the results with a schematic phase diagram. Finally, we discuss the findings of this study in the section following the results (Sect. 4).

2 Model

2.1 Switching Behaviour

Similar to the sigmoidal choice rule [3, 13], the probability of joining an attraction P_a is a function of the number of pedestrians who have already joined N_a and the number of pedestrians not stopping by the attraction N_0:

$$P_a = \frac{s(N_a + K_a)}{(N_0 + K_0) + s(N_a + K_a)}. \tag{1}$$

This suggests that larger N_a likely yields higher joining probability. In order to prevent indeterminate cases with $N_a = N_0 = 0$, two baseline values K_a and K_0 are introduced for N_a and N_0. Here, $s > 0$ is the strength of the social influence that can be also understood as pedestrians' awareness of the attraction. According to previous studies [3, 8, 13], we assumed that the strength of social influence can be different for different situations and can be controlled in the presented model. After joining the attraction, the individual will then stay near the attraction for an exponentially distributed time with an average of t_d, similar to previous works [3, 6, 10].

2.2 Pedestrian Movement

According to the social force model [6], the velocity $\mathbf{v}_i(t)$ of pedestrian i at time t is given by the following equation:

$$\frac{d\mathbf{v}_i(t)}{dt} = \frac{v_d\mathbf{e}_i - \mathbf{v}_i(t)}{\tau} + \sum_{j\neq i}\mathbf{f}_{ij} + \sum_{B}\mathbf{f}_{iB}. \tag{2}$$

Here, the first term on the right-hand side indicates the driving force describing the tendency of pedestrian i moving towards his destination with the desired speed v_d and a unit vector $\mathbf{e}_i$ pointing to the desired direction. The relaxation time τ controls how fast pedestrian i adapts its velocity to the desired velocity. The repulsive force terms $\mathbf{f}_{ij}$ and $\mathbf{f}_{iB}$ reflect his tendency to keep certain distance from other pedestrian j and the boundary B, e.g., wall and obstacles. A more detailed description of the pedestrian movement model can be found in previous works [6, 7, 9, 10].

2.3 Numerical Simulation Setup

Each pedestrian is modelled by a circle with radius $r_i = 0.25$ m. Pedestrians move in a corridor of length 55 m and width 6 m in the horizontal direction. They move with desired speed $v_d = 1.2$ m/s and with relaxation time $\tau = 0.5$ s, and their speed cannot exceed $v_{\max} = 2.0$ m/s. The desired direction points from the left to the right boundary of the corridor for one half of population and the opposite direction for the other half. On the lower wall of the corridor, three attractions are placed for every 15 m. The number of pedestrians in the corridor is associated with the pedestrian influx q, i.e., the arrival rate of pedestrians entering the corridor. The pedestrian arrival rate is assumed to follow a shifted exponential distribution $h = 1/q$ with a minimum headway $h_0 = 0.5$ s per unit width based on previous works [11, 12].

The joining probability (Eq. 1) is updated with the social force model (Eq. 2) for each simulation time step of 0.05 s. The individual can decide whether he will join the attraction when he enters the area of influence (see Fig. 1). The area of influence is defined as a square area of 15 m by 6 m, and its horizontal centre coincides with that of the attraction. Once the individual decides to join the attraction, he shifts his desired direction vector $\mathbf{e}_i$ towards the centre of the attraction. For simplicity, K_a and K_0 are set to be 1, meaning that both options are equally attractive when the individual would see nobody within his perception range. An individual i is counted as an attending pedestrian if his efficiency of motion $E_i = (\mathbf{v}_i \cdot \mathbf{e}_i)/v_d$ is lower than 0.05 within a range of 4 m from the centre of the attraction after he decided to join

Fig. 1 A schematic representation of the area of influence
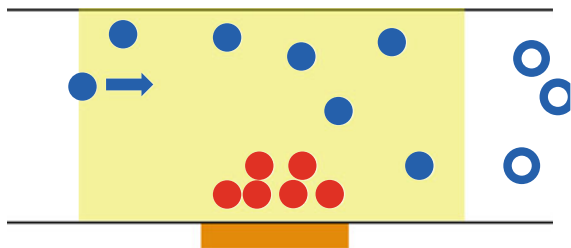
there (red circles in the yellow shade area, Fig. 1). Here, the individual efficiency of motion E_i indicates how much the driving force contributes to pedestrian i's motion with a range from 0 to 1 [4, 9]. The average of t_d is set to be 30 s.

3 Results and Discussion

For different levels of pedestrian influx q, different patterns of pedestrian movement appear. When q is low, one can observe a stable flow where attendees form standstill-like clusters near the attraction and such clusters do not impede pedestrian traffic near the clusters (see Fig. 2a). For large values of q, an unstable flow can be observed if the value of s is large. In the unstable flow, pedestrians form swirling clusters in which pedestrians near the attractions are being pushed away from the clusters by other pedestrians. Since increasing s makes more passers-by head for the attractions, pedestrians tend to rush into the attraction and push others, as shown in Fig. 2b.

In order to analyse the spatial distribution of the pedestrian flow interacting with attractions, this study evaluates local quantities, such as local density and local speed. Following previous studies [5, 9, 14], the local density and local speed are associated with a Gaussian distance-dependent weight function $f(d)$:

$$f(d) = \frac{1}{\pi R^2} \exp\left(-\frac{d^2}{R^2}\right) \tag{3}$$

with $R = 0.7$. The local density at a location $\mathbf{z}$ and time t is defined as

$$\rho(\mathbf{z}, t) = \sum_i f(d_{iz}), \tag{4}$$

where d_{iz} is the distance between location $\mathbf{z}$ and pedestrian i's position. Likewise, the local speed is given as
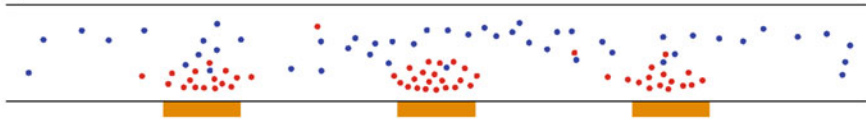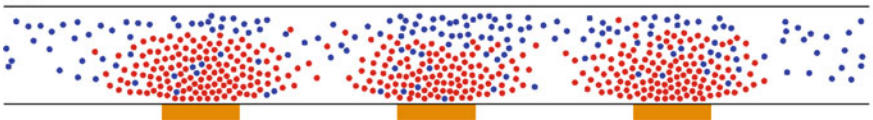
Fig. 2 Snapshots of a stable (*top*) and an unstable (*bottom*) flow. *Red circles* indicate pedestrians attracted by an attraction and *blue circles* pedestrians not attracted by the attraction. Snapshots of stable flow with $q = 0.05$ and $s = 0.2$ (**a**). Snapshots of an unstable flow with $q = 0.3$ and $s = 1.2$ (**b**)

$$V(\mathbf{z}, t) = \frac{\sum_i \|\mathbf{v}_i\| f(d_{iz})}{\sum_i f(d_{iz})}. \tag{5}$$

For different patterns, Figs. 3 and 4 show the local speed maps $V(\mathbf{z}, t)$ and the local density maps $\rho(\mathbf{z}, t)$ that have been averaged over the simulation period. In the stable flow, pedestrians form tighter clusters around the attraction as s increases, resulting in higher local density and lower local speed around the attractions (see Fig. 3). In the unstable flow, one can observe higher local density as s increases, similar to the observations from the stable flow. However, the local speed inside of
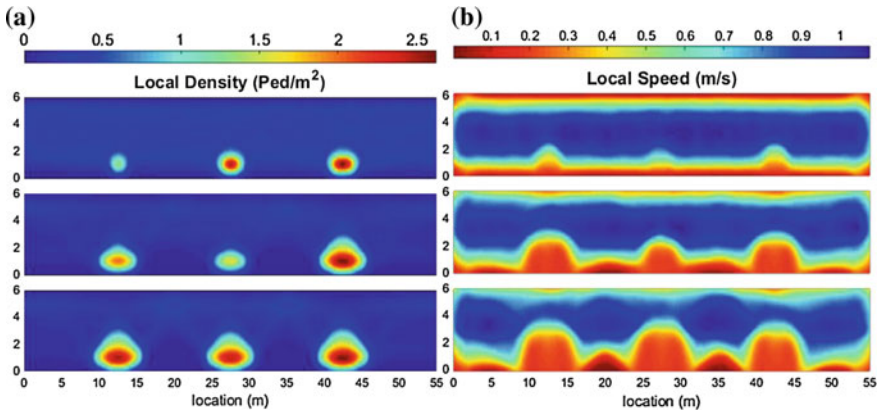
Fig. 3 Local speed **b** and local density **a** maps for stable flow with a low value of $q = 0.05$ Ped/m/s and different values of s: $s = 0.2, 0.6,$ and 1.2 (from *top* to *bottom*). In local speed maps, *red* and *blue colours* indicate lower and higher speed, respectively. In local density maps, *blue* and *red colours* indicate lower and higher density, respectively. The centre of each attraction is at $x = 12.5$, 27.5, and 42.5
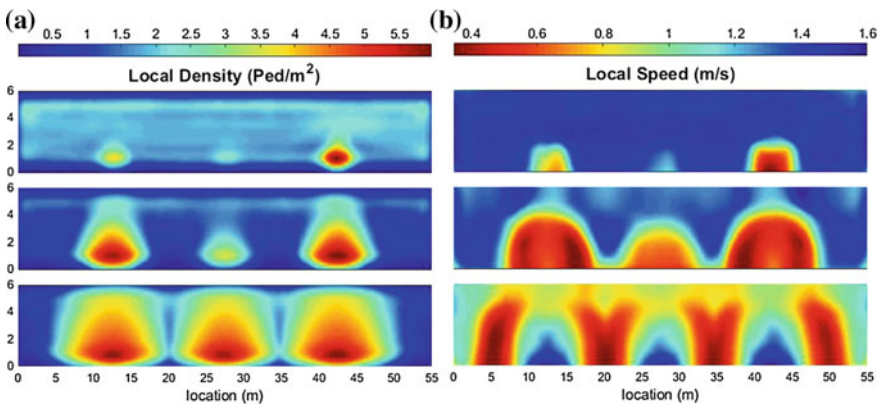
Fig. 4 Local speed **b** and local density **b** maps for unstable flow with a high value of $q = 0.3$ Ped/m/s and different values of s: $s = 0.2, 0.6,$ and 1.2 (from *top* to *bottom*)

the clusters decreases and then increases as s increases, while the local speed near the clusters begins to decrease when s is above a certain value (see Fig. 4).

In addition to the local quantities, one can better understand the spatial patterns of the pedestrian flow by means of collective quantities, such as the collective efficiency of motion E and the normalised kinetic energy K. As in previous studies [4, 9], E and K are measured as:

$$E = \left\langle \frac{1}{N} \sum_{i=1}^{N} \frac{\mathbf{v}_i \cdot \mathbf{e}_i}{v_d} \right\rangle = \left\langle \frac{1}{N} \sum_{i=1}^{N} E_i \right\rangle \tag{6}$$

and

$$K = \left\langle \frac{1}{N} \sum_{i=1}^{N} \frac{\|\mathbf{v}_i\|^2}{v_d^2} \right\rangle. \tag{7}$$

Here, $\langle \cdot \rangle$ represents an average over the simulation period after reaching the stationary state. Similar to E_i in the previous section, the collective efficiency reflects the contribution of the driving force in the collective pedestrian motion. The normalised kinetic energy has the value of 0 if no pedestrians move, otherwise it has a positive value.

Figure 5 shows how the collective efficiency $E(s, q)$ and the kinetic energy $K(s, q)$ depend on the social influence strength s and the pedestrian influx q. For each value of q, E decreases as s increases, indicating that more pedestrians are distracted from their initial destination due to the higher social influence (Fig. 5a). Depending on q, K reveals two distinct behaviours. First, for low values of q, the decreasing behaviour of K appears to be similar to that of E. This corresponds to
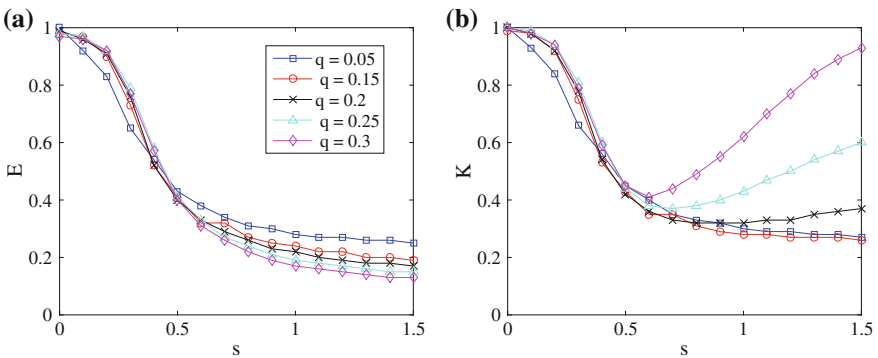
Fig. 5 Numerical results. Different symbols represent different levels of q. One can observe that $E(s)$ decreases as s increases for each given q. The behaviour of $K(s)$ is similar when the value of q is low. However, $K(s)$ decreases and then increases against s when q is large. The collective efficiency of motion $E(s, q)$ (**a**). The normalised kinetic energy $K(s, q)$ (**b**)

Fig. 6 A schematic representation of phase diagram. The *dashed line* indicates $\partial K / \partial s = 0$, the boundary between stable and unstable flow
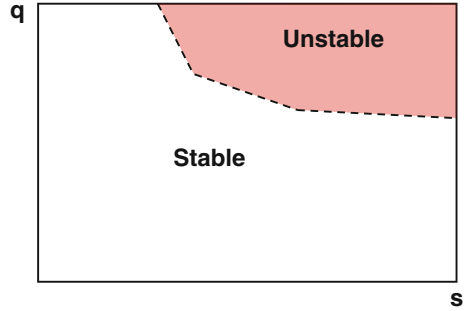
the stable flow that can be characterised by

$$\frac{\partial E}{\partial s} < 0 \text{ and } \frac{\partial K}{\partial s} < 0. \qquad (8)$$

Secondly, for large values of q, K decreases and then increases as s grows, indicating the unstable flow. This case can be characterised by

$$\frac{\partial E}{\partial s} < 0 \text{ and } \frac{\partial K}{\partial s} > 0. \qquad (9)$$

This reflects that higher s does not only yield more attendees around attractions, but also stronger repulsion among attendees. In this case, attendees near the attraction cannot reach a standstill and they are crowded out from the cluster by other attendees because of interpersonal repulsion. Consequently, expelled attendees from the cluster impede pedestrian flow between the left and right boundaries of the corridor, and thus this parameter region can be called the unstable flow. Those different patterns of pedestrian flow can be summarised in a schematic phase diagram, as shown in Fig. 6.

4 Conclusion

This study has numerically investigated the impact of impulse stops on pedestrian flow by employing the switching behaviour model. For low pedestrian influx, one can observe a stable flow in which attendees form standstill-like clusters. When the pedestrian influx and the social influence strength are high, on the other hand, one can see an unstable flow showing crowded out attendees from the clusters. Consequently, the expelled attendees impede the pedestrian flow near the clusters. We have also provided a schematic representation of phase diagram as a summary of the study results.

We believe that our study results can provide an insight into better management of pedestrian facilities where impulse stops may be expected to occur. For instance, during shopping holidays such as Black Friday in the United States and Singles day in China, the influx of people with extreme desire for merchandise may lead pedestrian incidents. The existence of the unstable flow suggests that controlling the pedestrian influx for expected level of social influence is necessary for safe and efficient use of pedestrian facilities.

The presented model can be further investigated for various scenarios. For instance, one can explicitly consider the capacity of the attractions, meaning that only a certain number of attendees can stay near the attractions. In addition, the length of stay t_d can be associated with the number of attendees near the attractions.

References

1. Bearden, W.O., Netemeyer, R.G., Teel, J.E.: Measurement of consumer susceptibility to interpersonal influence. J. Cons. Res. **15**(4), 473–481 (1989)
2. Borgers, A., Timmermans, H.: A model of pedestrian route choice and demand for retail facilities within inner-city shopping areas. Geogr. Anal. **18**(2), 115–128 (1986)
3. Gallup, A.C., Hale, J.J., Sumpter, D.J.T., Garnier, S., Kacelnik, A., Krebs, J.R., Couzin, I.D.: Visual attention and the acquisition of information in human crowds. Proc. Nat. Acad. Sci. **109**(19), 7245–7250 (2012)
4. Helbing, D., Farkas, I.J., Vicsek, T.: Freezing by heating in a driven mesoscopic system. Phys. Rev. Lett. **84** (2000)
5. Helbing, D., Johansson, A., Abideen, H.Z.A.: Dynamics of crowd disasters: an empirical study. Phys. Rev. E **75**(4), 046109 (2007)
6. Helbing, D., Molnár, P.: Social force model for pedestrian dynamics. Phys. Rev. E **51**(5), 4282–4286 (1995)
7. Johansson, A., Helbing, D., Shukla, P.: Specification of the social force pedestrian model by evolutionary adjustment to video tracking data. Adv. Complex Syst. **10**, 271–288 (2007)
8. Kaltcheva, V.D., Weitz, B.A.: When should a retailer create an exciting store environment? J. Mark. **70**, 107–118 (2006)
9. Kwak, J., Jo, H.H., Luttinen, T., Kosonen, I.: Collective dynamics of pedestrians interacting with attractions. Phys. Rev. E **88**(6), 062810 (2013)
10. Kwak, J., Jo, H.H., Luttinen, T., Kosonen, I.: Effects of Switching Behavior for the Attraction on Pedestrian Dynamics. PLoS ONE **10**, e0133–e0668 (2015)
11. Luttinen, T.: Properties of cowan's m3 headway distribution. Transp. Res. Rec. J. Transp. Res. Board **1678**, 189–196 (1999)
12. May, A.D.: Traffic flow fundamentals. Prentice Hall (1990)
13. Milgram, S., Bickman, L., Berkowitz, L.: Note on the drawing power of crowds of different size. J. Pers. Soc. Psychol. **13**(2), 79–82 (1969)
14. Moussaïd, M., Helbing, D., Theraulaz, G.: How simple rules determine pedestrian behavior and crowd disasters. Proc. Nat. Acad. Sci. **108**(17), 6884–6888 (2011)

Investigation on Cooperative Avoiding Behaviour in Bi-directional Flow

Daichi Yanagisawa

Abstract We have introduced an evolutionary game dynamics to a one-dimensional cellular automaton to investigate evolution and maintenance of cooperative avoiding behaviour in bidirectional flow of self-driven particles. In our model, there are two kinds of particles, which are right-going particles and left-going particles. Since the model is one dimension, they often face opponent particles. In order to avoid conflicts, the particles try to avoid their opponents by swerving to the right or left stochastically. The particles have a memory and reinforce their preference after their successful avoidance. Result of our simulation indicates that cooperative avoiding behaviour is achieved, i.e., swerving directions of the particles are unified, when the density of particles is close to 1/2 and the memory-loss rate is small. Application of our research will be useful to study evolution and maintenance of cooperative avoiding behaviour in pedestrian dynamics.

1   Introduction

Pedestrian dynamics has been vigorously studied both theoretically and experimentally in these two decades [4, 7, 9, 10]. Especially, bidirectional flow, which is one of the most popular themes in pedestrian dynamics, has been investigated by many researchers. Both continuous [5] and discrete space models [1, 2] have been developed, and experiments with real pedestrians have been also conducted [6, 11].

Bidirectional flow attracts many researchers since we observe lane formation. When there are right-going pedestrians and left-going pedestrians in a street, they try to follow the predecessors in the same walking direction, so that the lanes are formed as in Fig. 1. It is a self-organised as well as spontaneous symmetry breaking phenomenon. Pedestrians form lanes in order to avoid conflicts with opponent pedestrians. Besides, although the inflow from the right and left ends are same, the number of right and left-going lanes are not always equal.

D. Yanagisawa (✉)

Research Center for Advanced Science and Technology, The University of Tokyo,
4-6-1, Komaba, Meguro-ku, Tokyo 153-8904, Japan
e-mail: tDaichi@mail.ecc.u-tokyo.ac.jp
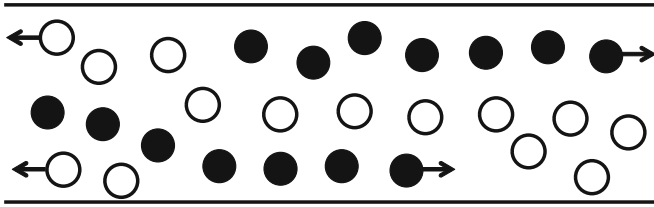
Fig. 1 Schematic view of the lane formation in bidirectional flow of pedestrians. Pedestrians depicted by *black* and *white* particles move to the *right* and *left*, respectively
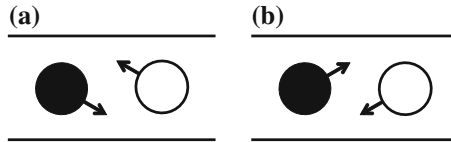
Fig. 2 Schematic view of swerving pedestrians: both pedestrians swerving to their right (**a**) and to their left (**b**) direction

In this paper, we consider swerving direction when pedestrians avoid their opponents (Fig. 2). Unification of the swerving directions of pedestrians, which smooths bidirectional flow, is a self-organised as well as spontaneous symmetry breaking phenomenon as lane formation. Pedestrians try to unify their swerving directions in order to avoid conflicts. Moreover, there are only right swerving pedestrians or left swerving pedestrians in the completely unified state. However, the mechanism of the lane formation and unification of the swerving directions are different. It is considered that the lane formation is achieved by the following behaviour of pedestrians. On the other hand, preferred swerving direction seems to be determined by the custom that pedestrians experience in their society.

Therefore, we develop a new model by combining one-dimensional cellular automaton and evolutionary game dynamics. Particles, which represent pedestrians, in the model have memories of their preferred swerving directions. They are updated by interaction with other pedestrians and memory-loss effect.

The remainder of the paper is organised as follows. In the next section, our model is introduced in detail, and the results of simulation are shown in Sect. 3. The final section is devoted to summary and conclusion.

2 Model

A schematic view of our model is depicted in Fig. 3. We consider one-dimensional discrete space with periodic boundary condition. The length of the space, i.e., the number of cell in the system, is L. Time is also discrete in the model, and the parallel-update rule is adopted.
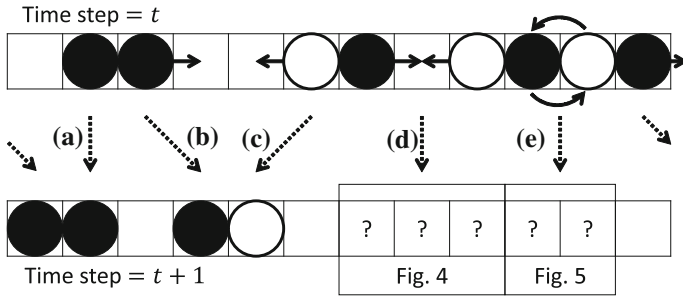
Fig. 3 Schematic view of the model. The *black* particle cannot move since its target cell is occupied by the other particle moving in the same direction (**a**). The *black* particle moves to the vacant right cell (**b**). The *white* particle moves to the vacant left cell (**c**). Interaction between the *black* and *white* particles occur (**d** and **e**)

There are two kinds of particles, which are right-going (black) and left-going (white) particles. The number of the right-going and left-going particles are N_R and N_L, respectively. Similarly, the density of the right-going and left-going particles are $\rho_R = N_R/L$ and $\rho_L = N_L/L$, respectively. The total number of the particles is $N = N_R + N_L$.

Every discrete time step, the right-going (left-going) particles move to the right (left) for one cell if their target cell is vacant (Fig. 3 case b, c). They cannot move if their target cell is occupied by the particles moving in the same direction (Fig. 3 case a).

When the right-going and left-going particles are moving to the same cell as in Fig. 3 case d, they try to avoid each other by swerving to the right or left with the probabilities p_i or $1 - p_i$, respectively (Fig. 4), where p_i is the right swerving probability of the particle $i \in [1, N]$. If the swerving directions of the two particles
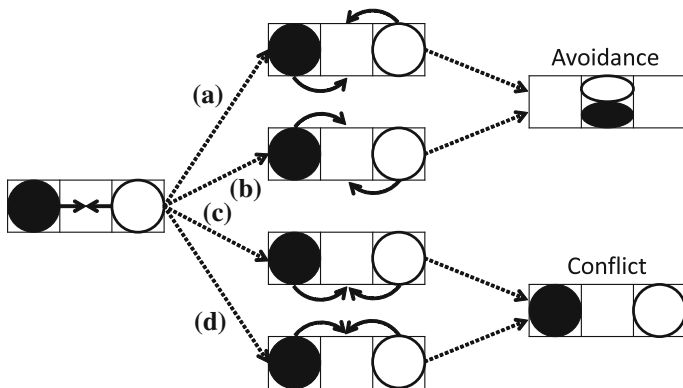
Fig. 4 Schematic view of avoidance and conflict when the two particles move to the same cell. Avoidance achieved by right swerving (**a**) and by left swerving (**b**). Conflict (**c** and **d**)
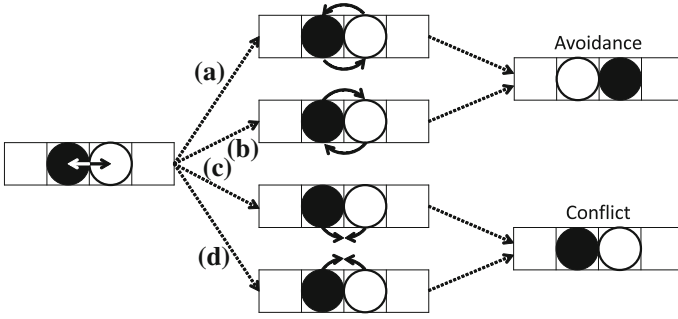
Fig. 5 Schematic view of avoidance and conflict when the two particles try to exchange their cell. Avoidance achieved by right swerving (**a**) and by left swerving (**b**). Conflict (**c** and **d**)

agree with the probability $p_i p_j + (1 - p_i)(1 - p_j)$ $(i, j \in [1, N], i \neq j)$, they avoid a conflict and stay at the same cell (Fig. 4 case a, b). In contrast, when the swerving directions disagree with the probability $p_i(1 - p_j) + p_j(1 - p_i)$, a conflict occurs and they remain at their cell (Fig. 4 case c, d). Similar rule is adopted when the right-going and left-going particles try to exchange their positions (Fig. 3 case e, Fig. 5).

Now, we introduce an evolutionary game dynamics to the model. Each particle has preference of right swerving and left swerving, which are described by $P_i^R \in \mathbb{R}_{\geq 0}$ and $P_i^L \in \mathbb{R}_{\geq 0}$, respectively. The right swerving probability, which is introduced in the previous paragraph is represented by the Logit model [3] using theses preferences.

$$p_i(t) = \frac{\exp\left(P_i^R(t)\right)}{\exp\left(P_i^R(t)\right) + \exp\left(P_i^L(t)\right)}. \tag{1}$$

The preferences are updated every time steps by the following equation

$$P_i^X(t+1) = (1 - \phi)P_i^X(t) + S_i^X(t), \tag{2}$$

where $X \in R, L, \phi \in (0, 1]$ is the memory-loss rate, and $S_i^X(t)$ is the payoff for the particle i at the time step t. The payoff $S^R = 1$ when the particles succeed in avoiding conflict by swerving to the right (Case a in Figs. 4 and 5). Similarly, $S^L = 1$ when the particles succeed in avoiding conflict by swerving to the left (Case b in Figs. 4 and 5). In the other cases, $S^R = S^L = 0$.

Therefore, if the particles often interact with the opponent particles and succeed in avoiding, their preference increase. By contrast, if they fail to avoid the opponent particles their preference does not increase. Furthermore, when there are few interactions, the preference decreases due to the memory-loss rate ϕ.

3 Simulation

Here, we consider the case where the same number of the right and left-going particles are moving in the system, i.e., $\rho_R = \rho_L (\equiv \rho)$. We control the density of the particles ρ and the memory-loss rate ϕ, and investigate the two quantities.

The first one is the unified ratio defined as follows:

$$U = \left| \frac{\sum_{i=1}^{N} 2(p_i - 1/2)}{N} \right| \in [0, 1]. \tag{3}$$

$U \cong 1$ implies that the unified phase is achieved, i.e., all the particles swerve to the same direction when they face their opponent particles. On the other hand, $U \cong 0$ indicates that the disordered phase is attained, i.e., all the particles do not have their preferred swerving direction, in other words, they swerve to the right and left with the equal probability $1/2$.

The other one is the flow of right-going particles $Q_R \in [0, 1]$. Note that the Q_R may be positive even if all the left-going particles cannot move.

We set the length of the system as $L = 50$ and perform simulation for 22000 time steps. For calculating the unified ratio and the flow, the results from $t = 2001$ to 22000 are used.

Figure 6 shows the unified ratio U as a function of the density ρ and memory-loss rate ϕ. We see two phases, which are the disordered and unified phases, and phase transition between them. When ϕ is large, quick memory-loss prevents the particles from keeping their preferences large, so that the disordered phase is achieved. Even if the memory-loss rate is small, the disordered phase is observed in the low and high density region. This is because there are few interactions between particles, which are opportunities to increase the preferences, in the low and high density cases. In the low density case, there are few particles to interact. In the high density case, it is difficult to move and interact since the cells are occupied by the other particles moving in the same direction. If the memory-loss rate is small and the density is medium,

Fig. 6 Unified ratio U as a function of the density $\rho(= \rho_R = \rho_L)$ and memory-loss rate ϕ. We see two clear phases, which are the disordered phase (*black top part*) and the unified phase (*light-grey bottom-middle part*)
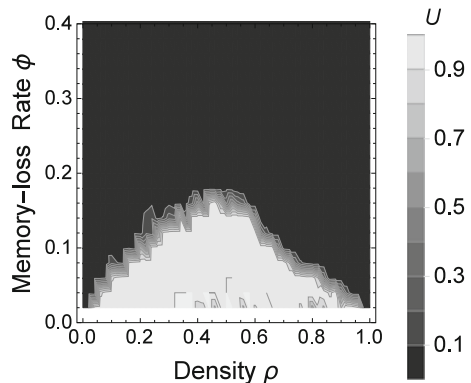
Fig. 7 Flow-density
diagram of the right-going
particles. We see that the
flow of the simulation
($\phi = 0.03$) agrees well with
that of the TASEP ($p = 1.0$)
in the most part of the figure
($\rho \leq 0.8$). By contrast, the
flow of the simulation
($\phi = 0.30$) agrees well with
that of the TASEP ($p = 0.5$)
in the high density region
($\rho \geq 0.5$)
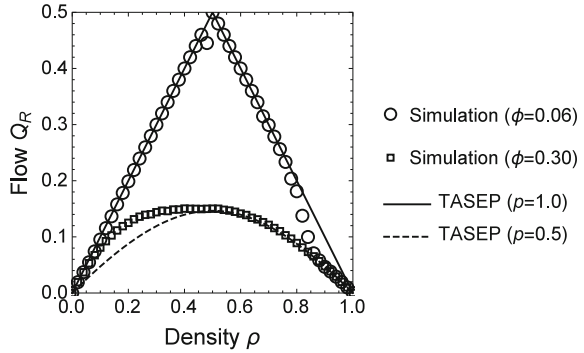
the unified phase is achieved. Many interactions between the particles reinforce the preference of them.

Figure 7 shows the flow of right-going particles Q_R as a function of the density ρ for the memory-loss rate $\phi = 0.03$ and 0.30. We see from Fig. 6 that the unified phase is achieved in the most density region in the case $\phi = 0.03$, whereas, the disordered phase is attained in all the density region when $\phi = 0.30$. The flows in the unified phase ($\phi = 0.03$, $\rho \leq 0.8$) are close to the higher curve and those in the disordered phase ($\phi = 0.03$, $\rho \geq 0.86$ and $\phi = 0.30$) are close to the lower curve. The curves represent the flow of the totally asymmetric simple exclusion process (TASEP) with the parallel-update rule [8]

$$Q_R = \frac{1 - \sqrt{1 - 4q\rho(1 - \rho)}}{2},\tag{4}$$

where q is the hopping probability of the particles. The higher and lower curves are the flow of the TASEP in the case $q = 1$ and $q = 0.5$, respectively. Thus, the probability of successful avoidance in the unified phase and disordered phase ($\rho \geq 1/2$) in our model corresponds to the hopping probability in the TASEP. In the disordered phase ($\rho \leq 1/2$) both the movement with the probability 1 (to the vacant cell) and 1/2 (interaction with the opponent particles) are included, so that the flow is not simply represented by the TASEP.

4 Summary and Conclusion

In this paper, we have developed the one-dimensional cellular automaton model with two kinds of particles, which are right and left-going ones. They try to avoid each other by swerving to the right or left stochastically. Evolutionary game dynamics is introduced in the model, so that the particles update their preference of swerving direction by interacting other particles. The effect of memory-loss is also considered.

The result of our simulation indicates that the swerving directions of the particles are unified (the unified phase is achieved) when the effect of memory-loss is weak and there are enough interaction between particles to increase the preference of swerving direction. If the condition in the previous sentence is not satisfied, the serving directions are not unified (the disordered phase is achieved), in other words, all the particles swerve to both right and left with the equal probability 1/2. It is also elucidated that the flow is well approximated by the totally asymmetric simple exclusion process (TASEP) with periodic boundary condition and the parallel-update rule. The flows in the unified phase and disordered phase in the high density region correspond those in the TASEP with the hopping probability equals to 1 and 1/2, respectively.

In this paper, we have focused on the case, where the number of right and left-going particles are same. Thus, the other cases should be also investigated in the near future. Moreover, further theoretical analyses are needed to be performed by applying the theories of the TASEP. Elucidation of the model helps us to understand when the cooperating avoiding behaviour is maintained in bidirectional flow.

References

1. Blue, V.J., Adler, J.L.: Cellular automata microsimulation for modeling bi-directional pedestrian walkways. Transp. Res. Part B: Methodol. **35**(3), 293–312 (2001)
2. Flötteröd, G., Lämmel, G.: Bidirectional pedestrian fundamental diagram. Transp. Res. Part B: Methodol. **71**, 194–212 (2015)
3. Hausman, J., McFadden, D.: Specification tests for the multinomial logit model. Econometrica: J. Econom. Soc. 1219–1240 (1984)
4. Helbing, D.: Traffic and related self-driven many-particle systems. Rev. Mod. Phys. **73**(4), 1067 (2001)
5. Helbing, D., Molnar, P.: Social force model for pedestrian dynamics. Phys. Rev. E **51**(5), 4282 (1995)
6. Hoogendoorn, S., Daamen, W.: Self-organization in pedestrian flow. In: Traffic and Granular Flow03, pp. 373–382. Springer (2005)
7. Schadschneider, A., Chowdhury, D., Nishinari, K.: Stochastic transport in complex systems: from molecules to vehicles. Elsevier (2010)
8. Schadschneider, A., Schreckenberg, M.: Cellular automation models and traffic flow. J. Phys. A: Math. Gen. **26**(15), L679 (1993)
9. Seyfried, A., Steffen, B., Klingsch, W., Boltes, M.: The fundamental diagram of pedestrian movement revisited. J. Stat. Mech: Theory Exp. **2005**(10), P10002 (2005)
10. Yanagisawa, D., Kimura, A., Tomoeda, A., Nishi, R., Suma, Y., Ohtsuka, K., Nishinari, K.: Introduction of frictional and turning function for pedestrian outflow with an obstacle. Phys. Rev. E **80**(3), 036110 (2009)
11. Zhang, J., Seyfried, A.: Empirical characteristics of different types of pedestrian streams. Procedia Eng. **62**, 655–662 (2013)

A Queuing Model Based on Social Attitudes

Gerta Köster and Benedikt Zönnchen

Abstract Modern pedestrian simulation models have to deal with queuing to obtain realistic results. Queues control the number of pedestrians entering or leaving an area and, through this, the number of pedestrians inside that area. Furthermore, they impede passing pedestrians. But how do humans decide on a queuing strategy? And how does this effect the form of the emerging queue? Based on dynamic floor fields for navigation and a simple heuristic decision mechanism we present a computer model that is able to capture different queuing patterns that we observe in every day life. For this, we assume that there are two basic attitudes, aggressive competition and cooperative getting in line. Pedestrians can switch between these strategies.

1 Introduction

Most people encounter queues as part of their everyday lives, including queuing in front of a public bathroom, a check-in booth at the airport, an escalator or the entrance of a concert. In many situations queues determine the exchange rate of pedestrians between two separated areas and thus the number of pedestrians at a location. For passing pedestrians physical queues are obstacles.

Queues form and dissolve for many reasons. Pedestrians in queues follow a variety of rules and norms that may be situation specific. Queues can be self-organised or controlled by queue managers. There can be physical constraints that structure the queue or an abstract mechanism, such as allocating numbers. Traditionally, queuing systems describe serving processes and can be used to model queuing in a strict line without queue-jumps. See [1, 2, 7, 19] for examples from the extensive literature.

This contribution focuses on self-organised physically loose queues. The goal is to extend an idea presented in [11] where loose queuing is induced by making the queue itself attractive to the pedestrians navigating along a floor field. In [11] every

G. Köster (✉) · B. Zönnchen
Munich Unversity of Applied Sciences, 80335 Munich, Germany
e-mail: gerta.koester@hm.edu

B. Zönnchen
e-mail: zoennchen.benedikt@hm.edu

pedestrian is cooperative. There is no jostling or queue-jumping. We now model the opposite strategy, aggressive competition for the position closest to the service point, by using a 'classic' floor field where the distance to the target determines the utility of a position. In fact, this is the agent behaviour in many simulation models that do not explicitly model the queuing process. See e.g. [4, 9, 10, 13, 15, 16] for the mushroom shaped crowd that then forms in front of a bottleneck. This shape can also be observed in reality, e.g. sometimes in front of ticket booths in India.

Next, we introduce queue-jumping and line cutting in a formerly cooperative queue by allowing pedestrians to switch between strategies with a certain probability. At this point we focus on the mechanism of the model and the analysis of emerging formations, keeping the switching process simple. Yet, a queue is a complete social system [14] where behaviour is governed by potentially very complex social rules and norms. Therefore we demonstrate how our simplistic process can be replaced by decision heuristics, in the spirit of [6], when more information about the waiting crowd is available.

The paper is structured as follows. First we describe how dynamic floor fields are used to model the basic strategies. This includes a novel method to detect the tail of the queue. Then, we explain the process of switching strategies. Depending on the parameter choice in the switching process different queue types emerge. Finally, we discuss the impact, limitations and next steps.

2 Results

Our goal is to find a simple and plausible mechanism to generate a variety of different queue formations as we experience them in daily life. We assume that there are two basic queuing strategies: cooperative getting in line and aggressive competition. We observe the types of queues that emerge when we allow pedestrians to switch between strategies.

2.1 The Model

In many pedestrian motion models agent navigate along floor fields that indicate the utility of a position 'on the floor'. For the two basic queuing strategies we extend ideas from [11] where we used dynamic floor fields to induce loose queuing. As many others [8, 12, 16] we store the arrival time $T(\mathbf{x})$ of an imaginary wave front in the floor field. This wave front propagates in the area of observation Ω starting from the target area $\Gamma \subset \Omega$. The travelling speed F of the wave may depend on travel conditions in the area such as obstacles, where the speed is zero, or surface conditions or, in our case, crowd agglomerations. The shorter the arrival time the higher the utility (set to the negative arrival time). In this contribution we use the Optimal Steps Model [16, 18] to locally maximise utility when stepping to the next

position. Thus, agents are guided along a path of high utility to the target. The queuing mechanisms should work for any other locomotion model with fine spatial resolution that uses floor fields for navigation, such as the Gradient Navigation Model [5], or varieties of the Social Force Model e.g. [3].

The arrival time T of the wave front is computed by solving the eikonal equation with Sethian's Fast Marching algorithm [17].

$$||\nabla T(\mathbf{x})|| = \frac{1}{F(\mathbf{x})}, \quad T(\mathbf{x}) = 0 \text{ if } \mathbf{x} \in \Gamma. \tag{1}$$

$F(\mathbf{x})$ stands for the travelling speed of the propagating front at $\mathbf{x}$. $F(\mathbf{x}) \geq 0 \ \forall \mathbf{x} \in \Omega$. Manipulating F is the key to both, avoiding and forming queues in [11]. F depends on the crowd density defined in [16]. Our idea is to use different travelling speed functions, and thus different floor fields (Fig. 1), to represent different queuing behaviours. Switching queuing strategy then simply means switching the floor field along which the agent navigates. The basic strategies are:

- Cooperative getting in line. We use a dynamic floor field where the travelling speed F of the imaginary wave front in Eq. 1 takes the changing queue into account. This corresponds to two sub-behaviours:

  1. Start queuing at the tail of the queue: *getting in line*.
  2. Keep queuing until the target is reached: *cooperative queuing*.

- Aggressive competition. We use a static floor field where the imaginary wave front propagates from the static target and does not consider pedestrian formations in the way. This corresponds to one sub-behaviour:

  3. Go to the target as fast as possible: *competitive queuing*.
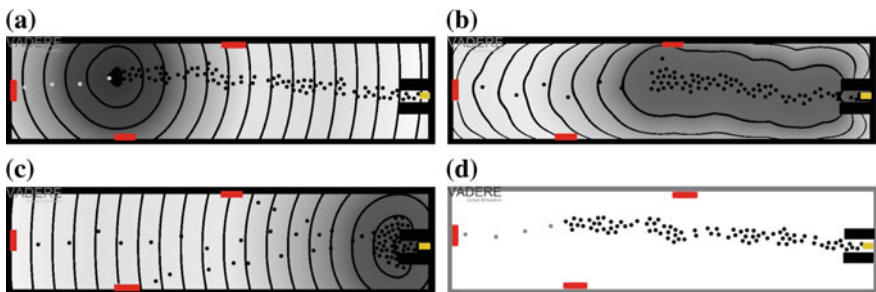
Fig. 1 Comparisons of the floor fields T induced by different wave speeds F. Agents navigate based on the displayed floor field. In *dark areas*, T is smaller than in *light areas*, that is, the utility is higher. *Black/grey agents* try to reach the *yellow target* at the right. *Grey agents* try to reach the queue tail. In the queue, all agents are cooperative forming a line without queue-jumpers. Floor field T for $F := F_{coop}^1$ seen by agents that need to get in line (**a**); floor field T for $F := F_{coop}^2$ seen by agents that queue cooperatively (**b**); floor field T for $F := F_{coop}^3$ seen by agents who try to cut the line (**c**); line formed by cooperative agents, joining the tail of the queue or queuing (**d**)

To construct the navigation field for all cooperative agents that have not yet joined the queue (behaviour 1) we solve Eq. 1 with the queue tail as target and the travelling speed function F:

$$F^1_{coop}(\mathbf{x}) = \frac{1}{1 + c_{ob} \cdot \rho_{ob}(\mathbf{x})} \tag{2}$$

As in [11] the 'obstacle density' ρ_{ob} makes sure that the utility decreases close to an obstacle—and the agents keep a certain distance; c_{ob} is a calibration parameter. Table 1 gives a list of the parameter values used in this contribution. Since the target position, the tail of the queue, changes we have to solve the eikonal equation with speed function F^1_{coop} for each time step. To detect the queue tail, we again solve the eikonal equation Eq. 1. This time we let the imaginary wave front propagate only through the space occupied by the queue. With this, we cannot only detect the tail of a winding queue, but we can also compare the travelling time of the propagating wave T at positions inside the queue. This yields a measure for the relative queue positions of agents that will be needed for decision strategies that take the position in the queue into account.

Once the agent has joined the queue, the travelling speed function for queuing F^2_{coop} is the same as in [11] with one little extension: we need to exclude the pedestrian density of aggressive pedestrians. Otherwise cooperative pedestrians would tend to follow aggressive pedestrians if they are near by.

$$F^2_{coop}(\mathbf{x}) = \frac{1}{1 - \min\left(c_{queue} \cdot \rho^b_{ped}(\mathbf{x}), 1 - \varepsilon\right) + c_{ob} \cdot \rho_{ob}(\mathbf{x})}, \tag{3}$$

with $0 \le (\rho^b_{ped} + \rho^a_{ped}) \le 1$ and $(1 - \varepsilon) > 0$; $\rho^b_{ped}(\mathbf{x})$ is the normalised pedestrian density from [16], but restricted to cooperative pedestrians; c_{queue} is a calibration parameter; $1 - \varepsilon$ levels out high densities in the middle of a crowd. See Table 1 for the parameter values. To model aggressive behaviour we let the agents be guided by a floor field computed with $F^3_{aggr} := F^1_{coop}$ from Eq. 2. But this time the propagating wave starts at the final target Γ. Utility is independent of the presence of others. If an competitive agent is still at a distance from the queue it will try to get as close as possible to the target. This may place it behind other agents but not at the end of a queue. Collisions are avoided by utility reducing short range potentials carried by each agent. As soon as an unoccupied position closer to the target opens, the agent will use it. That means some agents will step out of the queue, use a path parallel

Table 1 List of simulation parameters

Parameter	Usage	Value
c_{ob}	Controls distance to obstacles	3.5
c_{queue}	Controls the queue width	6.0
μ_a	Expected time in seconds a pedestrian will use the aggressive strategy (a)	Varies
μ_b	Expected time in seconds a pedestrian will use the cooperative strategy (b)	Varies

to the queue until they bump into others, reach the final goal, or, after a change of strategy, rejoin the queue. When an competitive agent changes strategy it rejoins the queue at the point in the queue it is closest to.

Next, we need to model how pedestrians decide which strategy to follow. We set the default strategy to cooperative getting in line. Then, directly after creation, agents adopt the strategy of the majority of all already existing agents, thus using the 'imitate the majority heuristic' from [6]. We then allow strategy changes. At this point, we want to keep the process of decision making rather simple and assume that it is similar to a birth process with a memoryless exponential distribution. We consider fixed sampling times t_i and $\Delta t_i = t_i - t_{i-1}$ and propose

$$P\left(ped \text{ changes strategy in } \Delta t_i\right) = \begin{cases} 1 - \exp\left(-\frac{\Delta t_i}{\mu_a}\right) & \text{if } ped \text{ is competitive} \\ 1 - \exp\left(-\frac{\Delta t_i}{\mu_b}\right) & \text{if } ped \text{ is cooperative,} \end{cases} \tag{4}$$

as probability for a strategy change in Δt_i. Since the actual strategy change could be at any moment in Δt_i we approximate it by t_i. Parameters μ_a or μ_b can be interpreted as the expected times pedestrians use competitive strategy (a) and cooperative strategy (b), respectively. If μ_b is large, infinite in the extreme case, a strategy change from cooperative to competitive is unlikely. With small μ_b, on the other hand, a strategy change to queue-jumping is likely: Pedestrians are impatient. A large μ_a also indicates impatience keeping competitive agents in queue-jumper mode. If $\mu_a \to \infty$, all competitive pedestrians will cut the line. Let us consider the two extreme cases:

1. $\mu_a \to \infty$ and $\mu_b \to 0$: A tendency to stick to competitive behaviour, and no patience, leads to a fully competitive line cut scenario with its typical jam in front of the bottleneck. See Fig. 2d.
2. $\mu_b \to \infty$ and $\mu_a \to 0$: With large μ_b for patience, and small μ_a for a quick return to cooperative behaviour, a fully cooperative line forms. See Fig. 2a.
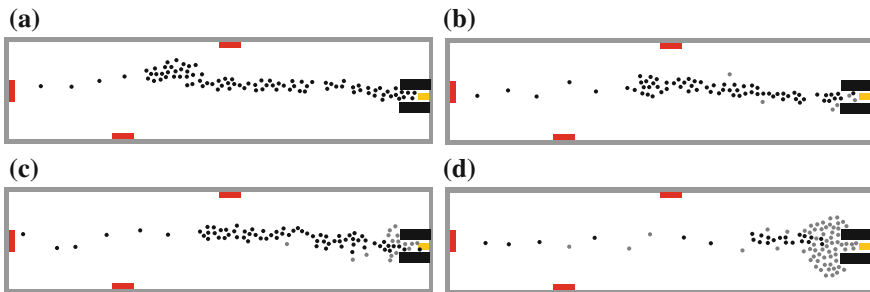
Fig. 2 Snapshots of different line cutting simulations ($\mu_a \to \infty$). The final goal is the *rectangle* at the *right*. *Light grey* pedestrians use aggressive strategy (a), *black* pedestrians cooperative strategy (b). The shape in *front* of the bottleneck depends on μ_b. $\mu_a \to \infty$, $\mu_b \to \infty$. Fully cooperative queue since agents start out cooperative (**a**); $\mu_a \to \infty$, $\mu_b = 300$ (**b**); $\mu_a \to \infty$, $\mu_b = 100$ (**c**); $\mu_a \to \infty$, $\mu_b = 40$ almost collpased queue (**d**)
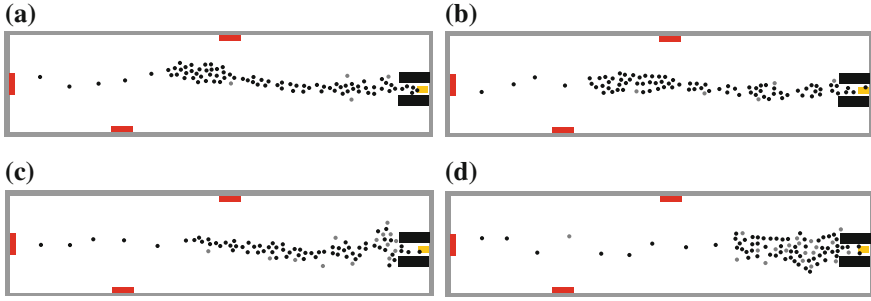
Fig. 3 Snapshots of different queue-jumping simulations. The final goal is the *rectangle* at the *right*. *Light grey* pedestrians use strategy (a), *black* pedestrians strategy (b). The shape of the whole queue depends on μ_a and μ_b. $\mu_a = 20$, $\mu_b = 300$ (**a**); $\mu_a = 2$, $\mu_b = 100$ (**b**); $\mu_a = 20$, $\mu_b = 80$ (**c**); $\mu_a = 5$, $\mu_b = 20$ (**d**)

Between those extremes, many variations are possible. The case $\mu_a \to 0$, $\mu_b \to 0$, for example, makes competitive agents quickly revert to queuing, while small μ_b makes agents in the queue impatient. Then we get a queue but with very frequent queue-jumping (Fig. 3c).

So far, the decision process can be said to depend on 'attitudes' such as patience (large μ_b) or aggressiveness (large μ_a) of the agents. This does not reflect character types or social or psychological states, since the values, μ_a, μ_b, are not attached to the agents, but to the current strategy of the agent. This can and should be changed with better knowledge of the crowd. Also, simple observations, that would naturally be part of a heuristic decision process, such as the position in the queue, or the elapsed waiting time, do not play a role.

We pick one example, the relative position in the queue, to show how this can be adapted. We propose that a presently cooperative pedestrian is less likely to start queue-jumping when he or she is close to the target. One might argue that he or she would risk the close position to the target by temporarily leaving the queue. Clearly further investigations are required to find heuristics that are substantiated by psychology. Here, we focus on the mechanism and replace μ_b by $\mu_b \cdot T_{queue}^{max} / T_{queue}(\mathbf{x})$, where $T_{queue}(\mathbf{x})$ is the travelling time of the propagating wave at $\mathbf{x}$ used to detect the tail of the queue and $T_{queue}^{max} = \max_{\mathbf{x} \in \text{queue area}}(T(\mathbf{x}))$. We set $T_{queue}(\mathbf{x}) = T_{queue}^{max}$ if $\mathbf{x}$ is outside the queue area. Since $T_{queue}^{max} / T_{queue}(\mathbf{x}) \geq 1 \; \forall \mathbf{x}$ we increase the expected time the pedestrian at position $\mathbf{x}$ sticks to the cooperative strategy.

2.2 Simulation Experiments

We show simulation results for varying parameters μ_a and μ_b. For simplicity, we select a single queue scenario. We let agents enter the room from three directions (left, top, bottom) to demonstrate how and where they join the queue (behaviour (1)). The all try to reach the service point (right). The service time of each pedestrian at the service point is 6 s and decision changes are allowed every 0.4 s.

First, we consider line cutting, that is, agents never change their strategy from being competitive (a) to being cooperative (b). With $\mu_a \to \infty$, once an agent is aggressive it sticks to this strategy until it reaches the final goal. For $\mu_b = 300$ the queue is a little shorter than the fully cooperative queue with $\mu_b \to \infty$. For $\mu_b = 40$ the queue almost collapses. See Fig. 2.

Second, we look at queue-jumping where pedestrians may switch from the competitive (a) to the cooperative (b) strategy before they reach the final goal. As a result, swelling of the queue may occur not only at the tail, but also at intermediate positions. Figure 3a, b look very similar, but in Fig. 3b the frequency of queue-jumps is higher resulting in the swelling at the middle of the queue. Since μ_b is smaller in Fig. 3c compared to Fig. 3a, the agents are less likely to stay cooperative and therefore more pedestrians stand near the goal. In Fig. 3c the queue is thick and short approaching the shape of a congestion as in Fig. 2. Table 1 lists the parameters used in the simulations for this contribution.

3 Discussion

In this paper we used floor fields to induce a variety of natural looking queues in a pedestrian motion model. We assumed two underlying attitudes and ensuing strategies, cooperative and competitive, that were each associated with a guiding floor field. Cooperative agents were attracted by first the tail of the queue, for which we presented a detection algorithm, then by the density of the queue itself, while competitive agents were attracted by the service point only. We allowed switches between the two attitudes to model queue-jumping and line cutting. The mechanism produces realistic looking queue formations and thus is a step forward from classic models in queuing theory that model the serving process, but neither the queue shape nor queue-jumping. However, while the two parameters in the decision process can be interpreted as patience or impatience, the process itself does not reflect natural heuristics. Nor does it consider behavioural norms that may arise from the condition of the crowd. The crowd may, for instance, be one with a high level of a shared identity which results in cooperative behaviour. Clearly rules that are based on findings from psychology must be identified. We believe that many such rules can be implemented by slightly adapting the decision process described in this contribution.

References

1. Arita, C., Schadschneider, A.: Density profiles of the exclusive queuing process. J. Stat. Mech: Theory Exp. **2012**(12), P12, 004 (2012)
2. Bungartz, H.J., Zimmer, S., Buchholz, M., Pflüger, D.: Modellbildung und Simulation: Eine anwendungsorientierte Einführung. eXamen.press. Springer, Heidelberg (2013)
3. Chraibi, M., Seyfried, A., Schadschneider, A.: Generalized centrifugal-force model for pedestrian dynamics. Phys. Rev. E **82**(4), 046, 111 (2010)

4. Chraibi, M., Ensslen, T., Gottschalk, H., Saadi, M., Seyfried, A.: Assessment of models for pedestrian dynamics with functional principal component analysis (2015). arXiv:1502.00528
5. Dietrich, F., Köster, G.: Gradient navigation model for pedestrian dynamics. Phys. Rev. E **89**(6), 062, 801 (2014)
6. Gigerenzer, G.: Why heuristics work. Perspect. Psychol. Sci. **3**(1), 20–29 (2008)
7. Gross, D., Shortle, J.F., Thompson, J.M., Harris, C.M.: Fundamentals of Queueing Theory, 4th edn. Wiley India Pvt Limited, London (2008)
8. Hartmann, D., Mille, J., Pfaffinger, A., Royer, C.: Dynamic medium scale navigation using dynamic floor fields. In: Weidmann, U., Kirsch, U., Schreckenberg, M. (eds.) Pedestrian and Evacuation Dynamics 2012, pp. 1237–1249. Springer (2014)
9. Hoogendoorn, S.P., Daamen, W.: Pedestrian behavior at bottlenecks. Transp. Sci. **39**(2), 147–159 (2005)
10. Kirik, E., Yurgel'yan, T., Krouglov, D.: An intelligent floor field cellular automation model for pedestrian dynamics. In: Proceedings of the 2007 Summer Computer Simulation Conference (2007)
11. Köster, G., Zönnchen, B.: Queuing at bottlenecks using a dynamic floor field for navigation. In: The Conference in Pedestrian and Evacuation Dynamics 2014. Transportation Research Procedia, pp. 344–352. Delft, The Netherlands (2014)
12. Kretz, T., Große, A., Hengst, S., Kautzsch, L., Pohlmann, A., Vortisch, P.: Quickest paths in simulations of pedestrians. Adv. Complex Syst. **10**, 733–759 (2011)
13. Liddle, J., Seyfried, A., Boltes, S.: Analysis of bottleneck motion using voronoi diagrams. In: Peacock, R.D., Kuligowski, E.D., Averill, J.D. (eds.) Pedestrian and Evacuation Dynamics, pp. 833–836. Springer (2011)
14. Mann, L.: Queue culture: the waiting line as a social system. Am. J. Sociol. **75**(3), 340–354 (1969)
15. Nishinari, K., Kirchner, A., Namazi, A., Schadschneider, A.: Extended floor field ca model for evacuation dynamics. IEICE Trans. Inf. Syst. **E87-D**, 726–732 (2004)
16. Seitz, M.J., Köster, G.: Natural discretization of pedestrian movement in continuous space. Phys. Rev. E **86**(4), 046, 108 (2012)
17. Sethian, J.A.: Level Set Methods and Fast Marching Methods: Evolving Interfaces in Computational Geometry, Fluid Mechanics, Computer Vision, and Materials Science. Cambridge University Press, Cambridge (1999)
18. von Sivers, I., Köster, G.: Dynamic Stride Length Adaptation According to Utility And Personal Space. Transport. Res. Part B-Meth. **74**, 104–117 (2015)
19. Zukerman, M.: Introduction to Queueing Theory and Stochastic Teletraffic Models. Cornell University Libraray (2013)

How Do People Queue? A Study of Different Queuing Models

Angelika Kneidl

Abstract Whenever there are crowded spaces, queuing occurs. Many different situations force people to queue: Waiting for a service counter, lining up for a train or bus, queuing in front of bottlenecks or simply waiting at a supermarket checkout. Such queuing evolves in many different ways, depending on the situation, the reason for queuing, the culture, the geometry and many more. Simulation models have to cope with such different situations and behaviours. This paper gives an overview on different queuing situations and corresponding models that exist for pedestrian modelling. Additionally, it introduces a new queuing model for organised queuing without demarcation tapes. First visual validations are shown.

1 Introduction

Since queuing occurs whenever we handle with large crowds, it is an essential building block when modelling and simulating pedestrians. However, there is not only one single type of queuing: Depending on the situation, the reason for queuing as well as the pedestrians' culture, queues can form very differently. Okazaki [7] has defined three different types of queuing: queuing in front of counters (type 1), queuing in front of gates (type 2) and queuing in front of doors of vehicles (type 3).

When considering the first type of queues (type 1), we can further distinguish between queues when flexible demarcation tapes or barriers dictate the formation of a queue and queues which form without demarcation utilities. A lot of research has been done for the type of queue with demarcation utilities, inspired from classical queuing theory [1, 7]. Here, the objective is to predict queue lengths and waiting times to make decisions about service provisions. Thus, a one-dimensional approach is sufficient, since the formation of the queue is given by the demarcation. The focus lies on waiting times and queue lengths.

The second type (type 2) of queue was examined by Köster and Zönnchen [6]. The authors state that people do not queue naturally in "mush-room"-shaped formations

A. Kneidl (✉)

accu:rate, Institute for Crowd Simulation, Munich, Germany
e-mail: ak@accu-rate.de

in front of bottlenecks. However, that is what most simulation models produce. In fact, the authors posit that pedestrian queue loosely in front of bottlenecks.

For the third type of queuing there has no explicit research been done, but there is a case study described by Davidich et al. [2] where German train stations have been observed.

In this contribution the different queuing models are described and a new model for self-organised queuing (type 1 without demarcation utilities) is introduced.

The outline of this papers is as follows: starting with a review of existing models, two queuing type models are described in more detail, followed by examples and first validations. The outlook of further studies concludes the paper.

2 Queuing Models at a Glance

Before taking a closer look on different queuing models, a definition of a queuing event is given.

Definition 1 We define queuing as a situation, when

1. More people are present than the capacity of a certain facility allows (e.g. service desks, bottlenecks)
2. A more or less ordered formation is observable, thus people do not push each other.

This definition excludes uncontrolled clogging situations in front of bottlenecks, which may occur in emergency situations.

In Table 1 we summarised and extended the typification of different queuing models suggested by Okazaki [7].

In the following sections these four types are described in more detail.

Table 1 Overview on queuing types

Queue type	Appearance	Characteristics	Simulation model
Organised queuing (demarcation tapes)	In front of service points (e.g. at airports)	Queue formation and length is given by demarcation tapes	One-dimensional approach
Queues in front of trains	At train boarding	Bulk of people next to opening doors	Definition of waiting zones
Queuing in front of bottlenecks	In front of bottlenecks	Loosely queue formation	Navigational fields with adjusted velocities
Organised queuing (no demarcation tapes)	In front of service points (e.g. at beer bar)	Queue width, length and form grows individually	Agent-based with knowledge about other queuing people

3   Organised Queuing with Demarcation Tapes

In front of service desks of infrastructural buildings such as train stations or airports, very often demarcation tapes are used to predefine the queue formation. Such queues are quite simple to model from a simulation point of view, since the location of the queue is given. The questions to be answered with such queues are waiting times and queue length to optimally provide services without long waiting times. The approaches which solve such questions have their origin in queuing theory [1, 7] and apply these theories to humans.

4   Queues in Front of Trains

When waiting for a bus or a train, people tend to queue in order to get on the bus or train. Depending on the culture and the country, such queues can form very differently. In front of trains people tend to wait left and right to the openings in order to let people get off the train. Such queues are more like an un-ordered but organised bunch of people. Such situations can be modelled by using waiting zones where people wait until passengers get off the train. Work has been done on that by Davidich et al. [2].

5   Queuing in Front of Bottlenecks

When people try to get through a narrow passage with less capacity, a loosely formed queue occurs. Such queues can differ a lot in their appearance: Depending on the relation of the direction pedestrians coming from and the direction of the bottleneck, such queues can form as well mushroom-shaped as tail-shaped. Such queues are characterised by their loosely queue formation and no clear order.

An example for such queues is depicted in Fig. 1. Here, people queue in front of an escalator. People tend to wait behind each other and do not overtake.

Simulation models can cope with such queues by using navigation fields. Navigation fields are calculated as a sum of different influencing utility functions for pedestrians on their way to their destination [6]. Such utility functions include the shortest path to the destination, the avoidance of obstacles on that path and the avoidance of other pedestrians. The latter utility function can be adapted in order to generate loosely formed queues.

Equation 1 describes the Eikonal equation, which solves the wave propagation. To construct the navigation field, we can use this wave propagation by starting from the destination and propagating to the position where a pedestrian is located [3]. The solution to this equation is the time the wave arrives at a certain location. Thus, the sooner the wave reaches a position, the more attractive the path is. The pedestrian

Fig. 1 A queuing example in front of an escalator: People approach the escalator from the front, thus a tail formation of the queue is observable

tends to always choose the position where the remaining travel time to the destination is lowest. Using the Fast Marching Method [10], this equation can be solved very efficiently.

The velocity of the propagation wave is constant in normal cases, but if we change the velocity $F(x)$, we can change the wave propagation speed and formation [3]. By defining $F(x)$ as in Eq. 2 stated, the speed is dependent the pedestrians' density $D(x)$ at a position x and a factor c [4]. This c can now be varied in order to create different shapes of queues. In [6] a study can be found on different values of c and the corresponding formation of the queue.

$$F(x)|\nabla T(x)| = 1 \; in \; \Omega,$$
$$T(x) = 0 \; in \; \Gamma. \tag{1}$$

$$F(x) = \frac{1}{c \cdot D(x)} \tag{2}$$

In order to reproduce the queue in front of the escalator as depicted in Fig. 1, c was set to 1. The simulation results are shown in Fig. 2.

As can be seen when comparing the simulation result with the real-world data, the queue forms quite similar to the queue observed in front of the escalator. The proposed model seems to model this type of queues quite well and is flexible enough to cope with different tail-shaped queues.
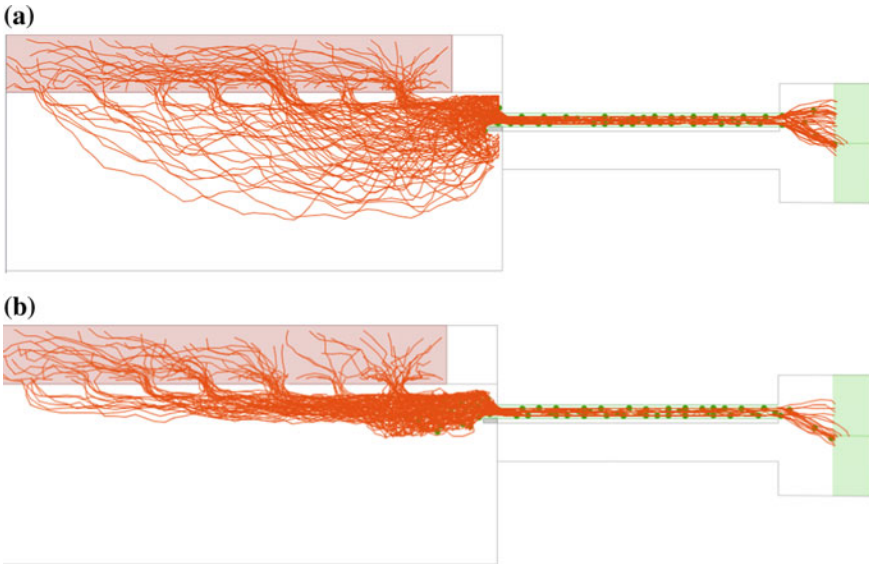
Fig. 2 A queuing example in front of an escalator: People approach the escalator from the front, thus a tail formation of the queue forms

6 Organised Queues Without Demarcation Tapes

For the last type of queues no queuing model could be found in literature. A very distinctive shape of such queues is depicted in Fig. 3.[1]

To cope with such queues, a new model is introduced: the model is integrated into an agent-based model. The optimal steps model [8] forms the locomotion layer of the model. The tactical layer is based on navigation graphs [5]. With this graphs, action plans and intermediate destinations can be defined. Such destinations are e.g. service points. Each agent moves according to utility functions: He wants to get fast towards his next destination whilst avoiding other moving agents and obstacles on the way to the next destination.

Based on this model, the agents try to queue behind each other by choosing a spot behind the last agent of the queue with a certain derivation angle.

The idea is as follows: The first agent approaching a service desk stops at a defined stopping line in front of the service desk (Fig. 4). If a second agent approaches the service desk as well, the agent 'sees' the first agent as soon as the first agent is within his perception radius. Once having spotted the last agent, the new approaching agent searches a waiting spot behind the agent. To avoid an artificial straight line of the queue, the agent searches a stopping spot within a certain derivation angle. This is done by defining a line which is of a certain distance to the waiting agent (Fig. 5).

---

[1] https://commons.wikimedia.org/wiki/File:Warteschlange_vor_dem_Eiffelturm.jpg.

Fig. 3 Queuing example for the Eiffel Tower in Paris. The queue forms individually and makes 'random' turns

Fig. 4 The model setup
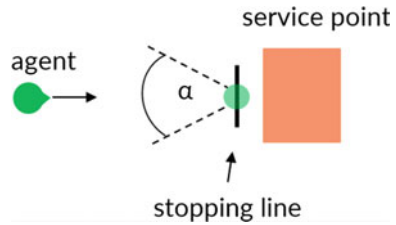
The distance of the line to the waiting agent is considered as the comfort distance and can be set dynamically. Between all possible valid spots on that line the spot is chosen randomly. For the next approaching agent, the same procedure is applied. By choosing the next position randomly from within a set of points, the queue starts evolving and turning.

The idea behind the derivation angle is the observation of the tendency of agents to queue slightly next to the already waiting agents in order to see where the head of the queue is located.

Results of such queues are depicted in Fig. 6. One can observe that the queue starts turning—the larger the derivation angle is chosen, the more turns the queue gets.

Since people often are not on their own but move within groups, we consider group queuing as well. The group model is based on [9]. To extend the queuing behaviour for groups, we extended the model as follows: If a group approaches a service desks, group members search waiting spots next to each other; Starting with the leader of the group (the agent who is closest to the tail of the queue) who searches a spot behind the last agent in queue as above, every following group member searches a waiting spot within a wider range of $\alpha = 180$. This leads to (a) wider queues which seems more realistic when looking to queues in real and (b) leads to less turns in the queue form. The results are shown in Fig. 7. We believe that the visual validations for the model look already quite promising. A next step will be to gather real-world data for more in-depth comparison.
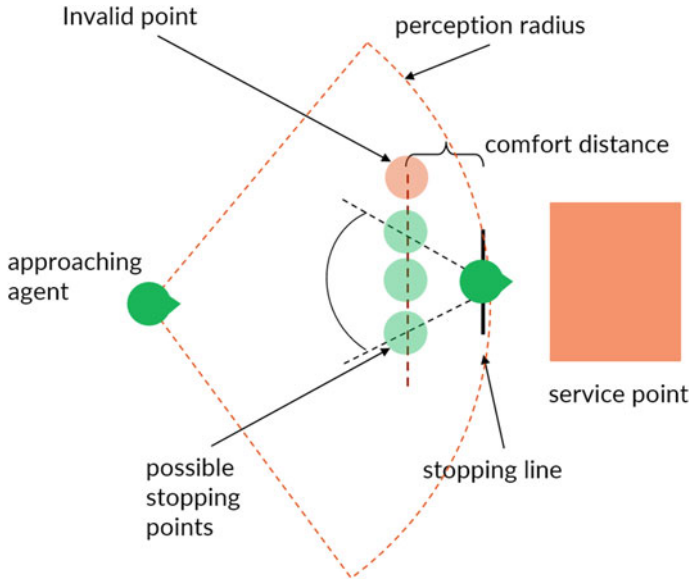
Fig. 5 Approaching agent searching for the next waiting spot
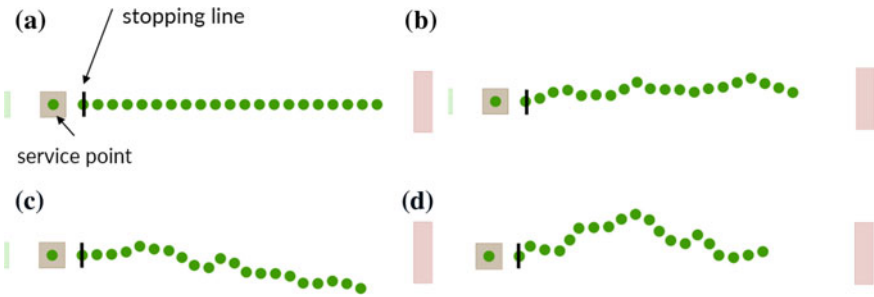
Fig. 6 Simulation results for different choices of α. The larger α is chosen the more the queue starts turning. $\alpha = 0°$ (**a**); $\alpha = 30°$ (**b**); $\alpha = 40°$ (**c**); $\alpha = 60°$ (**d**)
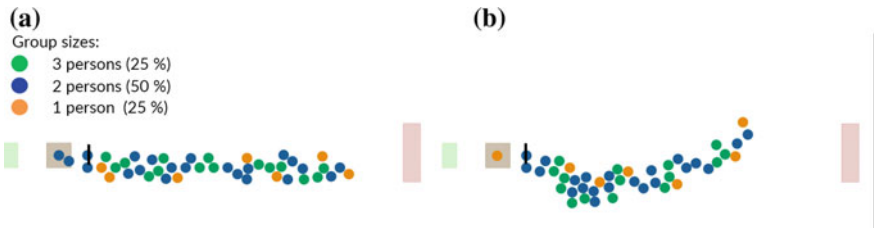
Fig. 7 Simulation results for group queuing for different choices of α. The larger α is chosen the more the queue starts turning. $\alpha = 0°$ (**a**); $\alpha = 60°$ (**b**)

7   Summary and Outlook

This paper summarised different queuing models. People do queue differently depending on the situation. Thus, different models have been developed and serve well for different occasions of queuing. For queuing without demarcation a new model was introduced. First visual validations show already promising results. Further studies have to be accomplished in order to further validate the model. Moreover, the reason for the turning and possible triggers have to be examined in more detail.

References

1. Arita, C., Schadschneider, A.: The dynamics of waiting: the exclusive queueing process. Transp. Res. Procedia **2**, 87–95 (2014)
2. Davidich, M., Geiss, F., Mayer, H.G., Pfaffinger, A., Royer, C.: Waiting zones for realistic modelling of pedestrian dynamics: a case study using two major German railway stations as examples. Transp. Res. Part C **37**(Complete), 210–222 (2013)
3. Hartmann, D.: Adaptive pedestrian dynamics based on geodesics. New J. Phys. **12**(4), 043, 032 (2010)
4. Hartmann, D., Mille, J., Pfaffinger, A., Royer, C.: Dynamic medium scale navigation using dynamic floor fields. In: Pedestrian and Evacuation Dynamics 2012, pp. 1237–1249. Springer (2014)
5. Kneidl, A., Hartmann, D., Borrmann, A.: Generation and use of sparse navigation graphs for microscopic pedestrian simulation models. Adv. Eng. Inf. **26**, 669–680 (2012)
6. Köster, G., Zönnchen, B.: Queuing at bottlenecks using a dynamic floor field for navigation. Transp. Res. Procedia **2**, 344–352 (2014)
7. Okazaki S., Matsushita, S.: A study of simulation model for pedestrian movement with evacuation and queuing. In: International Conference on Engineering for Crowd Safety, pp. 271–280 (1993)
8. Seitz, M., Köster, G.: Natural discretization of pedestrian movement in continuous space. Phys. Rev. E **86**(4), 046108–046116 (2012)
9. Seitz, M., Köster, G., Pfaffinger, A.: Pedestrian group behavior in a cellular automaton. In: Pedestrian and Evacuation Dynamics 2012, pp. 807–814. Springer (2014)
10. Sethian, J.A.: Level Set Methods and Fast Marching Methods: Evolving Interfaces in Computational Geometry, Fluid Mechanics, Computer Vision, and Materials Science, vol. 3. Cambridge university press (1999)

The Relationship Between the Waiting Crowd and the Average Service Time

Oliver Handel and André Borrmann

Abstract In this paper the relationship between the waiting crowd and the service time—the average duration to serve one single customer—is evaluated in the context of vendor stands (e.g. food stands, concession stands or kiosks). Drawing from traditional analytic queuing theory, a distribution function for the service time that remains steady is generally used. This steady state assumption is questioned in this paper by using computer simulation, empirical observation and qualitative reasoning. On the one hand, the impact of the amount of people waiting on the average duration of service time is examined. On the other hand, the effects of crowding on the choice of a customer are evaluated as well. Within this context different causal feedback relationships are identified that are expected to be of fundamental importance. The paper concludes that for the endogenisation of the service time, the incorporation of these feedback relationships is key to obtain more accurate results.

1 Introduction

While the time a person spends waiting in a queuing situation is commonly overestimated, the satisfaction tends to decrease the longer the waiting time is perceived [6, 9]. To avoid dissatisfaction of the people getting served, two different approaches can be distinguished. The first approach aims to manage the actual waiting time by predicting the demand and to provide a sufficient amount of servers to customers. But as services cannot be inventoried [18] and the demand for the service is hard to predict, waiting is often unavoidable if the cost of servers are not neglected. Various approaches from operational management research aim to minimise the actual waiting times, but because of the difficulties in providing the right amount of servers in every situation and to control therefore the actual wait duration, another approach aims to reduce not the actual waiting time, but the perceived waiting time by focusing

O. Handel (✉) · A. Borrmann
Technische Universität München, Arcisstr. 21, 80333 Munich, Germany
e-mail: oliver.handel@tum.de

A. Borrmann
e-mail: andre.borrmann@tum.de

209

on different characteristics of the service environment that affect time perception and thus make the waiting experience for the people waiting less dissatisfying [1]. This approach tries to influence the subjective perceived waiting time by drawing from theories from sociology, psychology and marketing. The perception of wait time and service satisfaction were discussed by [1, 12, 17] among others. Essential in this discussions are the degree of social interaction and distraction from the situation in the filled time gap [17], considerations about social justice (first-in-first-out-principle) and elements from the service environment (lightning, temperature, music, colour and furnishings) [1] that influence the perceived waiting time.

Although it is smart aiming to make the duration of the wait as comfortable as possible and thus to decrease the perceived waiting time and to avoid that the use of a service is overshadowed by the frustration of a perceived long wait, the even smarter way is to better optimise the actual waiting time and to overcome some obstacles in doing so. One key issue is the service time, defined as the duration to serve one single customer. Commonly the service time is seen as an input value that needs to be empirically collected, statistically aggregated and then inserted in the evaluation method as a fixed parameter or distribution function that remains the same over the whole time span. In this paper, the static service time assumption is questioned and the dynamic nature of the service time is pushed to the fore. Collected empirical data in the context of vendor stands at a music festival provides evidence that an endogenisation of the service time variable is necessary to increase the forecast accuracy for the length of waiting queues within the simulation. Before results from simulation are presented, analytic queuing theory is discussed in the next section with the outlook that there is need for simulation in this context.

2   Analytic Queuing Theory and Kendall's Notation

Analytic queuing theory aims to mathematically describe performance functions (e.g. average waiting time of a customer or server utilisation rate) of different queuing systems [5]. In this domain, queuing is not limited to queuing pedestrians, but also includes other queuing situations. Kendall's notation [10] prevailed to classify queuing systems. In this notation a queuing system is defined by a row of different letters: $A/S/c/K/N/D$ (A = arrival process / S = service time distribution / c = number of servers, K = capacity of the system / N = population size / D = service discipline). In case of pedestrian queuing, the short form of the Kendall notation $A/S/c$ can be generally used, because K and N are commonly assumed to be infinite and a FIFO service discipline is expected. A and S describe then different distribution functions, such as the Poisson, Degenerate, Erlang or Phase-type distribution. An abbreviation for each distribution function is used, plus the number for the amount of servers to define the queuing system. After having defined the queuing system, different performance functions can be specified. From a customer-focused perspective, the number of waiting customers and the average waiting time can be examined. From

a server-focused perspective, performance functions such as the idle and busy time of a server or the utilisation of the server can be measured.

Over the past hundred years, several scholars have contributed to solve different queuing systems analytically. An overview about which queuing systems is analytically solved can be found in [11]. It became a competition in probability and queuing theory to solve these commonly called *waiting time problems* [16], because—from a practical perspective—the only possibility to describe the performance of different pedestrian queuing systems was in times without computational simulation the analytic approach beside empirical observation. In other words, scholars who only had the analytic approach as their hammer saw every *waiting time problem* as a nail, nevertheless which limitations this approach embrace. Although it is of scientific value to solve queuing systems mathematically, some managerial implications remain especially in the domain of pedestrian queuing situations. Firstly, Kendall's notation includes the steady state assumption, as the arrival process and the service time distribution remain constant. Therefore, the formulas are helpful to get some quick benchmarks on how the queuing system would perform under the given narrow model boundary constrains, but taking into account more realistic scenarios with variations of the arrival pattern, the analytic approach is of limited help, if an overall evaluation is necessary and thus there is need for simulation. Simulation enables to take into account more dynamic arrival patterns or variations of the service time or to endogenise these key factors. Finally, in respect of the research topic, Kendall's notation may have contributed to the erroneous assumption that the amount of waiting people and the service time distribution are in each case two independent variables.

3   Simulation of Pedestrian Queuing

Simulation has several advantages. First of all, different from the analytic approach, simulation enables the generation of benchmarks for more complex queuing situations (e.g. oscillating batch arrivals). Secondly, in case of pedestrian queuing situations, the physical layout of the queuing environment—the servicescape [3]—can be taken into account, leading to minor delays, if a walking distance from the end of the queue to the server is necessary. And thirdly, simulation enables to endogenise key factors and therefore to push the model boundary forward.

The Java-based software Anylogic [4] is used here for the simulation of pedestrian queuing. In Fig. 1, a snapshot of an *M/M/5*-queuing system simulation is shown. The set-up consists of five servers and a single queue in front of the servers. The arrival process and the service rate are Poisson distributed. On the right hand side of the figure, the amount of waiting customers are depicted in the upper diagram and the utilisation rate of the servers is shown. In accordance with the amount of five servers and the given service time distribution with a mean value of 41.6 s and an arrival rate with a mean value of 250 arrivals per hour, a utilisation rate of around 80 % in steady state can be measured under the boundary condition that the amount of waiting people does not have an effect on the service time.
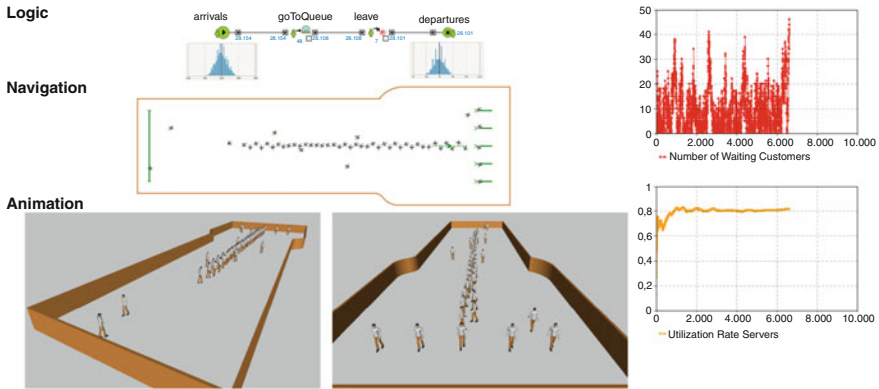
Fig. 1 Pedestrian queuing simulation with AnyLogic

If the arrival rate is increased step-wise from 100 to 450, Fig. 2 indicates that there is some qualitative moment of change, where the waiting time increases drastically and further increase leads to infinite waiting times. The diagram shows that, if the number of arrivals increases from 350 arrivals per hour to 400 arrivals per hour (15 % increment), the waiting time increases from 24 to 90 s (375 % increment) and goes from there on in the steady state quickly to infinity, because the waiting lines get theoretically endless long. The point where the queuing system cannot cope with the number of arrivals and the queues get endless long can be called a tipping point. The occurrence of tipping points in queuing systems has managerial implications, as the aim is to keep the queuing system away from the tipping point. The good news is that there are generally feedback effects leading to an increase of the maximum throughput of the queuing system, if waiting times get long. This form of systemic self-organisation will be discussed in the next section and results into the dynamic service time assumption.

Fig. 2 The relationship between the arrival rate and the average waiting time. The *blue dots* are the measured average waiting times as results from the simulation
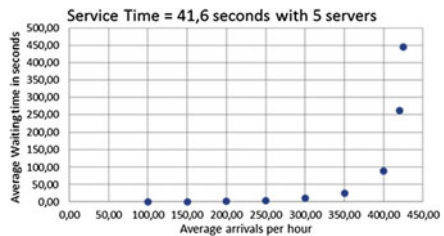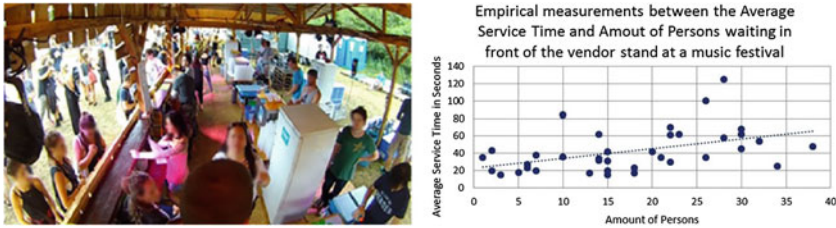
Fig. 3 Empirical collection of service times and the amount of people waiting at the same moment in front of a vendor stand at a music festival in Garching, Germany

4 Empirical Assessment and Findings

For the set-up of a microworld of an urban event case study, empirical data collection was conducted to gather essential input values such as the average time it takes to serve one customer. The data acquisition was carried out at a music festival in 2014 and 2015 in Garching, Germany. Video cameras have been used to assess the waiting crowd in front of several vendor stands (outdoor bars and food stands), mobile toilets and the entrance facility, and to get empirical values for the service times respectively durations of use. Post-evaluation of the primary video data was conducted to collect the secondary data material. A detailed report about the 2014 data collection and the spots observed can be found in [2].

In Fig. 3, the left picture shows exemplarily such an observed bar with different operational staff from the inside. On the right side of the figure, different measured data values for the time length of the collected service times are marked together with the information how many people waited in front of the vendor stand at this moment in time. Surprisingly there exists a positive correlation between both features (indicated by the linear trend line), i.e. the more persons waiting, the longer the average service time. A causal explanation about this counter-intuitive finding is shown with the next figure.

Figure 4 shows a dynamic hypothesis in form of a causal loop diagram. Through qualitative reasoning three main mechanisms (efficiency increase, grouping and postponement effect) are identified to be important in this context and are summarised in the figure. The first assumption is that an increase of waiting people in front of the vendor stand leads to an increased pressure on the employees and causes an efficiency

Fig. 4 The relationship between the number of people queuing and the service time in form of a causal loop diagram
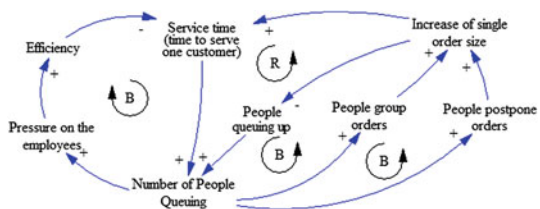
Fig. 5 A generic concept of an action selection mechanism. Internal and external states affect decision-making
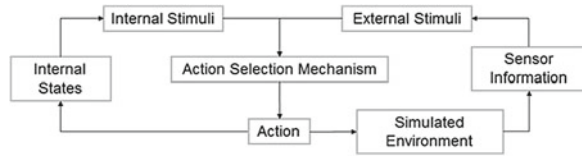
increase that reduces the service time per customer and thus the amount of people queuing. This effect is limited by an efficiency maximum. But beside this effect, if more and more people queue up, two other stronger mechanisms also begin to operate—so the second and third assumption—leading to the increase of the service time. One the one hand, if many people queue up, people start to group orders by asking a friend to bring along something for them and on the other hand, people start to postpone their orders, leading both to an increased single order size. If a fixed total order volume is assumed, the bigger the single orders are, the longer it takes to serve one customer (increase of the service time), but also the less amount of people need to be served. This effect is twofold counter-intuitive, because firstly the service time increases, but secondly—at the same time—the total order volume throughput increases. In compliance with the assumptions made, this finding is an example of positive self-regulation within a system.

To embed these mechanisms in a simulation, it is necessary to feedback from the amount of waiting people on the service time directly and on agent level on the decision architecture that defines under which conditions people decide to queue up, group and postpone orders. To make the simulation even more accurate, it is furthermore necessary to incorporate the grouping of orders effect as well. In Fig. 5, the generic concept of a decision architecture is shown. While the amount of waiting people is in this form a sensory information coming from the simulated environment and affects the dynamic decision-making of the agents and thus generate the grouping and the postponement of orders, the dynamic change of the service time will affect the simulated environment directly. More details about how crowding affects the choice of a customers to queue up are summarised in the next section.

5 Crowding, Customer Choice and Queue Shape Selection

In accordance with the context, different shape formations of the waiting crowd are possible. On the one hand, it is possible that very well organised queues are formed in the shape of a single or multiple queue structure. On the other hand, without according barriers it is often the case that an unorganised densely packed waiting crush forms. In Fig. 6, the implementation of different queuing models is depicted based on the AnyLogic software. These models allow to embed the different possible queuing formations in the simulation. How these different formations influences the choice of further customers to queue up are described in the following.
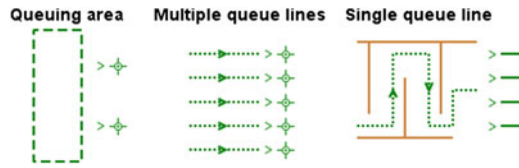
Fig. 6 Three different queuing models: (1). Service points with a queuing area. (2). Service points with separate queue lines. (3). Several service lines with one single queue line

Density and crowding are related to each other, but a differentiation is necessary [8]. Density refers to the physical condition—according to the spatial parameters [15] and crowding is more related to the unpleasant feeling of an individual in terms of the control perception to move freely in the environment. Schmidt et al. [14] used the term perceived control as an intervening variable between density and crowding that influences the behaviour of an individual. Drawing from the work of Hui et al. [8], perceived crowding affects negatively the emotional and behavioural responses of an individual and thus may hinder individuals to queue up, so the assumption. Handel et al. [7] argued that high-density conditions affect the risk-potential, as the velocity decreases in dense crowds. Therefore the question which queue shape to foster from a managerial perspective are quite straightforward to answer. The more perceived control the individual will have, the less likely that negative emotional responses are expected by the individual and the more likely that the individual not avoids to queue up. Therefore, the first choice should be to avoid the formation of an unorganised waiting crowd, and secondly in accordance with Rafaeli et al. [13], a single queue structure is more preferred than a multiple queue structure, because of fairness and predictability considerations.

6   Conclusion

In this paper, the relationship between the waiting crowd and the average service time have been evaluated. In the beginning, the classical analytic approach to solve queuing systems was discussed. Drawbacks of this approach have been mentioned, such as the non-endogenisation of essential key parameters and based on these considerations the assumption was made that the analytic approach strengthened the error-prone perception of a steady service time. From this point of view, the need of simulation was emphasised as simulation enables to take into account the physical layout of the queuing situation and to incorporate essential feedback effects to endogenise variables of the queuing system and therefore to see the queuing system not as isolated situation. Simulation of pedestrian queuing demonstrated the occurrence of tipping points, as the thresholds where the queuing system can either cope with the amount of arrivals or the waiting queues get theoretically endless long. Based on these considerations, several feedback effects between the waiting crowd and the average

service time that occur in the real-world and prevents the system from going beyond the tipping point, have been discussed. The efficiency increase, the postponement and the grouping effect was introduced based on a causal loop diagram and the incorporation of these effects into simulation was discussed. Finally, the effect of crowding on customer choice was elaborated and different queuing models have been introduced.

References

1. Baker, J., Cameron, M.: The effects of the service environment on affect and consumer perception of waiting time: an integrative review and research propositions. J. Acad. Mark. Sci. (1996)
2. Biedermann, D.H., Dietrich, F., Handel, O., Kielar, P.M., Seitz, M.: Using Raspberry Pi for scientific video observation of pedestrians during a music festival. Technical report, Technische Universität München, München (2015)
3. Bitner, M.: Servicescapes: the impact of physical surroundings on customers and employees. J. Mark. (1992)
4. Borshchev, A.: The Big Book of Simulation Modeling: Multimethod Modeling with AnyLogic 6. AnyLogic North America (2013)
5. Gross, D., Harris, C.M.: Fundamentals of queueing theory. Wiley (1988)
6. Groth, M., Gilliland, S.W.: The role of procedural justice in the delivery of services. J. Qual. Manage. **6**(1), 77–97 (2001)
7. Handel, O., Biedermann, D.H., Kielar, P.M., Borrmann, A.: A system dynamics based perspective to help to understand the managerial big picture in respect of urban event dynamics. Transp. Res. Procedia **2**, 669–674 (2014)
8. Hui, M., Bateson, J.: Perceived control and the effects of crowding and consumer choice on the service experience. J. Consum. Res. (1991)
9. Katz, K.L., Larson, B.M., Larson, R.C.: Prescription for the waiting-in-line blues: entertain, enlighten, and engage. Sloan Manage. Rev. **32**(2), 44–53 (1991)
10. Kendall, D.: Stochastic processes occurring in the theory of queues and their analysis by the method of the imbedded Markov chain. The Annals of Mathematical Statistics (1953)
11. Kleinrock, L.: Queuing systems. Wiley (1975)
12. Maister, D.: The psychology of waiting lines. The Service Encounter (2005)
13. Rafaeli, A., Barron, G., Haber, K.: The effects of queue structure on attitudes. J. Serv. Res. **5**(2), 125–139 (2002)
14. Schmidt, D., Keating, J.: Human crowding and personal control: an integration of the research. Psychol. Bull. (1979)
15. Stokols, D.: On the distinction between density and crowding: some implications for future research. Psychol. Rev. **79**(3), 275–277 (1972)
16. Takács, L.: Investigation of waiting time problems by reduction to Markov processes. Acta Math. Hungar. **6**(1–2), 101–129 (1955)
17. Taylor, S.: Waiting for service: the relationship between delays and evaluations of service. J. Mark. **58**(2), 56 (1994)
18. Zeithaml, V., Parasuraman, A., Berry, L.: Problems and strategies in services marketing. J. Mark. (1985)

How Do We Wait? Fundamentals, Characteristics, and Modelling Implications

Michael J. Seitz, Stefan Seer, Silvia Klettner, Oliver Handel and Gerta Köster

Abstract Pedestrian simulation models predominantly focus on the flow or motion of agents. However, in many real-world scenarios a large amount of pedestrians' time is spent waiting. Furthermore, the initial spatial distribution of visitors of a mass event may contribute significantly to the overall evacuation time. In this paper, we discuss social science concepts related to waiting, such as personal space requirements, and identify relevant aspects for the modelling of pedestrian behaviour. With this background, we develop measures and hypotheses for pedestrian waiting behaviour and apply them to a field observation of a train station platform in Vienna. We discuss implications for modelling approaches to waiting, which could be an important future extension to pedestrian simulations.

1 Introduction

Pedestrian simulations can be useful for a wide range of applications, such as safety engineering, transportation planning, or computer animation. The requirements for simulations vary across disciplines, but the underlying model always has to be

---

M.J. Seitz (✉) · G. Köster
Munich University of Applied Sciences, Lothstr. 64, 80335 Munich, Germany
e-mail: m.seitz@hm.edu

G. Köster
e-mail: gerta.koester@hm.edu

M.J. Seitz
Technische Universität München, Boltzmannstr. 3, 85747 Garching, Germany

S. Seer · S. Klettner
Austrian Institute of Technology, Giefinggasse 2, 1210 Vienna, Austria
e-mail: stefan.seer@ait.ac.at

S. Klettner
e-mail: silvia.klettner.fl@ait.ac.at

O. Handel
Technische Universität München, Arcisstr. 21, 80333 Munich, Germany
e-mail: oliver.handel@tum.de

217

validated according to some criteria. Hence, developing such a model must be based on knowledge of real pedestrians' behaviour, and its predictions are often compared to empirical data [15] gathered in field observations [17] or controlled experiments [11].

So far, research on emergent collective pedestrian behaviour has predominately focused on certain observable aspects, especially density and flow [18]. Although the flow is important for safety and efficiency considerations, humans often do not move but remain at a position for some time. They may have to wait or rest, or simply stay to chat with others. Waiting is also a common human activity in transportation systems but has been largely ignored in simulation models. Simulation approaches have been proposed for distributing pedestrians in waiting zones [2] and for modelling pedestrians to remain at a specified position within the social force model [8]. However, the individual choice of pedestrians to wait at a certain location and the respective underlying causes are widely unexplored.

We study *waiting* as a type of behaviour by individuals remaining at a position to pass time until an event they expect occurs. Waiting—according to this definition—stands in contrast to remaining at one position for other reasons, such as chatting with someone or enjoying the scenery. Standing in line can be considered a specific form of waiting—with distinct characteristics—but is not studied in this work.

In this paper, we focus on passengers waiting at a train station. We draw on the literature, especially from a social science perspective. Since the usage of space is correlated to the context, such as the built and social environment, we pay special attention to the context. This background from social sciences allows us to develop measures and hypotheses about pedestrian behaviour. We then evaluate the hypotheses with empirical data from a field observation.

2 Social Science Background

Environments are built with the intent that their functions and usage aim at regulating activities of individuals and groups [12]. According to Ruesch [14], both objects and spaces convey information just as spoken language, creating some symbolic meaning, categorisations or beliefs about a place. In that sense, what distinguishes one environment from another is "the nature of the rules embodied or encoded in it" ([13], p.14). Albeit the influence of environmental characteristics on human responses, their relation ought to be comprehended in a probabilistic way, i.e. the setting providing possibilities for choices by increasing or decreasing the probability for activities and behaviours [13]. In other words, choices and activities are not to be understood as determined by the environment, but as being mediated by an individual's characteristics (e.g. abilities, motivation, cognition), by subjective evaluations of space, as well as by (cultural) norms and conventions [3]. According to this understanding, it is the subjective reading of the context which affects activities in and the uses of space [9, 10].

Possibilities for such activities and behaviours can be communicated by the physical environment, its features [1], and/or by the subjective meaning of space [7, 9]. For example, being in public is different from being in private, revealing that individuals regulate their behaviours more in public environments [10]. At the same time, distinct physical features can trigger certain behaviours, such as position changes. Such influences can be grouped into two categories: push and pull factors. While push factors move individuals away from physical features, such as platform edges, pull factors attract and increase densities, such as by advertising screens.

Besides the physical environment, which provides possibilities for activities and decisions, it is the social environment and cultural accepted norms that regulate behaviour and social interactions, such as interpersonal distances to social group members (pull factors) or to non-social group members (push factors). Invisible boundaries around individuals and groups—often referred to as "small protective sphere or bubble" ([6], p.119)—are maintained to separate one from others [19] and to regulate privacy [6]. Entering somebody's intimate or personal sphere is normally an indication of familiarity and sometimes intimacy. While intimate distance (<0.45 m) is reserved for close relationships, friends, and family members, personal distance (0.45–1.2 m) is used for conversations with friends and associates. Social distance (1.2–3.6 m) on the other hand is held when being with strangers, newly formed groups, and new acquaintances, whereas at public distance (3.6–7.6 m), individuals are well outside the circle of involvement.

Another model used to understand spatio-temporal patterns that takes into account the social environment is Schelling's segregation model [16]. Applied in a microscopic context, its fundamental assumption is that individuals decide to change their waiting location once the share of neighbouring people with different social characteristics exceeds an individual-dependent threshold. In other words, the whereabouts of an individual depends on the social characteristics of the surrounding environment. Even though people are quite tolerant towards such differences (high acceptance threshold), segregation processes occur quite rapidly.

In modern society, especially in crowded urban communities, it can be difficult to maintain personal space requirements, such as when being in dense, impersonal situations, e.g. on crowded trains, elevators, or streets. In such situations, physical proximity might be perceived as psychologically disturbing and uncomfortable. Privacy and personal space may, however, be re-established by adjusting social interaction to a desired level by verbal, non-verbal, and physical processes [4], such as by increasing physical or perceived interpersonal distances (e.g. stepping away from others, avoiding eye contact).

3   Materials and Methods

The empirical data presented in this paper originates from observations in a metro station in Vienna consisting of a centre platform with tracks on each side, as illustrated in Fig. 1. The observed platform area was directly accessible for passengers via

Fig. 1 Observed platform area in the metro station. The tactile paving is shown in *grey* and the *line* indicating a safety distance is shown in *yellow*
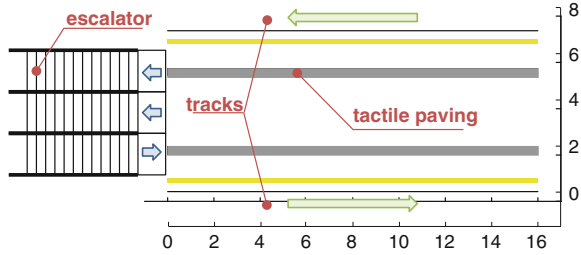
escalators and included tactile paving as well as yellow markings at the platform edges. Positions of waiting passengers were manually annotated in single video frames captured from an oblique camera view. Furthermore, all annotated waiting passengers were manually tracked over consecutive frames. We determined the point mapping between the image coordinate system and the world coordinate system using multiple reference points which were measured on-site. For our investigations, we used manual annotations from two video sequences each of 15 min length, which were recorded in the morning (7:00 AM with 38 passengers in 5 phases between consecutive trains) and evening (6:30 PM with 91 passengers in 4 phases between consecutive trains) with average train intervals of 80 s.

4   Results and Discussion

We analysed the data collected from the observation by clustering the spatial data in quadratic bins with a side length of 1 m. Figure 2 illustrates the spatial distribution of waiting passengers and the respective waiting times.

On the left in Fig. 2, the number of passengers occupying each bin was counted every second. The sum was divided by the overall observation time yielding a normalised measure for the occupancy. Warmer colours indicate positions that were occupied more often. We observed higher levels of occupancy in the evening compared to the morning. In both cases, passengers seemed to stay clear of close positions next to the platform edge, yet some individuals remained close to it. Additionally, only very few passengers waited close to the escalators on the left of the observation area.

On the right in Fig. 2, the mean remain time in seconds was calculated for each bin. Brighter colours indicate positions were passengers remained longer on average. Here, a similar picture can be observed as for the level of occupancy. We did not find any additional systematic distribution of the remain time. However, with additional data, this measurement methodology may yield interesting insights into waiting behaviour.
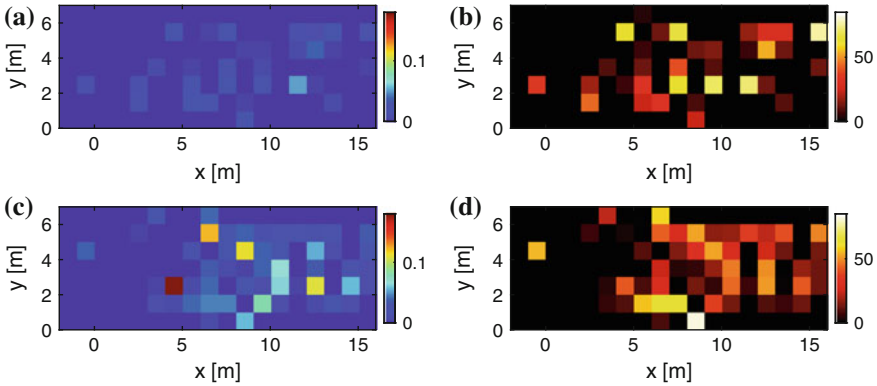
Fig. 2 On the *left*, passengers occupying one measurement bin were counted every second, and this sum was divided by the overall observation time. *Warmer colours* indicate a higher level of occupancy. On the *right*, the mean remain time was measured for each measurement bin. In both cases, measurement bins have side lengths of 1 m. Measure of occupancy, morning (**a**). Mean dwell time (s), morning (**b**). Measure of occupancy, evening (**c**). Mean dwell time (s), evening (**d**)

Looking at the data in detail, we evaluated two working hypotheses we expected to reject with the empirical observation. The first hypothesis states that passengers distribute uniformly over the platform. The second hypothesis postulates an exponential distribution for remain times. Both hypotheses were selected because of their simplicity and the assumption that they are used frequently in simulation models. In order to decide whether to reject the hypotheses, we explored the data with a series of histograms as reported in Fig. 3.

In Fig. 3a, the frequency of chosen positions over the width of the platform is shown. Again, this representation of the data reveals that passenger kept clear of close positions—up to 0.5 m—to the platform edge. Taken together with the spatial representations in Fig. 2, this strongly suggests that the hypothesis that passengers distribute uniformly can be rejected. Apart from the gaps close to the platform edge, a uniform distribution may still be a plausible statistical model for the data.

In Fig. 3b, the empirical distribution of remain times is shown. The hypothesis that the remain times are distributed exponentially seems implausible for two reasons. First, there is little weight for very short remain times, leaving a gap close to 0 s in the morning observation. Second, both distributions appear to be more heavy tailed compared to an exponential distribution—especially in the morning. From investigating the data we can conclude that the second hypothesis can be rejected as well. However, an exponential distribution may still be a useful simplified model for practical purposes.

In Fig. 3c, we report the distance kept for the chosen waiting position to the next waiting passenger. In the morning, passengers kept a mean interpersonal distance of 3.0 m. In the evening, pedestrians awaiting the train kept a mean distance of 1.2 m. Both empirical distributions could be modelled with a Gamma distribution, yet, with different parameters. In the morning, greater distances seemed to be more frequent.
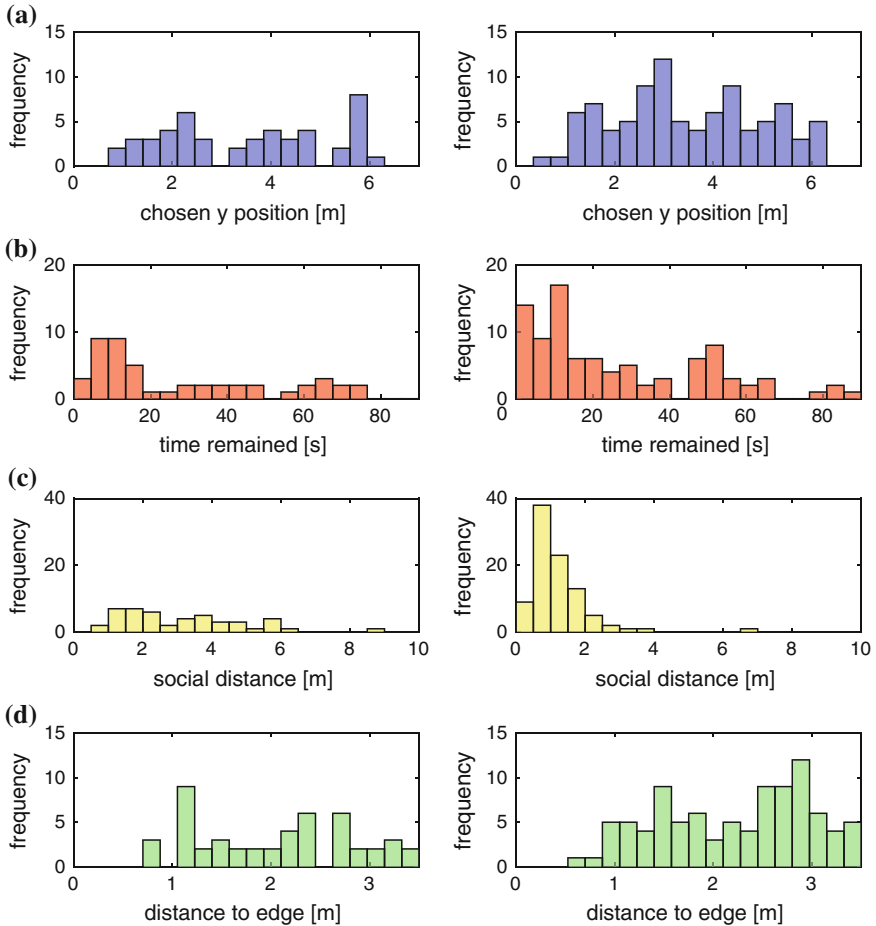
Fig. 3 Histograms summarising the waiting behaviour during the observation. *Left figures* refer to the morning, *right figures* refer to the evening. The frequency of chosen positions over the width of the platform (**a**). The times passengers remained at one position (**b**). Minimum distance kept to other passengers (positions were ignored when there were no other passengers on the platform) (**c**). Distance kept to the border of the platform (**d**)

However, it is important to mention that densities were higher in the evening and hence interpersonal distances are also more likely to decrease. Another reason for greater distances in the morning could be that more commuters who did not know each other were present. In contrast to that, in the evening, more passengers in social groups who stay closer together can be expected.

In reference to [6], proximities of 1.2 and 3.0 m are within the range of social distance. When chosen voluntarily, it reflects the distance held between strangers, newly formed groups, and new acquaintances. Following [6], one would expect larger distances, that are characteristic for public occasions. Yet, the limited platform space does not allow for much larger physical interpersonal distances.

Finally, in Fig. 3d, the empirical distribution of distances kept to the next platform edge are shown. As it was also observed in Fig. 2, passengers did not wait in a range from 0 up to 0.5 m and with low frequency in a range of 0.5 to 1 m. We propose two possible explanations for this. First, there was a yellow line indicating a safety distance people have to keep from the rails. This line is likely to encode the intended instruction to stay away from the platform edge and thus may suggests the observed behaviour (see [1, 9]). Second, the platform edge and the knowledge that trains arrive and departure there might induce a possible threat leading to the observed behaviour. Hence, the built environment itself and the familiarity of passengers with this context could be dominant. Finally, these two aspects together may encourage the observed behaviour.

While not often included, remain times and spatial distributions can be of great value for pedestrian simulation. Social distances and the distance to the platform edge could be modelled by push and pull factors. Additionally, we suggest to use heuristic decision making [5] to model waiting behaviour and propose the following four rules as working hypothesis for future research: (a) passengers get close to where the train arrives; (b) they keep a safety distance to the platform edge; (c) passengers keep a social distance to other passengers; (d) they stay away from the escalators.

5 Conclusions

In this paper, we reported a study of pedestrian waiting behaviour. First, we reviewed related concepts from social sciences. Second, we explored observational data from a train station platform and evaluated two simple working hypotheses. Finally, we proposed four heuristic rules that may be used in simulation models.

We argue that waiting behaviour is an important aspect in pedestrian interactions. Although waiting is especially relevant in public transportation systems, pedestrian simulation models have put less focus on waiting behaviour so far. Furthermore, quantitative data can also further the knowledge in social sciences. The measurement methodologies we used can be applied for other scenarios.

In the future, the proposed heuristics may be formalised, implemented, and studied in pedestrian simulations. The emergent effects can then be compared to empirical data, allowing for the validation of the proposed decision making model. For empirical research, however, it is crucial to collect more data from heterogeneous scenarios with different contexts. This would expose cultural similarities and differences, such as in European and Asian commuters' behaviour.

This contribution can be seen as a basis for the investigation of waiting behaviours in pedestrian research—both for empirical research and mathematical modelling. We emphasised the need to approach waiting behaviour in broader contexts, such as when taking into account the social environment (e.g. through social interactions) as well as the physical environment (e.g. spatial behaviour). The presented study can be used for future empirical measurements, mathematical modelling, and further studies in social sciences.

References

1. Campari, I.: Uncertain boundaries in urban spaces. In: Burrough, P.A., Frank, A. (eds.) Geographic objects with indeterminate boundaries. CRC Press (1996)
2. Davidich, M., Geiss, F., Mayer, H.G., Pfaffinger, A., Royer, C.: Waiting zones for realistic modelling of pedestrian dynamics: a case study using two major german railway stations as examples. Transp. Res. Part C: Emerg. Technol. **37**, 210–222 (2013)
3. Eibl-Eibesfeldt, I.: Similarities and differences between cultures in expressive movements. In: Non-verbal Communication, pp. 297–314. Cambridge University Press, Cambridge (1972)
4. Evans, G.W., Wener, R.E.: Crowding and personal space invasion on the train: please don't make me sit in the middle. J. Environ. Psychol. **27**(1), 90–94 (2007)
5. Gigerenzer, G., Todd, P.M.: A.B.C. Research Group: simple heuristics that make us smart. Oxford University Press, Oxford (1999)
6. Hall, E.T.: The Hidden Dimension. Doubleday (1966)
7. Huang, H., Klettner, S., Schmidt, M., Gartner, G., Leitinger, S., Wagner, A., Steinmann, R.: Affectroute—considering people's affective responses to environments for enhancing route-planning services. Int. J. Geogr. Inf. Sci. **28**(12), 2456–2473 (2014)
8. Johansson, F., Peterson, A., Tapani, A.: Waiting pedestrians in the social force model. Physica A **419**, 95–107 (2015)
9. Kallus, R.: From abstract to concrete: subjective reading of urban space. J. Urban Des. **6**(2), 129–150 (2001)
10. Matsumoto, D.: The psychological dimensions of context. Acta de Investigación Psicológica **2**(2), 611–622 (2012)
11. Moussaïd, M., Helbing, D., Garnier, S., Johansson, A., Combe, M., Theraulaz, G.: Experimental study of the behavioural mechanisms underlying self-organization in human crowds. Proc. Roy. Soc. B: Bio. Sci. **276**, 2755–2762 (2009)
12. Ozaki, R., Lewis, J.R.: Boundaries and the meaning of social space: a study of Japanese house plans. Environ. Plan. D Soc. Space **24**(1), 91–104 (2006)
13. Rapoport, A.: Human Aspects of Urban Form: Towards a Man? Environment Approach to Urban Form and Design. Pergamon Press, Oxford (1977)
14. Ruesch, J., Weldon, K.: Nonverbal Communication: Notes on the Visual Perception of Human Relations. University of California Press, Berkley and Los Angeles (1956)
15. Schadschneider, A., Klingsch, W., Klüpfel, H., Kretz, T., Rogsch, C., Seyfried, A.: Evacuation dynamics: empirical results, modeling and applications. In: Meyers, R.A. (ed.) Encyclopedia of Complexity and Systems Science, pp. 3142–3176. Springer, New York (2009)
16. Schelling, T.C.: Micromotives and macrobehavior. In: FELS Lectures on Public Policy Analysis. WW Norton & Company (1978)
17. Seer, S., Brändle, N., Ratti, C.: Kinects and human kinetics: a new approach for studying pedestrian behavior. Transp. Res. Part C Emerg. Technol. **48**, 212–228 (2014)
18. Seyfried, A., Passon, O., Steffen, B., Boltes, M., Rupprecht, T., Klingsch, W.: New insights into pedestrian flow through bottlenecks. Transp. Sci. **43**, 395–406 (2009)
19. Sommer, R.: Studies in personal space. Sociometry **22**(3), 247–260 (1959)

Collision-Free Speed Model for Pedestrian Dynamics

Antoine Tordeux, Mohcine Chraibi and Armin Seyfried

Abstract We propose in this paper a minimal speed-based pedestrian model for which particle dynamics are intrinsically collision-free. The speed model is an optimal velocity function depending on the agent length (i.e. particle diameter), maximum speed and time gap parameters. The direction model is a weighted sum of exponential repulsion from the neighbours, calibrated by the repulsion rate and distance. The model's main features like the reproduction of empirical phenomena are analysed by simulation. We point out that phenomena of self-organisation observable in force-based models and field studies can be reproduced by the collision-free model with low computational effort.

1 Introduction

Modelling of pedestrian dynamics have been strongly developed since the 1990s [1–3]. Microscopic models describe the movement of individuals in two-dimensional representation of space. They are used for theoretical purposes [4, 5], as well as for applications e.g. design and conception of escape routes in buildings [6, 7] or optimal organisation of mass events or public transport facilities (VISWalk [8], Legion [9], ...). In the microscopic class of models, pedestrians are represented as

A. Tordeux (✉) · M. Chraibi · A. Seyfried
Jülich Supercomputing Centre, Forschungszentrum Jülich GmbH,
Jülich, Germany
e-mail: a.tordeux@fz-juelich.de

M. Chraibi
e-mail: m.chraibi@fz-juelich.de

A. Seyfried
e-mail: a.tordeux@fz-juelich.de

A. Tordeux · A. Seyfried
Computer Simulation for Fire Safety and Pedestrian Traffic,
Bergische Universität Wuppertal, Wuppertal, Germany

autonomous entities (Lagrangian representation) with local interactions. Complex collective phenomena of self-organisation emerge from the interactions. Examples are the lane formation, clogging at bottlenecks, zipper effect or intermittent flow at bottlenecks, stop-and-go waves, herding, strip formation or circular flows (see [1, 10] and references therein). Even simple microscopic models can yield in rich dynamics [11, 12]. Yet, the relations between the microscopic model parameters and the emergence of phenomena of self-organisation are not straightforward. In most of the cases, they have to be analysed by simulation.

Microscopic pedestrian models could be defined in continuous or discrete time, space and state variables (see [3, Chap. 5]). One of the most investigated class is the class of *force-based* (or acceleration) models [11–13]. They use an analogy between pedestrian movement and Newtonian dynamics. Force-based approaches allow to describe a large variety of pedestrian dynamics [11, 12]. Yet, this model class describes particles with inertia and does not exclude particle collision and overlapping. This is especially problematic at high densities [13]. Moreover, the force-based approach may lead to numerical difficulties resulting in small time steps and high computational complexity, or use of mollifies [14].

Pedestrian behaviours result from repulsive and attractive forces with the acceleration models. They are based on the visual perception of distances or obstacle speeds resulting in instantaneous changing of the speed or the direction within the speed models. Also, this model class is generally called *vision-based*. One example is the *synthetic-vision-based steering approach* that notably allows to describe complex collective structures avoiding gridlocks [15]. Also the *velocity obstacle models* or *reciprocal velocity obstacle model* borrowed from robotics exist [16, 17]. These models are defined in discrete time and are driven by collision avoidance. They are by construction collision-free if the time step is smaller than a horizon time of anticipation. In the evacuation model by Venel, the pedestrians move as fast as possible to the desired destination with no overlapping [18]. There exist some variants of the model with different interaction strategies [19]. Note that there exists also rule based multi-agent models aiming to describe pedestrian psychology (see for instance [20, 21]) or mixed models, see for instance the *gradient navigation model* where the direction model is defined at first order while the speed is of second order [22]. In most of cases, these models need a large number of parameters with inherent calibration difficulties and, as for force-based models, high computational efforts.

In this paper, we aim to develop a minimal model for which the dynamics are by construction collision-free (i.e. overlapping-free). The model belongs to Maury and Venel mathematical framework [18]. We show by simulation that it allows to describe some expected phenomena of self-organisation observed in field studies or in simulations with forced based models. The model is defined in Sect. 2 while the simulation results are presented in Sect. 3. Conclusion and working perspective are given in Sect. 4.

2 Collision-Free Speed-Based Pedestrian Model

A continuous speed model is a derivative equation for the velocity. Typical examples are

$$\dot{\mathbf{x}}_i = \mathbf{v}(\mathbf{x}_i, \mathbf{x}_j, \ldots) \quad \text{or} \quad \dot{\mathbf{x}}_i = V(\mathbf{x}_i, \mathbf{x}_j, \ldots) \times \mathbf{e}_i(\mathbf{x}_i, \mathbf{x}_j, \ldots), \quad (1)$$

with $\mathbf{x}_i$ the pedestrian position and $\dot{\mathbf{x}}_i$ the velocity of pedestrian i (see Fig. 1). The velocity in regulated in one function for the first equality while the speed V and the direction $\mathbf{e}_i$ (unit vector) are regulated separately in the second approach.

2.1 Definition of the Model

The speed model is the optimal speed (OV) function depending on the minimal spacing in front. The approach is borrowed from road traffic model [23]. The OV approach has been already developed with a force-based model [24]. Here, we use the OV function at the first order with the minimal spacing in front.

For a given pedestrian i, the set of the pedestrians in front is defined by

$$J_i = \left\{ j, \ \mathbf{e}_i \cdot \mathbf{e}_{i,j} \le 0 \text{ and } |\mathbf{e}_i^\perp \cdot \mathbf{e}_{i,j}| \le \ell/s_{i,j} \right\}. \quad (2)$$

The pedestrians in front are the pedestrians overlapping the grey area in Fig. 1. The minimum distance in front s_i is

$$s_i = \min_{j \in J_i} s_{i,j}. \quad (3)$$

The model is

$$\dot{\mathbf{x}}_i = V\big(s_i(\mathbf{x}_i, \mathbf{x}_j, \ldots)\big) \times \mathbf{e}_i(\mathbf{x}_i, \mathbf{x}_j, \ldots), \quad (4)$$
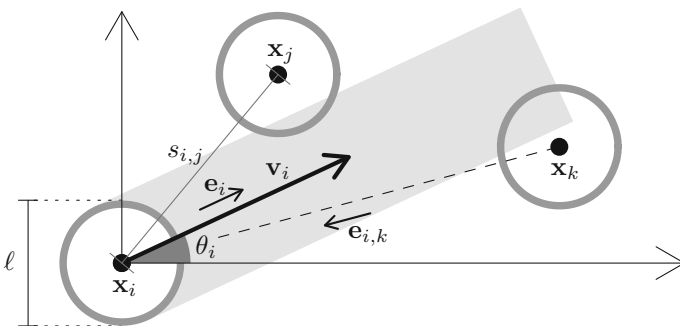
Fig. 1 Notations used: $\mathbf{x}_i$, $\mathbf{v}_i$ and θ_i are the position, velocity and direction of the pedestrian i; ℓ is the pedestrian size; $\mathbf{e}_{i,j}$ is the unit vector from $\mathbf{x}_j$ to $\mathbf{x}_i$; $\mathbf{e}_i = (\cos\theta_i, \sin\theta_i)$; $s_{i,j} = ||\mathbf{x}_i - \mathbf{x}_j||$
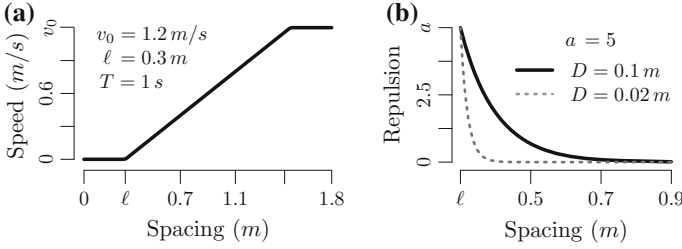
Fig. 2 Functions and associated parameters for the model: OV function, 3 parameters (**a**); repulsion function, 2 parameters (**b**)

with $V(\cdot)$ the OV function and $\mathbf{e}_i(\mathbf{x}_i, \mathbf{x}_j, \ldots)$ the direction model to define. As shown below, such model is by construction collision-free if

$$V(s) \geq 0 \quad \text{for all } s \quad \text{and} \quad V(s) = 0 \quad \text{for all } s \leq \ell. \tag{5}$$

In the following, the OV function is the piecewise linear $V(s) = \min\{v_0, \max\{0, (s - \ell)/T\}\}$, with v_0 the desired speed and T the time gap in following situations (ℓ is the pedestrian diameter, see Fig. 1). This OV function satisfies the collision-free assumption (Eq. 5). The direction model is a simplified version of the additive form of the *gradient navigation model* [22]. It is based on a repulsion function depending on the distances ($s_{i,j}$) with the neighbours

$$\mathbf{e}_i(\mathbf{x}_i, \mathbf{x}_j, \ldots) = \frac{1}{N} \left(\mathbf{e}_0 + \sum_j R(s_{i,j}) \, \mathbf{e}_{i,j} \right), \tag{6}$$

with $\mathbf{e}_0$ the desired direction given by a strategic model, N a normalisation constant such that $\|\mathbf{e}_i\| = 1$ and $R(s) = a \exp\left((\ell - s)/D\right)$ the repulsion function, calibrated by the coefficient $a > 0$ and distance $D > 0$. The parameter values used in the simulation are presented in Fig. 2.

2.2 Collision-Free Property

Oppositely to the force-based models, the presence of collision and overlapping can be controlled by construction with the speed-based models (non-overlapping constraint). If pedestrians are considered as discs with diameter ℓ, the set of collision-free configurations is for a given pedestrian i

$$Q_i = \left\{ \mathbf{x}_i \in \mathbb{R}^2, \ s_{i,j} \geq \ell \ \forall j \right\}. \tag{7}$$

The set of collision-free velocities

$$C_{\mathbf{x}_i} = \left\{ \mathbf{v} \in \mathbb{R}^4, \ s_{i,j} = \ell \ \Rightarrow \ \mathbf{e}_{i,j} \cdot \mathbf{v}_i \geq 0 \ \text{and} \ \mathbf{e}_{j,i} \cdot \mathbf{v}_j \geq 0 \right\} \tag{8}$$

is such that the speeds are nil or in opposite direction for a pedestrian in contact with an other (see [18] for more general conditions). Therefore, if initially $\mathbf{x}_i(0) \in Q_i$, then $\mathbf{x}_i$ remains in Q_i for any dynamics in $C_{\mathbf{x}_i}$. In these conditions Q_i is an invariant set for $\mathbf{x}_i$, i.e. the dynamics are collision-free (see also [25]). It is easy to see that the model (Eq. 4) belongs to this class if assumption (Eq. 5) is satisfied. Consider $s_{i,j} = \ell$ then either $\mathbf{e}_i \cdot \mathbf{e}_{i,j} \leq 0$ and then $j \in J_i$, i.e. $s_i \leq s_{i,j} = \ell$ and $V(s_i) = 0$, or neither $\mathbf{e}_i \cdot \mathbf{e}_{i,j} \geq 0$ and then $V(s_i) \geq 0$ since $V(\cdot) \geq 0$. Therefore $\mathbf{v}_i \cdot \mathbf{e}_{i,j} = V(s_i) \times \mathbf{e}_i \cdot \mathbf{e}_{i,j} \geq 0$ and the velocity belongs to $C_{\mathbf{x}_i}$. The arguments are valid for any direction model $\mathbf{e}_i$.

3 Model Features

We describe in this section by simulation some characteristics of the model with uni- and bi-directional flows. The parameter settings are given in Fig. 2. The simulations are done on rectangular systems with length $L = 9\,\text{m}$ and width $W = 3\,\text{m}$ from
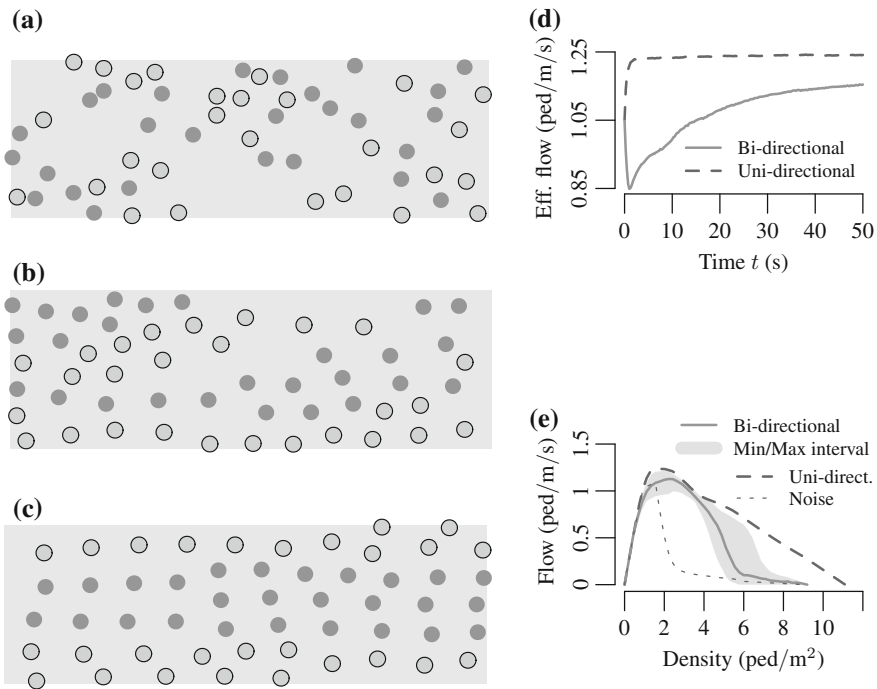
Fig. 3 Counter flows. t=0 (**a**); t=10 (**b**); t=50 (**c**); flow sequence by direction (**d**); fundamental diagram (**e**)

random initial configurations and by using explicit Euler numerical scheme with time step $dt = 0.01$ s.

3.1 Counter Flows and the Lane Formation

We observed with the model the formation of lanes by direction for counter flows (Fig. 3, left panels). Such phenomena frequently occur in real data (see for instance [26]). The system needs an organisation time for that the lanes emerge (Fig. 3, top right panel), where the mean flow to the desired direction for counter flows is compared to uni-directional ones). The formation of lanes is observed with the model for some density levels up to $\rho = 6$ ped/m^2 (Fig. 3, bottom right panel). As expected, the density threshold value for that the lanes appear depends on the pedestrian size ℓ (here $\ell = 0.3$ m). Note that the lane formation phenomenon disappears when a noise is introduced in the model (freezing by heating phenomenon, see [4] and in Fig. 3, thin dotted line in bottom right panel where a Brownian noise with standard deviation $\sigma = 0.1$ m/s is added to the model—the lane formation breaks as soon as $\rho \geq 2$ ped/m^2).
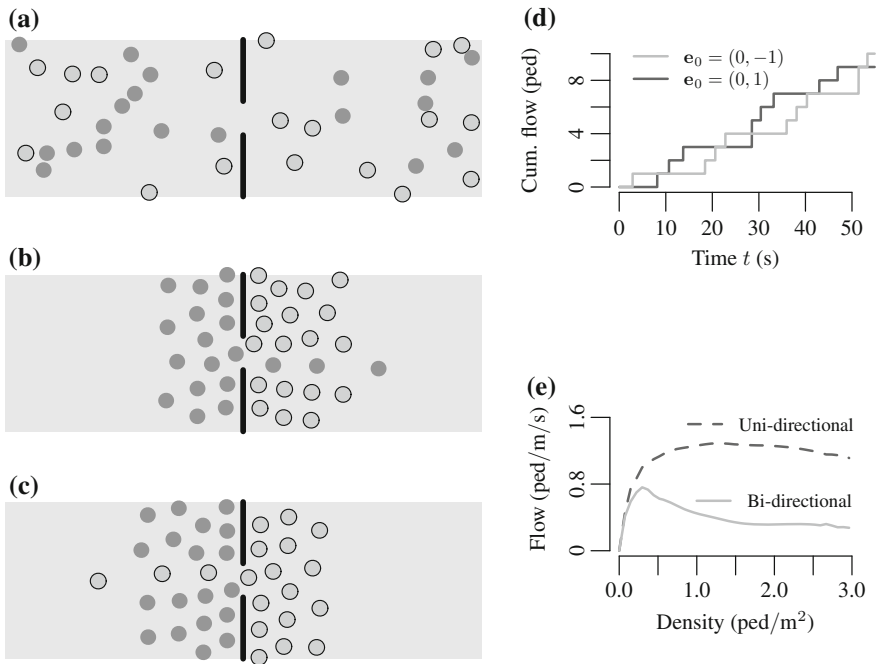
Fig. 4 Counter flows with bottleneck. t=0 (**a**); t=15 (**b**); t=25 (**c**); flow sequence by direction (**d**); fundamental diagram (**e**)

3.2 Intermittent Bottleneck Flows

Oscillating phenomena for counter flows in bottlenecks are observed with both real data and models [10, 12, 27]. Such phenomena are related as intermittent bottleneck flows in the literature [5]. We observe that the speed-based model is able to reproduce them (see Fig. 4, left and top right panels). The phenomenon occurs even at relatively high density levels (see Fig. 4, bottom right panel). Yet, it induces frictions and the flow volumes obtained for counter flows are less than the ones of uni-direction. As expected, the frictions tend to increase as the density increases. Some simulation results not presented here show that the intermittent flow phenomenon subsists for high density levels when D is sufficiently high and that the frequency of the flows oscillations tend to increase as the density increases.

4 Conclusion and Working Perspective

A new speed-based model is proposed for pedestrian dynamics in two dimensions. Oppositely to classical force-based approaches, the model is intrinsically collision-free and no overlapping phenomena occur, for any density level. The model has five parameters. Three of them concern the optimal speed function. They are the pedestrian length, desired speed and time gap with the predecessor. The two others calibrate the direction model. They are the repulsion rate and repulsion distance.

The model main properties are described by simulation. A large range of dynamics observed in real data and force-based models are reproduced. For instance, linear increase of flow with the bottleneck width, lane formation for counter flows (with the freezing by heating effect) or intermittent flows, are obtained with identical setting of the parameters. However, other well-known characteristic such that stop-and-go phenomena can not be described. Further mechanisms (and parameters) remain to be introduced to the model.

References

1. Chowdhury, D., Santen, L., Schadschneider, A.: Statistical physics of vehicular traffic and some related systems. Phys. Rep. **329**(4), 199–329 (2000)
2. Degond, P., Appert-Rolland, C., Moussaid, M., Pettré, J., Theraulaz, G.: A hierarchy of heuristic-based models of crowd dynamics. J. Stat. Phys. **152**(6), 1033–1068 (2013)
3. Schadschneider, A., Chowdhury, D., Nishinari, K.: Stochastic transport in complex systems: from molecules to vehicles. Elsevier (2010)
4. Helbing, D., Farkas, I.J., Vicsek, T.: Freezing by heating in a driven mesoscopic system. Phys. Rev. Lett. **84**(6), 1240 (2000)
5. Helbing, D., Johansson, A., Mathiesen, J., Jensen, M.H., Hansen, A.: Analytical approach to continuous and intermittent bottleneck flows. Phys. Rev. Lett. **97**(16), 168001 (2006)
6. GmbH, T.H.: Handbuch pedgo 2, pedgo editor 2. http://www.evacuation-simulation.com

7. Schneider V.K.R.: Simulating evacuation processes with aseri. In: Pedestrian and Evacuation Dynamics, pp. 303–314 (2002)
8. AG, P.: PTV Vissim 7.0—User Manual. PTV Group, Haid-und-Neu-Str. 15, D-76131 Karlsruhe, Germany (2014)
9. Berrou, J.L., Beecham, J., Quaglia, P., Kagarlis, M.A., Gerodimos, A.: Calibration and validation of the legion simulation model using empirical data. In: Pedestrian and Evacuation Dynamics, pp. 167–181 (2005)
10. Helbing, D.: Traffic and related self-driven many-particle systems. Rev. Mod. Phys. **73**(4), 1067 (2001)
11. Chraibi, M., Seyfried, A., Schadschneider, A.: Generalized centrifugal-force model for pedestrian dynamics. Phys. Rev. E **82**(4), 046111 (2010)
12. Helbing, D., Molnár, P.: Social force model for pedestrian dynamics. Phys. Rev. E **51**, 4282–4286 (1995)
13. Chraibi, M., Seyfried, A., Kemloh, U., Schadschneider, A.: Force-based models of pedestrian dynamics. Netw. Heterog. Media **6**, 425–442 (2011)
14. Köster, G., Treml, F., Gödel, M.: Avoiding numerical pitfalls in social force models. Phys. Rev. E **87**, 063305 (2013)
15. Ondřej, J., Pettré, J., Olivier, A.H., Donikian, S.: A synthetic-vision based steering approach for crowd simulation. ACM Trans. Graph. **29**, 123 (2010)
16. Van den Berg, J., Lin, M., Manocha, D.: Reciprocal velocity obstacles for real-time multi-agent navigation. In: IEEE International Conference on Robotics and Automation, 2008. ICRA 2008, pp. 1928–1935. IEEE (2008)
17. Fiorini, P., Shiller, Z.: Motion planning in dynamic environments using velocity obstacles. Int. J. Robot. Res. **17**(7), 760–772 (1998)
18. Maury, B., Venel, J.: Un modle de mouvement de foule. In: ESSAIM **18**, 143–152 (2007)
19. Venel, J.: Integrating strategies in numerical modelling of crowd motion. In: Pedestrian and Evacuation Dynamics 2008, pp. 641–646. Springer (2010)
20. Guo, R.Y., Wong, S., Huang, H.J., Zhang, P., Lam, W.H.: A microscopic pedestrian-simulation model and its application to intersecting flows. Physica A **389**(3), 515–526 (2010)
21. Pelechano, N., O'Brien, K., Silverman, B., Badler, N.: Crowd simulation incorporating agent psychological models, roles and communication. Technical Report, DTIC Document (2005)
22. Dietrich, F., Köster, G.: Gradient navigation model for pedestrian dynamics. Phys. Rev. E **89**(6), 062801 (2014)
23. Bando, M., Hasebe, K., Nakayama, A., Shibata, A., Sugiyama, Y.: Dynamical model of traffic congestion and numerical simulation. Phys. Rev. E **51**(2), 1035 (1995)
24. Nakayama, A., Hasebe, K., Sugiyama, Y.: Instability of pedestrian flow and phase structure in a two-dimensional optimal velocity model. Phys. Rev. E **71**(3), 036121 (2005)
25. Monneau, R., Roussignol, M., Tordeux, A.: Invariance and homogenization of an adaptive time gap car-following model. Nonlinear Differ. Equ. Appl. **21**(4), 491–517 (2014)
26. Zhang, J., Klingsch, W., Schadschneider, A., Seyfried, A.: Ordering in bidirectional pedestrian flows and its influence on the fundamental diagram. J. Stat. Mech. Theory Exp. **2012**(02), P02002 (2012)
27. Corradi, O., Hjorth, P.G., Starke, J.: Equation-free detection and continuation of a hopf bifurcation point in a particle model of pedestrian flow. SIAM J. Appl. Dyn. Syst. **11**(3), 1007–1032 (2012)

Finite Element Simulation of a Macroscopic Model for Pedestrian Flow

Rebekka Axthelm

Abstract We analyse the results of a finite element simulation of a macroscopic model, which describes the movement of a crowd, that is considered as a continuum. A new formulation based on the macroscopic model from Hughes [2] is given. We present a stable numerical algorithm by approximating with a viscosity solution. The fundamental setting is given by an arbitrary domain that can contain several obstacles, several entries and must have at least one exit. All pedestrians have the goal to leave the room as quickly as possible. Nobody prefers a particular exit.

1 Introduction

In Sect. 2, we introduce the underlying model equations to describe the process of pedestrian movement. We will present a reformulation, that is suitable with respect to a stable finite element-discretisation together with the corresponding boundary conditions. The description of the time-dependent density distribution ρ of pedestrians is based on the model introduced by Hughes [2]. This model is composed of two coupled, non-linear partial differential equations: the eikonal and the continuity equation. The solution of the eikonal equation determines the direction of the flow field. Areas of high density are avoided, because of the density-dependent external force. The density-dependent velocity is then given by a fundamental diagram. The continuity equation ensures the required conservation of mass of the crowd. With regard to a stable finite element-discretisation, we run over two equations in terms of viscosity solutions. The regularised eikonal equation is reformulated as a Helmholtz equation, which is a linear differential equation of second-order.

The discretisation in time of the new model is shown in Sect. 3 followed by a verification result. The finite element-discretisation in space completes the fully discretised model that finally presents itself as a system of linear equations.

R. Axthelm (✉)

Institute of Computational Physics, Zürich University of Applied Sciences,
Wildbachstr. 21, 8400 Winterthur, Switzerland
e-mail: rebekka.axthelm@zhaw.ch

233

As validation we compare evacuation results of our software pFlow with the corresponding results of the simulation tool Simwalk [4], which is based on a social forced modelling approach. As an outlook we apply the software for real-world situations. Corresponding outcomes can be found in Sect. 4.

2   Classical Model and Reformulation

First, we come from the model that is introduced by Hughes [2]. This is in short the coupling of the eikonal and the continuity equation:

$$|\nabla \Phi| = \frac{1}{f(\rho)} \tag{1}$$

$$u = -f(\rho) \frac{\nabla \Phi}{|\nabla \Phi|} \tag{2}$$

$$\rho_t + \nabla \cdot (\rho \, u) = 0 \tag{3}$$

The solution of the eikonal equation gives the walking direction. The right-hand side guarantees that high densities are disfavoured. The normalised gradient of Φ represents the walking direction and the velocity of the moving crowd is given by a fundamental diagram f. Together, we obtain the velocity field u. In order to require conservation of mass, because nobody dies and nobody materialises itself, we introduce the continuity equation. We formulate the corresponding boundary conditions after the reformulation of the model.

To begin with a new formulation of the model we get rid of the modulus in the eikonal equation by squaring Eq. (1):

$$(\nabla \Phi)^2 = \frac{1}{f^2(\rho)} \tag{4}$$

Adding an additional Laplace-operator to Eq. 4 greatly increases numerical stability. For sufficiently small $\varepsilon_1 > 0$ we obtain an approximation Φ_{ε_1} of the original solution Φ that is called the viscosity solution. Thus, we have to solve a non-linear partial differential equation of second-order:

$$- \varepsilon_1^2 \, \Delta \Phi_{\varepsilon_1} + (\nabla \Phi_{\varepsilon_1})^2 = \frac{1}{f^2(\rho)} \tag{5}$$

Φ_{ε_1} is a regularisation of Φ as it is shown in Fig. 1.

We replace Eq. 1 by Eq. 5 in our model. For simplicity, we write Φ instead of Φ_{ε_1} from now on. We now want to hide the non-linearity in (5). Defining

$$\Phi = -\varepsilon_1 \ln \psi \tag{6}$$
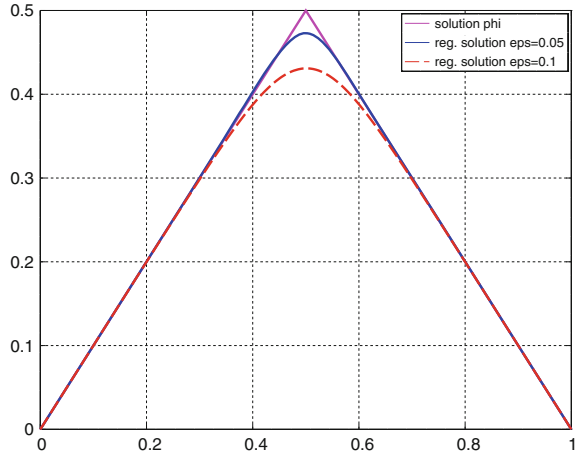
leads to the Helmholtz equation instead of the regularised eikonal equation. We then
have to solve a linear partial differential equation of second-order. For a given density
ρ and fundamental diagram $f(\rho)$ we are looking for ψ satisfying

$$\frac{1}{f^2(\rho)} \, \psi - \varepsilon_1^2 \, \Delta\psi = 0 \,. \tag{7}$$

The velocity field is composed as it is done in Eq. 2. As a showcase we imagine a
room split by a wall with a small passage in between. The shortest path from the
entry above to the exit on the right leads through the passage. We compare velocity
fields of an empty room at time $t = 0$ and a room where a crowd arose in front
of the passage at time $t = 120$. The normalised velocity fields in Eq. 2 computed
from Eqs. 6 and 7 in Fig. 2 show at which point the people decide to take the longer
way around the wall instead of squeezing themselves through the passage.

Also, for the continuity equation we restrict ourselves to a viscosity solution by
adding a Laplace-operator multiplied by a sufficiently small $\varepsilon_0 > 0$. All together,
with suitable boundary conditions the new model is made up as follows. In Ω we
solve

$$\frac{1}{f^2(\rho)} \, \psi - \varepsilon_1^2 \, \Delta\psi = 0 \,, \tag{8}$$

$$u = -f(\rho) \, \frac{\nabla\Phi}{\sqrt{|\nabla\Phi|^2 + \varepsilon_2^2}} \,, \quad \Phi = -\varepsilon_1 \, \ln\psi \,, \tag{9}$$

$$\rho_t - \varepsilon_0 \, \Delta\rho + \nabla \cdot (\rho u) = 0 \,. \tag{10}$$
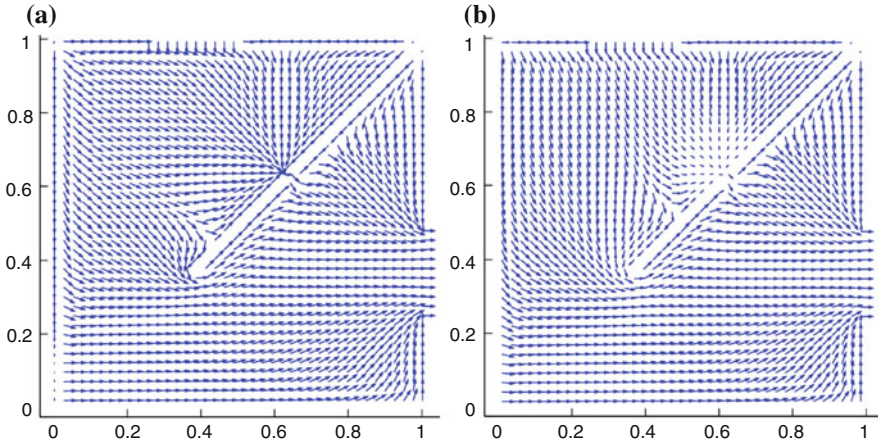
Fig. 2 Velocity field. $t = 0$ (**a**); $t = 120$ (**b**)

As the gradient of Φ may vanish we regularise the velocity field u. We have to postulate slip boundary conditions for the velocity field at walls due to the required conservation of mass: $u \cdot \nu = 0$, where ν is the outer normal to Ω at $\partial\Omega$. This is automatically fulfilled by choosing $\nabla \psi \cdot \nu = 0$. For the same reason we claim natural boundary conditions for the continuity equation at $\partial\Omega$. We have

$$\nabla \psi \cdot \nu = 0 \quad \text{on } \Gamma_{\text{wall}} \setminus \Gamma_{\text{exit}}, \tag{11}$$

$$\psi = 1 \quad \text{on } \Gamma_{\text{exit}}. \tag{12}$$

$$\nabla \rho \cdot \nu = 0 \quad \text{on } \partial\Omega, \tag{13}$$

$$\rho = \rho_{\text{in}} \quad \text{on } \Gamma_{\text{entry}}. \tag{14}$$

If there are any entries they feature non-zero Dirichlet boundary conditions ρ_{in} for the continuity equation. In practise we want to set a flow-rate-value (ρu) at entries and not the density itself. Actually, we do this and compute the Dirichlet boundary condition ρ_{in} by calculating the inverse of the specific power given by the fundamental diagram f. There are almost always two possibilities: many slow or few fast people entering. In- and out-flow occurs perpendicular to the domain boundary. This fixes the direction of the velocity field. In doing so, the velocity at entries is given, whereas it regulates itself at exits:

$$u = f(\rho)\, \nu \quad \text{on } \Gamma_{\text{exit}} \tag{15}$$

$$u = -f(\rho_{\text{in}})\, \nu \quad \text{on } \Gamma_{\text{entry}} \tag{16}$$

3 Discretisation and Verification

The time derivative of ρ is approximated by the Euler explicit method

$$\rho_t \approx \frac{1}{\delta}(\rho(t^{k+1}, \cdot) - \rho(t^k, \cdot)) \,. \tag{17}$$

Together with a semi-implicit time-discretisation for the whole model we decouple the equations from Eqs. 8 to 10. This leads in every time-step to a system of decoupled, linear partial differential equations of second-order. For a given initial density distribution $\rho^0 = \rho(t^0 = 0, \cdot)$ we iterate over k = 0,…

$$\frac{1}{f^2(\rho^k)} \psi^k - \varepsilon_1^2 \, \Delta \psi^k = 0 \,, \tag{18}$$

$$u^k = -f(\rho^k) \frac{\nabla \Phi^k}{\sqrt{\left|\nabla \Phi^k\right|^2 + \varepsilon_2^2}} \,, \quad \Phi^k = -\varepsilon_1 \, \ln \psi^k \,, \tag{19}$$

$$\rho^{k+1} - \delta \varepsilon_0 \, \Delta \rho^{k+1} + \delta \nabla \cdot (\rho^{k+1} u^k) = \rho^k \,, \tag{20}$$

including the additional boundary conditions from Eqs. 11 to 16. The discretisation in space is carried out by using piecewise linear finite elements, defined on a triangulated domain. For the Delauney triangulation of the domain the emc^2-software from [3] is used.

Table 1 shows the experimental order of convergence (EOC) for the stationary, regularised continuity equation in $\Omega = [0, 1]^2$ with the Dirichlet boundary condition on Γ. The computed example is given by Eq. 21 and its exact solution by Eq. (22).

$$-\Delta \rho + \nabla \cdot (\rho \, u) = F \tag{21}$$

$$\rho_{\text{ex}} = \frac{1}{2}(1 - x^2) \,, \; u \,, \; F \; \text{suitable} \tag{22}$$

From [1] we expect a L^2-error of second and H^1-error of first order:

$$\|\rho - \rho_h\|_{L^2} \leq C \, h^2 \quad \text{and} \quad |\rho - \rho_h|_{H^1} \leq C \, h^1 \tag{23}$$

Table 1 The experimental order of convergence for the stationary continuity Eqs. 21–22 shows the convergence order in Eq. 23

h	$\|\rho - \rho_h\|_{L^2}$	EOC	$|\rho - \rho_h|_{H^1}$	EOC
2.80e-02	3.39e-05	1.97	1.51e-03	1.01
1.38e-02	8.40e-06	2.02	7.39e-04	1.02
6.92e-03	2.09e-06	2.02	3.65e-04	1.01

4 Numerical Results

For all simulations we choose the fundamental diagram introduced by Weidmann [5] with $\rho_{max} = 5.4\,\text{Ped/m}^2$ and $u_{max} = 1.334\,\text{m/s}$.

The first example shows the comparison of our results (pFlow) to those from the commercial software Simwalk [4]. We consider a platform $\Omega = [0, 100] \times [0, n]$, $n \in \{2, 3\}$. Passengers are leaving the train through one or more doors with a certain flow-rate ($\rho_{in} u$). The exit is at right $\Gamma_{exit} = \{100\} \times [0, n]$. Everyone strives towards the exit. We count the passing pedestrians at the exit in both examples. We put an additional counter for the second example at the position of 80 m. The situations are illustrated in Fig. 3. In the continuous case we count people by measuring the flow-rate

$$\sum_{k=0}^{N} \delta \int_{\Gamma_{exit}} \rho^k \, u^k \cdot \nu \, do_x \,. \tag{24}$$

As we can see in Fig. 4 the graphs on the left show a good agreement between the two results. However, the right plot draws a discrepancy: the results of pFlow show that less pedestrians find themselves between the two counters. This can be explained by the additional diffusion term in Eq. 10. Hence, the overall walking speed of pedestrians is higher. That is why they leave the platform earlier.

As real-world situations we consider two public events in Zurich (Switzerland). The 'Münsterhof'-event (example 2a), where about 6,000 visitors appear, is a yearly celebration. The 'Zürifescht' (example 2b) with more than 60,000 visitors is organised every third year. The geographical location of these two festivals is shown in
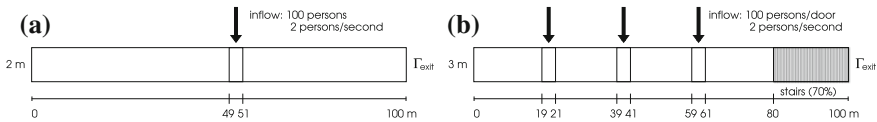
Fig. 3 Domain and boundary settings. Example 1a (**a**); example 1b (**b**)
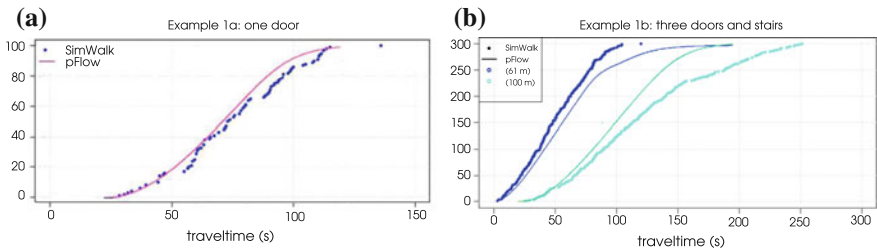
Fig. 4 Comparison between the results. pFlow (*lines* show measured value of Eq. 24) (**a**); SimWalk (*dots* show counted persons) (**b**)
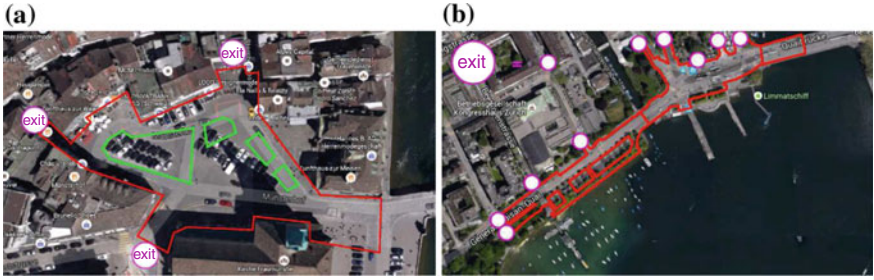
Fig. 5 Geographical positions; example 2a (**a**), example 2b (**b**). *Source* Google-maps
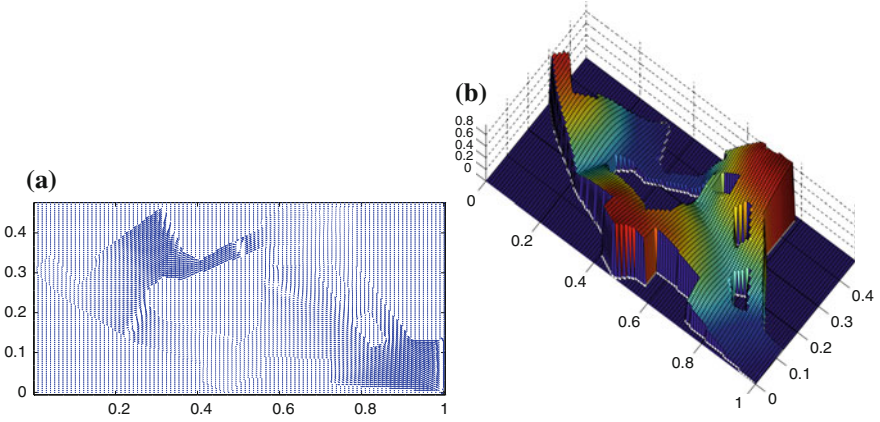
Fig. 6 Example 2a at $t = 589\,\mathrm{s}$ (*bottom*). Velocity field (**a**). Density distribution (**b**)

Fig. 7 Density distribution of example 2b at $t \approx 500\,\mathrm{s}$
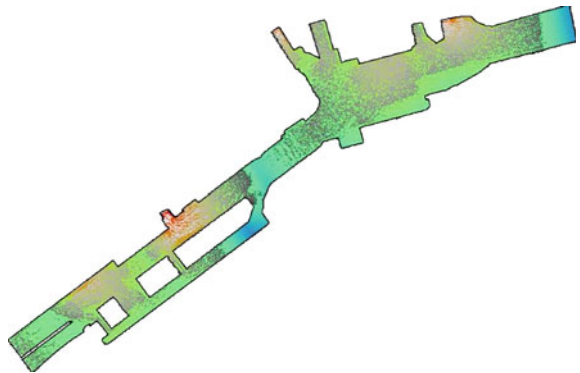
Table 2 Monitoring of the two real-world simulations

	P_0 [person]	diam(Ω) [m]	#Tri	Comp. time	Sim. time	Est. real time [min]	Max. power output	$\rho \in$
example 2a	5,960	100	2,086	≈ 27	≈ 9.5	≈ 15–20	≈ 5	[0.5, 1.3]
example 2b	58,570	459	6,800	≈ 64	≈ 21	≈ 30–40	≈ 9	[0, 4.6]

Fig. 5. We are interested in the evacuation time of both situations and the paths that pedestrians choose. Figure 6 shows qualitative results of example 2a: higher densities at the north-exit motivate more pedestrians to choose the west-exit.

Figure 7 presents the status after about 8 min where 58,570 people leave the Zürifescht-festival. A monitoring of computational-, simulation- and real-time data is given in Table 2.

References

1. Ciarlet, P.G.: The Finite Element Method for Elliptic Problems, vol. 40. Siam (2002)
2. Hughes, R.: A continuum theory for the flow of pedestrians. Transp. Res. Part B: Methodol. **36**(6), 507–535 (2002)
3. Saltel, E., Hecht, F.: EMC2 Wysiwyg 2D finite elements mesh generator. Inria Rep. **118** (1995)
4. Schmid, A.: Simwalk. Savannah Simulations AG. http://www.simwalk.com
5. Weidmann, U.: Transporttechnik der Fussgänger—Transporttechnische Eigenschaften des Fussgängerverkehrs (Literaturauswertung). Schriftenreihe des IVT **90** (1993)

A Unified Pedestrian Routing Model Combining Multiple Graph-Based Navigation Methods

**Peter M. Kielar, Daniel H. Biedermann, Angelika Kneidl
and André Borrmann**

Abstract   The navigation behaviour of pedestrians in street networks can be forecast by computer simulations based on routing models. These models characterise pedestrians' route choices regarding a variety of factors. However, the spatial cognition aspects are often omitted in routing models; thus, the diversity of predictable routes is limited. Here, we present a unified routing model that describes route choices of pedestrians by integrating the spatial cognitive aspects of allocentric-based and egocentric-based navigation. We achieved this by combining graph-based routing methods, each formalising a single spatial cognitive aspect. In addition, we present a generic calibration method for our model. For validation, we show that our model is able to correctly predict the routing behaviour of pedestrians in a case study.

1   Introduction

Every day, pedestrians navigate and walk in the street networks of cities. It is possible to forecast the pedestrians' navigational behaviour and predict the chosen routes by means of computer simulations. However, individual human navigation is influenced by many different factors [10] and there is still no pedestrian routing behaviour model that can predict the complete richness of pedestrian route choices.

In our previous research, different aspects of human spatial cognitive abilities were integrated successfully, and four different graph-based pedestrian navigation algorithms were presented [8]. Nonetheless, each method depicts only a specific type

P.M. Kielar (✉) · D.H. Biedermann · A. Borrmann
Technische Universität München, Arcisstr. 21, 80333 Munich, Germany
e-mail: peter.kielar@tum.de

D.H. Biedermann
e-mail: daniel.biedermann@tum.de

A. Borrmann
e-mail: andre.borrmann@tum.de

A. Kneidl
accu:rate GmbH Institute for Crowd Simulation, Rosental 5, 80331 Munich, Germany
e-mail: ak@accu-rate.de

of navigation behaviour—but, as shown by research on spatial cognition, human navigational abilities are more fine grained [5, 10]. Here, we present a Unified Pedestrian Routing Model that combines these four routing methods in a single model. By applying our approach to a pedestrian simulation, one can simulate a more diverse range of pedestrian way-finding behaviour.

1.1 Related Work

In contemporary research, there are several different approaches to model human navigation behaviour. Graph-based concepts utilise routing algorithms to determine an ordered set of street network joints to describe the path a pedestrian takes [7, 8]. Graph generation algorithms create the underlying routing network for the routing algorithms, based on the scenario geometry [3, 9]. The corridor map method is a concept that uses a route-map graph as well as clearance information to construct a corridor covering the traversable scenario layout from an origin to a destination [4]. When the corridor is completed, a simulated pedestrian navigates inside its boundaries towards a given destination. Another concept is the floor field method and its derivatives [1]. These methods compute distances on a grid that covers the simulation scenario as underlying data structure. Each grid cell is able to hold values—dynamically or statically—which are subject to gradual changes according to destination proximity and ground floor traversability.

1.2 Spatial Cognitive Concepts

The large field of research on spatial cognition contributes to improve our understanding of people's navigational abilities and limitations [10]. Human navigation abilities depend on the accuracy of perceiving spatial information, the competence to generate a spatial representation of the environment, as well as the efficiency of utilising the spatial representations [10]. In general, spatial representations of the environment are denoted as cognitive maps. Thus, way-finding abilities are directly related to the construction and processing of such maps [5].

Research on spatial cognitive abilities was able to prove that people use route-based, survey-based, or fuzzy intermediate strategies for navigation [5, 10]. The route-based navigation describes that a sequence of egocentric actions has to be carried out to recreate a route. Hence, little overall knowledge about the environment and relation between locations is needed. In contrary, the survey-based navigation approach is an allocentric strategy. People who use this strategy have a general understanding of relations and distances concerning a certain area, so they are able to find new direct paths from their current location to a not directly visible destination.

However, people do not simply choose one of these two strategies, but generate intermediate and mixed routing solutions based on the integrity of their cognitive

map, the reliability of their memory retrieval processes, their abilities to apply the information into actions, and the navigation task at hand [5, 10]. This predicts that intermediate variants of navigation methods must exist. The proposed Unified Pedestrian Routing Model captures these intermediates variants of route-based and survey-based navigation behaviour in a single way-finding model.

2 Graph-Based Navigation Methods

Graph-based routing methods for pedestrians predict walking paths from an origin to a destination either iteratively or directly in an algorithmic manner. The distinction is based on the egocentric routing strategy (iteratively) and the allocentric routing strategy (directly) outlined in Sect. 1.2. Direct routing solves the routing problem by providing an optimal path to the destination, based on shortest path solutions [2, 6]. In contrast, iterative routing algorithms provide the next vertex to visit stepwise, based on local optima. Previous work [8] includes the development of two direct routing methods—the Fastest Path (FP) and the Beeline Heuristics (BH)—as well as two iterative routing methods—the Greedy Beeline Heuristics (GBH) and the Straight and Long Legs (SALL). Figure 1 presents example routes generated by a pedestrian simulation that applies these methods on an artificial scenario.

2.1 Direct Routing Methods

We build upon two direct routing methods, the Fastest Path (FP) and Beeline Heuristics (BH) algorithms [8]. Both methods model routing behaviour of pedestrians who have a profound knowledge of the street network. The FP method is based on Dijkstra's algorithm [2]. The weight calculation method of FP combines the distance d_{ij} between current vertex i and a successor vertex j as well as a velocity v_{ij}, which is based on the number of pedestrians p_{ij} walking alongside a directed edge e_{ij}.
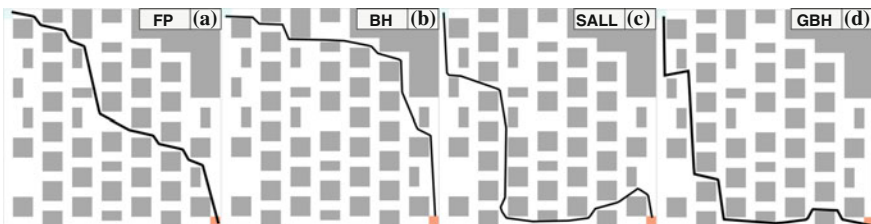
Fig. 1 The routes found by the four different basic routing models (**a–d**) in a pedestrian simulation. The pedestrians started at the *top-left* corners and walked to the corresponding *bottom-right* destination. The graph generation method of [9] was used for this artificial scenario

If an edge e_{ij} is not visible to a pedestrian, a standardised mean velocity v_m is used.

$$w_j = w_i + d_{ij}/v_{ij} \tag{1}$$

Because the FP algorithm has to be applied each time a pedestrian visits a vertex, the edge weights v_{ij} are updated corresponding to the velocities of the pedestrians v_{xij} on an edge e_{ij}. If the number of pedestrians p_{ij} at an edge is zero, a standardised mean velocity v_m is used for v_{ij}.

$$v_{ij} = \left(\sum_{x=1}^{k} v_{xij} \right) / p_{ij} \tag{2}$$

The BH algorithm is based on the A-Star algorithm [6] and describes the tendency to follow the beeline towards a destination. The algorithm of the weight calculation of the BH routing method integrates the beeline distance d_{jg} from the next vertex j to the destination vertex g, the distance d_{ij} between current vertex i and a successor vertex j, and a constant β. We omitted the random distance estimation error presented in [8]. Nonetheless, we kept the constant factor $\beta = 1.5$ of [8] to strengthen the beeline part of the calculation.

$$w_j = w_i + d_{ij} + d_{jg} \cdot \beta \tag{3}$$

The BH method's weight update uses the Dijkstra's Algorithm update procedure.

2.2 Iterative Routing Methods

The Greedy Beeline Heuristics (GBH) and the Straight and Long Leg methods (SALL) are the iterative routing concepts we build up upon [8]. They model the routing behaviour of pedestrians who are not familiar with the street network. The SALL method models the tendency to walk alongside straight and long streets. The route choice is based on the angle $\gamma_{aij} \in [0, \pi]$ in between the last vertex a and a next vertex j, as well as the relative distance reduction d_{jhg}/d_{jg} to the destination vertex g. The value d_{jhg} is calculated based on the vertex h, which is the farthest vertex within the projection of an arc of the angle of $\pm \mu$. The arc is centred alongside e_{ij} and its successor edges in succession. We set μ to $\pi/12$ for scenarios with rectangular street networks, and $\pi/9$ otherwise. For the calculation of the weight of a successor vertex j, the angle γ_{aij} improves the weight in the case of straight roads. The successor vertex with the smallest result is selected as the next vertex to visit.

$$w_j = (1 - \alpha) \cdot (d_{jhg}/d_{ig}) + \alpha \cdot (1 - |\gamma_{aij}|/180°) \tag{4}$$

The constant $\alpha = 0.75$ increases the influence of the angle parameter between zero and one. The value for α was determined by multiple pre-emptive test simulations.

The GBH describes a BH approach for pedestrians who are not familiar with the street network. Therefore, a simulated pedestrian can get lost by greedily following the beeline to the destination. For the route choice, the vertex with the smallest weight w_{ij} is selected as the next vertex to visit. The weight is influenced by the beeline distance d_{jg} from a successor vertex j to destination g only.

$$w_j = d_{jg} \tag{5}$$

3 The Unified Pedestrian Routing Model

The Unified Pedestrian Routing Model (UPRM) integrates all routing methods described in Sect. 2. By doing so, the integration is not a mutual exclusive application of routing algorithms, but a calculation-based integrative concept.

3.1 Merging the Graph-Based Methods

The UPRM is an iterative routing method to model the route-choice decision behaviour of selecting the next vertex to visit at a street junction, based on the four base algorithms. The weight calculation for UPRM is:

$$w_j = \zeta \cdot w_j^{FP} + \eta \cdot w_j^{BH} + \kappa \cdot w_j^{GBH} / \max\left(w_j^{GBH}\right) + \psi \cdot w_j^{SALL} / \max\left(w_j^{SALL}\right) \tag{6}$$

The successor vertex with the smallest weight w_j of the current vertex i will be selected as the next vertex to visit, as for the previous iterative methods.

The UPRM integrates the Greedy Beeline Heuristics (GBH) and Straight and Long Legs (SALL) methods by assessing the weights of all adjacent vertices j of vertex i. These weights are normalised by the maximal weight of all successor vertices of vertex i for each method separately. The Fastest Path (FP) and the Greedy Beeline (GB) algorithms contribute temporary calculations of the optimal paths, starting from vertex i. The first vertex of each optimal path is compared to the adjacent vertices j of the current vertex i. If a successor vertex of i is part of the optimal path, the weight w_j^{FP} (or respectively w_j^{BH}) is zero—and otherwise, it is one.

The resulting weights for each of the original methods are additively combined based on influence factors. These factors describe how strong a pedestrian is associated to a routing strategy. The factors ζ and η describe a high familiarity with the route network, whereas the factor κ and ψ describe a lesser knowledge of the network. The values range in [0, 1], but a single factor with a value larger than zero is mandatory. Hence, the factor concept also models interfering knowledge and uncertainty due to overlapping or under-represented factor combinations.

3.2 Model Calibration

The UPRM predicts the navigational paths based on the influence factors of the underlying routing algorithms. Therefore, a calibration method has to find influence factor combinations that yield realistic pedestrian routes for a scenario layout. We suggest a generic calibration approach that finds factors by a test simulation comprising a finite set of test pedestrians, initialised with random factors. We evaluated the calibration method by running a simulation with 1000 independent test pedestrians for an artificial world scenario. The simulated routes are compared by an extended version of the turning angle metrics [8]. The extended method removes redundant factor combinations that generate identical routes, based on the turning angles along the routing path. Hence, the method accepts only factor combinations that generate

Table 1 Factor combinations derived from the calibration method for an artificial scenario

	a	b	c	d	e	f	g	h	i	j	k	l	m	n	o	p	q	r
ζ	0.00	0.26	0.12	0.10	0.06	0.12	0.20	0.00	0.18	0.21	0.05	0.08	0.00	0.07	0.05	0.31	0.24	0.00
η	1.00	0.42	0.31	0.37	0.30	0.24	0.23	0.00	0.12	0.00	0.15	0.16	0.14	0.03	0.00	0.01	0.00	0.00
κ	0.00	0.81	0.75	0.99	0.94	0.40	0.75	0.00	0.02	0.03	0.50	0.75	0.33	0.43	0.99	0.57	1.00	1.00
ψ	0.00	0.78	0.45	0.02	0.15	0.87	0.71	1.00	0.75	0.76	0.62	0.95	0.91	0.68	0.67	0.73	0.69	0.00
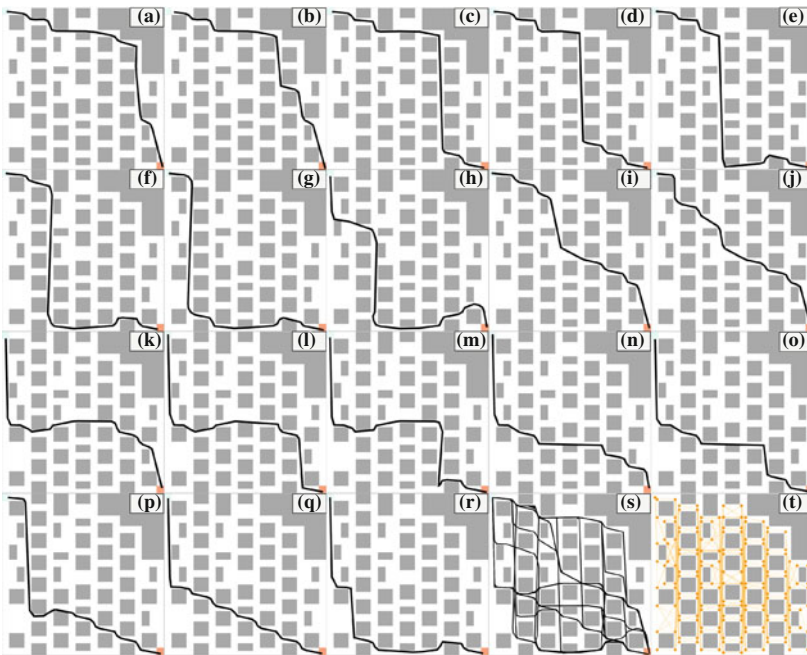
Fig. 2 Routes created by the UPRM based on Table 1 for the artificial simulation scenario. All routes start at the *top-left* and end at the *bottom-right* (**a–r**). All routes are shown in (**s**), and the used underlying graph is represented in (**t**) [9]

unique routes that reach the destination. Using this method, we found 18 feasible factor combinations for the artificial test scenario (see Table 1). Figure 2 shows the resulting routes based on the found factor combinations. Hence, our calibration method yields plausible and usable combinations for any layout.

4 Model Validation

We validated the Unified Pedestrian Routing Model (UPRM) in a case study, an annual music festival, by comparing the routes of real and simulated pedestrians. Thus, we captured the routing behaviour of approximately 700 of the 5000 festival visitors in 71 GPS measurements. The visitors travelled from a public transport station to the venue on walkways and streets that were closed for car traffic. Figure 3a–f shows the six different routes chosen by the visitors. For validation, we calibrated the model described in Sect. 3.2 and simulated the travellers' route choices. As visualised in Fig. 3g–k, the simulation results reveal that the UPRM predicts six different routes and forecast the route choices of the routes A to E correctly. The model could not predict route F completely, but misses to forecast one single route choice only— compare Fig. 3f, l. Naturally, the four original routing methods of [8] could predict the route choices of four routes correctly. In summary, the UPRM forecasts the route choices of pedestrian quite well, but seems to contain a minor flaw. We assume that the found uncertainty in predicting route F is based on a non-optimal calibration

Fig. 3 The measured walking routes of the festival visitors *A* to *F* (**a–f**). The simulation walking routes *A* to *F'* (**g–l**). The orange marker in (**l**) indicates the falsely predicted route choice. All routes start at the *bottom* and end at the *top*. An extended version of the graph generation method of [9] was used for the case study scenario

of the routing graph generation algorithm. It might be necessary to include further graph generation methods.

5 Conclusion

The Unified Pedestrian Routing Model (UPRM) represents a mathematical combination of pedestrian routing models from previous research. The model predicts route-based and survey-based navigation behaviour and, more importantly, intermediate and mixed variants of these routing strategies. By utilising pedestrian simulations, we showed that the UPRM is able to forecast a very large set of realistic navigation routes. Additionally, we validated the UPRM using a case study. We could forecast most of the pedestrian route choices of the study. Therefore, our approach of combining existing graph-based pedestrian routing methods to simulate more realistic routing behaviour was successful. Nonetheless, further validation studies are in preparation. We also aim to integrate herding-behaviour and a prediction of the relative frequency of route usage in further extensions of the UPRM.

References

1. Burstedde, C., Klauck, K., Schadschneider, A., Zittartz, J.: Simulation of pedestrian dynamics using a two-dimensional cellular automaton. Phys. A Stat. Mech. Appl. **295**(3–4), 507–525 (2001)
2. Dijkstra, E.W.: A note on two problems in connexion with graphs. Numer. Math. **1**(1), 269–271 (1959)
3. Geraerts, R., Overmars, M.H.: Creating high-quality roadmaps for motion planning in virtual environments. In: 2006 IEEE/RSJ International Conference on Intelligent Robots and Systems, pp. 4355–4361 (2006)
4. Geraerts, R., Overmars, M.H.: The corridor map method: a general framework for real-time high-quality path planning. Comput. Anim. Virtual Worlds **18**(2), 107–119 (2007)
5. Golledge, R.G.: Human wayfinding and cognitive maps. In: Wayfinding Behavior: Cognitive Mapping and Other Spatial Processes, pp. 5–45 (1999)
6. Hart, P.E., Nilsson, N.J., Raphael, B.: A formal basis for the heuristic determination of minimum cost paths. IEEE Trans. Syst. Sci. Cybern. **4**(2), 100–107 (1968)
7. Höcker, M., Berkhahn, V., Kneidl, A., Borrmann, A., Klein, W.: Graph-based approaches for simulating pedestrian dynamics in building models. In: eWork and eBusiness in Architecture, Engineering and Construction, pp. 389–394 (2010)
8. Kneidl, A., Borrmann, A.: Methoden zur Abbildung menschlichen Navigationsverhaltens bei der Modellierung von Fußgängerströmen. Ph.D. thesis, Technical University Munich (2013)
9. Kneidl, A., Borrmann, A., Hartmann, D.: Generation and use of sparse navigation graphs for microscopic pedestrian simulation models. Adv. Eng. Inform. **26**(4), 669–680 (2012)
10. Wolbers, T., Hegarty, M.: What determines our navigational abilities? Trends Cogn. Sci. **14**(3), 138–146 (2010)

Wayfinding and Cognitive Maps for Pedestrian Models

Erik Andresen, David Haensel, Mohcine Chraibi and Armin Seyfried

Abstract Usually, routing models in pedestrian dynamics assume that agents have fulfilled and global knowledge about the building's structure. However, they neglect the fact that pedestrians possess no or only parts of information about their position relative to final exits and possible routes leading to them. To get a more realistic description we introduce the systematics of gathering and using spatial knowledge. A new wayfinding model for pedestrian dynamics is proposed. The model defines for every pedestrian an individual knowledge representation implying inaccuracies and uncertainties. In addition, knowledge-driven search strategies are introduced. The presented concept is tested on a fictive example scenario.

1 Introduction

Microscopic simulations of pedestrian traffic flow are a suitable tool for designing both escape routes in buildings and pedestrian areas, e.g. malls, train and bus stations. Besides, simulations are used to investigate and analyse security risks in advance.

In the literature many elaborated microscopic pedestrian traffic flow models can be found. For a first overview see [1]. These models try to describe the locomotive actions of pedestrians, e.g. basic movement towards a certain location in space or steering (around obstacles to a certain destination).

E. Andresen (✉) · A. Seyfried
Faculty of Architecture and Civil Engineering, Bergische Universität Wuppertal,
Pauluskirchstr. 7, 42285 Wuppertal, Germany
e-mail: andresen@uni-wuppertal.de

A. Seyfried
e-mail: a.seyfried@fz-juelich.de

D. Haensel · M. Chraibi · A. Seyfried
Jülich Supercomputing Center, Forschungszentrum Jülich GmbH, 52425 Jülich, Germany
e-mail: d.haensel@fz-juelich.de

M. Chraibi
e-mail: m.chraibi@fz-juelich.de

However, they neither include the choice between currently accessible targets nor the planning of proceeding destinations (wayfinding tasks). These tasks are covered by the tactical level of pedestrian traffic flow modelling (see for example [2, 3]).

A majority of models concerning the tactical level assume the pedestrians to have a comprehensive knowledge about the spatial structure of their environment. Thus, the agents possess the ability to localise desired destinations in advance. They are, furthermore, able to evaluate or rather compare the quality of the routes which lead to the destinations. In many cases their evaluations are based on shortest path calculations or travel time optimisation.

The assumption that all pedestrians are provided with comprehensive global knowledge about a building's structure is a rough approximation, for example when pedestrians are not familiar with the facility. Even less, they are able to evaluate metric information about multiple routes so that an exact comparison is possible. In fact, the knowledge status of a group of pedestrians vary according to the number of visits and the capability to learn the spatial structure of new environments.

Human wayfinding is a complex process which includes the use of (in some cases inaccurate and incomplete) spatial memories [4], the use of signs and maps [4], search strategies and herding phenomena.

Although there are already approaches to represent wayfinding aspects including directional knowledge and uncertainties [5] there is room for improvements and continuations.

In this work we introduce a modelling approach enabling agents to make exit choice decisions based on inaccurate and incomplete knowledge about their environment and destinations.

1.1   The Cognitive Map

Although many mechanisms of perception and cognition enabling successful wayfinding are still unacquainted it is known that the hippocampal formation (part of the limbic system of the human brain) is mainly responsible to store and retrieve spatial memories which are essential to solve wayfinding issues [6]. John O'Keefe [6] and Maybritt and Edvard Moser [7] discovered place cells and grid cells in rats' brains that are involved in the formation of the so-called cognitive map. Similar systems of place-like and grid-like cells were discovered in many mammals' brains including the human brain [8].

The term cognitive map has been introduced by Tolman [9]. It depicts the mental representation of the spatial relationships between essential points, places, objects, etc. of our environment and possible connections between them [10]. Despite the prevailing opinion rats can only respond to stimuli, Tolman [9] conducted some experiments which gave evidence about the fact that rats possess clues about specific objects' positions relative to each other gathered from previous visits of the environment.

In the best case the cognitive map provides the possibility to locate the relative position to a specific destination and enables us to find or to plan a route leading to this destination [10, 11].

However, there is evidence that people get lost in several situations due to the fact that their cognitive maps are inaccurate, incomplete, distorted, or even wrong [10, 11].

Nevertheless, the cognitive map, although it does not provide detailed and much less accurate metric information, successfully helps us to find our way in most situations, especially in environments visited multiple times before. This results from the fact that humans possess the ability to store topological relations in a more accurate way [10, 11].

1.2   Generalised Knowledge

In many cases a wayfinding problem is not merely solved by information about the relations of explicit points or objects (the cognitive map). Additional knowledge called generalised knowledge is used as well. Human beings classify their environments and retrieve information, implications and expectations about the according classes, for example train stations, libraries, and office buildings [12, 13]. Generalised knowledge does not concern the explicit set-up of the specific environment itself but information about the environment's type or rather classification.

Within buildings we differentiate between two types of rooms (enclosed areas). On the one hand there are rooms serving the building's circulation or rather enabling people to reach efficiently their destination areas. Corridors, entrances, lobbies, stairs, ramps, etc. belong to this group of rooms. On the other hand there are rooms allotted to an explicit usage excluding the circulation. Concerning the second type of rooms we mention functional rooms, common rooms (offices, living rooms, cafeterias, etc.), store rooms, etc. as examples. We assume the majority of people to be capable to distinguish between both mentioned types due to their generalised knowledge about spatial structures.

Generalised knowledge provides the basis for various search strategies. To mention an example we consider a person to be located somewhere in a completely unfamiliar office building. The person is going to leave the building and is therefore looking for an exit. Due to knowledge about the purpose of circulation rooms he/she prefers to use them to reach the exit. Preferring circulation rooms instead of others is a simple but expedient and efficient strategy compared to a simple room exploration and thus facilitates the search for the exit severely.

2   Modelling Cognitive Map Knowledge

Following the findings mentioned in Sect. 1.1 we assume a simulated person to possess a cognitive map consisting of uncertain, inaccurate information. Thus, the agents possess only a vague idea of the exact (sub-)goals' position. For this purpose the
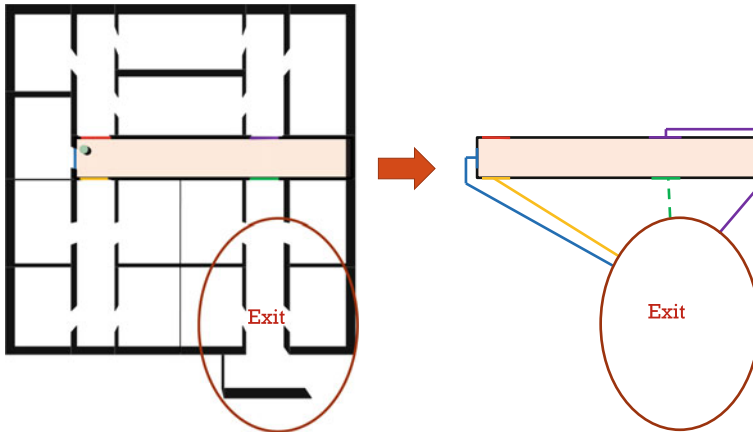
Fig. 1 The left figure shows the layout of a fictional building's floor. The agent's actual room is highlighted. The *ellipse* represents the agent's inaccurate idea of the exit's position. The right figure shows the agent's actual room and the ellipse without exception. The *lines* indicate possible routes to the exit region ignoring the spatial structure beyond the actual room. The shortest path from a doorway of the room to the exit area is shown *dashed*

inaccurate memories of the goals are not restricted to a point location but are represented by ellipses (see Fig. 1).

We assume that the agent searches a route leading him, preferably following the beeline, to the exit area. Therefore he chooses a doorway leading him as closely as possible to the destination area. Due to the fact that the agent has no knowledge about the remaining structure of the building his decision is only made by considering position and shape of the actual room (and its doors) and the ellipse representing the approximate position of the exit. Further rooms or rather their walls or obstacles beyond the actual room are not familiar to the agent. Hence, they are not taken into account within the decision making.

To determine the doorway which takes the agent as closely as possible to the ellipse the (lengths of the) shortest paths between every accessible doorway and the ellipse are calculated (see Fig. 1). The shortest path calculation is only performed under the consideration of the current room's walls (as obstacles). Even if the made assumption of an empty area beyond the current room may be inaccurate in most cases, this procedure will find the most appropriate doorway to come closer to the exit area if no spatial information of proceeding areas is available.

Depending on the length of their paths compared to paths from other possibilities the doorways are weighted differently. The doorway related to the shortest one of all shortest paths will be preferred by the pedestrian (see Fig. 1, right, dashed line).

If the agent has arrived at the target area (is located inside the ellipse) and there is still no exit in sight he has to rely on other information or strategies to look for the continuative way to the exit.

3   Examples

In the next section we demonstrate how the model presented performs in simple scenarios with respect to different degrees of spatial knowledge.

In every scenario an agent is situated in a room at the left lower corner of a fictional building (see Fig. 2) and searches a way to the outside. The entrance / exit can be found at the right lower corner.

3.1   Scenario 1: Cognitive Map Knowledge

With the help of this scenario we investigate the effects of using the modelling approaches concerning explicit cognitive map knowledge (see Sect. 2). The agent supposes the exit to be somewhere in the area depicted by the ellipse in the right lower region. At every choice point he decides to move to the direction taken him closer to the assumed area location of the exit.

Having started his journey the agent crosses the first corridor (lower left corner) heading to the opposing doorway as it is obviously the best choice to come closer to the exit area, assuming the lack of knowledge about the structure beyond the doors. However, as the agent recognises that he is located in a dead end he turns around trying to reach the exit area by moving through the crossing to the adjacent room. Eventually, he arrives at the corridor located in the middle of the building which enables him to travel to the right lower region of the building. Inside the ellipse depicting the exit area the agent proceeds to find the exit by exploring the rooms in the surrounding. He starts by heading to the nearest doorway. After having explored three further rooms within the exit area the agent finally reaches the exit.

Fig. 2 Trajectories of an agent situated in a fictional office building. The agent has access to cognitive map knowledge depicted with the help of the *ellipse*

Exit area

3.2 Scenario 2: Combination of Generalised and Cognitive Map Knowledge

Scenario 2 comprises the combination of generalised and cognitive map knowledge. To highlight the effects of this combination the agent is simultaneously provided with the ability to distinguish between common rooms and circulation rooms and with a directional sense of the exit's location. For this purpose the colour coded rooms are indicated as circulation rooms (see Fig. 3). Doorways leading to these rooms will be preferred by the agent. Furthermore, the agent is following the procedure explained in Sect. 2.

We assume the strategy to move to or to stay on a circulation room to be more expedient as to keep the direction to the destination. Following this assumption, the pedestrian will use circulation rooms even though he has to depart seriously from the beeline to the exit area.

Leaving the starting room the agent proceeds to the corridor in the middle of the building as it is the only adjacent corridor. Being located in the middle corridor the agent has to choose between three corridors. Obviously, the corridor in the right lower corner is the best possibility to come closer to the exit area. Within the exit area the agent again prefers the only proceeding corridor taking him eventually to the outside.

In this example scenario the agent is moving to the destination without making any detours. Hence, the search strategy (go to and stay on circulation rooms) and a vague idea about the location of the destination are sufficient in this example case.

Fig. 3 Trajectories of an agent situated in a fictional building. The agent has access to both cognitive map knowledge and generalised knowledge
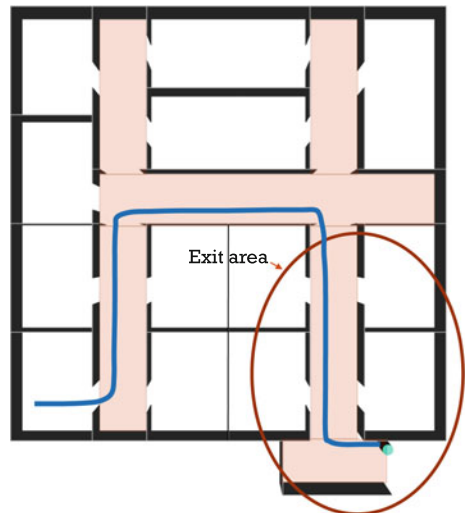
4 Summary and Outlook

The modelling approaches introduced in this paper provide simulated agents with restricted information about their environment instead of granting them access to global comprehensive knowledge about every part of the environment's structure. Additionally, the restricted information consists of uncertainties and inaccuracies. The information status of agents can be manipulated by modifying position and size or shape of ellipses modelling its actual cognitive map. In addition, it is conceivable to vary the knowledge degree of an agent compared to other agents by differing modifications.

Based on two examples we demonstrated the effects of different knowledge degrees. The first example showed that the agent does not instantly find an appropriate route to the outside by simply heading to the exit area. In the second example (Sect. 3.2) it has been shown that a vague, inaccurate idea of the destination's location in combination with the use of a search strategy is sufficient to find a route leading directly (without detours) to the desired destination.

Proceeding work implies the creation of a continuative framework modelling the human wayfinding process. On the one hand the framework is supposed to contain further mechanisms of the cognitive map, for example the involvement of landmarks and self localisation procedures. On the other hand it is supposed to include search strategies, recognition of signs and herding effects.

The affiliation of further models representing factors which contribute to exit choice decisions beside the wayfinding process is possible. Concerning further factors we mention sensory input models according to the evaluation of congestions [3] and smoke propagation [14].

References

1. Schadschneider, A., Klingsch, W., Klüpfel, H., Kretz, T., Rogsch, C., Seyfried, A.: Evacuation dynamics: empirical results, modeling and applications. In: Meyers, R.A. (ed.) Encyclopedia of Complexity and Systems Science, pp. 3142–3176. Springer, New York, NY (2009)
2. Crociani, L., Invernizzi, A., Vizzari, G.: A hybrid agent architecture for enabling tactical level decisions in floor field approaches. Transp. Res. Procedia **2**, 618–623 (2014)
3. Wagoum, A.U.K.: Route choice modelling and runtime optimisation for simulation of building evacuation. Schriften des Forschungszentrums Jülich **17** (2013)
4. Wiener, J.M., Büchner, S.J., Hölscher, C.: Taxonomy of human wayfinding tasks: a knowledge-based approach. Spat. Cogn. Comput. **9**(2), 152–165 (2009)
5. Kneidl, A.: Methoden zur abbildung menschlichen navigationsverhaltens bei der modellierung von fußgängerströmen. Ph.D. thesis, Technische Universität München (2013)
6. O'Keefe, J., Nadel, L.: The Hippocampus as a Cognitive Map. Clarendon Press, Oxford (1978)
7. Moser, E.I., Kropff, E., Moser, M.B.: Place cells, grid cells, and the brain's spatial representation system. Ann. Rev. Neurosci. **31**, 69–89 (2008)

8. Ekstrom, A.D., Kahana, M.J., Caplan, J.B., Fields, T.A., Isham, E.A., Newman, E.L., Fried, I.: Cellular networks underlying human spatial navigation. Nature **425**(6954), 184–188 (2003)
9. Tolman, E.C.: Cognitive maps in rats and men. Psychol. Rev. **55**(4), 189–208 (1948)
10. Golledge, R.G., Jacobson, R.D., Kitchin, R., Blades, M.: Cognitive maps, spatial abilities, and human wayfinding. Geogr. Rev. Jpn. Ser. B **73**(2), 93–104 (2000)
11. Ellard, C.: You Are Here: Why We Can Find Our Way to the Moon, But Get Lost in the Mall. Knopf Doubleday Publishing Group (2009)
12. Anderson, J.R.: Cognitive Psychology and Its Implications, 7th edn. Worth Publishers, New York (2010)
13. St. Pierre, M., Hofinger, G.: Human Factors und Patientensicherheit in der Akutmedizin, 3. aufl. edn. Springer, Berlin (2014)
14. Schröder, B., Haensel, D., Chraibi, M., Arnold, L., Seyfried, A., Andresen, E.: Knowledge- and Perception-based route choice modelling in case of fire. In: 6th International Symposium on Human Behaviour in Fire 2015, pp. 327–338. Interscience Communications Limited (2015)

Adaptive Tactical Decisions in Pedestrian Simulation: A Hybrid Agent Approach

Luca Crociani, Giuseppe Vizzari and Stefania Bandini

Abstract This paper presents the tactical level component of a hybrid agent architecture in which these decisions are enacted at the operational level by means of a floor-field based model, in a discrete simulation approach. This allows the agent to take decisions based on a static a-priori knowledge of the environment and dynamic perceivable information on the current level of congestion of visible path alternatives.

1   Introduction

Simulating human decision making activities and actions is extremely challenging, even if we focus on walking behaviour: different types of decisions are taken at different levels of abstraction: [8] provides a well-known scheme to model the pedestrian dynamics, describing 3 levels of behaviour: (i) *Strategic level*, managing abstract plans and final objectives motivating the overall decision to move (e.g., 'I am going to the University today to follow my courses and meet my friend Paul'); (ii) *Tactical level*, constructing sequences of activities to achieve the defined objectives (e.g., 'I'll take the 7:15 AM train from station X, get off at Y and then walk to the Department, then …'); (iii) *Operational level*, physically executing the defined plans (i.e.,. creating a precise walking trajectory, such as a sequence of occupied cells and related simulation turn in a discrete simulation).

Most of the literature has been focused on the reproduction of the physics of the system, so on the lowest level. Relevant recent works, such as [6, 9], start exploring the implications of tactical level decisions during evacuation. In particular, [6] modifies

L. Crociani (✉) · G. Vizzari · S. Bandini
CSAI Research Center, University of Milano-Bicocca, Milan, Italy
e-mail: luca.crociani@disco.unimib.it

G. Vizzari
e-mail: giuseppe.vizzari@disco.unimib.it

S. Bandini
e-mail: stefania.bandini@disco.unimib.it

S. Bandini
RCAST, The University of Tokyo, 4-6-1 Komaba, Meguro-ku, Tokyo 153-8904, Japan

the floor-field Cellular Automata approach for considering pedestrian choices not based on the shortest distance criterion but considering the impact of congestion on travel time. Wagoum[9] explores the implications of four strategies for the route choice management, given by the combination of applying the shortest or quickest path, with a local (i.e., minimise time to vacate the room) or global (i.e., minimise overall travel time) strategy. The global shortest path is calculated with the well-known Floyd–Warshall algorithm, implying computational times that can become an issue by having a large number of nodes or by considering special features in the simulated population (i.e., portion of the path where the cost differs from an agent to another). The work in this paper will propose an alternative and efficient approach to find a global path, where each agent will be able to consider additional costs in sub-paths without adding particular weight to the computation.

We must emphasise the fact that the measure of success and validity of a model is not the *optimality* with respect to some cost function, as in robotics, but the *plausibility*, the similarity of results to data acquired by means of observations or experiments. Putting together *tactical* and *operational* level decisions in a comprehensive framework, preserving and extending the validity that, thanks to recent extensive observations and analyses (see e.g., [2]), can be achieved at the operational level, represents an urgent and significant open challenge.

This paper presents the tactical level component of a hybrid agent architecture in which these decisions are enacted at the operational level by means of a floor-field based model, in a discrete simulation approach.

2   Brief Description of the Approach

The approach presented in this paper represents an extension and completion of a work started in [4], where a first hybrid agent architecture was defined, employing a floor-field operational level and a first knowledge-based tactical level component. The representation of the environment was derived by spatial annotations that were used to define obstacles, areas in which agents entered the simulation, areas that were target of their movements and way points. The derived spatial representation did not include information about distances among the areas that were mapped to nodes of a graph. In [5], this spatial representation was enhanced both to include this information, that is actually necessary to grant the agents proper way-finding capabilities, and also to consider computational issues related to model construction and execution. In fact, instead of having the agents performing individually path planning operations that required the inspection of the spatial representation, we decided to define and construct a data structure called *Paths Tree* comprising all plausible paths towards a destination and the associated expected travel cost not considering potential congestions in the relevant areas.

In the model set-up phase (while constructing the floor fields guiding agents at the operational level), this kind of structure is constructed for each possible destination and then agents can access these shared structures for finding the most appropriate

path towards its destination. While paths trees comprise static information about the travel time in free flow conditions, each agent is also granted the ability to estimate the added cost due to congestion close to the way points it is able to perceive: in this way, agents are able to choose a longer but non congested path, instead of a shorted one that would imply a significant queuing time. Agents are also able to re-evaluate an adopted plan, considering additional freshly acquired information (i.e., the perceived congestion in an area they just entered), and potentially perform a re-planning operation. Additional information about paths trees formal definition and construction algorithms are omitted for sake of space and they are available in [5].

3 Experiments and Evaluation

In order to show the potential and the possibility to fine tune the proposed approach, the evacuation in a hypothetical scenario has been simulated with a consistent incoming flow of people. A graphical representation of the environment and flow configuration is depicted in Fig. 1a: it illustrates a sample situation in which two flows of
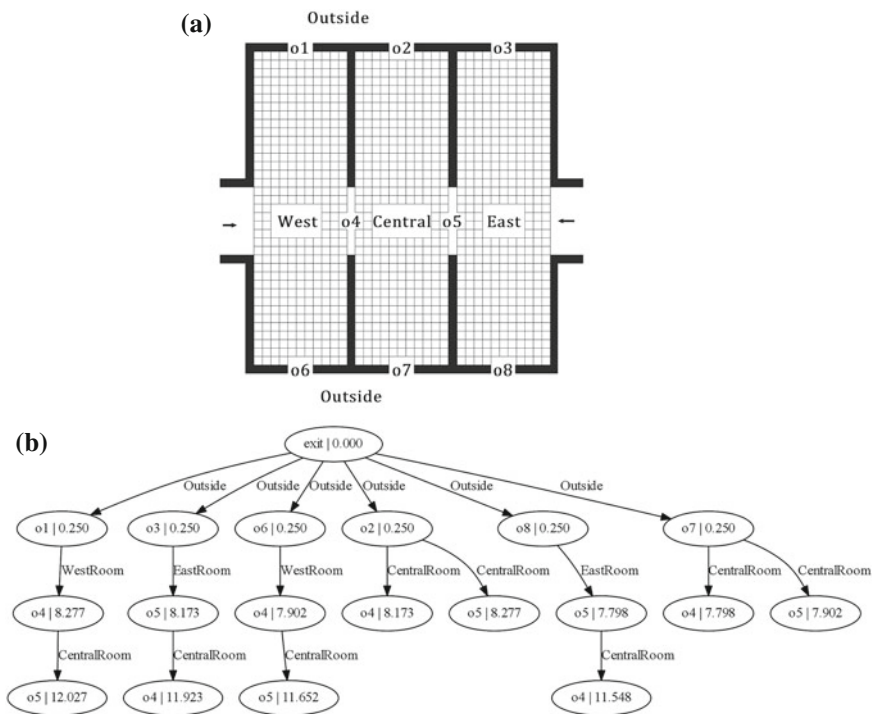
Fig. 1 The experimental scenario (**a**) and the associated paths tree (**b**)

(a)

(b)
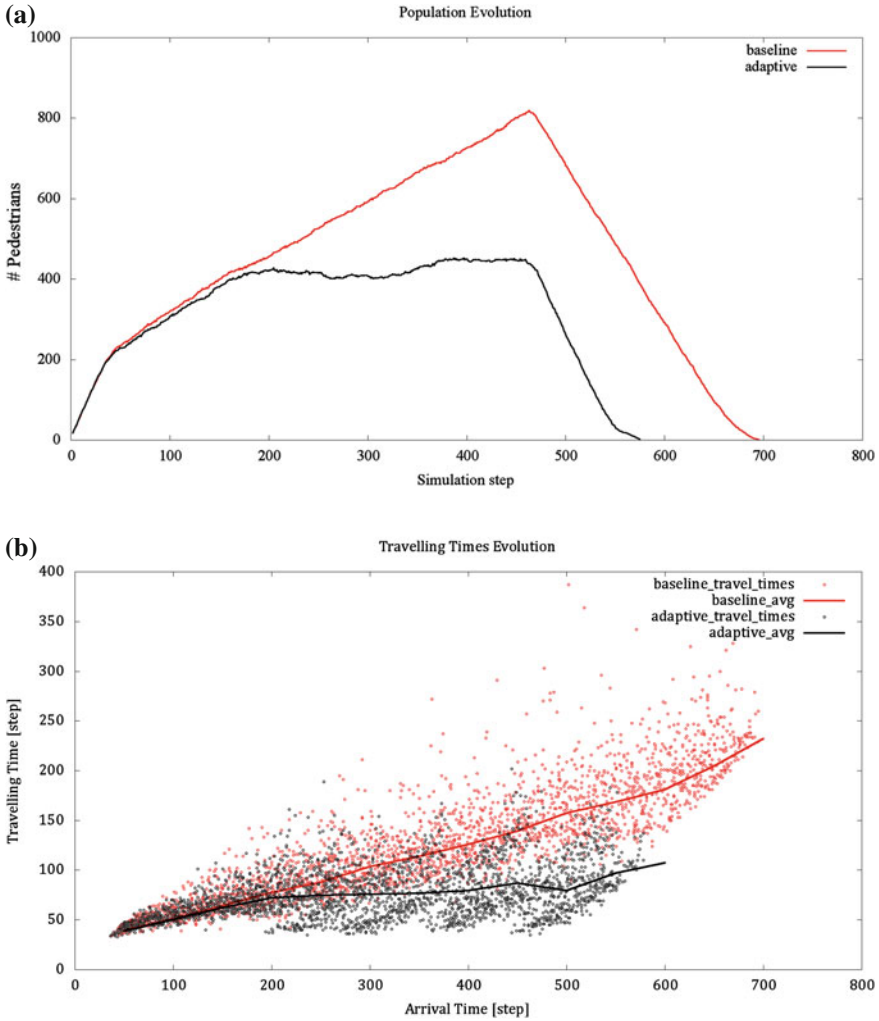
Fig. 2 Evolution over time. Number of pedestrians still in the scenario at a given time (**a**). Travel time for pedestrians entering the simulation environment at a given time (**b**)

pedestrians enter an area with six exits, distributed among 3 equal rooms, at a rate of 10 pedestrians per second. An important peculiarity is the slightly asymmetrical configuration of the environment, that causes shorter distances towards the three southern exits. This is reflected by the illustrated paths tree in Fig. 1b where, to give an example, the paths starting from *o4* and *o5* and leading out through *o2* take a little more time than the ones going out by using *o7*.

A diagram showing the evolution of the number of pedestrians still in the scenario through time is depicted in Fig. 2a and a graph showing the evolution of
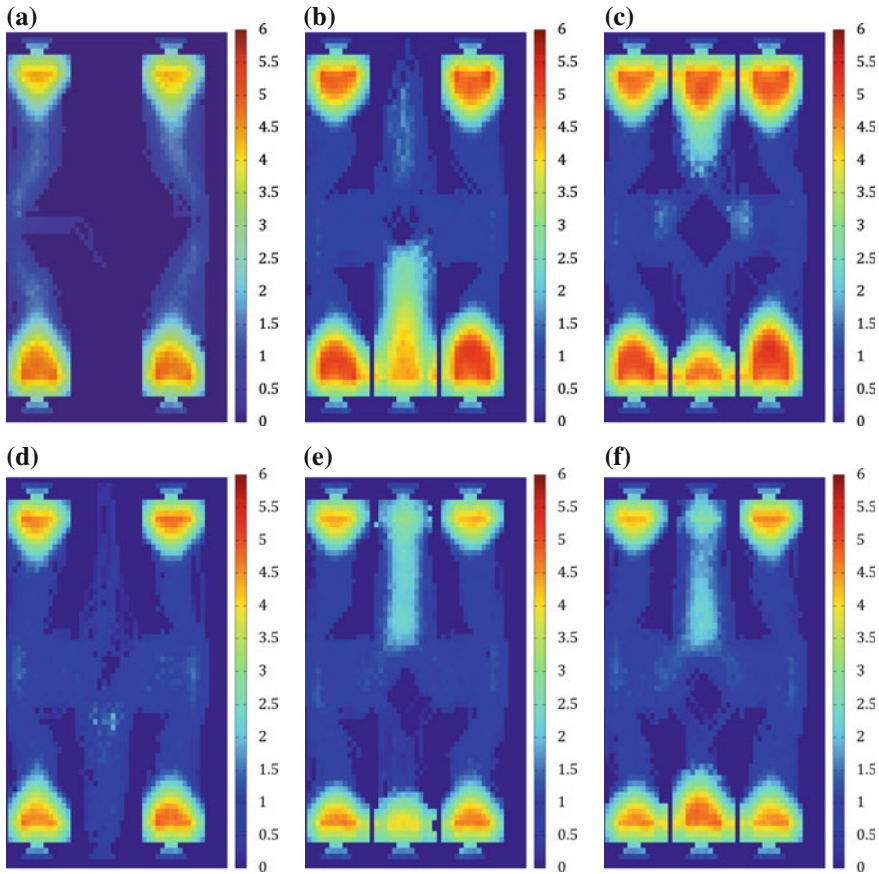
Fig. 3 The test scenario respectively without and with a random perturbation of the agent estimated travel time. Step 150–200, w/o RE (**a**); step 300–350, w/o RE (**b**); step 450–500, w/o RE (**c**); step 150–200, with RE (**d**); step 300–350, with RE (**e**); step 450–500, with RE (**f**)

travel time for pedestrians entering the simulation environment at a given time in Fig. 2b. Although the adopted approach is not actually aimed at finding the optimal planning solution for pedestrians, minimising the overall evacuation time, but rather a plausible one from the individual pedestrian perspective, the difference between the baseline tactical level, based on the shortest path choice, and the adaptive planning strategy, considering also the level of congestion, is apparent.

The slight asymmetry of the environment actually affected the results of the simulations, also shown with cumulative mean density maps [3][1] in Fig. 3.

---

[1]These heat maps describe the mean local density value in each cell. It is calculated in a time window of 50 steps where, at each step, only values of occupied cells are collected.

In particular, the results of two simulations in which different approaches have been implemented for the dynamic estimation of the path travelling times by the agents are shown. In the first approach, shown in the top row, all the agents perceived the same *congestion time* for the openings that they can detect during the simulation (i.e., the travel time corrected considering the path delay discussed in the previous section). In the second approach, instead, a random error of $\pm 10\,\%$ has been added to the overall calculation of the travelling time $Time(p)$ in order to consider the fact that pedestrians do not have an *exact* estimation of distances and delays caused by perceived congestion, in a more common sense spatial reasoning framework [1].

By comparing the results it is possible to notice that, counter-intuitively, the insertion of the random perturbation caused an optimisation of the flows in this overcrowded scenario. In the first 100 steps of the simulations, the dynamics for the two approaches is similar and described by the missed usage of the central room, since the distance between the northern and southern exits is quite small. The less precise calculation causes the agents to start using the central room and associated exits earlier than in the precise delay estimation case, in particular, around 130th step versus 150th step in the first scenario, generating lower level of densities and, thus, higher outgoing flow rates. Moreover, this error balances the attractiveness of middle southern and northern exits that are more evenly adopted than in the precise calculation approach (as shown in Fig. 3b, e, leading not only to a more efficient but especially more plausible space utilisation.

Finally, to analyse the overall trend of the computational times during the simulations, an additional simulation scenario has been designed and executed. Both benchmarks have been executed in a laptop PC with CPU Intel(R) i7 @ 2.3 Ghz, 16 GB RAM and operative system windows 8.1-x64.

The scenario consists of a relatively large area (200 m $\times$ 200 m) composed of three large rooms connected one by one by three doors of different sizes: a large one of 5 m and two small ones of 2 m. The environment configuration is shown in Fig. 4a. Figure 4b shows the results of the computational times analysis. It is possible to notice that the trend is linear (at least for the considered number of agents) and the results are characterised by a relatively small overhead due to the tactical level computation. The tactical level affects the time by means of three main activities, which are the perception of the congestion in the chosen path, the possible route recomputation and the calculation of the block probabilities for the estimation of the congestion time. The plan re-computation (the purple line in the figure) is the most significant one, since it 'bounces' from having the lowest value between the three activities to a much higher one sometimes also overcoming the floor field update of the operational level. In the end the trend of these activities is as well linear and the overall turn computation time remains lower than the actual simulated time until about 1000 agents are simultaneously simulated.
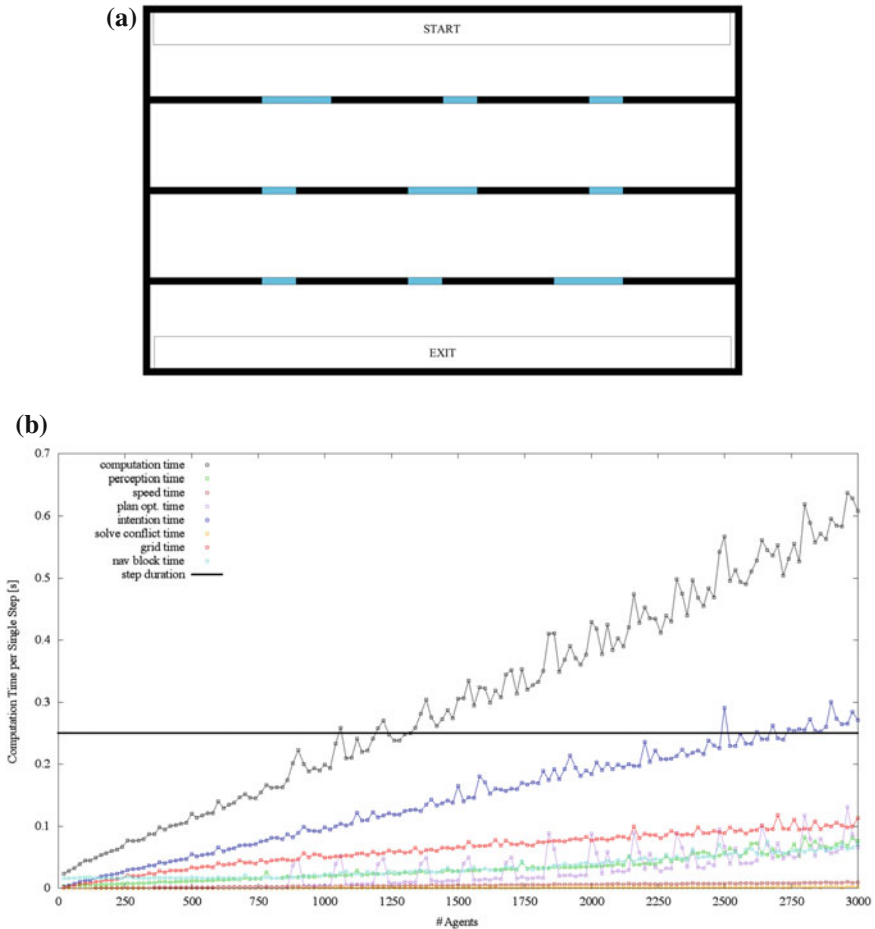
Fig. 4 The benchmark scenario used for the analysis of the computational times of the tactical level. Set-up (**a**); results (**b**)

4   Conclusions

The paper has presented a hybrid agent architecture for modelling tactical level decisions in pedestrian simulations. The agents make decisions based on a static a-priori knowledge of the environment and dynamic perceivable information on the current level of congestion of visible path alternatives. The model was experimented in a sample scenario showing the adequacy in providing adaptiveness to the contextual situation while preserving a plausible overall pedestrian dynamic: congestion is detected and, when possible, longer trajectories are adopted granting overall shorter travel times. The actual validity of this approach must still be proven, both in evacuations and other kinds of situations: this represents an open challenge, since there

are no comprehensive data sets on human tactical level decisions and automatic acquisition of this kind of data from video cameras is still a challenging task [7].

References

1. Bandini, S., Mosca, A., Palmonari, M.: Common-sense spatial reasoning for information correlation in pervasive computing. Appl. Artif. Intell. **21**(4–5), 405–425 (2007)
2. Boltes, M., Seyfried, A.: Collecting pedestrian trajectories. Neurocomputing **100**, 127–133 (2013)
3. Castle, C., Waterson, N., Pellissier, E., Le Bail, S.: A comparison of grid-based and continuous space pedestrian modelling software: analysis of two uk train stations. In: Pedestrian and Evacuation Dynamics, pp. 433–446. Springer (2011)
4. Crociani, L., Invernizzi, A., Vizzari, G.: A hybrid agent architecture for enabling tactical level decisions in floor field approaches. Transp. Res. Procedia **2**, 618–623 (2014)
5. Crociani, L., Piazzoni, A., Vizzari, G., Bandini, S.: When reactive agents are not enough: tactical level decisions in pedestrian simulation. Intell. Artif. **9**(2), 163–177 (2015)
6. Guo, R.Y., Huang, H.J.: Route choice in pedestrian evacuation: formulated using a potential field. J. Stat. Mech. Theor. Exp. **2011**(4), P04018 (2011)
7. Khan, S.D., Vizzari, G., Bandini, S.: Identifying sources and sinks and detecting dominant motion patterns in crowds. Transp. Res. Procedia **2**, 195–200 (2014)
8. Schadschneider, A., Klingsch, W., Klüpfel, H., Kretz, T., Rogsch, C., Seyfried, A.: Evacuation dynamics: empirical results, modeling and applications. In: Encyclopedia of Complexity and Systems Science, pp. 3142–3176. Springer (2009)
9. Wagoum, A.K., Seyfried, A., Holl, S.: Modelling dynamic route choice of pedestrians to assess the criticality of building evacuation. Adv. Complex Syst. **15**(7), 15 (2012)

Evacuation Dynamics of Asymmetrically Coupled Pedestrian Pairs

Frank Müller and Andreas Schadschneider

Abstract We propose and analyse extended floor field cellular automaton models for evacuation dynamics of inhomogeneous pedestrian pairs which are coupled by asymmetric group interactions. Such pairs consist of a leader, who mainly determines the couple's motion and a follower, who has a defined tendency to follow the leader. Examples for such pairs are mother and child or two siblings of different age. We examine the system properties and compare them to the case of a homogeneous crowd. We find a strong impact on evacuation times for the regime of strong pair coupling due to the occurrence of a clogging phenomenon. In addition, we obtain a non-trivial dependence of evacuation times on the followers' coupling to the static floor field, which carries the information of the shortest way to the exit location. In particular we find that systems with fully passive followers, who are solely coupled to their leaders, show lower evacuation times than homogeneous systems where all pedestrians have an equal tendency to move towards the exit. We compare the results of computer simulations with recently performed experiments.

1   Introduction

Human crowds and pedestrian traffic are usually composed of both social groups and individuals. Recent empirical studies brought to attention that in this context social groups are rather the normality than the exception (see several contributions in [1]). Moussaïd et al. [2] observed in a field study that up to 70 % of pedestrians walk in social groups and Xi et al. [3] found that most pedestrians walk in two-person-groups whereas individual pedestrian traffic is only second frequent. The high relevance of two-person-groups shows the importance of a deeper understanding of the impact such groups impose on evacuation processes.

F. Müller (✉) · A. Schadschneider
Institut für Theoretische Physik, Universität zu Köln, 50937 Cologne, Germany
e-mail: fm@thp.uni-koeln.de

A. Schadschneider
e-mail: as@thp.uni-koeln.de

We recently introduced models for evacuation processes including social groups which are inspired by methods of non-equilibrium physics [4]. From the perspective of physics the pivotal characteristic of these models is that social groups are *cohesive*, i.e. group members tend to maintain a spatial coherence. The current work focuses on asymmetrically coupled two-person-groups and aims to provide models for such pairs in evacuation processes. Being the smallest social group two-person-groups still can be very diverse. The strength and symmetry of interaction as well as the group members' level of orientation can differ significantly. Thus it has to be verified which set of models is applicable for simulations. The model types studied here can e.g. describe pairs like mother and child or siblings of different age where one part will dominantly determine the motion and the other part will have a defined tendency to follow. The dominating part will be called *leader* and the following part will be called *follower*. The proposed models are used for computer simulations and characteristic effects will be discussed.

The basic underlying model used for the computer simulations is the floor field cellular automaton model (FFCA). It is a stochastic model defined on a 2-dimensional grid with time evolution in discrete steps. A cell can be either empty or occupied by a particle representing a pedestrian. Particles can move by transition to a neighbouring cell. The transition will take place with a transition probability arising from different floor fields which encode the tendency to move towards the room's exit and the interaction between pedestrians—here the group cohesion. Further details and general properties of the FFCA can be found in [4].

The evacuation simulations are performed on a standard grid of 63×63 cells with a moderate pedestrian density of $\rho = 0.02$. Observables are averaged over at least 500 runs.

2   The DGFF and MTFF as Mediators of Group Interaction

The DGFF and MTFF are the central components which create the group cohesion in the models studied here. We introduced both concepts in [4] and will recap the most important properties in the following.

2.1   Properties of the DGFF

In the first proposed model the DGFF mediates the interaction between a leader and the follower. An FFCA with DGFF provides a model for crowds with two-person-groups which have a bond with a likelihood to permanently break up in higher densities.

The DGFF extends the dynamic floor field (DFF) introduced in [5] in several respects. It shares the basic idea that pedestrians increase a field value in the cell they leave when moving to a neighbouring cell while decay and diffusion can modify it

over time. This accounts for the important property that the DGFF is not related to position, but to the movement the leader has performed in preceding time steps. Each couple interacts via its individual DGFF. Only when the leader moves the field is built up and only the follower who is associated with the respective leader reacts on this leader's DGFF. If we do not take the SFF into account followers are most likely to transit to cells with a high associated DGFF value. This causes group members to tend moving on the same trajectory. The full transition probability for the follower including the SFF and the DGFF is

$$p_{ij}^{F(s)} = N \exp\left(k_S^F S_{ij}\right) \exp\left(k_D^F D_{ij}^{F(s)}\right) (1 - \eta_{ij})\xi_{ij} . \tag{1}$$

Here, $p_{ij}^{F(s)}$ is the transition probability for the follower of pair s, k_S^F is the coupling constant to the static floor field for followers and k_D^F is the coupling constant to the DGFF for followers, determining the coupling strength to this field. N is a normalisation term. The product $(1 - \eta_{ij})\xi_{ij}$ guarantees the exclusion principle and avoids transition into wall cells, see e.g. [5].

The transition probability for the leader only considers the SFF, which encodes the shortest way to the exit:

$$p_{ij}^{L(s)} = N \exp(k_S^L S_{ij})(1 - \eta_{ij})\xi_{ij} . \tag{2}$$

The DGFF can be understood as a field composed of field quanta (bosons[1]) with defined internal degrees of freedom. E.g. each field quantum carries the information by which particle it was produced. This allows particles to interact only with bosons of a special type. In particular it enables a follower particle to ignore all bosons, but these of its leader. The leader particles do not react with any boson type. This way an asymmetric group interaction can be established while self-interaction of particles is completely avoided.

It is an important characteristic of the DGFF concept that a moving particle increases the DGFF by $m \gg 1$ instead of only $m = 1$ as it is the case in [5]. Small values of m would not lead to sufficiently structured boson traces the followers could continuously follow since only one particle will contribute to the DGFF whereas in case of the DFF all particles contribute to the field. In addition a diffusion parameter $\alpha > 0$ is important for continuous group cohesion as it broadens the boson trace. Both factors highly increase the probability that followers do not lose the tracks of their leaders. Figure 1a illustrates the strong dependency of the average distance between leaders and followers d on the diffusion parameter α and the boson multiplicity m. d is a measure for group cohesion. While $m = 1$ does not create any noticeable pair bond, $m = 400$ causes strong group cohesion.

---

[1]Despite the denomination, 'bosons' should not be considered as quantum mechanical particles.

2.2 Construction of the Moving Target Floor Field

As explained in Sect. 2.1 the DGFF is solely increased in a cell when the leader leaves the cell by moving to a neighbouring cell. Thus the DGFF is depending on the leader's movement. The question arises how evacuation dynamics changes when the underlying floor field is solely depending on the leader's position. This is the case with the second model we examine here—the moving target floor field (MTFF).

In the FFCA model with MTFF group cohesion is achieved by an asymmetric interaction related to the relative position of the leader with respect to the follower. Every leader of pair s induces a group-specific floor field $M^{(s)}$ in the von Neumann neighbourhood of his associated follower:

$$M_{ij}^{(s)}(T) = \max_{(\tilde{i}, \tilde{j})} \left\{ \sqrt{(i_L(T) - \tilde{i})^2 + (j_L(T) - \tilde{j})^2} \right\} - \sqrt{(i_L(T) - i)^2 + (j_L(T) - j)^2}$$

(3)

$(i_L(T), j_L(T))$ denotes the position of the leader at time step T. The first term on the r.h.s. is a normalisation term where $(\tilde{i}, \tilde{j})$ runs over the cells in the von Neumann neighbourhood of the follower.

The MTFF contributes to the transition probabilities in an analogous manner as the DGFF in Sect. 2.1. The total transition probability of the follower F of pair s is

$$p_{ij}^{F(s)} = N \exp((k_S^F S_{ij} + k_M M_{ij}^{(s)})(1 - \eta_{ij})\xi_{ij} .$$

(4)

3 Impact of Pair Cohesion on Evacuation Dynamics

In this section we will investigate the question how the fragmentation of a pedestrian crowd into asymmetrically coupled pedestrian pairs impacts evacuation dynamics and how the resulting evacuation process compares to the scenario with a homogeneous crowd without pair bonds. We will analyse both DGFF and MTFF systems and compare the results.

3.1 Comparison of DGFF, MTFF and Homogeneous Model

For the purpose of comparison with a homogeneous crowd the model is configured such that leaders and followers are equipped with the same level of orientation, which is realised by an equal coupling constant with respect to the SFF. When $k_D^F = 0$ the configuration $k_S^L = k_S^F$ coincides with a homogeneous crowd with no interaction between the pedestrians.

First, we turn to the model with DGFF. For growing k_D^F the homogeneous crowd is fragmented into asymmetrically coupled pairs which increasingly maintain proximity and tend to move on the same trajectory. How will this impact evacuation dynamics?
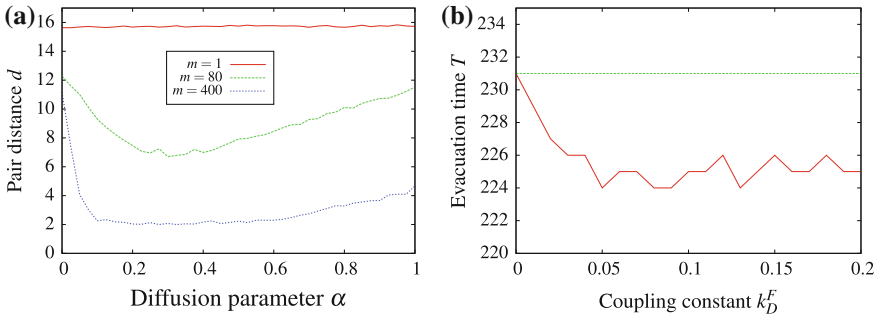
Fig. 1 Different views on the DGFF model. Dependence of the average pair distance d on the diffusion parameter α for different values of the boson multiplicity m (**a**), Dependence of T on k_D^F (**b**). The *dashed line* refers to $T = T_{hom}$, which is the average evacuation time of a homogeneous crowd without pair bonds

Figure 1b shows the dependence of T on k_D^F for the DGFF model: The coupling in pairs slightly improves the evacuation process. The effect is small, but it is clearly visible that T drops for growing k_D^F. The drop takes place in a comparably small interval since the boson multiplicity is high at $m = 400$. It is interesting to note that the effect does not coincide with a lower average number of conflicts per time step. An analysis of this number shows that conflicts are even increased for $k_D^F > 0$, but still T is lowered. The higher number of conflicts is due to the group cohesion. The continuous proximity of group members increases the likelihood that these choose the same cell for a transition which leads to an overall increase of conflicts.

The improvement of evacuation time T in this model becomes comprehensible when recalling the nature of the DGFF. It encodes spatio-temporal information about the path the leader has successfully moved on—not only spatial information about the leader. Without movement no DGFF builds up. Therefore, the information contributes to choose *successful* paths through the crowd.

The coupling mechanism of the MTFF highly differs from that of the DGFF since it is not related to the movement of the leader, but to his position. In fact simulations show that this difference translates to measurable differences in the respective evacuation processes. Figure 2a is the analogon of Fig. 1b for the MTFF model. It shows a non-trivial dependence of the evacuation time T on the coupling parameter k_M. The dashed line in Fig. 2a refers to the average evacuation time T of a homogeneous system without pair bonds. In both figures coupling to the SFF is at $k_S^L = k_S^F = 0.8$. In the domain of $k_M \lesssim 0.6$ the coupling in pairs results in a lower T while for $k_M \gtrsim 0.6T$ is increased. T remains nearly constant for $k_M \gtrsim 4$ ($T \approx 258$) until clogging processes increase T again. Clogging is discussed in Sect. 3.3.
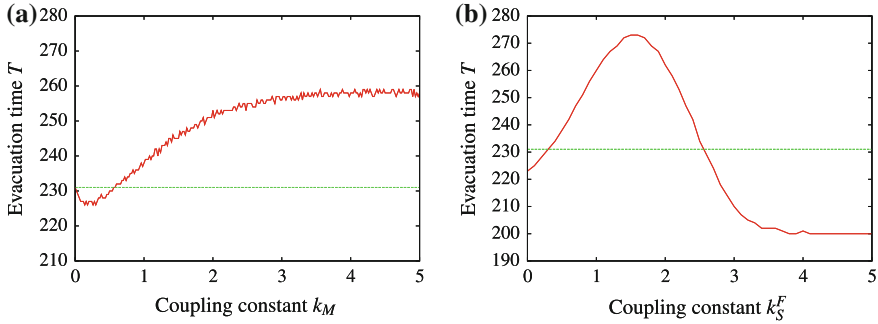
Fig. 2 Different views on the average evacuation time T for systems with MTFF. The *dashed line* visualises $T = T_{hom}$, which is the average evacuation time of a homogeneous crowd without pair bonds and $k_S = 0.8$. Dependence of evacuation time T on the coupling strength k_M in a configuration with $k_S^L = k_S^F = 0.8$ (**a**). Dependence of evacuation time T on k_S^F which controls the follower's coupling to the SFF. Pair coupling strength is constant at $k_M = 2$ and $k_S^L = 0.8$ (**b**)

3.2 Influence of the Follower's Coupling to the Static Floor Field

In this section we shift the point of interest to the question how the coupling of the follower to the static floor field (SFF) k_S^F influences the evacuation process. Apart from the coupling to the leader via MTFF the follower is also coupled to the SFF, which encodes the shortest way to the exit. $k_S^F = 0$ means that the follower's motion is not oriented at the exit at all whereas $k_S^F \to \infty$ leads to a deterministic movement on the shortest path to the exit. k_S^F can be interpreted as the follower's orientation towards the exit or more generally as the ability and will to reach the exit himself.

Figure 2b shows the resulting average evacuation time for a system with $k_M = 2$. The dashed line depicts the evacuation time T_{hom} of the homogeneous reference system without pair coupling and equal k_S. It is a counter-intuitive result that fully passive followers, who do not have any tendency to move to the exit themselves lead to a more efficient evacuation with lower evacuation times than a homogeneous crowd with an equally good orientation towards the exit. It appears to be beneficial if followers are solely led by their leaders. In contrary strong pair coupling together with the equally good orientation towards the exit ($k_S^L = k_S^F = 0.8$) slows down the evacuation. This result was also found in Fig. 2a.

The domain of $k_S^F \gtrsim 2.5$ where T falls below T_{hom} again arises from a situation where followers have such good ability to reach the exit themselves that despite their pair bond they overtake their leaders and reach the exit first. Here the overall average evacuation time benefits from the fast evacuation of the followers.

3.3 Clogging and Gridlocks

In [4] we had found clogging phenomena for the asymmetric fixed-bond leader–follower model. In this model the pair bond is fully fixed as for every cell transition the follower is positioned on the cell the leader had occupied previously. The pair distance is always $d = 1$. The question remained if such clogging phenomena can be found when the bond is dynamic and d can take on arbitrary values. Indeed this is the case for systems with MTFF.

In Sect. 3.1 it was addressed that for high k_M and the resulting high group cohesion clogging starts to increase the average evacuation time T. Figure 3a shows such increase. Here T fluctuates strongly and the standard deviation of T is accordingly high. The phenomenon occurs due to followers who maintain the nearest possible position to their leaders in front of the exit and impede their leaders from reaching the exit. If a configuration occurs where followers completely shield their leaders from exiting no particle will be evacuated until the situation dissolves. Figure 3b displays an example of such situations. For very high values of k_M the shielding followers have a nearly vanishing probability to ever leave the cell next to their leader and it comes to a final stop of the evacuation (gridlock). This is a situation which is not found in reality. However, clogging due to pairs who do not let go each other in a high density situation is well conceivable and a possible source of impediment in evacuation processes through a narrow door. The high standard deviation in the domain of clogging indicates that evacuation scenarios become increasingly unpredictable once clogging becomes a likely effect during the evacuation.

The described clogging phenomenon does not occur in systems with DGFF as this field is solely built up by the motion of the respective leader. While the MTFF only encodes spatial information about the leader the DGFF encodes spatio-temporal information about the path the leader has successfully moved on. When it comes to highly congested states the DGFF is only rarely increased and the decay mechanism
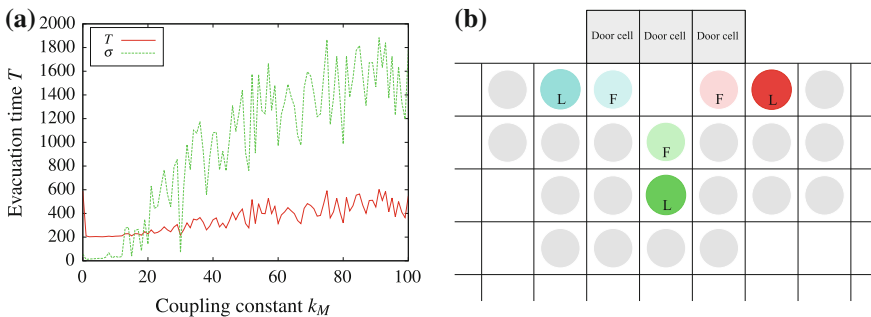
Fig. 3 Clogging in systems with MTFF. Dependence of evacuation time T on the coupling strength k_M with $k_S^L = 0.8$ and $k_S^F = 0.2$. High values of k_M lead to increased values of T and high $\sigma(T)$ due to clogging (**a**). Example for a typical clogging situation for a system with door width $d = 3$ (**b**)

brings the field strength down to low values or zero. Then movement is mainly governed by the SFF and particles start moving towards the exit again. Thus, systems with DGFF cannot develop long-term clogging or even gridlocks.

4 Conclusion

Quantitatively for moderate coupling both models show only small deviations from the average evacuation time T of a homogeneous reference system without pair coupling. This result is in line with the evacuation experiments we recently performed with students [6]. However, qualitatively the two models differ significantly from each other as the DGFF model always leads to a decreased T while the MTFF model shows two domains with decreased T for low and increased T for high coupling strength k_M. At present the collected data from experiment does not provide sufficient statistical significance to rank one model over the other. Further experiments will contribute to investigate this question.

For the MTFF system our simulations have shown a non-trivial dependency of T on k_S^F. The fragmentation of a crowd into couples with fully passive followers results in a more efficient evacuation process than a homogeneous crowd.

In the domain of strong coupling to the MTFF clogging leads to an increase of T and a high standard deviation, which makes the average evacuation time T less meaningful and a single evacuation process less predictable. This is an important factor when simulations are to predict evacuation times, e.g. for evacuation assistants to support decisions about optimum evacuation routes during emergencies.

References

1. Knoop, V., Daamen, W. (eds.): Proceedings of Traffic and Granular Flow 2015. Springer (In print)
2. Moussaïd, M., Perozo, N., Garnier, S., Helbing, D., Theraulaz, G.: The walking behaviour of pedestrian social groups and its impact on crowd dynamics. PLoS ONE **5(4)**, e10047 (2010)
3. Xi, J., Zou, X., Chen, Z., Huang, J.: Multi-pattern of complex social pedestrian groups. Transp. Res. Procedia **2**, 60–68 (2014)
4. Müller, F., Wohak, O., Schadschneider, A.: Study of influence of groups on evacuation dynamics using a cellular automaton model. Transp. Res. Procedia **2**, 168–176 (2014)
5. Kirchner, A., Schadschneider, A.: Simulation of evacuation processes using a bionics-inspired cellular automaton model for pedestrian dynamics. Phys. A **312**, 260–276 (2002)
6. von Krüchten, C., Müller, F., Svachiy, A., Wohak, O., Schadschneider, A.: Empirical study of the influence of social groups in evacuation scenarios. In: Knoop, V., Daamen, W. (eds.) Proceedings of Traffic and Granular Flow 2015. Springer (In print)

Granulometric Distribution and Crowds of Groups: Focusing on Dyads

Andrea Gorrini, Giuseppe Vizzari and Stefania Bandini

Abstract Pedestrian flows are characterised by the preponderant presence of groups, with particular reference to dyads. The paper presents a research focused on group and age-driven pedestrian behaviour in an urban crowded scenario. Data analysis was performed by using an open source tracker tool. Results showed that in situation of irregular flows (LOS B) dyads walked 30 % slower than singles, and that elderly walked 40 % slower than adults. The achieved results have been used towards the validation of the simulation platform `ELIAS 38`, with reference to the representation of the granulometric distribution of groups and heterogeneous speed profiles.

1 Introduction

Traditional approaches did not consider the impact of social relationships among people within the crowds [15] (generally defined as homogeneous systems composed of single entities), but more recent empirical contributions [12] have showed that pedestrian flows in crowded scenarios are characterised by the preponderant presence of groups. Analyses of crowd phenomena not considering this aspect have a reduced accuracy since grouping was found to negatively impact flow rate, speed and evacuation time. This is due to the difficulty in movement coordination among members (depending on the density level in the environment) [11], the need to maintain spatial cohesion to communicate while walking (i.e. *proxemic behaviour*) [9] and/or the urgency to evacuate together in case of emergency (i.e. *affiliative behaviour*) [10].

A. Gorrini (✉) · G. Vizzari · S. Bandini
Department of Informatics, Systems and Communication, CSAI Research Center,
University of Milano-Bicocca, Viale Sarca 336, 20126 Milan, Italy
e-mail: andrea.gorrini@unimib.it

G. Vizzari
e-mail: giuseppe.vizzari@disco.unimib.it

S. Bandini
e-mail: stefania.bandini@disco.unimib.it

S. Bandini
RCAST, The University of Tokyo, 4-6-1 Komaba, Meguro-ku, Tokyo 153-8904, Japan

Early studies [6] highlighted that the granulometric distribution of crowds is strongly affected by two-members groups (i.e. *dyads*), the most frequent and basic interacting elements of a crowd. Results achieved from a large data collection campaign [8] showed that pedestrian flows were characterised by 16 % single pedestrians, 44 % dyads, 17 % triples and 23 % groups of 4 or more members.

The presence of groups and their granulometric distribution in terms of size, but also the walking speed, are largely determined by the motivation by which people are gathered or move through a certain environment, and/or by the type of event they are participating to (i.e. *crowd profiling*) [4]. For example, train stations are mainly characterised by the presence of fast moving single commuters, while other venues such as pavilions or stadia are more often characterised by the presence of informal or guided groups of visitors, generally moving slower than the former type of pedestrian.

Moreover, pedestrian density widely affects the locomotion and proxemic behaviour of groups (i.e. *spatial patterns*) [5]. At low density dyad members walk side by side, forming a line abreast pattern but, when density increases, the linear formation turns into a diagonal pattern, with an individual positioned slightly behind in comparison to the other one. In situation of high density, the spatial distribution of the dyad members leads to a river-like pattern to minimise collisions with other pedestrians. Groups composed of three or more members often split into single individuals and dyads, in a dynamic process of mutation of the spatial configuration of the group (e.g., V-like pattern, spherical and ellipsoidal pattern) [11].

In this framework, the paper presents a research based on a field observation focused on small size group behaviour (i.e. *dyads*) in situation of irregular density condition. This is aimed at measuring the combined effect of grouping and density on pedestrians'speed, trajectories and spatial behaviour (e.g., spatial distance and degree of alignment between dyad members). Moreover, we focused on the implications of age on pedestrian behaviour. Compared to adult pedestrians, elderlies are characterised by lower speed and larger distances among group members while walking [3]. This is respectively due to the decreased perceptive and locomotor skills [16] and a subjective sense of psychological vulnerability [18].

Data collection was based on the video recorded observation of pedestrian dynamics in an urban crowded commercial-touristic walkway in Milan (the Vittorio Emanuele II gallery). Past data analysis of the video was manually performed, to achieve preliminary results on the observed dynamics [1] and later it led to the definition of a proper procedure for the detection of groups in the observed pedestrian population: a checklist (see Table 1), comprising a set of locomotion, communication and physical indicators, was used to detect groups and elderly pedestrians (approximately between 65 and 70 years old).

The data analysis performed for the present work used the Tracker Video Analysis and Modelling Tool,[1] an open source software built on the Open Source Physics

---

[1]http://physlets.org/tracker/.

Table 1 The checklist used by for detecting groups and elderly pedestrians

Group detection	
Locomotion Behaviour	• two or more people walking in the same direction
	• high spatial cohesion and coordination while walking
	• waiting dynamics to regroup in case of separation
	• leader/followers dynamics in sudden changes of direction
Verbal Behaviour	• talking while walking
Non Verbal Behaviour	• physical contact
	• body and gaze orientation to the each other
	• gesticulation while talking and/or indicating
Elderly detection	
Locomotion Behaviour	• slow and regular walking pace
	• stable trajectories towards the direction of movement
	• attentive in anticipating oncoming pedestrians by far
	• unsteady gait and lame posture
Physical Characteristic	• white hair/baldness
	• clothing (e.g., style, colours, hat)
	• use of artefact (e.g. stick, tripods)

(OSP) Java framework. Video images were calibrated[2] to achieve a zenith perspective of the area and analysed one frame every ten (every 0.4 s). The pedestrians' positions (X, Y) and the related frames (t) were exported for analysing data about trajectories and speed.

The achieved results have been used towards the validation of the agent-based simulation platform `ELIAS 38` [2, 14], with reference to the representation of the granulometric distribution of groups (starting initialisation of the simulated population and model calibration) and heterogeneous group and age-driven speed profiles. Moreover, the checklist used for data analysis (see Table 1) has been employed towards the development of automated analysis tools employing computer vision techniques.

The proposed approach is finally aimed at improving the walkability of congested urban areas and the security of large gathering-transit facilities (e.g., quality and comfort of sidewalks, route navigation, pedestrian-vehicular interaction), in an attempt to fulfil the prescriptions of the European Chart of Pedestrian Rights (1988) (i.e. *Pedestrian-friendly Cities*).

---

[2]The functions `Filter Perspective` and `Filter Resize` allowed to achieve a zenith perspective of the images and to maintain the proportion of the area adjusting the pixels. The function `Origin of the Axes` allowed to fix the origin of an orthogonal plane. The dimensions of the plane were calibrated by using a `Calibration Stick`, according to available spatial references. The function `Point Mass` allowed to manually track pedestrians, considering the space in between their feet (we did not use the position of their heads due to the image distortion).
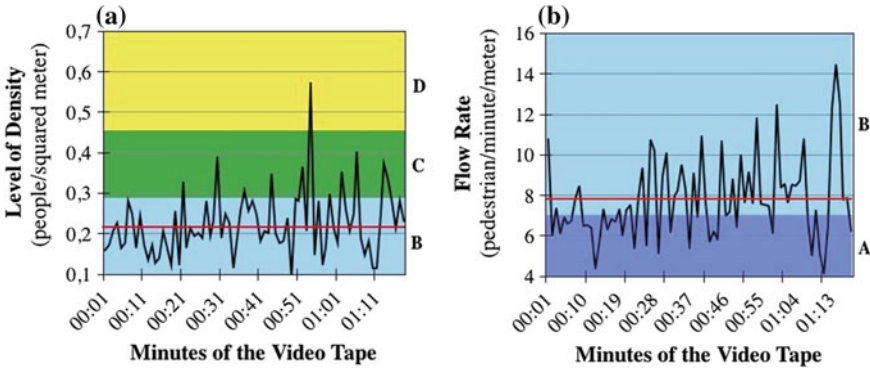
Fig. 1 Results. The *red lines* refer to average results. LOS are highlighted with a coloured background and labels. Level of density (**a**); pedestrian flow rate (**b**)

2 Level of Density

The average level of density was 0.22 ped/m^2 (see Fig. 1a). The average flow rate was 7.78 ped/min/m (see Fig. 1b). According to the Walkway Level of Service Criteria [7], results corresponded to LOS B: minor conflicts under low-medium density condition.

3 Speed and Trajectories

Results about speed and trajectories are presented in Fig. 2 and Table 2. 62 pedestrians were tracked under LOS B condition. The sample[3] was composed of: 15 adult singles (AS), 16 adult dyad members (AD), 15 elderly singles (ES), 16 elderly dyad members (ED).

A two-factor analysis of variance[4] showed a significant main effect for the *group* factor on speed [$F(1,58) = 28.61$, $p < 0.0001$], and a significant main effect for the *age* factor on speed [$F(1,58) = 105.97$, $p < 0.0001$]. Finally, results showed that the interaction between the *group* and *age* factors on speed was significant [$F(1,58) = 13.58$, $p < 0.001$]. A series of independent-samples t-tests showed a significant difference between the speed of: AS and AD, $t(29) = 2.05$, $p < 0.0001$; AS and ES, $t(28) = 2.05$, $p < 0.0001$; AS and ED, $t(29) = 2.05$, $p < 0.0001$; AD and ES, $t(29) = 2.05$, $p < 0.001$; AD and ED $t(30) = 2.04$, $p < 0.0001$. There was not a significant difference between the walking speed of ES and ED, $t(29) = 2.05$, $p = 0.21$.

---

[3]60 % single males and 40 % single females. 25 % male-male dyads, 25 % female-female dyads, 50 % mixed gender. 58 % pedestrians from South to North, 42 % from North to South. Pedestrians who stopped were not tracked, as well as mixed age dyads.

[4]All statistics hereby presented were conducted at the $p < 0.05$ level.
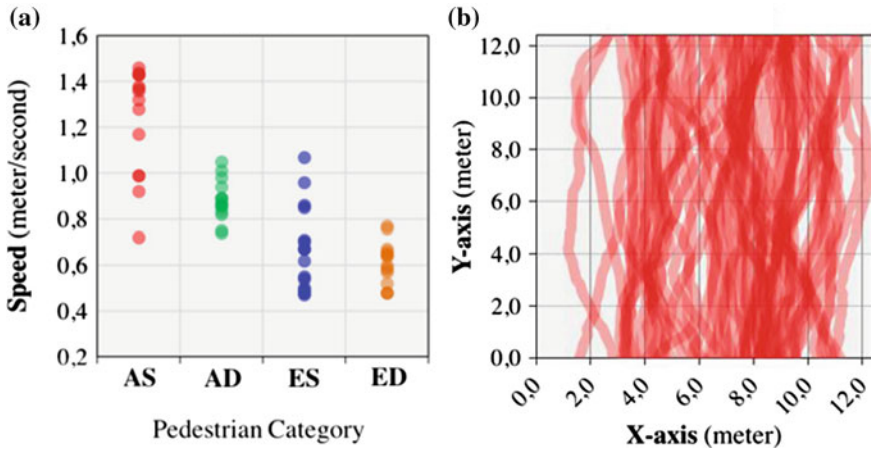
Fig. 2 Results: speed (**a**); trajectories (**b**)

Table 2 Results about speed, trajectories, spatial distance and alignment

	Adult singles	Adult dyads	Elderly singles	Elderly dyads
Speed (m/s)	1.25 m/s ± 0.23	0.88 m/s ± 0.08	0.68 m/s ± 0.19	0.61 m/s ± 0.09
Trajectories (m)	13.01 m ± 0.56	12.86 m ± 0.49	12.80 m ± 0.34	12.84 m ± 0.34
Distance (m)	–	0.64 m ± 0.31	–	0.65 m ± 0.2
Alignment (m)	–	0.17 m ± 0.18	–	0.21 m ± 0.17

A two-factor analysis of variance was conducted to compare the length of trajectories. Results showed that the *group* factor [$F(1,58) = 0.25$, $p = 0.62$] and *age* factor [$F(1,58) = 0.97$, $p = 0.33$] had not a significant main effect on trajectories. Results showed that the difference among the length of the trajectories of singles and dyads was not significant, like so comparing adults and elderly pedestrians.

Results showed that at LOS B dyads walked 30 % slower than singles, and that elderly walked 40 % slower than adults. Further analysis showed that *gender* and *direction of movements* had no significant effect on speed.

4 Dyad Proxemic Behaviour

The results about dyad proxemic behaviour are presented in Fig. 3 and Table 2. Spatial distance and alignment were measures as the distance between the *centroid* (geometrical centre of the group) and the relative positions of the group members along the X-axis and Y-axis.

An independent-samples t-test showed that the difference between the spatial distance of AD and ED was not significant, $t(725) = 1.96$, $p = 0.75$. Further t-test
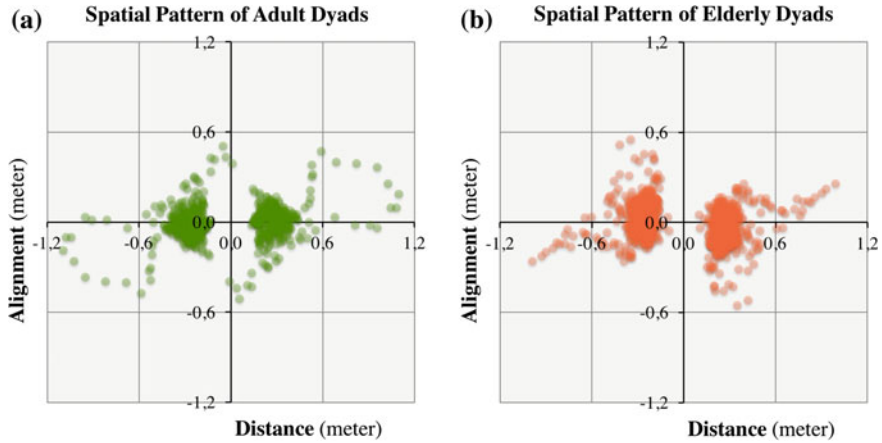
Fig. 3 Results about the spatial distance and degree of alignment: adult dyads (**a**); elderly dyads (**b**)

analysis showed a significant difference between the degree of alignment of AD and ED, t(725) = 1.96, p < 0.005. A linear regression analysis showed a significant impact of speed on the spatial alignment of ED [F(1,287) = 5.97, p < 0.02].

Results showed that at LOS B adult dyads walked with a line abreast pattern, while elderly dyads walked less aligned with a slight diagonal pattern. Further analysis showed that *gender* had no effect on spatial distance and degree of alignment among dyads.

5 Final Remarks

The current work has proposed a methodological framework based on the integration between empirical surveys and computer-based simulations. We investigated the impact of grouping and ageing on pedestrian circulation dynamics in urban contexts. Results showed that in situation of irregular flows dyads walked much slower than singles due to the need to maintain spatial cohesion to communicate; age significantly reduced the speed and the degree of alignment among group members due to locomotion skills decrease.

Although several empirical studies have been performed in this framework [13, 17], there is still a lack of contributions in the design of standardised methodology for the observation of pedestrian crowds in natural contexts. From the social science perspective, this approach allows a very limited control over the environment in which the empirical study takes place. However, this allows collecting empirical data about human behaviour considering the social context in which the subjects are situated. According to this approach, we propose hereby a general conceptualisation

of different walking behaviours based on this experience:

- *Time driven pedestrians*: people who have time constraints and walk through a certain environment constantly adjusting the trajectory between origin and destination to preserve a high speed (very often singles and commuters accessing public transport services);
- *Space driven pedestrians*: tourists or shoppers who visit for the first time a certain environment or have an exploratory attitude. Sometimes they are organised in large groups led by a guide. They stop more often, either for taking pictures of interesting spots or for shopping;
- *Social driven pedestrians*: strollers and inhabitants who amble thought a certain environment since they live or work nearby the area (more often small groups or families). They can stop their walk for an improvised conversation with somebody they know or for looking at the shop windows.

The proposed methodological approach is aimed at validating the pedestrian simulation platform `ELIAS 38`. Omitting the representation of grouping, heterogeneous behaviours and speed profiles could hardly compromise the accuracy of the results obtained by means of simulation campaigns execution. Although there are some objections about the simplified level of correspondence between simulations and real phenomena, once validated this method represents an innovative contribution for testing in advance the efficacy of alternative solutions for the design of complex spatial layouts and the management of pedestrian circulation dynamics. (i.e. *what-if scenarios*).

References

1. Bandini, S., Gorrini, A., Vizzari, G.: Towards an integrated approach to crowd analysis and crowd synthesis: a case study and first results. Pattern Recogn. Lett. **44**, 16–29 (2014)
2. Bandini, S., Mondini, M., Vizzari, G.: Modelling negative interactions among pedestrians in high density situations. Transp. Res. Part C Emerg. Technol. **40**, 251–270 (2014)
3. Burgess, J.W.: The social biology of human populations: spontaneous group formation conforms to evolutionary predictions of adaptive aggregation patterns. Ethol. Sociobiol. **10**(5), 343–359 (1989)
4. Challenger, W., Clegg, W., Robinson, A.: Understanding Crowd Behaviours: Guidance and Lessons Identified. Cabinet Office, UK (2009)
5. Costa, M.: Interpersonal distances in group walking. J. Nonverbal Behav. **34**(1), 15–26 (2010)
6. Federici, M.L., Gorrini, A., Manenti, L., Vizzari, G.: An innovative scenario for pedestrian data collection: the observation of an admission test at the university of Milano-Bicocca. In: Pedestrian and Evacuation Dynamics 2012, pp. 143–150. Springer, Switzerland (2014)

7. Fruin, J.J.: Pedestrian planning and design. Technical report. Metropolitan Association of Urban Designers and Environmental Planners, New York (1971)
8. Gorrini, A., Bandini, S., Vizzari, G.: Empirical investigation on pedestrian crowd dynamics and grouping. In: Traffic and Granular Flow '13, pp. 83–91. Springer, Switzerland (2015)
9. Hall, E.T.: The Hidden Dimension, vol. 14, pp. 103–124. Doubleday, Garden City (1966)
10. Mawson, A.R.: Mass Panic and Social Attachment: The Dynamics of Human Behavior. Ashgate Publishing Ltd. (2012)
11. Moussaïd, M., Perozo, N., Garnier, S., Helbing, D., Theraulaz, G.: The walking behaviour of pedestrian social groups and its impact on crowd dynamics. PloS One **5**(4), e10047 (2010)
12. Musso, A., Nuzzolo, A., Crisalli, U., Longo, G.: Editorial. Transp. Res. Procedia **5** (2015). SIDT Scientific Seminar 2013
13. Schultz, M., Schulz, C., Fricke, H.: Passenger dynamics at airport terminal nvironment. In: Pedestrian and Evacuation Dynamics 2008, pp. 381–396. Springer (2010)
14. Shimura, K., Ohtsuka, K., Vizzari, G., Nishinari, K., Bandini, S.: Mobility analysis of the aged pedestrians by experiment and simulation. Pattern Recogn. Lett. **44**, 58–63 (2014)
15. Templeton, A., Drury, J., Philippides, A.: From mindless masses to small groups: conceptualizing collective behavior in crowd modeling (2015)
16. Webb, J.D., Weber, M.J.: Influence of sensory abilities on the interpersonal distance of the elderly. Environ. Behav. **35**(5), 695–711 (2003)
17. Willis, A., Gjersoe, N., Havard, C., Kerridge, J., Kukla, R.: Human movement behaviour in urban spaces: implications for the design and modelling of effective pedestrian environments. Environ. Plann. B Plann. Des. **31**(6), 805–828 (2004)
18. Winogrond, I.R.: A comparison of interpersonal distancing behavior in young and elderly adults. Int. J. Aging Hum. Dev. **13**(1), 53–60 (1981)

Method for Simulating the Evacuation Behaviours of People in Dynamically Changing Situations

Tomoichi Takahahi, Toshinori Niwa and Rintaro Isono

Abstract Evacuation drills are executed to practice smooth rescue operations during emergencies. Evacuation simulation systems have been proposed to simulate evacuation behaviours of people in such situations, and to improve prevention plans. In this paper, we point out new features in simulating evacuation behaviours in dynamically changing situations and propose a simulation method in a case of closing fire shutters. Our simulation results show more realistic behaviours of evacuations than the traditional simulations and indicate potential to improve prevention plans for emergency situations and thus reduce fatalities, injuries, and damage from disasters.

1 Introduction

Multi-agent simulations (MAS) have been used to study the dynamics of social systems [2]. Disaster-related simulation is one field of application that makes it possible to simulate emergency scenarios that are difficult to replicate in the real world. MAS expresses the microscopic behaviours of humans and simulates evacuation behaviours of crowds. People make decisions and change their actions according to the guidance they receive from public announcement (PA) systems as the situation changes dynamically by unexpected events. Examples of announcements are "Please follow the warning lights leading to the emergency exit" or "The fire shutter closes automatically, so please use caution."

Fire shutters have been installed in buildings by law to prevent fire and smoke from spreading inside the buildings. Some shutters are designed to close automatically in a case of fire while other shutters are closed by human operations. The closing of shutters forces people to change their evacuation routes. Some people take note of

T. Takahahi (✉) · T. Niwa · R. Isono
Meijo University, 1-501 Shiogamaguchi, Tempaku, Nagoya 468-8502, Japan
e-mail: ttaka@meijo-u.ac.jp

T. Niwa
e-mail: 133430012@ccalumni.meijo-u.ac.jp

R. Isono
e-mail: 143430002@ccalumni.meijo-u.ac.jp

announcements from a PA system that broadcasts fire shutter closings and subsequently change their evacuation route. Others who do not notice the announcements may go to routes that are closed by the fire shutters. These actions change evacuation behaviours and make the required safe egress time (RSET) longer. RSET is one of the standards in fire prevention planning [3].

In this paper, we propose a method of simulating evacuation behaviours from buildings under dynamically changing situations. In Sect. 2, we show that it is common for environments to change during emergency situations and discuss problem setting in the changing situations. Section 3 describes an agent based evacuation simulation system, TENDENKO, and shows that a map is one of the important factors in the simulations. The map changes during simulations and cognitive maps that agents use will diverge from the real ones over time. The methods used to handle the changes and inconsistencies of maps, and the simulation results are presented in Sect. 4. Section 5 summarises our study.

2 Background and Problem Setting of Changing Situations During Evacuation

When emergencies occur, people start evacuation by sensing the emergency or they are guided by PAs. Emergency situations vary by the minute, and in the case of a fire, some rooms are filled with fire and smoke, thereby, activating an automatic fire alarm system. Sprinklers installed into the ceiling will spray water and fire shutters will close. During earthquakes, furniture can move over the floors, blocking occupants from smooth evacuation to exits.

Table 1 shows categories of changing situations during evacuations. Case 1 is a normal situation in everyday life, and the other four cases correspond to emergency situations. Case 2 corresponds to a situation during minor emergencies such as a small fire. The layout of the floor inside the buildings remains the same as Case 1 during the evacuation. Cases 3, 4, and 5 correspond to situations where some people may have trouble finding smooth evacuation to exits. Case 3 is a situation where an earthquakes causes furniture to fall to the floor and the changes hinder or prevent evacuations. In Case 4 human operations such as fire shutter closing, may block the evacuation routes. Case 5 is the situation in extreme disasters, where large

Table 1 Category of changing situations at evacuations

Case	Situations	Environment	Map	Fire shutter
1	Everyday	Static	Same	Open
2	Emergency	Static	Same	Open
3	Emergency	Dynamic	Different	Open
4	Emergency	Dynamic	Different	Closed
5	Emergency	Dynamic	Unknown	Open/closed

Table 2 List of evacuation simulation systems

	Building Exodus	SimTread	LEGION Studio	TENDENKO
MAP model	Network	CAD level	CAD level	CAD level
Order of evacuees	100,000	10,000	10,000	10,000
Evacuation type	Instant	Instant	Instant	Instant/after tasks/emergent
Communication	No	No	No	Among agents, broadcast

earthquakes cause so much destruction to parts of buildings that the floor layout is completely changed.

Evacuation drills are executed to practice smooth rescue operations during emergencies. However, it is difficult to execute the evacuation drills in preparation for the situations in Cases 3, 4, and 5. In fact, in those situations, real-time evacuation guidance is required to ensure smooth evacuations from buildings. Evacuation simulation systems are proposed to simulate evacuation behaviours of people in such situations, and to improve prevention plans in terms of available safe-escape time (ASET) and the RSET. Table 2 illustrates evacuation simulation systems [4], which handle Case 2 situations but do not function to simulate the evacuation scenarios in Cases 3 and 4.

In this paper, we perform and investigate evacuation simulations for a Case 4 situation. The following is our scenario: a fire breaks out at t_1, the fire alarm system detects the fire and warns occupants to evacuate to the outside at t_2, and operators at the prevention centre close the fire shutters at t_3. Agents are expected to follow a route to an exit to get outside the building after t_2. After t_3, the floor layout of the building changes and agents must change their route according to the situations. We propose a method of simulating agents' behaviour in changing environments and simulate 1,000 people evacuating from a building. The simulation results show the differences in some metrics such as RSET and evacuation rates. They are useful in improving prevention plans for emergency situations and for reducing fatalities, injuries, and damage from disasters.

3 Simulation System for Changing Environments and Evacuation Scenarios

3.1 Architecture of Agent Based Simulation System: TENDENKO

The Agent Based Simulation System (ABSS) consists of two parts; agents and environments [6]. Agents perceive data from the environment and decide their actions
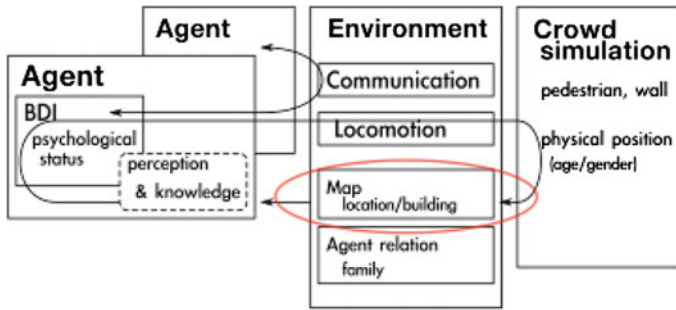
Fig. 1 System architecture of TENDENKO

according to their purposes. Their actions change the states of environment. Simulators in the environment also alter the environments, for example, they can simulate fire spreading and calculate human locations. ABSS repeats this simulation step. The situations represent the features of tasks that the ABSS is applied to, and they are conditions of simulations or parameters that affect the results of simulations. In a case of evacuation from buildings, the number of people in the building, their location at t_1, the floor layouts of buildings, public announcement from the prevention centre, and the rate of fire spread are the components of situations.

Figure 1 shows the general architecture of TENDENKO that we developed based on the RoboCup Rescue simulation system [5]. TENDENKO simulates agent behaviours in a three-dimensional world. The MAP refers to the data of the 3D world such as the floor layout of inside a building and roads of outside of the buildings. Agents use MAP information for route planning and a crowd simulator calculates the behaviours of agents with MAP.

3.2 Evacuation Behaviours in a Fire Shutters-Closing Situation

When a fire breaks out at t_1, the fire alarm system detects the fire and announces evacuation guidance at t_2. According to past reports on disasters, not all people evacuated at the same time [1]. Agents start their own evacuations after t_2: some agents evacuate instantly, other agents evacuate after finishing their jobs, and others stay there until they recognise the fire. The three types are referred to as instant evacuation, evacuation after tasks, and emergent evacuation in Table 2. Operators at the prevention centre close the fire shutters at t_3 when they decide this operation is necessary for fire fighting. Agents will notice the fire shutter closing at t_4 when they reach the fire shutter, and change their evacuation routes. From t_3 to t_4, the agents evacuate wrongly according to their own cognitive MAPs which have not been updated, and are the same as the ones in every day use.

Table 3 Inconsistency in the transition of MAPs
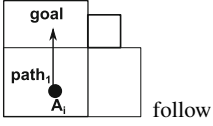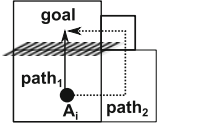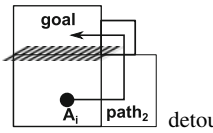
Time	Status of MAP_t^C & $MAP_t^{a_i}$	Agent's path planning in changing environment
$t_2 \sim t_3$	$_{initial}MAP_t^C = {}_{initial}MAP_t^{a_i}$	follow the shortest path
$t_3 \sim t_4$	$_{new}MAP_t^C \neq {}_{initial}MAP_t^{a_i}$	change the route in front of the shutter
$t_4 \sim$	$_{new}MAP_t^C = {}_{new}MAP_t^{a_i}$	detour to the exit

Table 3 illustrates the transition of MAPs of simulations and agents in the simulations. $MAP_k^{a_i}$ indicates a cognitive MAP that agent a_i has at time t_k, and MAP_k^C is a MAP that the crowd simulator use to calculate the locations of agents at time t_k. From start to t_3, $MAP_k^{a_i}$ is the same as MAP_k^C. At t_2, agents start evacuation and move to an exit that the agents think is the nearest exit. At t_3 when the prevention centre closes the fire shutters, the MAP_k^C in the simulator changes to a new one $_{new}MAP_k^C$ in which some paths are blocked. $_{new}MAP_k^C$ is then different from $MAP_k^{a_i}$ until the agent recognises the closing at t_4. After t_4, $_{new}MAP_k^C$ and $_{new}MAP_k^{a_i}$ becomes the same.

4 Evacuation Under Dynamically Changing Situations

4.1 New Feature and Multiple MAPs Among Agents and Simulators

Simulating evacuation behaviour in dynamically changing situations is one of the key functions which make ABSS useful in real applications. We point out that an understanding of the following three points is necessary for simulating evacuation from buildings.

(1)   **(2)**   **(3)**
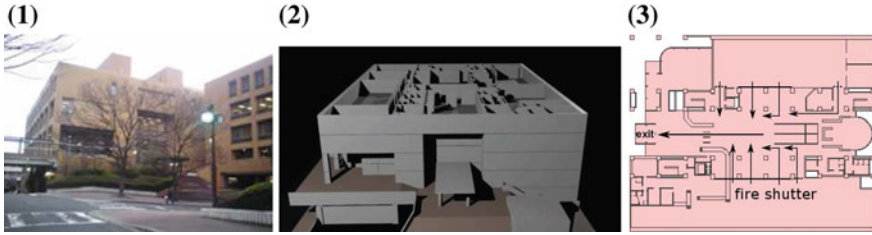
Fig. 2 The university library: building (**1**); CAD model (**2**); and layout of second floor (**3**)

1. The MAP that includes the floor layout of buildings changes dynamically during emergencies.
2. For some periods, there are inconsistencies between the MAP that the environment has and the cognitive MAPs that agents have.
3. When and how the agents recognise the changes in the MAP.

We implemented the functions in TENDENKO, limited to Case 4 in Table 1. In Case 4, human operations change the situation and we incorporated the fire shutter closing operation in our university library (Fig. 2), and simulated the evacuation of 1,000 agents from an exit on the second floor.

As it is pointed out, agents evacuate individually and differently. Even in a case where they evacuated instantly, they notice the fire shutter closing at different t_4 times. The agents have cognitive MAPs and at first, the MAPs of the simulator and agents are linked to $_{initial}MAP$. At t_3, the MAP in the simulator is linked to $_{new}MAP$ and agents' MAPs are linked to $_{new}MAP$ at t_{4i}. Figure 3 shows a timing diagram of the evacuation simulation with fire shutters closing. When agent$_i$ comes to an area in front of the shutter at t_{4i}, the kernel sends a message to the agent that the path to an exit is blocked and the agent recognises that the fire shutter is closed.

4.2 Discussions of Simulation Results

The top snapshot in Fig. 3 shows the evacuation behaviours from t_2 to t_3. During this period, agents evacuated to the nearest exit through the shortest path. At t_3, the fire shutter was closed. From t_3 to t_4, agents who do not know the change caused by closing the shutter followed the route planned with the initial map and stopped at the shutter. The middle snapshot in Fig. 3 illustrates a congested situation in the front of the shutter. Individual agents noticed the shutter closed at t_4^i, and they changed their own cognitive map, namely they changed MAP to $_{new}MAP$. The bottom snapshot shows that the behaviour of the agents who changed their evacuation routes.

Figure 4 shows the rate of evacuation for three cases. Simulation, S1, corresponds to case C2 where there are no fire shutters. The other two simulations, S2 and S3, are in the category of C4 with the closing of the fire shutters. Agents did not recognise
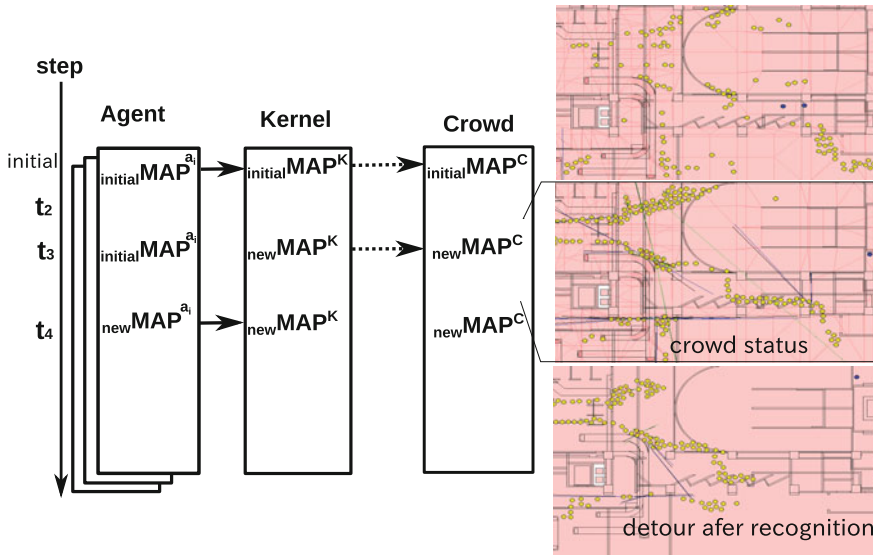
Fig. 3 Timing diagram among agents, kernel and simulator, and snapshots are situations at, $t_2 \sim t_3$, $t_3 \sim t_4$ and $t_4 \sim$ from *top* to *bottom*

Fig. 4 Evacuation rates of 1,000 people from the library
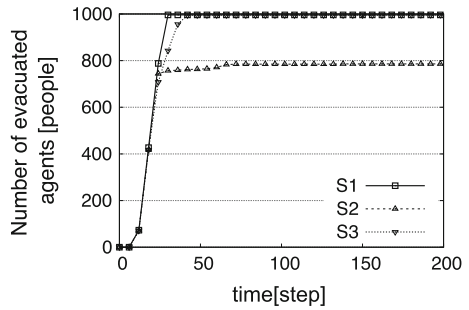
the fire shutters closing in S2; however, agents recognised the shutters were closed in S3. The vertical axis shows how many people evacuate from the building and the horizontal axis is simulation step. The three graphs correspond to scenarios S1, S2 and S3.

The evacuation rate of S2 shows that not all the people evacuate because some agent stay in front of the shutters. In S1 and S3, all people evacuate. Around 30 steps, the evacuation rate of S3 is lower than the rate of S1. This caused that some evacuees to detour to the exit. The simulation results of S3 appear more realistic than the results for S1.

5 Summary

Evacuation drills are undertaken to ensure smooth rescue operations. Proper evacuation guidance is required to make smooth evacuations from buildings. However it is difficult to execute the evacuation drills for emergencies where the situation changes dynamically.

In this paper, a method for simulating an evacuation during dynamically changing situations is proposed. We examined evacuation situations where fire shutters close and noted three key points concerning MAP in ABSS. The method is implemented in TENDENKO and the simulations of 1,000 evacuations from a building were demonstrated. The result is a more realistic prediction of behaviours during evacuations than those obtained by traditional simulations. Additionally, the results indicate a potential to improve prevention plans for emergency situations and thus reduce fatalities, injuries, and damage from disasters.

References

1. Averill, J.D., Mileti, D.S., Peacock, R.D., Kuligowski, E.D., Groner, N.E.: Occupant behavior, egress, and emergency communications (NIST NCSTAR 1-7). Technical report, Gaitherburg, MD: National Institute of Standards and Technology (2005)
2. Hawe, G.I., Coates, G., Wilson, D.T., Crouch, R.S.: Agent-based simulation for large-scale emergency response. ACM Comput. Surv. **45**(1), 1–51 (2012)
3. ISO:TR16738:2009: Fire-safety engineering—technical information on methods for evaluating behaviour and movement of people
4. Kuligowski, E.D.: Review of 28 egress models. In: NIST SP 1032; Workshop on Building Occupant Movement During Fire Emergencies (2005)
5. Okaya, M., Niwa, T., Takahashi, T.: TENDENKO: agent-based evacuation drill and emergency planning system (demonstration). In: The Autonomous Agents and MultiAgent Systems (AAMAS), pp. 169–1670 (2014)
6. Weiß, G. (ed.): Multiagent Systems: A Modern Approach to Distributed Artificial Intelligence. MIT Press, Cambridge, MA, USA (1999)

Efficacy of Pedestrian Evacuation Time Estimate Using Agent Based Queuing Network Model

Bharat Kunwar, Filippo Simini and Anders Johansson

Abstract There is an increasing risk of exposure to disasters due to rising instances of extreme events (Munich et al. Topics Geo: Natural Catastrophes 2013: Analyses, Assessments, Positions. Munchener Ruckversicherungs-Gesellschaft, Munich, 2014, [7]) and growing urban settlements (United Nationsin World economic and social survey 2013: sustainable development challenges, 2013, [9]). As such, it is important that we explore ways measure preparedness to such disasters. In a previous work (Kunwar et al. in Evacuation time estimate for a total pedestrian evacuation using queuing network model and volunteered geographic information, 2015, [5]), we used agent based modelling (ABM) to investigate 50 cities in the UK and draw a link between their attributes such as spatial size, population, exit width and their evacuation time estimates (ETE) for a full city evacuation, one of the most stressing mobility use cases for a city. In this work, we examine the efficacy of those results by looking at how sensitive they are to fundamental diagram parameters. We found the overall ETE to be most sensitive to density threshold for minimum velocity with variations as large as an order of magnitude. We observed that ETE is also sensitive to maximum density limit but the results keep within the same order of magnitude. We also saw an increasing gap in ETE for lowest and highest values of density threshold for minimum velocity with every doubling of population. We reached a conclusion that it is necessary to carefully establish the input parampAGNeters if a robust result is desired for a network-based 'mesoscopic' modelling.

B. Kunwar (✉) · F. Simini · A. Johansson
Faculty of Engineering, University of Bristol, Bristol, UK
e-mail: b.kunwar@bristol.ac.uk

F. Simini
e-mail: f.simini@bristol.ac.uk

A. Johansson
e-mail: a.johansson@bristol.ac.uk

289

1 Introduction

There is a greater risk of exposure to disasters than ever before due to rising instances of extreme events [7] and growing urban settlements [9]. It is important for us to be prepared in advance and determining evacuation time estimate (ETE) [11] is an essential component of proactive evacuation planning. A full city evacuation is one of the most stressing mobility use case for a city and one of the ways of understanding the result of interaction between large numbers of autonomous agents to establish ETE is by running an agent based model (ABM) simulation [3].

In a previous work [5], we investigated 50 regions in the UK similar in size to the 'City of Bristol' using OpenStreetMap data [1]. We used a modified queuing network model described in [4]. We established a link between parameters that describe a city (spatial size, population, exit width) and its ETE. In this work, we examine the efficacy of those results by looking at how sensitive the results are to fundamental diagram parameters.

Since a fundamental diagram is a description of aggregate pedestrian crowd behaviour, it cannot describe system dynamics far from equilibrium (i.e. high density crowds). We used Weidmann's fundamental diagram [12] in [5] to establish ETE. It has been shown that keeping a constant lower limit on the net-time headway is a key mechanism behind dynamics of pedestrian streams [2]. This is more apparent in the high density regime where density-velocity relationship transitions to a minimum velocity 'stop-and-go' wave phase for a moving crowd. While a mesoscopic model cannot replicate the exact microscopic interactions, it is possible to study how sensitive the observed evacuation time is to density limit beyond which velocity remains constant and the maximum density limit allowed on any given link.

Related work include sensitivity analysis of ETE route choice mechanisms, risk area population, route degradation etc. [6, 8, 10]. There appears to be a gap in identifying sensitivity of ETE to the shape of the fundamental diagram.

2 Methodology

For our analysis, we use OpenStreetMap data for 'Carlisle', a UK city that has historically been prone to flooding. We assume a single catchment area to the south of the city, an area to which all agents in the simulation evacuate to (Fig. 1). For reference, 90 % of agents in 'Carlisle' lie within 5371 m of the exit as shown in Fig. 2.

We use Weidmann's [12] fundamental diagram to carry out the sensitivity analysis for which the pedestrian density-velocity relationship written as follows:

$$v(k) = v_f(1.0 - e^{-1.913(\frac{1.0}{k} - \frac{1.0}{k_{max}})}) \tag{1}$$
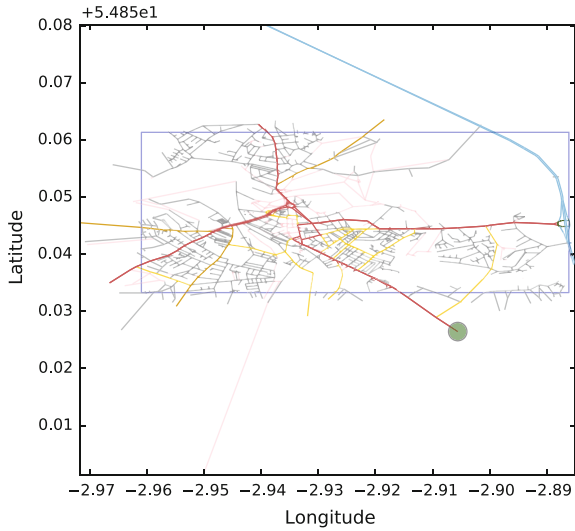
Fig. 1 Catchment area indicated by the inner *rectangular box* for 'Carlisle' where the *green circle* indicates the exit
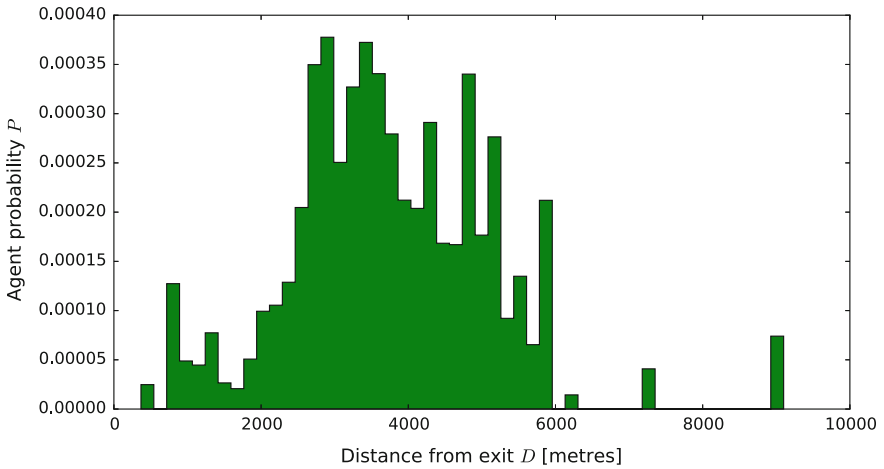
Fig. 2 Distribution of agent distance D away from the catchment area exit. 90 % of agents in 'Carlisle' lie within 5371 m of the exit

Consequently, the relationship between density k and flow rate Q is as follows:

$$Q(k) = kv(k) = kv_f(1.0 - e^{-1.913(\frac{1.0}{k} - \frac{1.0}{k_{max}})})$$ (2)
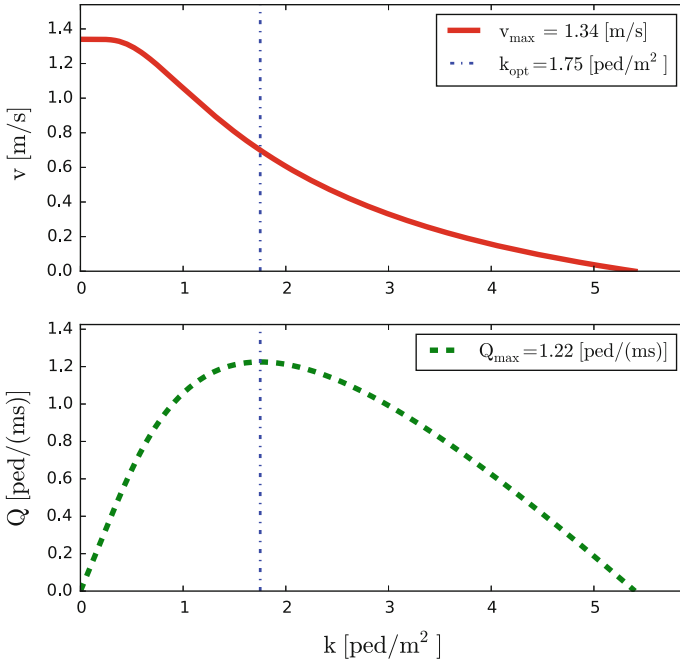
Fig. 3 Weidmann's density-velocity and density-flow relationships as described by equations $v(k) = v_f(1.0 - e^{-1.913(\frac{1.0}{k} - \frac{1.0}{k_{max}})})$ and $Q(k) = kv(k)$ respectively. At a density of $k = 5.4$ ped/m^2, velocity $v = 0$. Similarly, a maximum flow rate $Q_{max} = 1.22$ ped/ms is possible at an optimum density $k_{opt} = 1.75$ ped/m^2

We can see these equations represented graphically in Fig. 3. We can determine using these equations that a maximum flow rate of $Q_{max} = 1.22$ ped/ms can be achieved at an optimum density of $k_{opt} = 1.75$ ped/m^2.

For the sensitivity analysis, we have three variables: a density threshold to enable a minimum velocity in the high density region $k_{v,min}$ which we expect the simulation time to be most sensitive to (step = 0.1), maximum density upper limit k_{lim} which we are not certain what effect it has on the outcome but keen to understand the general trend (step = 0.5) and doubling range of population size N in order to determine its effect on the result space. The range of parameters are listed in Table 1.

In order to understand what these parameters mean visually, we present density-velocity/density-flow diagrams for extreme values of $k_{v,min}$ and k_{lim} within our parameter space in Table 2. The vertical green dotted lines indicate the position of $k_{v,min}$ and the vertical red dotted lines indicate the position of k_{lim}.

Using these parameters, we run our ABM using queuing network model adapted from [4]. For each of the 360 configurations, we measure the overall simulation time T, which can be described as the time it takes the last agent to reach the exit.

Table 1 The range of three parameters to be examined: density threshold for minimum velocity $k_{v,min}$, maximum density limit k_{lim} and catchment area population N. In total, we have $10 \times 9 \times 4 = 360$ individual configurations

Index	$k_{v,min}$	k_{lim}	N
1	4.4	5.0	25,000
2	4.5	5.5	50,000
3	4.6	6.0	100,000
4	4.7	6.5	200,000
5	4.8	7.0	
6	4.9	7.5	
7	5.0	8.0	
8	5.1	8.5	
9	5.2	9.0	
10	5.3		

Table 2 Density-velocity/density-flow diagrams obtained as we vary the density threshold for minimum velocity $k_{v,min}$ and maximum density limit k_{lim} parameters
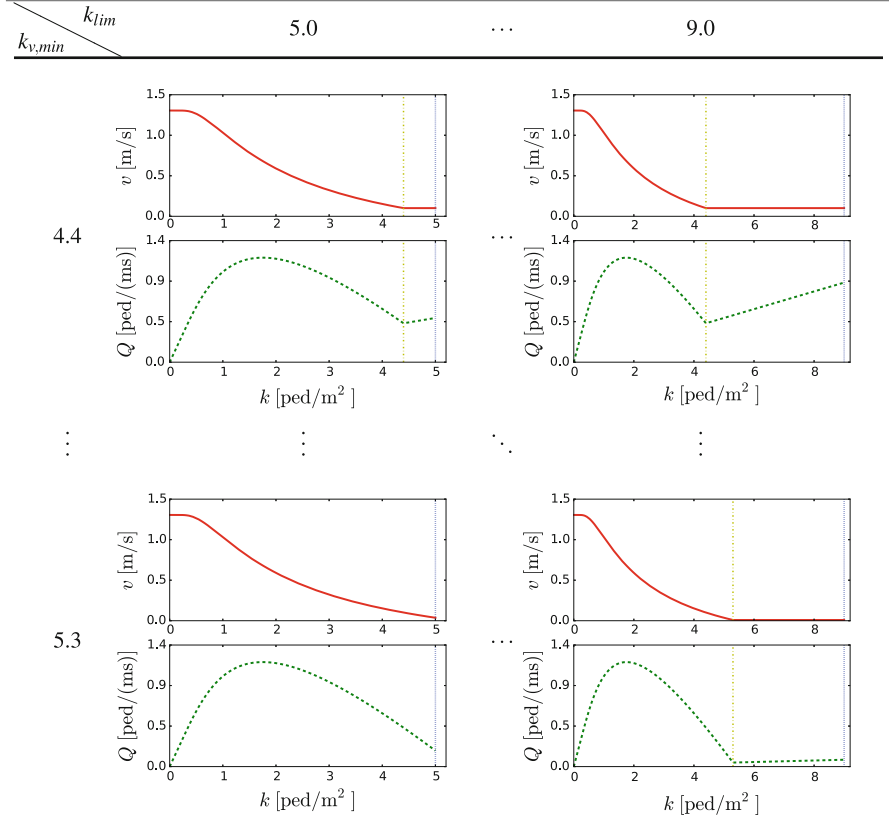
We present the diagrams for extreme values of $k_{v,min}$ and k_{lim} within our parameter space. The vertical green dotted lines indicate the position of $k_{v,min}$ and the vertical red dotted lines indicate the position of k_{lim}
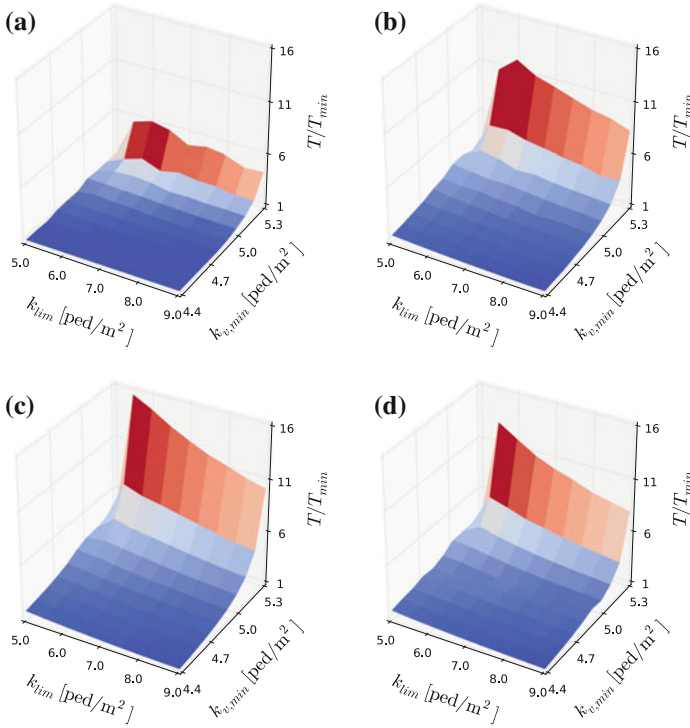
Fig. 4 3-dimensional plots for each value of N where we have $k_{v,min}$ and k_{lim} on the *horizontal axes* and T/T_{min} on the *vertical axes*. T_{min} is the minimum observed value of T for each value of N. The value of N and T_{min} used to normalise the *vertical axes* are given next to each of the labels: $N = 25000$, $T_{min} = 138$ mins (**a**); $N = 50000$, $T_{min} = 166$ mins (**b**); $N = 100000$, $T_{min} = 288$ mins (**c**); $N = 200000$, $T_{min} = 737$ mins (**d**)

3 Results

We present 3-dimensional plots for each value of N in Fig. 4 where we have $k_{v,min}$ and k_{lim} on the horizontal axes and T/T_{min} on the vertical axes. T_{min} is the minimum observed value of T for each value of N.

As we hypothesised, the simulation time T appears to be much more sensitive to $k_{v,min}$ as it approaches 5.4 ped/m^2 where $v = 0$ m/s.

It appears that with increasing k_{lim}, there is a gradual reduction in T apart from a slight kink when $k_{lim} < k_{v,min}$. However, the values keep within the same order of magnitude.

As N doubles, we see an increasing gap between T at minimum and maximum values of $k_{v,min}$ from ≈ 6 when $N = 25000$ to a maximum gap of ≈ 16 in the case of $N = 100000$. The gap closes again to ≈ 13 in the case of $N = 200000$.

4 Conclusion

The overall simulation time appears to be most sensitive to density threshold for minimum velocity as hypothesised with variations as large as an order of magnitude. It is therefore important to consider how we define this value, either empirically or through microscopic modelling. ETE is somewhat sensitive to maximum density limit but the results keep within the same order of magnitude. We also saw an increasing gap in ETE between lowest and highest values of density threshold for minimum velocity with every doubling of population. In conclusion, we stress to anyone considering network-based 'mesoscopic' modelling about the need to carefully establish the input parameters if a robust result is desired.

References

1. Haklay, M., Weber, P.: Openstreetmap: user-generated street maps. IEEE Pervasive Comput. **7**(4), 12–18 (2008). http://www.openstreetmap.org/
2. Johansson, A.: Constant-net-time headway as a key mechanism behind pedestrian flow dynamics. Phys. Rev. E **80**(2), 26120 (2009)
3. Johansson, A., Batty, M., Hayashi, K., Al Bar, O., Marcozzi, D., Memish, Z.A.: Crowd and environmental management during mass gatherings. Lancet. Infect. Dis. **12**(2), 150–156 (2012)
4. Kunwar, B., Simini, F., Johansson, A.: Large scale pedestrian evacuation modeling framework using volunteered geographical information. Transp. Res. Procedia **2**, 813–818 (2014)
5. Kunwar, B., Simini, F., Johansson, A.: Evacuation time estimate for a total pedestrian evacuation using queuing network model and volunteered geographic information (2015)
6. Lindell, M.K.: EMBLEM2: an empirically based large scale evacuation time estimate model. Transp. Res. Part A Policy Pract. **42**(1), 140–154 (2008)
7. Munich, R.E., Kron, W., Schuck, A.: Topics Geo: Natural Catastrophes 2013: Analyses, Assessments. Positions. Munchener Ruckversicherungs-Gesellschaft (2014)
8. Sinuany-Stern, Z., Stern, E.: Simulating the evacuation of a small city: the effects of traffic factors. Soc. Econ. Plann. Sci. **27**(2), 97–108 (1993)
9. United Nations. Department of Economic and Social Affairs.: World Economic and Social Survey 2013: Sustainable Development Challenges. United Nations, New York (2013)
10. Urbanik II, T.: Evacuation time estimates for nuclear power plants. J. Hazard. Mater. **75**(23), 165–180 (2000)
11. Urbanik II, T., Desrosiers, A.E.: An Analysis of Evacuation Time Estimates Around 52 Nuclear Power Plant Sites Analysis and Evaluation. Technical report. Pacific Northwest National Laboratory, Richland (1981)
12. Weidmann, U.: Transporttechnik der Fussgänger: Transporttechnische Eigenschaften des Fussgängerverkehrs (Literaturauswertung). ETH, IVT (1993)

Modelling Pedestrian Evacuation Movement on a Swaying Ship

Juan Chen, Jian Ma and Siuming Lo

Abstract With the advance in living standard, cruise travel has been rapidly expanding around the world in recent years. The transportation of passengers over the water has also made a rapid development. It is expected that ships will be more and more widely used. Unfortunately, recent ship disasters caused serious losses. It raised concerns on the effectiveness of passenger evacuation on ships. The present study thus focuses on pedestrian evacuation features on ships. On ships, passenger movements are affected by the periodical water motion and thus are quite different from the characteristic when walking on a static horizontal floor. Taking into consideration this special feature, an agent-based pedestrian model is formulated and the effect of ship swaying on pedestrian evacuation efficiency is investigated. Results indicated that the proposed model can be used to quantify the special evacuation process on ships.

1   Introduction

In the past decades, cruise travel has been a rapid expanding field around the world. A worldwide annual growth rate of 6.55 % for passage by sea from 1990 to 2019 has been recorded which is expected to grow. The transportation of passengers over water has also made a rapid development. It is expected that ships will be more and more widely used in transporting passengers. Unfortunately, several ship disasters

J. Chen (✉) · S. Lo
Department of Architecture and Civil Engineering, City University of Hong Kong,
Hong Kong SAR, China
e-mail: juanchen6-c@my.cityu.edu.hk

S. Lo
e-mail: bcsmli@cityu.edu.hk

J. Ma
National United Engineering Laboratory of Integrated and Intelligent Transportation,
School of Transportation and Logistics, Southwest Jiaotong University,
Chengdu 610031, China
e-mail: majian@mail.ustc.edu.cn

occurred recently which caused serious losses to people's lives and properties. It raised concerns on the effectiveness of large crowd passenger evacuation on ships.

To mitigate the effect of an emergency, evacuating passengers from ships will be necessary. The International Maritime Organisation (IMO) has already developed guidelines for passenger ship evacuation. However, these guidelines and regulations, like most building codes, only enforce the capacity of individual components such as exits and passenger way width, thus can barely provide efficient setting and management strategies. Computer simulation, on the contrary, can be helpful by performing simulations even at the ship design stage. The International Conventions for the Safety of Life at Sea (SOLAS) now requires evacuation analysis at the early stage of ship design (IMO MSC.1/Circ.1238, 2007). Thus, some simulation models have been built to perform computer simulation based evacuation analysis.

When compared to building evacuation, passenger ship evacuation is still a new research topic and only limited publications can be found. Existing works were more or less inspired by the IMO guidelines. The two full scale drill exercise projects, i.e., 'FIRE-EXIT' and 'SAFEGUARD' have provided valuable information for model validation, especially for 'maritime-Exodus' [5]. Some other models have also been established, including AENEAS [11], EVI [1] and VELOS [6]. The former two models are grid-based models, and thus have great advantage in computing efficiency, yet the discretisation may affect their ability to model the environmental space and detailed pedestrian motion when compared to the last two continuous space models. The influences of ship motion on pedestrian movement in these models are almost mimicked by speed reduction considering different inclination angles rather than considering the coupled-forced pedestrian movement features.

In the present paper we establish an evacuation model taking into account forced pedestrian movement patterns. The rest of the paper is organised as follows. In Sect. 2, we introduce the model which takes into account the ship swaying effect. In Sect. 3, we first compare several single pedestrian movement features under different conditions and then analyse a ship evacuation process. In the last section, conclusions are drawn.

2 Ship Evacuation Model

Basically, the design layout of the cruise ships is the same as that of hotels on the ground, which includes separated accommodation cabins, restaurants, sports facilities, etc., so that cruise ships can be regarded as mobile hotels. However, one of the important differences between them is that the deck of a cruise ship has a complex motion pattern as a result of periodical water movement. Thus, pedestrians on board would be affected by the inertial force, which makes pedestrian movement characteristic different from when walking on a static horizontal floor. Taking into consideration this special feature, an agent-based pedestrian model is formulated, and the effect of ship swaying on pedestrian evacuation efficiency is investigated.
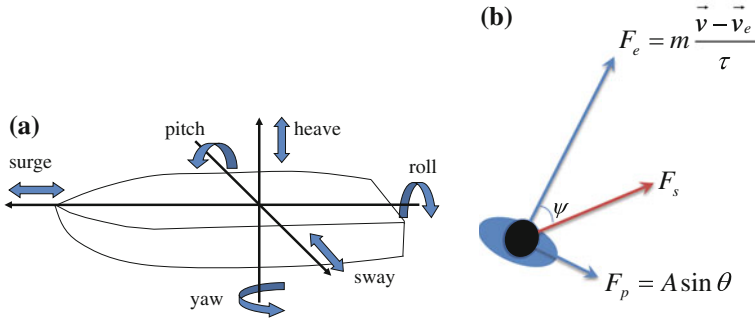
Fig. 1 Movement and forces. Scheme of ship motion types (**a**). Force analysis for an onboard passenger (**b**)

2.1 Ship Swaying Features

As mentioned before, ship movement in the water is very complex. It displays a six-degree-of-freedom motion feature because of the periodical water movement and wind influence, as shown in Fig. 1a. These motions include linear translation motions (surge, sway and heave) and non-linear rotation motions (pitch, roll and yaw). Swaying refers to the linear side-to-side motion, while rolling and pitching represent the tilting rotation of a ship about its front-back axis and side-to-side axis, respectively. Due to combined motions of swaying, rolling and pitching, the deck of a cruise ship may get inclining and then recovering periodically as a result of the counter-rotating torque. Hereinafter, we do not distinguish these motion types and use swaying instead. This special combined movement feature can be quantified by two parameters, swaying amplitude $B(t)$ and phase $\varphi(t)$. It should be noted that here, $\varphi(t)$ is periodically changing with time t. The exact form of ship motions in seaways should be based on water movement and wind influence features, however, for simplicity and without loss of generality, we assume,

$$\varphi(t) = M \times sin(t), \tag{1}$$

where M indicates the maximum ship ground inclining degree.

2.2 Pedestrian Movement Features

When a pedestrian moves smoothly on a horizontal floor and there is no swaying, the pedestrian movement is driven by the internal self-driven force, F_e, as shown in Fig. 1b. This internal driven force makes the pedestrian move with a speed not far

away from his expected speed v_e, thus the required evacuation time can be estimated based on walking speed, queuing length, and emergency exit capacity [3]. However, it should be noticed that the movement of a pedestrian is accomplished step by step, using their two legs. As a consequence, there is a gait cycle, as reported in [9, 10]. Thus, when the ground is swaying, the pedestrian gait would be affected by the new force component, the inertial force F_s, as shown in Fig. 1b. This new force component can be projected onto two directions, i.e., the pedestrian movement direction and the direction perpendicular to his movement direction. The force component along pedestrian movement direction, $F_{e\parallel}$, would affect the maximum speed that pedestrians can achieve, while the force component along the lateral direction would affect the gait cycle, so we introduce a periodically changing force component along the lateral direction, i.e., F_p to quantify this influence.

For the internal self-driven force, as in other force-based models [2, 7], we take the following form,

$$F_e = m \frac{\mathbf{v} - \mathbf{v_e}}{\tau} \tag{2}$$

where $\tau = 0.5\,\text{s}$ is selected according to Ma et al. [8]. The ship swaying induced parallel force component $F_{e\parallel}$ can be denoted as,

$$F_{e\parallel} = F_s \times cos\psi \tag{3}$$

where ψ means the angle between F_s and F_e. For the step by step lateral movement of the pedestrian, we assume that,

$$F_p = A \times sin\theta \tag{4}$$

It should be noted that a pedestrian can sense the ship swaying, and can as a result adjust his gait, thus in Eq. (4), A quantifies the influence of the ship swaying amplitude $B(t)$, while θ represents his gait cycle, which can be determined by

$$A = f(B) = F_s \times sin\psi = \beta B(t)sin\psi \tag{5}$$

$$\frac{d\theta}{dt} = \Omega + cB(t)sin(\varphi - \theta + \alpha) \tag{6}$$

Here, c quantifies pedestrians' sensitivity to ship swaying amplitude $B(t)$ and phase $\varphi(t)$. Ω is a random step frequency, which can be estimated following the pedestrian movement experiments [4]. α is a phase lag parameter. β represents the effect of friction when a pedestrian walks on an inclining ground.

3   Results and Discussion

Equations (1) to (6) in Sect. 2 together describe the forced movement pattern for a pedestrian on a swaying ship. It should be noted that in reality, the ship swaying induced force component F_s for a pedestrian might be very complex. So, in the present section, we explore its effects by performing two simple case studies.

Firstly, we place a pedestrian 5 m away from his target, as shown in Fig. 2a. The pedestrian has a free movement speed of 1.2 m/s. Three scenarios were considered:

1. The pedestrian is moving on a horizontal ground, without ship swaying.
2. The ship is swaying along the direction perpendicular to the pedestrian's movement direction.
3. The ship is swaying along the direction parallel to the pedestrian movement direction.
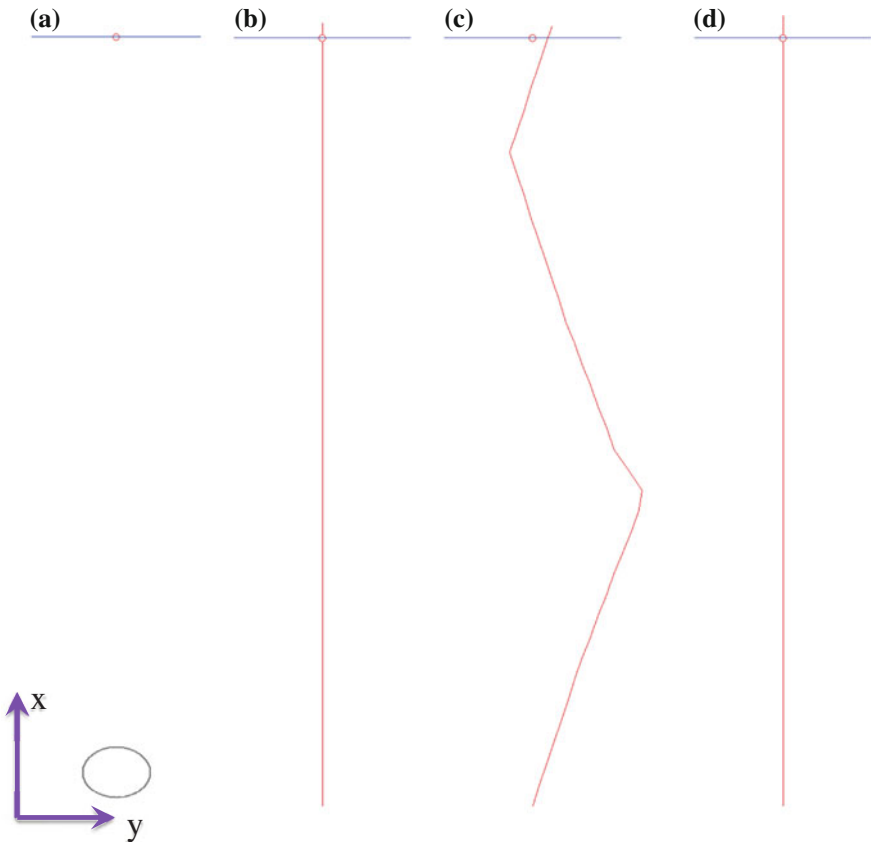
Fig. 2   Single pedestrian movement trajectories under different conditions: initial configuration (**a**); no sway (**b**); Y-direction sway (**c**); X-direction sway (**d**)

(a)

(b)
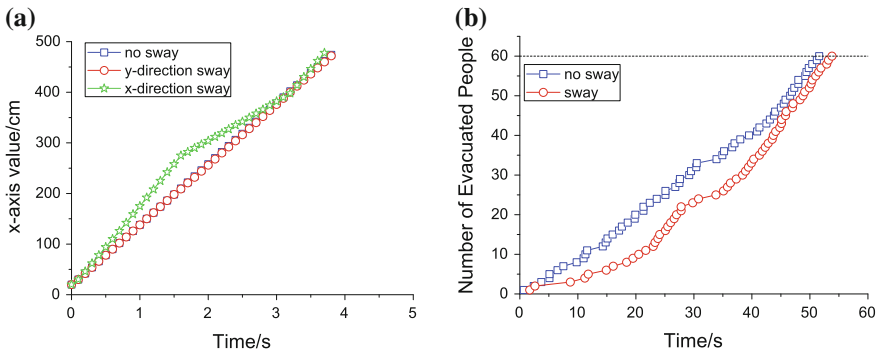
Fig. 3 Effect of ship swaying: pedestrian movement features (**a**); ship passenger evacuation process (**b**)

Simulation snapshots for these three different scenarios can be found in Fig. 2b, c, d, respectively. As can be found in these figures, when there is no swaying, the pedestrian can move freely towards his target. When the ship is swaying perpendicular to the pedestrian movement direction, we can see as a result of the swaying, the pedestrian makes lateral movements when approaching his target. That is due to the ship swaying induced inertial force exerted on that pedestrian, which changed his gait. We can also find that, although the pedestrian made lateral movements, the movement towards his direction has barely been influenced, as can be found in Fig. 3a. When the ship is swaying along the direction parallel to the pedestrian movement direction, as shown in Fig. 2d, his trajectory seems like the one when there is no ship swaying, as in Fig. 2b. We further compared the spatio-temporal feature of these trajectories shown in Fig. 2b, d, and found, as shown in Fig. 3a, that the pedestrian accelerates at first and then decelerates, meaning he keeps changing his speed during the process when he moves towards his target in the case when the ship is swaying along the direction parallel to his movement direction. We can see that the ship swaying affects pedestrian microscopic features even in these simple conditions.

Secondly, scenarios of a ship evacuation with/without swaying were simulated. In case of emergency, prior to any decision to actually abandon the ship, passengers on a ship have to be evacuated to the assembling site. That is because if abandoning is unavoidable, these passengers can be evacuated immediately, and if there is no need to abandon ship, dealing with the emergency would be much easier with no passengers around. So, passengers were ordered to evacuate to the assembling area on the right side, i.e., front of the ship in the present case, as shown in Fig. 4. There were in total 60 passengers on the ship. In Fig. 4a, b we show the trajectories of those passengers on the ship when there is no sway and when there is sway, respectively. Comparing these figures, we can easily find that due to ship swaying, passengers made lateral movements during evacuation. The lateral movement slowed down the evacuation process, as shown in Fig. 3a. We can also find that for those passengers

(a)

(b)
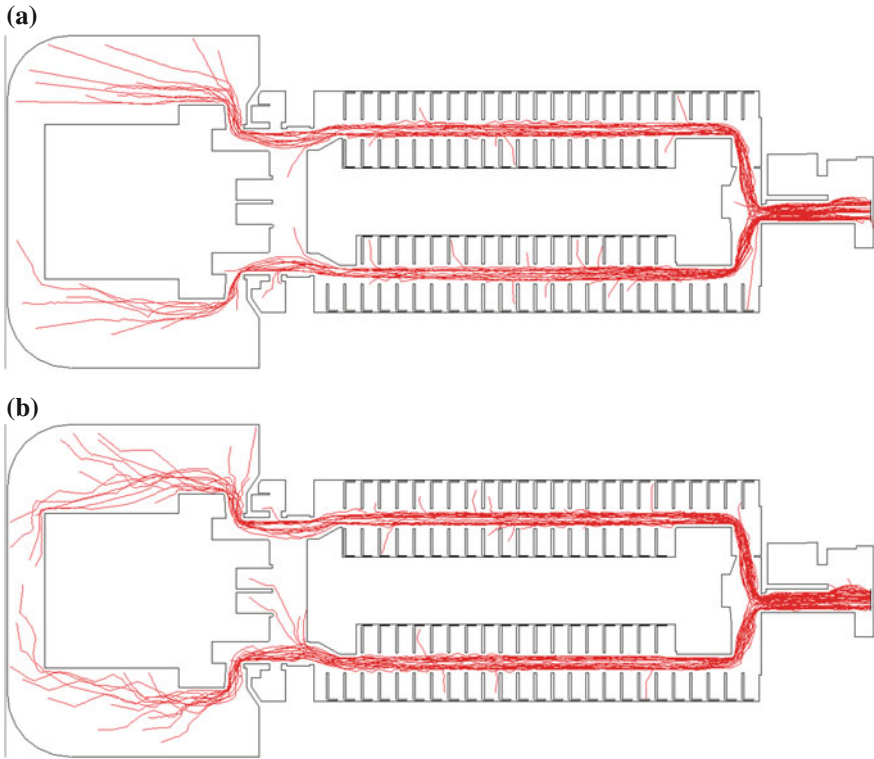
Fig. 4 Passenger evacuation simulation snapshots: no ship sway (**a**); ship swaying (**b**)

initially located in the relatively open area, as shown in the left part of Fig. 4, their trajectories show clear curved features when the ship is swaying. When there is no sway, these trajectories were almost linear, representing these passengers can move freely towards their targets. For those who were located in the long channel, as can be found in the right part of Fig. 4, they were barely influenced by the swaying ship. The reason is that the channel is so narrow that passengers' lateral movements were hindered by those chairs and walls.

When we compare the evacuation process, as can be found in Fig. 3b, when there was no ship swaying, the total assembling time for 60 passengers is only slightly shorter than when there was ship swaying. That is because the evacuation processes were mainly performed in the long channel section, as shown in Fig. 4. However, the assembling efficiency when there was no sway is always higher, as indicated by the number of assembled people shown in Fig. 3b. That is because, passengers located on the back and front sections had to make movement along the ship swaying direction, which would slow them down, as shown in Fig. 3a.

4 Conclusion

An agent-based passenger evacuation model was built. Each agent in the model can sense ship swaying and adjust its own gait. This way, forced pedestrian movement feature as a result of ship swaying was mathematically quantified. Simulations of single pedestrian movement show that the angle between pedestrian movement direction and ship swaying direction may influence spatio-temporal features of a pedestrian. Thus, under the situation of total evacuation, the passenger assembling efficiency would be affected. The simulated assembling time provides a very important criterion to evaluate the total evacuation time needed for an orderly evacuation. It should also be noticed that the computed evacuation time gives an estimate of the time the passengers need to get out of the ship interior and reach a boarding site, thus the influence of the ship interior can be evaluated to find bottlenecks.

References

1. Azzi, C., Pennycott, A., Mermiris, G., Vassalos, D.: Evacuation simulation of shipboard fire scenarios. In: Fire and Evacuation Modeling Technical Conference (2011)
2. Chraibi, M., Seyfried, A., Schadschneider, A.: Generalized centrifugal-force model for pedestrian dynamics. Phys. Rev. E **82**(4), 046111 (2010)
3. Daamen, W., Hoogendoorn, S.P.: Emergency door capacity: influence of door width, population composition and stress level. Fire Technol. **48**(1), 55–71 (2012)
4. Fang, Z.M., Song, W.G., Liu, X., Lv, W., Ma, J., Xiao, X.: A continuous distance model (CDM) for single-file pedestrian movement considering step frequency and length. Phys. A: Stat. Mech. Appl. **391**(1–2), 307–316 (2012)
5. Galea, E.R., Deere, S., Brown, R., Filippidis, L.: An experimental validation of an evacuation model using data sets generated from two large passenger ships. J. Ship Res. **57**(3), 155–170 (2013)
6. Ginnis, A.I., Kostas, K.V., Politis, C., Kaklis, P.D.: Velos: a VR platform for ship-evacuation analysis. Comput. Aided Des. **42**(11), 1045–1058 (2010)
7. Helbing, D., Farkas, I., Vicsek, T.: Simulating dynamical features of escape panic. Nature **407**(6803), 487–490 (2000)
8. Ma, J., Song, W., Fang, Z., Lo, S., Liao, G.: Experimental study on microscopic moving characteristics of pedestrians in built corridor based on digital image processing. Build. Environ. **45**, 2160–2169 (2010)
9. Ma, J., Song, W., Lo, S.M., Fang, Z.: New insights into turbulent pedestrian movement pattern in crowd-quakes. J. Stat. Mech. Theor. Exp. **2013**(02), P02028 (2013)
10. Olivier, A.H., Marin, A., Crétual, A., Pettré, J.: Minimal predicted distance: a common metric for collision avoidance during pairwise interactions between walkers. Gait Posture **36**(3), 399–404 (2012)
11. Valanto, P.: Time dependent survival probability of a damaged passenger ship iievacuation in seaway and capsizing. HSVA Report (1661) (2006)

Granularity of Pre-movement Time Distribution in Crowd Evacuation Simulations

Jakub Porzycki, Jarosław Wąs, Robert Lubaś and Grzegorz Bazior

Abstract This paper addresses issues of spatial distribution of pre-movement time. Three different, real life cases of egress are analysed. In all the analysed cases a coarse spatial distribution of pre-movement time is observed. On the basis of the examples the authors investigate whether this phenomenon has a significant influence on the evacuation process. It has been found that in more complex scenarios, the spatial distribution of pre-movement time affects the evacuation process, while in simple scenarios (like large room evacuation) no significant influence is observed. Finally, some factors that increase the magnitude of the observed phenomenon were identified, namely the complicated geometry of the facility, evacuees confusion, existence of groups and appearance of a leader. As a consequence of the findings, it is recommended to include coarse spatial distribution of pre-movement times in simulations of complex scenarios.

1 Introduction

In practice *pre-movement time* is a significant component of the total evacuation time. In general, the term *pre-movement time* refers to the time before evacuation of an area. More precisely, pre-movement time is *the interval between the time at which the alarm signal is given and the time at which the decision is made and person starts the evacuation process* [1].

With respect to fire safety engineering, there are two terms crucial from a safety point of view: RSET (Required Safe Evacuation Time) and ASET (Available Safe

J. Porzycki (✉) · J. Wąs · R. Lubaś · G. Bazior
AGH University of Science and Technology, Mickiewicza 30, 30-059 Kraków, Poland
e-mail: porzycki@agh.edu.pl

J. Wąs
e-mail: jarek@agh.edu.pl

R. Lubaś
e-mail: lubas@agh.edu.pl

G. Bazior
e-mail: bazior@agh.edu.pl

305
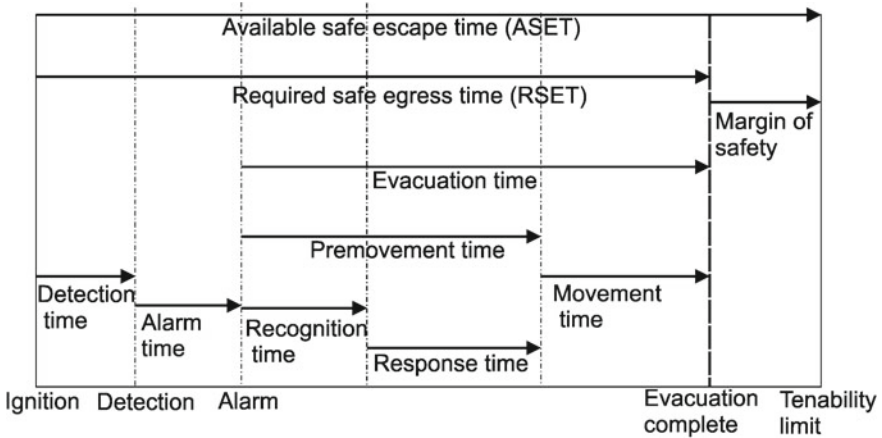
Fig. 1 Classification of evacuation time components according to SFPE Handbook of Fire Protection Engineering

Evacuation Time). On the one hand, RSET refers to *the time required for escape*, on the other hand, ASET is defined as *the time to loss of tenability* [5]. According to the methodology proposed in the SFPE Handbook of Fire Protection Engineering [1], particular components of the evacuation time are classified as follows (Fig. 1):

The response of occupants in buildings and other facilities during hazardous situations depends on many factors. The sample factors are occupant alertness (awakens, long term occupancy, medical care etc.) [1], occupant familiarity with a facility/environment, complexity of a facility/environment, social affiliation, occupant density, and effectiveness of the alarming system (poor, average or good) [4].

One can also point out many other factors influencing pre-movement times such as frequency of false alarms, training of occupants, commitment (it is usually reluctant to turn attention of people committed to an activity) [1].

The issue of pre-movement time has been a subject of an intensive research during the past few years. Zhang et al. analysed evacuation times of students from a classroom [8] and finally discovered that it corresponds to log-normal distribution and varies within a region of about 30 % of the mean value. Another interesting observation in the article is that the first arrival student has a great significance on the evacuation results and optimises influence of pre-movement time due to the coordination among evacuees.

D'Orazio et al. recently presented an interactive wearable system for reducing pre-movement time [2]. The system consists of two main parts: a Zig-Bee-based localisation module which identifies the occupants positions after the alarm and individual electronic devices generating a personal stimulus to latecomers.

Rogsch et al. [6] tested the correlation between initial distribution of occupants in a building and the distributions of evacuation times. They concluded that the range of the pre-movement time interval has a major influence of the pedestrian movement inside the building, especially the pre-movement time interval influences the density inside the staircases.
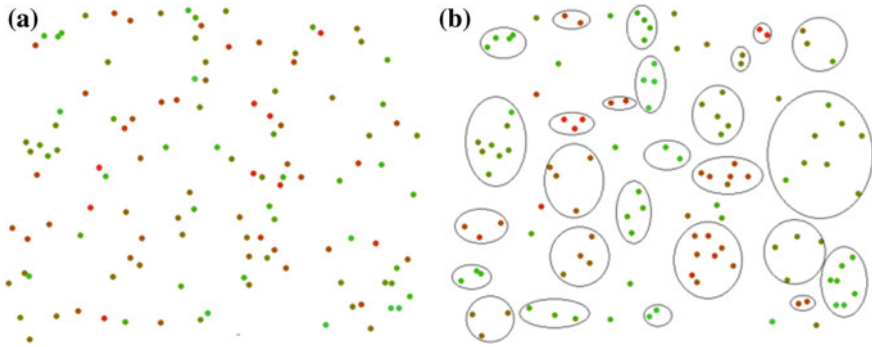
Fig. 2 Illustration of the stated hypothesis. Pedestrians are represented as *dots*, the *redder* the *dot*—the longer is its pre-movement time. In both figures the overall distribution is the same (normal): classical approach, with fine spatial granularity (**a**); coarse spatial granularity, where similar pre-movement times appears among all the members of the groups (**b**)

2 Hypothesis of Coarse Spatial Granularity

In the vast majority of crowd dynamics simulation the only assumption about pre-movement time is that it can be described using predefined distribution (uniform, normal, log-normal or exponential) [6, 8]. It is also the only requirement in documents that define validation and verification procedures [3, 7]. However, no attention is given to its spatial distribution (see Fig. 2). It is assumed that every pedestrian starts his/her movement independently from each other.

Contrary to this classical approach, the authors claim that the pedestrians pre-movement time strongly depends on its position and behaviours of its neighbours. Therefore, in real life situation we observe rather coarse, than fine spatial granularity of pre-movement time distribution. In order to investigate this hypothesis we analysed a number of real life evacuation and normal condition egress scenarios.

3 Observations of Real Life Evacuation Scenario

3.1 Egress of a Football Stadium Tribune

We analysed a normal condition egress of the football stadium tribune with five sectors and capacity of 5,806 persons. During the observation of the event tribune was occupied by approximately 5,000 fans (see Fig. 3a). Significant differences in the behaviour of persons occupying the particular sectors of the stadium were observed. In the first sector (on the left) and fifth sector (faintly visible on the right) the vast majority of fans began to leave the stadium quickly after the match, only *small groups* stayed longer in their places. On the other hand, in the three central sectors
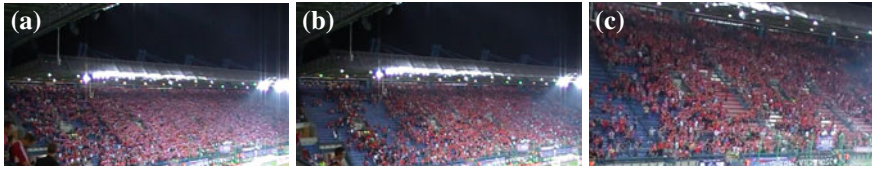
Fig. 3 Consecutive stages of normal condition egress of the Wisla Krakow stadium. Easily observable evidence of coarse spatial granularisation of pre-movement times: initial state (moment when referee ends the match) (**a**); 2 min, 53 s differences in behaviour of whole sectors (**b**); 4 min, 28 s large spots of empty seats, nearby the dense crowd (**c**)

only *small groups* of fans began to leave early, while most of them decide to stay longer to thank the team. This situation is visible in Fig. 3a. At this moment one can observe coarse granularity on two levels—different decision between sectors, as well as *groups* decision to behave differently than its sector.

Figure 3c shows the three central sectors a few minutes after ending the match. Coarse spatial granularisation at the group level is clearly visible. There are dense groups of fans next to a relatively large area of empty seats. In the case of the classical approach to pre-movement times distribution we would rather observe tribunes with a uniform sparse crowd, without large empty spots.

3.2   Announced Fire Drill in a Lecture Hall

Another test is an announced evacuation of a lecture hall containing 450 students. Participants were informed about the evacuation and instructed what they should do. The population was young and prepared for evacuation, therefore the total evacuation time was short (1 min 57 s). The observed minimal and maximal pre-movement times were only 1 and 6 s, respectively.

The initial state, at the moment of triggering the alarm (time = 0 s), is presented in Fig. 4a. After 2.5 s one can observe the number of students that already stood up. Even in the case of such a short pre-movement time coarse granularity of its spatial distribution is visible. Figure 4c shows the situation at time = 6 s—all students have begun to move towards the exit, and the first persons have already left the lecture hall. Finally, the evacuation state at time = 25 s is shown in Fig. 4d—high density, clogging exit areas and queues forming are observed.

Generally, efficient evacuation is observed: occupants evacuate without any hesitation and delay. All the participants try to leave the hall as quickly as possible, however no competitive behaviour is observed. Clogging appears only in the close vicinity of exits.

Fig. 4 Consecutive stages of an announced evacuation of a lecture hall. One can observe how quickly all the occupants begin their movement towards the exits. In the last figure the clogging of exit areas is visible: initial state (**a**); 2 s after drill (**b**); 6 s after drill (**c**); 25 s after drill (**d**)

3.3 Unannounced Fire Drill in an Academic Building

A completely different behaviour was observed during unannounced evacuation test of an academic building. The fire alarm was triggered at 9:20 a.m. when all the occupants (approximately 350 persons in the monitored area) perform their normal activity: several lectures and laboratories were taking place, a number of researchers was in their rooms, as well as some office staff. The whole evacuation process took 16 min 45 s, while 95 % persons were evacuated in 14 min 40 s.

The beginning of the evacuation process is presented in Fig. 5a. One should note the behaviour of a lecturer (a person in a white shirt): after the siren, he goes downstairs to check the authenticity of the alarm, returns to lecture hall and instructs the students to evacuate. Approximately 30 s later a security guard appears and checks the consecutive rooms to make sure that everyone was informed about the evacuation (Fig. 5b). Both lecturer and security staff are the leaders that trigger off the evacuation of rooms.

Figure 5c shows the moment, when a few persons join the pedestrian stream from the lecture hall. Single persons were able to join the stream without any qualitative change of its flow. Contrary to this, when a larger group (17 persons) joins the stream, one can observe the formation of queue (Fig. 5d).

It is worthwhile to note, that the man with a blue-grey hood (Fig. 5c) is an example of a person who goes upstairs instead of evacuating the area. There could be two reasons of such a behaviour: one does not receive the information about evacuation

Fig. 5 Unannounced fire drill in an academic building: a lecturer (*white shirt*) - leaves the classes to check the authenticity of the evacuation (40 s) (**a**); evacuation of lecture halls begins, security staff appears (1 min 12 s) (**b**); single person joins the stream from another room (**c**); a larger group joining the same stream (**d**)

or ignores the information. During the whole experiment, there were approximately 25 persons who went upstairs.

The outflow of the discussed evacuation was measured in the staircase, below the corridor shown in Fig. 5. This is presented in Fig. 6. During the evacuation process there are peaks in flow, when consecutive groups are evacuating. Between peaks there are long breaks (30–120 s) when no one appears on the staircase. In the whole building there are no obstacles or bottlenecks that can slow down the evacuees in such
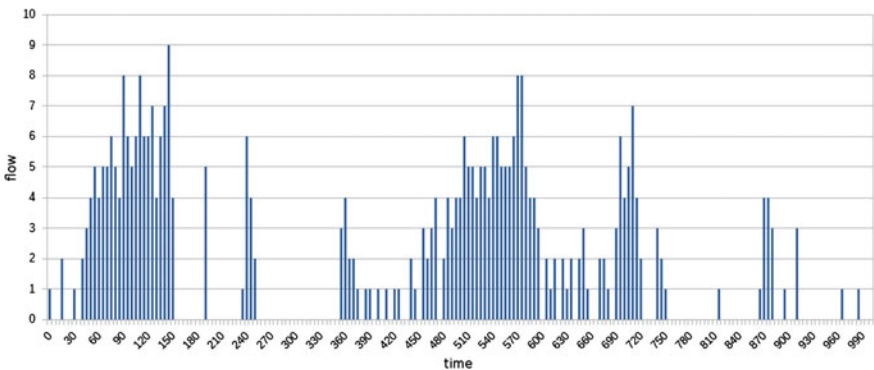
Fig. 6 Outflow in the staircase below the corridor. Each *bar* in the chart shows the number of pedestrians passing through, in consecutive 5 s time windows

a way. Therefore, it is clear that the observed outflow pattern is caused mainly by coarse spatial pre-movement time distribution, where groups of people start moving at the same time.

4 Analysis

In all analysed real life scenarios, one can observe that the spatial granularity of pre-movement time is coarse. In the stadium, the large spots of empty seats and dense crowd nearby are clearly visible. Moreover, on a larger scale the pre-movement time distribution differs significantly between sectors. During the unannounced evacuation, the existence of groups that make the decision to begin evacuation at the same time can be detected by the analysis of the outflow plot. In the case of the announced evacuation in the lecture hall, the coarse granularity of pre-movement time was more subtle, due to the fact that it takes only 6 s to complete the pre-movement time phase by all the participants, however it was noticeable. Having such evidence it should be clear that coarse granularity of pre-movement time distribution is a fact. Thus, two questions should be asked: *Does observed phenomenon significantly affect the evacuation process? Should it be included in crowd dynamics simulations?*

The only example where the evacuation process was not quantitatively influenced by spatial distribution of pre-movement time is the announced evacuation of the lecture hall. In this case the occupants were in the same room and were well prepared for the evacuation.

The fans in the stadium are also prepared to leave, but they do not receive a clear signal to leave—it is their decision to leave or to stay while longer. Moreover, the visibility of the actions in the other sectors was reduced.

During the unannounced fire alarm one can observe that spatial time distribution is strongly related with the existence of leaders (lecturer or security staff etc.), they trigger the evacuation of larger groups of pedestrians. This is especially significant when people are unprepared for evacuation and do not have the full knowledge as what they have to do. The fact that the occupants were in different rooms magnified the granularity of pre-movement time distribution. One can observe the queue before staircase when two groups of pedestrians merge, such a situation will probably not occur if we assume fine spatial distribution—there will be no numerous groups.

It is worthwhile to note that, in both the stadium case and the unannounced fire alarm case the pre-movement time was a significant part of the total evacuation time, while in the case of announced evacuation it takes only a few seconds. On the basis of the discussed examples, we presume that spatial distribution of pre-movement time can be omitted in simulation of simple scenarios (occupants prepared for evacuation, clear signal, simple geometry, lack of groups and leaders). However, in the case of complex scenarios of multi-room and multi-floor buildings, in the case of pedestrians unprepared for evacuation, where they can follow the groups or some leaders, the spatial distribution of pre-movement times is coarse and can significantly change the evacuation process.

5   Summary

The phenomenon of coarse spatial distribution of pre-movement time was discussed in this paper. Three real live cases: stadium tribune normal condition egress, announced evacuation of a lecture hall and an unannounced fire alarm in academic building were analysed. We have shown that in terms of spatial relations the distribution of pre-movement time is coarse-grained. Pedestrians have a tendency to start their movement according to decision of group, neighbours or leaders.

There is a big class of complex scenarios where simulation results can be strongly affected by the pre-movement time spatial distribution. We identify the list of factors that can increase this influence: complex geometry with multiple rooms, presence of persons unprepared for evacuation, lack of knowledge what action should be taken, existence of groups or appearance of leaders. Contrary to this, in simple scenarios one cannot identify no significant influence.

According to our knowledge, the coarse spatial granularity of pre-movement time distribution is not taken into account in neither crowd dynamics simulations nor verification and validation tests. In conclusion we would like to emphasise, that in real life complex scenarios this phenomenon can change the evacuation process and it should be considered in models.

References

1. DiNenno, P.J. (ed.): SFPE Handbook of Fire Protection Engineering, 3rd edn. National Fire Protection Association, Bethesda, MD (2008)
2. D'Orazio, M., Longhi, S., Olivetti, P., Bernardini, G.: Design and experimental evaluation of an interactive system for pre-movement time reduction in case of fire. Autom. Constr. **52**, 16–28 (2015)
3. IMO: Guidelines for evacuation analysis for new and existing passenger ships. msc.1/circ.1238. Technical report. International Maritime Organization (2007)
4. Proulx, G., Fahy, R.F.: The time delay to start evacuation: review of five case studies. Fire Saf. Sci. **5**, 783–794 (1997)
5. Purser, D.: ASET and RSET: addressing some issues in relation to occupant behaviour and tenability. Fire Saf. Sci. **7**, 91–102 (2003)
6. Rogsch, C., Galster, R., Luthardt, T., Mohr, D.: The effect of pedestrian placement and pre-movement times on evacuation simulation. Transp. Res. Procedia **2**, 291–299 (2014). The Conference on Pedestrian and Evacuation Dynamics 2014 (PED 2014), 22–24 Oct 2014, Delft, The Netherlands
7. Ronchi, E., Kuligowski, E.D., Reneke, P.A., Peacock, R.D., Nilsson, D.: NIST Technical Note 1822, the process of verification and validation of building fire evacuation models. Technical report. NIST (2013)
8. Zhang, J., Song, W., Xu, X.: Experiment and multi-grid modeling of evacuation from a classroom. Phys. A Stat. Mech. Appl. **387**(23), 5901–5909 (2008)

Estimation of Discretised Motion
of Pedestrians by the Decision-Making Model

Pavel Hrabák, Ondřej Ticháček and Vladimíra Sečkárová

Abstract The contribution gives a micro-structural insight into the pedestrian decision process during an egress situation. A method how to extract the decisions of pedestrians from the trajectories recorded during the experiments is introduced. The underlying Markov decision process is estimated using the finite mixture approximation. Furthermore, the results of this estimation can be used as an input to the optimisation of a Markov decision process for one 'clever' agent. This agent optimises his strategy of motion with respect to different reward functions, minimising the time spent in the room or minimising the amount of inhaled CO.

1 Introduction

This study can be used as an auxiliary calibration tool for microscopic models of pedestrian flow with spatially discretised motion of agents, as e.g. floor-field model [4] or optimal-steps model [7]. The results can be applied in the navigation robotic systems [8]. The introduced method builds upon the floor-field model. Thanks to the restriction to the discretised motion of pedestrian we are able to express the local decisions of pedestrian in the terms of Markov decision process [5].

For the analysis of the real data, we use the experimental data from a passing-through experiment [1]. In this experiment, pedestrians were instructed to pass through a simple room equipped by one entrance with controlled inflow and one exit of the width 60 cm. Since we are mainly interested in the pedestrian interaction, we used the data from the rear camera covering the space of 2.5 m in front of the exit and short part of the corridor behind the exit.

P. Hrabák (✉) · O. Ticháček · V. Sečkárová
The Institute of Information Theory and Automation of the Czech Academy of Sciences,
Pod Vodarenskou Vezi 4, 182 08 Prague 8, Czech Republic
e-mail: hrabak@utia.cas.cz

O. Ticháček
e-mail: tichaond@utia.cas.cz

V. Sečkárová
e-mail: seckarov@utia.cas.cz

Throughout the article, we use the notation related to Markov decision processes (MDP) adopted from [5]. The main task of the contribution is to express the basic entries of the MDP theory in the scope of pedestrian flow dynamics. This is necessary to use the optimisation technique described in [5, Chap. 4].

2 Basic Concept

Let us describe the MDP in general. The considered decision process (DP) is characterised by a sequence $(s_1, a_1, s_2, a_2, \ldots, s_{T-1}, a_{T-1}, s_T)$ of states $s_t \in S$ and performed actions $a_t \in A$. Here, T plays the role of a finite time horizon used for the optimisation. At time t an agent, who is making the decision, observes the system to be in state s_t and based on this observation performs an action a_t with conditional probability $p_t(a_t \mid s_t)$. The system reacts to the action stochastically and the state changes to s_{t+1} with conditional probability $p_t(s_{t+1} \mid s_t, a_t)$. This probability can be understood as the agent's image of the environment behaviour. The Markov property is hidden in the fact that both, the decision part $p_t(a_t \mid s_t)$ and the environmental model $p_t(s_{t+1} \mid s_t, a_t)$, depend only on the situation at time t. Then, the probability of a sequence $(s_1, a_1, s_2, a_2, \ldots, s_{T-1}, a_{T-1}, s_T)$ is given as

$$\Pr(s_1, a_1, s_2, a_2, \ldots, s_{T-1}, a_{T-1}, s_T) = p(s_1) \prod_{t=1}^{T-1} p_t(a_t \mid s_t) p_t(s_{t+1} \mid s_t, a_t). \quad (1)$$

This concept can be easily applied to the floor-field model [4] (For more details about the model we refer the reader to [6]). The floor-field model is a particle hopping model defined on a rectangular lattice L representing the discretised layout of the simulated facility. Particles are hopping between cells stochastically according to the hopping probabilities, which are influenced by the static floor field S. Usually $S(y) = \text{dist}(y, \mathbf{E})$ refers to the distance of the cell y to the exit $\mathbf{E}$ in defined metric dist. Let the state of the system at time t be denoted by $\tau_t \in \{0, 1\}^L$, where $\tau(x) = 1$ refers to an occupied cell and $\tau(x) = 0$ to an empty cell. Let further $n_t = \sum_x \tau_t(x)$ be the number of agents in the lattice at time t.

In each algorithm step $t \to t + 1$, every agent $i \in \{1, \ldots, n_t\}$ chooses his future position $y_{i,t}$ given he is sitting in $x_{i,t}$ with probability

$$p(y_{i,t} \mid x_{i,t}, \tau_t) \propto \exp\{-S(y_{i,t})\} \mathbf{1}_{\{\text{dist}(x_{i,t}, y_{i,t}) \leq 1\}} \quad (2)$$

according to floor-field model. The model of the environment is then a consequence of the choices of future positions of all agents, i.e., the dynamics is driven by the environment model

$$p\left(\tau_{t+1} \mid \tau_t, y_{i,t}, i \in \{0, \ldots, n_t\}\right) = F(p(y_{i,t} \mid x_{i,t}, \tau_t), i \in \{0, \ldots, n_t\}), \quad (3)$$
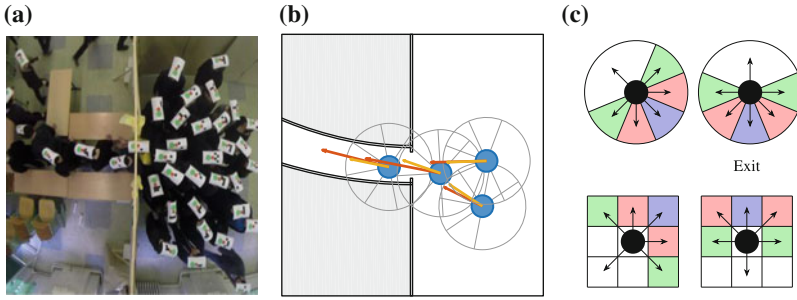
Fig. 1 Transformation of trajectory record to actions: trajectories are extracted from video records, figure from [1] (**a**); transformation to motion within sectors (**b**); interpretation as motion in the lattice (**c**)

where F is a function that reflects conflicting situation where two agents choose the same target cell.[1]

3 Estimating $p_t(a_t \mid s_t)$

This section focuses on the probabilistic decision $p_t(a_t \mid s_t)$ from the data recorded during evacuation experiment [1].

Let us assume that the pedestrians act similarly to the floor-field particles, i.e., all pedestrians are following the same decision strategy, which does not change in time and space. Furthermore, we assume that pedestrians react only on their immediate neighbourhood reflecting the direction towards the exit, but not their absolute position. Therefore, the state s_t in MDP can be associated with the state of the immediate neighbourhood. Contrary to the floor-field model we consider the neighbourhood to be oriented with respect to the direction towards the exit. The actions are associated with direction angle a pedestrian can choose, see Fig. 1.

The experimental data for trajectory analyses have been provided by our colleague Marek Bukáček (Czech Technical University). The data are in the form of paths records $\left(\mathbf{x}_i(t), t \in [t_i^{\text{in}}, t_i^{\text{out}}]\right)$, where t_i^{in} and t_i^{out} is the time of the first and the last appearance of the pedestrian i on the screen respectively. $\mathbf{x}_i(t)$ is the position of the pedestrian on the screen at time t. To match the discrete nature of the decision-making process, the motion of pedestrians has been discretised in time with the discretisation step $\Delta t = 1$ s. The vector of motion at time t is then $\Delta \mathbf{x}_i(t) = \mathbf{x}_i(t + \Delta t) - \mathbf{x}_i(t)$ and the direction of motion $\vartheta_i(t)$ is an angle given by

$$\cos \vartheta_i(t) = \frac{[\mathbf{E} - \mathbf{x}_i(t)] \cdot \Delta \mathbf{x}_i(t)}{\|\mathbf{E} - \mathbf{x}_i(t)\| \cdot \|\Delta \mathbf{x}_i(t)\|}. \tag{4}$$

This angle is then associated to the action $a \in A$ according to the Table 1. The set of actions is $A = \{\otimes, \leftarrow, \nwarrow, \nearrow, \uparrow, \downarrow, \rightarrow\}$, e.g., an angle $\vartheta_i(t) = 20°$ corresponds

---

[1]Without conflicting situations the function is just a product of the entries.

Table 1 Action set in detail

Action	$\otimes$	$\leftarrow$	$\nwarrow$	$\swarrow$	$\uparrow$	$\downarrow$	$\rightarrow$
Angle	$\emptyset$	$\left(-\frac{\pi}{8}, \frac{\pi}{8}\right)$	$\left(-\frac{\pi}{8}, -\frac{3\pi}{8}\right)$	$\left(\frac{3\pi}{8}, \frac{\pi}{8}\right)$	$\left(-\frac{3\pi}{8}, -\frac{5\pi}{8}\right)$	$\left(\frac{5\pi}{8}, \frac{3\pi}{8}\right)$	$\left(-\pi, -\frac{5\pi}{8}\right) \cup$ $\left(\frac{5\pi}{8}, \pi\right)$
Colour	Black	Blue	Red	Red	Green	Green	White

Direction angle towards the exit is 0. Colours refer to Fig. 1

to the forward motion $\leftarrow$, while $\vartheta_i(t) = 30°$ corresponds to the left-forward motion $\swarrow$. Every motion performed with velocity $v_i(t) = \|\Delta\mathbf{x}_i(t)\|/\Delta t$ less than 0.5 m/s has been considered as standing ($\otimes$).

In Fig. 2, the frequency of chosen direction with respect to the direction angle is plotted. Two main clusters for forward stepping and standing can be distinguished, the latter dominates. The data are aggregated over all pedestrians and all records for each. From this graph we can conclude that the majority of pedestrians preferred standing in line and moving forward centimetre by centimetre rather then trying to push through the crowd or overrunning it.

For the estimation of the decision process we associate the state s_t in the decision process $p(a_t \mid s_t)$ with the occupancy of the immediate neighbourhood. By the neighbourhood $N(\mathbf{x})$ of a position $\mathbf{x}$ we understand a circle around $\mathbf{x}$ with the radius 0.75 m (maximal step size) divided into 6 sectors $\{\leftarrow, \nwarrow, \swarrow, \uparrow, \downarrow, \rightarrow\}$ defined in previous section. The state $s_{i,t}$ for the decision $p(a_{i,t} \mid s_{i,t})$ of the agent i is then a vector from $\{0, 1\}^6$, where $s_{i,t}(y) = 0$ for empty sector y and $s_{i,t}(y) = 1$ for occupied sector. Here $y \in \{\leftarrow, \nwarrow, \swarrow, \uparrow, \downarrow, \rightarrow\}$. The sector is considered occupied if it contains at least one position vector of another agent or if it is covered by a wall by at least 40%. Since the data are aggregated over all pedestrians, the index i will be further omitted.

Most natural way how to estimate the decision process $p(a_t \mid s_t)$ is to compare the frequency of chosen directions (actions) given the occupancy of the neighbourhood. However, this method fails in the case of the trajectory data from considered experiment, since most of the combinations (a_t, s_t) appear very rarely. For this reason we
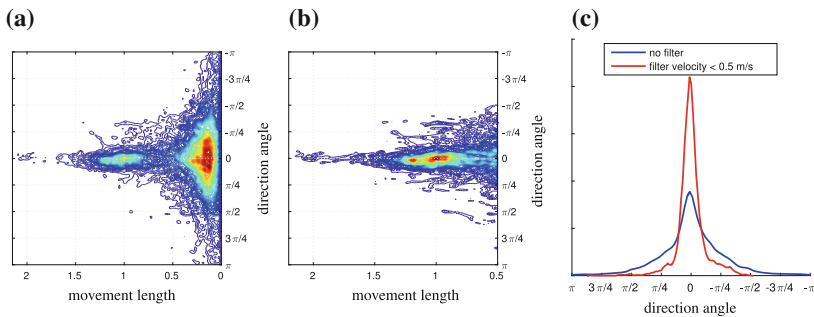
Fig. 2 The frequency of occurrence of the motion length in given direction angle. The graphs are oriented similarly to the snapshot from the experiment in Fig. 1: no filter (**a**); filter velocity < 0.5 m/s (**b**); gaussian-kernel estimation of the distribution of chosen direction (**c**)

applied the approximation of the decision by finite mixture model with forgetting [3]. The idea consists in approximation of the complex decision process $p(a_t \mid s_t)$ by the convex combination of marginal decision processes $\Theta(a_t \mid s_t(y))$, i.e.,

$$p(a_t \mid s_t) \approx p(a_t \mid \Theta, s_t) = \sum_{y \in N(\mathbf{x}_t)} \alpha_y \Theta(a_t \mid s_t(y)), \qquad (5)$$

where α_y is the coefficient of influence of the state of y to the decision; $\sum_y \alpha_y = 1$. For more details see [2].

The resulting values of the mixture model are given in Table 2. The following phenomena can be observed analysing the values in the table. The occupancy of a neighbouring sector almost always contributes with the highest value to the decision "to stand" ($\otimes$). However, a free neighbouring sector does not always tend to imply motion, see the forward sector ($\leftarrow$). The most diverse influence of the empty and occupied states show the "slightly right" ($\nwarrow$) and "slightly left" ($\nearrow$) sectors. The explanation for this may be a zipper-like effect of agents passing through a narrow exit and corridor.

The table also implies, that the occupancy of right and left sectors ($\uparrow$, $\downarrow$) does not play a significant role in agent's decision as it does not restrain him from moving in desired (forward) direction. Finally, although in principle, the occupancy of the back sector ($\rightarrow$) should not affect the agent's decision in his desire to go straight, this sector is mostly occupied if the agent is in a high-density situation (e.g. a jam) and therefore its occupancy reflects the agent's (in)ability to move at all.

4 Optimising $p_t(a_t \mid s_t)$

This chapter offers an alternative view on the application of MDP to pedestrian flow modelling. Let the result of previous section be used as the behavioural frame of the majority of pedestrians, which determines the environmental model $p_t(s_{t+1} \mid s_t, a_t)$ described by Eq. (3). The aim of this section is to equip one of the pedestrian agent by an optimal decision strategy how to move among the pedestrians following the majority behaviour.

Table 2 Influence of regressors y to decision a for two states of sector occupancy ($\circ$ symbolises empty sector, $\bullet$ occupied)

y	$\leftarrow$		$\nwarrow$		$\nearrow$		$\uparrow$		$\downarrow$		$\rightarrow$	
$\widehat{\alpha}$	0.9212		0.0749		0.0014		0.0002		0.0002		0.0021	
a	$\circ$	$\bullet$	$\circ$	$\bullet$	$\circ$	$\bullet$	$\circ$	$\bullet$	$\circ$	$\bullet$	$\circ$	$\bullet$
$\otimes$	**0.76**	**0.94**	0.03	**0.97**	0.05	**0.52**	0.11	0.12	0.12	0.11	0.07	**0.69**
$\leftarrow$	**0.22**	0.06	**0.63**	0.01	**0.73**	0.12	0.39	0.23	0.35	0.24	**0.68**	0.10
$\nwarrow$	0.01	0.01	0.02	0.01	0.05	0.06	0.09	0.11	0.10	0.11	0.06	0.04
$\nearrow$	0.01	0.01	**0.27**	0.00	0.04	0.08	0.09	0.11	0.10	0.11	0.06	0.04
$\uparrow$	0.00	0.00	0.02	0.00	0.04	0.06	0.08	0.11	0.09	0.11	0.04	0.04
$\downarrow$	0.00	0.00	0.02	0.00	0.03	0.05	0.08	0.11	0.08	0.11	0.04	0.03
$\rightarrow$	0.00	0.00	0.02	0.00	0.06	0.10	0.15	0.20	0.16	0.22	0.06	0.06

$\widehat{\alpha}$ is the weight of the regressor
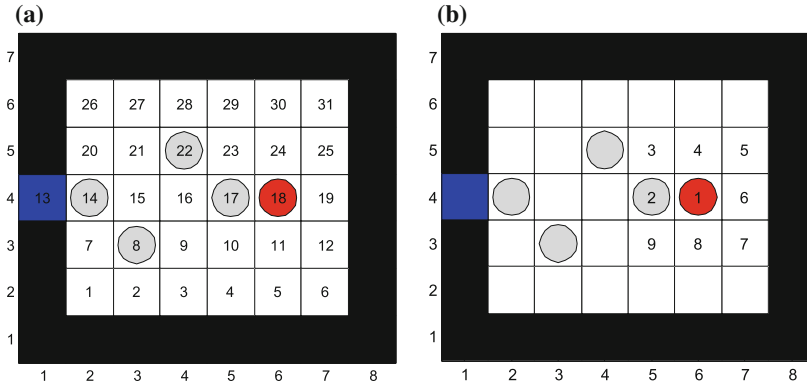
Fig. 3 An example of the state of the lattice with one clever agent (*red*) and 4 floor-field particles (*grey*): The state is $s_t = (x_t, z_t)$, where $x_t = 18$, $z_t = \{8, 14, 17, 22\}$ (**a**); The numbering of directions corresponding to actions $a_t \in \{1, \ldots, 9\}$ (**b**)

Let us in the following, for simplicity, return to the Floor-field basis of the simulation. Consider that there is one 'clever' particle among the ordinary undistinguishable floor-field particles behaving according to Eq. (2) or (5). By the optimal strategy of the clever particle we understand the sequence $(d_1, d_2, \ldots, d_{T-1})$, where $d_t(s_t) = q$ is the distribution on the set of actions A playing the role of the decision process, i.e., $p(a_t \mid s_t) = q(a_t)$. The strategy is optimised with respect to given reward function $R(s_1, a_1, \ldots, s_T)$, which can be used to model different preferences of the clever particle.

Contrarily to Sect. 3 we consider in the following the position and the orientation to be absolute, i.e., there are not preferred positions on the lattice regarding the distance or orientation towards the lattice. The optimising algorithm is supposed to find the shortest path given the maximal reward R itself. The state of the system is expressed by the position of the clever agent x_t and by the set of positions of all floor-field particles z_t, where $|z_t| = n_t - 1$ (compare to previous section, where only the neighbouring pedestrians play role). Let the positions be numbered by natural numbers as shown by an example in Fig. 3.

The actions an agent can choose are related to the 8 neighbouring sites and a possibility to stay in current position. Therefore the action set can be chosen as $A = \{1, 2, \ldots, 9\}$, where the directions are numbered as depicted in Fig. 3, i.e., $a_t = 1$ means to choose as next target site the current position $x_t = 18$; $a_t = 2$ corresponds to the target site x_t '+' $(-1, 0) = 17$, etc. Here, we note that, similarly to the floor-field, the chosen target site can be entered by a near floor-field particle. The choice of the target site is therefore influenced by the probability that other particles can change their positions.

For the purposes of this contribution we have chosen a simple updating scheme in which the clever agent moves after all other particles performed their actions. Then, the environmental model $p_t(s_{t+1} \mid s_t, a_t) = p(x_{t+1}, z_{t+1} \mid x_t, z_t, a_t)$ decomposes into a stochastic part $p(z_{t+1} \mid x_t, z_t)$ and a deterministic part $p(x_{t+1} \mid x_t, a_t, z_{t+1})$ as

$$p(x_{t+1}, z_{t+1} \mid x_t, z_t, a_t) = p(z_{t+1} \mid x_t, z_t) p(x_{t+1} \mid x_t, a_t, z_{t+1}). \tag{6}$$

In our case, the transition probability (5) can be simplified to the form

$$p(z_{t+1} \mid x_t, z_t) \propto \exp\{-U(z_{t+1})\}, \qquad U(z_{t+1}) = \sum_{j=1}^{|z_{t+1}|} \mathrm{dist}(z_{t+1}(j), \mathbf{E}) \quad (7)$$

for all states z_{t+1} reachable from z_t by the motion of floor-field particles by one site. The introduced potential U supports the states in which particles are closer to the exit and therefore suppresses the random motion away from the exit.

The above mentioned concept fits the finite time optimisation of the MDP strategies using the backward induction algorithm described in [5, Sect. 4.5]. The final step is to define properly the reward function R. The reward function is defined as a cumulation of local rewards $r_t(s_t, a_t)$ and the final reward $v_T(s_T)$, i.e.,

$$R = \sum_{t=1}^{T-1} r_t(s_t, a_t) + v_T(s_T), \qquad r_t(s_t, a_t) = \sum_{s_{t+1}} p(s_{t+1} \mid s_t, a_t) r_t(s_{t+1}, s_t, a_t). \quad (8)$$

The final reward is the same for all agents preferences taking into account the distance to the exit multiplied by a factor of 2, i.e., $v_T(s_T) = -2\, \mathrm{dist}(x_T, \mathbf{E})$. The local reward then reflects the agent's preferences. We introduce two main approaches: minimising the time spent in the room and minimising the amount of inhaled carbon monoxide (CO) related to the aim to minimise number of lost conflicts.

The reward function minimising the time simply subtracts one reward unit for each step an agent spends outside the exit, i.e.,

$$r_t(s_{t+1}, s_t, a_t) = \begin{cases} 0 & x = \mathbf{E}, \\ -1 & x \neq \mathbf{E}. \end{cases} \quad (9)$$

The reward function minimising the amount of inhaled CO takes into account the possibility that the agent can choose a site which becomes occupied by another particle. Such choice can be interpreted as running to another pedestrian, which causes a significant loss of energy with no improvement of the distance to the exit. Such situation costs 2 reward units, while standing only one half. Therefore

$$r_t(s_{t+1}, s_t, a_t) = \begin{cases} 0 & x_t = \mathbf{E}, \\ -1/2 & a_t = 1, \\ -1 & a_t \neq 1,\ x_{t+1} \notin z_{t+1}, \\ -2 & a_t \neq 1,\ x_{t+1} \in z_{t+1}. \end{cases} \quad (10)$$

5 Conclusions and Future Plans

The main goal of this paper was to introduce a concept of Markov decision process (MDP) to the pedestrian flow simulation. Two aspects have been studied by means

of this concept: the estimation of pedestrian behaviour within crowded area and the optimisation of the decision with respect to given pedestrian preferences. Both approaches are motivated by the cellular floor-field model used for simulation of pedestrian evacuation.

The estimation of pedestrian behaviour have been analysed from experimental trajectories. By means of the space discretisation and finite mixture approximation we have been able to extract the pedestrians decision in relation to the occupation of his immediate neighbourhood. The analysis showed that the main influence to the decision has the occupation of the area in the forward direction towards the exit. Further, most of the decisions pedestrians performed was to move forward or stay at the position. The overrunning of the crowd was rather a rare event.

The results of the experiment analyses can be then used as the input to the optimisation task of one 'clever' agent among usual floor-field particles. We have introduced a technique of expressing the pedestrian evacuation model in terms of the MDP. Furthermore, two different reward functions have been introduced to simulate different preferences of the clever agent: to minimise the time spent in the room and to minimise the amount of inhaled carbon oxygen, i.e. minimising the number of conflicts. In the future we plan to test the combination of those two strategies in order to prove that optimal is the combination of the two above mentioned strategies.

References

1. Bukáček, M., Hrabák, P., Krbálek, M.: Experimental study of phase transition in pedestrian flow. In: Daamen, W., Duives, D.C., Hoogendoorn, S.P. (eds.) Pedestrian and Evacuation Dynamics 2014, Transportation Research Procedia, vol. 2, pp. 105–113. Elsevier Science B.V. (2014)
2. Hrabák, P., Ticháček, O.: Prediction of pedestrian decisions during the egress situation: application of recursive estimation of high-order Markov chains using the approximation by finite mixtures. Technical report 2346, ÚTIA AV ČR, POBox 18, 182 08 Prague 8, Czech Republic (2015)
3. Kárný, M.: Recursive estimation of high-order markov chains: approximation by finite mixtures. Inf. Sci. **326**, 188–201 (2016)
4. Kirchner, A., Schadschneider, A.: Simulation of evacuation processes using a bionics-inspired cellular automaton model for pedestrian dynamics. Phys. A: Stat. Mech. Appl. **312**(12), 260–276 (2002)
5. Puterman, M.L.: Markov Decision Processes: Discrete Stochastic Dynamic Programming, 1st edn. Wiley, New York, NY, USA (1994)
6. Schadschneider, A., Chowdhury, D., Nishinari, K.: Stochastic Transport in Complex Systems: From Molecules to Vehicles. Elsevier Science B.V., Amsterdam (2010)
7. Seitz, M.J., Köster, G.: Natural discretization of pedestrian movement in continuous space. Phys. Rev. E **86**, 046108 (2012)
8. Spaan, M., Veiga, T., Lima, P.: Decision-theoretic planning under uncertainty with information rewards for active cooperative perception. Auton. Agents Multi-Agent Syst. **29**(6), 1157–1185 (2015)

Oppilatio: The Forecast of Crowd Congestions on Street Networks During Public Events

Daniel H. Biedermann, Peter M. Kielar and André Borrmann

Abstract At many events, the arrival of visitors depends mainly on public transport services. On such occasions, people walk from the station or bus stop to the event site. This can lead to crowd congestions since the visitors arrive in large numbers according to the schedules of the public transport services. Unfortunately, organisers of such events have very limited information about the arrival behaviour of their visitors. Normally, they only know the number of incoming visitors on the event site and the timetable of the public transport service. It is difficult to perform crowd management successfully with so little data. Oppilatio uses this limited data to determine the most likely routing paths of incoming visitors. This allows an early recognition of potential crowd congestions on the access routes and therefore the initiation of countermeasures.

1 Motivation

Size and significance of public events have increased in the last decades [1]. Therefore, research about crowd control has become more and more important. A vital aspect of crowd control is pedestrian dynamic simulations, which serves to predict the visitors' movement behaviour and can be distinguished into three different model types. Macroscopic approaches describe pedestrians as flowing densities [5] and reduce the scenario to a simple network graph. Mesoscopic approaches describe pedestrians as discrete objects that move on a cellular grid [4]. Another model type are microscopic models which simulate individual and discrete pedestrians on a continuous scenario [8]. Each model type has different attributes according to computational effort and spatial resolution [3]. Additionally, two types of hybrid modelling exist. The first type combines pedestrian models of different spatial resolutions [3]. The

D.H. Biedermann (✉) · P.M. Kielar · A. Borrmann
Technische Universität München, Arcisstraße 21, 80333 Munich, Germany
e-mail: daniel.biedermann@tum.de

P.M. Kielar
e-mail: peter.kielar@tum.de

A. Borrmann
e-mail: andre.borrmann@tum.de

second type couples pedestrian dynamic simulations with simulation models from other research fields [2]. A proper use of simulations requires valid data about all boundary conditions of the scenario (e.g. number of visitors) and background knowledge about pedestrian dynamics (e.g. for the specification of input parameters).

Unfortunately, most organisers of public events are lacking such background knowledge. Furthermore, the acquisition of valid data according to boundary conditions is difficult to achieve, especially if an event is carried out for the first time. However, knowledge about the visitors' walking behaviour is essential for organisers to successfully perform crowd control. Many visitors arrive with public transport services like subways or shuttle buses. These transport services carry the visitors to a subway station or bus stop, from which they walk to the event site. Since many events take place in an urban environment [1], the access routes are often narrow and insufficient for large crowds. It is important to forecast possible congestions and therefore to prevent hazardously high densities. Broad video observation of all access routes would be useful, but this is expensive and difficult to execute due to government regulations according to data privacy. In order to fill this gap, we developed the Oppilatio method to estimate route choices based only on public transport schedules and data of arriving visitors. Oppilatio is a real time data analysis approach which helps organisers to survey incoming pedestrian streams. Contrary to simulations, no background knowledge about pedestrian dynamics is necessary and the needed input data can be easily collected (see Fig. 1):

1. Arrival times of public transport services at the station
2. Accessible routes from station to the event site
3. Time-stamped counting of incoming visitors at the event site

Local transport operators provide timetables of their public transport services. Possible pathways from the station to the event site can be determined by openly-licensed
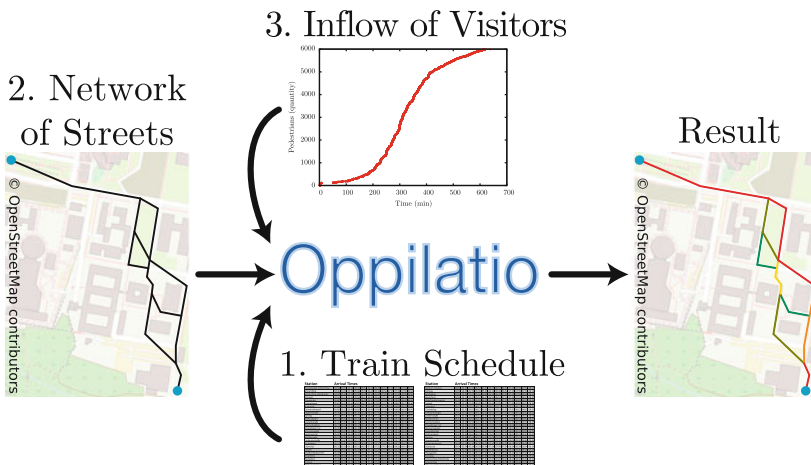
Fig. 1 Based on data commonly accessible for event organisers, it is possible for Oppilatio to calculate the routing behaviour of incoming visitors to an event site

geo-databases. The accessible routes are entered as a network of edges and nodes into Oppilatio: streets are represented by edges and intersections are represented by nodes. Time-stamped counting of incoming visitors can be acquired easily by event organisers (e.g. time-stamped entrance tickets). Solely based on this information, Oppilatio can calculate the most likely routes for each incoming visitor p_i, using algorithms described in Sects. 2 and 3.

2 Allocation of Arrival Times at the Station

We use the arrival time t_i at the event site to determine the time a visitor p_i started at the public transport station. For this calculation, we need the pedestrian's velocity, a parameter which is unknown. Therefore, we have to estimate this value based on the classical velocity distribution by Weidmann [13]. It is a normal distribution with a mean value of $v_\varnothing = 1.34$ m/s and a standard deviation of $\sigma_v = 0.26$ m/s. We assume a minimal velocity $v_{min} = v_\varnothing - 2\sigma_v$ and a maximal velocity $v_{max} = v_\varnothing + \sigma_v$. The assumption is based on our field observation, that visitors of public events have a significantly lower minimal velocity, since many of them stop on their way to the event site to communicate and socialise with other visitors.

$$\varphi_i(v_i) = \frac{1}{\sqrt{2\pi \sigma_v^2}} \exp\left(-\frac{(v_i - v_\varnothing)^2}{2\sigma_v^2} \right) \tag{1}$$

A new velocity v_i has to be determined if a velocity value larger than v_{max} or smaller than v_{min} is calculated by Eq. 1. Parameter Λ describes the set of all accessible routes $\lambda_l \in \Lambda$ from the station to the event site. The length d_l of a route λ_l is the sum of all straight route section lengths $|\mathbf{s}_{l,m}|$. The index $m = 1...M$ classifies the singular edges and nodes of a route λ_l. The sequence of indices describes the chronological order a pedestrian on route λ_l visits the nodes and edges. Therefore, the length d_l of a route λ_l with M nodes can be calculated as:

$$d_l = \sum_{m=1}^{M-1} |\mathbf{s}_{l,m}| \tag{2}$$

The parameter d_{min} defines the length of the shortest route $\lambda_{min} \in \Lambda$, and d_{max} the longest. Therefore, we can determine a minimal walking time $\Delta t_{min} = d_{min}/v_{max}$, or maximal walking time $\Delta t_{max} = d_{max}/v_{min}$. If a pedestrian enters the event site at t_i, he or she has left the station in the time interval $\tau_i \in \Delta D_i = [t_i - \Delta t_{max}, t_i - \Delta t_{min}]$. Thus, only arrival times of public transport services during this time interval can be starting times of a pedestrian p_i. If multiple transport services arrive at the station during the time interval ΔD_i, a clear assignment of starting times τ_i is not possible. In this case, we assume a normal distribution as a probability distribution to distinguish between multiple possibilities of starting times:

$$\psi_i(t) = \begin{cases} \frac{1}{\sqrt{2\pi\sigma^2}} \exp\left(-\frac{(t-\mu_i)^2}{2\sigma^2}\right) & t \in \Delta D_i \\ 0 & t \notin \Delta D_i \end{cases} \tag{3}$$

The expected value $\mu_i = t_i - \frac{1}{2}(\Delta t_{max} + \Delta t_{min})$ describes the mean value of the time interval ΔD_i. The behaviour of the normal distribution is given by the standard deviation. If we assume that our interval ΔD_i includes about 95 % of all possible values, we can determine the standard deviation as $\sigma = \frac{1}{4}(\Delta t_{max} - \Delta t_{min})$. In the next step, we determine the probability that the arrival time τ_k of a public transport service is chosen as the starting time of pedestrian p_i at the station:

$$\Psi_{i,k} = \frac{\psi_i(\tau_k)}{\sum_j \psi_i(\tau_j)} \tag{4}$$

Parameter τ_j with $j = 1...J$ corresponds to all possible arrival times of public transport services at the station relating to their timetable. If multiple starting times τ_i are possible, one starting time $\tau_i = \tau_k$ is chosen randomly relating to its probability $\Psi_{i,k}$.

3 Allocation of Routes from Station to the Event Site

In the next step, we determine the most likely route a pedestrian has chosen from the station to the event site. Thus, we introduce a rating system which is based on the physical boundary conditions of the scenario and on the cognitive routing behaviour of humans. The time a visitor p_i needed to walk from the station to the event site equals $\Delta \tau_{i,k} = t_i - \tau_k$. This corresponds to an estimated walking distance of $d_i = v_i \cdot \Delta \tau_{i,k}$. The smaller the difference between d_i and the total length d_l of a route λ_l, the higher the probability that this route was chosen by pedestrian p_i. Thus, we introduce a rating system Ξ to rate all possible routes for a visitor p_i. The route with the highest score will be assumed as the route the pedestrian has chosen:

$$\Xi(p_i, \lambda_l) = \begin{cases} \xi(p_i, \lambda_l) & v_{min} \cdot \Delta \tau_{i,k} \leq d_l \leq v_{max} \cdot \Delta \tau_{i,k} \\ 0 & \text{else} \end{cases} \tag{5}$$

In a first step, the score depends only on the difference between the estimated walking distance d_i and the total length d_l of a route λ_l. According to the potential time interval ΔD_i of a visitor, a walking distance d_i must be between $v_{min} \cdot \Delta \tau_{i,k}$ and $v_{max} \cdot \Delta \tau_{i,k}$. Thus, we can normalise the distance between d_i and d_l by:

$$\alpha(d_i) = 1 - \frac{|d_l - d_i|}{(v_{max} - v_{min}) \cdot \Delta \tau_{i,k}} \tag{6}$$

Unfortunately, the matching of walking distance d_i and total route length d_l is not sufficient, since the assumed velocities v_i are only approximations. Cognitive sciences suggest, that the navigation behaviour of humans is a complex process [11].

Some routes are more likely to be used even if the lengths between the predicted walking distance and the existing routes to the event site match not perfectly. Thus, we correct the rating $\xi(p_i, \lambda_l)$ of routes λ_l according to their attractiveness for the human navigation process. For example, pedestrians prefer routes which run close along the beeline from their position to their target Θ [9]. Based on these scientific findings, we extend the rating $\Xi(p_i, \lambda_l)$ by a factor $\beta(o_l)$ to describe the preference of beeline-oriented routes. We calculate the mean derivation $o_{l,m}$ from the beeline for each section $\mathbf{s}_{l,m}$. The beeline from a certain intersection to the target is given by $\Gamma_{l,m} = \Theta - \mathbf{e}_{l,m}$. Since the intersection $\mathbf{e}_{l,m}$ is located at the beginning of section $\mathbf{s}_{l,m}$, we can calculate the mean derivation of this section as (see Fig. 2):

$$o_{l,m} = \frac{1}{2} \left| \mathbf{e}_{l,m} + \frac{(\mathbf{e}_{l,m+1} - \mathbf{e}_{l,m}) \circ \Gamma_{l,m}}{\Gamma_{l,m} \circ \Gamma_{l,m}} \cdot \Gamma_{l,m} - \mathbf{e}_{l,m+1} \right| \tag{7}$$

The total derivation o_l equals the sum $o_l = \sum_m o_{l,m}$ of all sections of route λ_l. For the rating, we scale $o_{m,l}$ by the average beeline derivation $o_\emptyset = \frac{1}{L} \sum_{l=1}^{L} o_l$ of all routes:

$$\beta_l(o_l) = \begin{cases} 1 - \Delta p & o_\emptyset/o_l < 1 - \Delta p \\ o_\emptyset/o_l & 1 - \Delta p \le o_\emptyset/o_l \le 1 + \Delta p \\ 1 + \Delta p & o_\emptyset/o_l > 1 + \Delta p \end{cases} \tag{8}$$

According to a field experiment from Kneidl [10], 71.2 % of all routes chosen by the participants were beeline-oriented and 28.1 % were not [9]. Thus, we limited the influence of the rating to $\Delta p = \pm 0.5 \cdot (71.2 - 28.1)\% = \pm 21.6\%$. Another important aspect is the preference of humans to choose routes with a small number of direction changes [10]. A direction change occurs if the angle $\omega_{l,m}$ between two sections $\mathbf{s}_{l,m-1}$ and $\mathbf{s}_{l,m}$ differs by more than $\omega_0 = \pi/18$ [9]. The angle $\omega_{l,m}$ can be calculated by the scalar product of the neighbouring edges (see Fig. 2). The total number of direction changes h_l for a route λ_l can be calculated by the Heaviside-function:

$$h_l = \sum_m \mathscr{H}\left(\omega_{l,m} - \omega_0\right) \tag{9}$$

The rating $\gamma(h_l)$ is analogue to the calculation of the beeline factor $\beta(o_l)$ with $h_\emptyset$ as the average number of direction changes per route:
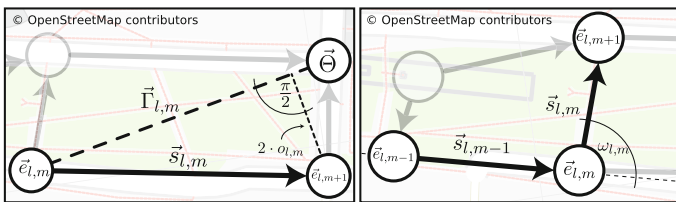
Fig. 2 Scoring calculation for the preference of beelines (*left*) and few direction changes (*right*)

$$\gamma(h_l) = \begin{cases} 1 - \Delta q & h_\varnothing / h_l < 1 - \Delta q \\ h_\varnothing / h_l & 1 - \Delta q \leq h_\varnothing / h_l \leq 1 + \Delta q \\ 1 + \Delta q & h_\varnothing / h_l > 1 + \Delta q \end{cases} \tag{10}$$

Rating parameter Δq is based on Kneidl's experiment [10]. 73.2 % of all routes selected by the participants had few direction changes, where as 26.8 % had many direction changes. Therefore, the influence of the number of direction changes was limited to $\Delta q = \pm 0.5 \cdot (73.2 - 26.8)\% = \pm 23.2\%$. Additionally, the navigation of humans is influenced by the surrounding density of pedestrians. Persons with low local knowledge often use the route choice of other people to navigate. A sufficient description of this behaviour was described by Schadschneider et al. [12], who applied the established ant-algorithm from Dorigo et al. [6] to pedestrian dynamics. At this, the influence of other humans on the route choice is valid only if these people are visible for the pedestrian p_i. Additionally, other people can decrease the attractiveness of a route: a too crowded street ($\rho \geq 0.5\,\mathrm{P/m}^2$) affects the operational behaviour of pedestrians [13]. Thus, people will avoid such sections. A density depending algorithm can model both contrary aspects. Since each unique section $\mathbf{s}_{l,m}$ runs linear between $\mathbf{e}_{l,m}$ and $\mathbf{e}_{l,m+1}$, we can assume that each pedestrian on a section $\mathbf{s}_{l,m}$ is visible to any other pedestrian on this section. This means, that a pedestrian p_j is visible on $\mathbf{s}_{l,m}$ for a time period $[T_{l,m,j}^-, T_{l,m,j}^+]$ with the starting time $T_{l,m,j}^- = \tau_j + \sum_{k=1}^{m-1} |\mathbf{s}_{l,k}|/v_j$ and the ending time $T_{l,m,i}^+ = \tau_i + \sum_{k=1}^{m} |\mathbf{s}_{l,k}|/v_j$. The sum of all visible pedestrians determines the density of this section for a pedestrian p_i:

$$\rho_{l,m,i} = \frac{N_{l,m,i}}{|\mathbf{s}_{l,m}| \cdot b_{l,m}} \tag{11}$$

The parameter $b_{l,m}$ describes the width of a section $\mathbf{s}_{l,m}$. The number of all pedestrians p_j, which are visible for a pedestrian p_i at a section $\mathbf{s}_{l,m}$ are given by:

$$N_{l,m,i} = \sum_j \mathscr{H}\left(t_{l,m,i} - T_{l,m,j}^-\right) \cdot \mathscr{H}\left(T_{l,m,j}^+ - t_{l,m,i}\right) \tag{12}$$

Parameter $t_{l,m,i}$ is the moment a pedestrian p_i would enter the intersection $\mathbf{e}_{l,m}$. At this time, the pedestrian p_i has to decide which section they choose next. Therefore, the local density at this moment would influence the decision making process. This point in time can be calculated by $t_{l,m,i} = \tau_i + \sum_{k=1}^{m-1} |\mathbf{s}_{l,k}|/v_i$. We use the established parabolic relation from Greenshields [7] to model this density depending behaviour. It is based on the fundamental relation of traffic sciences and describes the density dependency of traffic flow. Our scoring system is based on this approach to model the contrary density behaviour of pedestrians:

$$\zeta_{l,i} = \sum_{m=1}^{M} \frac{\rho_{l,m,i}}{\rho_{max}}\left(1 - \frac{\rho_{l,m,i}}{\rho_{max}}\right) \tag{13}$$

The parameter $\rho_{max} = 5.4\,P/m^2$ describes the amount of density, at which crowd flow stops [13]. The rating of each route is compared to the average value $\zeta_\varnothing$:

$$\delta(\rho_{l,i}) = \begin{cases} 1 - c & \zeta_{l,i}/\zeta_\varnothing < 1 - c \\ \zeta_{l,i}/\zeta_\varnothing & 1 - c \leq \zeta_{l,i}/\zeta_\varnothing \leq 1 + c \\ 1 + c & \zeta_{l,i}/\zeta_\varnothing > 1 + c \end{cases} \qquad (14)$$

The factor $c = 0.01$ determines the influence of the density dependencies and is based on our experimental observations. Finally, we can calculate the total score of a route λ_l. The route with the highest score is assigned to pedestrian p_i.

$$\xi(p_i, \lambda_l) = \xi(d_i, o_l, h_l, \rho_{l,i}) = \alpha(d_i) \cdot \beta(o_l) \cdot \gamma(h_l) \cdot \delta(\rho_{l,i}) \qquad (15)$$

4 Field Study and Outlook

The Oppilatio method was implemented and afterwards tested on a local music festival with 5000 visitors. We tracked 700 visitors on their way from the subway station to the actual event site to verify the routing suggestions. The field study was executed by student assistants, who followed visitor groups to record their trajectories with GPS devices. Based on this data, we determined the probability that visitors use a specific section $s_{l,m}$ on their way to the event site. These probabilities were compared with the probabilities calculated by Oppilatio. The results (see Fig. 3 and Table 1) were averaged over 30 calculation runs and corresponded quite good to the data. Larger differences to the experiment exist in section sequence 02–04 (see Fig. 3). The reason is mainly due to problems with the data acquisition. During the field study, about ten student assistants tracked the visitors from the station to the event site. At the peak hours, as most of the visitors arrived, the number of student assistants was too small to record a proportional share of visitors. Thus, the route choices of these visitors are under-represented in the experimental data. Due to herding behaviour, nearly all of them walked along the section sequence 01-03-06-09-11-13. Thus, our experiment has most likely underestimated the total number of pedestrians on this section sequence. In further research, various extensions are planned for Oppilatio. One main issue concerns the layout input: at the current state, event organisers have to set possible routes from station to event site on their own. We will couple the

Fig. 3 Layout of the researched field study with section-wise identification numbers for Table 1
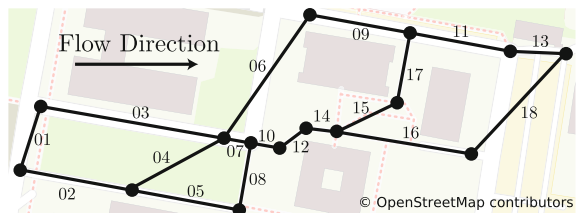
Table 1 Experimental pedestrian distributions compared with the results from Oppilatio

Section	01	02	03	04	05	06	07	08	09
Study (%)	82.5	17.5	82.5	12.2	5.3	74.9	19.8	5.3	74.9
Oppilatio (%)	98.2	1.9	98.2	1.1	0.9	83.8	15.5	0.9	83.8
Section	10	11	12	13	14	15	16	17	18
Study (%)	25.1	74.9	25.1	74.9	25.1	2.1	22.9	2.1	22.9
Oppilatio (%)	16.3	84.6	16.3	84.6	16.3	0.9	15.5	0.9	15.5

Oppilatio method with an network design approach, which calculates optimal route networks based on information from open geo-databases.

References

1. Betz, G., Hitzler, R., Pfadenhauer, M.: Zur Einleitung: Eventisierung des Urbanen. In: Urbane Events, pp. 9–24. Springer (2011)
2. Biedermann, D.H., Kielar, P.M., Aumann, Q., Osorio, C.M., Lai, C.T.W.: Carped a hybrid and macroscopic traffic and pedestrian simulator. In: Proceedings of the 27th Forum Bauinformatik, pp. 228–236 (2015)
3. Biedermann, D.H., Kielar, P.M., Handel, O., Borrmann, A.: Towards transitum: a generic framework for multiscale coupling of pedestrian simulation models based on transition zones. Transp. Res. Procedia **2**, 495–500 (2014)
4. Blue, V.J., Adler, J.L.: Cellular automata microsimulation for modeling bi-directional pedestrian walkways. Transp. Res. Part B: Methodol. **35**(3), 293–312 (2001)
5. Colombo, R.M., Rosini, M.D.: Pedestrian flows and non-classical shocks. Math. Methods Appl. Sci. **28**(13), 1553–1567 (2005)
6. Dorigo, M., Maniezzo, V., Colorni, A.: Ant system: optimization by a colony of cooperating agents. IEEE Trans. Syst. Man Cybern. Part B: Cybern. **26**(1), 29–41 (1996)
7. Greenshields, B., Channing, W., Miller, H., et al.: A study of traffic capacity. In: Highway Research Board proceedings, National Research Council (USA), Highway Research Board, vol. 1935 (1935)
8. Helbing, D., Molnar, P.: Social force model for pedestrian dynamics. Phys. Rev. E **51**(5), 4282 (1995)
9. Kneidl, A.: Methoden zur Abbildung menschlichen Navigationsverhaltens bei der Modellierung von Fußgängerströmen. Ph.D. thesis, Technische Universität München (2013)
10. Kneidl, A., Borrmann, A.: how do pedestrians find their way?. In: Results of an Experimental Study with Students Compared to Simulation Results, Emergency Evacuation of People from Buildings (2011)
11. Kuipers, B.: The cognitive map: could it have been any other way? In: Spatial orientation, pp. 345–359. Springer (1983)
12. Schadschneider, A., Kirchner, A., Nishinari, K.: From ant trails to pedestrian dynamics. Appl. Bionics Biomech. **1**(1), 11–19 (2003)
13. Weidmann, U.: Transporttechnik der Fußgänger: transporttechnische Eigenschaften des Fußgängerverkehrs. Literaturauswertung, ETH Zürich (1992)

Simulation-Based Forecasts of Crowd Flows at Major Events Using Real-Time Measurements

Thomas Matyus, Stefan Seer and Helmut Schrom-Feiertag

Abstract The complexity and dynamic nature of large events arise the need for decision makers to assess the current situation and to derive multi-temporal forecasts in order to identify critical situations in a timely manner and to initiate appropriate countermeasures. In this work, we present a fast mesoscopic simulation model which incorporates measurements from counting and Bluetooth sensors, thus providing real-time forecasts of crowd flows at major events. With this approach already a sparse placement of sensors at strategic points on an event area is sufficient to achieve the necessary spatial and temporal resolution for a complete characterization of the current crowd flows. For model verification and validation, we investigated case studies from two music festivals in Austria in 2012 and 2013 where extensive measurements on human motion data were obtained to evaluate the deviations of the simulation results from the measured walking times.

1 Introduction

Despite extensive pre-event planning and well-developed security concepts, the complexity and dynamic nature of large events can lead to unforeseen, tragic incidents. While real-time sensor measurements on human motion may deliver essential quantitative data, complete coverage of an entire large outdoor event area with counting sensors to provide all required data is prohibitively expensive. Here, the combination of fast crowd simulation tools with various types of real-time pedestrian flow measurement technologies can achieve the required spatial and temporal resolution for estimating the distribution, densities and walking speed of pedestrians. In [1]

T. Matyus (✉) · S. Seer · H. Schrom-Feiertag
Mobility Department, AIT Austrian Institute of Technology,
Giefinggasse 2, 1210 Vienna, Austria
e-mail: thomas.matyus@ait.ac.at

S. Seer
e-mail: stefan.seer@ait.ac.at

H. Schrom-Feiertag
e-mail: helmut.schrom-feiertag@ait.ac.at

an evacuation assistant has been developed which allows forecasting the emergency egress of large crowds in complex buildings by using data of video-based person counting as input for a real-time simulation. Extending this concept to a monitoring and decision support system of large outdoor events requires the ability to handle dynamic origin-destination-relations (OD-relations). Whereas the OD-relations during an evacuation are predefined and nearly static, pedestrian flows between multiple areas of a venue are highly dynamic. These dynamic OD-relations can be determined by detecting mobile devices at predefined positions for example by using Bluetooth sensors.

In this work we present a pedestrian simulation model based on a mesoscopic Cellular Automaton which simulates crowd flows at major events faster than real-time and incorporates measurements from counting and Bluetooth sensors. This enables decision makers to assess the current situation and to derive multi-temporal forecasts in order to identify critical situations in a timely manner and to initiate appropriate countermeasures. From the measured motion data, the following input for the simulation model is derived: (1) Pedestrian generation rate at each entrance, (2) exit rates and (3) the OD-relations. The first two are provided by counting sensors which have to be deployed at neuralgic points such as entrances and exists. The third input data is obtained by Bluetooth sensors. Depending on the number and locations of Bluetooth sensors, in general, the resulting data reveals the relations between origin and final destination points as well as the relations between intermediate targets. Thus, the model is required to deal with dynamic OD-matrices which are extended by intermediate targets.

In the following section the data model is described which is used to prepare the raw sensor data for the input into the simulation model. The latter is presented in Sect. 3. For the model verification (in Sect. 4) and validation, we investigated case studies from two music festivals in Austria in 2012 and 2013 where extensive measurements on human motion data were obtained. The results are summarised in Sect. 5 and concluded in Sect. 6.

2 Data Model

2.1 Types of Sensors

There are a variety of sensor technologies available to measure crowd flows and densities. It is very important to select reliable and affordable sensors that allow counting people at cross-sections and detecting people movements at outdoor festival areas under all light and weather conditions. The two types of sensors chosen for our framework are (1) laser based counting sensors and (2) Bluetooth sensors. The counting sensor is the laser based LD PeCo 3100 [6] with head detection for wide passage areas with high visitor frequencies especially suitable for outdoor use. The number of people passing the counting sensor in and out are recorded and transmitted

directly via GSM to a server and aggregated every quarter of an hour. For Bluetooth detection the BLIDS Bluetooth sensor network [3] was chosen which is cost-efficient and easy to instal. The BLIDS sensor detects Bluetooth-enabled mobile devices in its vicinity but provides no information about directions. Direction information can be obtained in a sensor network over the sequence of those sensors where the specific device was detected. The BLIDS network enables the real-time acquisition of crowd flow data and similar to the counting sensors the data are buffered locally and transmitted via GSM to a server. The data stored are the detection log from the Bluetooth sensor network which consists of timestamp, sensor id and device id.

2.2 Data Preperation

To calculate the people counts based on the number of detected Bluetooth-enabled mobile devices the correlation between the measurements of a certain Bluetooth sensor and the number of pedestrians passing this sensor has to be estimated. For this purpose, a linear regression model is fitted to the dataset using the least squares method.

The final result is a graph (for example see Fig. 1) consisting of nodes representing all sensor locations and all possible connections between sensors with complete information about the crowd flow on each arc in the last quarter hour. The graph and its data serve as input for the simulation model in order to initialise it with the current situation. This enables the simulation to predict the movements of the crowd for a specified time horizon.
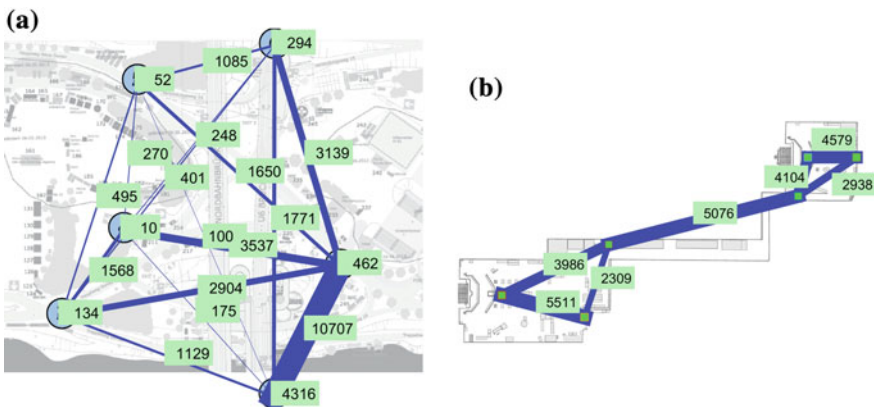
Fig. 1 Number of detected Bluetooth-enabled mobile devices over all three days: Donauinsel festival 2013 (**a**); Nova Rock festival 2012 (**b**)

3 Simulation Model

The mesoscopic simulation model is based on a Cellular Automaton model [2]. With respect to the data model the navigation model has to be adapted: the infrastructure consisting of walkable regions, obstacles, etc. is represented by polygons. For each entry in the OD-matrix a corresponding decision point is generated in the walkable region. The value of the OD-relation is interpreted as the probability for the pedestrian to choose the corresponding destination as next goal. Between the decision points the pedestrians are routed on the shortest path by applying Dijkstras algorithm [4] on a visibility graph.

The operational model is based on a regular $1 \times 1\,m$ grid with Moore-neighbourhood. The maximum density of a cell is 5 persons per square metre. The velocity for movements within a cell corresponds to Helbings Fundamental Diagram [5]. Since Helbing's data offer no values for densities lower than 1.0 persons per square metre the dataset is extended by data points from Weidmann's Fundamental Diagram [7].

The real-time input data of the crowd flow are obtained from the sensor network: (1) Pedestrian generation rate at each entrance and (2) the exit rates which are updated every 15 min and (3) the OD-relations in real-time.

4 Model Verification

For a proof of concept we tested the computational performance of the implemented mesoscopic simulation model applied to data recorded at the Donauinsel festival 2013 in Vienna. It is an open access festival on an island in the river Danube lasting for three days with overall three million visitors. For this purpose, we restricted the observation area to that part of the festival site with the highest crowd flows. Namely, the area where the visitors leave the island via two bridges towards the two nearest subway stations. Figure 1 shows the OD-relations of all three festival days extrapolated from the recorded Bluetooth data (see Sect. 2). The highest pedestrian flow occurred in the hour after midnight on the second festival day. We used the 15 min data of this period to test if the implementation of the mesoscopic simulation model reproduces the OD-relations correctly, if the temporal resolution is suitable and if it is fast enough for forecasts during the festival. At the maximum of the crowd flow 42,000 visitors have been simulated simultaneously on a typical laptop ten times faster than real-time.

5   Model Validation

In order to validate the simulation model we compared the walking times in a corridor measured by Bluetooth sensors, with the forecasts of a simple macroscopic model and with results computed by the proposed mesoscopic simulation model. As test site we chose the 'Nova Rock' festival 2012.

The festival area is located on a flat and open terrain and the whole area is surrounded with security fencing. The festival area inside is divided into a camping zone and a core zone which in turn is again separated from the camping zone by a fence. In Fig. 2 the festival area with the camping zone as well as the core zone with its two stages, the Blue and the Red Stage are shown. The two stages are far apart and connected over a corridor with a length of 600 m and a width ranging from 23 at the widest to 16 m at the narrowest point. The core zone has only two entrances, one near the Blue stage and one near the Red stage. For crowd control 14 line-up gates at the entrance of the Blue and 12 line-up gates at entrance of the Red Stage were installed.

5.1   Data Analysis

The correlation between the number of persons and the Bluetooth measurements as shown in Fig. 3 was estimated by a linear regression model (see Sect. 2). The results of the linear regression are: 41.41 for the linear coefficient, nearly zero for the p-value of the t-statistic and 607 for the root mean squared error. The regression model cannot
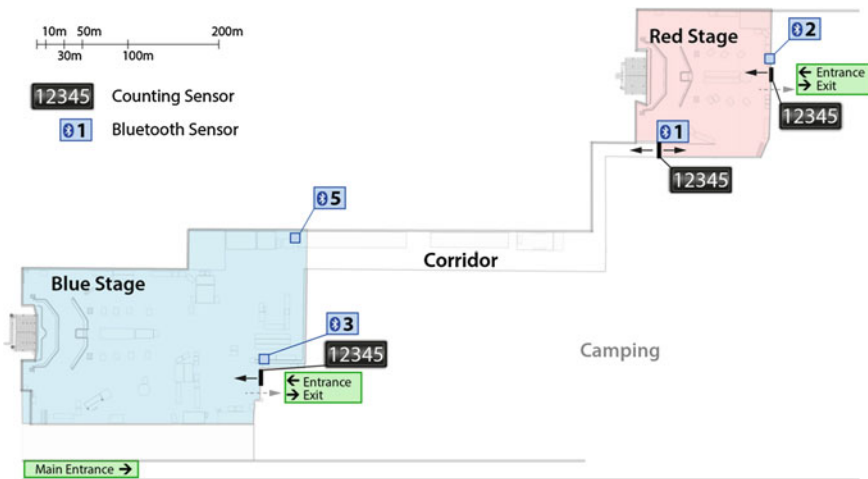
Fig. 2 Overview of the Nova Rock festival site with its main parts (*Blue stage*, Corridor, *Red Stage* and Camping area) and the sensor locations
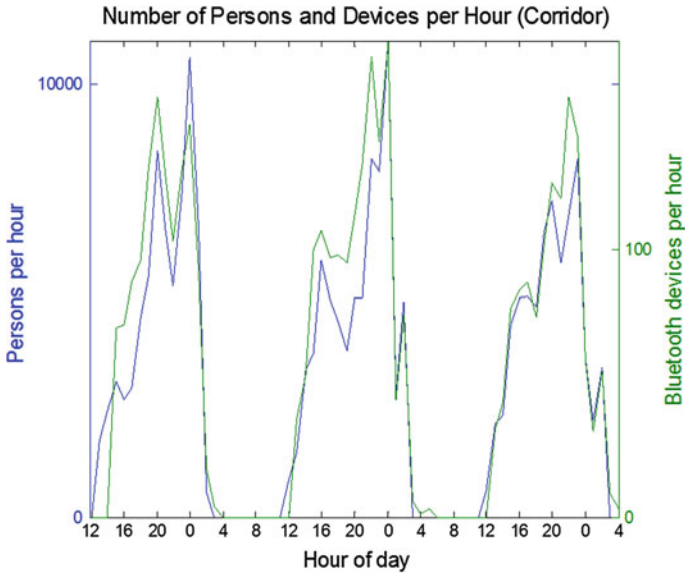
Fig. 3 Number of persons (*blue line*) and number of detected Bluetooth-enabled mobile devices (*green line*) per hour for all three festival days

be determined at the beginning of the festival without having data. Therefore, the linear model is updated constantly during the progress of the event having a current linear coefficient.

5.2 Macroscopic Model

The macroscopic model was used to calculate the walking times by estimating the mean velocities for each 15 min time slot. This was done by applying the Fundamental Diagram, given in Sect. 3, on the corresponding average densities in the corridor. Of course, this underlies the assumption that all visitors are distributed uniformly in the corridor. In order to determine the number of pedestrians. we extracted the walking time distribution from the Bluetooth measurements of the previous hour. This rather long time interval was chosen because there were small stages located inside the corridor which induced some visitors to remain in the corridor instead of just passing through. For each time point within the next hour the number of pedestrians staying inside the corridor was estimated. This was done by drawing from the generated distribution and integrating the inflow into the corridor which we got from the corresponding counting data. Thus, the average densities inside the corridor and subsequently the mean velocities were determined.

5.3 Results

For the model validation we considered two periods on the second festival day. A longer one which lasted from 08.00 pm until 00.15 am on the next day and a shorter one from 11.00 pm until 00.15 am. At 11.00 pm a thunderstorm warning induced a heavy and continuous crowd flow through the corridor whereas in the hours before we observed the usual crowd behaviour with lingering visitors. Based on the sensor measurements of these two periods we calculated the deviation between the measured walking times and the walking times estimated first, by the macroscopic model as described before and secondly, by the mesoscopic simulation model. As it can be seen in Fig. 4 both models, the macroscopic model and the mesoscopic simulation model, predict the walking times quite well and the difference between the deviations of the two can hardly be detected. Nevertheless, the detailed results presented in Table 1 reveal that the assumption of the macroscopic model that all pedestrians are distributed uniformly in the corridor does not hold. The simulation is able to model the pedestrian flows inside the corridor more precisely and hence, produces better results. Especially, in the hour when the corridor was crowded, the mesoscopic simulation model reduced the average walking time deviation by -17% and the median deviation by -31% compared to the results of the macroscopic model.
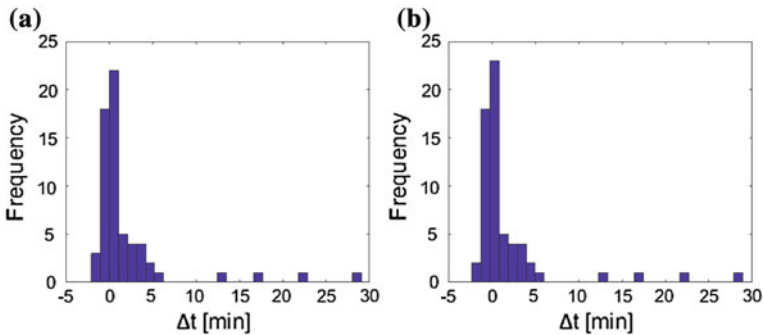
Fig. 4 The histograms of the walking time deviations from the measured data for the period between 11.00 pm and 00.15 am: macroscopic model (**a**); mesoscopic simulation model (**b**)

Table 1 Comparison of the walking time data of the macroscopic model and of the mesoscopic simulation

Period	Mean deviation			Median deviation		
	Macroscopic [min]	Simulation [min]	Delta [%]	Macroscopic [min]	Simulation [min]	Delta [%]
20:00–0:15	18.18	18.13	−0.24	1.45	1.41	−2.92
23:00–0:15	1.25	1.03	−17.30	0.54	0.37	−31.23

6   Conclusions

We presented a fast mesoscopic simulation model for real-time forecasts of crowd flows at major events which incorporates measurements from counting and Bluetooth sensors. Data from counting sensors showed a good correlation to data from Bluetooth sensors and the combination of them can be considered as an appropriate method for crowd flow acquisition with respect to spatial and temporal resolution. Based on these real-time measurements the presented mesoscopic simulation model is able to improve forecast quality compared to a macroscopic model. Of course, future investigations how the computational performance and the quality of the simulation results of the mesoscopic simulation model can be increased are necessary. Therefore, we are pursuing several options such as improving the implementation, calibrating the simulation model, searching for alternative models and extending the sensor network with alternative technologies, such as WiFi scanners or video-based counting and crowd flow analysis. For this purpose, it is indispensable to acquire more data for case studies and to test the forecast for diverse real-life events. Finally, the validation process presented herein can only be seen as a first approach and has to be further refined.

References

1. Holl, S., Schadschneider, A., Seyfried, A.: Hermes: An Evacuation Assistant for Large Arenas. Springer (2014)
2. Klüpfel, H.: A cellular automaton model for crowd movement and egress simulation. Ph.D. thesis, Universitt Duisburg-Essen (2003)
3. Blids® network.: http://www.blids.cc
4. Dijkstra, E.: A note on two problems in connexion with graphs. Numerische Mathematik **1**(1), 269–271 (1959)
5. Helbing, D., Johansson, A., Al-Abideen, H.: Dynamics of crowd disasters: an empirical study. Phys. Rev. E **75** (2007)
6. Personenzählsystem LD-PeCo.: http://www.sick.com
7. Weidmann, U.: Transporttechnik der Fussgänger—Transporttechnische Eigenschaften des Fussgängerverkehrs (Literaturstudie). Literature Research 90, Institut für Verkehrsplanung, Transporttechnik, Strassen- und Eisenbahnbau IVT an der ETH Zürich, ETH-Hönggerberg, CH-8093 Zürich (1993). In German

Level of Safety Concept for Major Events

Stefan Holl, Maik Boltes and Armin Seyfried

Abstract Most of the international guidelines for the dimensioning of pedestrian traffic facilities are built on the 'Level of Service' concept. It is well suited for a lot of traffic conditions like unidirectional pedestrian flows on pavements or in corridors. However, the concept reaches its limit in case of more complex situations like bi- and multi-directional streams, e.g. at railway stations, airports or large public events. Several disasters in context of large public events revealed the lack of applicable rules. The deficit is explainable against the background of missing experience. Neither emergency forces and responsible authorities nor researchers in the area of pedestrian dynamics have a valid database to describe multi-directional streams in high densities. As part of the research project 'BaSiGo—Bausteine für die Sicherheit von Großveranstaltungen', large-scale laboratory experiments with about 2,000 pedestrians have been conducted in 2013. The aim of the work is to convert the 'Level of *Service*' concept into a 'Level of *Safety*' concept for large public events. A first approach for the new concept, based on a traffic light system (green, yellow, red), is presented in this article.

1 Introduction

Various accidents at mass events in the past years (e.g. the 'Loveparade' disaster in Duisburg 2010) revealed some serious problems: First of all, it had to be noted, that there are no generally obliging rules for the approval of large public events. In the past, such outdoor events were often treated as such in buildings. In Germany, the

S. Holl (✉) · M. Boltes · A. Seyfried
Forschungszentrum Jülich GmbH, Jülich Supercomputing Centre, Jülich, Germany
e-mail: st.holl@fz-juelich.de

M. Boltes
e-mail: m.boltes@fz-juelich.de

A. Seyfried
School of Architecture and Civil Engineering, University of Wuppertal,
Wuppertal, Germany
e-mail: a.seyfried@fz-juelich.de

Regulations on Places of Assembly,[1] which normally applies for assembly buildings, was used frequently. Neither this regulation nor the guidelines for the design of road traffic facilities [1] include binding criteria for the assessment of pedestrian areas in case of high densities, such as found at large public events. This is not surprising, because there is no adequate empirical database until today. Field studies and experiments are already carried out for many years, but only in recent years it is possible to observe the microscopic correlations inside the pedestrian flows. The topic of the project 'BaSiGo—Bausteine für die Sicherheit von Großveranstaltungen' [2] has been to define safety and security modules for large public events. In about 30 setups typical traffic facilities at large public events like corridors, intersections, entrances, corners, etc. have been investigated. At various runs up to 1,000 probands have participated. The pedestrian density in these experiments reached up to six and more persons per square metre. The results of the project will be incorporated step by step into the new 'Level of Safety' concept.

2 State-of-the-Art

Most regulations in context of pedestrian traffic are based on the 'Level of Service' concept [3–5], which focuses on comfort, but not on safety aspects. Multi-directional traffic is usually not taken into account, it is assumed that the pedestrian traffic takes place in only one or two directions. The most popular guideline for the design of road traffic facilities in Germany is the 'Handbuch für die Bemessung von Straßen-verkehrsanlagen (HBS)' [1]. The method therein for pedestrians is based on Weid-mann's fundamental diagram

$$J_s = \rho \cdot v_0 \cdot \left(1 - e^{-1.913 \cdot \left(\frac{1.0}{\rho} - \frac{1.0}{5.8}\right)}\right) \tag{1}$$

where J_s is the specific flow, ρ the density and v_0 the desired speed. According to this fundamental diagram six quality levels are defined, which are indicated by the letters A to F (see Fig. 1). The limit, which normally should be complied, is level D. The threshold values have been identified in field studies. Since in these studies only densities up to $\rho = 0.63$ m^{-2} could be observed, the high density areas were simulated by a microscopic model [6, p. 26]. For major events, however, the people densities are generally much higher. Densities of more than five persons per square metre are not uncommon. On the other hand, the fine-scaled classes in the low density areas are only relevant for comfort aspects. Although the HBS has been proven useful for standard traffic situations, it should not be used for major events.

---

[1]The building codes in Germany are regulated by the federal states. The conference of the ministers of construction works out the 'Muster-Versammlungsstättenverordnung' (MVStättV). It is a proposal for the federal ordinances. In North Rhine-Westphalia places of assembly are regulated in a Special Construction Regulation (Part 1: Assembly Areas).
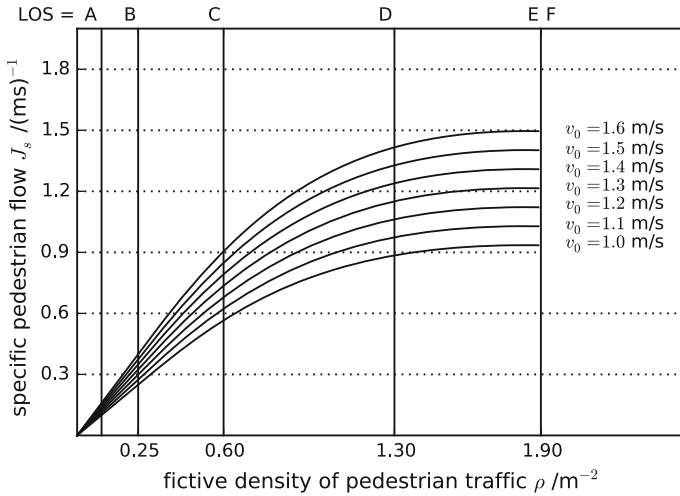
Fig. 1 Level of Service diagram according to HBS [1, Fig. S9–4a and Table S9–1]. The *curves* are defined by the fundamental diagram of Weidmann and depend on the free velocity v_0. In the 'fictive density of pedestrian traffic' different factors, such as the oncoming traffic or the manner of walking are taken into account. Footnote in HBS: For safety reasons, the fictive density of pedestrian traffic may not exceed the value of $1.90\,\text{ped/m}^2$

3 Level of Safety Concept

First of all, it is necessary to distinguish between the different traffic situations at major events. There are three typical conditions associated with the priority use of the areas:

1. Traffic areas, which are used for movement, e.g. pavements or entrances
2. Common areas, e.g. waiting zones or areas in front of stages
3. Mixed used areas, e.g. in the centre of flea markets or parish fairs

The Level of Safety concept applies to areas which serve the movement. Stationary individuals—who do not want to move—may only be considered as barriers to the flow of traffic. Nevertheless, the concept is also interesting for the escape routes of common and mixed used areas. The crucial criterion for these areas is the possibility to reach the escape routes and exits in adequate short time. In common or mixed used areas (e.g. directly in front of the stage at a musical event) the acceptable local density can be significantly higher than in areas, which are used for movement.

The concept should be easy to apply and the focus should be on safety aspects. Therefore the HBS method is used as a template but the classification is simplified: instead of levels A to F, a traffic light system (red, yellow, green) is used. These three levels are based on the elementary zones of the fundamental diagram (see Fig. 2). The figure does not intend to describe all states exactly. High densities for example
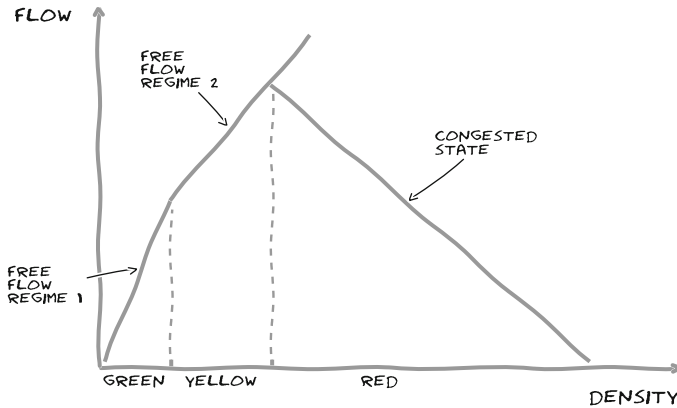
Fig. 2 Schematic representation of the fundamental diagram. The elementary zones are correlated with the safety levels 'green', 'yellow' and 'red'

show additional effects, like stop-and-go-traffic. For the safety levels, however, these effects have no relevance. Nevertheless, there are three basic zones:

- Free flow regime I: rare interferences and free velocities
- Free flow regime II: interaction between pedestrians with needs for changes of velocity and direction but still a stable flow
- Congested state: traffic jams up to stoppages which could lead to critical situations

At the transition between 'yellow' and 'red' we have a special situation because of the overlap which is defined as red. In this transient region, the dependency of flow and density is no longer unique. For a given density in the transient region the flow may either be free or congested, depending on the circumstances. The state of metastability is insufficiently researched until today.

As a result of the laboratory experiments in the projects Hermes [7] and BaSiGo [8] (see Fig. 3) the fundamental diagrams for various geometries could already be determined. The analyses are based on individual trajectories [9–11]. To describe the traffic conditions the methods developed by Steffen [12] and Zhang [13, 14] are used. Based on this data the first threshold values for uni- and bidirectional traffic are set (see Table 1 and Fig. 4).

4 Procedural Steps

For practical use of the Level of Safety concept six steps have to be executed:

1. Visualisation of site and traffic
2. Specification of pedestrian flows
3. Conversion into 2-minute-intervals
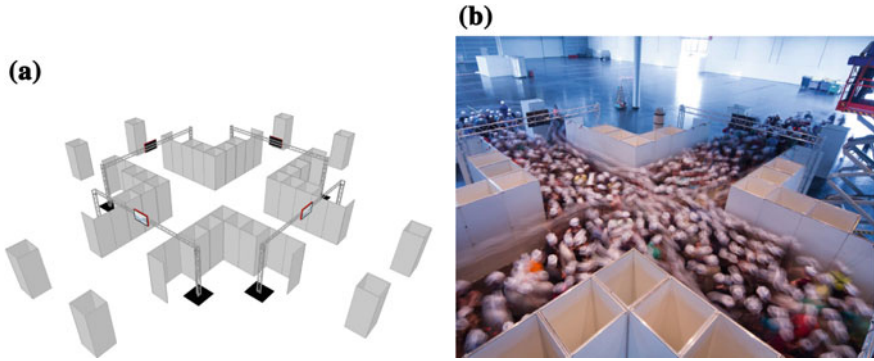
Fig. 3 Image sequence of an intersection experiment, one of the large-scale laboratory experiments in BaSiGo project: experiment setup, each entrance has a width of four metre, the streams cross at an angle of 90° (**a**); experiment with more than 600 probands. The density exceeded six persons per square metre (**b**)

Table 1 Level of Safety classification

Type of traffic	Level of Safety		
	Green	Yellow	Red
Unidirectional	$J_s \leq 1.3\,(\text{ms})^{-1}$	$J_s \leq 1.6\,(\text{ms})^{-1}$	$J_s > 1.6\,(\text{ms})^{-1}$
	$\rho \leq 1.0\,\text{m}^{-2}$	$\rho \leq 1.7\,\text{m}^{-2}$	$\rho > 1.7\,\text{m}^{-2}$
Bidirectional	$J_s \leq 0.6\,(\text{ms})^{-1}$	$J_s \leq 1.2\,(\text{ms})^{-1}$	$J_s > 1.2\,(\text{ms})^{-1}$
	$\rho \leq 0.5\,\text{m}^{-2}$	$\rho \leq 1.0\,\text{m}^{-2}$	$\rho > 1.0\,\text{m}^{-2}$
Intersections, corners, waiting areas, ...	Current analysis of BaSiGo results		
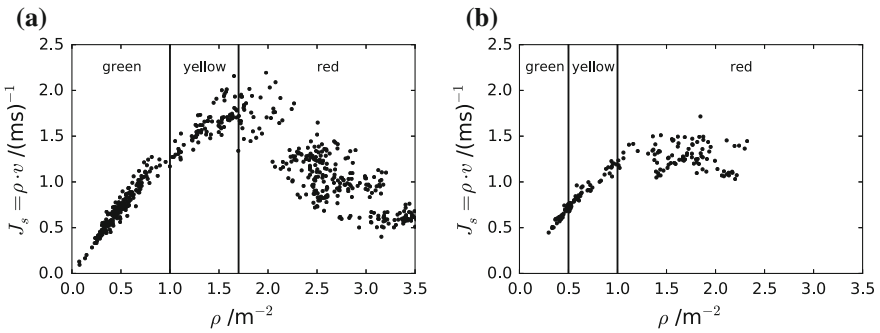
Fig. 4 Level of Safety zones: for unidirectional flow (**a**); bidirectional flow (**b**). The fundamental diagrams originate from Zhang [13]. The *vertical lines* mark the boundaries between the safety levels 'green', 'yellow' and 'red'

4. Calculation of effective width
5. Calculation of specific flow
6. Level of Safety classification

Maybe the most important step is the *visualisation of site and traffic*. The planner has to pay close attention to all the upcoming traffic flows. In this step he does it just in a qualitative way. The traffic—induced by the event just as additional everyday traffic—is visualised on a true-to-scale site plan. As a basis for these plans municipal cadastral plans are recommended. The presentation is done in scale 1:500 (1 cm $\widehat{=}$ 5 m), but in no case at a scale smaller than 1:1,000 (1 cm $\widehat{=}$ 10 m). For each time period of arrival, the event itself and the departure a separate plan (or separate CAD layer) is created on which the traffic streams are shown as coloured arrows. In particular load peaks (e.g. due to the timing of public transport or special attractions), it may be useful to shorten the intervals for the presentation on 60, 30 or 15 min. Based on the visualisation it can be determined which critical sections are relevant for detailed analysis. Particular attention should be addressed on the identification of bi- and multi-directional traffic at intersections and bottlenecks (e.g. at barriers and entrance gates).

The second step is the *specification of pedestrian flows*. For each relevant section the traffic is predicted hourly (or for shorter intervals in case of special load peaks). Relevant for the further consideration are the time intervals with the largest flow of people. In case of hourly prediction the pedestrian flow is referred as q_{60}.

In the previous step, the traffic volumes were usually acquired for 60-min-intervals. For further calculations, the flow values are *converted into* 2-min-intervals. For this, the conversion factors of the HBS are used. The conversion of units and a surcharge which accounts the fluctuations in traffic flow are already contained in these factors. Example: For the transition from sixty to two minutes a surcharge of 1.8 is set. This produces a conversion factor of $0.06 = 1.8 \cdot 2/60$ min (see Table 2).

Next step is the *calculation of the effective width*. The effectively available width of the walking area is decisive for the number of persons which can pass the section within the specified period. For the calculation of usable width b_{eff} obstacles (walls, masts, trees, bollards, bins, etc.) are considered in their geometrical width plus additional distance to boundaries (0.25 to 1.00 m each side) [1, 15].

Table 2 Factors for translation into 2-min-intervals (see HBS [1, Fig. S2–2 and Table S2–3])

Prediction interval [/min]	Surcharge	Conversion factor [/(Δt min/2 min)]
60	1.80	0.06
30	1.50	0.10
15	1.35	0.18
10	1.25	0.25

Example: $q_{60} = 30,000 \frac{\text{ped}}{60 \text{ min}} \Rightarrow q_2 = 30,000 \frac{\text{ped}}{60 \text{ min}} \cdot 0.06 \cdot \frac{60 \text{ min}}{2 \text{ min}} = 1,800 \frac{\text{ped}}{2 \text{ min}}$

The next to last step is the *calculation of the specific flow*. For this purpose, the following equation can be used:

$$J_s = \frac{q_2 \cdot \frac{2\,\text{min}}{120\,\text{s}}}{b_{eff}} \tag{2}$$

For the example in Table 2 and an effective width $b_{eff} = 10$ m results:

$$J_s = \frac{q_2 \cdot \frac{2\,\text{min}}{120\,\text{s}}}{b_{eff}} = \frac{1,800\,\frac{\text{ped}}{2\,\text{min}} \cdot \frac{2\,\text{min}}{120\,\text{s}}}{10\,\text{m}} = 1.5\,\frac{\text{ped}}{\text{ms}} \tag{3}$$

Final step is the *Level of Safety classification*. For unidirectional traffic the comparison with Table 1 shows that the exemplary calculated specific flow is still in the yellow range. However, for bi-directional traffic this value is already in the red zone. In this case, safety-critical situations have to be expected.

References

1. Handbuch für die Bemessung von Straßenverkehrsanlagen (HBS), Teil S, Stadtstraßen. Forschungsgesellschaft für Straßen- und Verkehrswesen (FGSV), Köln (2015)
2. Bausteine für die Sicherheit von Großveranstaltungen (BaSiGo). http://www.basigo.de/
3. Fruin, J.J.: Designing for Pedestrians: A Level of Service Concept. Ph.D. thesis, Polytechnic University of Brooklyn (1970)
4. Fruin, J.J.: Pedestrian Planning and Design, revised edn. Elevator World (1987)
5. Weidmann, U.: Transporttechnik der Fussgänger: Transporttechnische Eigenschaften des Fussgängerverkehrs (Literaturauswertung), Schriftenreihe des Instituts für Verkehrsplanung, Transporttechnik, Strassen- und Eisenbahnbau, ITH Zürich, vol. 90. Zürich (1993)
6. Alrutz, D., Friedrich, B., Mennicken, C., Bohle, W., Busche, K., Irzik, M., Rose, M.: Bemessungsgrundlagen für Fußgängerverkehrsanlagen: Kurzbericht zum FE 77.452/2000. Planungsgemeinschaft Verkehr und Institut für Verkehrswirtschaft, Straßenwesen und Städtebau der Universität Hannover, Hannover (2003)
7. Holl, S., Seyfried, A.: Hermes—an evacuation assistant for mass events. In: SiDE, vol. 7(1), pp. 60–61 (2009)
8. Holl, S., Seyfried, A.: Laboratory experiments on crowd dynamics. In: SiDE, vol. 11(2), pp. 102–103 (2013)
9. Boltes, M., Seyfried, A.: Collecting pedestrian trajectories. Neurocomput. Spec. Issue Behav. video **100**, 127–133 (2013)
10. Boltes, M., Seyfried, A., Steffen, B., Schadschneider, A.: Automatic extraction of pedestrian trajectories from video recordings. In: Klingsch, W.W.F., Rogsch, C., Schadschneider, A., Schreckenberg, M. (eds.) Pedestrian and Evacuation Dynamics 2008, pp. 43–54. Springer, Berlin (2010)
11. Mehner, W., Boltes, M., Seyfried, A.: Methodology for generating individualized trajectories from experiments. In: Traffic and Granular Flow 2015 (2015)

12. Steffen, B., Seyfried, A.: Methods for measuring pedestrian density, flow, speed and direction with minimal scatter. Phys. A **389**(9), 1902–1910 (2010)
13. Zhang, J.: Pedestrian fundamental diagrams: comparative analysis of experiments in different geometries. Schriften des Forschungszentrums Jülich, IAS series, vol. 14. Jülich (2012)
14. Zhang, J., Klingsch, W., Schadschneider, A., Seyfried, A.: Transitions in pedestrian fundamental diagrams of straight corridors and T-junctions. J. Stat. Mech. Theory Exp. **6**, 06004–06004 (2011)
15. Nelson, H.E., Mowrer, F.W.: Emergency movement. In: DiNenno, P.J., Drysdale, D., Beyler, C.L., Walton, W., Douglas, C., Richard, L.P., Hall, J.R., Watts, J.M. (eds.) SFPE Handbook of Fire Protection Engineering, pp. 3–367–3–380. National Fire Protection Association, Quincy, Massachusetts (2002)

Brazilian Legislation and the Boate Kiss Tragedy: Computational Modelling of Evacuation

Henrique C. Braga, Gray F. Moita and Paulo E. M. Almeida

Abstract Brazil was recently the scenario of a great tragedy in the nightclub Boate Kiss, where 242 people were killed. The starting point of the fire was the use of a pyrotechnic device over an acoustic coating made of a kind of polyurethane foam. The causalities were caused mainly by asphyxia and by the inhalation of toxic gases. However, several additional causes contributed to the amount of damage and human losses. The investigation emphasised the necessity to discuss details in the applicable Brazilian legislation. In this work, the Boate Kiss tragedy is presented and the some of their mainly aspects discussed. The software FUGA, used to simulate the evacuation process, is also summarised. A computational model for evacuations in environments similar to the Boate Kiss is built and analysed. Finally, some considerations are made in order to improve the current Brazilian safety codes.

1 Introduction

In 2013 a great tragedy occurred in Brazil. A fire at nightclub Boate Kiss, in the city of Santa Maria—state of Rio Grande do Sul (RS), Brazil, killed 242 people, most of them young university students. About 680 people were injured, many seriously. This was the second largest Brazilian official tragedy by fire and the largest in the last 50 years. Historically [6], accidents in environments such as nightclubs (even in small ones) can be considered critical in terms of safety. The Boate Kiss tragedy presented similarities to what happened in the fire at a nightclub in Rhode Island—USA, in 2003, and, mainly, with the tragedy at República Cromañon in Argentina, in 2004.

H.C. Braga (✉) · G.F. Moita · P.E.M. Almeida
Post-Graduate Program in Mathematical and Computational Modelling,
Centro Federal de Educação Tecnológica de Minas Gerais, CEFET-MG,
Belo Horizonte, MG, Brazil
e-mail: bragaseg@yahoo.com.br

G.F. Moita
e-mail: gray@dppg.cefetmg.br

P.E.M. Almeida
e-mail: pema@lsi.cefetmg.br

Unfortunately, the knowledge acquired in these earlier tragedies was neglected by many, including the authorities.

The starting point of the fire was the use of a cheap pyrotechnic device called 'Sputnik'—prohibited for indoor use—over an acoustic coating made of a kind of polyurethane foam. The causalities were caused mainly by asphyxia and toxic gases inhalation, such as hydrocyanic, from the smoke generated by the burning foam [2, 4]. In spite of the causative main factor, the investigations pointed out that, as it usually happens in great tragedies such as this one, several additional causes contributed to the amount of damage and human casualties [3, 7]. Therefore, the necessity to discuss many of the crucial technical details in the applicable Brazilian legislation was also emphasised [9].

In this work, the Boate Kiss tragedy is presented and some of the main points related to the incident discussed. It is important to highlight that this is a recent event and that the investigations are still in progress. Some of the information provided is provisional and subject to modification. The software FUGA [5] used to simulate the evacuation process is briefly described. Afterwards, computational simulations of evacuations in environments externally similar to the nightclub are performed. No considerations about the internal design are taken into account at this moment. All simulations are made considering an occupancy of 350, 700 (approximately the maximum legal occupancy of Boate Kiss) and 1000 persons. The environments are considered with a single exit of 3.2 m (the real situation in the location) and with some alternative situations, with a wider exit and with additional exits.

The dynamics of people flow is evaluated by checking the flow capacity of the exits, the time and flow profile and the possibility of the occurrence of internal collisions. It is demonstrated that even if all of the requirements of the Brazilian codes were thoroughly followed, serious accidents could still potentially occur in certain situations, demonstrating the need for a greater discussion of the codes applied to these types of environments in Brazil. At the end, some considerations are made in order to improve the existing Brazilian fire and safety codes.

2 Background

2.1 Boate Kiss Tragedy

The nightclub Boate Kiss was located in a residential and commercial area, in the centre of Santa Maria, and the noise generated caused a big problem with the neighbourhood, specifically during the nights. Thus, the entire nightclub was sealed as a way to avoid noise dispersion. There were absolutely no windows or alternatives ways to eliminate the smoke. The fire started in the roof above the main stage after the ignition of a cheap pyrotechnic device by a member of the band that was performing in the premises. Soon after the beginning of the fire, a fire extinguisher was used in an attempt to extinguish the fire in the roof, but to no avail (the fire extinguisher was not fully operational).

The spreading of the smoke was accelerated by the air conditioning system of the place. There are evidences reporting that it took no more than three minutes to engulf almost the entire club. It was really a very fast phenomenon. Furthermore, there was no kind of smoke suppression system installed in the nightclub. The smoke generated took a critical importance in this tragedy.

The nightclub was overcrowded. According to the original project (from 2009), its maximum occupancy should be 691 people [9], but the real number could be significantly higher. Additionally, instead of applying the correct (and approved) project, the owners have changed themselves the environment design (there is no official or updated project elaborated by an architect or an engineer). Several obstacles and iron bars in the exit route were added, causing a bottleneck effect. This alteration by the owners in exit route was done to avoid unauthorised people to leave and to facilitate the bill payment (all food and beverage consumption within the nightclub was paid when the costumer left the premises).

The excerpt below, a transcript of the police investigation of the tragedy [3], helps to illustrate some of the numerous problems which have occurred:

> Panic took hold of individuals who were in the club, causing people to despair and try to leave the place, but Boate Kiss had only one exit that led to the outside. That exit was absolutely insufficient to give flow to the amount of people throng in desperate attempt to leave the area, many of which have died trying to. Not only the single exit, the existence of several physical barriers, guard rails (containment bars) in the exit routes, stairs, emergency lighting disability, lack of indication or escape routes signalling, in addition to the crowded site, also contributed to the resulting damage, factors that together hampered the rapid evacuation of the spot (free translation)

To better exemplify one of the above points: to comply with the Brazilian standards Boate Kiss had two emergency exits [1], but these exits were placed side by side, so that in fact it had only a single double sized emergency exit. Later on, experts considered that this single exit was irregular [10], but this is a point not fully covered (or dealt with) in the applicable Brazilian codes [9]. During the investigation, it was shown that the (effective) unique double exit was of the knowledge of the municipal government and also of the local Fire Department. However, these authorities did not restrain this condition, probably due to gaps created by the wording of the prescriptive rules and the institutionalised relaxation and disregard with the inspection of fire safety [10]. In RS, the simplification in the process to obtain a legal license was such that even a nightclub of the size and occupation of Boate Kiss could get its authorisation of conformity against fire without an updated fire protection design made by a specialist [3, 10].

Particularly for Boate Kiss, despite numerous irregularities in statements, a senior officer of CBMRS (State Fire Department) said to the press:

> I have been telling that it (the premises) was regular with respect to fire prevention; the code itself is a very, very limited code.[1] That property was in compliancy with the Brazilian

---

[1]Discovery Channel, Documentary 'Tragédia em Santa Maria', 2013.

Fig. 1 Images of the escape route of Boate Kiss (adapted from [9])

standards for fire safety, including the emergency exit, the anti-panic bars, the emergency lighting and the fire extinguishers. Everything was ok[2] (free translations).

Finally, Fig. 1 shows some images of the escape route, taken after the tragedy.

2.2 *Brazilian Code*

The legal code used in this work to determine the dimension of the exits is the Brazilian standard ABNT 9077 [1]. It is important to state that, in reality, as a substitute of the national standard, each Brazilian state has its own legislation, but in general they are very similar and comply with ABNT.

In ABNT 9077, the total width of the exits is given by the following equation:

$$N = P/C \tag{1}$$

---

[2]https://esportes.yahoo.com/fotos/boate-estava-regular-diz-bombeiro-photo-185217717.html
(2013). Accessed 13 Nov 2015.

where N = number of passages unit (PU), rounded to the higher natural number; P = occupation (according specific criterions); and C = capacity of PU (referential number of people to get through the doorway in one minute).

The value of P and C are obtained in ABNT 9077 (Sects. 4.3 and 4.4.1.1 and Table 5 of ABNT 9077 Appendix). One PU represents 0.55 m. The width can never be less than 1.1 m (or 2 PU).

For example, a nightclub with 350 m² useful floor area (areas like bathrooms or staircases are not considered as useful areas) will admit a population of 700 people. As C is equal to 100, according to Eq. 1 the minimum width of all exits must be equal to 7 PU (or 3.85 m). The code for this environment imposes the necessity of a minimum of two exits. There is no specification about the best positioning for the exits. Additionally, the use of hydrant, sprinkler, alarm or smoke suppression systems are not mandatory for a night club like Boate Kiss.

Independent of the technical laws, another important point is that the facilities for a night club (as almost all kind of company) work without a fire license in Brazil.

2.3 The Software FUGA

In order to simulate the evacuation, the software FUGA v. 1.0 was used. Its conception is based on a discrete automaton modelling, considering as paradigms the ergonomics aspects relate to the human movement and the fuzzy logic to emulate the human decision making process. Two results were obtained from the simulations: the time for the effective escape of the environment and the possibilities of occurrence of internal collisions (POIC) among the persons during the evacuation.

The effective escape time is normally considered as the sum of three times: the perception time, the reaction time and the effective movement time. With FUGA, it is possible to consider, or not, the perception and reaction times. However, in the current evacuation simulations, the whole crowd immediately begins to move in the direction of the nearest available exit. Thus, in these cases the considered escape time is only the effective movement time up to the exits.

The parameter POIC can be used as a qualitative indicator of the jamming or congestion possibilities [5]. There are four kinds of POIC. POIC 1 indicates how many times, during the escape up to the exit, persons have the first option of movement obtained by the fuzzy system blocked. POIC 2 indicate how many times, during the escape up to the exit, the first and the second options of movement of persons obtained by the fuzzy system are blocked. By applying the same rules, POIC 3 indicates how many times the first, the second and the third options of movement are blocked, and, finally, POIC 4 indicates how many times all possibilities of movement are blocked (in this situation, even if a person wants to move, he or she has to remain in the same place). Consequently, a low value for POIC 1 indicates a low possibility of the occurrence of internal collisions or jamming; however, a high POIC 4 indicates a true chance of jamming occurrence during the escape, specially in case of non-adaptive behaviour [8].
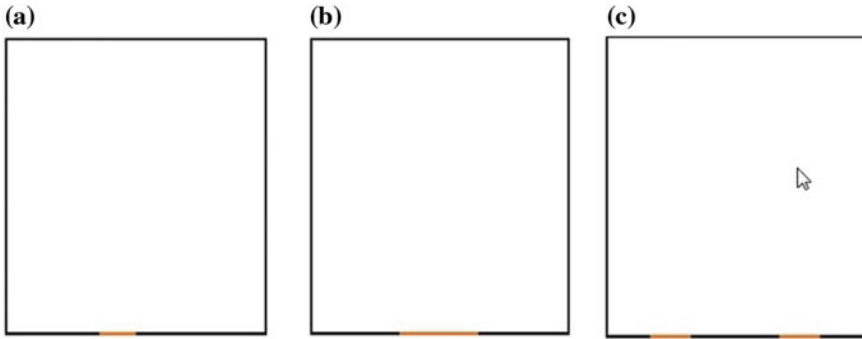
Fig. 2 Different exits configuration adopted in the evacuation simulation (*top* view, with the external walls in *black* and the exits in *orange*). Configurations 1 (real): 1 exit of 3.2 m (**a**); 2: 1 exit of 7 m (**b**); 3: 2 exits of 3.5 m in the facade (**c**)

3 Results and Discussions

All the evacuation simulations were performed by FUGA in environments externally similar to the nightclub Boate Kiss (rectangular, with dimensions 23.18 m long by 26.45 m wide). No obstacles or inner walls were considered. Three different exit configurations were possible. The first is similar to the real Boate Kiss, a single exit with 3.2 m. The second configuration considers a single exit with 7 m in the centre of the building façade. The third configuration considers two exits, each one with 3.5 m. Figure 2 shows each exit configuration adopted in the simulations. Each exit environment configuration was simulated considering occupancies of 350, 700 and 1000 persons. Figure 3 shows an example of the different occupancy profiles.
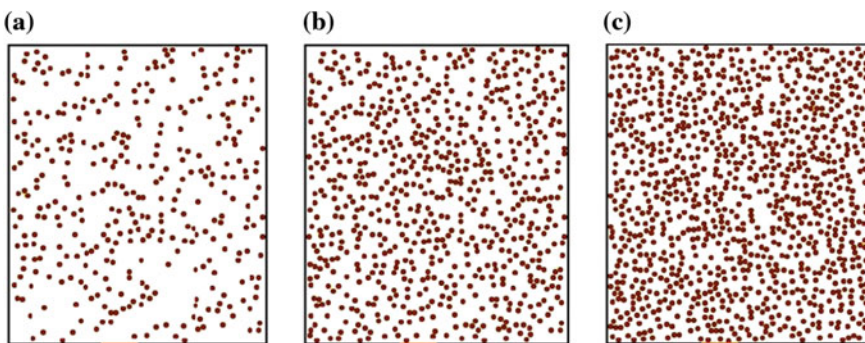
Fig. 3 Examples of the adopted occupancy profiles (initial random distribution): 350 persons (**a**); 700 persons (**b**); 1000 persons (**c**)
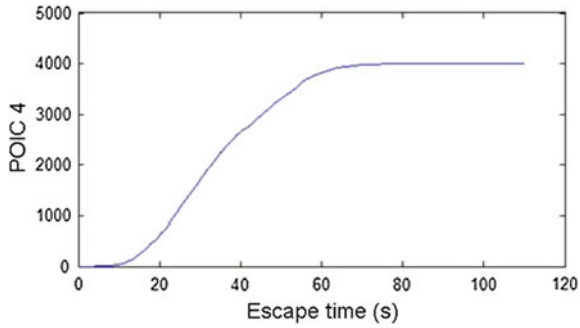
Fig. 4 Evolution of POIC 4 as a function of escape time for the real external environment (exit configuration 1) and occupancy of 700 persons

Table 1 Result of evacuation simulations

Exit configuration	Occupancy	Total escape time (s)	POIC4
Configuration 1: 1 exit of 3.2 m	350	60	70
	700	110	4,000
	1000	153	13,300
Configuration 2: 1 exit of 7 m	350	44	15
	700	70	700
	1000	90	2,800
Configuration 3: 2 exits of 3.5 m in the same side	350	40	0
	700	62	140
	1000	82	1,700

As example, Fig. 4 shows, for the real environment (externally), i.e., exit configuration 1, the evolution of POIC 4 as a function of the escape time. Finally, the results of all evacuation simulations are summarised in Table 1.

The results of Table 1 show that the real environment is the worst exit configuration, i.e., by increasing the width of total exit all safety aspects become better. However, an important point noted is that even if the total escape time for the real environment could be considered to be satisfactory (about 2.5 min to evacuate all environment even in an overcrowded situation), the POIC values indicate high possibilities of congestion in all simulated configurations for the most critical situation (1000 persons). This happens even in normal legal occupancy (700 persons) on the real external environment (configuration 1).

Hence, the evacuation results indicate that the exit width of 3.2 m is reasonably safe in the environment only if the abandonment happens in an organised manner. If the evacuation takes place with a non adaptable behaviour (such as in panic situations), there is a large probability of congestion and accidents to occur. It is noteworthy to

emphasise that no considerations were made about the internal configuration of the environment; thus, the real possibility of congestion in panic situation is higher than what is shown here.

4 Final Considerations

The minimum legal exit width is capable to ensure safety (in terms of escape time) during an evacuation in case of no panic (organised behaviour), but incapable to ensure safety in case of panic (non-adaptive behaviour). Thus, the control of the internal layout, of the materials used in edifications, of the smoke generated and the use of fire fighting systems like hydrants and sprinklers are paramount in order to keep safety and avoid losing control in a panic situation. However, these are not mandatory requirements for environments like Boate Kiss in Brazil nowadays. Additionally, it is clear that the overcrowded situation and the alteration by Boate Kiss owners of the internal layout, and also the sound isolation materials used had great influence on this fatal situation.

Thus, the results of this work showed that Brazilian legal codes for safety in environments such as nightclubs are really weak and the situation is worsened by the weakness of the public system of licensing and inspection.

References

1. ABNT: NBR 9077—Emergency Exits—procedure. Associação Brasileira de Normas Técnicas (2001)
2. Antonio, A.C.P., Castro, P.S., Freire, L.O.: Smoke inhalation injury during enclosed-space fires: an update. Jornal Brasileiro de Pneumologia **39**(3), 373–381 (2013)
3. Arigony, M., Meinerz, S., Vianna, M., Zanella, G., Souza, L.: Final Report - Police Investigation n 94/2013/150501. First Police Department of Santa Maria—RS, Santa Maria (2013)
4. Bassi, E., Miranda, L.C., Tierno, F., Ferreira, C., Cadamouro, F., Damasceno, M., Malbouisson, L.: Assistance of inhalation injury caused by fire in confined spaces: what we learned from the tragedy at santa maria. Revista Brasileira de Terapia Intensiva **26**(4), 421–429 (2014)
5. Braga, H.C., Moita, G.F., Camargo, F., Almeida, P.E.M.: Simulation of the movement of people in emergency situations: ergonomic and computational aspects with fuzzy automata and its application in architectural design. Ambiente Construído **14**(2), 61–77 (2014)
6. Duval, R.F.: NFPA Case Study: nightclub fires. NFPA (2006)
7. Meinerz, S., Souza, L.: Police Inquiry—report n 001/2013. 3a DPR—RS (2014)
8. Pan, X., Han, C.S., Dauber, K., Law, K.H.: A multi-agent based framework for the simulation of human and social behaviors during emergency evacuations. AI Soc. **22**(2), 113–132 (2007)
9. Silva, L., Wengrover, C., Saldanha, M., Brentano, T., Rodrigues, E.: Analysis of the Sinister at Kiss Nightclub in Santa Maria. RS, CREA-RS (2013)
10. Trevisan, M., Jesus, I.: Civil action for conviction for acts of administrative impropriety. Prosecutors of Justice of Santa Maria, Santa Maria (2013)

Simulation of Crowd in the Corridor
of Ziara in Masjid-e-Nabwi, Madinah

Abdullah Alshehri, Muhammad Arif and Emad Felamban

Abstract Visitors to Saudi Arabia for Hajj and Umrah from around the globe are constantly increasing with each passing year and hence visitors to the Prophet Muhammad (S.A.W)'s mosque, in Madina Munawara are also increasing. This paper investigates numerically the corridor of Ziara Place which is the most congestion place in the mosque. In order to improve crowd management and minimise the occurrence of emergency situations or hazardous conditions necessary arrangements e.g. decreasing the waiting time, avoiding barriers, controlling the crowd size and optimising the queuing process, are suggested. Certain simulation scenarios are studied in helping to reduce the risk of people colliding into each other, as well as helping to reduce long waiting times in this particular area. Visitor's behaviour, crowd density, and crowd flow around the Prophet (S.A.W)'s grave is analysed for varying crowd densities.

1 Introduction

With the advances in the computational power and availability of huge memory, crowd simulation is not only becoming a tool for creation of virtual environment and rendering the crowd but also to study the behaviour of crowd in different scenarios [6]. There are enormous applications in the field of education, training and entertainment [9, 10]. Behaviour analysis of the crowd has many applications in the area of crowd management, public space design, visual surveillance, virtual and intelligent environments [5] etc. Crowd simulation can be done as goal-driven collision free navigation of group of agents or individual agents. According to the literature, there

A. Alshehri (✉) · E. Felamban
TCMCORE, Umm Alqura University, Makkah, Saudi Arabia
e-mail: alshehri@tcmcore.org

E. Felamban
e-mail: eafelamban@uqu.edu.sa

M. Arif
College of Computer and Information Systems, Umm Alqura University,
Makkah, Saudi Arabia
e-mail: mahamid@uqu.edu.sa

are numerous methods to avoid collisions between agents, and collisions between agents and environments. Computing collision free paths of an agent through velocity obstacles helps generate a simulation of multiple agents in a moving obstacles environment with pre-calculated roadmaps [3]. Some collision avoidance techniques consider only the agents in a small area and ignore the agents which are distant from that area, this helps reduce computational cost [4]. Models that help in understanding crowd behaviour in various scenarios are proposed in the literature. Intrinsic information of the crowd like direction of the crowd flow, velocity profiles in these crowds, and motion anomalies can be studied in order to model crowd behaviour [5].

Crowd behaviours in emergency and evacuation scenarios are different from normal behaviours. In these scenarios, people tend not to process situations logically and are prone to act irrationally [1]. Santos and Aguirre [7] presented a critical review of some evacuation simulation models including flow based, cellular automata, agent based, and activity based models. Similarly seven methodologies including cellular automata, lattice gas models, social force model, fluid dynamic model, agent based model and game theoretic model are studied and advantages and disadvantages of these models are highlighted in relevance to crowd evacuation [11]. Different crowd behaviours in panic conditions are reported in [8] and empirical results are elaborated for the various models.

2 Methodology

Based on the recorded videos of the Prophet (S.A.W)'s Mosque during the Hajj season of 2013 [2], a randomly selected sample of people were manually tracked to trace their walking speed and total time spent in the corridor of the Ziara place. The corridor is divided into two regions (Fig. 2). Distance from the entrance gate to the Ziara place is 69.7 m, while distance from Ziara place to the exit door is 22.2 m. The corridor is 8 m wide. The exit door is 3.13 m wide. The first region is the incoming/approach region leading from the entrance gate to the Ziara place. It was observed in this region, that people move at relatively normal speeds. However, when near the Ziara place, they tend to walk as fast as they can within a reason of respect. The second region is in front of Ziara place where people slow down to pay salam to Prophet Muhammad and the two companions. Our team tracked 100 randomly selected individuals from different videos to calculate the average speed and standard deviation in both regions. The average walking speed in the approach region was 1.2 m/s with a standard deviation of 0.3 m/s. In the region in front of the Ziara place, the average walking speed slowed to 0.42 m/s with a standard deviation of 0.2 m/s. These parameters are used in setting up agent profiles for MassMotion in these two regions (Fig. 1).

MassMotion is a pedestrian simulation tool for designing and optimising high occupancy facilities. It is the world's most advanced system of its kind, featuring 3D environments, automatic path-finding, discrete event logic, etc. MassMotion is designed for the creation and execution of large scale (1,000,000 + individuals)

Fig. 1 Crowded view of Ziara place
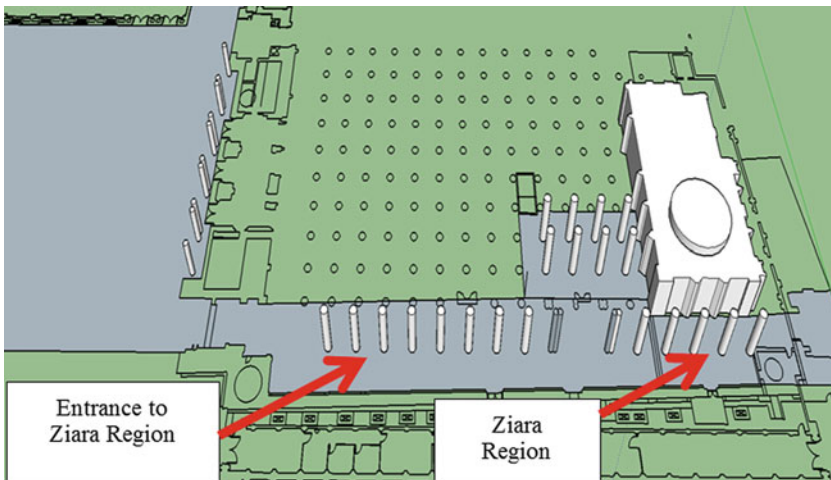
Fig. 2 3D sketch of the investigated area

3D crowd simulations. The MassMotion toolset has been successfully applied to some of the most demanding pedestrian environments in the world including mass-transit stations, performance venues, airports, and stadiums. MassMotion enables us to make informed decisions about crowd management pertaining to the design and operations of complex facilities.

3 Results and Discussions

In this section, results of the crowd simulations are discussed for two modes, namely full crowd mode and batch crowd mode. In the full crowd mode, simulations are conducted for ten cases starting from 1000 agents, gradually going up to 16,000 agents [2]. All agents are simultaneously released from the entrance gate and the

Table 1 Mean time (mm:ss) spent in two regions for different number of agents, standard deviation in between brackets

Agents		1000	6000	8000	10000	12000	14000	16000
En—Z	Time duration	1:41	8:47	11:53	15:08	18:00	20:29	22:31
	Standard deviation	0:28	4:58	6:52	8:47	10:40	12:35	14:16
Z—Exit	Time duration	1:04	1:56	1:59	2:02	2:13	2:45	3:22
	Standard deviation	0:18	0:38	0:37	0:37	0:45	1:19	1:52

simulation runs until all agents have crossed the exit door. The results of the all the simulation in full crowd mode (number of agents from 1000 to 16,000) are summarised in Table 1. Mean and the standard deviation of the time spent by agents in both regions (Entrance to start of Ziara En-Z and Start of Ziara to Exit door Z-Ex) are reported. Agents pass through the entrance gate to reach the Ziara place and the time spent in the region of En-Z can be considered as the waiting time for agents in queue to reach the Ziara place. It can be seen from the table that as the number of agents increase, the time spent in the first region En-Z also increases, as it reaches an approximate average of 23 min. Due to the proximity of the second region to the exit, the crowd disperses faster than it gathers. Although time spent in front of Ziara place has increased but it is not significant in comparison to the first region.

Let $d_a(t, k)$ be the number of agents at time t in the agent density slot k (according to Table 2). The percentage of the agent's experienced kth density slot over all the times is defined as PDR_k and calculated as below,

$$PDR_k = \frac{\sum_t d_a(t, k)}{\sum_k \sum_t d_a(t, k)} \tag{1}$$

Values of PDR_K for simulations of different number agents are summarised in Table 2. It can be seen from the table that for 1000 agents, the highest percentage is in the

Table 2 PDR_K for simulation of different number of agents

Agents	Crowd density range							
	<0.31	0.31–0.43	0.43–0.72	0.72–1.08	1.08–2.17	2.17–3.17	3.17–4.17	>4.17
1000	2.69	4.38	10.00	14.58	29.17	16.71	13.94	8.52
2000	0.65	1.10	2.60	4.25	22.78	14.73	13.20	40.70
4000	0.15	0.32	0.66	1.13	5.34	5.67	16.50	70.23
6000	0.07	0.18	0.35	0.52	2.45	2.67	7.57	86.18
8000	0.04	0.10	0.20	0.29	1.33	1.62	4.72	91.70
10000	0.02	0.07	0.12	0.19	0.85	1.07	3.32	94.36
12000	0.02	0.05	0.09	0.14	0.62	0.80	2.50	95.77
14000	0.01	0.04	0.06	0.09	0.45	0.58	1.79	96.97
16000	0.01	0.03	0.05	0.08	0.34	0.44	1.29	97.76

Table 3 Batch calculation for fixed number of agents (16,000)

Number	Crowd Density (P/m^2)	Initial batch	Batch increment	Time between batches (s)
A1	2	1115	355	113
A2	3	1673	533	170
A3	4	2230	710	227
A4	5	2788	888	284
A5	6	3346	1066	340
A6	7	3903	1243	397

density slot of 1.08 to 2.17. Small percentage of the agents (8.5%) experienced the highest density slot. As the number of agents has increased, peak of *PDR* is moved towards highest density slot (>4.17). In the simulations where the number of agents surpassed is 8000, *PDR* for the density slot (>4.17) reached above 90%. It shows that increasing the total number of agents is inversely proportional to the comfort level of the indicated agents.

In the batch mode, the crowd is divided into batches. Batch sizes and time interval between batches are varied according to the target crowd density values. Total number of agents is restricted to 16,000 for all simulations. Table 3 shows 6 scenarios where different initial batch sizes, batch increments and intervals are selected [2].

Table 4 shows PDR_k for all settings. It can be seen how with settings higher than A3, the percentage of highest density slot grows beyond 50%. However, this is still far less than the 97% in case of full crowd mode. Average and standard deviation of the time spent in both regions are tabulated in Table 6 for each setting. In the previous section we learnt that in full crowd mode (16,000 agents), the average duration of time spent in the first region was 22, and 3:22 min in the second region. Whereas in the batch mode, the duration of time spent in region 1 is below 5 min for all the settings. This is also very comforting and encouraging for the agents as region 1 is considered the waiting region.

Table 5 shows total time taken by each setting to complete the ziara for all agents. It was observed that at the expense of increasing the crowd density, for a short duration of time, the overall time reduces from setting A1 down to setting A6. When

Table 4 PDR_k for simulation of different number of agents

Agents	Crowd density range							
	<0.31	0.31-0.43	0.43-0.72	0.72-1.08	1.08-2.17	2.17-3.17	3.17-4.17	>4.17
A1	5.50	7.64	12.25	12.41	25.43	10.97	5.86	19.95
A2	3.24	4.58	8.27	10.49	24.13	12.41	9.01	27.88
A3	1.92	2.76	5.19	7.37	22.82	11.90	12.45	35.60
A4	1.58	2.25	4.29	6.40	21.63	6.22	9.40	48.24
A5	0.79	1.22	2.38	3.82	17.02	9.83	13.14	51.79
A6	0.51	0.84	1.67	2.62	13.29	9.25	12.50	59.32

Table 5 Time duration (mm:ss) spent in two regions as Mean (standard deviation)

Settings	A1	A2	A3	A4	A5	A6
En-Z	1:53 (0:35)	2:12 (0:47)	2:35 (1:07)	3:02 (1:34)	3:35 (2:06)	4:15 (2:41)
Z-Exit	0:56 (0:19)	1:04 (0:26)	1:12 (0:32)	1:20 (0:34)	1:28 (0:37)	1:36 (0:38)

Table 6 PDR_k for simulation of different settings (Modified Exit Door)

Agents	Crowd Density Range							
	<0.31	0.31–0.43	0.43–0.72	0.72–1.08	1.08–2.17	2.17–3.17	3.17–4.17	>4.17
A1	6.57	9.62	15.33	15.97	22.96			18.82
A2	4.34	6.02		12.89	28.54			24.11
A3	2.77	3.86			30.41	9.40		28.50
A4	1.84	2.67			29.23	11.17	10.21	33.04
A5	1.32	1.90			27.01	12.22	10.97	37.57
A6	0.95	1.37			22.83	14.20	12.07	41.78

comparing with the full crowd mode (approximately 57 min), total time of A6 setting (approximately 72 min) is quite comparable with a more comfortable flow of the agents. The difference between setting A1 and setting A6 is also not great, given the fact that the door's throughput (width 3.13 m) is limited, so by increasing the batch size, we do not affect the total time significantly.

4　Structural Modification: Exit Door Width Is Modified

It is observed in the results of above simulations that width of the exit door is a bottleneck to improve the throughput and increased agent density in the Ziara place. Hence we have modified the width of the exit door and increased it to the width of the corridor (8 m). Figure 3 shows the modification in the layout for wider exit door. The door's width is increased from 3.13 to 8 m. In the batch mode, we have done two sets of simulations. In the first set of simulations, batch sizes and time between batches are kept similar to the case of batch mode in the existing door width. In the other set of simulation time between batches are reduced as the throughput from the exit door is increased. Simulations for the batch mode are run for this modification. Table 6 shows that agent densities are better, compared to the full crowd mode with modified door width.

　　Based on the simulations done and results discussed, following recommendations are made. Crowd management should be done in the batch mode with appropriate selection of the batch sizes and timing between batches. To ensure smooth flow of the crowd strong motivation from the security personnel especially in the high density cases is recommended. With the existing door, A4 batch mode setting is suggested to compromise the operation completion time and lower crowd density in the regions. It is suggested that following mechanism can be adopted for the batch mode control of the crowd.
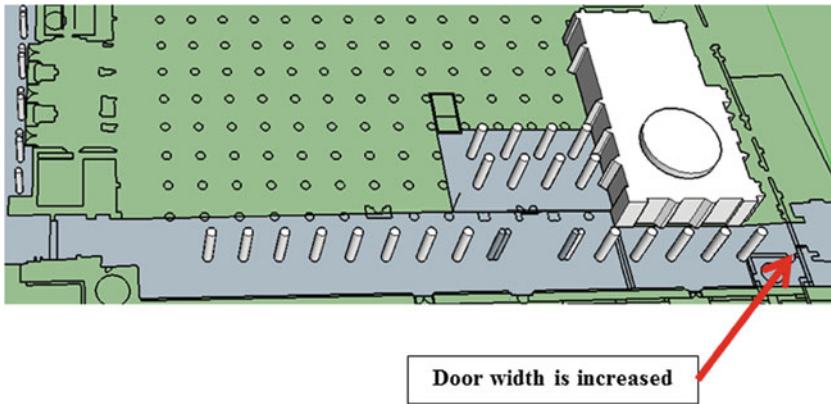
Fig. 3 Layout of the Ziara place with modified door
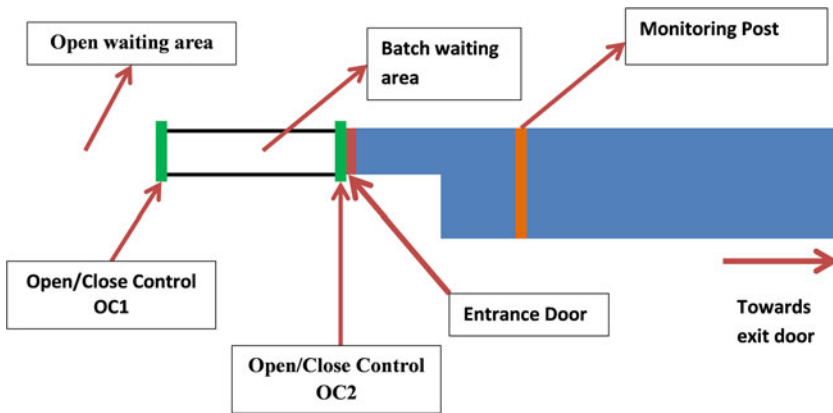
Fig. 4 Proposed Batch mode control plan

Figure 4 shows the proposed batch mode control plan. There are two control points outside the entrance door. First control point OC1 brings the people from outside to the batch waiting area. Length of these two points depends on how much will be the batch size. Initially, initial batch is allowed in the batch waiting area by opening OC1 and OC2 is closed. Then, OC1 is closed and OC2 will be open to let the batch into the mosque through entrance door. A security personal will be placed on monitoring post. The distance of monitoring post from the entrance door depends on the batch size. Once the whole batch enters in the mosque, OC2 is closed. The OC1 is open to bring another batch in the waiting area. When the security personal signals the crossing of last person of batch from the monitoring line, new batch is entered by opening OC2. This procedure keeps repeating until all persons complete ziara or outside waiting crowd falls below certain threshold. Proper motivation to move is required in front of Ziara place to keep the flow smooth.

5   Conclusion

In this paper, crowd simulation is done in various scenarios including full crowd mode and batch mode. Simulation results are compared to find out the best crowd management policy. It was found that batch mode strategy is better to compromise between throughput of the crowd from the exit door and the crowd density levels inside the Ziara place. It was found that existing door width is a bottleneck in the maximum throughput of the crowd and the increased crowd density levels in the Ziara place. It is therefore suggested that exiting door should be modified to make the width of the door equals to the width of the corridor so that there can be no congestion near the exit door. Simulation results should the efficacy of the structural modification in the exit door.

References

1. Almeida, J.E., Rosseti, R.J., Coelho, A.L.: Crowd simulation modeling applied to emergency and evacuation simulations using multi-agent systems (2013). arXiv preprint arXiv:1303.4692
2. Alshehri, A., Arif, M., Alkhemi, M., Felemban, E.: Analysis of crowd movement in the prophet (saw) mosque in the city of madinah, saudi arabia. In: Proceedings of the Third International. Conference on Advances in Computing, Electronics and Electrical Engineering—CEET 2015, pp. 151–160 (2015)
3. van den Berg, J., Patil, S., Sewall, J., Manocha, D., Lin, M.: Interactive navigation of multiple agents in crowded environments. In: Proceedings of the 2008 Symposium on Interactive 3D Graphics and Games. I3D '08, pp. 139–147. ACM, New York, NY, USA (2008)
4. Guy, S.J., Chhugani, J., Curtis, S., Dubey, P., Lin, M., Manocha, D.: PLEdestrians: a least-effort approach to crowd simulation. In: Proceedings of the 2010 ACM SIGGRAPH/Eurographics Symposium on Computer Animation. SCA '10, pp. 119–128. Eurographics Association, Aire-la-Ville, Switzerland, Switzerland (2010)
5. Jacques, J. Jr., Raupp Musse, S., Jung, C.: Crowd analysis using computer vision techniques. IEEE Sig. Process. Mag. **27**(5), 66–77 (2010)
6. Pelechano, N., O'Brien, K., Silverman, B., Badler, N.: Crowd simulation incorporating agent psychological models, roles and communication. Technical report, DTIC (2005)
7. Santos, G., Aguirre, B.E.: A critical review of emergency evacuation simulation models (2004)
8. Schadschneider, A., Klingsch, W., Klüpfel, H., Kretz, T., Rogsch, C., Seyfried, A.: Evacuation dynamics: Empirical results, modeling and applications. In: Meyers, R.A. (ed.) Extreme Environmental Events, pp. 517–550. Springer, New York (2011)
9. Sung, M., Gleicher, M., Chenney, S.: Scalable behaviors for crowd simulation (2004)
10. Ulicny, B., Ciechomski, D.H.P., Thalmann, D.: Crowdbrush: Interactive authoring of real-time crowd scenes. In: Proceedings of the 2004 ACM SIGGRAPH/Eurographics symposium on Computer animation, pp. 243–252 (2004)
11. Zheng, X., Zhong, T., Liu, M.: Modeling crowd evacuation of a building based on seven methodological approaches. Build. Environ. **44**(3), 437–445 (2009)

Pedestrian Dynamics at Transit Stations: An Integrated Pedestrian Flow Modelling Approach

Emily Porter, Samer Hamdar and Winnie Daamen

Abstract The objective of this chapter is to explore an integrated modelling framework that captures pedestrian walking behaviour in congested and uncongested conditions and covers different traffic dynamics caused by complex geometric and operational characteristics such as those observed in transit stations. The integrated modelling framework is built using concepts from the Social Force model, behavioural heuristics, and materials science. Pedestrian trajectory data provided by the Delft University of Technology were used to test the validity of the aforementioned modelling framework. A simulation study showed that the model reproduces realistic trajectory patterns in an environment similar to that at the Foggy Bottom METRO station in Washington, D.C, USA.

1 Introduction and Motivation

Pedestrians play an increasingly important role in the traffic scenes of the modern world. This role is particularly important in urban areas, such as Washington D.C., where pedestrians often dominate the traffic flow [3]. By accurately modelling pedestrian behaviour, design of civil infrastructures may be improved by increasing the number of pedestrians who can safely flow through the corresponding geometric components (i.e. pedestrian infrastructure capacity). Of particular interest is the flow of pedestrians through public transit stations [1, 6, 12]. Transit stations must be able to hold large numbers of travellers while also allowing pedestrians to move safely and efficiently from one location to another. Accurately modelling pedestrian behaviour

E. Porter (✉) · S. Hamdar
The George Washington University, 800 22nd Street NW, Washington DC, USA
e-mail: emilyporter@gwmail.gwu.edu

S. Hamdar
e-mail: hamdar@gwu.edu

W. Daamen
Delft University of Technology, Stevinweg 1, P.O. Box 5048, 2600 GA
Delft, The Netherlands
e-mail: w.daamen@tudelft.nl

through transit stations allows identifying areas with critical densities that might be dealt with through changing the corresponding geometric features or through offering some level of control (pre-timed or real time). Many models of pedestrian behaviour have been previously suggested, however, a relatively recent review of crowd models suggested that model usability is highly dependent on the application for which the model was originally developed [4]. In this chapter, the model is intended to be used for crowd management and control for the Washington, DC METRO system. As such, the model must be able to accurately show high-density situations, run in real time, and consider the complex nature of human decision making. Although some existing pedestrian models are computationally efficient, these models frequently capture one-to-one interactions and fail to consider the complexities of decision making that occur in crowded conditions [9, 11].

The objective is to accurately and efficiently model pedestrian operational behaviour (focusing on walking behaviour), using a combination of the Social Force model [7], the behavioural heuristics model [10], and concepts from materials science such us multi-body potential molecular interactions [5]. The resulting integrated model (IM) rules are programmed in a JAVA simulation platform constructed by the authors. Realistic parametric values were initially taken from the literature and later calibration efforts were conducted using experimental data obtained by the Transport and Planning Department at the Delft University of Technology. The basic manual calibration was aimed to reproduce the observed densities in a bidirectional flow experiment. Afterwards, simulations were run to look into the reproducibility of trajectory patterns observed in 4 additional experiments. After this introduction, Sect. 2 presents the model itself, including a description of the models formulation and basic calibration. Section 3 contains an analysis of the results obtained from model simulation related to the 5 experimental scenarios previously described in addition to an exploratory study on simulating pedestrian movements in a transit station. In Sect. 4, the paper concludes and suggests future research recommendations.

2 Model Formulation and Calibration

In this section, some IM related details are explained, beginning with the formulation framework, which specifies the aspects of the suggested model that were adapted from other sources as well as the method by which they were combined. Afterwards, the calibration efforts that were undertaken for this model are described.

The motivation behind offering the suggested integrated modelling framework is the hope that the resulting formulation will benefit from the attraction/repulsive force concepts offered by the social force models (offering realistic one-to-one interactions), the flexibility of the behavioural heuristics (incorporating multiple psychological and physiological pedestrian characteristics) and the theoretical foundation from materials science. Accordingly, the basic interaction between 'bodies' (i.e. pedestrians or obstacles) is adapted from the Social Force model [7]. The Social Force model essentially uses Newtonian physics to describe how pedestrians move.

The model defines attractive and repellent forces which push and pull pedestrians along their path of motion. On the other hand, the behavioural heuristics model utilised in this paper considers that pedestrians take advantage of their eyesight and cognitive perception of their surrounding environment to determine which direction is the most efficient to reach their local destination (i.e. operational navigation) [10]. Finally, an essential concept from materials science is incorporated; this concept states that molecular interactions can be well modelled by taking into account directly neighbouring molecules. This greatly simplifies the complexity of the calculations since not all surrounding objects need to be considered. This conceptual hypothesis is to be tried in this paper: when applied to pedestrian dynamics, this concept implies that accurately modelling pedestrian behaviour requires 'social force' calculations not only between the two closest bodies (i.e. pedestrians or obstacles), nor all surrounding bodies, but rather between multiple bodies (i.e. multi-body potential interactions) within the corresponding field of view [5]. In our model, based on the findings of the research conducted in materials science [5], the closest three other pedestrians/obstacles are taken into account when determining a specific pedestrians course of action. It should be noted that this number may be a parameter to be calibrated depending on surrounding traffic conditions.

Given the aforementioned modelling framework, manual calibration was conducted using a bidirectional flow experiment data set provided by TU Delft (Fig. 1c). A more detailed review of these experiments is provided by [2]. From this data, macroscopic information such as average flows and densities were extracted. The mean and standard deviation of the pedestrians speed in the experimental data (assuming a normal distribution) was applied to the modelled pedestrians as their desired speed.

The density from the model was recorded at every time step and compared to the actual density recorded in the data. In this case, the density consists of the number of pedestrians in the entire walking area ($40\,m^2$). These density recordings taken from the data were used to determine how closely the model was representing the experimental results on a macroscopic level. The resemblance between the experimental data (i.e. observed density) and the model output (i.e. simulated density) was measured based on a simple relative error term expressed as the absolute (positive) difference between the two values (i.e. observed density simulated density) divided by the observed data (i.e. observed density). The parameter values in the model were changed using a tabu-search approach in order to reproduce results similar to those seen in the experimental data. The error resulting from the density comparisons is 24.6 % error for the IM approach. Such error is outside the acceptable error ranges [8] despite the low density values recorded; the integrated model still obtained the lowest error if compared to the BH and SF models implemented by the authors.

Section 3 describes the numerical results gathered from simulation, including a comparison between the experimental data and the integrated approach model output for 5 scenarios: a unidirectional flow scenario, a bidirectional flow scenario, a crossing scenario, a wide bottleneck scenario and a narrow bottleneck scenario. The simulation study is further extended to explore some trajectory patterns produced by the integrated model at a transit station.
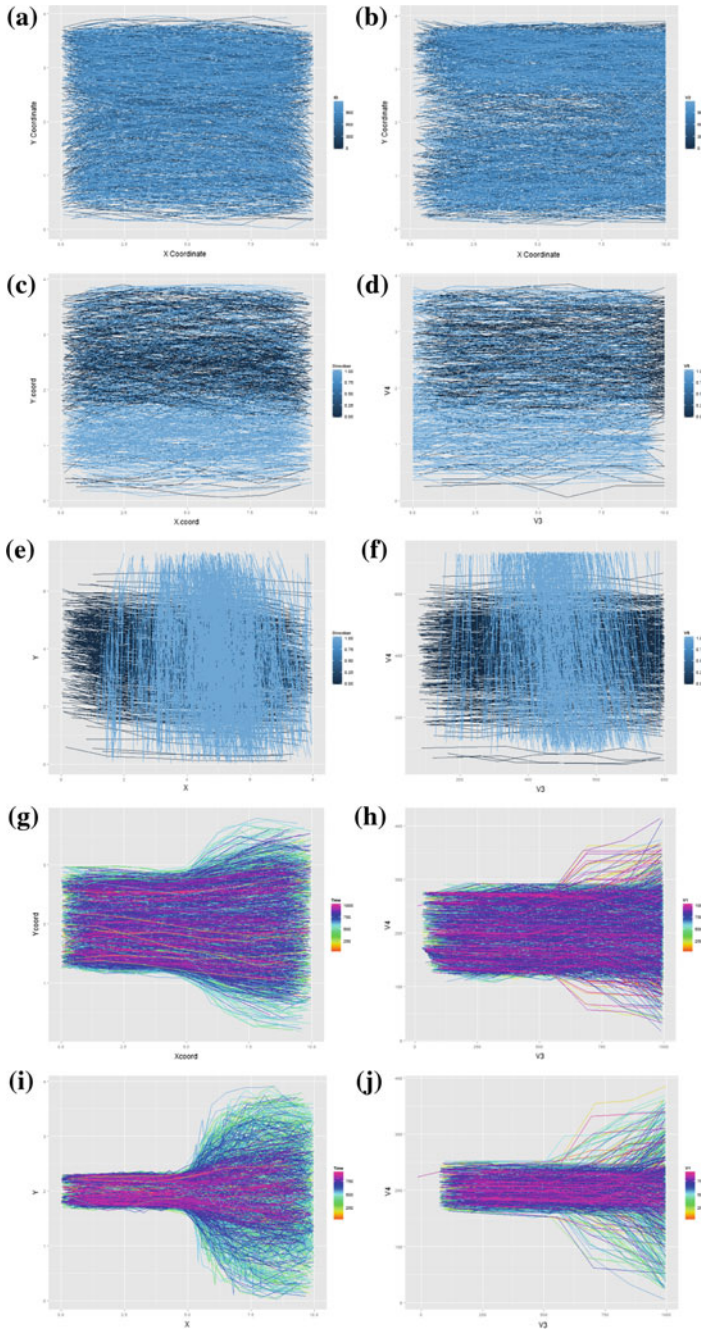
Fig. 1 Comparison of data and model trajectory results for 5 experimental scenarios. Unidirectional flow: data (**a**), model (**b**); bidirectional flow: data (**c**), model (**d**); crossing flow: data (**e**), model (**f**); wide bottleneck: data (**g**), model (**h**); narrow bottleneck: data (**i**), model (**j**)

3 Simulation

Figure 1 presents a trajectory comparison between experimental data gathered by TU
Delft and the corresponding trajectories that were gathered from the IM model (using
the parameters that produced the lowest error). From the top, the images show: one
directional flow, two directional flow (left to right in blue and right to left in black),
crossing (right to left in black and top to bottom in blue), wide bottleneck (colours
based on entrance time: red most recent and orange yellow, less recent), and narrow
bottleneck. The sharp changes in direction seen in the IM trajectories are due to the 1
second time step that has been employed. Aside from this obvious difference, there
are numerous similarities between the experimental trajectories and the simulated
trajectories. The one directional flow indicates consistency in the area occupied by
pedestrians. In the two directional flow situation, in addition to matching in terms
of area occupied by pedestrians (i.e. area mainly occupied by pedestrians moving
from right to left—black trajectories—versus area occupied mainly by pedestrians
moving from left to right—blue trajectories), the simulation suggests lane formation
similar to that seen in the data, although this phenomena cannot be definitively
observed with all of the trajectories plotted at once. The simulated pedestrians in the
crossing scenario are also seen to have similar trajectory patterns as those observed
in the experiment. It seems there is a major crossing area and a minor crossing area
towards the left of the corresponding plots). The last two scenarios illustrated in the
figure correspond to bottlenecks. The simulated wide bottleneck scenario provides
more similarities with the observed trajectories if compared to the narrow bottleneck
scenario; such results at this exploratory level of the study is somewhat expected
due to the increasingly complex interactions that occur at narrow bottlenecks [8]. In
both simulated bottleneck results, the funnelling effect can be seen as the pedestrians
fan outwards before entering the bottleneck area. The experimental results from the
narrow bottleneck show sharp zig-zagging trajectories from pedestrians travelling on
the outermost edge of the funnel shape who are attempting to enter the central area,
whereas the simulation shows these trajectories as smooth. The zig-zagging seen in
Fig. 1i is caused by the swaying effect, which is visible at low speeds, and occurs
when pedestrians shift their weight from their right foot to their left foot.

Since the IM is ultimately intended to be used at the Washington DC METRO
system, a simulation was conducted based on the layout of the station at Foggy
Bottom. In the corresponding scenario, it was assumed that pedestrians entered the
platform from the escalator near the right side of Fig. 2a (descending escalators) as
well as from train doors. Pedestrians were able to leave the platform via the more
centrally located escalator (ascending escalators) as well as by entering train doors.
The simulation was conducted with pedestrians entering from the escalator at a
uniform arrival rate.

Figure 2a shows the simulated trajectory data with the train doors and escala-
tors shown. Figure 2b is a density plot, which shows the areas with the highest
'congestion', which correspond primarily to waiting areas. The darkest areas in
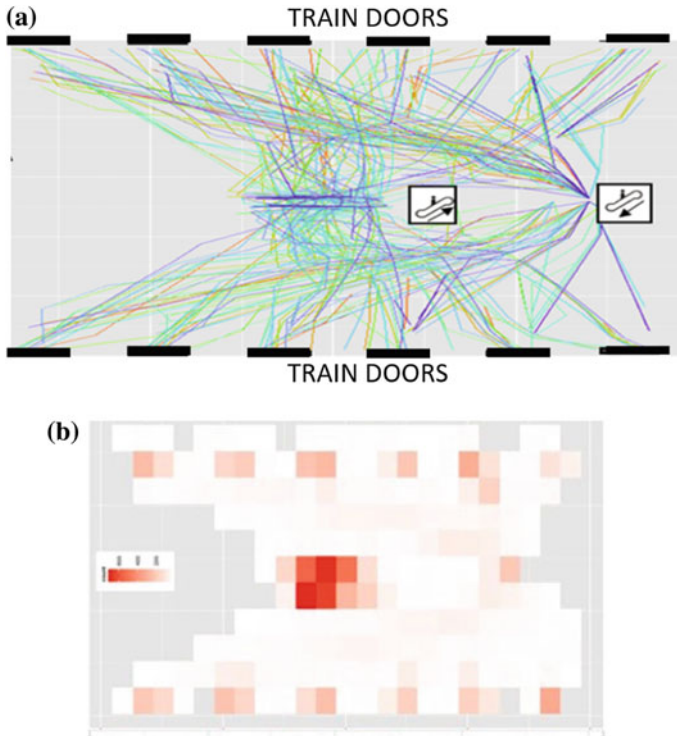
Fig. 2 Transit scenario results: simulated trajectories at transit station (**a**); density distribution for transit simulation (**b**)

Fig. 2b indicate areas in which pedestrians have spent prolonged periods of time (more than 1 s). These dark points correspond to waiting areas, such as those located near train doors where pedestrians who have descended on the escalator are awaiting their train and the area in front of the escalator where pedestrians are waiting to exit the station. The pedestrians waiting for the escalator are experiencing delays due to congestion, which may be mitigated by crowd control, whereas the pedestrians waiting near the train doors are waiting for their train to arrive, which is controlled by the train scheduling. The highest density area occurs near the escalator that leads from the platform to the stations exit, where pedestrians can be seen queuing. This result is expected, especially considering trains from both directions arrived at the same time. This causes a queue to build up in front of the escalator as pedestrians await their turn to leave. This result resembles the real-world lane formation, which shows pedestrians queuing in straight lines (rather than half a circle) before entering the escalator. This queuing is shown by the green and red points in front of the escalator in Fig. 2a. Although the transit simulation cannot be numerically verified by empirical data at this stage (the same traffic patterns observed in real-life are observed in the simulation), the results appear to accurately reflect basic densities and crossing

areas on the station platform. These results, in addition to the proximity between the empirical data and the simulation results shown above (Fig. 1), indicate that the IM approach is well-suited for performing in transit situations, and further work should be conducted to reinforce this indication.

4 Conclusions

Pedestrian modelling faces numerous challenges, ranging from covering heterogeneity among the behaviour of individuals to a lack of commonly used datasets. These difficulties affect models in different ways the heterogeneity of pedestrians contributes to the non-existence of a single model that can accurately describe all types of scenarios, and the lack of common data sets contributes to different approaches taken by authors to validate their models. Furthermore, there is a lack of commonly accepted calibration and validation methods as well as a lack of agreement on which phenomena and behaviours a model should be able to capture, which adds to the difficulty of verifying that a particular model is working well. Although the pedestrian modellers ultimate goal, of being able to realistically simulate all types of situations with a single model, has not yet been reached, there are many models which are capable of reproducing specific situations. One such model has been presented here. The IM approach is intended to be used in high-density situations, and this paper discusses the initial calibration and validation efforts that have been taken towards achieving that goal. In order to further improve this model, experimental data gathered in high-density situations will need to be used for calibration. Additionally, a sensitivity analysis must be conducted, in addition to more intensive calibration efforts, in order to verify that the IM approach is capable of simulating all types of scenarios that are seen in transit stations. Future calibration efforts will consist of a thorough macroscopic and microscopic calibration in addition to specifying individual pedestrian information, such as sight angle and distance. The primary future goal identified by the authors of this paper is to collect data from high-density experiments, which will be invaluable to this model, as well as to other models with similar objectives.

References

1. Daamen, W.: Modelling passenger flows in public transport facilities. Ph.D. thesis, Delft University of Technology (2004)
2. Daamen, W., Hoogendoorn, S.: Experimental research of pedestrian walking behavior. Transp. Res. Rec.: J. Transp. Res. Board **1828**, 20–30 (2003)
3. District of Columbia Department of Transportation: District of columbia pedestrian master plan. Technical report, District of Columbia Department of Transportation (2009)
4. Duives, D., Daamen, W., Hoogendoorn, S.: State-of-the-art crowd motion simulation models. Transp. Res. Part C: Emerg. Technol. **37**, 193–209 (2013)
5. Gniewek, P., Leelananda, S., Kolinski, A., Jernigan, R.A.K.: Multibody coarsegrained potentials for native structure recognition and quality assessment of protein models. Proteins: Struct. Funct. Bioinf. **79**(6), 1923–1929 (2011)
6. Hänseler, F., Farooq, B., Muhlematter, T., Bierlaire, M.: An aggregated dynamic flow model for pedestrian movement in railway stations. In: Proceedings of the 13th Swiss Transport Research Conference, pp. 1–14 (2013)
7. Helbing, D., Molnar, P.: Social force model for pedestrian dynamics. Phys. Rev. E **51**(5), 4282 (1995)
8. Hoogendoorn, S., Daamen, W.: Microscopic calibration and validation of pedestrian models: cross-comparison of models using experimental data. In: Traffic and Granular Flow Conference. Berlin, Germany (2005)
9. Jian, X.X., Wong, S., Zhang, P., Choi, K., Li, H., Zhang, X.: Perceived cost potential field cellular automata model with an aggregated force field for pedestrian dynamics. Transp. Res. Part C: Emerg. Technol. **42**, 200–210 (2014)
10. Moussaïd, M., Helbing, D., Theraulaz, G.: How simple rules determine pedestrian behavior and crowd disasters. Proc. Natl. Acad. Sci. **108**(17), 6884–6888 (2011)
11. Tao, W., Jun, C.: An improved cellular automaton model for urban walkway bi-directional pedestrian flow. In: International Conference on Measuring Technology and Mechatronics Automation, vol. 3, pp. 459–461. IEEE (2009)
12. Zhang, R., Zhihong, L., Hong, J., Han, D., Zhao, L.: Research on characteristics of pedestrian traffic and simulation in the underground transfer hub in Beijing. In: Fourth International Conference on Computer Sciences and Convergence Information Technology, pp. 1352–1357 (2009)

PedVis: Pedestrian Flow Visualisations

**Jimmy Schmid, Harald Klingemann, Arne Scheuermann,
Judith Bühling, Nicolo Bernasconi and Michael Flückiger**

Abstract More and more people are using public transport. The Swiss Federal
Railways (SBB) are expanding their railway stations and redesigning them so that
all passengers will in future still reach their destinations safely and quickly. In this
context, the depiction, planning and simulation of people flows (customer flows,
movement patterns) are of increasing importance. This project will open up new
access points in this field. Starting with seven topical clusters, different aspects of
people flows will be analysed and depicted anew, based on a comprehensive collection
of images. The prototypes for new visualisations developed from this have been
validated using a Delphi survey of expert opinions and tested for their future potential.
The SBB have been presented with a catalogue of recommendations with all the
visualisation models, and a practice manual will be developed during the last phase
of the project.

J. Schmid (✉) · H. Klingemann · A. Scheuermann · J. Bühling ·
N. Bernasconi · M. Flückiger
Bern University of the Arts, Fellerstrasse 11, 3027 Bern, Switzerland
e-mail: jimmy.schmid@hkb.bfh.ch

H. Klingemann
e-mail: harald.klingemann@hkb.bfh.ch

A. Scheuermann
e-mail: arne.scheuermann@hkb.bfh.ch

J. Bühling
e-mail: judith.buehling@hkb.bfh.ch
N. Bernasconi
e-mail: nicolo.bernasconi@hkb.bfh.ch

M. Flückiger
e-mail: michael.flueckiger@hkb.bfh.ch

1 Introduction

Influencing people flows is becoming increasingly important on account of user numbers and limited space in the halls and surfaces of railway stations. Such space was not a rare commodity at stations in the past. However, it is rare today, and will presumably remain so in the future [9, 13].

Assessing the dynamic of people flows in railway stations means answering relevant, specific questions such as: which trains should arrive on adjacent platforms? Which trains are involved when people have to change trains? What constellations of trains and public facilities create minimum flows of people? What constellations create the smallest distances to be covered? How do demographic change and multilingualism influence orientation behaviour?

The paths taken by travellers and shoppers can be influenced by measures taken in the realms of structure, design, atmosphere and operations, as well as through customer information and customer guidance. Attention must be paid here to the fact that in the spaces of a railway station, *four systemically linked* worlds come together:

- Public facilities: entrances/exits; pedestrian underpasses and overpasses; access points to the platforms (ramps/stairs/lifts); platforms;
- Actual station operations: which trains stop when, and at which platforms; train lengths;
- Local environment: city planning, public spaces, non-motorised traffic, public transport, motorised private transport, ...;
- Human behavioural patterns (e.g. pedestrian speed of movement, interpersonal proximity, whether people proceed over certain distances in isolated fashion or in a crowd) [5].

Models, simulations and calculations in the context of people flows and the dimensions of stations are all ultimately based on assumptions about precisely this human behaviour. The more accurately such behaviour can be characterised, the greater is the prognosis strength of the models, simulations and calculations developed.

The interdisciplinary approach necessary when monitoring and influencing people flows, is contingent upon models and simulations [8]. Currently, multiple databases are available that describe people flows from an external perspective (including sensor readings, counts, films ...), from internal perspectives (questionnaires, eye-tracking ...) and models and statements derived from them. However, these have been insufficiently exploited, have been depicted in a suboptimal fashion, and are correspondingly limited in what they are able to interpret.

They also often remain incomprehensible outside a small circle of experts. There is a need—inadequately met at present—for appropriate, public-friendly depictions of ideal and actual spatial uses that are suitable for other target groups [1, 2].

This is the starting point for the project presented here, which offers new approaches for a contemporary form of communication about people flows that is appropriate to the context and to the needs of the public [14].

2 Methods

The research design encompasses three phases: (1) A design analysis and inventory of existing visual depictions and knowledge visualisations; (2) Developing practicable prototypes for context-appropriate knowledge visualisations; (3) Monitoring the added value of the prototypes and the potential of alternative visualisation models when compared to current solutions. For this, a three-round Delphi survey was carried out from a pool of $n = 43$ SBB experts in May, 2015. Delphi surveys are used to assess trends and prognoses [12], also within the context of system tasks and topic evaluations, and are thus suitable for use in our current context [11]. Experts who have no direct contact with each other are presented with a list of questions or statements and comment on them over the course of several rounds, each time getting feedback on the group opinion [4, 6]. This step-by-step procedure enables the development of a group consensus. The Delphi method was developed as an alternative to expert meetings in which there is often the danger of a distorting influence on the part of dominant participants in the group, with the group consequently losing sight of the actual aim of its discussions. As a suitable *tool* for a complex on-line survey [7] that provides an optimal view of the static and dynamic visualisation models and offers interfaces to statistical evaluations, we chose 'Qualtrics Research Suite' (http://www.qualtrics.com/research-suite/). The method and the tool were subjected to a 'pre-test' between 27 April 2015 and 21 May 2015 in which three members of the research team took part, along with the person responsible for the project; together, they produced a finalised version.

The *participation level* in the Delphi survey can be regarded as very satisfactory—in total there was a response rate of between 64 and 76 %. The absolute number of 14 participants in all three rounds also corresponded to the optimal group size for Delphi surveys as stated in the literature, which suggests a minimum of 10 and a maximum of 16 participants [11].

Above and beyond this, we must still investigate the extent to which the *professional profile of the participants might have shifted over the course of the rounds.* When recruiting and compiling the initial list, the assumption was made, that three types of target groups should be taken into consideration which represent the different forms of familiarity and experience with such visualisations. It emerged that these target groups were almost equally represented in the group of the first round, namely *users* (n = 9), *authors* (n = 11) and *recipients* (n = 9). This picture remained largely unaltered, with a distribution in the second round of *users* (n = 8), *authors* (n = 8) and *recipients* (n = 6) and in the third round of *users* (n = 6), *authors* (n = 4) and *recipients* (n = 4). Thus, we achieved a *broad spectrum of opinions* representing the data base for the analysis.

3 Results

The following results of the project highlight intermediate stages of the *interdisciplinary* design and research process. Using social scientific methods, the alternative visualisation strategies and prototypes are tested by eliciting feedback from experts and end-users. This information informs subsequent stages of design solutions as part of an open process.

3.1 Cluster Identification

A thematic classification has been developed of the visual language of the SBB on the topic of 'people flows' [10]. The inventory of this depictional world of the SBB has been complemented by the opinions on current visualisation practices of key persons from different functional areas (see target groups above). This way, we have prioritised subject areas for subsequent work (subject clusters).

The focus of our work has been on the design development of prototypes to depict the different parameters of spaces and movement, and their impact on each other in specific time windows. Here, it was necessary to pay greater attention to linkages of the subject clusters with the terminology of existing guidelines ('Assessing public facilities and development projects from the perspective of people flows') and the important time dimension. This led to the identification of new subject clusters ('Connection times of people types' and 'Platform occupancy') and to the derivation of further visualisation prototypes ('Space-time axis' and 'Platform occupancy topology') [3]. Visualisations were subsequently prepared (Figs. 1, 2, and 3) and the on-line Delphi expert survey was carried out.
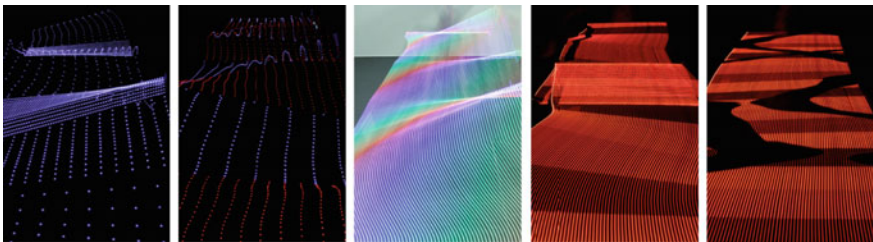
Fig. 1 Explorative, experimental arrangement for visualising people flows by means of LED printing: using long exposures of a programmable LED strip moved in space, strips of light are created. According to how the blinking speed, duration and colour are set, and according to the movement in the space, different impressions and associations arise
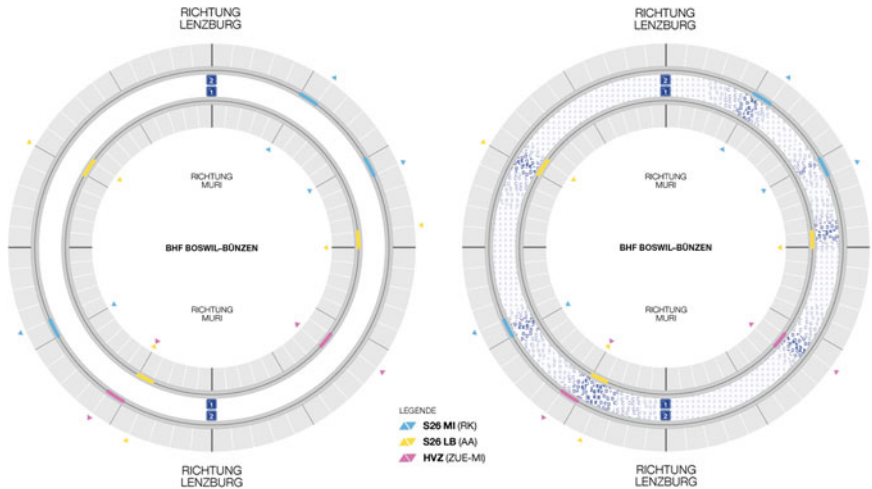
Fig. 2 This visualisation offers an overview of all regular train movements at the different platforms in a specific railway station. Thus a glance at the graphic offers information on the arrivals and departures of trains during a specific hour, and the time they spend at platforms. This circular map may also be expanded, by adding further data, such as people density, so that the volume of people on the platform is visible

3.2 Expert Feedback

More specifically, the expert feedback from the three Delphi rounds showed, that the majority of the innovative visualisation strategies was considered a clear improvement on the status quo. Specific suggestions were screened by the research team and provided input for the finalised solutions. More specifically, this positive picture emerged particularly from the first round with the highest participation of $n = 29$ experts; the highest rating was received by the new visualisation of the topic 'Arriving and departing travellers' ($x = 3.3$ on a scale from 1–4) and only the topic 'heat map' was attributed a potential similar to that of existing plans. During the second and third rounds with $n = 22$ and $n = 14$ participants, a more critical assessment prevailed; however, eight out of twelve suggestions for new topical visualisations were still considered to be superior to plans used so far.

Most notably, as a result of the second round, specific *comments from the participants highlighted the pros and cons of the alternative and conventional visualisation strategies:* From a pragmatic point of view, participants in the second round remarked that the expense of making realistic isometric depictions would be far too great, and that it must be possible to edit the depictions *oneself.* Conciliatory positions were adopted in that different degrees of information for the usual plans and alternative solutions may be emphasised paradigmatically: thus the necessary widths of pedestrian overpasses and underpasses were adopted from the old plan, while the new plan offers information on high people densities. Furthermore, it was suggested that it
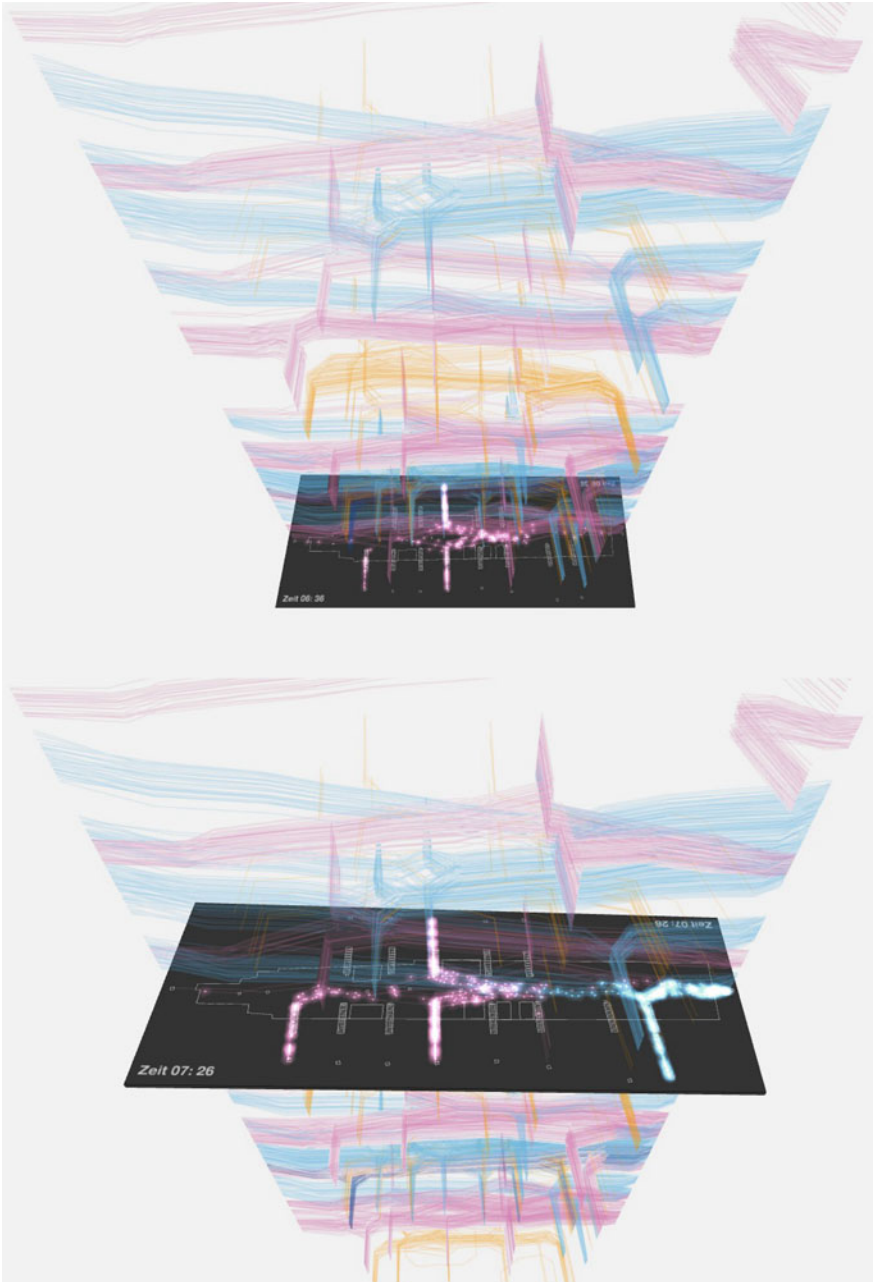
Fig. 3 Based on a situational ground plan, people flows in this interactive model are depicted as a function of the pre-set points of departure and destination. The colour coding in each case refers to a train (source or goal). Every person is depicted by a line. Depending on the increase or decrease in the volume of people, the model can display problematic intersections or cumulative people flows

should be possible *to switch between 2D and 3D depictions* to a varied degree—for example, if individual people are to be counted on the platforms, then a 2D-depiction is surely easier to read. In order to display the density of travellers on the platforms and to get an idea of this, however, a 3D-depiction would be appropriate. It would correspondingly be advantageous if one could switch between these two depiction options.

3.3 Modifications and Practical Relevance

In general, the participants propose a sequential approach when offering alternative depictions in the form of follow-ups. In other words, if information is lacking in a depiction, then a second or complementary depiction should be made possible that would focus on this particular lacuna.

While this feedback makes evaluating additional potential dependent on the *specific question to be answered* in each case, a second focus arose during the group echo on the *problem of the target public and aspects of communication*: a further expansion was proposed for communicating to laypeople. When communicating with laypeople, more could be gained from using an expanded palette in the SBB colour world, while project-related work should focus on primary colours. In addition, it was pointed out that alternative visualisations have considerable communication potential for *external presentations.* It was accepted that they could make it possible to explain clearly and simply to a town or local authority why a railway station should be subjected to further development. All the relevant information would thereby be made available.

At the same time, the opinion was expressed that readability was important for all stakeholders, both laypeople and experts, and that the old depictions were also not 'management-friendly'. As in round 1, obstacles in the organisational area were highlighted that could make an adjustment process necessary among technical experts and planners. Often, it is not recognised that utilising alternative visualisations can make it unnecessary to use special software or to carry out complex surveys. Instead, they make it possible to use empirical data or observations on the spot.

This opinion also surfaces in the closing section of round 2: '... and what I still wanted to say—group forum'. Here, the focus was once more on the implementation of alternative visualisations, i.e. when they should be used, and for what target groups. Here two tendencies became clear. First, the opinion that the alternative depictions are *exclusively* appropriate as a means of communication to laypeople; and secondly, that the alternative depictions should take a *broad spectrum* of addressees into consideration that also includes new employees and internal specialists who do not concern themselves with these topics on a regular basis.

3.4 Limitations and Outlook

As a *general conclusion* from the feedback of the Delphi rounds it became clear that the research team had not successfully communicated the idea of a 'modular toolbox' to be applied across topics and the optional use of existing and new visualisations; the latter need not necessarily replace current practices. A perceived loss of information or a requirement to learn new ways of reading more complex alternative visualisations emerged as additional factors impacting on the acceptance of innovative solutions.

To summarise, the findings gained from the project—especially the findings of the Delphi survey—will provide the basis for a manual that demonstrates the variety of possible visualisations and describes their respective strengths and possible applications.

References

1. Andrienko, N., Andrienko, G.: Visual analytics of movement: an overview of methods, tools and procedures. Inf. Vis. (2012)
2. Andrienko, N., Andrienko, G., Gatalsky, P.: Exploratory spatio-temporal visualization: an analytical review. J. Vis. Lang. Comput. **14**(6), 503–541 (2003)
3. Boyandin, I., Bertini, E., Bak, P., Lalanne, D.: Flowstrates: An approach for visual exploration of temporal origin-destination data. In: Computer Graphics Forum, vol. 30, pp. 971–980. Wiley (2011)
4. Delbecq, A.L., van de Ven, A.H., Gustafson, D.H.: Group techniques for program planning: a guide to nominal group and Delphi processes. Scott, Foresman Glenview, IL (1975)
5. Farber, S., O'Kelly, M., Miller, H.J., Neutens, T.: Measuring segregation using patterns of daily travel behavior: a social interaction based model of exposure. J. Transp. Geogr. **49**, 26–38 (2015)
6. Geist, M.R.: Using the Delphi method to engage stakeholders: a comparison of two studies. Eval. Program Plann. **33**(2), 147–154 (2010)
7. Gordon, T., Pease, A.: Delphi RT: an efficient, round-less almost real time Delphi method. Technol. Forecast. Soc. Change **73**(4), 321–333 (2006)
8. Jin, J., Wang, Y.H., Li, M.: Prediction of the metro section passenger flow based on time-space characteristic. Appl. Mech. Mater. **397**, 1038–1044 (2013)
9. Loukaitou-Sideris, A., Taylor, B.D., Voulgaris, C.T.: Passenger flows in underground railway stations and platforms. MTI report, pp. 12–43 (2015)
10. Noble, I., Bestley, R.: Visual Research. AVA publishing (2005)
11. Okoli, C., Pawlowski, S.D.: The Delphi method as a research tool: an example, design considerations and applications. Inf. Manag. **42**(1), 15–29 (2004)
12. Scapolo, F., Miles, I.: Eliciting experts' knowledge: a comparison of two methods. Technol. Forecast. Soc. Change **73**(6), 679–704 (2006)
13. Scheuermann, A.: RailCity oder Hauptbahnhof? Eine designtheoretische Interpretation von Transportstroemen und Einkaufserlebnissen im Hauptbahnhof Bern. Archimaera **1**(1), 105–111 (2008)
14. Zeng, W., Fu, C.W., Arisona, S.M., Erath, A., Qu, H.: Visualizing mobility of public transportation system. IEEE Trans. Vis. Comput. Graph. **20**(12), 1833–1842 (2014)

Facing Needs and Requirements of Crowd Modelling: Towards a Dedicated Computer Vision Toolset

Sultan Daud Khan, Giuseppe Vizzari and Stefania Bandini

Abstract The modelling and simulation of pedestrians and crowd dynamics require empirical evidences and quantitative data describing the relevant phenomena that models must be able to reproduce. Computer vision can provide several tools both to semi-automatically acquire the demand of a given situation and actually configure a simulation model, as well as to gather information for the sake of model calibration and validation. This paper proposes methods supporting the segmentation and pedestrian counting of crowd flows, the identification and characterisation of main flows in an analysed scene and the detection of social groups in an observed population. The methods are briefly introduced and the achieved results are presented and discussed with reference to the current state of the art.

1   Introduction

Crowds of pedestrians are, at the same time, complex entities to study by means of observations, analyses and simulation and also extremely relevant to the activities of architects, designers, urban planners and organisers of events involving a large public participation in relatively constrained spaces. Pedestrians show a variety of individual and collective behaviours, such as competition for the space shared and collaboration due to generally shared (at least in a given scenario) social norms. Individual goal orientation, based on the least effort principle, is often in conflict with contextual conditions pushing pedestrians to adapt their behaviour to avoid congested areas or

S.D. Khan (✉) · G. Vizzari · S. Bandini
CSAI Research Center, University of Milano-Bicocca, Milan, Italy
e-mail: sultan.khan@disco.unimib.it

G. Vizzari
e-mail: giuseppe.vizzari@disco.unimib.it

S. Bandini
e-mail: stefania.bandini@disco.unimib.it

S. Bandini
RCAST, The University of Tokyo, 4-6-1 Komaba, Meguro-ku, Tokyo 153-8904, Japan

Fig. 1 Integration of analysis and synthesis
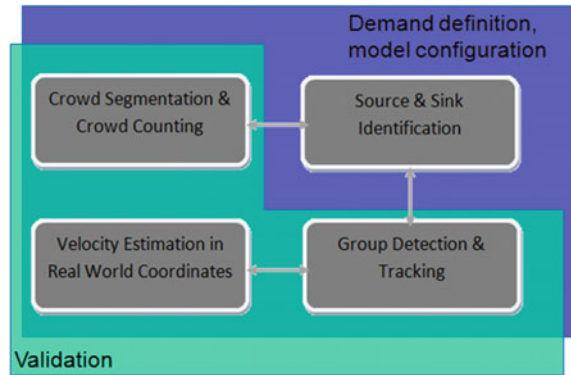
to negotiate their individual preferences with those of other members of a group they belong to.

Crowd studies represent successful applications of researches carried out both in the context of computer simulation and computer vision. Comprehensive simulation studies require the synthesis of pedestrians and crowd behaviour, but the developed models must be (i) calibrated and validated by means of data acquired in the field and (ii) informed by the specific contextual conditions of the simulated environment. Synthesis requires thus the results of analysis. In turn, the analysis of crowding phenomena can benefit from results on the side of synthesis: researches on the latter often produce formalisation of phenomena and lead to the definition of metrics and indicators to evaluate the generated dynamics. These concepts and mechanisms can represent a useful contribution towards the automation of the analysis techniques that, thanks to the development of computer vision techniques, can actually produce useful information even from cluttered scenes like those taken from security cameras in public spaces. In this paper, we discuss different specific contributions from the computer vision area that are also schematised in Fig. 1 and that provide different kinds of support to the definition of the demand or simulation model configuration on a specific situation, as well as useful elements for validation of achieved results, considering naturalistic videos as inputs.

2 Elements of the Toolset

2.1 *Crowd Flow Segmentation and Crowd Counting*

In this section we briefly describe a framework proposed in [3] that tackles the problems of crowd flow segmentation and, at the same time, people counted in the different flows. The segmentation of crowd flows provides a clutter free visualisation of the dynamics taking place in the scene, and it supplies a first characterisation of the overall dynamics in an environment. The fact that flows are immediately characterised
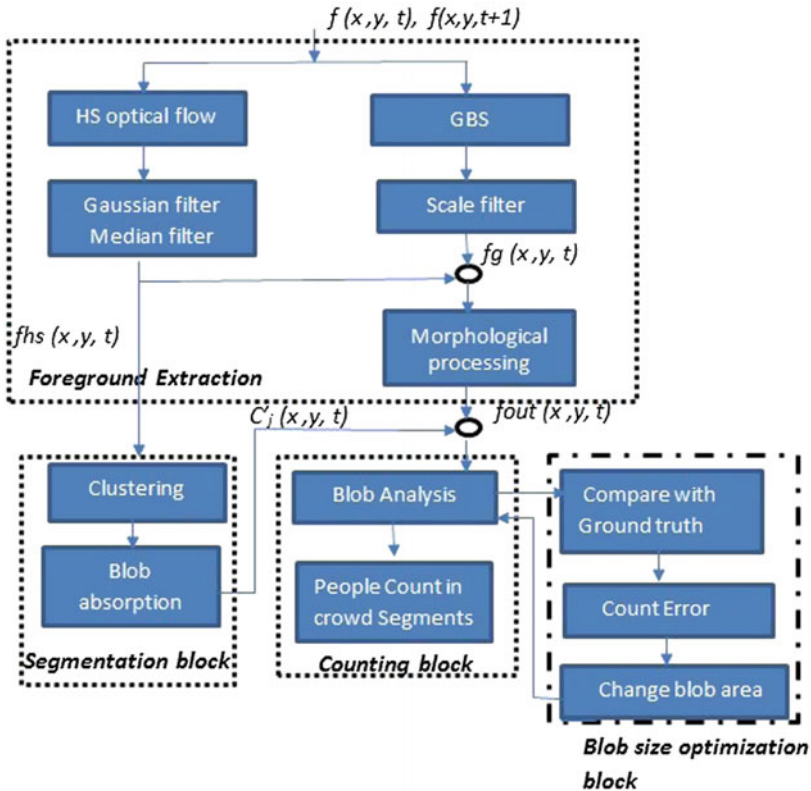
Fig. 2 Crowd flow segmentation and counting

in terms of an estimation of the number of pedestrians they are made up of makes it useful also for quantifying the demand.

The framework consists of three main parts: foreground extraction, crowd flow segmentation, and crowd counting as depicted in Fig. 2. The first component works according to two different ways, the first one aimed at capturing motion information describing the overall pedestrian flows, and the other focused on the identification of shapes that could represent pedestrians. The first sub-component is implemented by means of optical flow computation followed by Gaussian and Median filtering operations, extracting the foreground in terms of areas of the picture showing significant changes due to the movement of pedestrians. The results of this elaboration represents the input to the block performing the segmentation: the different portions of the picture are in fact clustered (using K-means algorithm) according to the direction of movement associated to the pixels into a configurable set of directions (e.g. four ones: up, down, left and right). Since small sets of pixels, associated (for instance) to parts of pedestrian bodies, can actually move in different directions from the body (e.g. an arm swinging backwards), we also employ the blob absorption method. Small blobs are either absorbed by a dominant cluster or by the background.

The second foreground segmentation block employs the Gaussian Background Subtraction (GBS) technique, which is quite effective in separating objects from the background. The result of this task undergoes a scale filtering and morphological analyses to support a subsequent analysis of the achieved blobs, to identify those associated to pedestrians. The size of a blob to be considered as a pedestrian can undergo an optimisation phase that could require a minimal human intervention.

Experiments revealed that crowd flow segmentation does not produce high quality results unstructured crowds, which involve complex and conflicting movement of people like in airports, stations, shopping malls, etc. For this purpose, in the next section, we propose another framework tackling this problem.

2.2 Characterisation of Main Flows

Pedestrians in videos from fixed cameras tend to appear and disappear at precise locations (e.g. doors, gateways, edges of the scene). We refer to locations where pedestrians appear as *sources* (potential origins) and the locations where they disappear as *sinks* (potential destinations). Intuitively, detecting sources and sinks implies detection and tracking of pedestrians, however, those operations generally fail in high density situations because of the severe clutter and occlusions. Therefore, we propose a different algorithm in [2] employing a more robust approach. A set of particles is overlaid to the scene, to initialise a dynamical system based on optical flow. Time integration of the dynamic system over a segment of the video provides particle trajectories (tracklets) that represent motion patterns in the scene for a certain time interval associated to the analysed segment. We detect sources, sinks and main flows in the segment by analysing motion patterns followed by clusters of tracklets, obtained using an unsupervised hierarchical clustering algorithm, where the similarity is measured by the Longest Common Sub-sequence (LCSS). The proposed framework is shown in Fig. 3.

As depicted in Fig. 3, the input video is divided into N number of segments s, each containing K frames. Next, we compute the optical flow field between two consecutive frames of every segment. We employ the method proposed by [1]. The next step is to advect grid of particles over the optical flow field, that corresponds to the
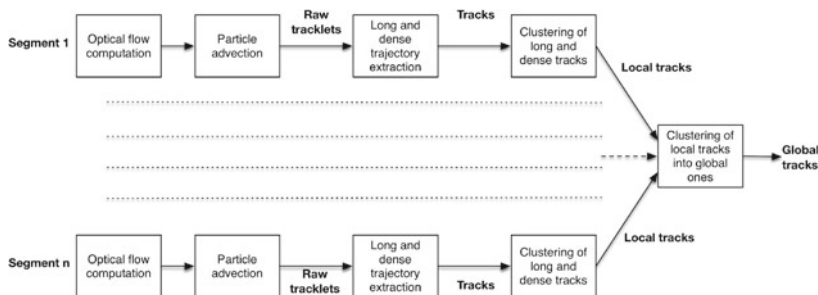
Fig. 3 Source and sink identification framework

time interval 1 to T for each segment. As a result of this evolution of particles, small tracklets are generated. These tracklets represent a relatively raw kind of information, plausibly about the movement of an individual, and they can be fruitfully grouped to provide a more concise description of overall flows in the scene. In the next step, therefore, we cluster those that are spatially close to each other and have similar direction of motion by employing Longest Common Sub-Sequence (LCSS).

The trajectories produced by this method represent dominant motion patterns in the scene. The source and sink points of the trajectories give us the precision starting and stopping locations of the group of people moving in different directions.

2.3 Social Group Detection

A crowd is generally composed of several small groups of people, for instance due to social relationships (families or friends) or a common goals, like reaching a certain point of the environment. Since group membership actually influences overall pedestrian dynamics, it is important to detect their presence in a given situation and, for this purpose, we propose a framework described more in detail in [4].

The overall approach is described in Fig. 4: the input is a video sequence in which individual pedestrians are detected, and tracked. We adopted a semi-automated detection techniques and the Generalised Minimum Clique Graphs (GMCP) [5] method for tracking. The next step is to construct an *Association Matrix*, that captures the joint distribution of source and sink locations of all pedestrians to all other pedestrians in the scene. A single pedestrian (not member of a group) tends to move or stop freely in the environment, changing his/her speed and keep a distance from other pedestrians or obstacles, pursuing his/her own goals. This behaviour uniquely identifies his/her source and sink locations. Members of a group generally move and stop together, preserving a certain distance between them despite the obstacles and counter flows.

To define groups based on the trajectories, we defined a bottom-up hierarchical clustering approach following three step process. We first assign distinct cluster identifiers by treating each pedestrian as a separate cluster. Then, we discover couples by measuring the difference between distribution of each pedestrian with the distribution of all other pedestrians in the scene employing *Kullback-Leibler (KL) divergence*, also known as relative entropy. This process always proposes for each pedestrian the best possible partner to form a couple, although this candidate partner might even be a bad partner, since the pedestrians do actually not follow similar paths. The next step
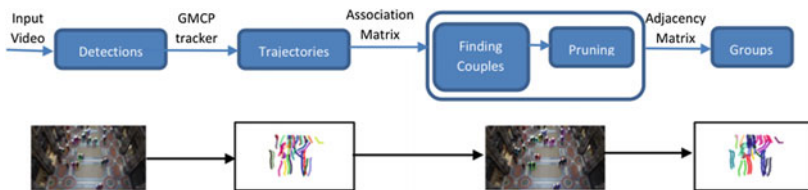
Fig. 4 Framework for group detection

is thus to prune these bad couples. After pruning, an adjacency matrix is generated which captures the connectivity information among all pedestrians. In the third step of the algorithm, groups of couples, those having strong intergroup closeness are merged into a larger group.

3 Experimental Results

3.1 Crowd Flow Segmentation and Crowd Counting

This framework consists of two major parts, respectively focuses on *segmentation* and *counting*, so experiments are carried out in two steps. In Fig. 5, we qualitatively compare segmentation results with state of the art methods: the proposed approach detects relatively small groups and highlights clear boundaries among different flows.

For the same video, we report the counting results in Table 1: since two dominant flows are detected, we estimate the number of people in these two segments. Table shows counting results of random frames taken from analysed video, where F.n. represents frame number of the analysed sequence. The rise and fall in people count in different frames represents the fact that people are entering or leaving the scene affecting people count at different time. To check the counting accuracy of the proposed framework, ground truth (G.T.) for each direction (East (E), West (W), North (N), South (S)) is found for the frames after random intervals and count error (Err) is computed by comparing results with the ground truth data.

3.2 Characterisation of Main Flows

The results of the source and sinks detection and characterising main flows are qualitatively depicted in Fig. 6. Different colour codes are used for representing different flows, while source and sink points are always marked with yellow and red circles respectively. Two extremes situations are depicted, since *Unimib* sequence is characterised by medium-low density and a structured crowd while *Gallery* covers high density and extremely complex and unstructured crowd. The framework correctly extracts semantic regions with the corresponding source and sink points in the *Unimib* video, while providing plausible results also for the *Gallery* video.

3.3 Social Group Detection

We used different videos that include both structure and unstructured crowds with different density condition. We evaluated the approach by using two coding schemes:
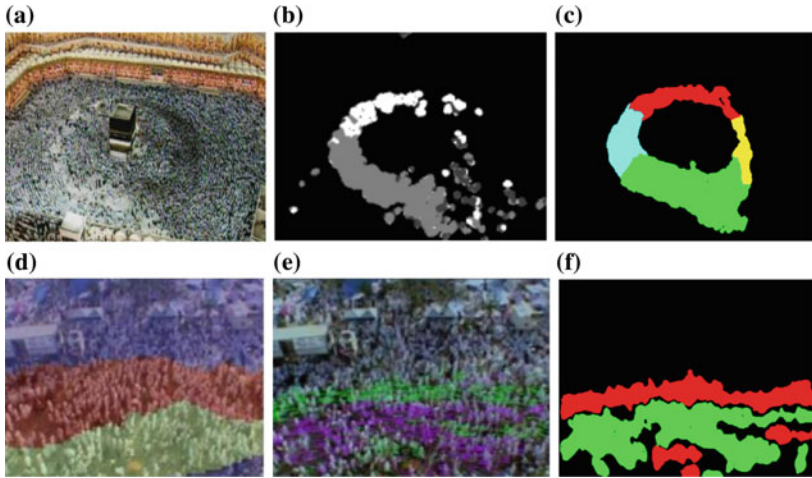
Fig. 5 Comparing results: sample frame (**a**); histogram curve (**b**); our approach (**c**); sample frame (**d**); histogram curve (**e**); our approach (**f**)

Table 1 Hajj video people counting in sequence of frames

F.n.	G.T.(E)	G.T.(W)	Cnt.(E)	Cnt.(W)	Err(E) (%)	Err(W) (%)
12	151	159	170	154	12.58	3.14
20	153	161	167	154	9.15	4.35
29	185	185	195	194	5.41	4.86
37	176	187	192	201	9.09	7.49
45	187	186	200	191	6.95	2.69
55	187	187	195	188	4.28	0.53
63	189	185	194	194	2.65	4.86
Average error					7.16	3.99
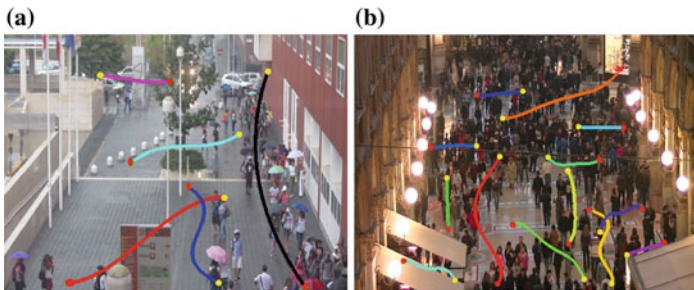
Fig. 6 Results of sources and sinks detection framework: unimib sequence (**a**); gallery sequence (**b**)
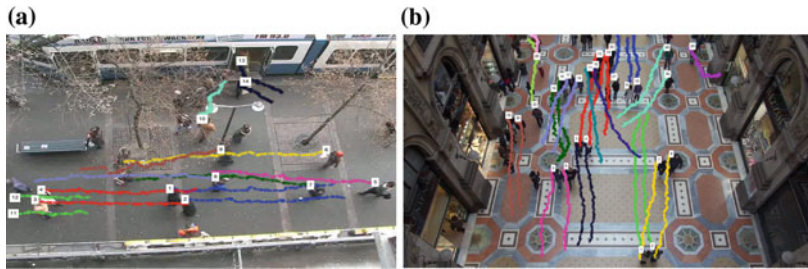
Fig. 7 Qualitative results of different video sequences: hotel sequence (**a**); gallery sequence (**b**)

Table 2 Dichotomy and Trichotomy on different video sequences

Videos	τ_s	Dichotomoy (%)	Trichotomy (%)
ETH	10^{-10}	100.0	95.0
HOTEL	10^{-15}	100.0	92.0
GALLERY	10^{-19}	96.3	89.9
SU2-L	10^{-12}	90.70	86.7
SU2-H	10^{-12}	81.06	77.2

Dichotomous and *Trichotomous*. In the former, we checked whether a pedestrian is alone or in group while in the trichotomous scheme we also determine the size of the group. The accuracy of our results using different videos is reported in Table 2. Figure 7 shows qualitative results of the proposed framework.

References

1. Brox, T., Bruhn, A., Papenberg, N., Weickert, J.: High accuracy optical flow estimation based on a theory for warping. In: Computer Vision-ECCV 2004, pp. 25–36. Springer (2004)
2. Khan, S.D., Bandini, S., Basalamah, S., Vizzari, G.: Analyzing crowd behavior in naturalistic conditions: Identifying sources and sinks and characterizing main flows. Neurocomputing **177**, 543–563 (2016)
3. Khan, S.D., Vizzari, G., Bandini, S., Basalamah, S.: Detecting dominant motion flows and people counting in high density crowds (2014)
4. Khan, S.D., Vizzari, G., Bandini, S., Basalamah, S.: Detection of social groups in pedestrian crowds using computer vision. In: Advanced Concepts for Intelligent Vision Systems, pp. 249–260. Springer (2015)
5. Zamir, A.R., Dehghan, A., Shah, M.: Gmcp-tracker: Global multi-object tracking using generalized minimum clique graphs. In: Computer Vision–ECCV 2012, pp. 343–356. Springer (2012)

Part II
Vehicular Traffic

Computer-Aided Bifurcation Analysis for a Novel Car-Following Model with Relative Velocity Effect

Akiyasu Tomoeda, Tomoyuki Miyaji and Kota Ikeda

Abstract The global behaviour of mathematical models for traffic flow is important in order to understand their characteristics because of the bistable property observed in real traffic. This bi-stability can be discussed in a bifurcation analysis. In fact, bifurcation analysis of optimal velocity models in several studies has revealed the global bifurcation structure of the model, which shows a loss of stability due to the Hopf bifurcation and bistable property. Shamoto et al. proposed a novel car-following model with relative velocity effect (STNN model), which was not introduced into the optimal velocity model, but is important in real traffic scenarios. They discussed the linear stability of homogeneous traffic flow; however, they did not reveal the global bifurcation structure of the STNN model. In this paper, we numerically investigated the global bifurcation structure of the STNN model and observed that the strength of the relative velocity effect drastically changes the bifurcation structure. This result provides a possibility of implementing (semi-)automatic driving systems to alleviate traffic jams.

1 Introduction

Various types of self-driven particle systems, such as vehicular traffic and pedestrian dynamics, have attracted a great deal of attention during the last few decades in a wide range of fields, such as natural sciences, applied sciences, and engineering, for the potential practical use of investigation results [2, 5, 9]. Especially, a better understanding of traffic flow has been achieved by developing sophisticated mathematical models. One of the common goals among these modelling approaches is

A. Tomoeda (✉)
Musashino University, Ariake 3-3-3, Koto-ku, Tokyo, Japan
e-mail: a_tomo@musashino-u.ac.jp

T. Miyaji · K. Ikeda
Meiji University, Nakano 4-21-1, Nakano-ku, Tokyo, Japan
e-mail: tmiyaji@meiji.ac.jp

K. Ikeda
e-mail: ikeda@meiji.ac.jp

to understand the spontaneous occurrence of traffic jams when the average density of vehicles exceeds a certain critical value. This transition in flow behaviour is considered as a dynamical phase transition and can be discussed in terms of instability of homogeneous flow. That is, jamming flow occurs as a result of the instability of homogeneous traffic flow due to fluctuations of the driving behaviour over the critical density; the instability leads to the transition of the homogeneous traffic flow to a jamming flow due to enhancement of fluctuations.

Linear stability analysis is very useful for detecting critical density. As the loss of stability is often accompanied by a bifurcation, one may expect a jamming flow to exist. The linear stability analysis, however, does not provide any information regarding a bifurcating solution. It is important to understand the global bifurcation structure of periodic solutions bifurcating from the critical density because bi-stability, which is regarded as one of the characteristics of transition to a jamming flow, is not a local property. Moreover, the features of a global bifurcation structure provide us with hints for controlling traffic flow by changing the parameters of a model. Thus, global bifurcation analysis is important from both theoretical and practical viewpoints. Several researchers have investigated the global bifurcation structure of a car-following type model by describing the dynamics of N vehicles on a circular road via special continuation codes [4, 6–8].

Gasser et al. [4] focused on an optimal velocity (OV) model, which is described as

$$\frac{d^2}{dt^2}x_j(t) = a\left\{V(h_j(t)) - \frac{d}{dt}x_j(t)\right\}, \tag{1}$$

where x_j ($j \in N$) and $h_j = x_{j+1} - x_j$ are the position of the jth vehicle, and the headway distance between the jth vehicle and the vehicle in front, respectively. The function $V(h_j)$ is called the OV function, which provides an ideal velocity decided by the headway. This model (Eq. 1) was originally proposed by Bando et al. [1], and they considered the OV function as $V(h) = \tanh(h - 2) + \tanh(2)$. In [4], they proved that the loss of stability is generally due to a Hopf bifurcation, and they analytically showed a quantity related to the first Lyapunov coefficient of the bifurcation, which determine if Hopf bifurcation is supercritical or subcritical for general OV function satisfying a few basic properties. This result mentioned that the type of Hopf bifurcation depends on the OV function, length of the circuit, and the number of vehicles. Moreover, they numerically investigated the global bifurcation structure for periodic solutions and revealed a complete picture of OV model dynamics. From these numerical results, the behaviour of a Hopf bifurcation is locally supercritical, but macroscopically subcritical under some situations, i.e., the OV model shows bi-stability. One of their conclusions was that the Hopf bifurcation is not necessarily subcritical, which depends on the optimal velocity function. Moreover, they concluded that a stable periodic solution may (co-)exist even in the stable region; in particular, this coexistence does not depend on the type of Hopf bifurcation, but on the global bifurcation structure.

Orosz et al. [6–8] proposed a novel OV model with driver reaction time delay, which is described as

$$\frac{d^2}{dt^2}x_j(t) = a\left\{V(h_j(t-\tau)) - \frac{d}{dt}x_j(t)\right\}, \tag{2}$$

where τ is the reaction time of the drivers in perception, which is different from the relaxation time $T = \frac{1}{\alpha}$ in action to adjust the vehicle's velocity. They also showed the loss of stability due to Hopf bifurcation and the global behaviour of the system (Eq. 2) numerically, although their computational technique was different from the one in [4] because of the delay effect. As a result, they also observed branches of oscillating solutions connecting Hopf bifurcation points, where the OV function determines whether the Hopf bifurcation is supercritical or subcritical, and then they revealed the existence of the regions of bi-stability.

These investigations are very significant in order to understand the complete picture of each traffic model in detail; however, these models did not consider the relative velocity effect, and the parameters in these models were difficult to be estimated by real experiments, i.e., difficult to be controlled in practical use. Thus, in this paper, we investigate the global bifurcation structure of a model proposed by Shamoto et al. (STNN model) [10], in which the relative velocity effect is introduced, and the parameters are estimated by real experiments. Moreover, we show the changing the global bifurcation structure based on variation in the relative velocity effect as a possibility of the strategy to alleviate traffic jams, as the strength of relative velocity effect is varied.

This paper is organised as follows. In Sect. 2, we briefly review the STNN model proposed by Shamoto et al. [10] and modify the model to a suitable form for use with numerical bifurcation algorithm in AUTO [3]. The computational results are shown in Sect. 3. Finally, Sect. 4 is devoted to the concluding discussions.

2 STNN Model and Its Rewritten Form

Recently, Shamoto et al. proposed a novel car-following model (STNN model) in [10], which takes into account the relative velocity effect. Their model is described in the following form :

$$\frac{d}{dt}v_j = a - b\frac{v_j}{(h_j - d)^2}\exp\left(-c\Delta v_j\right) - \gamma v_j, \tag{3}$$

where a, b, c, d and γ are positive parameters. The parameter a represents the maximum acceleration. The initial acceleration of the vehicles, when they start to move forward, is determined by a. The parameter d indicates the headway when vehicles stop completely. The other parameters $b, c,$ and γ denote the strength of interaction with the vehicle in front, the weight of the relative velocity effect, and the strength

Fig. 1 The definition of the variables y_j to suppress translation symmetry in the periodic condition
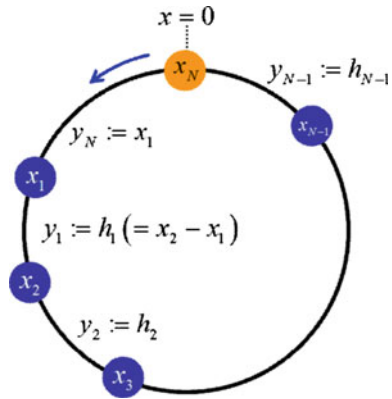
of friction, respectively. The advantages of the STNN model are that it is experimentally accessible, and it is easy to understand the physical meaning, although the model has only five parameters. Actually, the parameter values were estimated by circuit experiments in [10]. They mentioned that their model showed a metastable homogeneous flow around the critical density from the linear stability analysis. That is, if the traffic density exceeded the critical density, the homogeneous flow became unstable because of a small perturbation that changes into another branch (a jamming flow). However, their results are local and do not give us any insight into the stability of the other branch and the changes in the global bifurcation structure, as a parameter is varied. We thus use the software AUTO [3] to numerically obtain and investigate the global behaviour of their model (Eq. 3).

The STNN model in the periodic system has a continuous family of solutions corresponding to the homogeneous traffic flow due to the translation symmetry. This feature is unsuitable for analysis by using AUTO, as AUTO can follow only a one-parameter family of solutions.

Let $N \in \mathbb{N}$ and $L > 0$. N is the number of vehicles, and L is the length of the circuit. We regard $x_{N+1} = x_1 + L$. Obviously, we have

$$\sum_{j=1}^{N} h_j = L. \tag{4}$$

That is, the sum of headways is equal to the length of the entire circuit.

We suppress the translation symmetry by introducing variables $y = (y_1, \cdots, y_N)$ (see Fig. 1), which satisfy

$$y = (y_1, \ldots, y_N) = (h_1, \ldots, h_{N-1}, x_1). \tag{5}$$

Note that this transformation of variables is regular. Indeed, the inverse is given by

$$x_j = y_N + \sum_{k=1}^{j-1} y_k, \quad j = 1, 2, \ldots, N, \tag{6}$$

where the sum is taken only when $j - 1 > 1$.

The STNN model can be written in the following form:

$$\ddot{x}_j = a - \dot{x}_j W(h_j, \dot{h}_j), \quad j = 1, 2, \ldots, N, \tag{7}$$

where a is a positive parameter, which is the same as the original model. W is, for example,

$$W(h_j, \dot{h}_j) = \frac{b}{(h_j - d)^2} e^{-c\dot{h}_j} + \gamma. \tag{8}$$

Here, we consider the case of N vehicles. In general, y is governed by

$$\ddot{y}_j = -(\dot{y}_N + \sum_{k=1}^{j} \dot{y}_k) W(y_{j+1}, \dot{y}_{j+1}) + (\dot{y}_N + \sum_{k=1}^{j-1} \dot{y}_k) W(y_j, \dot{y}_j), \tag{9}$$

$$\ddot{y}_{N-1} = -\left(\sum_{k=1}^{N} \dot{y}_k\right) W(L - \sum_{k=1}^{N-1} y_k, -\sum_{k=1}^{N-1} \dot{y}_k) + (\dot{y}_N + \sum_{k=1}^{N-2} \dot{y}_k) W(y_{N-1}, \dot{y}_{N-1}), \tag{10}$$

and

$$\ddot{y}_N = a - \dot{y}_N W(y_1, \dot{y}_1), \tag{11}$$

where $j = 1, 2, \ldots, N - 2$. y_N is just an integral of $\dot{y}_N$. Note that the problem is reduced to a system on $\mathbb{R}^{2N-1}$.

3 Numerical Bifurcation Analysis

In this section, we show bifurcation diagrams of Eq. 3. In particular, we focus on the effect of relative velocity. First, we consider the case when $c = 0$. Next, we consider the case when $c \neq 0$ by computing a two-parameter bifurcation diagram. We regard L and c as the primary and the secondary parameters, respectively. The remaining parameters are assigned the same values estimated in [10], that is, $a = 0.73$, $b = 3.25$, $d = 5.25$, and $\gamma = 0.0517$. Moreover, now we assign the number of vehicles $N = 30$.

(a)

(b)
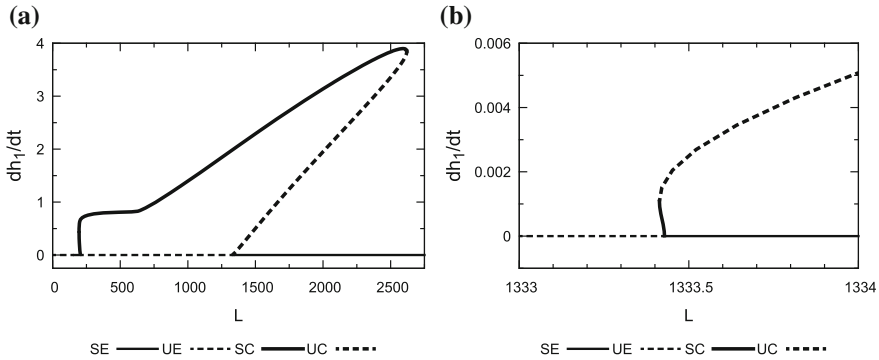
Fig. 2 Bifurcation diagram. Abbreviations: Stable Equilibrium (SE), Unstable Equilibrium (UE), Stable Cycle (SC), and Unstable Cycle (UC). Global bifurcation diagram of STNN model for the parameters $a = 0.73, b = 3.25, c = 0, d = 5.25$, and $\gamma = 0.0517$ (**a**); close-up picture of the right Hopf bifurcation point (**b**)

3.1 Without Relative Velocity Effect ($c = 0$)

First, we investigate a global bifurcation structure in the case of $c = 0$, where the model has no relative velocity effect. Under this condition, the model should reflect the characteristics that are in common with the OV model.

Figure 2 illustrates a bifurcation diagram, which has L on the horizontal axis and the relative velocity of the first vehicle on the vertical axis. The left image shows the entirety of the bifurcation diagram and the right image is the close-up picture at $L = 1333.43$. The solid line (curve) and the dashed line (curve) indicate a stable solution and an unstable solution, respectively. From these figures, we reveal the birth of a supercritical Hopf bifurcation as the parameter L becomes small (density becomes large). That is, if one moves along the horizontal line ($\frac{dh_1}{dt} = 0$) from right to left, one can find at first a stable equilibrium point ($L = 1333.43$) that eventually loses its stability in favour of a periodic solution branch. Subsequent to that, two saddle-node bifurcations ($L = 1333.41$ and $L = 2619.25$) take place on this periodic solution branch. In the region $1333.43 < L < 2619.25$, both the homogeneous solution and the periodic solution are stable, that is the traffic flow shows bi-stability. This global bifurcation structure is qualitatively similar to the structure of the OV model shown in [4], that is, the behaviour of a Hopf bifurcation is locally supercritical, but macroscopically subcritical.

3.2 With Relative Velocity Effect ($c \neq 0$)

Next, we consider the case when $c \neq 0$. A Hopf bifurcation point and a saddle-node bifurcation point draw a curve in two-parameter plane when an additional parameter
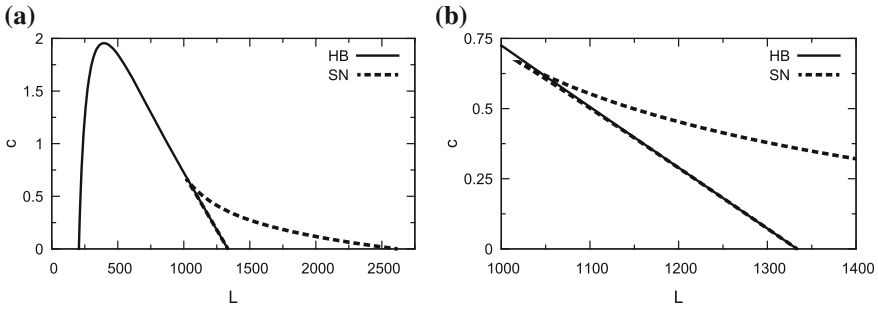
Fig. 3 Two-parameter bifurcation diagram: behaviours of Hopf Bifurcation points (HB) and Saddle-Node points (SN) on (L, c)-plane for the parameters $a = 0.73$, $b = 3.25$, $c = 5.25$, $\gamma = 0.0517$ (**a**); close-up picture at the cusp point (**b**)

is varied. We vary c as well as L to numerically compute the curves starting at two Hopf bifurcation points $((L, c) = (205.612, 0), (1333.41, 0))$ and two saddle-node bifurcation for Eq. 3 with $c = 0$.

Figure 3 shows the two-parameter bifurcation diagram and its close-up view. The curve of Hopf bifurcation points turns down at $(L, c) = (395.55, 1.955)$, and no Hopf bifurcation is found for $c > 1.995$. From phenomenological point of view, this implies that the enhancement of relative velocity effect leads drivers to a good response and eventually makes the homogeneous flow stable for a fluctuation. Thus, we have found that homogeneous flow becomes stable in all densities in a parameter region $c > 1.955$. On the other hand, the curve of saddle-node bifurcation points meets at a cusp point $(L, c) = (1019.23, 0.6664)$. This implies that the bi-stability as shown in Fig. 2 does not appear when $c > 0.6664$. Thus, we have three intervals $0 < c < 0.6664$, $0.6664 < c < 1.955$, and $1.955 < c$ in which bifurcation diagrams are qualitatively different. It should be noted that here we discuss only two Hopf bifurcation points. Other Hopf bifurcation points exist at the region $205.612 < L < 1333.41$ and may show another stable periodic solution branch, which implies multi-stability. These features will be also investigated in the near future.

4 Conclusion and Discussion

In this paper, we investigated the global bifurcation structure of the periodic solutions bifurcating from the critical density for STNN model, wherein the relative velocity effect is introduced. In the case when $c = 0$, which corresponds to the model without the relative velocity effect, the global bifurcation structure shows features that are similar to the OV model; the model shows that the loss of stability in homogeneous flow is due to a Hopf bifurcation, and the behaviour of a Hopf bifurcation is locally supercritical, but macroscopically subcritical. Moreover, we have found that two Hopf bifurcation points turn down at a point on (L, c)-plane, and two

saddle-node points merge and make a cusp point in the case of $c \neq 0$, where the model takes into account the relative velocity effect. In particular, this result shows that the instability of the homogeneous flow disappears, and the homogeneous flow becomes stable in a parameter region $c > 1.955$. This situation might not be realistic in non-automatic driving, but could provide a solution in the near future for implementing (semi-)autonomous driving systems, such as the adaptive cruise control system, to alleviate traffic jams.

References

1. Bando, M., Hasebe, K., Nakayama, A., Shibata, A., Sugiyama, Y.: Dynamical model of traffic congestion and numerical simulation. Phys. Rev. E **51**(2), 1035 (1995)
2. Chowdhury, D., Santen, L., Schadschneider, A.: Statistical physics of vehicular traffic and some related systems. Phys. R. **329**(4), 199–329 (2000)
3. Doedel, E., Oldeman, B.: Auto-07p: Continuation and bifurcation software for ordinary differential equations. Technical report, Concordia University; Montreal, Canada (2012)
4. Gasser, I., Sirito, G., Werner, B.: Bifurcation analysis of a class of car following traffic models. Phys. D: Nonlinear Phenom. **197**(3), 222–241 (2004)
5. Helbing, D.: Traffic and related self-driven many-particle systems. Rev. Mod. Phys. **73**(4), 1067 (2001)
6. Orosz, G., Krauskopf, B., Wilson, R.E.: Bifurcations and multiple traffic jams in a car-following model with reaction-time delay. Phys. D: Nonlinear Phenom. **211**(3), 277–293 (2005)
7. Orosz, G., Stépán, G.: Subcritical Hopf bifurcations in a car-following model with reaction-time delay. Proc. R. Soc. London A: Math. Phys. Eng. Sci. **462**(2073), 2643–2670 (2006)
8. Orosz, G., Wilson, R.E., Krauskopf, B.: Global bifurcation investigation of an optimal velocity traffic model with driver reaction time. Phys. Rev. E **70**(2), 026207 (2004)
9. Schadschneider, A., Chowdhury, D., Nishinari, K.: Stochastic transport in complex systems: from molecules to vehicles. Elsevier (2010)
10. Shamoto, D., Tomoeda, A., Nishi, R., Nishinari, K.: Car-following model with relative-velocity effect and its experimental verification. Phys. Rev. E **83**(4), 046105 (2011)

Lane Change Strategies on Freeways: A Microscopic Simulation Study

Mehdi Keyvan-Ekbatani, Victor L. Knoop, Vincent Grébert and Winnie Daamen

Abstract Understanding the influence of lane changing manoeuvres on the capacity, stability, and breakdown of traffic flows is a crucial issue. In a recent study, four distinct lane change strategies on freeways have been found: (1) Speed Leading; (2) Speed Leading with Overtaking; (3) Lane Leading; (4) Traffic Leading. To the best of our knowledge, combining speed choice and lane preference is not currently considered in most driving behaviour models. The principal aim of this paper is to investigate the impact of the forenamed lane change strategies on freeway traffic operations. The developed strategy-based lane change model has been implemented in a microscopic simulation environment. The study revealed that different lane change strategies may have various impact on the lane flow distribution and consequently on the freeway capacity. It has been seen that an unbalanced distribution of flow on a multi-lane freeway may lead to reduction of capacity. In addition, it has been found that the lane change rate variates under different lane change strategies. The highest traffic stability has been observed under speed leading and speed leading with overtaking strategies.

M. Keyvan-Ekbatani (✉) · V.L. Knoop · V. Grébert · W. Daamen
Delft University of Technology, Stevinweg 1, 2628 CN Delft, The Netherlands
e-mail: m.ekbatani@tudelft.nl

V.L. Knoop
e-mail: v.l.knoop@tudelft.nl

V. Grébert
e-mail: vincent.grebert@entpe.fr

W. Daamen
e-mail: w.daamen@tudelft.nl

V. Grébert
École Nationale des Travaux Publics de l'État (ENTPE),
University of Lyon, Lyon, France

395

1 Introduction

Microscopic simulation tools might be applied in various traffic and transportation studies. They can be utilised for analysing traffic incidents or providing a virtual environment to evaluate new traffic management policies and evaluating their impacts. Modelling of the movement of vehicles on freeways is mimicked by a combination of a longitudinal (car-following) and a lateral (lane change (LC)) model. The validity of the aforementioned microscopic sub-models is currently a challenging issue. Comprehending the influential factors of the driver's lane change behaviour and the corresponding decisions seems to be an essential issue for developing realistic and accurate models.

Knoop et al. [1] addressed that there are large discrepancies between the principles modelled and the observations for discretionary lane changes (DLC). Empirical studies have revealed that drivers show different driving behaviour in practice (see [2] for lane changing and [3] for car-following behaviour).

Without asking people, the motive and stimulus behind the lane change decision process cannot be known. Thus, Kondyli and Elefteriadou [4] applied interview techniques for a study on driving behaviour in merging areas. Later, the same authors conducted a test-drive with an instrumented vehicle [5]. Keyvan-Ekbatani et al. [2] combined an interview-based study with a test-drive (using an instrumented car). The test-persons were requested to drive on a freeway sketch in a camera-equipped vehicle. Immediately after the drive, the participants were interviewed and questioned regarding their decisions (i.e. for changing lane or not) during the test. The study led to a categorisation of lane change decision process (i.e. strategies). Four distinct lane change strategies for DLC behaviour were unveiled based on the aforementioned study: (1) *Speed Leading*; (2) *Speed Leading with Overtaking*; (3) *Lane Leading*; (4) *Traffic Leading*.

The research objective is to study the impact of the forenamed strategies on the traffic flow characteristics. The four lane change strategies have been implemented in the microscopic simulation tool MOTUS [6]. A three-lane freeway stretch without considering any on- and off-ramps has been applied as a test-bed. It should be noted that this paper only focuses on the simulation part of the strategy-based lane change model and does not discuss the modelling and implementation details.

The remainder of the paper is organised as follows. The methodological details (i.e. brief introduction of the four lane change strategies and simulation set-up) are addressed in Sect. 2. The simulation results are presented in Sect. 3. Finally, a brief summary and conclusion are included in the last section.

2 Methodology

In this section, the four lane change strategies found in [2] are introduced briefly. Then, the defined simulation scenarios along with some technical details of the simulation set-up are discussed.

2.1 Lane Change Strategies

The four lane change strategies found in [2] (i.e. *Speed Leading*, *Speed Leading with Overtaking*, *Lane Leading* and *Traffic Leading*) are defined as follows:

Speed Leading: The drivers who follow this strategy choose a desired speed and try to keep it. They change lanes such that they can drive with their desired speed. Drivers choose their speed based on their driving style and preference. Drivers using cruise control are usually speed leading.

Speed Leading with Overtaking: Drivers driving with this strategy choose a speed and stay at the rightmost lane possible with that speed. In case the speed on that lane decreases (i.e. presence of a vehicle with a lower speed), the driver will change lanes. In other words, the drivers applying this strategy consider this action as an overtaking and increase their speed while being in the more left lane. The motivation for increasing the speed is that 'an overtaking manoeuvre takes less time'.

Lane Leading: In this strategy drivers choose a lane based on their perceived relative driving speed. In other words, drivers settle for a lane and adapt their speed to that of vehicles in that lane. The combination of speed and lane choice is the incentive in this strategy.

Traffic Leading: Drivers follow the speed of the other drivers in a stream. There is no desired speed or lane in this strategy. Drivers may join faster vehicles or slower ones. Faster drivers might drive faster in busier conditions, since there is a higher probability of existence of a driver with higher desired speed.

2.2 Simulation Set-Up

The main goal of this paper is to investigate the impact of the different lane change strategies on the traffic flow characteristics. To this end, the strategy-based lane change model has been implemented in a microscopic simulator. More specifically, lane flow distribution, lane change rate, creation of stop-and-go wave and the road capacity under each lane change strategy have been investigated. Four different simulation scenarios have been defined. In scenarios (1)–(3), 100 % of drivers drive with the strategies *Speed Leading*, *Speed Leading with Overtaking* and *Lane Leading*, respectively. Scenario (4) includes 50 % of the drivers driving with *Traffic Leading* and 50 % with *Speed Leading* strategy. Drivers with *traffic leading* adapt their speed to other drivers. However, if all drivers are traffic leading, no reference speed is available. This implies that a flow composition cannot only consist of *traffic leading* vehicles. We therefore choose a traffic composition of 50–50. A longitudinal neighbourhood of 100 m from the front and 50 m from the back of the vehicle linearly distance-weighted (highest weight for the closest vehicle) has been considered. For the lateral neighbourhood, the vehicles on the same lane, adjacent lane and next to the adjacent lane have the weights 1, 0.8 and 0.6. If the vehicle drives on the middle lane, the left and the right lanes are equally weighted (i.e. 0.8). Trucks are not considered in these scenarios.

(a)

(b)
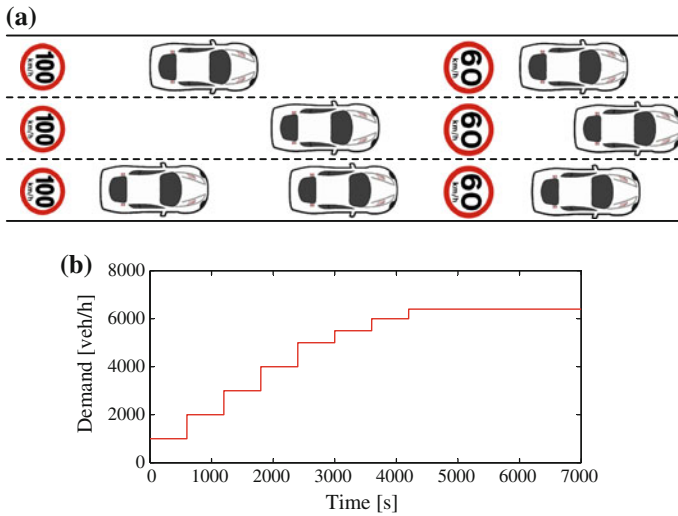
Fig. 1 Simulation set-up: three-lane freeway stretch applied as test-bed (**a**); two-hour demand profile (**b**)

MOTUS is an open-source microscopic traffic simulation package which is developed in java. MOTUS is stochastic, thus different simulation runs (replications) with different random seeds may lead to different results. For this reason, 10 different replications have been utilised for each investigated scenario and then the average value of the 10 runs for each simulation result has been calculated. As shown in Fig. 1a, a three-lane freeway stretch (7 km) without any off- and on-ramp has been modelled in the microscopic simulation MOTUS. To create a bottleneck (for reproducing a part of the congested branch of the fundamental diagram), a speed limit has been imposed on the last 2 km of the modelled road layout. A step-wise demand increase has been implemented for the two-hour simulation (see Fig. 1b). The car-following model utilised for this simulation is IDM+ [7]. In scenarios (1), (2) and (4) a speed limit of 100 km/h for the first 5 km and for scenario (3) different speed limits (i.e. 100, 85 and 70 km/h for the left, middle and right lanes, respectively) have been set. The speed limit in the last 2 km of the freeway is 60 km/h in all scenarios. The desired speed of the drivers are produced based on a Gaussian distribution function with an average value of 100 km/h and a standard deviation of 10 % (or 10 km/h).

3 Simulation Results

In this section, we describe the simulation results for the previously introduced scenarios. First, we discuss the speed contour plots (for one replication), followed by the fundamental diagram, the lane flow distribution and the lane change rates. The
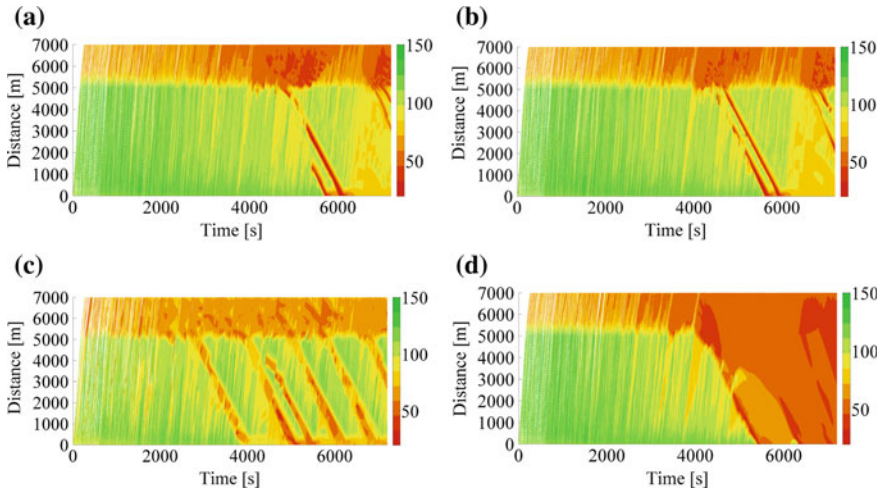
Fig. 2 Speed contour plots for the four simulation scenarios: speed leading (**a**); speed leading with overtaking (**b**); lane leading (**c**); speed leading + traffic leading (**d**)

trajectory data of a section of 1000–5000 m has been considered for derivation of the last three plots.

Figure 2a–d display the speed contour plots for scenarios (1) to (4), respectively. In all scenarios, congestion starts at the bottleneck (after 5 km) and propagates upstream. As it is realised from Fig. 2a, b, the instabilities (stop-and-go waves) are similar for the first two scenarios. For scenario (3), a different pattern of stop-and-go waves can be seen. The traffic conditions showed more unstable under this lane change strategy (more waves are visible) compared to two previous scenarios. The most congested traffic condition can be seen in scenario (4). After 4000 s the entire freeway stretch is affected by the congestion created upstream of the bottleneck. This might be due to the speed adaptation concept of this scenario. The drivers adapt their speed to the speed of the vehicles in their neighbourhood, thus reduction of speeds at the bottleneck might affect the drivers upstream more and faster.

The fundamental diagrams for the different simulation scenarios are found in Fig. 3a, b, c, d, (10 different replications shown by different colours). A rough estimation of the capacity might be determined by taking the maximum value in the fundamental diagrams. The highest observed flows of the *speed leading*, *speed leading with overtaking* and *traffic leading* strategies appear to be larger than the *lane leading* strategy. All scenarios except scenario (3) reach a flow value of around 2500 veh/h/lane. The flow in scenario (3) does not exceed 2000 veh/h/lane (see Fig. 3c). This might be due to the suboptimal distribution of flow over lanes and consequently congestion occurrence on specific lanes. In the cases of *speed leading* strategies, drivers will merge into the faster lane if needed and also merge back to the right, and high flows will be obtained in all lanes.

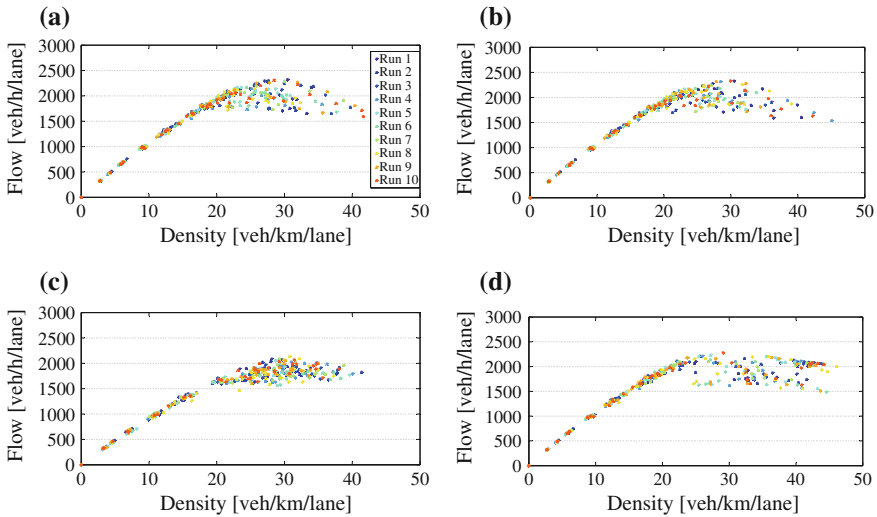**Fig. 3** Fundamental diagrams for the four simulation scenarios: speed leading (**a**); speed leading with overtaking (**b**); lane leading (**c**); speed leading + traffic leading (**d**)

For the *traffic leading* strategy, much more noise and scatter have been found in the fundamental diagram after the onset of congestion (around the density of 30–40 veh/km/lane) compared to the other three strategies. Apparently, drivers accept different speeds at the same densities. This is in line with the fact that drivers adapt the speed in this strategy.

Figure 4 displays the lane flow distribution on different lanes versus density in the four introduced simulation scenarios, averaged over 10 different runs. As it can be realised from Fig. 4a and b, under *speed leading* and *speed leading with overtaking* strategies, most of the traffic is on the right and the middle lane in the low-flow conditions. In higher densities, gradually, traffic utilises the middle lane and the median lane more. A similar pattern has been found in empirical data for Dutch freeways [8]. In the study with real data [8], it was found that near capacity, the left lane has an excess load, because drivers do want the 'spots in the overtaking lane'. This is partially found in the simulation data: indeed, there is the high flow in the left lane, but this at densities which are slightly lower than capacity. In *speed leading with overtaking*, the reduction of right lane usage is less sharp than in speed leading. In the *lane leading* strategy, the flow distribution is not as balanced as in the other scenarios. This might be one of the reasons of the lower capacity compared to the other scenarios (see Fig. 3). In *traffic leading* strategy, drivers distribute quite well over the lanes. This could be a reason of the high capacity despite of the more congested traffic state.

Figure 5 shows the lane change rate vs. density for each of the scenarios. For the *speed leading* strategy, the number of lane changes depends strongly on the density. For lower densities, drivers change lanes often (approximately 0.5 lane change per km). As the densities increase, drivers keep their lane for a longer time.
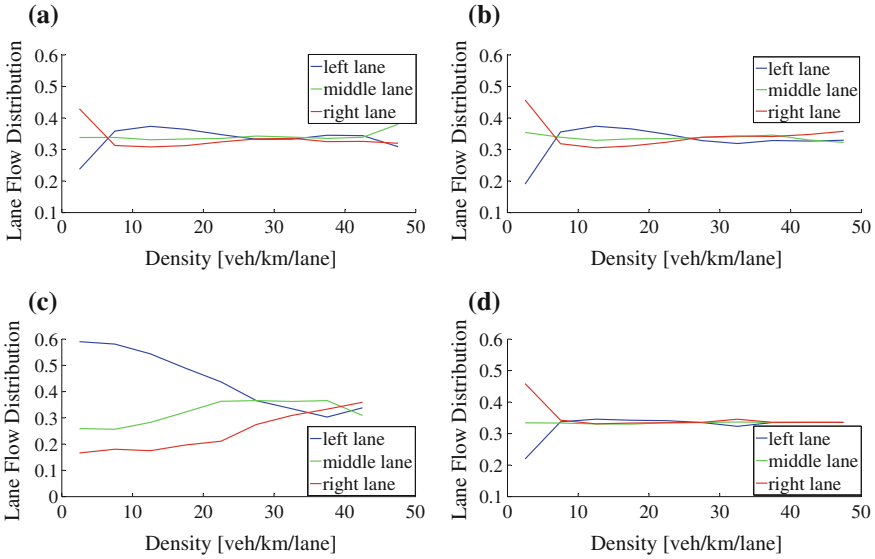
Fig. 4 Lane flow distribution for the four simulation scenarios (averaged over 10 runs): speed leading (**a**); speed leading with overtaking (**b**); lane leading (**c**); speed leading + traffic leading (**d**)

Fig. 5 Lane change rate for the four simulation scenarios (averaged over 10 runs)
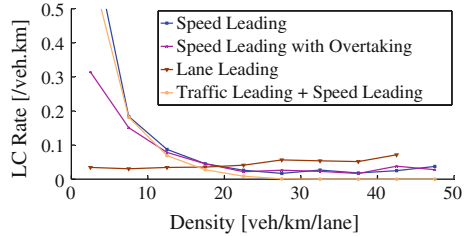
This can be explained by the fact that the speeds in all lanes become similar, taking away the necessity of a lane change. A similar pattern is visible for the *speed leading with overtaking strategy*. As anticipated, the number of lane changes for the *lane leading* strategy is very low. Note that the number of lane changes increases with an increasing density. This can be explained by the fact that if there are no other vehicles, the *lane leading* drivers will follow the lane. The most remarkable pattern is found for the *traffic leading* strategy. In cases of low density, drivers tend to follow other drivers, which might have a different speed. Hence, the lane changes are relatively high. For higher densities, the number of lane changes decreases to the lowest values found for all strategies (they even stop changing lane). *Traffic leading* drivers will simply follow the traffic, and if there are drivers in front, driving at a reasonable speed, they have no incentive to leave the lane and change lane, since there is neither a desired lane where they should head to, nor a desired speed.

4   Conclusions

In this paper, the recently found lane change strategies are implemented in a microscopic simulation environment. The impact of each strategy on the freeway traffic operations has been investigated. In particular, it has been realised that under different lane change strategies, various stop-and-go waves can occur. Under *speed leading* and *speed leading with overtaking* strategies the highest stability has been observed. In addition, for higher densities, the number of lane changes decreases to the lowest values in all strategies. Various lane flow distributions have been found under different lane change strategies. It has been seen that an unbalanced distribution of flow on a multi-lane freeway may lead to reduction of capacity.

Future research directions in this area include investigating the traffic operations under different combinations of lane change strategies, sensitivity analysis of the model parameters, validation and calibration of the model.

References

1. Knoop, V., Hoogendoorn, S., Shiomi, Y., Buisson, C.: Quantifying the number of lane changes in traffic: empirical analysis. Transp. Res. Rec. J. Transp. Res. Board **2278**, 31–41 (2012)
2. Keyvan-Ekbatani, M., Knoop, V.L., Daamen, W.: Categorization of the lane change decision process on freeways. Transp. Res. Part C: Emerg. Technols. (2015)
3. Ossen, S., Hoogendoorn, S., Gorte, B.: Interdriver differences in car-following: a vehicle trajectory-based study. Transp. Res. Rec.: J. Transp. Res. Board **1965**, 121–129 (2006)
4. Kondyli, A., Elefteriadou, L.: Driver behavior at freeway-ramp merging areas: focus group findings. Transp. Res. Rec. J. Transp. Res. Board **2124**, 157–166 (2009)
5. Kondyli, A., Elefteriadou, L.: Modeling driver behavior at freeway-ramp merges. Transp. Res. Rec. J. Transp. Res. Board **2249**, 29–37 (2011)
6. Motus (2015). http://homepage.tudelft.nl/05a3n/
7. Schakel, W., Knoop, V., van Arem, B.: Integrated lane change model with relaxation and synchronization. Transp. Res. Rec.: J. Transp. Res. Board **2316**, 47–57 (2012)
8. Knoop, V.L., Duret, A., Buisson, C., van Arem, B.: Lane distribution of traffic near merging zones influence of variable speed limits. In: 2010 13th International IEEE Conference on Intelligent Transportation Systems (ITSC), pp. 485–490. IEEE (2010)

When Is a Bottleneck a Bottleneck?

Andreas Schadschneider, Johannes Schmidt and Vladislav Popkov

Abstract Bottlenecks, i.e. local reductions of capacity, are one of the most relevant scenarios of traffic systems. The asymmetric simple exclusion process (ASEP) with a defect is a minimal model for such a bottleneck scenario. One crucial question is "What is the critical strength of the defect that is required to create global effects, i.e. traffic jams localised at the defect position". Intuitively, one would expect that already an arbitrarily small bottleneck strength leads to global effects in the system, e.g. a reduction of the maximal current. Therefore, it came as a surprise when, based on computer simulations, it was claimed that the reaction of the system depends in non-continuous way on the defect strength and weak defects do not have a global influence on the system. Here, we reconcile intuition and simulations by showing that indeed the critical defect strength is zero. We discuss the implications for the analysis of empirical and numerical data.

1 Introduction

One of the most important scenarios in any traffic system are bottlenecks, i.e. (local) flow limitations. Typical examples are a reduction in the number of lanes on a highway, local speed limits or narrowing corridors or exits in pedestrian dynamics. The identification of bottlenecks gives important information about the performance of the system. E.g. in evacuations, egress times are usually strongly determined by the relevant bottlenecks. Therefore, a proper understanding of bottlenecks and their influence on properties like the flow is highly relevant.

One of the most natural questions is "When does a bottleneck lead to a traffic jam?" Does any bottleneck immediately lead to jam formation or is there a minimal

A. Schadschneider (✉) · J. Schmidt · V. Popkov
Institut für Theoretische Physik, Universität zu Köln, 50937 Cologne, Germany
e-mail: as@thp.uni-koeln.de

J. Schmidt
e-mail: schmidt@thp.uni-koeln.de

V. Popkov
e-mail: vladipopkov@gmail.com

bottleneck strength required? Intuitively, one would say that even a small bottleneck strength leads to macroscopically observable effects, like a reduction of the maximal current or jams. However, other scenarios have been considered as well and have even been part of legal guidelines. One prime example in pedestrian dynamics is the dependence of the current on the width of a corridor [10, 13]. Originally it was believed that the current increases stepwise, i.e. non-continuously, with increasing bottleneck width. This increase was assumed to happen when the corridor width allows an additional lane of pedestrians to be formed (Fig. 1). Taking the corridor width as measure for the bottleneck strength (rather its inverse) this implies that an increasing bottleneck strength not necessarily leads to smaller current values or jam formation. In the meantime, we know that this scenario is not correct and the current increases linearly with the width [13]. However, it is still possible that there are situations where lane formation is relevant and this scenario is more adequate, e.g. in colloidal systems [14].

In the following, we will take a theoretical physics point of view by considering a minimal model for bottlenecks. Experience shows that the results capture the generic nature of bottleneck transitions.

2 Bottlenecks in the ASEP

The Asymmetric Simple Exclusion Process (ASEP) is a paradigmatic model of non-equilibrium physics (for reviews, see e.g. [2, 4, 7, 9, 12]) and arguably the simplest model that captures essential features of traffic systems, i.e. directed motion, volume exclusion and stochastic dynamics. It describes interacting (biased) random walks on a discrete lattice of N sites, where an exclusion rule forbids occupation of a site by more than one particle. A particle at site j moves to site $j + 1$ with rate p if site $j + 1$ is not occupied by another particle (Fig. 2). In the following we will mainly use a random-sequential update. If sites are updated synchronously (parallel update) the model is the $v_{max} = 1$ limit of the Nagel-Schreckenberg model [8, 9]. Many exact results are known for the homogeneous case of the ASEP, e.g. the fundamental diagram and the phase diagram in case of open boundary conditions [2, 4, 7, 9, 12].
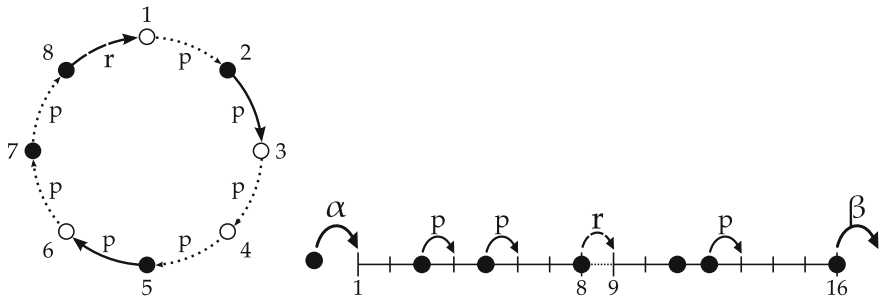
Fig. 2 ASEP with a defect (slow bond) where the hopping probability is $r < p$. $r = p$ corresponds to the homogeneous case. *Left* Periodic boundary conditions with $N = 8$ sites, the slow bond is between sites 8 and 1. *Right* Open boundary conditions with $N = 16$ sites, the slow bond is between sites 8 and 9

A simple but generic model for a bottleneck is obtained by replacing one of the hopping probabilities p by a defect, or slow bond, with hopping probability $r < p$ (Fig. 2). Many properties of this defect system have been obtained in a seminal paper by Janowsky and Lebowitz [6]. They have shown that the shape of the fundamental diagram can be understood by a simple mean-field theory. In the stationary state the current can be obtained by matching the current J_{hom} in the homogeneous system with the current J_{def} at the defect. Neglecting correlations at the defect site one finds that the defect has no influence on the system for low densities $\rho < \rho_1$ and large densities $\rho > \rho_2$.[1] The density remains uniform throughout the whole system and the current is identical to that of the homogeneous system (Fig. 3).

For densities $\rho_1 < \rho < \rho_2$, on the other hand, the fundamental diagram exhibits a plateau where the current is independent of the density (Fig. 3). The plateau value J_{plat} corresponds to the maximal current that is supported by the defect. In this density regime the stationary state is no longer characterised by a uniform density. Instead phase separation into a high and a low density region is observed. The high density region corresponds to a jam that is formed at the defect position (Fig. 4). For periodic boundary conditions the jam length shows characteristic fluctuations (Fig. 4a) [6].

For the ASEP with periodic boundary conditions, random-sequential update and a defect r mean-field theory makes quantitative predictions for the phase-separated regime [6]. The value of the current in the plateau region is given by

$$J_{plat} = \frac{pr}{(p + r)^2} \tag{1}$$

and the densities in the low and high density region by

$$\rho_\ell = \frac{r}{p + r} \qquad \text{and} \qquad \rho_h = \frac{p}{p + r} \tag{2}$$

---

[1]For the ASEP, due to particle-hole symmetry, $\rho_1 = 1 - \rho_2$.
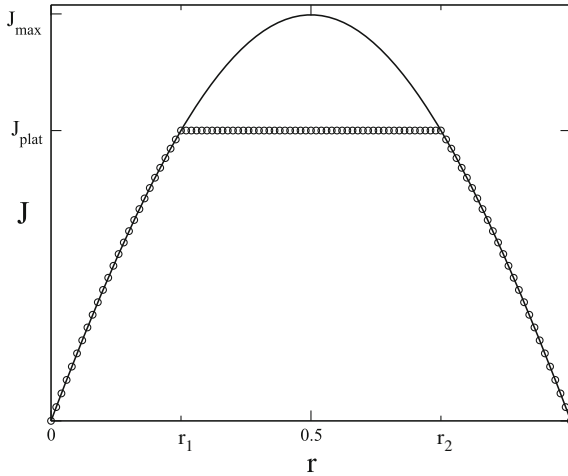
Fig. 3 Fundamental diagram of the ASEP with a defect r (*circles*). The full *line* is the fundamental diagram of the homogeneous system without defect. The current $J(r)$ is independent of the global density ρ for $\rho_1 < \rho < \rho_2$. The plateau value J_{plat} in this region is smaller than the maximal flow J_{max} in the homogeneous system
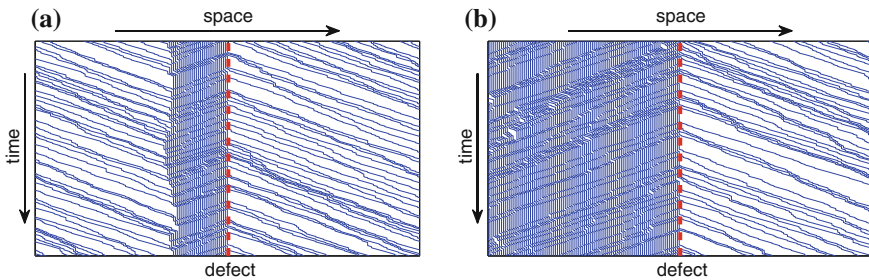
Fig. 4 Phase separation in the plateau regime: particle trajectories for Periodic boundary conditions (**a**); open boundary conditions (**b**)

The critical densities ρ_1, ρ_2 which determine the plateau regime $\rho_1 < \rho < \rho_2$ are simply

$$\rho_1 = \rho_\ell \quad \text{and} \quad \rho_2 = \rho_h \tag{3}$$

The mean-field results are supported by systematic series expansions [3].

Figure 5 shows the resulting phase diagram. For any defect $r < p$ only currents up to the plateau value J_{plat} can be realised in the system which then phase separates into a high density region pinned at the defect and a low density regime. For currents $J < J_{\text{plat}}$ the density is uniform. The important point is that $J_{\text{plat}} < J_{\text{max}}$ for any $r < p$ where J_{max} is the maximal current in the homogeneous system. In other words: any bottleneck leads to a reduction of the current and a phase-separated state (at intermediate densities).

Fig. 5 Phase diagram of the ASEP with defect according to [6]. The full *line* shows the current at the plateau as function of the defect hopping rate r. Any $r < p$ leads to a reduction of the maximal current compared to that of the homogeneous system J_{max}. In the phase of uniform density the defect has only local effects
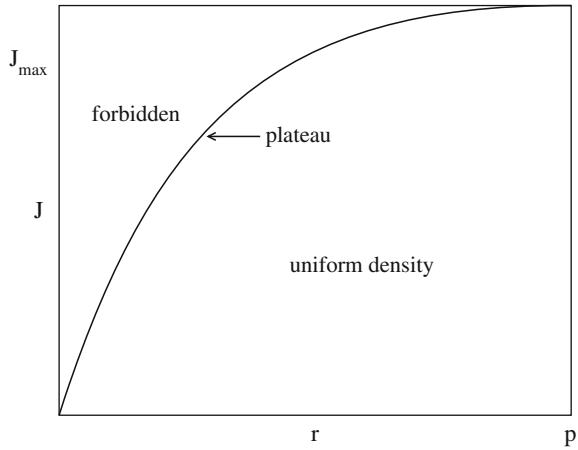
3 What Is the Critical Bottleneck Strength?

Mean-field theory predicts that any bottleneck $r < p$ leads to the formation of a plateau in the fundamental diagram and the associated phase-separated state [6]. Defining the bottleneck strength by

$$\Delta p = \frac{p - r}{p} \tag{4}$$

implies that the critical bottleneck strength $(\Delta p)_c$ at which the defect has global influence on the system (e.g. its current or the density) is predicted to be

$$(\Delta p)_c = 0, \quad \text{i.e. } r_c = p \tag{5}$$

As mentioned in the introduction this is what is intuitively expected. Therefore it came as quite a surprise when it was claimed [5], based on extensive computer simulations, that $r_c \approx 0.8$, i.e.

$$(\Delta p)_c^{(\text{Ha})} \approx 0.2 \tag{6}$$

The corresponding phase diagram is shown in Fig. 6. In contrast to Fig. 5, for defects $r > r_c$ all currents up to J_{max} can be realised and there is no phase separation at any density for weak defects! In this case the bottleneck has only *local* effects which can be observed near the defect, but not in the whole system.

Due to this apparent contradiction with expectations we have revisited the ASEP defect problem in [11] based on highly accurate Monte Carlo simulations. Similar to [5] we have simulated the ASEP with open boundary conditions, random-sequential dynamics (with $p = 1$) and a defect in the middle of the system (Fig. 2). However, choosing $\alpha = \beta = \frac{1}{2}$ as in [5], corresponds exactly to the phase boundary of the

Fig. 6 Phase diagram of
ASEP with defect according
to [5]. Defects with
$r_c < r \leq p$ have no
influence on the current J
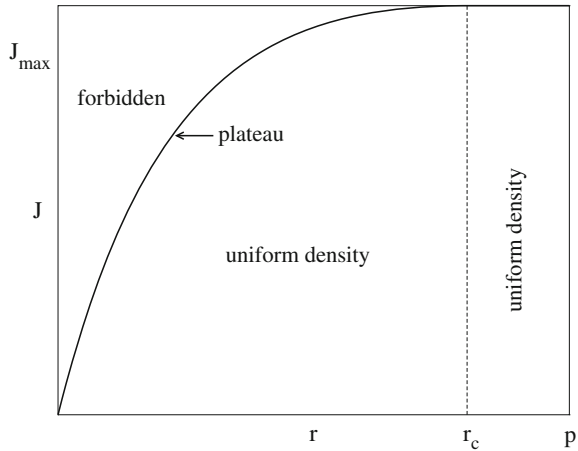
high, low and maximal current phase [4, 9, 12]. Fluctuations in finite-size systems
will systematically underestimate the defect current $J(r)$ [11]. We have therefore
chosen $\alpha = \beta = 1$ well inside the maximal current phase which allows to obtain a
much better statistics.

To determine rather subtle bottleneck effects, very good statistics and advanced
Monte Carlo techniques are required. To minimise errors induced by pseudo-random
number generators we have used the Mersenne Twister [11].

Measurements of bottleneck effects for small defect strengths are easily hidden
by fluctuations. Instead of using independent measurements for each defect strength
r the systems are evolved in parallel, i.e. with the same protocol and the same set of
random numbers, which leads to a strong suppression of fluctuations [11].

In order to minimise finite-size corrections, system lengths of up to $N = 200,000$
were considered (Fig. 7) which is two orders of magnitude larger than the systems
considered in [5].

To estimate the global effects of the defect we first considered the finite-size cur-
rent $J(N, r)$ through a system of length N and with a defect r. Due to the fact that
finite-size corrections lead to an enhanced current, i.e. $J(r, N) > J(r, N = \infty)$,
one finds a lower bound for the critical hopping rate by satisfying $J(N, r_c) -
J(N = \infty, r = 1) < 0$. However, in this way we only could derive a lower bound
$r_c \geq 0.86$ for the critical hopping rate (Fig. 7). Assuming the existence of an essential
singularity at $r_c = 1$, i.e. $j(1) - j(r) \sim \exp(-a/(1 - r))$ [3], further improve-
ment of the lower bound for the critical defect r_c by increasing the system length is a
hopeless enterprise: e.g. a numerical proof of $r_c > 0.9$, $r_c > 0.95$, $r_c > 0.99$ would
require $N > 10^{10}$, $N > 10^{22}$, $N > 10^{147}$, respectively.

A much better quantity to determine the global influence of the defect (see e.g.
Fig. 4, right) is the density profile or rather the difference between the density profile
of the defect system with a corresponding homogeneous system (Fig. 8). Using the
approach of parallel evolving systems we could clearly show a non-local influence on
the density profile for defect strengths up to $r = 0.99$ (Fig. 8). This strongly supports
the mean-field prediction $r_c = 1$.

Fig. 7 Finite-size corrections to the current. The exactly known current in the infinite homogeneous system is $J(N = \infty, r = 1) = 1/4$
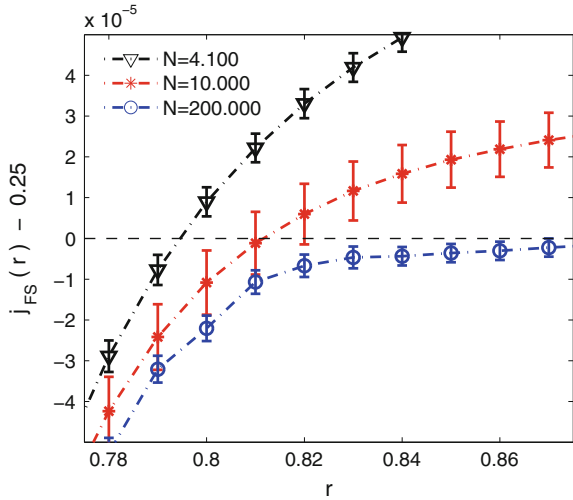
Fig. 8 Arbitrary defects r have a non-local effect on the density profile. The figure shows the difference between the density profile $\rho_r(x)$ with and that without defect $\rho_{r=1}(x)$ where $x = j/N$ is the rescaled position
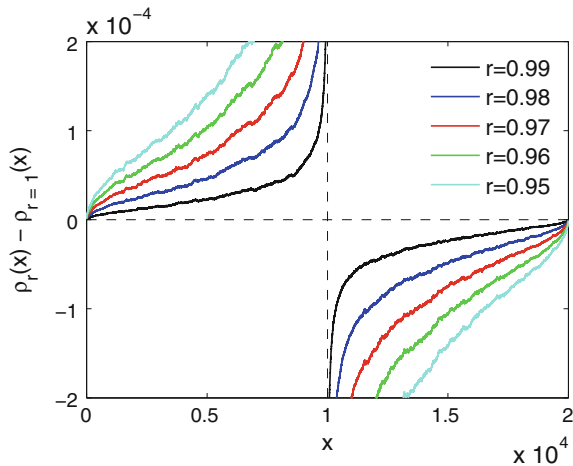
4 Discussion and Relevance for Empirical Results

Despite its relevance for applications some fundamental aspects of bottlenecks are not fully understood. Even for a minimal model like the ASEP with a defect the influence of weak bottlenecks is rather subtle and can be easily lost in fluctuations.

We have shown how to reconcile computer simulations with the intuition that even small defects have a global influence on the system. These effects are not easily seen in a reduction of the current which presumably shows a non-analytic dependence on the bottleneck strength. Bottlenecks are better identified by their effects on the density profile which spreads throughout the whole system.

Based on a careful statistical analysis of Monte Carlo simulations we have found strong evidence that an arbitrarily weak defect $\Delta p \to 0$ in the ASEP has a global influence on the system. Meanwhile, a mathematical proof of $(\Delta p)_c = 0$ has been announced in [1].

These results are believed to be generic for bottleneck systems. As a consequence the identification of weak bottlenecks in noisy empirical data is extremely difficult. Even for computer simulations very good statistics is required. Since the effect on the current is rather small, the density profile might be a better indicator for the presence of weak bottlenecks.

References

1. Basu, R., Sidoravicius, V., Sly, A.: Last passage percolation with a defect line and the solution of the slow bond problem (2014). arXiv:1408.3464
2. Blythe, R.A., Evans, M.R.: Nonequilibrium steady states of matrix-product form: a solver's guide. J. Phys. A Math. Theor. **40**(46), R333 (2007)
3. Costin, O., Lebowitz, J., Speer, E., Troiani, A.: The blockage problem. Bull. Inst. Math. Acad. Sin. **8**(1), 49–72 (2013)
4. Derrida, B.: An exactly soluble non-equilibrium system: the asymmetric simple exclusion process. Phys. Rep. **301**(1), 65–83 (1998)
5. Ha, M., Timonen, J., den Nijs, M.: Queuing transitions in the asymmetric simple exclusion process. Phys. Rev. E **68**(5), 056–122 (2003)
6. Janowsky, S.A., Lebowitz, J.L.: Finite-size effects and shock fluctuations in the asymmetric simple-exclusion process. Phys. Rev. A **45**(2), 618 (1992)
7. Liggett, T.M.: Stochastic interacting systems: contact, voter and exclusion processes, vol. 324. Springer Science & Business Media (2013)
8. Nagel, K., Schreckenberg, M.: A cellular automaton model for freeway traffic. Journal de physique I **2**(12), 2221–2229 (1992)
9. Schadschneider, A., Chowdhury, D., Nishinari, K.: Stochastic transport in complex systems: from molecules to vehicles. Elsevier (2010)
10. Schadschneider, A., Seyfried, A.: Empirical results for pedestrian dynamics and their implications for modeling. Netw. Heterog. Media **6**, 545–560 (2011)
11. Schmidt, J., Popkov, V., Schadschneider, A.: Defect-induced phase transition in the asymmetric simple exclusion process. EPL (Europhys. Lett.) **110**(2), 20008 (2015)
12. Schütz, G.M.: Exactly solvable models for many-body systems far from equilibrium. Ph. Trans. Crit. Phenom. **19**, 1–251 (2001)
13. Seyfried, A., Passon, O., Steffen, B., Boltes, M., Rupprecht, T., Klingsch, W.: New insights into pedestrian flow through bottlenecks. Trans. Sci. **43**(3), 395–406 (2009)
14. Vissers, T., Wysocki, A., Rex, M., Löwen, H., Royall, C.P., Imhof, A., van Blaaderen, A.: Lane formation in driven mixtures of oppositely charged colloids. Soft Matter **7**(6), 2352–2356 (2011)

Jam Avoidance with Autonomous Systems

Antoine Tordeux and Sylvain Lassarre

Abstract Many car-following models have been developed for jam avoidance in highways. Two mechanisms are used to improve the stability: feedback control with autonomous models and increasing of the interaction within cooperative ones. In this paper, we compare the linear autonomous and collective optimal velocity (OV) models. We observe that the stability is significantly increased by adding predecessors in interaction with collective models. Yet, autonomous and collective approaches are close when the speed difference term is taken into account. In the linear OV models tested, the autonomous models including speed difference are sufficient to maximise the stability.

1 Introduction

Recently, many car-following models have been developed for jam avoidance in highways. Models have equilibrium homogeneous solutions where all vehicle speeds and spacings are constant and equal. 'Jam avoidance property' is investigated through analysis of the stability of such solutions. Most of the approaches are extended versions of the *optimal velocity* (OV) model [1]. The basic model is solely based on the distance spacing with the predecessor (local next-neighbour interaction). Several studies have shown that speed and spacing feedback mechanisms in autonomous OV models allow to improve the stability of the homogeneous solution and to avoid jam formation [2, 6, 9, 10, 16]. Similar results are obtained with the *intelligent driver* (ID) model for specific parameter values [7, 8].

A. Tordeux (✉)
Jülich Supercomputing Centre, Forschungszentrum Jülich, Germany and Computer Simulation for Fire Safety and Pedestrian Traffic, Bergische Universität Wuppertal, Wuppertal, Germany
e-mail: a.tordeux@fz-juelich.de

S. Lassarre
GRETTIA/COSYS – IFSTTAR, Marne-la-Vallée, France
e-mail: sylvain.lassarre@ifsttar.fr

Several vehicles in the neighbourhood are included in the interaction for collective (or cooperative) systems. Many studies show improvements of the stability if the number of predecessors in interaction increases [3, 4, 11, 15]. Comparable results are obtained with symmetric interaction (interaction with predecessors and followers, see for instance [12, 13]). Opposite to autonomous models for which the variables can be directly measured, cooperative systems require that the vehicles are connected to communicate their states. This makes their implementation difficult.

In this paper, autonomous linear OV models and extended ones with speed difference term are compared to their collective versions including several predecessors in interaction. Both extended and collective OV models describe significant improvement of the stability. More precisely, we observe that the number of predecessors in interaction in the collective models and the speed difference term in the autonomous approaches have similar roles in the dynamics. The paper is organised as follows. The linear jam avoidance models are introduced in Sect. 2. The results of the simulation experiment of a jam are presented in Sect. 3, while the Lyapunov exponents of the different autonomous and collective models are calculated in Sect. 4. Section 5 gives the conclusion and outlook.

2   Linear Jam Avoidance Models

The optimal velocity model is

$$\ddot{x}_n(t) = \frac{1}{T}\big(V(\Delta x_n(t)) - \dot{x}_n(t)\big), \tag{1}$$

with $x_n(t)$ the position of the vehicle n at time t, $\Delta x(t) = x_{n+1}(t) - x_n(t)$ the distance spacing with $x_{n+1} > x_n$ the predecessor position (see Fig. 1), and $T > 0$ the relaxation (or reaction) time [1]. A jam avoidance should have stable homogeneous solution. More precisely, it should be locally stable with no oscillation (LSNO) to avoid collision and globally stable (GS), see for instance [14, Chap. 15]. The conditions ensure a collision-free convergence of the system to the homogeneous solution for any initial condition. In the OV model, the linear LSNO and GS conditions are respectively:

$$V' < \frac{1}{4T} \quad \text{and} \quad V' < \frac{1}{2T}. \tag{2}$$

Fig. 1 Notations used. x_n is the position and Δx_n is the spacing of the vehicle n
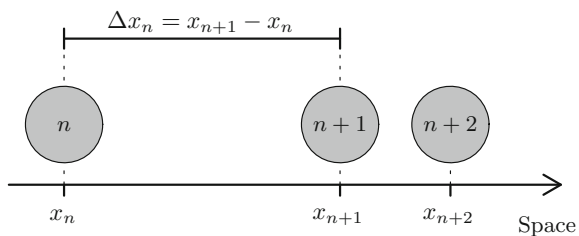
Note that the first condition implies the second. The *full velocity difference* (FVD) is an extended OV model including a speed difference term [5]:

$$\ddot{x}_n(t) = \frac{1}{T_1}\big(V(\Delta x_n(t)) - \dot{x}_n(t)\big) + \frac{1}{T_2}\Delta \dot{x}_n(t). \tag{3}$$

It includes two relaxation times $T_1 > 0$ and $T_2 > 0$. The model is the same as the OV model at the limit $T_2 \to \infty$. For the FVD model, the LSNO and GS conditions are respectively:

$$V' < \frac{1}{4T_1}\left(1 + \frac{T_1}{T_2}\right)^2 \quad \text{and} \quad V' < \frac{1}{2T_1} + \frac{1}{T_2}. \tag{4}$$

These conditions are simply $V' < 1/T$ if $T_1 = T_2 = T$ (the first inequality implies the second if $T_1 < 3T_2$). Clearly, the speed difference has a stabilisation effect on the dynamics. The LSNO and GS conditions always hold at the limit $T_2 \to 0$.

The models (Eqs. 1 and 3) are autonomous: they are solely based on distance spacing and speed difference with the predecessor. Collective models depend on several predecessors in front. Generally, collective OV models have the form $\ddot{x}_n(t) = \sum_{k=1}^{K} F_k\big(\Delta x_{n,k}(t), \dot{x}_n(t), \Delta \dot{x}_{n+k}(t)\big)$, where K is the number of predecessors taking into account and $\Delta x_{n,k} = x_{n+k} - x_k$ is the distance to the vehicle $n+k$. F_k represents the influence of the vehicle k on the acceleration rate of the considered vehicle. In the *Multi-anticipative* (MA) model [11], this influence is

$$F_k = \frac{\alpha_k}{T}\big(V\big(\Delta x_{n,k}(t)/k\big) - \dot{x}_n(t)\big). \tag{5}$$

The *velocity difference multi-anticipative* (VDMA) model includes speed difference terms

$$F_k = \alpha_k\left[\frac{1}{T_1}\big(V\big(\Delta x_{n,k}(t)/k\big) - \dot{x}_n\big) + \frac{1}{T_2}\Delta \dot{x}_{n+k}(t)\right]. \tag{6}$$

Here, the positive coefficients (α_k) are such that $\sum_k \alpha_k = 1$. They specify the interaction with the predecessors. In the following we set $\alpha_k = 1/K$ for all k (uniform interaction) in order to maximise the stability [3, 11]. Note that the MA model is the OV one and the VDMA model is the FVD one for $K = 1$, while the VDMA model is the MA one at the limit $T_2 \to \infty$. The tested models are resumed in Table 1.

3 Simulation of a Jam

In this section, the models (Eqs. 1, 3, 5 and 6) are simulated with periodic boundary conditions from jam initial conditions by using explicit Euler schemes with time step 0.001 s. $N = 20$ vehicles are considered with the settings: $V' = 1 \text{ s}^{-1}$, $T = T_1 = 0.25$ s (fix), and $T_2 = 2, 0.5, 0.1$ s, $K = 2, 4, 10$ veh (tested). The settings are defined

Table 1 Name, acronym, type and parameters of the tested models

Name	Acronym	Type	Parameter
Optimal velocity	OV	Autonomous	V', T
Full velocity difference	FVD	Autonomous	V', T_1, T_2
Multi-anticipative	MA	Collective	V', T, K
Velocity difference multi-anticipative	VDMA	Collective	V', T_1, T_2, K
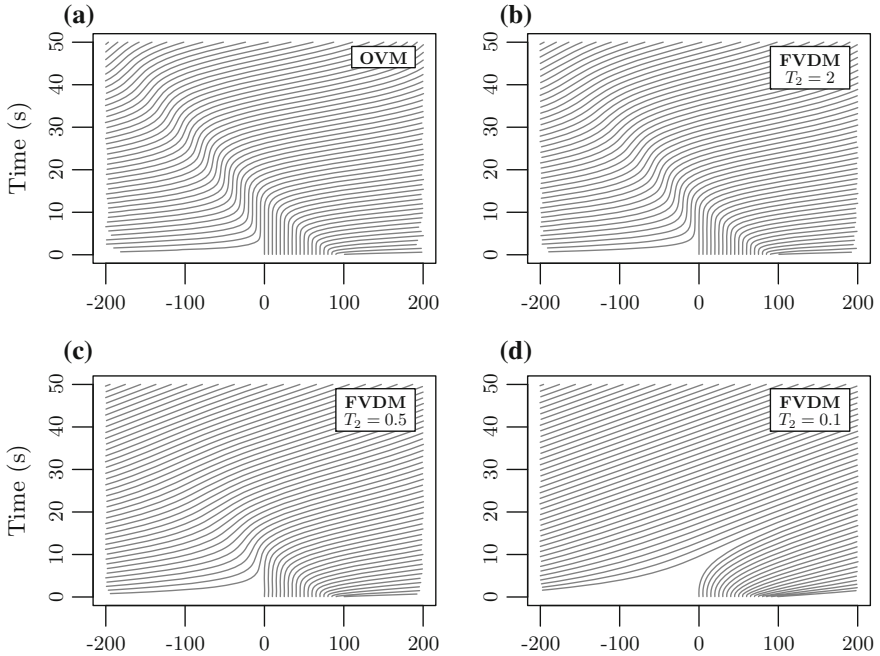
Fig. 2 Trajectories with the OV and FVD models from jam initial configuration

so that the LSNO and GS conditions occur for any model. The trajectories obtained with OV and FVD autonomous models are presented in Fig. 2. The convergence speed to the homogeneous solutions increases as $T_2 \to 0$. The same phenomenon occurs with MA model as $K \to \infty$, see Fig. 3. However, there is no clear improvements of the stability with the VDMA model if T_2 is sufficiently small (see Fig. 4).

The speed of convergence of the system to the uniform solution can be quantified by spacing standard deviation sequence (Lyapunov function):

$$\sigma_{\Delta x} = \sqrt{\frac{1}{N} \sum_{n=1}^{N} (\Delta x_n - \Delta \bar{x}_n)^2} \quad \text{with} \quad \Delta \bar{x}_n = \frac{1}{N} \sum_{n=1}^{N} \Delta x_n. \tag{7}$$

In Fig. 5, the logarithms of the spacing standard deviation are plotted according to the time for the different models. We observe linear evolution, meaning that the
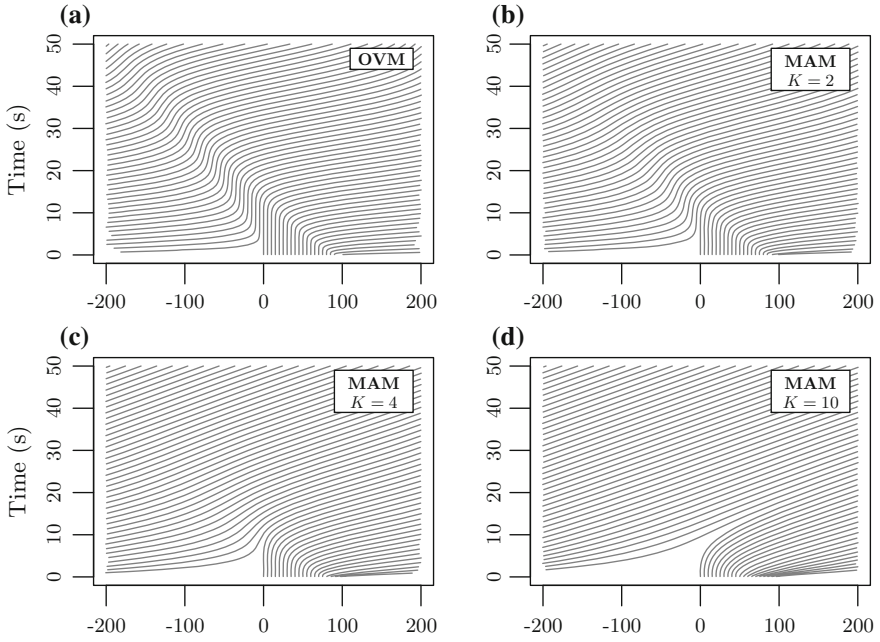
Fig. 3 Trajectories with the OV and MA models from jam initial configuration
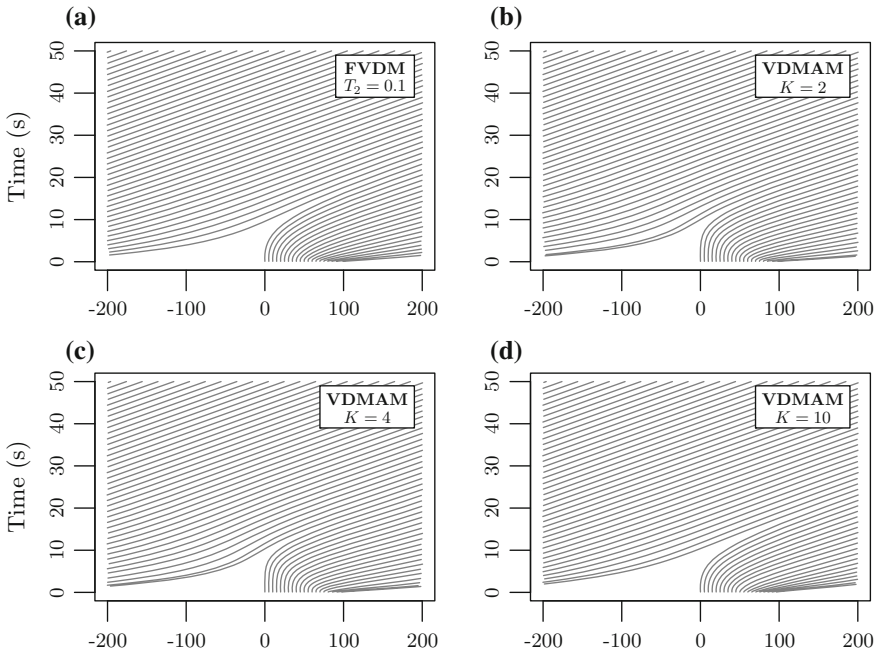
Fig. 4 Trajectories with the FVD and VDMA models from jam initial configuration
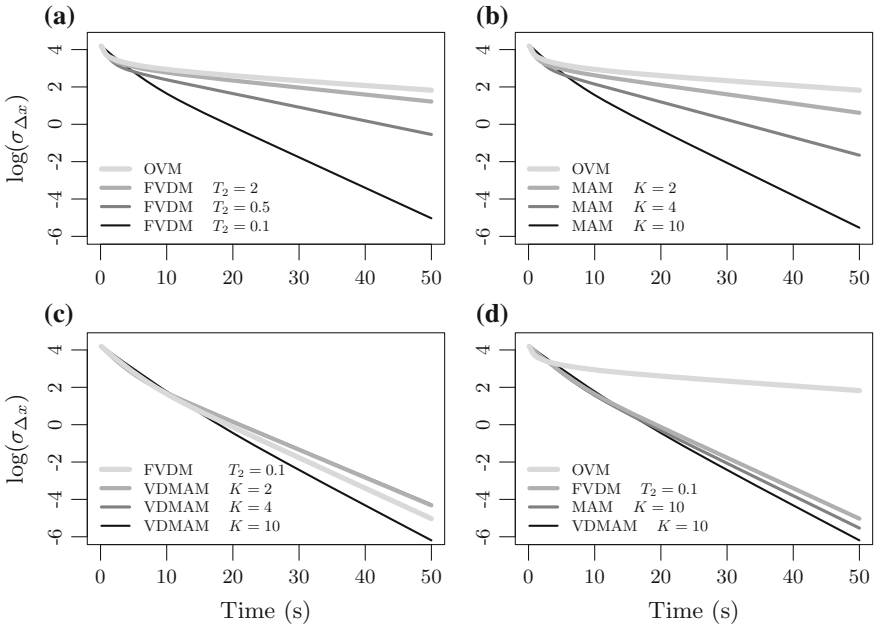
Fig. 5 Sequences of the spacing standard deviation logarithm with OV, FVD, MA and VDMA models

deviation tends to zero with exponential speed. As expected, the slope of the logarithm (i.e. the convergence speed) increases as T_2 decreases with the autonomous models (see Fig. 5a), while the speed depends on the number of predecessors in interaction K with the collective MA model (see Fig. 5b). As we observed previously, the speed does not change significantly if K increases with VDMA model (see Fig. 5c). In fact, the speeds of convergence of FVD, MA, and VDMA models are close (see Fig. 5d); they are strongly faster than the convergence speed of ordinary OV model. Such results suggest that speed difference term with the autonomous models and the number of predecessors in interaction with the collective ones have similar roles in the dynamics. The convergence speed to the homogeneous solution is maximised as $T_2 \to 0$ or as $K \to \infty$.

4 Lyapunov Exponents

The solution of the linear systems are a linear combination (LC) of exponential terms

$$x_n(t) = \text{LC}\big(\exp(\lambda_l t), t \exp(\lambda_l t) \big) \tag{8}$$

with (λ_l) the Lyapunov exponents of the system (i.e. the eigenvalues of the system Jacobian matrix). In our stable case, all the exponents have strictly negative real
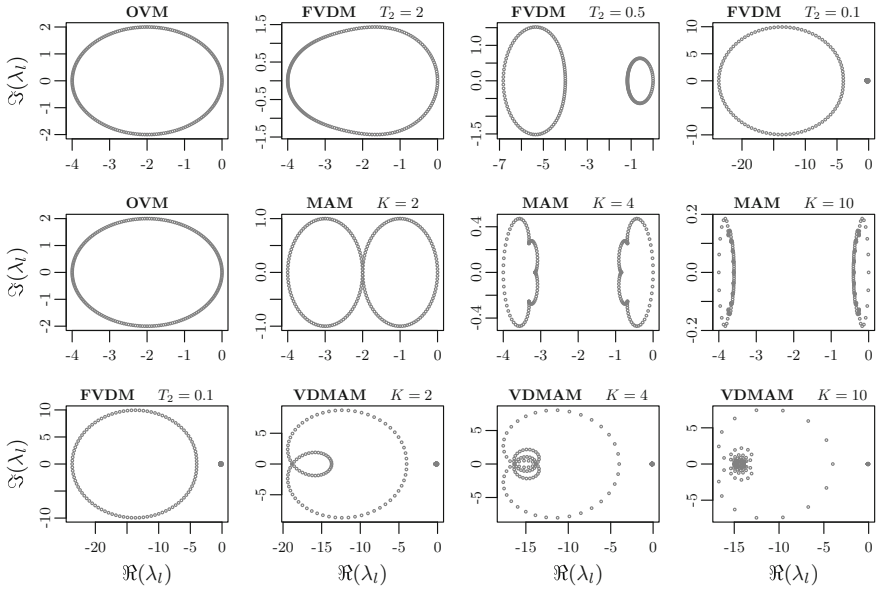
Fig. 6 Lyapunov exponents for OV, FVD (*top figures*), MA (*middle figures*) and VDMA (*bottom figures*) models with $N = 100$

parts, excepted one equal to zero. Moreover, we can expect that the convergence to the homogeneous solution gets faster as the exponents go the left of the imaginary axis. With the optimal velocity we investigate, the exponents are:

$$\lambda_l = \frac{1}{2}\sum_{k=0}^{K}\beta_k \iota_l^k \pm \frac{1}{2}\Big[\Big(\sum_{k=0}^{K}\beta_k \iota_l^k\Big)^2 - 4\sum_{k=1}^{K}\alpha_k(1-\iota_l^k)\Big]^{1/2} \qquad (9)$$

with $\iota_l = \exp(2i\pi l/N)$, $l = 1,\ldots N$, N being the vehicles number, $\alpha_k = \frac{1}{kT_1}\frac{V'}{K}$, $\beta_0 = -\frac{1}{T_1} - \frac{1}{T_2}$ and $\beta_k = -\frac{1}{KT_2}$ for all $k = 1,\ldots N$. The Lyapunov exponents are plotted in Fig. 6 for the different models. We observe that they converge to a double mode pattern as $T_2 \to 0$ with the autonomous FVD model, and $K \to \infty$ with the MA collective model. They remain double mode with the collective VDMA model as K increases. Such results confirm qualitatively the ones observed by simulation. The speed difference behave in the dynamics as the number of predecessors in interaction. Also increasing the interaction seems not necessary to maximise the stability.

5   Conclusion

The convergences to the homogeneous solution of linear jam avoidance OV models are compared. We observed that extending the OV model with speed difference term significantly improves the stability. In a similar way, the adding of neighbours in

interaction gives stability enhancements. However, increasing the interaction does not improve the stability with the extended OV model. This suggests that both the number of predecessors in interaction in the collective models and the speed difference term in the autonomous approaches allow to maximise the convergence speed to homogeneous solutions. Also, the connection between the vehicles, hard to implement, may not be necessary to optimise the stability and efficiently avoid jam formation. Further investigations remain to be carried out to validate this hypothesis. For instance, the influence of the geometry, initial conditions or vehicle density have to be investigated. The shape of the Lyapunov exponents and their impact on the stability are not explicit. Furthermore, nonlinear models may present better convergence speed than the basic linear models we analysed. These subjects will the topic of future works.

References

1. Bando, M., Hasebe, K., Nakayama, A., Shibata, A., Sugiyama, Y.: Dynamical model of traffic congestion and numerical simulation. Phys. Rev. E **51**(2), 1035–1042 (1995)
2. Davis, L.C.: Effect of adaptative cruise control systems on traffic flow. Phys. Rev. E **69**, 066110 (2004)
3. Hasebe, K., Nakayama, A., Sugiyama, Y.: Dynamical model of a cooperative driving system for freeway traffic. Phys. Rev. E **68**, 026102 (2003)
4. Hu, Y., Ma, T., Chen, J.: An extended multi-anticipative delay model of traffic flow. Commun. Nonlinear Sci. Numer. Simul. **19**(9), 3128–3135 (2014)
5. Jiang, R., Wu, Q., Zhu, Z.: Full velocity difference model for a car-following theory. Phys. Rev. E **64**, 017101 (2001)
6. Jin, Y., Hu, H.: Stabilization of traffic flow in optimal velocity model via delayed-feedback control. Commun. Nonlinear Sci. Numer. Simul. **18**(4), 1027–1034 (2013)
7. Kesting, A., Treiber, M., Schönhof, M., Helbing, D.: Adaptive cruise control design for active congestion avoidance. Trans. Res. Part C Emerg. Technol. **16**(6), 668–683 (2008)
8. Kesting, A., Treiber, M., Schönhof, M., Kranke, F., Helbing, D.: Jam-avoiding adaptive cruise control (ACC) and its impact on traffic dynamics. In: Traffic and Granular Flow'05, pp. 633–643 (2007)
9. Konishi, K., Kokame, H., Hirata, H.: Coupled map car-following model and its delayed-feedback control. Phys. Rev. E **60**, 4000–4007 (1999)
10. Konishi, K., Kokame, H., Hirata, K.: Decentralized delayed-feedback control of an optimal velocity traffic model. Eur. Phys. J. B-Condens. Matter Complex Syst. **15**(4), 715–722 (2000)
11. Lenz, H., Wagner, C., Sollacher, R.: Multi-anticipative car-following model. Eur. Phys. J. B-Condens. Matter Complex Syst. **7**(2), 331–335 (1999)
12. Monteil, J., Billot, R., Sau, J., El Faouzi, N.E.: Linear and weakly nonlinear stability analyses of cooperative car-following models. IEEE Trans. Intell. Trans. Syst. **15**(5), 2001–2013 (2014)
13. Nakayama, A., Sugiyama, Y., Hasebe, K.: Effect of looking at the car that follows in an optimal velocity model of traffic flow. Phys. Rev. E **65**, 016112 (2001)
14. Treiber, M., Kesting, A.: Traffic Flow Dynamics. Springer, Berlin (2013)
15. Wilson, R., Berg, P., Hooper, S., Lunt, G.: Many-neighbour interaction and non-locality in traffic models. Eur. Phys. J. B-Condens. Matter Complex Syst. **39**(3), 397–408 (2004)
16. Zhao, X., Gao, Z.: Controlling traffic jams by a feedback signal. Eur. Phys. J. B-Condens. Matter Complex Syst. **43**(4), 565–572 (2005)

Modelling Backward Travelling Holes in Mixed Traffic Conditions Using an Agent Based Simulation

Amit Agarwal, Gregor Lämmel and Kai Nagel

Abstract A spatial queue model in a multi-agent simulation framework is extended by introducing a more realistic behaviour, i.e. *backward travelling holes*. Space corresponding to a leaving vehicle is not available immediately on the upstream end of the link. Instead, the space travels backward with a constant speed. This space is named a 'hole'. The resulting dynamics resemble Newell's simplified kinematic wave model. Furthermore, fundamental diagrams from homogeneous and heterogeneous traffic simulations are presented. The sensitivity of the presented approach is tested with the help of flow density contours.

1 Introduction

Use of an iterative algorithm to determine the dynamic user equilibrium in simulators is common, but simulating large scale scenarios within a reasonable time frame is rare [11]. A simple queue model is very helpful in traffic flow models due to its computational efficiency [11, 16]. In these models, vehicles move along a link at free flow speed until the end of the link. At the end of the link, if the inflow is higher than the maximum possible outflow (link capacity), a queue appears. A simple approach is the point queue model in which vehicles are stacked on top of each other as vertical stack [19, 20]. In such models, the storage capacity is assumed to be infinite and therefore, the queue length is zero, and spillover into other links does not occur. Shortcomings of the point queue model are the ignorance of the physical length of the queue, unclear interaction between links and missing intra-link congestion [19]. In urban settings spillover often occurs at many intersections

---

A. Agarwal (✉) · K. Nagel
Technische Universität Berlin, Sek. SG 12, Salzufer 17–19, 10587 Berlin, Germany
e-mail: amit.agarwal@campus.tu-berlin.de

K. Nagel
e-mail: nagel@vsp.tu-berlin.de

G. Lämmel
Forschungszentrum Jülich, Institute for Advanced Simulation, 52425 Jülich, Germany
e-mail: g.laemmel@fz-juelich.de

in particular during peak hours. Spillover is considered in spatial queue models (see, e.g., [16]). This is achieved by assigning storage capacities to links based on length of the link and number of lanes. Spatial queue models observe those storage capacities by verifying the available space on the downstream link before allowing vehicles to enter it. Consequently, queues can spillover onto the upstream link(s).

In the *spatial* queue model, queuing occurs upstream of the bottleneck links as observed in real-life, but it is assumed that the space originating from leaving vehicle is available immediately at the upstream end of the link. Thus, in both point and spatial queue models, intra-link congestion is not incorporated.

Intra-link flow dynamics is described by the LWR model [12, 15] and by Newell's simplified kinematic wave model (KWM) [14]. Daganzo has proposed the cell transmission model (CTM) to solve the kinematic wave equation [6, 7]. A link transmission model (LTM) is introduced by Yperman [17]. In this model, traffic propagation is consistent with KWM.

Differences between point queue model, spatial queue model and cell transmission model under dynamic network loading condition are shown by [19]. The authors show that the point queue model considerably underestimates the dynamic network travel time. In addition, for heavily congested networks with spillback, spatial queues without kinematic waves can also underestimate the impact of congestion. The limitations of the point and spatial queue models are shown also in a previous study by Frederix et al. [10] by comparing the results of toy scenarios with LTM.

One way to incorporate KWM like flow dynamics into spatial queue models is the introduction of backward travelling holes (or gaps) [5, 8]. The present study continues this line of research by using the backward travelling holes in the spatial queue model.

In most of the developing economies, a variety of vehicles are prevalent on the streets, which can be differentiated based on their static (dimension) and dynamic (speed, acceleration etc.) attributes. In this direction, the LWR model is extended analytically for mixed traffic by Zhang and Jin [18]. However, to avoid computational complexities, the present study focuses only on extending the queue model with holes for mixed traffic rather than addressing more general LWR model.

2 Modelling

The multi-agent transport simulation framework MATSim [13] is used for all simulation experiments. The minimal inputs are physical boundary condition (the road network) and daily plans of individual travellers as an initial condition. Daily plans are loaded simultaneously using a network loading algorithm which is embedded into an iterative co-evolutionary algorithm [4]. The network loading algorithm of the MATSim framework is a so-called queue model [11, 16]. The queue model in MATSim allows spillback, thus, from here onwards in the present study, the queue

model refers to the spatial queue model. In the present study, the queue model with holes is presented in detail. A brief introduction of the queue model with holes for link dynamics is given in two previous studies [1, 2].

2.1 Race Track Experiment

A race track experiment is set up to establish the relation between the three fundamental quantities of traffic flow, i.e. flow (q), density (ρ) and speed (v). A triangular race track is taken as experimental network in which agents keep travelling until a steady state is achieved [3]. Each side of the track is 1000 m long and the maximum allowed speed on all links is 60 km/h. Maximum flow capacity and density of each link are 2700 PCU/h and 133.33 PCU/km. Here, PCU refers to passenger car unit. Further, in order to check the behaviour of heavy vehicles, truck mode is also used. The maximum speeds and PCUs of car, truck, motorbike, and bike modes are assumed as 60, 30, 60, 15 km/h, and 1, 3, 0.25, 0.25 respectively.

Corresponding to each discrete density point and modal split, the number of agents on the race track is determined. These agents are allowed to run on the track until the fluctuations in the flow and speed of each mode are damped. This situation is referred to as steady state. Flow and speed corresponding to each density point are then recorded. The average values for each mode are recorded. Data is not recorded if a steady state is not achieved.

2.2 Queue Models Without 'Holes'

For reference, two link dynamics—namely, first-in-first-out (FIFO) and passing of queue model without holes—are presented here briefly.

2.2.1 FIFO

The queue model in MATSim follows the traditional *first-in-first-out* (FIFO) approach and processes the vehicle queue on each road segment (link) according to FIFO order. In the MATSim framework, a link l has a number of attributes e.g. link length ℓ_l, flow capacity c_{flow}, storage capacity $c_{storage}$, maximum allowed speed on the link $v_{l,max}$, etc. The flow capacity (link outflow) controls the maximum number of vehicles that can leave the link, whereas storage capacity controls the link density, i.e. maximum number of vehicles that can be placed on the link. For each entering vehicle with maximum vehicle speed $v_{v,max}$, an earliest link exit time (or free speed travel time, t_{free}) is computed as $= \ell_l / min(v_{l,max}, v_{v,max})$. Afterwards, the vehicle is added to the queue data structure, from where the vehicle is moved across the downstream intersection provided: (1) the vehicle has spent free speed time (t_{free}) on the link;

(2) flow capacity of the link is available; (3) the downstream link has enough space. The queue model controls vehicles only at entries and exits, and never in between, which makes it computationally efficient.

2.2.2 Passing

In order to simulate a traffic mix that consists of vehicles with different maximum speed ($v_{v,max}$) and physical characteristics, the MATSim queue model is modified by a passing queue [3] as follows:

1. A passenger car unit (PCU) equivalent is assigned to each vehicle type to consume the flow and storage capacities on the link.
2. The queue data structure is sorted based on the earliest link exit time (t_{free}). Thus, it allows faster vehicles to overtake slower vehicles.

2.3 Queue Model with 'Holes'

In the FIFO and passing queue models, it is assumed that when a vehicle leaves the downstream end of the link, the freed space is available immediately on the upstream end of the link. As stated earlier, this is unrealistic: in real-life it takes some time for the free space to arrive at the upstream end of the link [5, 8]. Therefore, the present study continues by introducing backward travelling holes into the queue simulation. As the name indicates, in this approach, there are holes and they travel backwards, i.e. opposite to the direction of the traffic flow. The approach works as follows:

- Whenever a vehicle leaves the downstream end of the link, the space freed is called a 'hole'. Every hole has a size equivalent to the PCU of the leaving vehicle.
- The space freed by the leaving vehicle is then occupied by the following vehicle and thus the hole propagates one step backward. This process continues until the free space (hole) arrives at the upstream end of the link.
- Consequently, the space on the upstream end of the link is not available instantly; instead it reaches the upstream end of the link after time t_{hole}. Each hole is equipped with upstream arrival time which is defined as $= \ell_l / v_{hole}$, where v_{hole} is the hole speed. This speed corresponds to the speed of the backward travelling kinematic wave in the KWM and mainly depends on the reaction time of the drivers.
- In this study, a constant hole speed of 15 km/h is assumed. This hole speed corresponds to a time headway of about 2 s between two subsequent vehicles.
- After a certain density, no vehicle can enter the link until free space reaches the upstream end of the link. Therefore, in contrast to the queue model without holes, in this approach, vehicles wait for the free space. Consequently, in addition to the existing outflow link capacity, an implicit inflow link capacity is introduced.

2.3.1 Comparison of with and Without Holes Models

Figure 1a, b show a comparison of both queue model approaches—with and without holes—for a car only simulation. In the free flow regime, the primary relationship between the three fundamental variables of traffic flow ($q = \rho \cdot v$) holds for queue models with and without holes. As already described in Sect. 2.2.1, in the queue model without holes, the free space on the upstream end of the link is available instantly and therefore, in capacity regime, a horizontal section is observed corresponding to the outflow capacity [16] and afterwards, at higher densities, this horizontal section joins together with a nearly vertically downward sloping congested branch (see golden points in Fig. 1a). In contrast, in the queue model with holes, the slope of the congested branch is reduced to the speed of the backward travelling holes. This branch is then met with the upward sloping free flow branch at a capacity below the outflow capacity. It can also be observed that the critical density at which speed starts decreasing is less for the queue model with holes than for the queue model without holes. Thus, the maximum flow for queue model with holes mainly depends on the backward travelling hole speed and the maximum speed of the vehicle [9]; this can also be verified from Fig. 1c.

2.3.2 FIFO

Initially, FDs for single mode simulations, namely car, truck, motorbike, and bike are plotted (see Fig. 1c, d). Car and motorbike modes have different PCUs and same speed, therefore, when plotting density in PCU/km, the FDs for these two modes are similar. The FDs are not able to achieve the maximum flow due to implicit inflow link capacity as described in Sect. 2.3. Moreover, for truck and bike the maximum flow is even lower due to (1) lower maximum speed of these modes and (2) implicit inflow link capacity. The former can also be confirmed from FDs for queue model without holes, in which lower bike speed results in lower maximum flow [3]. The maximum flow for trucks and bikes is achieved at a higher density than for cars and motorbikes due to lower maximum speeds.

2.3.3 Passing

The queue model with holes is also applied to passing link dynamics. It is assumed that the reaction time of all vehicle types is the same, which results in a constant backward travelling hole speed for all vehicle types. In order to show the FDs for passing link dynamics in the queue model with holes, car and bike modes are simulated in equal PCU units. The resulting FDs are shown in Fig. 1e, f.

Clearly, cars can overtake the slower bike mode. Car mode has the maximum flow at a lower density than bike because of slower speed of bike mode; this can be also verified from Fig. 1c in which maximum flow for bike mode occurs at a higher density.
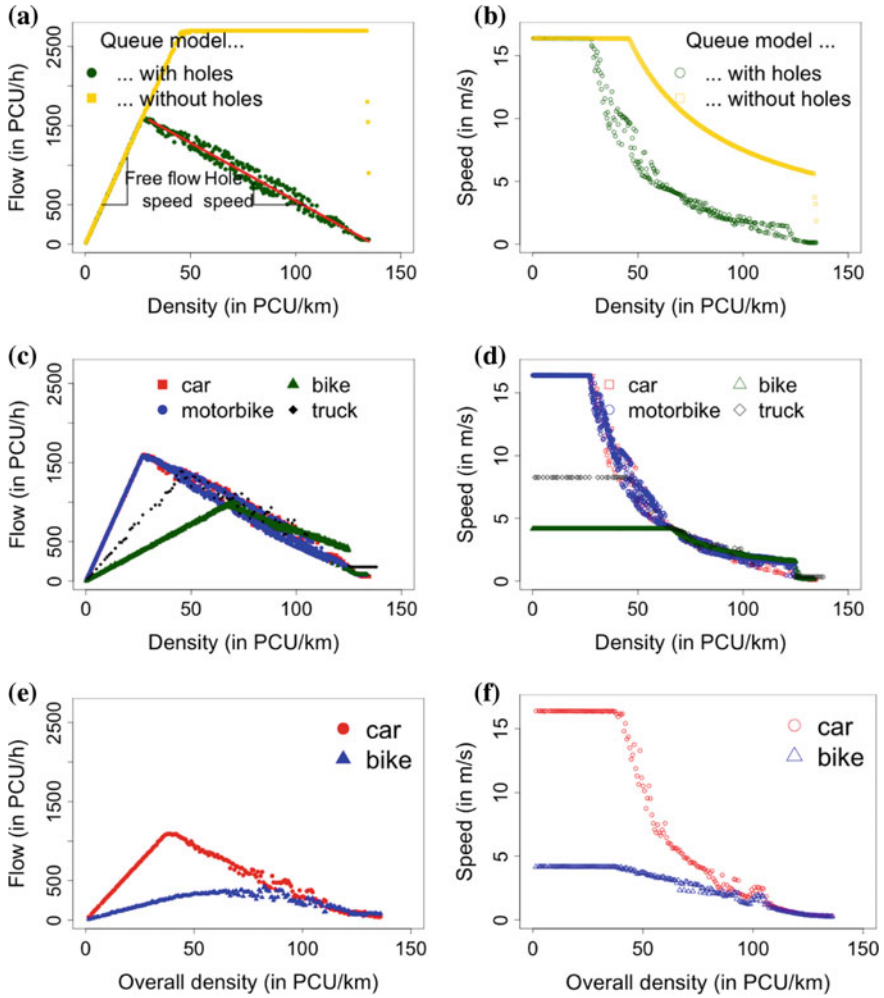
Fig. 1 Fundamental diagrams: flow density plot for with and without holes queue models (**a**); speed density plot for with and without holes queue models (**b**); flow density plot from one mode simulations for with holes queue model (after [2]) (**c**); speed density plot from one mode simulations for with holes queue model (after [2]) (**d**); flow density plot for passing queue model with holes (**e**); speed density plot for passing queue model with holes (**f**)

3 Sensitivity

In order to check the sensitivity of the queue model with holes, flow density contours are plotted in Fig. 2 for different modal split variation of car and bike simulations on the race track. Figure 2a, b show the flow density contours for the queue models with and without holes respectively. Clearly, at higher densities (diagonal values) the
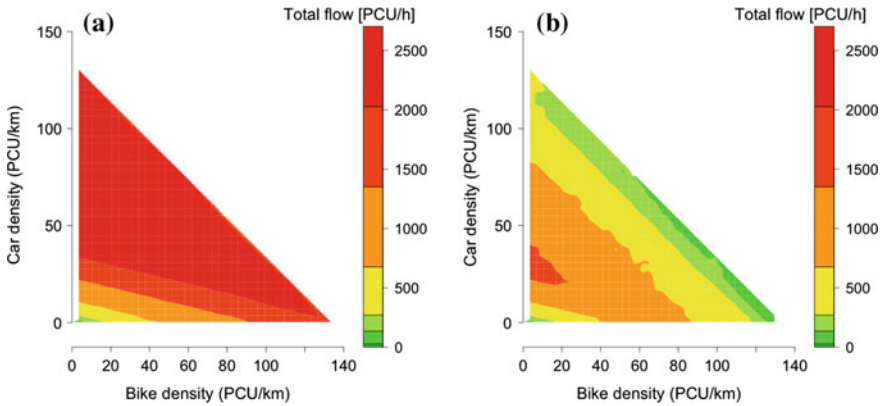
Fig. 2 Flow density contours for car bike simulation and passing link dynamics. Queue model: without holes (**a**); with holes (**b**)

queue model with holes has a clearer jammed regime compared to the queue model without holes. Furthermore, it can be observed that the queue model with holes is not able to reach the link capacity due to the limited inflow caused by the backwards travelling holes.

4   Conclusion

This study extended spatial queue model in a computationally efficient multi-agent simulation framework by introducing a more realistic behaviour, i.e. backward travelling holes. Since, in this concept, space freed by leaving vehicles is not immediately available on the upstream end of the link, the link inflow capacity is restricted implicitly. This eliminated the previously present unclear dynamics in jammed regime of the fundamental diagrams.

In order to validate the model, first, fundamental diagrams for one mode simulations were presented. Later, to test the mixed traffic behaviour, combination of car and bike were simulated and corresponding fundamental diagrams were presented. The sensitivity of the model was tested by comparing the flow density contours from with and without holes queue models. The presented queue model with holes is able to simulate mixed traffic more realistic and still is applicable to large scale scenarios.

References

1. Agarwal, A., Lämmel, G.: Modeling seepage behavior of smaller vehicles in mixed traffic conditions using an agent based simulation. In: 3rd Conference of the Transportation Research Group of India. Kolkata, India (2015). Also VSP WP 15-09, see http://www.vsp.tu-berlin.de/publications
2. Agarwal, A., Lämmel, G.: Seepage of smaller vehicles under heterogeneous traffic conditions. Procedia Comput. Sci. **52**(C), 890–895 (2015)
3. Agarwal, A., Zilske, M., Rao, K., Nagel, K.: An elegant and computationally efficient approach for heterogeneous traffic modelling using agent based simulation. Procedia Comput. Sci. **52**(C), 962–967 (2015)
4. Balmer, M., Rieser, M., Meister, K., Charypar, D., Lefebvre, N., Nagel, K., Axhausen, K.: MATSim-T: Architecture and simulation times. In: Bazzan, A., Klügl, F. (eds.) Multi-Agent Systems for Traffic and Transportation, pp. 57–78. IGI Global (2009)
5. Charypar, D., Axhausen, K., Nagel, K.: Event-driven queue-based traffic flow microsimulation. Trans. Res. Rec. **2003**, 35–40 (2007)
6. Daganzo, C.: The cell transmission model: a dynamic representation of highway traffic consistent with the hydrodynamic theory. Trans. Res. Part B Methodol. **28**(4), 269–287 (1994)
7. Daganzo, C.: The cell transmission model, part II: network traffic. Trans. Res. Part B Methodol. **29**(2), 79–93 (1995)
8. Eissfeldt, N., Krajzewicz, D., Nagel, K., Wagner, P.: Simulating traffic flow with queues (2006). See http://www.vsp.tu-berlin.de/publications
9. Flötteröd, G.: Queueing representation of kinematic waves. In: Horni, A., Axhausen, K.W., Nagel, K. (eds.) The Multi-Agent Transport Simulation MATSim, chap. 37 (in preparation)
10. Frederix, R., Viti, F., Tampère, C.: A density-based dynamic OD estimation method that reproduces within-day congestion dynamics. In: 2010 13th International IEEE Conference on Intelligent Transportation Systems (ITSC), pp. 694–699 (2010)
11. Gawron, C.: An iterative algorithm to determine the dynamic user equilibrium in a traffic simulation model. Int. J. Mod. Phys. C **9**(3), 393–407 (1998)
12. Lighthill, M.J., Whitham, J.B.: On kinematic waves. I: flow movement in long rivers. II: a Theory of traffic flow on long crowded roads. Proc. R. Soc. A **229**, 281–345 (1955)
13. MATSim: MultiAgent Transport SIMulation webpage http://www.matsim.org (2004). Accessed 2014
14. Newell, G.: A simplified theory of kinematic waves in highway traffic. I: General theory. II: Queueing at freeway bottlenecks. III: Multi-destination flows. Trans. Res. Part B Methodol. **27B**, 281–313 (1993)
15. Richards, P.: Shock waves on the highway. Oper. Res. **4**, 42–51 (1956)
16. Simon, P., Esser, J., Nagel, K.: Simple queueing model applied to the city of Portland. Int. J. Mod. Phys. **10**(5), 941–960 (1999)
17. Yperman, I.: The link transmission model for dynamic network loading. Ph.D. thesis, Katholieke Universiteit Leuven (2007)
18. Zhang, H.M., Jin, W.L.: Kinematic wave traffic flow model for mixed traffic. Trans. Res. Rec. J. Trans. Res. Board **1802**, 197–204 (2007)
19. Zhang, H.M., Nie, Y.: Modeling network flow with and without link interaction: properties and implication. In: Presented at the 84th annual meeting of the Transportation Research Board (2005)
20. Zhou, X., Taylor, J.: DTALite: a queue-based mesoscopic traffic simulator for fast model evaluation and calibration. Cogent Eng. **1**(1), 961345 (2014)

Analysis in Kantorovich Geometric Space for Quasi-stable Patterns in 2D-OV Model

Ryosuke Ishiwata and Yuki Sugiyama

Abstract The two-dimensional optimal velocity (2D-OV) model, which consists of self-driven particles, reproduces a big variety of dynamical patterns as seen in biological collective motions (Sugiyama (2009) Natural Computing. Springer Japan, Tokyo [7]). We perform simulations of the 2D-OV model in a simple maze. Dynamically stable patterns are observed from the simulation results. The stability of the patterns seems to be related to a kind of degeneracy of a state. In order to look for some physical quantity, which can indicate the relation between the stability and the degeneracy, we construct a geometric space based on the Kantorovich distance among patterns and represent the changing of flow pattern as the trajectory in the geometric space. As a result, a point corresponding to distributions of particles for the quasi-stable pattern converges to the localised region in the space.

1 Two-Dimensional Optimal Velocity Model

The optimal velocity model is first introduced for a mathematical model of traffic flow as a motion in one dimensional space. The model well describes the phenomena of forming a traffic jam.

The model is easily extended to a two-dimensional version (2D-OV model) [6]. Every particle moves as the equation of motion as

$$\frac{d^2}{dt^2}\mathbf{x}_i(t) = a\left\{\sum_j \mathbf{V}(\Delta\mathbf{x}_{ij}(t)) - \frac{d}{dt}\mathbf{x}_i(t)\right\}. \tag{1}$$

R. Ishiwata (✉) · Y. Sugiyama
Department of Complex Systems Science, Nagoya University, Nagoya, Japan
e-mail: ishiwata@phys.cs.is.nagoya-u.ac.jp

Y. Sugiyama
e-mail: sugiyama@phys.cs.is.nagoya-u.ac.jp

Fig. 1 Illustration for the
interaction of 2D-OV ith
particle moving with the
velocity $\dot{x}_i$ interacting with
jth and kth particles
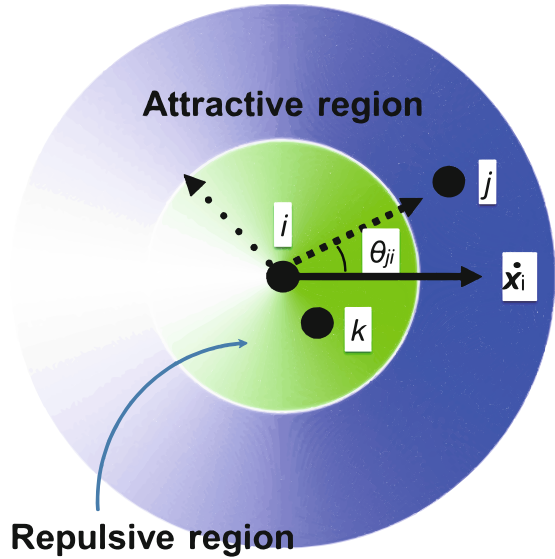
$\mathbf{x}_i$ is the position of a particle. $\varDelta\mathbf{x}_{ij} = \mathbf{x}_j - \mathbf{x}_i$ is the difference between two particles.
$\mathbf{V}$ is the interaction between two particles, so called an optimal velocity function.

$$\mathbf{V}(\varDelta\mathbf{x}_{ij}) = f(r_{ij})(1 + \cos\theta_{ij})\,\mathbf{n}_{ij}, \tag{2}$$
$$f(r_{ij}) = f_0\{\tanh m(r_{ij} - d) + c\}, \tag{3}$$

where r_{ij} is the distance of two particles, and $\mathbf{n}_{ij}$ is a unit vector for the direction
of the jth particle to the moving direction of ith particle. The strength of the inter-
action depends on r_{ij}, and is polarised in the direction of motion by $(1 + \cos\theta_{ij})$,
which expresses asymmetric interaction. The parameter c, $(-1 < c < 1)$, controls
the threshold of attractive and repulsive interactions. According to the value c, each
particle surrounding the ith particle contributes to an interaction dependent of the
distance, which is illustrated in Fig. 1. The model is applicable to a pedestrian flow
and collective bio-motion [2, 5].

The 2D-OV particles show several pattern-formations for group motions after
a relaxation time, depending on the control parameter c. For example, a cluster
flow like a fleet at $c = 0.0$ is organised, as shown in Fig. 2a. In this case, particles
have a repulsive interaction in short distance (exclusive behaviour) and an attractive
interaction in long distance (following behaviour). In another example at $c = 1.0$,
particles have only attractive interaction at any distance. Particles form several sizes
of moving strings bending easily as shown in Fig. 2b, owing to the dominance of
following behaviour. In this paper, we use this case for further study.
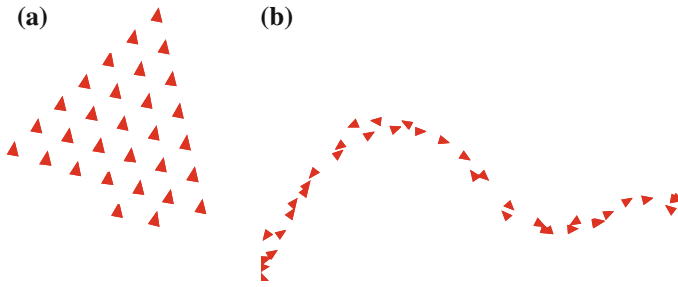
Fig. 2 Collective motions of 2D-OV particles. A cluster flow of 2D-OV particles at $c = 0.0$. All particles move in the same direction with the same velocity forming a homogeneous distribution with hexagonal pattern (**a**), A string-like flow of 2D-OV particles at $c = 1.0$. Each particles move along a formed string. A string moves with deforming continuously (**b**)

2 Formation of a Solution for a Maze

Collective bio-motions create several phenomena of collective behaviours, so called 'group intelligence'. For example, amoeboid organisms solve a maze, that is, they organise the optimal path between the two locations of food in a maze [4].

Similarly, collective motions of 2D-OV particles organise an optimal path of flow pattern between two gates connected with the periodic boundary condition in a maze. The wall of the maze is an elastic boundary.

We set a simple maze shown in Fig. 3. An appropriate number of 2D-OV particles for $c = 1.0$, $a = 20$, $N = 130$, are initially distributed homogeneously in random motions. In the intermediate state, particles create several sizes of moving strings. After a relaxation time, they compose a unit string with moving particles, which solves a maze.

There are two quasi-stable solutions as shown in Fig. 4. One is Fig. 4a, which shows a solution of motions of the optimal path reflecting two elastic opposite boundaries. The second one is the solution of the periodic boundary, as shown in Fig. 4b, where particles move along the optimal path through the gate of the periodic boundary.

Fig. 3 A simple maze filled with 2D-OV particles distributed homogeneously in random moving

(a)   **(b)**
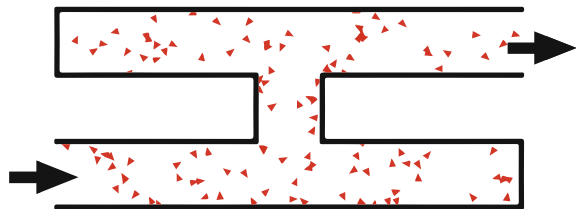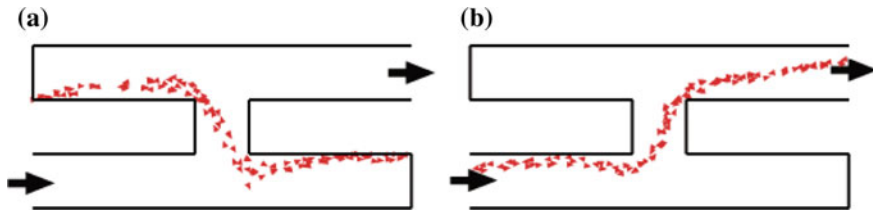
Fig. 4 Two optimal patterns formed by motions of OV particles. The motions of particles: by elastic reflection by two opposite walls (**a**); the motions of particles through the two gates connected with periodic boundary condition (**b**)

3 Kantorovich Metric Space

We briefly present the metric space of measuring affinity of patterns [1] in the context of a many-particle system. A pattern is represented to a point in this space, and we can measure how similar the two patterns are, using the distance of two corresponding points.

We denote two patterns as P_i and P_j. We set each pattern to consist of N identical particles. A pattern is given by the positions of N particles. Suppose that we transport all particles of a pattern P_i to another pattern P_j. We have several plans of transportation of points from P_i to P_j in Fig. 5. The distance of affinity between two patterns is defined by the minimum cost of transportation from a pattern to another pattern, which is denoted by $Kr(P_i, P_j)$. Cost should be appropriately defined as the situation of the problem. In our case, we simply define the total sum of path lengths for transportation as a cost. In mathematics, this is related to the 'Optimal Transportation problem' [8].

In our context for dynamics of many-particle system in pattern formation, we consider a time sequence of patterns: $P(t_1) \rightarrow P(t_2) \rightarrow P(t_3) \rightarrow \cdots \rightarrow P(t_n)$. Now, we define the 'affinity matrix' as $B_{i,j} := Kr(P(t_i), P(t_j))$, meaning measuring the affinity of every pair between each pattern appearing in the whole sequence. We

Fig. 5 Transport of particles from pattern P_i, at their positions, $x_1, x_2, \cdots, x_N$, to another P_j at $x'_1, x'_2, \cdots, x'_N$
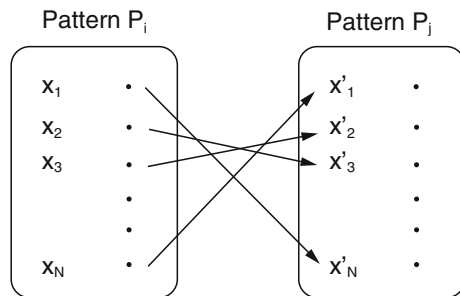
Transportation of the points
of particles from P_i to P_j

Fig. 6 Time evolution of forming pattern in the Kantorovich metric space: Time steps goes from *red* through *blue to green*. The first quasi-stable pattern as Fig. 4a corresponds to the clump of states with a *purple colour*. The second quasi-stable pattern as shown in Fig. 4b corresponds to the states *coloured green*
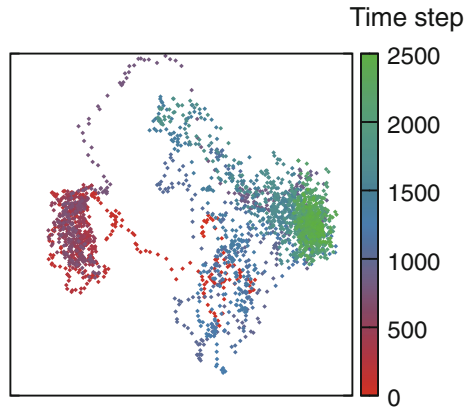
diagonalise the matrix and obtain the eigenvectors ψ and corresponding eigenvalues λ as

$$\psi_1, \quad \psi_2, \quad \ldots, \quad \psi_r$$
$$\lambda_1 > \lambda_2 > \cdots > \lambda_r, \tag{4}$$

where $r = rank\ B$.

We represent a pattern P_i consisted with particles as a vector in the Kantorovich metric space as

$$c_1\psi_1 + c_2\psi_2 + \cdots, \tag{5}$$

which is mapped in Euclidean space R^r, We usually take the first two eigenvectors with two largest eigenvalues for constructing sufficiently coarse variables for describing a pattern. In the present case of group formation with particles, it is sufficient to describe a difference between patterns. This means a dimensional reduction of degrees of freedom of particles R^N to $R^r \sim R^2$ [3].

Thus, we have constructed the Kantorovich metric space describing a pattern in the real space as a point in that space. The time evolution of forming a pattern consisting of many particles is represented as a trajectory in the low dimensional Kantorovich metric space.

4 Time Evolution of Forming Optimal Flow Patterns in the Kantorovich Metric Space

Starting the initial pattern as Fig. 3, which is at the centre point in the Kantorovich space, the whole time evolution of group formation in 2500 time steps is shown in Fig. 6.

There are two quasi-stable patterns forming in the period of 2500 time steps. The first formed pattern is the optimal path moving and reflecting between two opposite boundaries as shown in Fig. 4a. After a while, the second pattern emerges, which is the optimal path through the periodic boundary as shown in Fig. 4b. Either of the two quasi-stable patterns of particle-flow is represented as a localised region in the Kantorovich metric space.

5 Discussions

We have shown quasi stationary states in 2D-OV particles as macroscopic patterns as optimal flow in a maze. The patterns are represented as points in localised regions in a low dimensional Kantorovich metric space. We would like to insist that we have shown an example that the quasi stationary state in a non-equilibrium many-body system can be represented as a localised region in the Kantorovich metric space, which is constructed with the basis of a few macroscopic variables.

Time evolution of a system converging to a localisation in a space of variables indicates that the time sequence of changing a state can be expressed by a gradient flow of some potential in this space. We have a possibility to find such a potential using a few macroscopic variables made of microscopic variables in an original many-body system. We suppose that the potential is some sort of 'free energy' or 'thermo dynamical potential' for the non-equilibrium many-body system, which controls a state of the system for changing its stability.

Actually, we may understand the search of a solution in a maze using 2D-OV particles as follows. Group motion of 2D-OV particles for $c = 1$, which has purely attractive interaction, form a free moving string with continuous deformation of a shape. This indicates the formed pattern has continuous degree of freedom for bending freely. This corresponds the high degeneracy of ground state of a 'thermo dynamical potential'. When the 2D-OV particles for appropriate number put in a maze, they spontaneously form a flow pattern fitting the boundary conditions of the maze, that is finding a solution of the maze as an optimal flow.

References

1. Baba, A., Komatsuzaki, T.: Construction of effective free energy landscape from single-molecule time series. Proc. Natl. Acad. Sci. U.S.A. **104**(49), 19297–19302 (2007)
2. Ishiwata, R., Sugiyama, Y.: Flow instability originating from particle configurations using the two-dimensional optimal velocity model. Phys. Rev. E **92**(6), 062830 (2015)
3. Miura, Y., Sugiyama, Y.: A coarse analysis method using diffusion maps: Application to bifurcation analysis of the optimal velocity model. New J. Phys. (Submitted)

4. Nakagaki, T., Yamada, H., Tóth, A.: Maze-solving by an amoeboid organism. Nature **407**(6803), 470 (2000)
5. Nakayama, A., Hasebe, K., Sugiyama, Y.: Effect of attractive interaction on instability of pedestrian flow in a two-dimensional optimal velocity model. Phys. Rev. E **77**(1), 016105 (2008)
6. Nakayama, A., Sugiyama, Y.: Group Formation of Organisms in 2-Dimensional OV Model. In: Traffic and Granular Flow'03, pp. 399–404. Springer Berlin Heidelberg, Berlin (2005)
7. Sugiyama, Y.: Asymmetric interaction in non-equilibrium dissipative system towards dynamics for biological system. In: Natural Computing, pp. 189–200. Springer Japan, Tokyo (2009)
8. Villani, C.: Optimal transport: old and new. Die Grundlehren der mathematischen Wissenschaften, Springer (2009)

Fractal Analysis of Empirical and Simulated Traffic Time Series

Thomas Zaksek and Michael Schreckenberg

Abstract Time series can show signs of fractal and multi-fractal behaviour. An analysis from this perspective can unearth features of time series that remain hidden for analysis with standard statistics. We analyse the multi-fractal spectra of traffic time series with the help of Multi-fractal Detrended Fluctuation Analysis (MDFA). Empirical time series of traffic flows and velocities measured by loop detectors are compared with time series gathered from traffic simulations. As a second focus, we analyse multi-fractal features of time series from different vehicle classes, i.e. passenger and transport traffic.

1 Introduction

Time series can not only describe systems with fractals features (e.g. systems with chaotic behaviour and strange attractors), but also the graph of a time series itself can be a fractal (e.g. time series of full developed turbulence or financial time series like the S&P500). Not only statistical self-similarity but also roughness of time series is quantified by signatures of fractal behaviour like box counting dimension [3].

Some studies indicate that time series of traffic data show fractal and especially multi-fractal behaviour [10]. In this context velocity traffic time series from Beijing were analysed [11]. We present an analysis of empirical and simulated time series of German motorway traffic with focus on multi-fractal spectra.

The empirical traffic data for this study were gathered from the motorway network of the German State of North Rhine-Westphalia. Based on empirical traffic data, synthetic traffic time series are created from simulations with a cellular automaton approach using a Nagel-Schreckenberg-alike model.

T. Zaksek (✉) · M. Schreckenberg
Physics of Transport and Traffic, University of Duisburg-Essen, Essen, Germany
e-mail: thomas.zaksek@uni-due.de

M. Schreckenberg
e-mail: michael.schreckenberg@uni-due.de

We obtain multi-fractal spectra for time series of velocity and flow with Multi-fractal Detrended Fluctuation analysis (MDFA) and also calculate estimates for fractal dimensions. This indicators of (multi-)fractal behaviour are used to compare the empirical data with the simulated data and also to compare time series of different classes of vehicles. We try to give explanations for the differences and similarities in the multi-fractal spectra of the traffic time series.

2 Methodology

In this study we use a multi-fractal formalism that gives us multi-fractal spectra by calculating a hoelder grain exponent α and plotting the graph of the scaling function $\tau(\alpha)$ versus α.

A Multi-fractal Detrended Fluctuation Analysis [5–7] ansatz is used here on the assumption that traffic time series most of the time have trends on many scales (e.g. intra day because of commuters, weekly because of workdays and weekend, or seasons). As a first step, we profile the time series:

$$X_p(i) = X(i) - \langle X \rangle, \quad i = 1 \dots N$$

for a discrete time series X with length N.

The time series is divided in dyadic intervals of degree n (i.e. 2^n non overlapping intervals with length 2^{-n} each).

$\alpha_{n,k}$ is the exponent such that the coefficients

$$D(I_n(k)) = \left(\frac{1}{\#I_n(k)} \sum_{\chi \in I_n(k)} \left(X_p(\chi) - P_i^{dp} \right)^p \right)^{1/p}$$

show a power law behaviour to the interval size:

$$\alpha_{n,k} = \frac{\log(D_x(I_n(k))}{\log(2^{-n})}$$

(with $I_n(k)$ the kth dyadic interval at scale n, $\#I$ the cardinality of the points in I, P_i^{dp} a polynomial fit of degree dp fitting the $X \in I$).

Due to method and partitioning in dyadic intervals, the grain exponents α drift with dependency on scale n. It is necessary to normalise the signal (see [6]).

Now, we calculate the Legendre spectrum

$$\tau_{X,n}^*(\alpha) = \inf_{q \in \mathbb{R}} \{\alpha q - t_{x,n}(q)$$

with

$$t_{x,n}(q) = -\frac{1}{n} \log_2 \sum_{I \in \xi_n} 2^{-nq\alpha_X(I)}$$

for a range of $q \in [-50, 50]$.

We analyse the multi-fractal spectrum $\tau^*(\alpha)$ over α at different scales n. Qualitatively the width of these spectra relate to multi-fractal properties of the time series. Theoretically, each value for the width above zero gives us some degree of multi-fractality, but in practice, small values (<0.1) are just some artefact because of the finite length or resolution of the time series. The peak of the spectra (if it exists) and mean of the spectra can be both interpreted as an estimator of the likeliest fractal dimension of the time series.

3 Empirical Data and Simulations

We use measurements from loop detectors on the A3 freeway from the German province of North Rhine-Westphalia, located north of Cologne. The time series in this study are gathered from a detector at the second lane (three lanes altogether) and include separate transport traffic (including heavy trucks, light trucks and buses). The data set we analyse includes flow and velocity, separated into passenger car and transport traffic.

For comparison we use simulated traffic data from the autobahn.nrw project. The simulation uses a multi-lane variety of the Nagel-Schreckenberg-Model [1, 2, 4, 8]. The simulated network spans the whole freeway network of North Rhine-Westphalia. Every minute the simulation runs trough a tuning process where the state of the simulation is compared and balanced with real time empirical data. In the simulated network virtual detectors are placed to gather the time series. The placement of the virtual detectors covers approximately the same positions as the corresponding detectors on the real freeway. For an in depth description of the autobahn.nrw simulation see [1].

For this study we use a time series of traffic flow and velocity with 16,348 data points (about 1 week of data, a power of two was chosen for convenience with dyadic scales). Each data point corresponds to one minute. Traffic flow is cumulated over one minute, velocity is averaged over one minute. Figure 1 shows a comparison of an empirical traffic flow time series and the corresponding simulated traffic flow time series.

Fig. 1 Empirical and
simulated time series (traffic
flow, 2048 min)
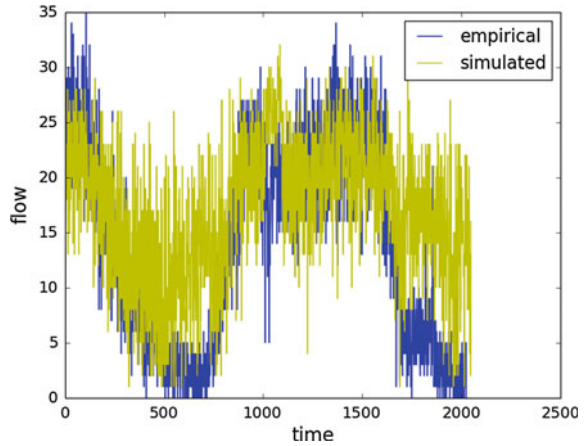
4 Results and Discussion

Figure 2 shows a comparison of multi-fractal spectra for empirical and simulated
passenger car velocity time series for $n = 8, \ldots, 11$. Both spectra show signs of
multi-fractal behaviour with a width of 0.5 respectively 0.7. The estimated likeliest
fractal dimension for these time series is about 1.8 respectively 1.7.

Figure 3 shows a comparison of multi-fractal spectra for empirical and simulated
traffic flow time series for $n = 8, \ldots, 11$. Both spectra show weaker multi-fractal
behaviour than the velocity time series with a width of about 0.3 to 0.4. The estimated
likeliest fractal dimension for these time series is about 1.9. For traffic flow, both
spectra resemble each other much more than for the velocity time series.

Fig. 2 Multi-fractal
spectrum of passenger traffic
velocities. Empirical
measurements and simulated
data with 16,348 data points
each
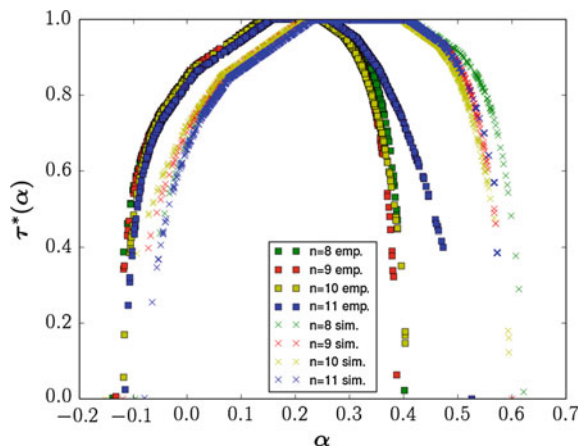
Fig. 3 Multi-fractal spectra of traffic flows. Empirical measurements and simulated data with 16348 data points each
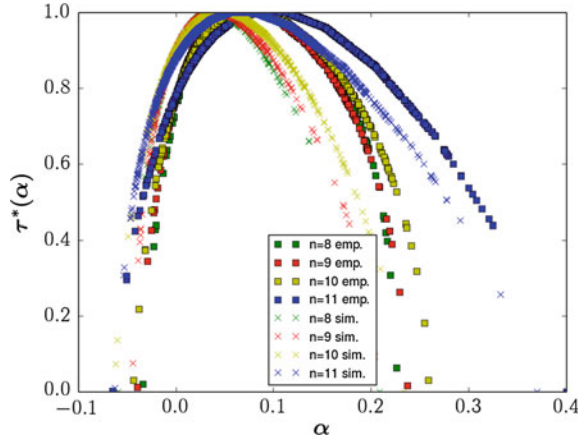
In [9] it was shown that multi-fractal properties of velocity time series can origin both from long range correlations and a broad probability distribution. We suppose that the differences between the spectra of empirical and simulated velocity time series originate in part from the fact that the cellular automata model uses a step wise car velocity and acceleration. This may lead to a different probability distribution, a more unsteady behaviour of the single cars and as a result to a rougher, more volatile velocity time series. On the other hand, the traffic flow time series from simulated data resembles the time series from empirical data. This may be due to both empirical and simulated measurements are integer count data and the simulation by construction resembles the distribution of the empirical flows. The weaker signs of multi-fractal behaviour for the flow compared to the velocity may originate from the less volatile nature of the traffic flow and its relative insensitivity to changes of the traffic state (e.g. free flow and synchronised traffic may have the same amount of traffic flow).

In Figs. 4 and 5 part of the time series is split into windows of 2048 data points. We compare the multi-fractal spectra of each of these intervals. On a qualitative level, there is not much difference between the different intervals, both for empirical and simulated data. The slight differences may be due to the changing traffic situation on different days. Overall, this shows that multi-fractal analysis with MDFA is a robust tool for analysis of traffic time series. Multi-fractal spectra seem to have a low dependence concerning specific date and time of the day.

Figures 6 and 7 compare multi-fractal spectra of velocities for passenger and transport traffic and the multi-fractal spectra of total traffic flow and transport traffic flow. The multi-fractal spectra of the transport traffic velocity differs wildly from the spectrum of the passenger car velocity. The former shows a much narrower spectrum, i.e. the behaviour of these time series seems to be more mono-fractal than multi-fractal. The traffic flow time series on the other hand show only a slight shift of the peak. The striking difference in the velocity time series may arise from the
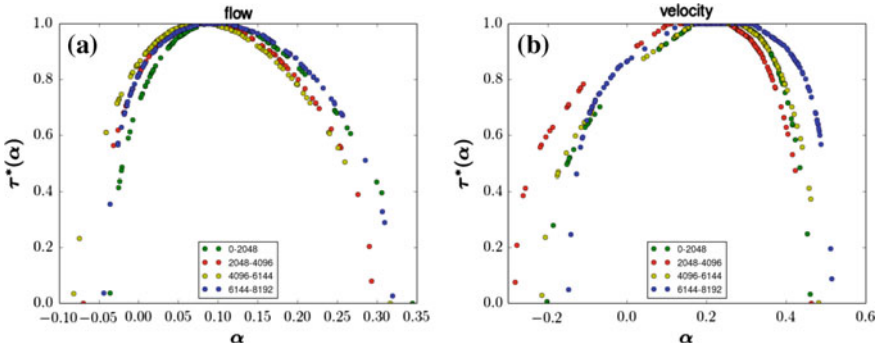
Fig. 4 Intervals of 2048 data points, empirical data set
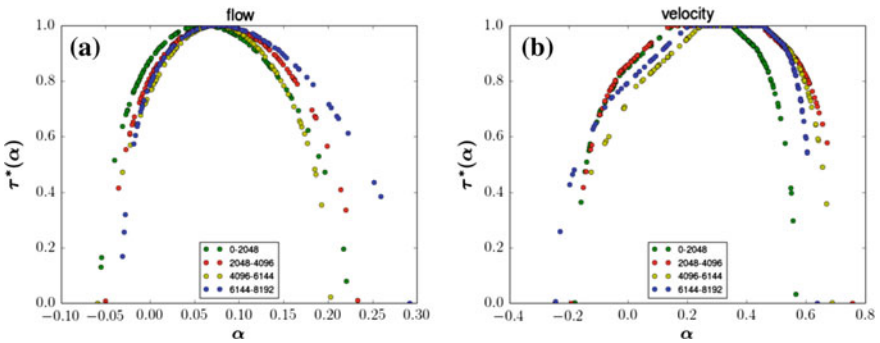
Fig. 5 Intervals of 2048 data points, simulated data set

Fig. 6 Multi-fractal spectra of traffic velocity time series. Comparison between passenger and transport velocities
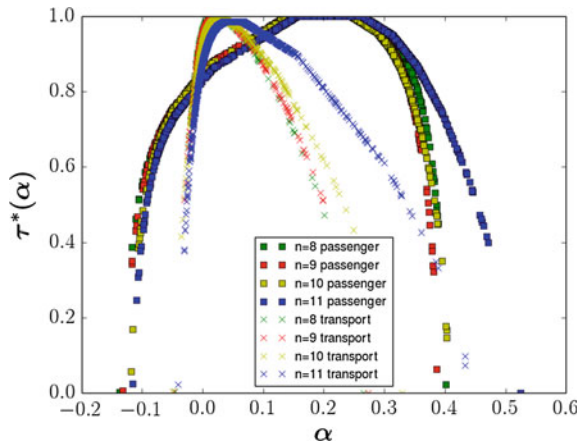
Fig. 7 Multi-fractal spectra
of traffic flow time series.
Comparison between time
passenger and transport
traffic flow
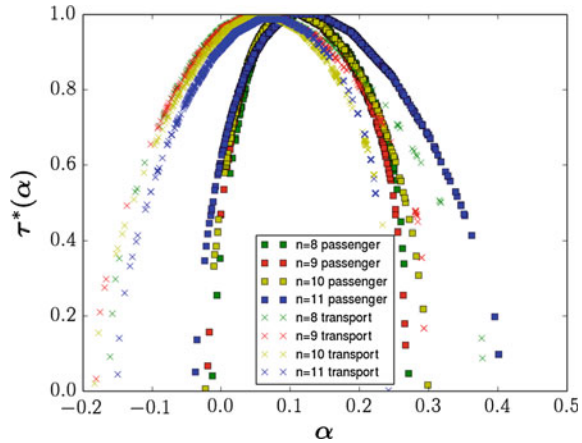
fact that transport traffic in general has a much more steady pace due to speed limits
and temporary driving in large convoys.

There arise some apparent questions from the multi-fractal point of view on traffic
time series. If and how fractal behaviour of traffic time series changes with time of
the day, different traffic situations, a different share of heavy transport traffic? Can
we use fractal analysis for traffic forecasting and to improve traffic simulations? How
different traffic models differ in their multi-fractal behaviour?

Conclusions

This paper discusses the multi-fractal behaviour of different traffic time series.
We analyse multi-fractal spectra generated with MDFA. Especially the spectra
of velocity time series show signatures of multi-fractal behaviour. We found
deviations of the spectra of simulated time series compared to spectra from
empirical data. We also show that the multi-fractal spectra of transport traffic
velocities differ strikingly from passenger traffic. Multi-fractal analysis can be
another helpful tool to characterise and compare traffic time series apart from
standard statistics.

References

1. Brügmann, J., Schreckenberg, M., Luther, W.: A verifiable simulation model for real-world microscopic traffic simulations. Simul. Model. Pract. Theory **48**, 58–92 (2014)
2. Chrobok, R., Pottmeier, A., Wahle, J., Schreckenberg, M.: Traffic forecast using a combination of on-line simulation and traffic data. In: Fukui, M., Sugiyama, Y., Schreckenberg, M., Wolf, D. (eds.) Traffic and Granular Flow 01, pp. 345–350. Springer, Berlin Heidelberg (2003)
3. Davies, S., Hall, P.: Fractal analysis of surface roughness by using spatial data. J. R. Stat. Soc. Ser. B (Stat. Methodol.) **61**(1) (1999)
4. Habel, L., Schreckenberg, M.: Asymmetric lane change rules for a microscopic highway traffic model. In: Cellular Automata—11th International Conference on Cellular Automata for Research and Industry, ACRI 2014, pp. 620–629 (2014)
5. Kantelhardt, J.W., Zschiegner, S.A., Stanley, H.E.: Multifractal detrended uctuation analysis of nonstationary time series. Phys. A **316**, 87–114 (2002)
6. Loiseau, P., Médigue, C., Gonçalves, P., Attia, N., Seuret, S., Cottin, F., Chemla, D., Sorine, M., Barral, J.: Large deviations estimates for the multiscale analysis of heart rate variability. Phys. A: Stat. Mech. Appl. **391**(22), 5658–5671 (2012)
7. Meyer, M., Stiedl, O.: Self-affine fractal variability of human heartbeat interval dynamics in health and disease. Eur. J. Appl. Physiol. **90**(3–4), 305–316 (2003)
8. Nagel, K., Schreckenberg, M.: A cellular automaton model for freeway traffic. Journal de Physique I **2**(12), 2221–2229 (1992)
9. Shang, P., Lu, Y., Kamae, S.: Detecting long-range correlations of traffic time series with multifractal detrended fluctuation analysis. Chaos, Solitons & Fractals **36**(1), 82–90 (2008)
10. Vojac, S., Vehel, J., Danech, M.: Multifractal description of road traffic structure. In: 7th IFAC/IFORS Symposium on Transportation Systems: Theory and Application of Advanced Technology (1995)
11. Wang, J., Shang, P., Cui, X.: Multiscale multifractal analysis of traffic signals to uncover richer structures. Phys. Rev. E **89**(3), 032916 (2014)

Wide Scattering of Nagel-Schreckenberg Fundamental Diagram Under Traffic Bottlenecks

Wei Liang Quek and Lock Yue Chew

Abstract Based on current traffic flow studies, there are several traffic cellular automaton (TCA) models, in which the wide scattering of flow-density data are observed. In this study, we propose that the physical mechanism behind the observed wide scattering is the variability of cluster formation in congested traffic. By simulating road bottlenecks on highways using the Nagel-Schreckenberg (NaSch) model, varying degrees of wide scattering is observed. Numerical analysis of the results shows a strong correlation between the variance in the number of clusters and the width of scattering in the flow-density data. By studying the microscopic dynamics of the NaSch model, we proposed the physical mechanism of wide scattering in TCA models to be the heterogeneity of cluster formation in congested traffic flow. In addition, the results were compared with Tian (2012)'s Average Space Gap Model (ASGM) and through qualitative analysis, we suggest that the wide scattering observed is due to the AGSM mechanism favouring statistically unfavourable cluster configurations.

1 Introduction

In the past 30 years, there has been a large variety of studies on vehicular traffic, which range from quantitative studies of extensive traffic data to the modelling of traffic flow through computer simulations. In general, the common goal of these studies is to gain an understanding of the nature of traffic flow and how various traffic patterns (congestions) emerge in homogeneous traffic flow. One such feature is the flow-density relation of vehicular traffic, which is also known as the fundamental diagram.

W.L. Quek (✉) · L.Y. Chew
Division of Physics and Applied Physics, School of Physical and Mathematical Sciences,
Nanyang Technological University, Singapore, Singapore
e-mail: S130019@e.ntu.edu.sg; quekweiliang@gmail.com

L.Y. Chew
e-mail: lockyue@ntu.edu.sg

Nagel and Schreckenberg proposed one of the most used simulation models [4], the Nagel-Schreckenberg (NaSch) Cellular Automata (CA) model, in 1992. By modelling the microscopic behaviour of cars, the model exhibits spontaneous emergence of congestion in homogeneous traffic flow (without bottlenecks), which was later reproduced experimentally by Sugiyama [7]. The fundamental diagram obtained from this model shows a roughly functional relationship between flow and density, which highlights 2 distinct phases in traffic flow—free flow and congestion. When the results are compared to real traffic, the existence of two distinct phases were also apparent, even though real traffic has a wider spread of flow-density data in the congested phase [1].

In Three Phase Traffic Theory (3PT) [2], Kerner proposed that the origins of wide scattering is not trivial. Traffic is classified into 3 phases: free flow (F), synchronised flow (S), and wide moving jam (J), with the (S) phase covering a 2-D region in the flow-density plane. To capture this phase, Kerner proposed the Kerner-Klenov-Schreckenberg (KKS) model [3], which is a NaSch model modified with mechanisms of anticipation and competition effects. This leads to a numerical fundamental diagram that better reflects the wide scattering of flow-density data.

While the KKS model is successful in reproducing many traffic features and patterns, its critics [6] found it too complex in its description of the physics of captured traffic features. For example, the exact mechanisms that lead to wide scattering in TCA models were not established [6]. This drives current research in working on a simpler model that is able to capture various phenomena that the traditional two-phase models failed to. Out of these studies, a few captured the wide scattering in TCA models. Tian [8] proposed the Average Space Gap Model (ASGM), which is a NaSch model modified with slow-to-start and anticipation mechanisms. Neto [5] proposed the defensive driving model (DD Model), which is also a NaSch Model modified with defensive reactions. Compared to the KKS model which requires 13 additional mechanisms [6], these models are much simpler with significantly less added mechanisms (<5). Despite their simpler nature, both models are able to capture a certain degree of wide scattering in their simulated flow-density data. In this study, we aim to investigate a physical mechanism that could lead to wide scattering in TCA models using a simple NaSch model modified with a traffic bottleneck. With that, the relationship between this mechanism and the existence of wide scattering in various TCA models will be studied quantitatively and qualitatively.

2 Preliminary Studies

2.1 Simulation Model

In an exploratory study of simulating a road bottleneck, we found that one of the effects of bottlenecks in the NaSch simulation is a wider spread in the numerical flow-density data plot in the congested phase (Fig. 1). In traffic studies, a road bottleneck has been defined as the result of the merging of a two-lane traffic flow into a single
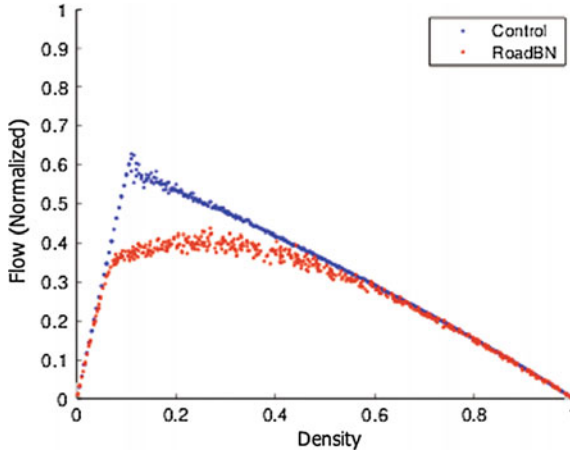
Fig. 1 Plot of NaSch fundamental diagram with and without the effects of road bottleneck

Fig. 2 Illustration of implementation of bridge bottleneck which was proposed in [9]

lane. The general concept of our implementation of road bottleneck is based on the 'bridge bottleneck' described by Xiao [9], and illustrated in Fig. 2. While the details of this implementation are documented in the Appendix, the crucial point is that we are able to obtain a tunable parameter, which systematically varies the width of scattering of the fundamental diagram.

The typical parameters used in our study are given in Table 1. Since this study is carried out only with periodic boundary conditions, i.e., $Position(L + 1) = Position(1)$, the number of cars is conserved. In addition, the road bottleneck involves an additional tunable parameter, the Lane interface probability.

Wide scattering of flow-density states is defined as the existence of a multitude of steady flow-density states. While one of the motivations behind Kerner's 3PT traffic is wide scattering, the width of scattering was not properly defined throughout his studies. As such, we have to define our own measure. By definition, the absence of wide scattering means that flow-density has a functional (1–1) relation. Hence, for

Table 1 Parameters used in this study

Parameter	Symbol	Value
Maximum velocity	v_{max}	6
Random deceleration	p	0.2
Road length	L	1000
Simulation time	t	1000
Transient time	t_0	$5L = 5000$
Lane interface probability	p_{loop}	0.5

Fig. 3 *Plot* of width of scattering versus tunable parameter (loop probability). Results taken from an average of 10 realisations of 10,000 time-step simulations
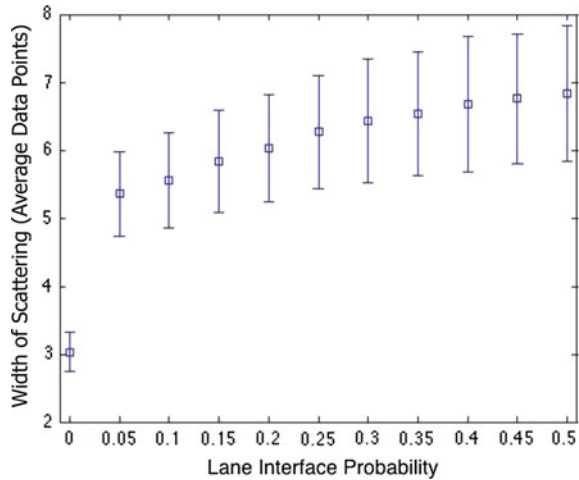
each particular density point, we can define the width as the number of flow rate data that corresponds to that density. Since the focus of this study is the fundamental diagram as a whole (over the full density range), the width of scattering presented will be value averaged over the discretised values of density, which in this case is 1000 data points (step size of density = 0.001).

Figure 3 shows the relationship between the loop interface probability (p_{loop}) and the width of scattering. Since this TCA simulation results in a monotonic relationship between width of scattering and a tunable parameter, this model can be used as a systematic study between the width of scattering and the proposed mechanism.

2.2 Proposed Mechanism

In the congested state, vehicles bunch up randomly, forming clusters of various sizes. From the rules of the NaSch model, cluster formation has a direct effect on the fluctuation of the flow rate. While the stochasticity of the NaSch CA model does contribute to the flow rate variations, the hypothesis of this study is that wide scattering, i.e., macroscopic flow variations is due to the variability of clustering in congested traffic states.

With this hypothesis, we will go on to discuss the objective function of our study. In this study, a cluster is defined as one or more vehicles connected spatially without any space between them. With the cluster count—no. of clusters—fluctuating in time, the standard deviation of this fluctuation quantifies this variability. Using the varying degrees of wide scattering obtained in our simulation work, Fig. 4 plots the standard deviation of the cluster count as a function of the width of scattering. As presented, the monotonic relation between the variance of cluster count with the width of scattering supports our hypothesis that variability in cluster formation could result in macroscopic flow variations in the form of wide scattering.

Fig. 4 *Plot* of cluster variance versus width of fundamental diagram. Cluster variance taken as the standard deviation of 10,000 simulations. Width is derived from 10,000 flow-density data points
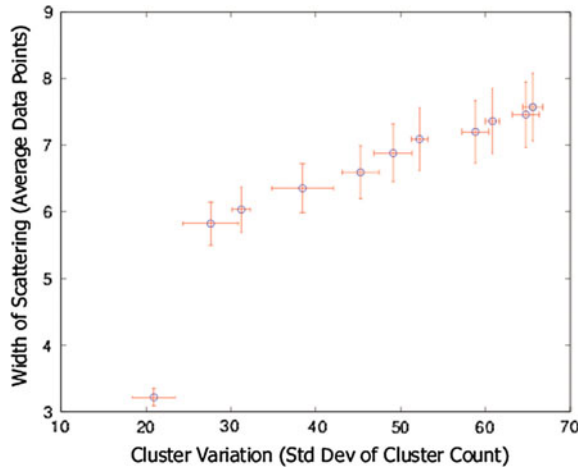
3 Analysis on Existing TCA Models

In the previous section, we proposed the methods that cluster formation could lead to wide scattering in TCA models. This is supported by numerical results that displays a strong association between the width of scattering and the variance of the time series cluster count. However, before further conclusions are made, it is important to take a closer look at the wide scattering thus far. The weakness of this study is that it could be overly ambitious to claim that the wide scattering results we obtained under traffic bottlenecks have the same nature as those claimed by the other TCA models. Hence in this section, we will apply a similar approach on one of the two mentioned studies: the Average Space Gap Model (ASGM) by Tian [8].

The average space gap model is a TCA model based on the NaSch model, modified with slow-to-start and velocity anticipation rules. The values for the parameters are shown in Table 2.

Using the same approach as before, Table 3 is the tabulation of the cluster variability and the width of scattering of the fundamental diagram, with and without the added ASGM mechanism.

Table 2 Parameter values used, values taken from [8]

Parameter	Value
ρ_a	0.95
ρ_b	0.60
$\rho_c = p$	0.20
a	2
b	1
t_c	6
m_l	3

Table 3 Width of scattering and cluster variation between ASGM and NaSch Model

	Width of scattering	Cluster variation
Control	49.5 ± 3.3	18.3 ± 0.4 (Mean = 136.2)
ASGM	76.7 ± 1.9	32.3 ± 0.7 (Mean = 64.9)

Data obtained for density = 0.16, sampled over 10 sets of 100 readings

As presented, the addition of the ASGM mechanism in the NaSch model increases the width of scattering by about 50 %. At the same time, we see that this increase corresponds with the increase in cluster variation, measured as the standard deviation of the cluster count. In fact, the percentage variation in cluster count increases from 13 to 50 %. This numerical result further supports our claim that the wide scattering in TCA model are highly associated and possibly caused by the increased variations of cluster formation.

However, unlike the previous studies, the ASGM does not provide a systematic way of varying the cluster count to substantiate the hypothesis. However, a qualitative analysis can be done based on the additional rules of the ASGM. These rules are the speed adaptation, and the slow-to-start rule.

Our hypothesis claims that wide scattering is a result of cluster variation in the TCA models. This is illustrated in Fig. 5. In this figure, the densities of both roads are the same. However, according to the rules of the NaSch model, their overall flow rates are 6 and 15 respectively.

For each car in the ASGM, the speed adaptation rule assesses the speeds of the preceding cars, and synchronises the vehicles speeds with the vehicles in front of them. With regard to clustering, this causes the system to favour a multiple single vehicle cluster, which are otherwise statistically unfavourable. This state corresponds to flow rates that were otherwise statistically unfavourable too. This accessibility to high flow rates are reflected as wide scattering of flow-density data.

The effect of the slow-to-start (STS) rule is the same, but instead it favours flow rates that are lower than those which are statistically favoured. The hypothesis behind the STS is that the vehicles stopped for an extended period of time will take a longer time to start up as compared to the vehicles that had stopped for a comparatively shorter time span. This results in the STS favouring large clusters because the vehicles take a comparatively longer time to leave the cluster than to join it. In our hypothesis, this configuration leads to very low flow rates, which are statistically unfavoured in
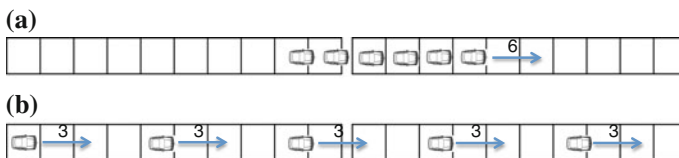
Fig. 5 Illustration of different cluster configurations in the NaSch model and how they could lead to a fluctuation of flow rates. Cluster configuration: cluster count = 1; flow rate = 6 **(a)**; cluster count = 6; flow rate = 15 **(b)**

the NaSch CA model. Hence, the same conclusion can be made regarding how this rule leads to the wide scattering of flow-density data.

To summarise, between the ASGM model and the NaSch model, the additional mechanism of the ASGM model only seems to accentuate the effects of extreme cluster configurations, which are otherwise statistically unfavourable. This leads to the system occupying comparatively more flow-density states, which is reflected in the observed wide scattering in the flow-density diagram.

4 Conclusion

In this study, we aim to propose a physical mechanism—the variations of cluster formation in congested traffic flow—which captures the wide scattering of flow-density data in traffic cellular automata (TCA) models. Using the standard deviation of cluster count fluctuation as the objective function, and a simulation of tunable width of scattering, we obtained a monotonic relationship that shows a strong association between the variations of clustering and the width of scattering.

An additional test of this hypothesis was done on the Average Space Gap Model (ASGM) [8], which also captures wide scattering in the flow-density data. While there is limited numerical analysis to supporting this argument, qualitative analysis presents how the wide scattering in the ASGM could be a result of the model favouring statistically unfavourable cluster configurations.

Appendix

The bridge bottleneck implemented by Xiao (2003) [9] involves splitting a road into 5 different segments, with $L_1 L_2$ and $L_4 L_5$ as 2 pairs of lanes and L_3 as the single bridge lane. Since each segment has its own specific boundary condition, the evolution rules are implemented separately for each lane. These conditions are:

1. At 2-lane-1-lane interface, only the car from one of the two lanes can enter L_3 at each time step
2. At the 1-lane-2-lane interface, there is a 50 % chance the car will enter either lane, L_4 and L_5 from L_3 at each time step

Since the rule 184 CA model [9] is an elementary model where vehicles can only move at unit velocity, implementing the bridge bottleneck as 5 different segments (L_1 to L_5) is still relatively simple and computationally efficient. However, the NaSch model involves the velocities that range from 0 to 6 and its evolution involves two parallel matrices (position and velocity). Hence, implementing the road bottleneck in the NaSch model in this manner will be highly inefficient. Since one of the successes of the NaSch CA model lies in the computational efficiency of the cellular automaton, modifications have to be made in order to preserve this aspect in the road bottleneck case.

Instead of splitting the simulation into 5 different road segments, we proposed to split the entire model into only two different loops called the primary and secondary

loops, with the primary loop containing three of the original lanes, and the secondary containing two. The new proposed loops are dynamical, such that the grouping changes for each time step under the following algorithm:

if $rand() < p_{loop} = 0.5$ **then**
  primary loop $= L_1 \rightarrow L_3 \rightarrow L_4$
  secondary loop $= L_5 \rightarrow L_2$
else
  primary loop $= L_2 \rightarrow L_3 \rightarrow L_5$
  secondary loop $= L_4 \rightarrow L_1$
end if

From there, the 4-step evolution rule will first be done on the primary loop and the secondary loop separately. Since the secondary loop is not connected to the single lane L_3, only one car from L_1 and L_2 can enter the single lane at each time step. This randomised selection of lanes as each time-step forms the 2-lane-to-1-lane (and vice-versa) interface condition similar to that of Xiao (2003). With the 4-step evolution taking these sets of lanes as a whole, and the choice of the loops taking care of the conditions at the interfaces, our implementation of the road bottleneck took 25.4 % of the time taken by Xiao's 5-segment implementation of the bridge bottleneck in the NaSch model.

Due to this proposed methods of implementing the road bottleneck as two dynamic loops, we are able to favour one of the lanes by varying the probability, p_{loop} of choosing each loop. The physical analogue of favouring one of the lanes is a street merging with a major highway. Most importantly, we are able to vary the width of scattering systematically as seen in Fig. 3.

References

1. Chowdhury, D., Santen, L., Schadschneider, A.: Statistical physics of vehicular traffic and some related systems. Phys. Rep. **329**(4), 199–329 (2000)
2. Kerner, B.S.: Introduction to Modern Traffic Flow Theory and Control. Springer, Berlin (2009)
3. Kerner, B.S., Klenov, S.L., Schreckenberg, M.: Simple cellular automaton model for traffic breakdown, highway capacity, and synchronized flow. Phys. Rev. E **84**, 046110 (2011)
4. Nagel, K., Schreckenberg, M.: A cellular automaton model for freeway traffic. Journal de Physique I **2**(12), 2221–2229 (1992)
5. Neto, J.P.L., Lyra, M.L., Da Silva, C.R.: Phase coexistence induced by a defensive reaction in a cellular automaton traffic flow model. Phys. A: Stat. Mech. Appl. **390**(20), 3558–3565 (2011)
6. Schnhof, M., Helbing, D.: Criticism of three-phase traffic theory. Trans. Res. Part B: Methodol. **43**(7), 784–797 (2009)
7. Sugiyama, Y., Fukui, M., Kikuchi, M., Hasebe, K., Nakayama, A., Nishinari, K., Tadaki, S.i., Yukawa, S.: Traffic jams without bottlenecks experimental evidence for the physical mechanism of the formation of a jam. New J. Phys. **10**(3), 033001 (2008)
8. Tian, J., Yuan, Z., Treiber, M., Jia, B., Zhang, W.Y.: Cellular automaton model within the fundamental diagram approach reproducing some findings of the three-phase theory. Phys. A Stat. Mech. Appl. **391**(11), 3129–3139 (2012)
9. Xiao, S., Kong, L., Liu, M.: A cellular automaton model for a bridge traffic bottleneck. Acta Mech. Sin. **21**(3), 305–309 (2005)

A General Scheme for Deterministic Microscopic Traffic Models. Part I: Theoretical Construction

Bo Yang and Christopher Monterola

Abstract We propose a theoretical construction of the master model for the deterministic microscopic traffic models with the assumption of identical drivers. The construction is based on a renormalisation like procedure that integrates out unimportant degrees of freedom. This leads to a universal mathematical structure of such models, enabling us to carry out a controlled expansion, allowing all deterministic microscopic traffic models to be compared and classified systematically. We illustrate the controlled expansion with a few examples. The theoretical construction also paves the way for us to obtain the master model from the microscopic empirical data, which will be discussed in *A General Scheme for Deterministic Microscopic Traffic Models. Part II: Empirical Verifications*.

1 Introduction

Modelling the traffic system has been the active field of research for both the physicists and the transportation engineers, due to its theoretical interest and practical applications [4, 8, 11]. While in many cases only macroscopic quantities such as flow and density are used for the applications of urban planning, they will not be sufficient when the flow and density are high and the interaction between vehicles can not longer be ignored. Good traffic models are thus needed that can capture the essential features of human driving behaviours. Such models are indispensable for the numerical simulation, which is an efficient and economic way of studying the urban planning and evaluation of new technologies such as the adaptive cruise control [6, 12, 13] and the urban intersection control [14].

B. Yang (✉) · C. Monterola
Complex Systems Group, Institute of High Performance Computing, A*STAR,
Singapore 138632, Singapore
e-mail: yangbo@ihpc.a-star.edu.sg

C. Monterola
e-mail: monterolac@ihpc.a-star.edu.sg

451

The traffic system is intrinsically difficult to model due to the non-linear interaction and the lack of symmetry. In the simplest possible case, the traffic flow is modelled as a one-dimensional flow of particles moving in a viscous media with anisotropic nearest neighbour interactions. The non-linear nature of the interaction makes the validation of the model difficult, since many features of the model can only be obtained numerically, with the time evolution very sensitive to the initial conditions. The lack of symmetry implies that there are very few constraints to the traffic theory and modelling. Indeed, in contrast to the more conventional physical systems, not only is there a lack of translational invariance both in space and time, even individual components are not identical to one another. This results in a plethora of traffic models being proposed in the literature. Even for the microscopic traffic models, many different models have been proposed with different assumptions and intuitions [8, 11]. Comparing numerical simulations with empirical data are further complicated by the fact that the empirical traffic flow cannot be easily controlled in the same way as a physical experiment.

The over-abundance of the microscopic traffic models reflects a lack of fundamental principles in the construction of such models. The real human driving behaviour is highly nuanced, and it is the goal of the simple models to capture only the important characteristics of such behaviour so as to make useful predictions of the dynamics of the traffic flow. It is thus important to have a theoretical framework to understand unambiguously the assumptions made in various models in a universal way, so that different models can be meaningfully compared. In addition, such framework should also allow empirical verifications of the assumptions made in the models at the microscopic level. The framework should also be general enough so as to be applicable to most, if not all, of the proposed microscopic traffic models, including the three-phase traffic models proposed in accordance to the three-phase traffic theory [8].

In this paper, we propose such a general framework in Sect. 2 that was explained in more details in [17], but here we illustrate it with more examples in Sect. 3. In Sect. 4 we briefly summarise our results and show how they can be connected to the empirical verifications described in *A General Scheme for Deterministic Microscopic Traffic Models. Part II: Empirical Verifications*, in which a more complete conclusion and discussion will be presented.

2   The Universal Mathematical Structure

We assume it is possible to model most of the essential empirical features with a single agent, and start with the most general model for such an agent, exploring its general mathematical structures based on a few simple physical arguments. Such mathematical structures are thus universal to any microscopic traffic models with the assumption of identical drivers, as we will illustrate with specific examples in Sect. 3.

2.1 The Master Model

In general, the driver decides to accelerate or decelerate based on his/her own velocity, as well as the distance and velocity of the vehicle in front of him/her. We assume all other factors, including the intrinsic stochasticity of the driving behaviour, have a much weaker effect, compared to the vehicle's own velocity and its interaction with the vehicle in front, so they can be properly averaged to obtain the following master model [11]:

$$a = f(h, v, \Delta v) \tag{1}$$

Here, a is the acceleration of the vehicle, v is its velocity, h is the bumper-to-bumper distance to the vehicle in the front, and Δv the approach velocity to the vehicle in the front. The functional form f is the renormalised model after unimportant degrees of freedom are averaged, including the variation of the driving behaviours between different vehicles [17]. It is thus potentially different from observing the behaviour of a single, or a few vehicles in an experimental setting, and is in general also a very complex function. All proposed microscopic models in the literature can be taken as its special cases, when the complex RHS of Eq. 1 is replaced by simple functions in the hope of still retaining the essential features of the common driving behaviours.

Due to the lack of the symmetry not much can be said about the possible forms of f, other than certain stability requirements [11] that are also based on the intuitive driving experience. We exploit the fact that now the traffic system is described for identical drivers, and make the reasonable assumption that for each headway h there exists one or more preferred velocity at which the driver will neither accelerate or decelerate. For a chain of vehicles travelling in one direction this corresponds to zero approach velocity, and all vehicles are equally spaced travelling at the same constant velocity. This state of the traffic flow, if undisturbed, will last forever, and this is the fundamental assumption of the traffic system we study, which implies the solutions to the following equation exist:

$$f(h, v, 0) = 0 \tag{2}$$

For a fixed headway h, the solutions give a set of optimal velocities $V_{op}^{(k)}$ such that $f\left(h, V_{op}^{(k)}, 0\right) = 0$. Note that in some models the optimal velocity function is shown explicitly [1, 2, 5, 7], while in other models it is not [15, 16]. The solutions of Eq. 2 show that the optimal velocity function is intrinsic for any deterministic model.

We thus define Eq. 1 as the master model of the deterministic microscopic traffic models with the assumption of the identical drivers travelling in a single lane without overtaking. Note that for the same vehicle density there may be more than one preferred or optimal velocities. The two-phase models are characterised by a unique optimal velocity at any vehicle density, whereby in three-phase models such relationship is no longer unique [8, 9].

2.2   The Controlled Expansion

We now proceed to assume the master model of Eq. 1 is analytic. For the traffic system consisting of many vehicles, all the variables in Eq. 1 are labelled with a subscript n, which is the car index. Note the function f is the same for all vehicles. The steady states are thus given by $h_n = h_0, v_n = V_{\text{op}}^{(k)}$. We can now undertake a well-defined Taylor expansion around these states as follows:

$$a_n = \sum_{p,q} \kappa_{p,q}\,(h_n)\,\left(v_n - V_{op}^{(k)}\,(h_n)\right)^p \Delta v_n^q \tag{3}$$

$$\kappa_{p,q}\,(h_n) = \frac{1}{p!q!} \left.\frac{\partial^{p+q} f}{\partial^p v_n \partial^q \Delta v_n}\right|_{\substack{v_n = V_{op}(h_n) \\ \Delta v_n = 0}} \tag{4}$$

Note that the expansion can be carried out for any $V_{\text{op}}^{(k)}$, if it is not unique. While Eq. 3 may potentially contain an infinite number of terms, it is mathematically equivalent to Eq. 1. In particular, for any specific traffic model with a given functional form of f, Eq. 3 can be carried out. The differences between any two specific models can be quantitatively characterised by the differences between $V_{\text{op}}^{(k)}$, and the set of the coefficients of expansions. It is also clear that in general the set of coefficients of expansion depends on h_n, each of them giving the relative importance of the driver's reacting to his/her velocity deviating from the optimal velocity and the approach velocity. Such reactions are thus dependent on the density of the traffic.

The universal mathematical structure of the microscopic models, as illustrated by Eq. 3, not only allows us to evaluate quantitatively the different assumptions built in the model, but also to simplify the model in a systematic way. Both the coefficients of expansion and the optimal velocity function are in general very complicated in Eq. 1, and can be replaced with simple functions as long as the essential features of the master model are retained. It is also generally the case that higher order terms in the Taylor expansion can be truncated because they are small, without affecting the quantitative and qualitative features of the numerical simulations [17]. Thus, seemingly very different models can actually be shown to be effectively similar, after the unimportant terms in the expansions are removed.

3   Case Studies of Existing Traffic Models

In this section we will employ the controlled expansion of some of the popular microscopic traffic models proposed in the literature, and to illustrate the main differences between these models under this general framework. We focus on popular two-phase traffic models. For the discussions regarding three-phase models more details can be found in [17].

3.1 Optimal Velocity Models

The optimal velocity models [1] are arguably the simplest class of traffic models that can especially capture the evolution of the wide moving jams from the dense traffic flow. The optimal velocity is explicitly defined in such models, and the most popular form is given by

$$a_n = \kappa \left(V_{\text{op}} (h_n) - v_n \right) + g \left(\Delta v_n \right) \tag{5}$$

Thus, the assumption here is that at any vehicle density there is only one optimal velocity, and only the lowest order of $\left(V_{\text{op}} - v_n \right)$ is kept. If the second term on the right is ignored, it is the original Bando's model [1]. If $g \left(\Delta v_n \right)$ is linear, then Eq. 5 is the full force model [7]; if it is non-linear with even powers, then Eq. 5 is the asymmetric full force model [2].

An important characteristic of the optimal velocity models is that all the coefficients of expansion are independent of the density. The cluster solutions of such simplified models are easier to understand with well-defined emergent properties [3, 10, 18]. From the empirical perspective, however, the human's response time and sensitivity to the vehicle's environment in general should depend on whether the road is empty or packed. It is thus reasonable to generalise the car-following models by making the parameters dependent on h_n in the appropriate way. We will now show this is implicitly done by other more realistic models proposed in the literature.

3.2 Intelligent Driver Model

The intelligent driver model [16] is a popular model proposed to more realistically simulate the human driver behaviour, with the following specific functional form:

$$a_n = a \left(1 - \left(\frac{v_n}{v_0} \right)^{\delta} - \left(\frac{h^* (v_n, \Delta v_n)}{h_n} \right)^2 \right) \tag{6}$$

$$h^* (v, \Delta v) = s_0 + s_1 \sqrt{\frac{v}{v_0}} + T v + \frac{v \Delta v}{2 \sqrt{ab}} \tag{7}$$

Comparing to the optimal velocity model, the acceleration and deceleration patterns as predicted by this model have a much better match to the empirical data from the sensor equipped vehicles. To explicitly compare the IDM model and the optimal velocity model, we carry out the controlled expansion by first finding the intrinsic optimal velocity function given by solving

$$1 - \left(\frac{v}{v_0} \right)^{\delta} - \left(\frac{h^* (v, 0)}{h} \right)^2 = 0 \tag{8}$$

Fig. 1 The coefficients of expansion of the IDM in Eq. 6 as the function of the bumper-to-bumper distance h, and λ_{pq} is defined in Eq. 9 and normalised to have the same dimensions. We use the parameters in the original IDM from [16], and the *plot* is taken from [17]
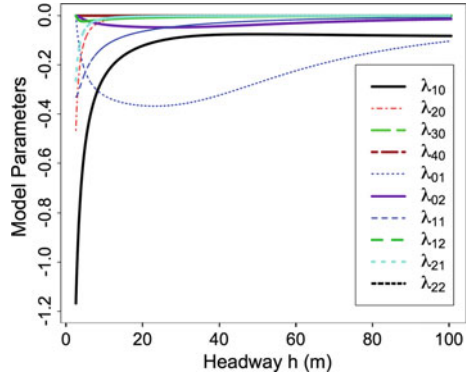
In this case, the optimal velocity is also unique for any value of h, and the Taylor expansion around such ground states gives

$$a_n = \sum_{p=0,q=0}^{p=4,q=2} \lambda_{p,q} \left(v_n - V_{op}\left(h_n\right)\right)^p \Delta v_n^q \tag{9}$$

Thus, not only the higher orders of expansion are present, all the coefficients of expansion, $\lambda_{p,q}$, are explicitly dependent on h_n, or the local density of the vehicles.

Not all terms in Eq. 9 are important, and some can be completely ignored. We now plot these coefficients of expansion in Fig. 1. It is obvious that only λ_{10}, λ_{01} and λ_{11} play significant roles in the effective modelling. When the density of the traffic is fixed, the dependence of the acceleration on Δv_n is always rather linear. At high density, the terms quadratic in $\left(V_{op} - v_n\right)$, as well as the terms coupling $\left(V_{op} - v_n\right)$, Δv_n are also important, reflecting hard braking at very high density when either the approach velocity or the deviation of the velocity from the near-zero optimal velocity is large. For intermediate density, however, the dependence of the acceleration on $\left(V_{op} - v_n\right)$ and Δv_n is both quite linear, though the coefficients strongly depend on the density. At low density the coefficients depends only weakly on the density.

The Taylor expansion reveals in detail the qualitative and quantitative assumptions of the human driving behaviours made by the IDM. In particular, one can also truncate all the unimportant terms, so that the IDM model can be understood as a simple generalisation of the OV model, as verified by numerical simulations [17]. The IDM is more realistic because of the appropriate dependence of the coefficients of expansion on the density. However, it does not distinguish between the acceleration and braking behaviour, since the model is predominantly linear in Δv_n [15].

3.3 Shamoto's Car-Following Model

Shamoto's car-following model [15] is claimed to be more realistic than the IDM especially for the braking behaviour. It also has an artificial divergence of the accel-

Fig. 2 The coefficients of expansion of the Shamoto's model in Eq. 10 as the function of the bumper-to-bumper distance h, and λ_{pq} is defined in Eq. 11 and normalised to have the same dimensions. We use the parameters in the original model from [15]
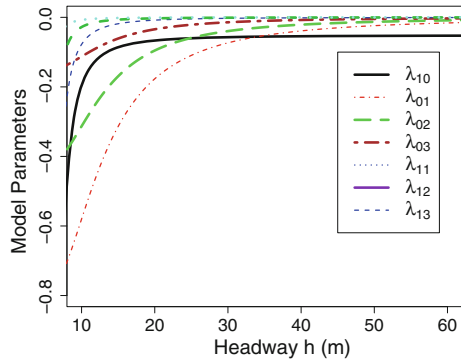
eration when the bumper-to-bumper headway approaches some small value. The model and its optimal velocity function is explicitly given by

$$a_n = A - B \frac{v_n}{h_n - D} e^{C \Delta v_n} - \gamma v_n, \qquad V_{\mathrm{op}} = \frac{A (h_n - D)^2}{B + \gamma (h_n - D)^2} \qquad (10)$$

For this model the expansion around the steady state will yield an infinite number of terms due to the exponential in the model. However, the coefficients of expansion for the higher order terms with the power of Δv_n greater than 3 are very small and can be ignored. The full expansion is given by

$$a_n = \lambda_{10} \left(V_{\mathrm{op}} - v_n \right) + \sum_{p=1}^{\infty} \left(\lambda_{0,p} + \lambda_{1,q} \left(V_{\mathrm{op}} - v_n \right) \right) \Delta v_n^p \qquad (11)$$

We again plot the significant coefficients of expansion as a function of the average headway in Fig. 2. All coefficients of expansion diverges when h approaches D. The main difference between Shamoto's model and the IDM is that the former emphasises on the non-linearity in Δv_n, especially in the region of high density. For Shamoto's model, at low density the drivers are paying more attention to their own velocities as compared to the approach velocity. This is presumably more realistic, in the sense when the vehicle in the front is far away, it is difficult for the driver to judge the approach velocity.

4 Conclusions

In summary, we have proposed a theoretical construction of the master model for the deterministic microscopic traffic models, which can be used to systematically understand all such models proposed in the literature with the assumption of identical drivers. In particular, we propose such models can be completely characterised by the intrinsic optimal velocity function (as well as its multiplicity), and the set of

coefficients of expansions. In this way, not only can different models be compared quantitatively, the underlying assumptions of the human driving behaviours for each model can also be understood in a universal way.

The master model can also be measured from the microscopic empirical data, which we describe in more detail in *A General Scheme for Deterministic Microscopic Traffic Models. Part II: Empirical Verifications*.

References

1. Bando, M., Hasebe, K., Nakayama, A., Shibata, A., Sugiyama, Y.: Dynamical model of traffic congestion and numerical simulation. Phys. Rev. E **51**(2), 1035 (1995)
2. Gong, H., Liu, H., Wang, B.H.: An asymmetric full velocity difference car-following model. Phys. A Stat. Mech. Appl. **387**(11), 2595–2602 (2008)
3. Hayakawa, H., Nakanishi, K.: Theory of traffic jam in a one-lane model. Phys. Rev. E **57**(4), 3839 (1998)
4. Helbing, D.: Traffic and related self-driven many-particle systems. Rev. Mod. Phys. **73**(4), 1067 (2001)
5. Helbing, D., Tilch, B.: Generalized force model of traffic dynamics. Phys. Rev. E **58**(1), 133 (1998)
6. Jerath, K., Ray, A., Brennan, S., Gayah, V.V.: Dynamic prediction of vehicle cluster distribution in mixed traffic: a statistical mechanics-inspired method. IEEE Trans. Intell. Trans. Syst. **16**(5), 2424–2434 (2015)
7. Jiang, R., Wu, Q., Zhu, Z.: Full velocity difference model for a car-following theory. Phys. Rev. E **64**(1), 017101 (2001)
8. Kerner, B.S.: Introduction to modern traffic flow theory and control: the long road to three-phase traffic theory. Springer Science & Business Media (2009)
9. Kerner, B.S.: Criticism of generally accepted fundamentals and methodologies of traffic and transportation theory: A brief review. Phys. A Stat. Mech. Appl. **392**(21), 5261–5282 (2013)
10. Kerner, B.S., Konhäuser, P.: Structure and parameters of clusters in traffic flow. Phys. Rev. E **50**(1), 54 (1994)
11. Kesting, A., Treiber, M.: Traffic Flow Dynamics: Data, Models and Simulation. Springer, Berlin (2013)
12. Lunge, A., Borkar, P.: A review on improving traffic flow using cooperative adaptive cruise control system. In: 2015 2nd International Conference on Electronics and Communication Systems (ICECS), pp. 1474–1479. IEEE (2015)
13. Montanaro, U., Tufo, M., Fiengo, G., Santini, S.: A novel cooperative adaptive cruise control approach: Theory and hardware in the loop experimental validation. In: 2014 22nd Mediterranean Conference of Control and Automation (MED), pp. 37–42. IEEE (2014)
14. Papageorgiou, M., Diakaki, C., Dinopoulou, V., Kotsialos, A., Wang, Y.: Review of road traffic control strategies. Proc. IEEE **91**(12), 2043–2067 (2003)
15. Shamoto, D., Tomoeda, A., Nishi, R., Nishinari, K.: Car-following model with relative-velocity effect and its experimental verification. Phys. Rev. E **83**(4), 046105 (2011)
16. Treiber, M., Hennecke, A., Helbing, D.: Congested traffic states in empirical observations and microscopic simulations. Phys. Rev. E **62**(2), 1805 (2000)
17. Yang, B., Monterola, C.: Classification and unification of the microscopic deterministic traffic models. Phys. Rev. E **92**(4), 042802 (2015)
18. Yang, B., Xu, X., Pang, J.Z., Monterola, C.: Cluster statistics and quasisoliton dynamics in microscopic car-following models (2014). arXiv:1407.3177

A General Scheme for Deterministic Microscopic Traffic Models. Part II: Empirical Verifications

Bo Yang, Jiwei Yoon and Christopher Monterola

Abstract We describe the techniques for the extraction of the microscopic empirical data from high frame-rate videos of the traffic flows in Singapore. Such data include accelerations, velocities, headways and approach velocities. Following the discussions and the proposal from *A General Scheme for Deterministic Microscopic Traffic Models. Part I: Theoretical Construction*, we aggregate the collected microscopic empirical data by the proper sampling and the averaging of the unimportant factors influencing the driving behaviours, and present some of the tentative results in mapping the master model for the deterministic microscopic traffic models.

1 Introduction

Empirical verification of the traffic models is an important topic in the research of traffic modelling and simulation [3, 5]. The complexity of the traffic system, especially due to the diversity of the interacting vehicles and the intrinsic stochasticity, makes the task highly non-trivial. The non-linear interaction between the vehicles, as well as the inability to control the traffic system the same way as a physical experiment, also makes the tuning of the models based on the comparison between numerical simulations and empirical observations controversial [4, 10, 11]. Many efforts on tuning the models based on microscopic vehicle dynamics from a small number of sensor equipped vehicles or with video analysis [2, 6–9] lead to much better understanding of the viable range of parameters in many models. They do not,

B. Yang (✉) · C. Monterola
Complex Systems Group, Institute of High Performance Computing, A*STAR,
Singapore 138632, Singapore
e-mail: yangbo@ihpc.a-star.edu.sg

C. Monterola
e-mail: cmonterola@ihpc.a-star.edu.sg

J. Yoon
Department of Materials Science and Engineering, UC Berkeley, Berkeley, USA
e-mail: zeidae@berkeley.edu

however, provide conclusive resolutions to the plethora of existing traffic models or to the controversies between the two-phase and the three-phase traffic models [4, 10, 11].

In this paper, we aim to implement the theoretical construction of the master deterministic microscopic traffic model in *A General Scheme for Deterministic Microscopic Traffic Models. Part I: Theoretical Construction*, by collecting microscopic empirical data at a large scale from the highway traffic flow in Singapore. We use a commercially available high-speed video camera to record the traffic flows of Queensway, one of the major expressways in Singapore. Advanced video-processing techniques are employed to extract velocity, acceleration, headway and approach velocity of each passing vehicle. Our algorithm combines machine learning, edge detection and adaptive averaging to give accurate measurements of velocities and accelerations, with errors close to the systematic limit. This is an on-going project and some tentative results will be presented.

2   Empirical Verification of the Traffic Model

While it is useful to understand various types of assumptions in different models in an intuitive way, we would also like to be able to verify such assumptions from the microscopic empirical data. We start with a formal and statistically rigorous approach, whereby the master model (as proposed in *A General Scheme for Deterministic Microscopic Traffic Models. Part I: Theoretical Construction*) is obtained via a renormalisation procedure where all the unimportant details are averaged over. In this section, we will present the theoretical framework in obtaining such a master model from the microscopic empirical data.

In principle, the driver's decision to accelerate or decelerate depends on many factors. Though we would expect the major factors to include the velocity, headway as well as the approach velocity, other factors should also be taken into account, because their collective impact on the driving behaviour is rather non-trivial. Formally, using the subscript n as the vehicle index, the acceleration of the vehicle is given by

$$a_n = \mathscr{F}_{n,\{s_i\}_n}\left(\{t_i\}_n\right) \tag{1}$$

where $\{t_i\}_n$ contains all factors influencing the nth vehicle that are considered important, on which the dependence of the acceleration will be studied in detail whereby $\{s_i\}_n$ contains all other factors, so in principle Eq. 1 is the complete model, though it is not very useful for analytical or numerical studies by itself. One can, however, average over all the unimportant factors as follows [11]:

$$\bar{a}_n = \frac{1}{N_0} \sum_{\{s_i\}_n} \mathscr{F}_{n,\{s_i\}_n}\left(\{t_i\}_n\right) = \bar{f}_n\left(\{t_i\}_n\right) \tag{2}$$

where N_0 is the appropriate normalisation factor. The summation is done over all possible values of $\{s_i\}_n$, weighed by their respective possibility. In practice, one

cannot list all possible factors in $\{s_i\}_n$, so to obtain the averaged function in Eq. 2, a large number of the pairs $\{a_n, \{t_i\}_n\}$ are sampled from a single vehicle. The functional form is thus obtained by averaging over all values of a_n for each set of $\{t_i\}_n$.

Since we are looking for a microscopic model with identical drivers, different types of drivers and vehicles can be treated as another 'unimportant' factor, and can be averaged over in a similar way:

$$\bar{a}_n = \frac{1}{N} \sum_{k=1}^{N} \bar{f}_k \left(\{t_i\}_n\right) = \bar{f}_0 \left(\{t_i\}\right) \tag{3}$$

In practice, this can also be done by sampling over a large number of vehicles appearing in the traffic system. The resulting dependence of the acceleration on $\{t_i\}_n$ is now given by $\bar{f}_0$ that is renormalised by the average of all other factors, and may well be different from what is obtained from a few sensor equipped vehicles in test driving. In particular, $\bar{f}_0$ depends explicitly on the vehicle composition in the traffic system under study, as well as on the statistical distribution of the conditions in $\{s_i\}$ during the period of study, including the demographic composition of the drivers.

To study the dynamics of the traffic flow, we choose $\{t_i\}_n = \{h_n, v_n, \Delta v_n\}$. The possible dependence of the driving behaviours on the vehicles at the back, as well as the vehicles further ahead, are thus treated as unimportant factors and averaged over. The resulting Eq. 3 is thus the renormalised master model for all the deterministic microscopic models in which the acceleration only depends on headway, velocity and approach velocity.

3 Extraction of Microscopic Empirical Data

To obtain Eq. 3 empirically, we video-taped the traffic flow of a fixed segment of the expressway in Singapore, over the period of six months. The video is shot with a camera with a high frame rate to reduce the systematic error. With the full videos available, it is easy to implement the virtual 'double-loop sensor' for the measurement of the velocities, and the 'triple loop sensor' for the measurement of the accelerations. One should be aware of, however, the intrinsic systematic error due to the finite resolution of the video, as well as the finite frame rate of the camera. They lead to inaccuracies both in the spatial and time domain. In our empirical measurements, a video camera of 250 frames per second was aimed at a section of the Queensway in Singapore. The resolution of each frame is 640 pixels in width and 360 pixels in height.

The following steps are implemented in generating the empirical data of interest:

1. *Pre-processing the raw videos*: in Fig. 1 we illustrate the pre-processing of the raw videos before detection and analysis are executed. Firstly, every frame of the video was un-tilted and cropped to the region of interest using the comprehensive video editing software FFmpeg. The cropped video is then converted into the moving edges by the Canny Edge Detection algorithm [1].

Fig. 1 The *top segment* part
is the complete view of the
video; the *middle segment* is
the cropped part where we
focus on the fast lane of the
traffic from *left to right*. The
bottom segment is the result
after conversion of the
original video into moving
edges using the Canny Edge
Detection algorithm

2. *Extraction of Detector Time Series*: a series of virtual detectors were placed
   along the fastest moving lane in the edge detected videos to detect the sum of
   pixel values. In total, there are more than 500 detectors along a lane, resulting in
   a maximum of 500 velocity measurements for each passing vehicle.

   Figure 2 shows the normalised sum of the pixel values as detected by a virtual
   detector, from the edges of the moving vehicles shown in Fig. 1 (bottom). The high
   signal-to-noise ratio is evident from the non-discernible baseline of Fig. 2. Even
   with strong overhead sun and the associated shadows of the trees, the empirical
   signal-to-noise ratio remains above 100:1.

3. *Peak Detection and Temporal Positioning*: the peak series in Fig. 2 needs to be
   further processed to extract the time of incidence of a moving object. We employ a
   two-step approach. In the first step, we identify the approximate temporal position
   of the peaks. In anticipation of the background noise we employ a baseline sensi-
   tive method to identify first the approximate temporal position of the peaks. The
   $[N1, N2]$ percentile of the signals of the consecutive segments of a pre-specified
   time window (on the order of less than a few minutes) of the video was sampled
   to measure the fluctuation of the baseline. Signals within the $[N1, N2]$ percentile
   give us a sampling of the local baseline. Both values of $N1$ and $N2$ are chosen
   empirically.

   In the second step, we perform a test to identify the rising wall and then find
   the exact time of the rise. Consecutive points around the approximate temporal
   positions identified by the first step are compared to identify the rising wall. We
   then employ a descent method to find the exact time which satisfies the condition

Fig. 2 The time series of the pixel values of a single virtual detector, measuring the accumulation of the bright pixels in the converted video (see Fig. 1 *bottom segment*). Each peak indicates a moving vehicle having reached and passed the virtual detector
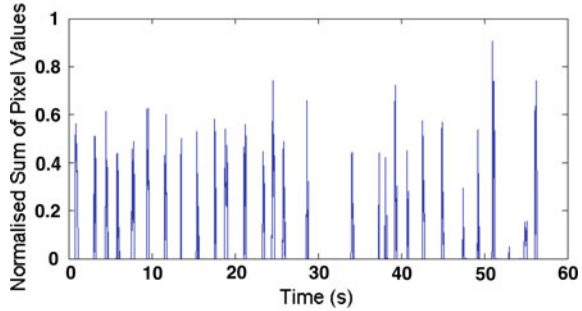
that the local change in signal value is within the range of the fluctuation of the signal around the local mean, in both the forward and backward direction in time.

4. *Velocity and Acceleration Calculation and Averaging*: from the list of time of incidences of the objects on each detector, we find the same object on two detectors that are distance d apart. To that end, we define a search time period $\triangle t$, for the Nth object on the Mth detector. The search time period was chosen to be the time from the incidence of the Nth object to that of the $(N + 1)$th object on the Mth detector. We search for the incidence of an object on the $(M + d)$th detector within $\triangle t$ and associate the two events to the same object. We can then calculate the velocity by dividing the separation distance with the time separation.

   To reduce the noise of the data, velocity averaging for the Nth detector was done by associating the calculated velocities that are within the time period $\triangle t$ from the Nth to the $(N + N)$th detector. A simple average and standard deviation were calculated (see Fig. 4). The method of calculating acceleration is identical to the method of calculating velocity.

5. *Machine-Learning Classification of Vehicles:* as we are only interested in the interactions between large vehicles (cars, trucks, buses, etc.), we trained a machine learning Haar classifier to identify them. This was done using the OpenCV package with C++ code. A total of 3000 positive samples of cars and 400 negative samples were cropped. Figure 3 shows some of the positive and negative samples. The positive samples include vehicles that are occluded by trees. The negative samples include a segment of road with lane markers, trees and road divider, as well as shadows and motorcycles. For the classification, we use FFmpeg to seek for the frame at which velocity calculations were made. The classifier is used to identify the cars in the frame.

4   Tentative Empirical Results

We now proceed to discuss the results from the simple analyses of the dataset. In Fig. 4 we plot the theoretical systematic error and the average empirical error in the velocity calculation against velocity. The theoretical systematic error curve assumes that the velocity is kept constant. Therefore, the error is entirely due to
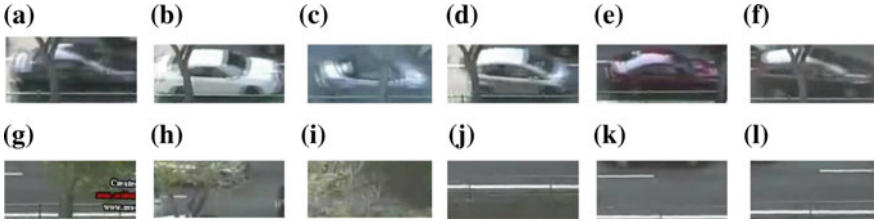
Fig. 3 Examples of the positive (**a–f**) and negative samples (**g–l**) for the Haar classifiers in machine learning
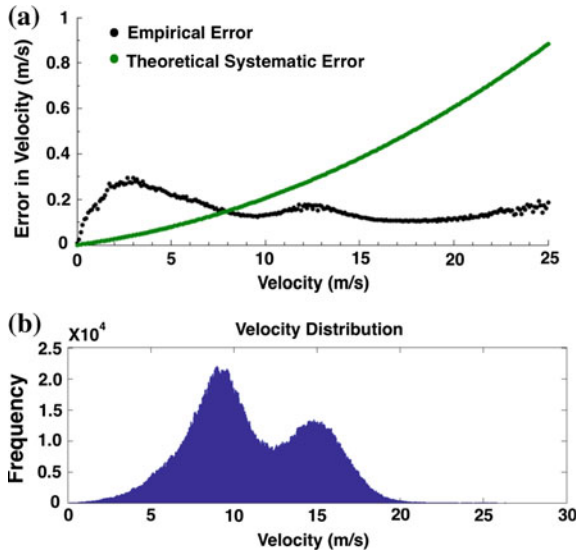
Fig. 4 Results. The empirical and theoretical errors of the velocity measurements. The empirical error is calculated after averaging over the velocity measurements from very closely spaced detectors (one pixels apart), while the theoretical errors are calculated from the video resolution and camera frame rate (**a**), the frequency distribution of the velocities measured, showing two peaks giving the most common velocities at the congested phase and the free-flow phase respectively (**b**)

the spatial granularity of the frame and the finite time frame. On the other hand, empirically derived velocity over a finite separation distance is susceptible to an additional error source due the acceleration of the vehicle. This error tends to be more pronounced for smaller velocities as the vehicles have more time to accelerate in the finite detector separation. This explains the larger empirical error as compared to the theoretical systematic error. At $\sim$8 m/s the two curves meet, suggesting that the error due to acceleration becomes less significant than the theoretical error. For the measured velocity frequencies we observe two peaks, one at 9 m/s and another at 18 m/s, corresponding to the most common velocities in the congested flow and the free flow respectively. Also, the average empirical errors are all below $\sim$0.3 m/s.

A large number of such data has been collected for the past six months. We attempt to construct the master model of Eq. 3 by mapping the dependence of the averaged

acceleration as a function of the headway, velocity and approach velocity, $\{h, v, \Delta v\}$. Significant noises are expected when the number of data points is small for each set of $\{h, v, \Delta v\}$. It is empirically observed that the noises decrease with the increase of the number of the data points, and the averaged accelerations tend to converge to specific values when more than one thousand of measured accelerations with the same $\{h, v, \Delta v\}$ are averaged over, leading to a smooth manifold of the acceleration as a function of the three parameters in Eq. 3.

While this is still work in progress and the acceleration is only converged for a small sub-domain in the three-dimensional parameter space, we show some well-converged results in Fig. 5, where the acceleration is plotted as a function of the velocity at various different headways, with *zero* approach velocity. The plots are rather smooth, with the uncertainty value given by the size of the black dots in the plot. One can see clearly that the x-axis intersection increases with the headway, which gives the optimal velocity as a function of the headway. Detailed features of the velocity dependences at $h = 10$ m and $h = 11$ m indicate multiple steady states with different velocities corresponding to the same density, as evidenced by the formation of the plateau around zero acceleration. This is potentially strong microscopic empirical evidence for the three-phase traffic theory [3], whereby the synchronisation gap can now be measured empirically.

5   Conclusion and Discussions

In summary, we have shown how the average human driving behaviours can be measured from the microscopic empirical data and used to validate various assumptions in the traffic models. We also presented some tentative results on the microscopic empirical data collected from the real traffic flow in Singapore, and showed how we

Fig. 5 The dependence of the averaged acceleration as a function of the velocity, measured at zero approach velocity and different headway. Each data point is averaged over more than 5000 measurements and is well-converged, with the error bar the same size of the *black dots* in the plot. Headway = 4 m (**a**), Headway = 8 m (**b**), Headway = 10 m (**c**), Headway = 11 m (**d**)
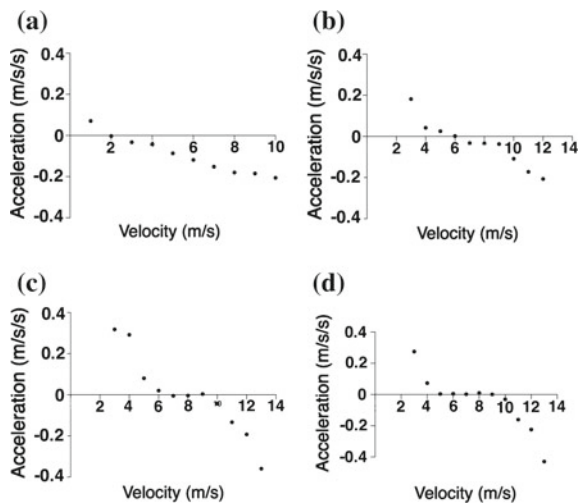
used it to construct the master model empirically under the same theoretical framework. The partial results we have obtained already show very interesting behaviours of the human driving behaviours especially when the traffic is congested, suggesting that at the same density, there is a range of preferred average velocity for the traffic flow. It remains to see how various popular traffic models in the literature, and in particular the three-phase traffic models, compare with the microscopic empirical data. This can potentially be very useful for both understanding the nature of the traffic flow and for the construction and tuning of the most appropriate traffic models.

The relevant technical details can also be found in [11], the complete results of the microscopic empirical data are still work in progress and will be published soon. From the modelling perspective, the general framework proposed in those references and in this paper should provide a standard way in treating deterministic microscopic traffic models with the assumption of identical drivers. The raw microscopic empirical data we have also contain information on the driving behaviours of different vehicle species (i.e., cars and trucks) as well as the statistical distribution of the stochastic part of the human driving behaviours. Further analysis of such data can lead to a more complete traffic model, in which different vehicles species and the stochasticities can be taken into account.

References

1. Canny, J.: A computational approach to edge detection. IEEE Trans. Pattern Anal. Mach. Intell. **6**, 679–698 (1986)
2. Helbing, D., Tilch, B.: Generalized force model of traffic dynamics. Phys. Rev. E **58**(1), 133 (1998)
3. Kerner, B.: The Long Road to Three-Phase Traffic Theory. Springer (2009)
4. Kerner, B.S.: Criticism of generally accepted fundamentals and methodologies of traffic and transportation theory: a brief review. Phys. A Stat. Mech. Appl. **392**(21), 5261–5282 (2013)
5. Kesting, A., Treiber, M.: Traffic flow dynamics: Data, models and simulation (2013)
6. Neubert, L., Santen, L., Schadschneider, A., Schreckenberg, M.: Single-vehicle data of highway traffic: A statistical analysis. Phys. Rev. E **60**(6), 6480 (1999)
7. Shamoto, D., Tomoeda, A., Nishi, R., Nishinari, K.: Car-following model with relative-velocity effect and its experimental verification. Phys. Rev. E **83**(4), 046105 (2011)
8. Sugiyama, Y., Nakayama, A., Fukui, M., Hasebe, K., Kikuchi, M., Nishinari, K., Tadaki, S.i., Yukawa, S.: Observation, theory and experiment for freeway traffic as physics of many-body system. In: Traffic and Granular Flow03, pp. 45–58. Springer (2005)
9. Tadaki, S., Kikuchi, M., Fukui, M., Nakayama, A., Nishinari, K., Shibata, A., Sugiyama, Y., Yosida, T., Yukawa, S.: Phase transition in traffic jam experiment on a circuit. New J. Phys. **15**(10), 103034 (2013)
10. Treiber, M., Kesting, A., Helbing, D.: Three-phase traffic theory and two-phase models with a fundamental diagram in the light of empirical stylized facts. Trans. Res. Part B Methodol. **44**(8), 983–1000 (2010)
11. Yang, B., Xu, X., Pang, J.Z., Monterola, C.: Cluster statistics and quasisoliton dynamics in microscopic car-following models (2014). arXiv:1407.3177

Influence of Various Traffic Densities on 1/f Noise

Reuben Thieberger

Abstract Previously, we examined 1/f noise for a simple cellular automata model. For illustrative purposes, we considered a specific case of approaching a city. The case involves a traffic light where one continues on the main road, where additional cars are entering at the light. At this intersection an alternative route begins, which is longer, but where no additional cars are entering. In this paper we add a 'slow to start' model. We calculate the Fourier transform of the average velocity for each traffic light cycle. We consider different average 'slow to start cases' and obtain different results for different cases. All cases can be written as $1/f^{\alpha}$. We check by least squares the value of α. We compare qualitatively our results to experiments. When we do not assume cars which are 'slow to start', the results differ from the experiment, but when we introduce 'slow to start' cars, the results are similar to the experimental values. We consider different densities of cars. There are different characteristics for low densities, mid range and high densities.

1 Introduction

In a previous study [9], we examined a specific traffic problem. In this study we introduce the 'slow to start' model. The motivation for this improvement in our model is that we wish to improve the agreement between our calculations and the experimental results.

To make our exposition clearer we describe again the procedure given in our previous study. This traffic problem mimics to a certain degree a real situation. We did not try to obtain the actual values as we wish here just to show the feasibility of our approach. The real situation we encounter when entering the city of Beer Sheva, Israel, from the North-East. Therefore the main question posed is how does the amount of 'slow to start' cars influence α (in the noise term, Eq. 1).

Empirical observations of traffic show that at high enough densities the behaviour of traffic becomes quite complex. Cellular Automata is one of the most used meth-

R. Thieberger (✉)
Department of Physics, Ben Gurion University, 84105 Beersheba, Israel
e-mail: thieb@bgu.ac.il

467

ods for evaluating traffic, because of their speed and complex dynamic behaviour. Cellular Automata were first studied by Ulam and von Neumann [4]. An important contribution to the field was in the work of Wolfram [8] who introduced classifications, used in the present study. The elementary Cellular Automaton is a collection of cells arranged on a one dimensional array. Each cell can obtain just two possible numbers: 1 and 0. The 'time' is discrete and at each time step all the cell values are updated synchronously. The value of each cell depends just on the values in the previous step of that cell and its two neighbours. Wolfram names each elementary Cellular Automaton with a binary numeral, which he calls 'rule'. This value results from reading the output when the inputs are lexicographically ordered. This will become clearer when we will explain the rules we use. The rules we used are taken from the Cellular Automata model proposed by Gershenson and Rosenblueth [3]. Our main interest in this paper is the power spectrum of the average velocities over a cycle. This value gives us the main contribution to the noise. All cases can be written as $1/f^\alpha$. We check by least squares the value of α. We will consider this expression in the section dedicated to calculating the noise.

2 The Model

We will deal here only with the 'microscopic' models where we consider each individual vehicle. Our highways are represented by an array of cells, each cell has the values 0 or 1. 1 represents a vehicle and 0 an empty portion of the highway. We assume that the magnitude of a cell corresponds to the average length of a vehicle. In Fig. 1, we show the layout of our model. At a certain point we have a bifurcation where there are two different ways to proceed and they merge again at a later point. This model represents in a simplistic way the possibility of using two alternative routes (the main route and the 'bypass') when approaching a city from a certain direction of suburbs. We add the possibility that additional cars are coming into the main road and are removed when approaching the city. So that overall the number of vehicles is preserved. The rules, which are the same as used by Gershenson and Rosenblueth [3], are given in Table 1.

In this paper we have one modification, which is quite significant. Previously the model enabled a car to move if there was an empty space in front of it. In this study we assume that a certain part of the cars do not follow into the empty space in front of them. This is equivalent to having some cars which are slow to start. This is a more realistic model than the one we used in our previous study. This is called the *slow to start rule* [1] and we expect that it will give more realistic results.

In our analysis we distinguish four regions:

1. The 'bypass region' (denoted by iq).
2. The region on the main road between the entrance and exit of the 'bypass' (denoted by ipe).

Table 1 Wolfram rules used in this model

$t - 1$	t_{184}	t_{252}	t_{136}
000	0	0	0
001	0	0	0
010	0	1	0
011	1	1	1
100	1	1	0
101	1	1	0
110	0	1	0
111	1	1	1

3. The whole of the main road (denoted by ip).
4. The part of the main road from the second traffic light and on (denoted by t).

In this paper we will be dealing only with the fourth region, therefore we can omit the letter 't'.

2.1 Measures

The density, ρ, is given by the number of 'ones' (i.e. vehicles) divided by the general number of cells. Initially we take this value to be the same for the three sections. We check how this value changes in the different regions. Here, we are interested only in the equilibrium values. The velocities, v, denoted by v_p, v_q, v_{pe} and v_t, are given by the number of cells which change in one step from 0 to 1.

In our calculation, space and time are just abstract quantities. Still if concrete numbers are desired, one can quote [3] where one cell represents five metres, and a time step represents a third of a second, which gives us about 50 km/h, roughly the speed limit within a city.

2.2 The Grid

The schematic picture of our specific problem is given in Fig. 1.

In Fig. 2 we show schematically the movements of the vehicles. We have two traffic lights (denoted by '1' and '2' on the diagram). When the movement is on the 'main road' diagram 'a' gives us the movement. When we enter or exit the 'bypass' then 'b' gives us the rules.

We have a parameter telling us the amount of 'cars' added to the main road at the junction of the bypass. This same amount is deducted from the 'main road' further away and is done in order to preserve the total number of vehicles. The actual addition of cars is governed by a random number which depends on the parameter (i.e., the percentage of cycles when a car is added).

Fig. 1 The route of vehicles

Fig. 2 The movement of vehicles
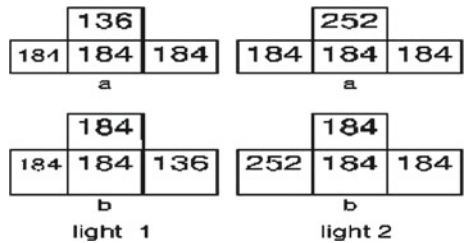
We have a parameter telling us what part of cars do not move, even when they could move according to our rules. We denote this parameter by crr, and it changes between 0 and 1.

3 Noise

Traffic noise is one of the most important sources of noise pollution. It is well known that this is a health hazard. In this study we wish to check the frequency distribution of the noise. It was shown by Takayasu and Takayasu [6], that we obtain $1/f$ noise. Let us explain here this term: '$1/f$ noise' refers to the phenomenon of the spectral density, $S(f)$, of a stochastic process having the form:

$$S(f) = const./f^\alpha \tag{1}$$

Here, $S(f)$ is the spectral density and f the frequency. When $\alpha = 0$, we say that we have white noise. If $\alpha = 1$, we say we have pink noise. If $\alpha = 2$, we say we have brown noise. To understand better this term, we refer to [2, 5]. An Indian group [7] made measurements in a number of selected locations from busy roads of Aurangabad and obtained mostly pink noise in a large range of frequencies. To obtain $S(f)$ we make the Fourier transform of the velocities. To perform our Fourier transform we take the averages over each traffic light cycle and study the frequencies of these averages over all cycles taken in our calculations. We compare the results to $1/f^\alpha$ by a least square test.

4   Results and Discussion

We used a fixed grid. The main road was comprised of 1200 cells, the 'bypass' 300 cells and the distance between the two traffic lights was 120 cells. We used the 'green wave' regime. As we have just two traffic lights, it was shown by Gershenson and Rosenblueth [3], that in this case one does not get different results using the 'self-organising' regime.

We introduce a vehicle on the first intersection for 40 % of the steps and we eliminate the same number of vehicles on the last point of our main route, again per unit time.

In the next figure we show the results for the case of no 'slow to start' cases. This figure appeared in our previous paper. The purpose of showing it here again is to understand better the effect of the 'slow to start' rule.

We averaged the velocities over a traffic light cycle and studied the power spectrum. The value we are interested in is α, in the expression $1/f^{\alpha}$. We give this value in Fig. 3.

This is an interesting result. When we increase the density so that we reach the transition from free flow to the jammed region, the noise shoots up from white noise to brown noise and then settles in the region of pink noise. This result does not correspond to a real situation where α is close to 1 [1]. Our purpose in the present study is to see if introducing the improved model, i.e. the model with 'slow to start', we obtain a better agreement with the experiment.

In the next figures we show the effect of the 'slow to start' probability. In Fig. 4 we show the values of $\alpha(t)$ for the low densities. This is the region of free movement therefore there is no significant change for different 'slow to start' scenarios.

In Fig. 5 and in Fig. 6 we present the results for α at mid range densities and for high densities.

We see in Fig. 5, that even a very small percentage of cars which are slow to start results in α being closer to the pink noise just as is given by the experimental results [7].

Fig. 3 The values of α as a function of density
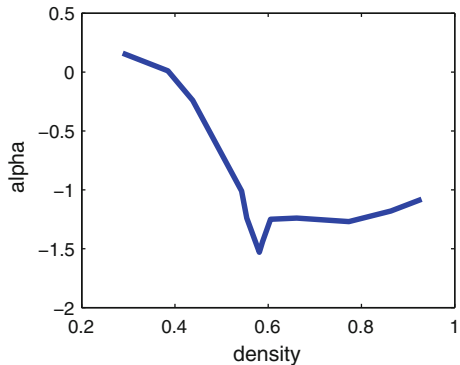
Fig. 4 α values as function of change in probability of slow to start values for low densities
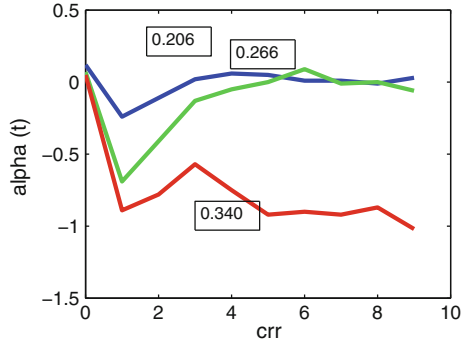
Fig. 5 The values of α as a function of change in probability of slow to start at mid range densities
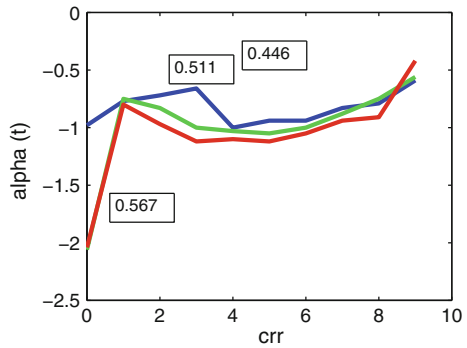
Fig. 6 The values of α as a function of change in probability of slow to start at high densities
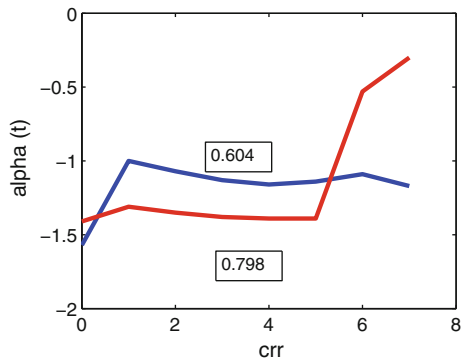
In conclusion, we can say that our calculations give us a wide range of information which can be applied for specific cases. It shows us the importance of modifying the simple rule by adding the 'slow to move' rule.

References

1. Barlovic, R., Santen, L., Schadschneider, A., Schreckenberg, M.: Metastable states in cellular automata for traffic flow. Eur. Phys. J. B-Condens. Matter Complex Syst. **5**(3), 793–800 (1998)
2. Erland, S., Greenwood, P.E., Ward, L.M.: $1/f\alpha$ noise is equivalent to an eigenstructure power relation. EPL (Europhys. Lett.) **95**(6), 60006 (2011)
3. Gershenson, C., Rosenblueth, D.A.: Modeling self-organizing traffic lights with elementary cellular automata (2009). arXiv:0907.1925
4. Neumann, J.V., Burks, A.W.: Theory of self-reproducing automata. University of Illinois Press (1966)
5. Procaccia, I., Schuster, H.: Functional renormalization-group theory of universal 1 f noise in dynamical systems. Phys. Rev. A **28**(2), 1210 (1983)
6. Takayasu, M., Takayasu, H.: 1/f noise in a traffic model. Fractals **1**(04), 860–866 (1993)
7. Thieberger, R.: WorldComp 2014 Proceedings. http://worldcomp-proceedings.com/proc/p2014/PDP4123.pdf
8. Wolfram, S.: Theory and applications of cellular automata, vol. 1. World scientific Singapore (1986)
9. World Academy of Science: Proceedings of the 2014 World Congress in Computer Science, Computer Engineering, and Applied Computing (2014)

A Multi-class Vehicular Flow Model for Aggressive Drivers

Wilson Marques Jr., Rosa María Velasco and Alma Méndez

Abstract The kinetic theory approaches to vehicular traffic modelling have given very good results in the understanding of the dynamical phenomena involved [3, 8]. In this work, we deal with the kinetic approach modelling of a traffic situation where there are many classes of aggressive drivers [5]. Their aggressiveness is characterised through their relaxation times. The reduced Paveri-Fontana equation is taken as a starting point to set the model. It contains the usual drift terms and the interactions between drivers of the same class, as well as the corresponding one between different classes. The reference traffic state used in the kinetic treatment is determined by a dimensionless parameter. The balance equations for the density and average speed for each class are obtained through the usual methods in the kinetic theory. In this model, we consider that each class of drivers preserve the corresponding aggressiveness, in such a way that there will be no adaptation effects [6]. It means that the number of drivers in a class is conserved. As preliminary results, we have obtained a closure relation to derive the Euler-like equations for two drivers classes. Some characteristics of the model are explored with the usual methods.

1 Introduction

In the literature, traffic flow in highways is described through different approaches going from the microscopic to the macroscopic points of view [1, 3, 8]. All have advantages as well as problems in their development. Our goal in this work is the

W. Marques Jr. (✉)
Departamento de Fisica, Universidade Federal Do Paraná, Curitiba 81531-990, Brazil
e-mail: marques@fisica.ufpr.br

R.M. Velasco
Departamento de Física, Universidad Autónoma Metropolitana, 09340 Iztapalapa, Mexico
e-mail: rmvb@xanum.uam.mx

A. Méndez
Departamento de Matemáticas Aplicadas y Sistemas,
Universidad Autónoma Metropolitana, 05348 Cuajimalpa, Mexico
e-mail: amendez@correo.cua.uam.mx

construction of a macroscopic model starting from a kinetic approach for multiple-user class of drivers, in particular, we will focus in two classes of drivers which have certain aggressiveness. We characterise it by means of the response time, which is shortly called the relaxation time, one for each class τ_1, τ_2, $\tau_1 \neq \tau_2$. Our treatment starts with the Reduced Paveri-Fontana equation (RPF) for the distribution function $f_i(c, x, t)$ where we have introduced a model for the averaged desired speed, then the homogeneous steady state (equilibrium) in the system leads to a parameter α which contains the aggressiveness parameter, the characteristic density and average speed proper to this state ρ_1^e, ρ_2^e, v_1^e, v_2^e [6]. The kinetic model is averaged over the speed c to obtain the macroscopic equations with the interaction terms. Then, the distribution function corresponding to equilibrium is written in terms of the local densities and speeds and they are taken to calculate the passive and active interaction integrals, leading to a closure relation in the macroscopic description.

2   The Model

The kinetic model we consider to construct our macroscopic description is the reduced Paveri-Fontana equation (RPF), which comes from an integration over the desired speed giving place to an average speed called as $c_0(c, x, t)$ where c is the instantaneous speed of vehicles. On the other hand, the interaction terms are separated according to an active $\psi_i(c)$ or passive $\xi_i(c)$ interaction as follows

$$\frac{\partial f_i(c)}{\partial t} + c\frac{\partial f_i(c)}{\partial x} + \frac{\partial}{\partial c}\left(\frac{c_0(c) - c}{\tau_i} f_i(c)\right) = (1 - p)\sum_j [\rho_i f_j(c)\xi_i(c) + \rho_j f_i(c)\psi_j(c)] \quad (1)$$

where p is the probability of overpassing and the interaction terms are defined as

$$\psi_i(c) = \int_{w<c} (w - c)\frac{f_i(w)}{\rho_i}dw, \qquad \xi_i(c) = \int_{w>c} (w - c)\frac{f_i(w)}{\rho_i}dw, \quad (2)$$

where it should be noted that we have written only the instantaneous speed dependence to shorten the notation. Clearly, the distribution functions and the densities depend on (x, t). The densities and average speeds are defined as

$$\rho_i(x, t) = \int f_i(c)dc, \qquad v_i(x, t) = \int c\frac{f_i(c)}{\rho_i}dc = \langle c \rangle_i. \quad (3)$$

The average over c taken in Eq. 1 leads to the density equations

$$\frac{\partial \rho_i}{\partial t} + \frac{\partial \rho_i v_i}{\partial x} = -(1 - p)\sum_j \rho_i \rho_j [v_j - v_i + \langle \psi_i \rangle_j - \langle \xi_j \rangle_i], \quad i = 1, 2 \quad (4)$$

where $\langle ... \rangle_i$ means the average over the f_i distribution function, and it should be noted that $\langle \psi_j \rangle_i - \langle \psi_i \rangle_j = v_j - v_i$. As a consequence, we obtain that both densities

satisfy conservation equations as it is expected due to their lack of adaptation between classes of drivers. Also, the macroscopic equations for flux are obtained from Eq. 1 after the multiplication by c and the corresponding integration

$$\frac{\partial \rho_i v_i}{\partial t} + \frac{\partial}{\partial x}(\rho_i v_i^2 + \mathscr{P}_i) = \frac{\rho_i}{\tau_i}(V_i^0 - v_i) + (1 - p)\sum_j \rho_i \rho_j [\langle c\xi_i \rangle_j + \langle c\psi_j \rangle_i],$$

(5)

where $V_i^0(x, t)$ comes from the average of the desired speed now taken over the instantaneous speed c, $\Theta(x, t) = \int (c - v_i)^2 f_i(c) dc$ is the $i-$class speed variance and $\mathscr{P}_i$ is the traffic pressure. In this case, we do not have conservation equations. Instead, we obtained a kind of relaxation equation from the average flux $\rho_i v_i$ to $\rho_i v_i^*(x, t) = \rho_i [V_i^0 + \tau_i \sum_j \rho_j(\langle c\xi_i \rangle_j + \langle c\psi_j \rangle_i)]$, which depends explicitly on the interaction of both within $(i - i)$ and between $(i \neq j)$ classes.

Let us call the interaction integrals as

$$\mathscr{I}_{ij} = \langle c\xi_i \rangle_j + \langle c\psi_j \rangle_i,$$

(6)

and we must calculate them with a distribution function $f_i(c)$ which is a solution of the kinetic Eq. 1. Here, we will use the local distribution function obtained for one class of drivers, which is given as

$$f_i(c, x, t) = \rho_i \frac{\alpha}{\Gamma(\alpha)v_i} \left(\frac{\alpha c}{v_i}\right)^{\alpha-1} exp\left(-\frac{\alpha c}{v_i}\right),$$

(7)

where the (x, t) dependence is understood in the local variables (ρ_i, v_i) and $\Gamma(\alpha)$ is the gamma function [9].

Then, when considering the interaction between vehicles in the same class it is immediately obtained that $\mathscr{I}_{ii} = -\rho_i \Theta_i$. On the other hand, the case where $i \neq j$ can be calculated in a closed way in terms of hypergeometric functions. In fact, we have found that they can be approximated by a simpler expression with the step function $\mathscr{H}(v_i - v_j)$

$$\mathscr{I}_{ij} = v_i v_j \left\{ 2 - \left(\frac{\alpha + 1}{\alpha}\right)\left(\frac{v_j}{v_i} + \frac{v_i}{v_j}\right)\mathscr{H}(v_i - v_j)\right\}.$$

(8)

3 Two Classes of Drivers

In order to analyse the macroscopic model we consider just two classes of drivers, though it is clear that the treatment can be done in a more general case. Besides, one class goes faster than the other $v_2 > v_1$ in such a way that there is only one nonvanishing interaction integral between them $\mathscr{I}_{12} = 0$, $\mathscr{I}_{21} \neq 0$.

Also, the traffic pressure chosen corresponds to the usual model for one class of drivers, it contains the speed variance $\Theta_i = v_i^2/\alpha$ and an anticipation term proportional to the average speed gradient and a coefficient similar to the viscosity, then

$$\mathscr{P}_i = \rho_i \frac{v_i^2}{\alpha} - \mu_i \frac{\partial v_i}{\partial x}. \tag{9}$$

Here, the first term comes from our equilibrium state solution in which $1/\alpha$ can be identified with the variance prefactor obtained from the empirical records in the literature [7]. In a general case, the variance prefactor is a function of the density and within a good approximation, it becomes a constant at low densities. In fact, it can be seen that the dimensionless parameter $\alpha \sim 100$, a value which allows us to make some approximations.

3.1 The Equilibrium State

Now, we write the set of macroscopic Eqs. 4 and 5 for this particular case

$$\frac{\partial \rho_1}{\partial t} + \frac{\partial \rho_1 v_1}{\partial x} = 0, \tag{10}$$

$$\frac{\partial \rho_2}{\partial t} + \frac{\partial \rho_2 v_2}{\partial x} = 0, \tag{11}$$

$$\frac{\partial v_1}{\partial t} + v_1 \frac{\partial v_1}{\partial x} = -\frac{1}{\rho_1} \frac{\partial \mathscr{P}_1}{\partial x} + \frac{v_1^* - v_1}{\tau_1}, \tag{12}$$

$$\frac{\partial v_2}{\partial t} + v_2 \frac{\partial v_2}{\partial x} = -\frac{1}{\rho_2} \frac{\partial \mathscr{P}_2}{\partial x} + \frac{v_2^* - v_2}{\tau_2}, \tag{13}$$

where the interaction integrals are given as

$$\mathscr{I}_{11} = -\frac{v_1^2}{\alpha}, \quad \mathscr{I}_{12} = 0, \quad \mathscr{I}_{21} \simeq -(v_2 - v_1)^2, \quad \mathscr{I}_{22} = -\frac{v_2^2}{\alpha}, \tag{14}$$

$$v_1^* = wv_1 - \tau_1(1 - p_1)\frac{\rho_1 v_1^2}{\alpha}, \quad v_2^* = wv_2 - \tau_2(1 - p_2)\frac{\rho_2 v_2^2}{\alpha} - \tau_2(1 - p_2)\rho_1(v_2 - v_1)^2, \tag{15}$$

with the traffic pressure written as in Eq. 9.

The solution for the equilibrium state is obtained in a direct way in terms of the equilibrium densities. First, we find that $v_1^* = v_1^e(\rho_1^e)$ which will be written in terms of a chosen fundamental diagram here simply called v_1^e, specified at the end of the calculation. From Eq. 13, the equilibrium speed for the second class is written as

$$\left(\frac{v_2^e}{v_1^e}\right)^{\pm} = \delta\left\{\frac{\beta + 2\alpha \pm \sqrt{(\beta + 2\alpha)^2 - 4(1 + \alpha\delta)\alpha/\delta}}{2(1 + \alpha\beta)}\right\}, \qquad (16)$$

where $\delta = \frac{\rho_1^e}{\rho_2^e}$, $\beta = \frac{\tau_1}{\tau_2}$ are dimensionless quantities written in terms of the model parameters and the equilibrium densities for both classes. It should be noted that both values for the quotient v_2^e/v_1^e are positive and their values depend on both the model parameters and the densities in the equilibrium state.

Now, according to Eq. 16 we have two equilibrium states and we have to decide which one has a physical meaning. First of all, the average speeds must be positive which means that the speed goes in the direction of the flow, both solutions satisfy such criteria. Second, we will ask that a free flow regime must be stable at least in a certain set of parameters values, otherwise, the model would be not able to reproduce the free flow stage. Then, our next step will be the linear stability calculation.

4 Stability Analysis

As a first step in the model analysis, we will take a small perturbation around the equilibrium state and calculate the conditions for the stability of the corresponding equilibrium solution. Hence

$$\rho_i = \rho_i^e + \hat{\rho}_i exp(ikx - \sigma t), \quad v_i = v_i^e + \hat{v}_i exp(ikx - \sigma t), \qquad (17)$$

where the perturbation has been expanded in modes with a wave vector k and a complex frequency called σ in such a way that the stability condition for the equilibrium state is determined by the condition $\mathscr{R}e(\sigma) > 0$.

In order to linearise the dynamical equations, it is necessary to make a comment about the density dependence in the probability of overpassing. In fact, we have taken the usual modelling and express it in terms of an effective density, then $1 - p = \rho_{eff}$, where $\rho_{eff} = \rho/\rho_{max}$. Besides, in the two classes model it has been argued [2, 10] that the effective density for the slow class (class-1 in our case) is given as $(\rho_1)_{eff} = \rho_1/\rho_{max}$. On the other hand, for the fast class $(\rho_2)_{eff} = (\rho_1 + \rho_2)/\rho_{max}$.

The direct substitution of Eq. 17 in the set of Eqs. 10–13 and the corresponding linearisation can be written in terms of a matrix in which its determinant must vanish to obtain the dispersion relation,

$$\begin{pmatrix} -\sigma + ikv_1^e & 0 & ik\rho_1^e & 0 \\ \frac{(v_1^e)^2 ik}{\alpha\rho_1^e} - \frac{\gamma_{11}^e}{\tau_1} & 0 & -\sigma + \frac{\alpha+2}{\alpha}ikv_1^e + \frac{\mu_1}{\rho_1^e}k^2 + \frac{1}{\tau_1} & 0 \\ 0 & -\sigma + ikv_2^e & 0 & ik\rho_2^e \\ -\frac{a_1}{\tau_2} & \frac{ik(v_2^e)^2}{\alpha\rho_2^e} - \frac{a_2}{\tau_2} & -\frac{a_3}{\tau_2} & -\sigma + \frac{\alpha+2}{\alpha}ikv_2^e + \frac{\mu_2 k^2}{\rho_2^e} + \frac{1-a_4}{\tau_2} \end{pmatrix}$$

$$(18)$$

The quantities a are given as

$$a_1 = -\frac{\tau_2 \rho_2^e (v_2^e)^2}{\alpha \rho_{max}} - \frac{\tau_2}{\rho_{max}}\left[2\rho_1^e(\rho_1^e + \rho_2^e)(v_2^e - v_1^e)\gamma_{11}^e + (2\rho_1^e + \rho_2^e)(v_2^e - v_1^e)^2\right] \tag{19}$$

$$a_2 = -\frac{\tau_2}{\alpha \rho_{max}}(\rho_1^e + 2\rho_2^e)(v_2^e)^2 - \frac{\tau_2 \rho_1^e}{\rho_{max}}(v_2^e - v_1^e)^2 \tag{20}$$

$$a_3 = \frac{2\tau_2}{\rho_{max}}\rho_1^e(\rho_1^e + \rho_2^e)(v_2^e - v_1^e) \tag{21}$$

$$a_4 = \omega - \frac{2\tau_2 \rho_2^e}{\alpha \rho_{max}}(\rho_1^e + \rho_2^e)v_2^e - \frac{2\tau_2 \rho_1^e}{\rho_{max}}(\rho_1^e + \rho_2^e)(v_2^e - v_1^e), \tag{22}$$

all of them can be written in terms of the dimensionless parameters.

Due to the fact that the macroscopic equations are valid in a kind of hydrodynamical limit ($k \to 0$), we will expand the roots in the dispersion relation around $k = 0$ and take terms up to order k^2,

$$\sigma = \sigma_0 + k\sigma_1 + k^2\sigma_2 + \mathcal{O}(k^3), \tag{23}$$

and there will be four different roots, which will be called as Σ_i. The results being given as follows

$$\Sigma_1 = ikc_1 + \frac{k^2\tau_1}{\alpha \rho_1^e}\left[c_1^2 - (\alpha + 1)(\gamma_{11}^e \rho_1^e)^2\right] \tag{24}$$

$$\Sigma_2 = \frac{1}{\tau_1} + \frac{ik}{\alpha}(2v_1^e + \alpha v_1^e - \alpha \gamma_{11}^e \rho_1^e) + \frac{k^2}{\alpha \rho_1^e}\left[\alpha \mu_1 - \tau_1 \rho_1^e\left((v_1^e)^2 + 2\rho_1^e v_1^e \gamma_{11}^e - \alpha(\rho_1^e \gamma_{11}^e)^2\right)\right], \tag{25}$$

$$\Sigma_3 = \frac{ik}{a_4 - 1}\left[(a_4 - 1)v_2^e - a_2\rho_2^e\right] + k^2\Sigma_{32} \tag{26}$$

$$\Sigma_{32} = -\frac{\tau_2}{\alpha(a_4 - 1)^3}\left[(a_4 - 1)^2(v_2^e)^2 - a_2\rho_2^e\left(2v_2^e(a_4 - 1) + \alpha a_2\rho_2^e\right)\right],$$

$$\Sigma_4 = \frac{1 - a_4}{\tau_2} + \frac{ik}{\alpha(a_4 - 1)}\left[(a_4 - 1)v_2^e(2 + \alpha) + \alpha a_2\rho_2^e\right] + k^2\Sigma_{42} \tag{27}$$

$$\Sigma_{42} = \frac{1}{(a_4 - 1)^3 \alpha \rho_2^e}\left[(a_4 - 1)\rho_2^e v_2^e \tau_2\left((a_4 - 1)v_2^e - 2a_2\rho_2^e\right) + \alpha\left[(a_4 - 1)^3 \mu_2 - \rho_2^e \tau_2(a_2\rho_2^e)^2\right]\right],$$

where $\gamma_{11}^e = (dv_1^e/d\rho_1)^e$ and can be calculated once the fundamental diagram for the slow class is chosen.

The mode determined by Σ_1 associated with the slow class density (ρ_1) propagates with a speed $c_1 = v_1^e + \gamma_{11}^e \rho_1^e$ and the real part of it determines a time scale which tends to zero as k^2. However, this real part must be positive to have stability, it means that the quantity $c_1^2 - (\alpha + 1)(\gamma_{11}^e \rho_1^e)^2 > 0$ and it depends on the slow class fundamental diagram. Note that this condition corresponds to the usual one for Payne-like models, it is known that in this case there exists stability regions [4]. The root Σ_2 has a leading term independent of the wave vector magnitude given by
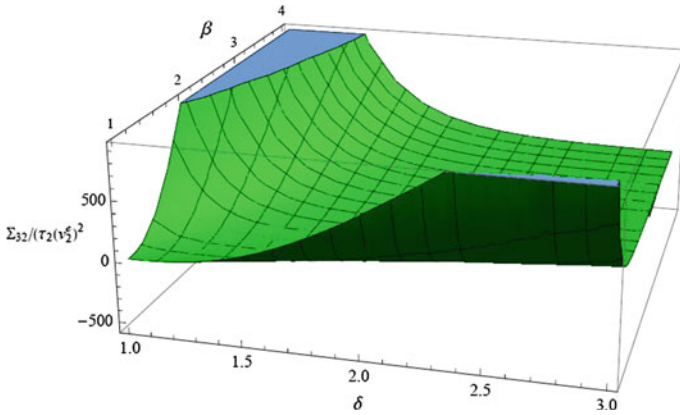
Fig. 1 Real part of root Σ_{32} for $\alpha = 100$. We recall that δ and β correspond to the quotient between the equilibrium densities and the relaxation times τ_1, τ_2
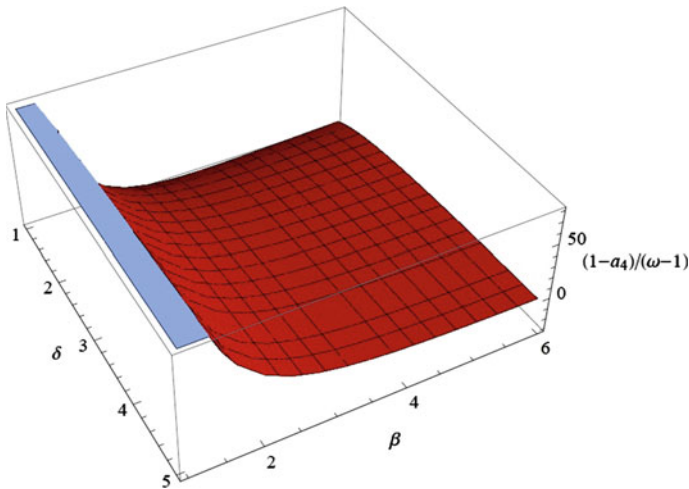
Fig. 2 The effective relaxation time determined by the leading term in root Σ_4

the relaxation time in the slow class (τ_1), obviously positive. This root is associated with mode v_1, which also propagates with a speed determined by the fundamental diagram.

The modes in the fast class (ρ_2, v_2) also propagate and both of them determine the stability condition. First, the real part in root Σ_3 is given through Σ_{32} and it can be written as

$$\frac{\Sigma_{32}}{\tau_2(v_2^e)^2} = \frac{1}{\alpha(a_4 - 1)^3}\left[(\alpha + 1)\left(\frac{a_2\rho_2^e}{v_2^e}\right)^2 - \left(\frac{c_2}{v_2^e}\right)^2\right], \tag{28}$$

where $c_2 = \frac{1}{1-a_4}[(a_4 - 1)v_2^e - a_2\rho_2^e]$ is the propagation speed for mode ρ_2.

Lastly, the leading term in root Σ_4 determines an effective relaxation time given as $(1 - a_4)/\tau_2$, which must be positive to have the interpretation given as time of response in the fast class. Figure 1 shows this characteristic for a region of the parameters δ, β with $\alpha = 100$. It should be mentioned that this characteristic is valid only for the equilibrium state $(v_2^e/v_1^e)^-$ meaning that this equilibrium state represents a physical point of interest. Its behaviour is shown in Fig. 2, where we can see that the region of stability coincides with the stability situation for Σ_{32}.

5 Concluding Remarks

The kinetic model based on the reduced Paveri-Fontana equation when applied to two classes of drivers leads to a macroscopic model where the interaction between user classes plays an important role. In fact, even in the simplest case studied in this paper we have found that the free flow is stable only for a region of densities and relaxation times. The analysis and figures shown tell us that the stability occurs for certain regions in the δ and β. First, $\delta > 1$ which means that the density of the slow vehicles must be greater than the density of fast vehicles. Besides the fact that $\beta > 1$ shows that the relaxation time for the slow class is bigger than the corresponding relaxation time for the fast class. Both conditions together lead to the stability of just one equilibrium state for which it is possible to obtain free flow, at least in a small region. It should be mentioned that this result represents a step in the complete analysis of the model and some simulations must be performed in the unstable region to possibly find other traffic phases.

References

1. Helbing, D.: Traffic and related self-driven many-particle systems. Rev. Mod. Phys. **73**(4), 1067 (2001)
2. Hoogendoorn, S., Bovy, P.: Modeling multiple user-class traffic. Trans. Res. Rec. J. Trans. Res. Board **1644**, 57–69 (1998)
3. Kerner, B.S.: Introduction to modern traffic flow theory and control: the long road to three-phase traffic theory. Springer Science & Business Media (2009)
4. Kerner, B.S., Konhäuser, P.: Cluster effect in initially homogeneous traffic flow. Phys. Rev. E **48**(4), R2335 (1993)
5. Marques, W., Méndez, A.: On the kinetic theory of vehicular traffic flow: Chapman-Enskog expansion versus grads moment method. Phys. A Stat. Mech. Appl. **392**(16), 3430–3440 (2013)
6. Méndez, A., Velasco, R.: Kerner's free-synchronized phase transition in a macroscopic traffic flow model with two classes of drivers. J. Phys. A Math. Theor. **46**(46), 462001 (2013)
7. Shvetsov, V., Helbing, D.: Macroscopic dynamics of multilane traffic. Phys. Rev. E **59**(6), 6328 (1999)
8. Treiber, M., Kesting, A.: Traffic Flow Dynamics, Data, Models and Simulation. Springer, Berlin (2013)
9. Velasco, R., Marques Jr, W.: Navier-stokes-like equations for traffic flow. Phys. Rev. E **72**(4), 046102 (2005)
10. van Wageningen-Kessels, F., Van Lint, H., Vuik, K., Hoogendoorn, S.: Genealogy of traffic flow models. EURO J. Trans. Logist. **4**(4), 445–473 (2015)

Microscopic Simulations of Oversaturated City Traffic: Features of Synchronised Flow Patterns

Gerhard Hermanns, Peter Hemmerle, Hubert Rehborn, Boris S. Kerner and Michael Schreckenberg

Abstract Understanding the physics of vehicular traffic and the emergence of traffic patterns in city traffic is important for the implementation of traffic management measures. Recently, the synchronised flow pattern has been found in empirical GPS probe vehicle data of oversaturated city traffic (Phys Rev E 90:032810, 2014 [13]). Traffic simulation models based on classical theories cannot reproduce this synchronised flow. We present simulation results of oversaturated city traffic with the stochastic microscopic Kerner-Klenov traffic flow model that is based on Kerner's three-phase traffic theory. These results show features of synchronised flow. It is found that the drivers speed adaptation effect plays the key role in the understanding of the emergence of synchronised flow in oversaturated city traffic. The physical meaning of the speed adaptation effect in oversaturated city traffic is explained. The influence of the speed adaptation effect on the average speed and travel time in oversaturated city traffic is investigated.

G. Hermanns (✉) · B.S. Kerner · M. Schreckenberg
Physics of Transport and Traffic, University of Duisburg-Essen,
Lotharstr. 1, 47057 Duisburg, Germany
e-mail: gerhard.hermanns@uni-due.de

B.S. Kerner
e-mail: boris.kerner@uni-due.de

M. Schreckenberg
e-mail: michael.schreckenberg@uni-due.de

P. Hemmerle · H. Rehborn
Daimler AG, RD/RTF, HPC: 059-X832, 71063 Sindelfingen, Germany
e-mail: peter.hemmerle@daimler.com

H. Rehborn
e-mail: hubert.rehborn@daimler.com

1   Oversaturated City Traffic

On an urban road with a traffic signal various congested traffic patterns can be observed. The understanding of these city traffic phenomena is important for the development of effective tools for traffic management and intelligent transportation systems.

Traffic signals at city intersections act as bottlenecks determining the main features of city traffic. Urban traffic on a multi-lane road with a traffic signal at its end can either be oversaturated or undersaturated. In undersaturated city traffic all vehicles waiting in a queue in front of a traffic signal during the red light phase can pass the signal in the next green light phase. In oversaturated city traffic on the other hand, not all vehicles can pass and therefore the queue of waiting vehicles grows with each cycle of the signal. In accordance with classical theories as in [2, 3, 18, 20–22], when the flow rate increases above some signal capacity value, a transition occurs from under- to oversaturated traffic which consists of a series of moving queues, sequences of stopped vehicles interrupted by sequences of vehicles that move from one moving queue to the next adjacent queue downstream. The mean duration of a vehicle stop within a moving queue does usually not change while the moving queue propagates upstream of the signal.

Based on simulations in the framework of the three-phase theory [7, 8, 10], Kerner et al. recently predicted that in addition to classical sequences of moving queues, in oversaturated traffic synchronised flow pattern(s) (SP) should also occur [17]. Empirical synchronised flow has recently been found in an empirical study of anonymised GPS probe vehicle traces measured in navigation systems of TomTom company [6, 13] and common empirical characteristics and features of synchronised flow have been revealed. In this paper, based on the use of the Kerner-Klenov stochastic microscopic traffic flow model for two-lane city road [9, 11, 12, 14–16] in the framework of Kerner's three-phase theory, we make a classification of different spatio-temporal patterns which can occur in oversaturated traffic with different parameters of drivers speed adaptation.

2   Kerner-Klenov Simulation Model

In contrast with two-phase traffic flow models with a fundamental diagram (e.g., [1, 4, 19], in the stochastic model [14–16] used for all simulations, there is a 2D-region of synchronised flow associated with the fundamental hypothesis of three-phase theory (see Chap. 3.2 in [8]). When a driver approaches a slower moving preceding vehicle and he cannot overtake it, the driver begins to decelerate and adapts its speed to the speed of the preceding vehicle, when the gap g to the preceding vehicle becomes smaller than a synchronisation gap G. This driver's speed adaptation occurs under condition $g_{\text{safe}} \leq g \leq G$, where g_{safe} is a safe gap.

We use a discrete version of a stochastic three-phase microscopic model of Kerner and Klenov [14–16]. The physics of the model variables are explained in [7, 8].

The parameters of the model have been adapted for city traffic in [9, 11, 12]. All simulations are made with the same set of parameters as in [12].

In the model, if a vehicle reaches the upstream front of a moving queue at a signal it decelerates as it does at the upstream front of a wide moving jam propagating on a road without traffic signals [7, 8]. During the green light phase, vehicles accelerate at the downstream front of the moving queue (queue discharge) with a random time delay as they do at the downstream jam front. During the yellow phase a vehicle passes the signal location, if the vehicle can do it until the end of the yellow phase; otherwise, the vehicle comes to a stop at the signal.

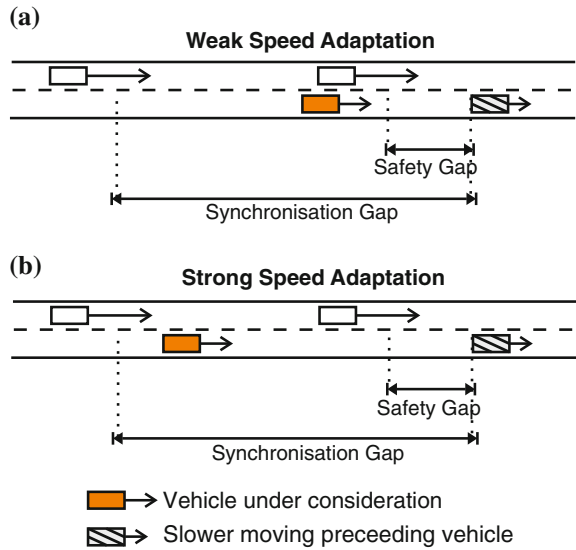## 2.1 Speed Adaptation Effect

A key role in the simulation of synchronised flow plays the driver's speed adaptation for which we use a stochastic description through the probabilities p_1 and p_2 in Eq. (14) of [12]. We write these probabilities as follows:

$$p_1 = \min(1, (1 + \varepsilon)p_1^{(0)}), \quad p_2 = \min(1, (1 + \varepsilon)p_2^{(0)}(v_n)), \tag{1}$$

where $p_1^{(0)} = 0.3$, $p_2^{(0)}(v_n) = 0.48 + 0.32\Theta(v_n - v_{21})$, ε is the coefficient of speed adaptation. The larger ε, the stronger the speed adaptation and, therefore, the larger the mean space gap (the longer the mean time headway) between vehicles in synchronised flow. This can be explained as follows. If on a multi-lane road a driver approaches a slower moving vehicle in front and if he cannot change lane, the driver has to decelerate. In the model he can start to decelerate as soon as he enters the synchronisation gap to his leader. The driver will decelerate if his distance to the leader becomes smaller than the safety gap, and he will accelerate if the distance becomes greater than the synchronisation gap (Fig. 1). But in contrast to models based on classical theories, in three-phase traffic flow models a vehicle does not try to abide to a specific distance to the preceding car, usually the safety gap. Instead, the vehicle tends to adapt its speed to the speed of the preceding car, but it will do this while taking an arbitrary distance to it as long as it stays within the synchronisation gap.

Therefore, the driver could decelerate gradually to the speed of the leader as soon as he enters the synchronisation gap, which would lead to a short headway to the preceding vehicle (Fig. 1a). This situation, described with $\varepsilon = 0$, is called usual or weak speed adaptation and leads to the classical behaviour of stop-and-go traffic: the mean duration of the stops of the vehicles remain almost constant along the moving queues that build upstream of the signal [17]. Alternatively, the driver can decelerate more sharply when reaching the synchronisation gap distance, which would lead to a large headway to the preceding vehicle (Fig. 1b). This situation, described with $\varepsilon > 0$, is called strong speed adaptation and leads to the behaviour that cannot be described by classical theories: the mean duration of the stops of the vehicles decreases the further upstream of the traffic signal the moving queue is located [17]. The growth of the space gap leads to the dissolution of the jam upstream of the traffic signal. So, in oversaturated city traffic adjacent to the traffic signal there is still the classical

Fig. 1 Explanation of speed
adaptation effect: weak
speed adaptation (**a**);
strong speed adaptation (**b**)

(a)

Weak Speed Adaptation

Safety Gap

Synchronisation Gap

(b)

Strong Speed Adaptation

Safety Gap

Synchronisation Gap

Vehicle under consideration

Slower moving preceeding vehicle

stop-and-go behaviour of the vehicles, but further away from the signal synchronised
flow emerges due to the dissolution of the jam.

3 Synchronised Flow in Oversaturated City Traffic

To investigate the influence of the speed adaptation effect, we made simulations
with constant inflow rate on a two-lane road of 5 km length with a traffic signal with
constant phases. Figure 2 shows simulation results for weak ($\varepsilon = 0$) speed adaptation:
not all vehicles waiting in front of the traffic signal are able to pass in the same green
phase, the queue of waiting vehicles grows (Fig. 2a). Vehicles approaching the ends
of the moving queues start to decelerate to a standstill, then after some time accelerate
out of the queue, drive a short distance and decelerate again when they reach the next
queue downstream. This is repeated until the vehicles reach the traffic signal. The
evolving traffic pattern is that of classical Moving Queues as shown in Fig. 2b–d: the
vehicles marked red and blue pass through several moving queues. It should be noted
that Figs. 2b and 3a, b show trajectories of vehicles in the right lane only, except for
the red and blue marked vehicles that are independent on lane changes.

In contrast to the classical behaviour, Fig. 3 shows simulation results for strong
speed adaptation (left: $\varepsilon = 1.33$, right: $\varepsilon = 2$). The length of the queues in front of
the traffic signal does not increase further upstream than a few hundred metres, so
the vehicles do not have to pass more than one or two moving queues in front of the
traffic signal. With increasing value of the speed adaptation coefficient ε the queue
length decrease as they dissolve into the synchronised flow upstream. In both cases
$\varepsilon = 1.33$ and $\varepsilon = 2$, the vehicles drive with relatively small speed of around 10–
20 km/h and do not decelerate to a standstill for most part of the road. The vehicles
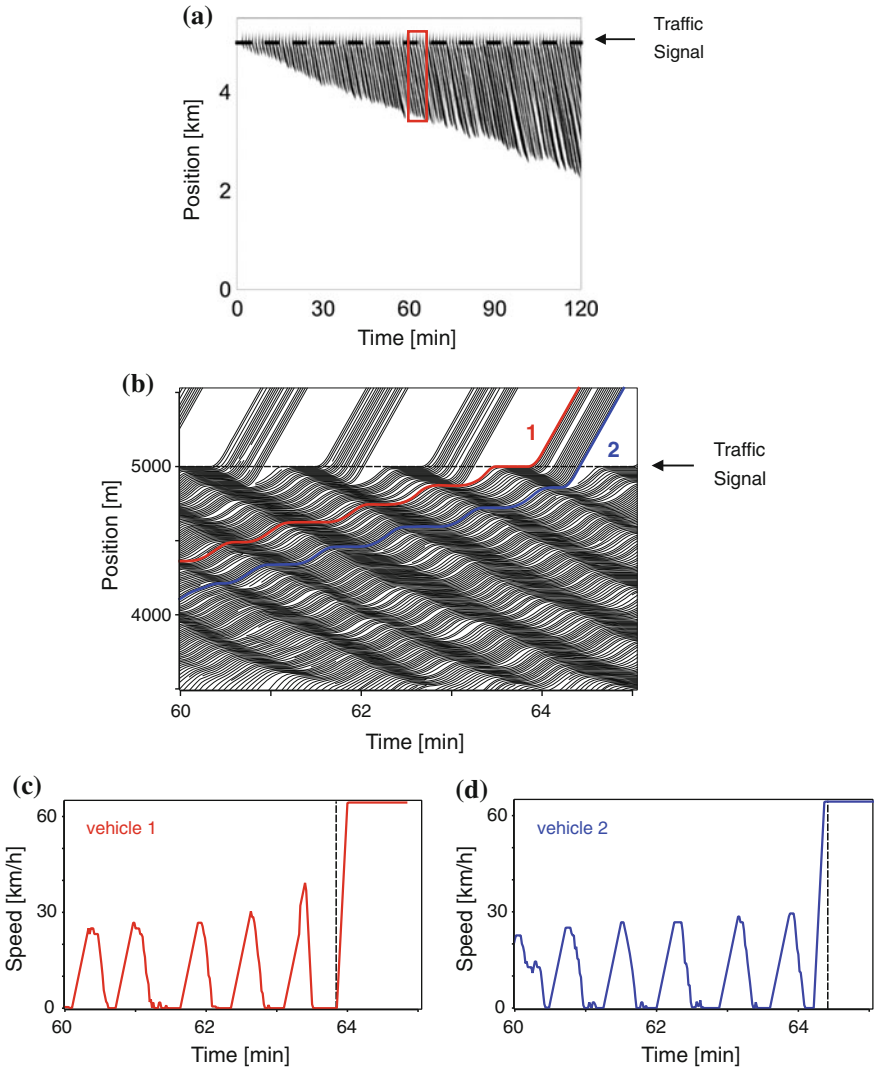
Fig. 2 Simulation results for weak ($\varepsilon = 0$) speed adaptation. *Dotted lines* denote the position of traffic signal and time instant when vehicles pass the traffic signal, respectively. $q_{in} = 948$ veh/h/lane, $\vartheta = 70$ s, $T_R = 35$ s, $T_Y = 4$ s: speed in space and time (**a**); in white regions the speed is higher than 30 km/h, in black regions speed is 0 km/h. Trajectories upstream of traffic signal (**b**); speed profile of vehicle 1 (**c**); speed profile of vehicle 2 (**d**)

driving slowly and not stopping is a characteristic behaviour of the Synchronised Flow phase. This driver behaviour is shown with the microscopic speed profiles in Fig. 3c–f of vehicles marked with numbers 3–6 in Fig. 3a, b.

It is also apparent that the increase of the speed adaptation coefficient leads to higher average speeds of the vehicles and therefore to lower travel times. Table 1
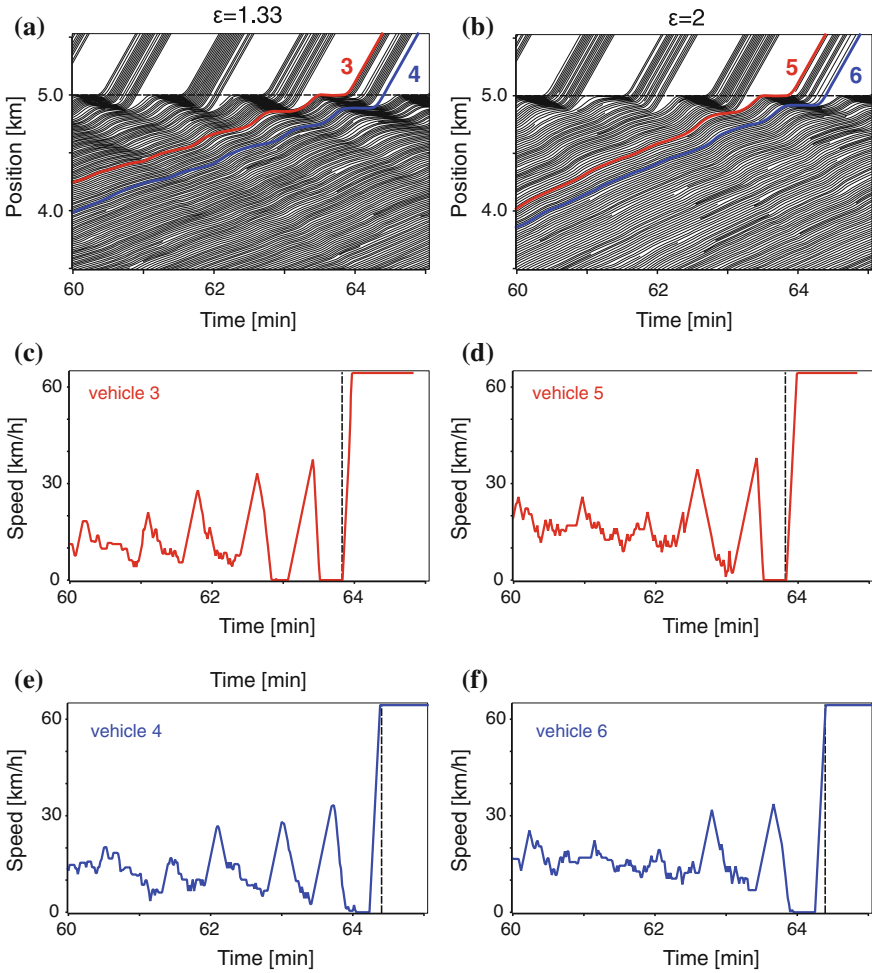
Fig. 3 Simulation results for strong speed adaptation (left: $\varepsilon = 1.33$, right: $\varepsilon = 2$). Dotted lines denote the position of traffic signal and time instant when vehicles pass the traffic signal, respectively. $q_{in} = 948$ veh/h/lane, $\vartheta = 70$ s, $T_R = 35$ s, $T_Y = 4$ s: strong speed adaptation ($\varepsilon = 1.33$): Trajectories upstream of traffic signal (**a**); strong speed adaptation ($\varepsilon = 2$): Trajectories upstream of traffic signal (**b**); speed profile of: vehicle 3 (**c**); vehicle 5 (**d**); vehicle 4 (**e**); vehicle 6 (**f**)

shows average speed and travel time for vehicles numbered 1–6 in Figs. 2 and 3, calculated for the final 800 m upstream of traffic signal. Vehicle 1 drives under the condition of weak speed adaptation ($\varepsilon = 0$) and as it approaches the traffic signal, it is forced to pass several moving queues. This leads to a low average speed of $v_{avg} = 9.6$ km/h and a high travel time of almost 5 min ($T_{tr} = 299$ s) for 800 m. Vehicle 5 drives under the condition of strong speed adaptation ($\varepsilon = 2$) and as it approaches the traffic signal, it drives quite regularly for the first part of the road. Only when it reaches the last part of the road in front of the traffic signal it is forced to stop. This leads to a

Table 1 Average speed and travel time[a] dependent on coefficient of speed adaptation

Coefficient of speed adaptation	Vehicle number	Average speed (km/h)	Travel time (s)
0	1	9.6	299
0	2	11.8	245
1.33	3	16.6	174
1.33	4	19.3	149
2	5	25.7	112
2	6	25.3	114

[a]Speed and travel time calculated for the last 800 m upstream of traffic signal

rather high average speed of $v_{\mathrm{avg}} = 25.7$ km/h and a travel time of only $T_{\mathrm{tr}} = 112$ s for 800 m.

This means that the average speed for vehicles driving under the condition of weak speed adaptation is lower and the travel time is higher than for vehicles driving under strong speed adaptation. It can be explained as follows. Under the condition of a high speed adaptation factor, the vehicles in average tend to greater space gaps (headways) to the preceding vehicles as they decelerate more sharply when they reach the synchronisation gap than under the condition of weak speed adaptation. This also leads to a reduction of the speed fluctuations as can be seen in Fig. 3c–f, respectively. The higher the coefficient of speed adaptation, the more the vehicles spend their time moving.

In conclusion, one can say that the reproduction of the synchronised flow pattern in oversaturated city traffic in the simulation is a direct result of the use of the speed adaptation effect.

4 Conclusions

Oversaturated city traffic has been simulated with the Kerner-Klenov three-phase traffic flow model and the use of the drivers speed adaptation effect. The simulations show that under strong speed adaptation synchronised flow patterns that have previously been found empirically can be produced with this model. Under weak speed adaptation the classical moving queue pattern is reproduced. Strong speed adaptation is associated with an average increase of the space gaps (time headways) that drivers choose while moving in oversaturated city traffic. The higher the speed adaptation factor, the higher the average speed of the vehicles and the lower the average travel time.

The existence of the synchronised flow phase has an important impact on fuel consumption calculations in oversaturated city traffic. As shown recently [5] the fuel consumption of vehicles driving in a moving queue pattern is considerably higher than that of vehicles driving in a synchronised flow pattern.

References

1. Barlovic, R., Santen, L., Schadschneider, A., Schreckenberg, M.: Metastable states in cellular automata for traffic flow. Eur. Phys. J. B Condens. Matter Complex Syst. **5**(3), 793–800 (1998)
2. Dion, F., Rakha, H., Kang, Y.S.: Comparison of delay estimates at under-saturated and over-saturated pre-timed signalized intersections. Transportation Research Part B: Methodological **38**(2), 99–122 (2004)
3. Gartner, N.H., Stamatiadis, C.: Traffic networks, optimization and control of urban. In: Encyclopedia of Complexity and System Science, pp. 9470–9500. Springer (2009)
4. Gipps, P.G.: A behavioural car-following model for computer simulation. Transp. Res. Part B: Methodological **15**(2), 105–111 (1981)
5. Hemmerle, P., Hermanns, G., Koller, M., Rehborn, H., Kerner, B.S., Schreckenberg, M.: Macroscopic consumption matrix for on-line energy-efficient route guidance. In: Transportation Research Board 94th Annual Meeting, 15-2751 (2015)
6. Hemmerle, P., Koller, M., Rehborn, H., Hermanns, G., Kerner, B.S., Schreckenberg, M.: Increased consumption in oversaturated city traffic based on empirical vehicle data. In: Advanced Microsystems for Automotive Applications 2014. Smart Systems for Safe, Clean and Automated Vehicles, pp. 71–79. Springer (2014)
7. Kerner, B.S.: The Physics of Traffic: Empirical Freeway Pattern Features, Engineering Applications, and Theory. Springer (2004)
8. Kerner, B.S.: Introduction to Modern Traffic Flow Theory and Control: The Long Road to Three-Phase Traffic Theory. Springer (2009)
9. Kerner, B.S.: Physics of traffic gridlock in a city. Phys. Rev. E **84**(4), 045102 (2011)
10. Kerner, B.S.: Criticism of generally accepted fundamentals and methodologies of traffic and transportation theory: a brief review. Phys. A **392**(21), 5261–5282 (2013)
11. Kerner, B.S.: The physics of green-wave breakdown in a city. EPL (Europhys. Lett.) **102**(2), 28010 (2013)
12. Kerner, B.S.: Three-phase theory of city traffic: moving synchronized flow patterns in under-saturated city traffic at signals. Phys. A **397**, 76–110 (2014)
13. Kerner, B.S., Hemmerle, P., Koller, M., Hermanns, G., Klenov, S.L., Rehborn, H., Schreckenberg, M.: Empirical synchronized flow in oversaturated city traffic. Phys. Rev. E **90**, 032810 (2014)
14. Kerner, B.S., Klenov, S.L.: A microscopic model for phase transitions in traffic flow. J. Phys. A **35**(3), L31 (2002)
15. Kerner, B.S., Klenov, S.L.: Microscopic theory of spatial-temporal congested traffic patterns at highway bottlenecks. Phys. Rev. E **68**, 036130 (2003)
16. Kerner, B.S., Klenov, S.L.: Phase transitions in traffic flow on multilane roads. Phys. Rev. E **80**, 056101 (2009)
17. Kerner, B.S., Klenov, S.L., Hermanns, G., Hemmerle, P., Rehborn, H., Schreckenberg, M.: Synchronized flow in oversaturated city traffic. Phys. Rev. E **88**(5), 054801 (2013)
18. Little, J.D.: The synchronization of traffic signals by mixed-integer linear programming. Oper. Res. **14**(4), 568–594 (1966)
19. Nagel, K., Schreckenberg, M.: A cellular automaton model for freeway traffic. J. Phys. I **2**(12), 2221–2229 (1992)
20. Newell, G.F.: Approximation methods for queues with application to the fixed-cycle traffic light. Siam Rev. **7**(2), 223–240 (1965)
21. Robertson, D.I.: Transyt: a traffic network study tool (1969)
22. Webster, F.: Traffic signal settings, road research technical paper no. 39. Road Research Laboratory (1958)

Traffic Simulations with Empirical Data: How to Replace Missing Traffic Flows?

Lars Habel, Alejandro Molina, Thomas Zaksek, Kristian Kersting and Michael Schreckenberg

Abstract For the real-time microscopic simulation of traffic on a real-world road network, a continuous input stream of empirical data from different locations is usually needed to achieve good results. Traffic flows for example are needed to properly simulate the influence of slip roads and motorway exits. However, quality and reliability of empirical traffic data is sometimes a problem for example because of damaged detectors, transmission errors or simply lane diversions at road works. In this contribution, we attempt to close those data gaps of missing traffic flows with processed historical traffic data. Therefore, we compare a temporal approach based on exponential smoothing with a data-driven approach based on Poisson Dependency Networks.

1 Introduction

Microscopic road traffic simulations based on a real-world topology usually need many preparations to deliver reliable results. At first, a promising simulation model has to be chosen and the topology has to be converted into a model-friendly representation. When the simulation shall use traffic data from real-world detectors, they

L. Habel (✉) · T. Zaksek · M. Schreckenberg
Physik von Transport und Verkehr, Universität Duisburg-Essen,
47057 Duisburg, Germany
e-mail: lars.habel@uni-due.de

T. Zaksek
e-mail: thomas.zaksek@uni-due.de

M. Schreckenberg
e-mail: michael.schreckenberg@uni-due.de

A. Molina · K. Kersting
Fakultät für Informatik, Technische Universität Dortmund,
LS VIII, 44221 Dortmund, Germany
e-mail: alejandro.molina@tu-dortmund.de

K. Kersting
e-mail: kristian.kersting@cs.tu-dortmund.de

and the belonging areas to fill in (or remove) vehicles according to the data have to be implemented as well. For complex topologies, this means that the simulation results then not only depend on the quality of the model and the topology representation, but also on a possibly huge number of empirical traffic detectors.

Usually, empirical traffic detectors provide new traffic flow data every minute. This data is then used in the simulation to reproduce all the recent traffic in- and outflows of the real-world system. Therefore, the permanent availability of empirical data is necessary especially at on- and off-ramps. Unfortunately, the reliability of empirical detectors is often not good enough to ensure this requirement minute by minute. This contribution provides a comparison of two approaches to close the resulting gaps in empirical data, one working on temporal level, the other one on level of dependencies between multiple detectors.

2 Methods

In case of missing data, a decision has to be made how the simulation shall handle this issue. Principally, different strategies are possible: Some detectors are redundant, so the missing data simply could be ignored because the coverage of neighbouring detectors is sufficient enough. However, it is often difficult to decide whether a detector is important or not. The importance of such a redundant detector can also rise when neighbouring detectors go off-line. Additionally, each detector often has a complex neighbourhood, which is sometimes not fully known because the given location data is lacking precision or is outdated. The same issues can also occur on temporal level because it is usually unknown how long a detector will be off-line. This is especially problematic when the simulation is used in a real-time context, i.e. in a traffic information system [1], and thus new empirical data is queried by the simulation at run time.

The described problem is somewhat related to short-term traffic forecasting methods and to interpolation methods for incomplete time series in general. These topics have already been addressed by numerous approaches (see e.g. [8] for a summary). However, these are often complicated to understand or to apply, or they also need e.g. a complete set of historical data or a working detector neighbourhood. As described, these preconditions are often not met. Because of this, we focus on two simple and resilient methods for filling these gaps in real-time.

2.1 Exponential Method

The temporal approach [2] is based on exponential smoothing a set **j** of historical traffic flows. **j** comprises previously collected traffic flows from up to 30 timestamps t measured at the particular detector, which are chosen by a clustering algorithm that distinguishes between different weekdays, school holidays and public holidays. The

predicted flow j_t^* is then obtained by

$$j_t^* = \alpha j_t + \alpha \sum_{i=1}^{t-1} (1-\alpha)^i j_{t-i} + (1-\alpha)^t j_0 , \qquad (1)$$

where j_t is the most recent historical traffic flow. We use $\alpha = 0.8$ for long-term gap filling [3].

2.2 *Poisson Dependency Network (PDN)*

For the dependency-based gap filling, we use the recently proposed Poisson Dependency Networks [4]. Dependency networks are graphical models, meaning that each graph node represents a single detector and each edge between nodes describes dependencies between them. Note that neighbouring detectors on the road do not have to be strongly connected in the PDN.

Here, the set $\mathbf{j}$ comprises traffic flows from other detectors, but measured at the same time. The probability function to obtain a traffic flow for detector a given all the other flows $\mathbf{j}_{\backslash a} = \mathbf{j} \setminus \mathbf{j}_a$ at that time is then denoted as

$$p(j_a | \mathbf{j}_{\backslash a}) = \frac{\lambda_a^{j_a}(\mathbf{j}_{\backslash a})}{j_a!} e^{-\lambda_a(\mathbf{j}_{\backslash a})} , \qquad (2)$$

where $\lambda_a(\mathbf{j}_{\backslash a})$ is a function which contains all knowledge about correlations between detector a and the others. In this contribution, each λ is modelled by Poisson regression trees which have been learned by the R-package `rpart`.

3 Comparison Setup

For the comparison, we use empirical traffic data from the Cologne orbital motorway network in Germany, which is formed by the motorways A1, A3 and A4 and is about 100 km long. Traffic data is provided by 187 detectors at 95 cross-sections.

Both approaches use historical traffic data in a certain sense. In the Exponential Method, there is usually a window of 1 week between each time stamp t, because Eq. (1) is not suitable for intra-day traffic forecasting, as it does not take the intra-day shape of a traffic flow time series into account. For the calculation of Eq. (1), historical timestamps with missing values and timestamps of different classes (i.e. holidays, see Sect. 2) have to be removed, meaning that the effective window between two timestamps is sometimes more than 1 week.

To create a level playing field for the comparison, the PDN approach uses data from the preceding week as well to learn $\lambda_a(\mathbf{j}_{\backslash a})$, see Fig. 1 for a graphical explanation. A sufficient number of timestamps has to be in the training set to reflect the correlations, so we decided to use a 60-min window from that week. Note that in contrast to the Exponential Method, the PDN gets data from n detectors. The set of all 187 detectors is resized dynamically to n for each prediction, because detectors without passed
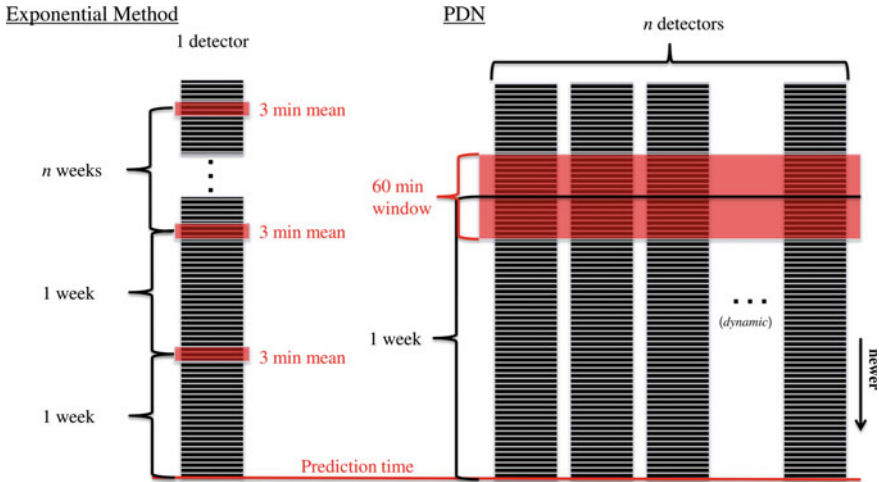
Fig. 1 Visualisation of different data sets used for the predictions. Each column represents a time series of a single detector. Highlighted rows are used for the prediction at the next new time stamp

traffic (i.e. with $\text{var}(\mathbf{j}_a) = 0$) during the 60-min window have to be excluded. Also, missing values have to be removed. This can be done row-wise by removing the whole time stamp, but usually a huge number of missing values is produced by a small subset of detectors. We have excluded them column-wise first, if more than 5 % of their values were missing.

We used traffic data from 21/09/2015 to 27/09/2015 to test the predictions and data from the preceding week to train the PDN. The exponential method got data from the preceding week and up to 30 weeks before.[1]

4 Results

To compare the accuracy of both strategies, we calculated the root-mean-square error between all N predicted traffic flows $\mathbf{P}$ and observed traffic flows $\mathbf{O}$

$$\text{RMSE} = \sqrt{\frac{1}{N} \sum_{i=1}^{N} (P_i - O_i)^2} \tag{3}$$

and its normalised variant

$$\text{NRMSE} = 100 \frac{\text{RMSE}}{\text{sd}(\mathbf{O})}, \tag{4}$$

where $\text{sd}(\mathbf{O})$ is the standard deviation of all observations.

The overall prediction accuracies are shown in Table 1. There, every time stamp of the whole test week is included. It is obvious that both prediction methods are

---

[1] These values had been calculated in advance as a part of OLSIM [1].

Table 1 Overall prediction accuracy

Method	RMSE (vehs/min)	NRMSE (%)
Exponential	4.93	53.2
PDN	**4.50**	**48.6**

bold numbers show better results

not faultless, because both of them basically perform a 1-week-prediction of 1-min count data.

For a deeper analysis, it is typically better to use a subset of data from working days only. We also categorised the data by time interval[2] and created a spatial visualisation, which is shown in Fig. 2, by using the R-package ggmap [6].

The visualisation reveals that prediction problems typically are bound to topological problems: The north-eastern part of the network around the motorway junction between A1 (connects north-east and west) and A3 (connects northeast and south-east) was affected by several construction sites at time of this analysis. On the A1 a speed limit of 60 km/h had to be implemented because of repairs on a damaged bridge, also trucks were not allowed to pass that bridge. Parallel, works on the A3 started to upgrade the road cross-section from three to four lanes per direction. These required temporally closed lanes and driving on the hard shoulder. Hence, these sites and the related upstream road sections were heavily affected by congestion because of their huge bottleneck impact. They can be identified in Fig. 2 by the size of the dots, which denote the mean empirical velocity at test time.

The colours of the dots in Fig. 2 show the mean differences between predicted and observed traffic flows per lane, meaning that negative differences indicate an ongoing underestimation of flow by the prediction. As can be seen, the Exponential Method underestimated traffic on the A3 inside and upstream of the bottleneck heavily. One reason for this are the temporal lane closures. Then, the distribution of vehicles on the remaining lanes changes in contrast to the preceding weeks and thus the exponential predictions become incorrect. The predictions from the PDN clearly benefit from the learned correlations, although it was trained with historical data as well. However, the PDN sometimes overcompensated the lane closure, albeit an overestimation of traffic flow is usually less of a problem than underestimation: Traffic breakdowns happen at high traffic flows and with an underestimation, a potentially unstable traffic situation would be missed by the simulation. Also, common microscopic traffic models tend to underestimate the spatial extent of congestion [7], so that a slight overestimation usually will not harm the simulation results.

One has to note that although the mean differences are often very low outside the hotspot areas, the RMSE is usually higher, because positive and negative differences balance each other out from minute to minute. This is shown in Fig. 3, which also shows that the (N)RMSE rises heavily inside a jam. However, the PDN is always a bit more accurate.

Most of the time, time series of observations and both predictions have a quite similar shape. Figures 4 and 5 show typical examples of special situations, where

---

[2]Time intervals (in local time): morning 05:00–09:59, midday 10:00–13:59, afternoon 14:00–17:59, evening 18:00–21:59, night 22:00–04:59.

(a)

(b)
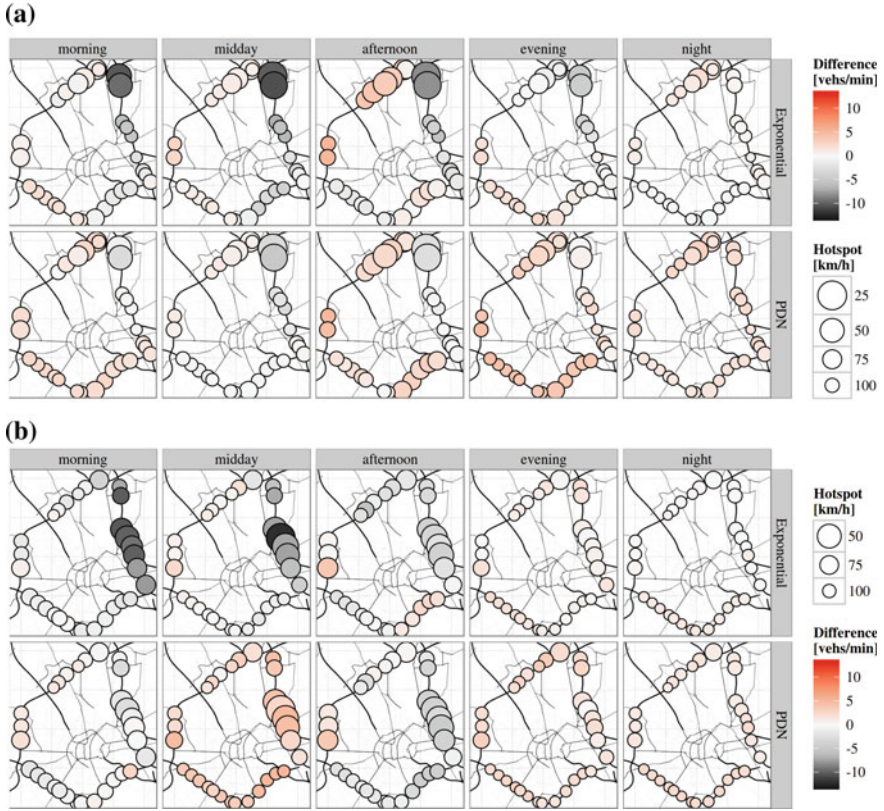
Fig. 2 Spatial visualisation of differences between predicted and observed traffic flows on working days by time interval. Each dot represents a detector cross-section in clockwise (**a**) or anti-clockwise driving direction (**b**). The size of each dot shows the mean empirical velocity measured in the corresponding time interval during the test week. *First row* Exponential Method, *Second row* PDN
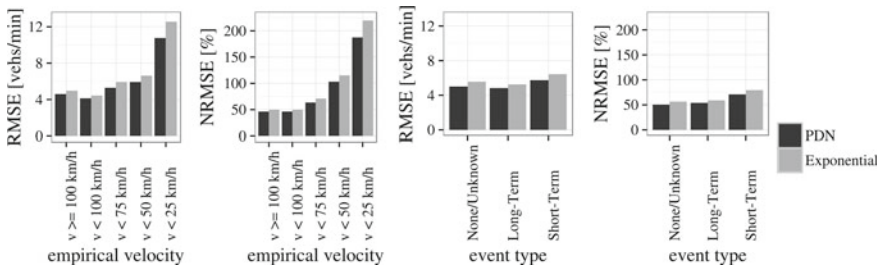
Fig. 3 Prediction accuracy in congested traffic on working days in anti-clockwise direction. Results are divided into different classes of empirical velocities and TMC event type at test time
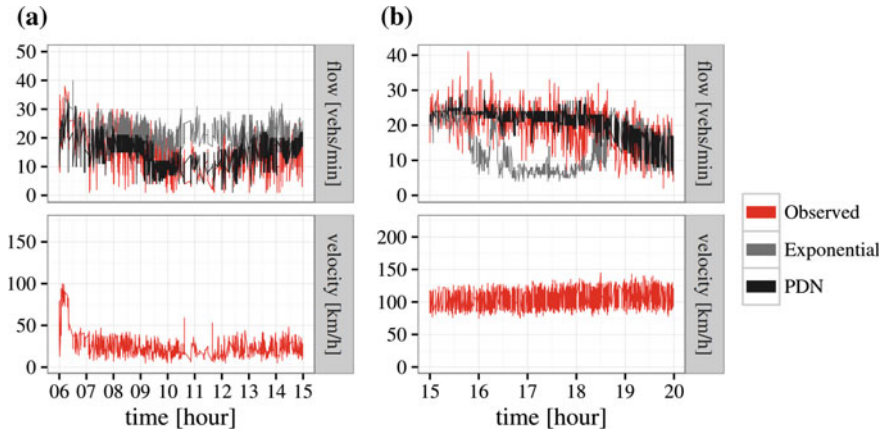
Fig. 4 Different time series with diverted traffic: less traffic than usual on the northbound A3. Some data points are missing because of missing observed data (**a**); more traffic than usual on the eastbound A4 avoiding the jammed north-eastbound A1 (**b**)
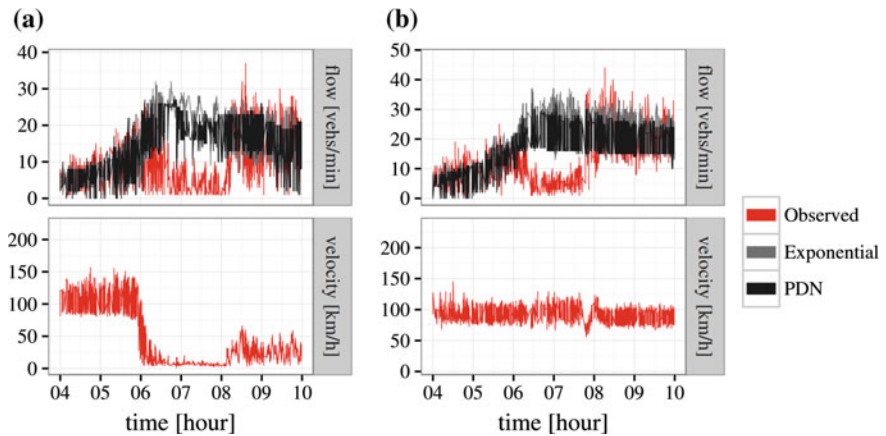
Fig. 5 Time series with an accident on the A3 in northbound direction: upstream of the bottleneck (**a**); downstream of the bottleneck (**b**)

Fig. 6 Established links and the corresponding weights in the PDN for a northbound detector on the motorway A3, located in the south-eastern corner of the map. The hotspot area determines the upstream traffic conditions
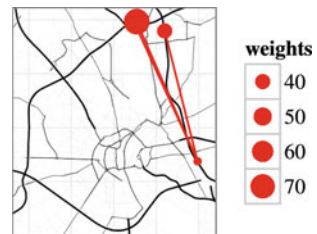
the predictions differ. When traffic uses different ways than usual (see Fig. 4), the PDN approach has a clear advantage, because it implicitly detects the necessary dependencies to deal with the situation. However, it is not able to avoid any misprediction. Figure 5 shows time series with a big accident during the rush hours, where prediction accuracy of traffic flow was not only affected upstream of the incident, but also downstream, because the flow was drastically reduced by the accident. This event was not foreseeable for both methods.

5 Conclusion

In this contribution, we have analysed the prediction accuracy of Poisson Dependency Networks in the context of traffic simulations in comparison to an older approach. It is interesting to see how good the PDN performed, given the fact that we did not implement the detector network topology explicitly. Further improvements are planned, namely using a more flexible window of training data as well as trying out different strategies for learning $\lambda_a(\mathbf{j}_{\backslash a})$.

Also, a detailed analysis of the graphical structure of the PDN seems to be promising. An example for the correlations the PDN is revealing is shown in Fig. 6. With the described training window, the PDN only established up to 4 edges per node. When used with more learning data it uses more edges, even to the other side of the ring, as we showed in [5] in a different context.

References

1. Brügmann, J., Schreckenberg, M., Luther, W.: Real-time traffic information system using microscopic traffic simulation. In: Al Begain, K., Al Dabass, D., Orsoni, A., Cant, R., Zobel, R. (eds.) EUROSIM 2013—8th EUROSIM Congress on Modelling and Simulation, pp. 448–453. EUROSIM, IEEE, Cardiff, Wales (2013)
2. Chrobok, R., Kaumann, O., Wahle, J., Schreckenberg, M.: Three categories of traffic data: historical, current, and predictive. In: Schnieder, E., Becker, U. (eds.) Proceedings of 9th IFAC Symposium Control in Transportation Systems, pp. 250–255. Pergamon (2001)
3. Chrobok, R., Kaumann, O., Wahle, J., Schreckenberg, M.: Different methods of traffic forecast based on real data. Eur. J. Oper. Res. **155**(3), 558–568 (2004)
4. Hadiji, F., Molina, A., Natarajan, S., Kersting, K.: Poisson dependency networks: gradient boosted models for multivariate count data. Mach. Learn. **100**(2–3), 477–507 (2015)
5. Ide, C., Hadiji, F., Habel, L., Molina, A., Zaksek, T., Schreckenberg, M., Kersting, K., Wietfeld, C.: LTE Connectivity and vehicular traffic prediction based on machine learning approaches. In: 2015 IEEE Vehicular Technology Conference (VTC Fall) (2015)
6. Kahle, D., Wickham, H.: ggmap: Spatial visualization with ggplot2. R J. **5**(1), 144–161 (2013)
7. Knorr, F., Schreckenberg, M.: On the reproducibility of spatiotemporal traffic dynamics with microscopic traffic models. J. Stat. Mech. Theory Exp. **2012**(10), P10018 (2012)
8. Vlahogianni, E.I., Karlaftis, M.G., Golias, J.C.: Short-term traffic forecasting: where we are and where we're going. Transp. Res. Part C: Emerg. Technol. **43**, 3–19 (2014)

Dynamic Model for Assignment in a 'Sky-Car' Transit System: Spatial Interactions with Other Common Transport Modes

Kwami Sossoe and Jean-Patrick Lebacque

Abstract This paper provides a Lagrangian dynamic fluid model of the traffic of Personal Rapid Transit (PRT) system or of personal rapid maglev-transporters. The transport system using these maglev-transporters or sky-podcars operates in the style of demand-responsive systems. The advantage of the sky-podcars is that they are fast and that they do not operate in the same physical space as the other ground transportation modes. Thus they will contribute to alleviate congestion. We model the dynamics of the sky-podcars transportation system and we solve the problem of relocation with minimum cost in this maglev system. An analysis of assumptions of effective operation of the PRT is carried out. Reactive dynamic assignment in such PRT system is described. In a multi-modal transport system where the maglev-transporters mode is taken into account, we describe the multi-modal dynamic assignment and its spatial interactions with other common transportation systems.

1 Introduction

Transport demands of passengers increasingly grow nowadays in big cities and business cities all over the world. Those demands of traffic in view of networks supplies of relatively small size lead to traffic incidents, especially problems of traffic congestions. Researchers and engineers construct, and deploy many scientific tools in the sense that these tools can handle these issues. That is in the line of network traffic flow management. Different traffic flow models, built at different scales of details and representations, such as link and node based flows, and network-based flows, abound in the literature. However, one still observes that operators' services are not

K. Sossoe (✉)
IRT SystemX, 8 Avenue de la Vauve, 91120 Palaiseau, France
e-mail: kwami.sossoe@irt-systemx.fr

J.-P. Lebacque
IFSTTAR, 14-20 Boulevard Newton, Cité Descartes, Champs sur Marne,
77447 Marne-La-Vallée Cedex 2, France
e-mail: jean-patrick.lebacque@ifsttar.fr

quite performing to provide non-congested and fluid traffic for their correspondent networks, in many cities.

In order to address traffic issues, many new transport vehicles and transport systems are being built. We notice autonomous vehicles, automated vehicles, and further special technologies such V2V (vehicle-to-vehicle) communication and also V2I (vehicle-to-infrastructure) communication for traffic management. This paper focuses on a new demand-responsive transportation system, namely sky-car transportation system. This is a new generation of Personal Rapid Transit (PRT) system [7], and is being held by the project skyTran. skyTran is a new project for the construction of rapid vehicles (podcars or sky-cars) that use maglev system relying on magnetic levitation rather than wheels (or conventional motors). The maglev propels podcars along sky railways lanes, resulting in nearly silent transportation. The maglev system makes safe, reliable form of travel, with high speed up to 240 km/h; thus, allowing local, regional and national networks to be built. Further, skyTran extends the transport network area by creating a new traffic game area at twenty feet from the ground. In order to prevent congestion on the main sky railways, podcars are pulled off onto the sidetracks for dropping off and picking up the passengers. Since the chosen context is futurist, a study has been carried out on the reliability and the efficiency of the sky-car system. Its impacts and its spatial interactions with the common already existing transport modes such as classic car, taxi, bus, bike, ride-car, carpooling, tram or train are studied. An implementation of such a sky-car system shall obtain an evaluation of the proposed solution in this paper in Sects. 2 and 3.

The contents of the paper are the following: we recall graph approach for modelling network in Sect. 2 with few extending components. Section 3 addresses the fluid model of the dynamic of podcars by describing motions of the personal rapid maglev-transporters. Some assumptions on how the sky-car transportation system may work efficiently have made. We establish control laws in Sect. 3 and design algorithms for traffic control and for good interactions with other transport modes.

2 Background

2.1 Sky-Car Network—Notion of Maglev-Graph

In connection with transport graph as well, the maglev-graph includes a few different components. We describe this graph, denoted by G_M, by a quadruple of sets (N_M, A_M, L_M, P_M), where N_M is the set of all nodes (that are the intersections, the poles of stations, the departure and the arrival portals at stations) of the maglev system, A_M is the set of arcs connecting two nodes of the same maglev-lanes. There are different maglev-lanes such as deceleration lanes, non-stop guideways, acceleration non-stop guideways (or acceleration lanes) which are vertically set up above the former. We denote by L_M the set of all lanes. P_M denotes the set of all pairs of

portals (departure and arrival) that physically represent the stations or the sky-car stops location. At any station, there is an 'off line guideway' which keeps sky-cars that are at rest waiting for passengers to board. There are diverging and merging zones, that is to say intersection or nodes, that allow podcars for switching from 'acceleration lane' onto 'low non-stop guideway', and inversely.

2.2 Traffic Models for Demand-Responsive Transports

Taxi services work as demand-responsive transport services, and they have been improved to a more flexible way to respond to transport demands. A succinct review on taxi systems and urban demand-responsive systems are given in [1–6, 8] where multi-agent-based models of simulation are provided for urban dynamic traffic services. These models also addressed the problem of traffic congestions and accidents, CO_2 emissions, air pollution, financial costs, and other environmental damages.

3 Model of the System—Lagrangian Coordinates

This section describes the model of the system: first the sky-car motion formulation, then the demand optimisation, followed by the spatial interactions with other modes.

3.1 Sky-Car Motion Formulation

To set ideas on the dynamic of podcars along sky railways, the following assumptions have made on the functioning of the PRT system.

1. The number of sky-car stations in the system can be as high as desired to reach all transport demands.
2. Sky-cars do not takeover each other except at internal intersection.
3. Capacity of a sky-car is limited, taking a finite number of passengers with a similar profile.
4. Any sky-car is available for only one transport demand.
5. For each transport demand in the system, more than one passenger can enter in the sky-car at the starter station to a target destination station.
6. Two maglev-lanes of the same level cannot intersect with each other at any station; maglev-lanes of different levels interconnect together with poles. That allows avoidance of collisions. The transfer of traffic is made between two lanes of different levels through poles by switches.

7. Generally, we assume that the considered demand-responsive transportation system is equipped with an adaptive cruise control that increases the driving comfort, reducing traffic accidents and increasing the traffic flow throughput.
8. We assume that accelerations of pods do not cost anything while they are offset by decelerations, in term of energy consumption of the system. However, we do not address this aspect which concerns the control of the energy consumption of the system.

Let S be the set of all stations $s \in S$ of the maglev system. Let x denote the position of podcar, $t \geqslant 0$ the time and a the podcar index. $\{x_a(t), t \in \mathbb{R}^+\}$ refers to the trajectory of the podcar $a \in \Lambda$, Λ being the total number of podcars of the transit system, and $x_a^j(t)$ referring to the position of a on the arc $(j) \in A_M$. Let $u_a(t)$ be the speed of the podcar a at the time t, and $w_a(t)$ the acceleration–deceleration of the pod a at the time t. Assuming that vehicles are labelled according to a snapshot of line from downstream to upstream, the podcar labels will increase with the position x. Therefore, $r_a(t) = x_{a-1}(t) - x_a(t)$ is the spacing between vehicle a and its leader $a - 1$ at time t, and $v_a(t) = \dot{r}_a(t) = \dot{x}_{a-1}(t) - \dot{x}_a(t) = u_{a-1}(t) - u_a(t)$ is its relative velocity at the same time t.

Let us describe the dynamic of the vehicles along the sky transit network. Along the same lane, and on a line section without intersection and without switch pole, the dynamic of sky-car is governed by the following system of equations: $\forall t \geq 0, \forall a \in \Lambda, \exists!(j) \in A_M$ such that:

$$\begin{cases} x_a^j(t+1) = x_a^j(t) + \delta t u_a^j(t) \\ u_a^j(t) = \min \left(U_e\left(r_a^j(t)\right), u_{p_a}\left(x_a^j(t)\right) \right). \end{cases} \tag{1}$$

$U_e\left(r_a^j(t)\right)$ is the speed equilibrium relationship depicted by Fig. 1. $u_{p_a}\left(x_a^j(t)\right)$ is the sky-car velocity profile that may depend on the vehicle a, the charge of the current link (j) or current arc (j) and the mission of the podcar a. In the sake of capturing all cases, one may apply a following dynamic system (2) instead of the system of governing Eq. (1):
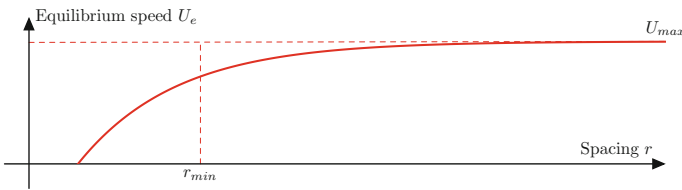
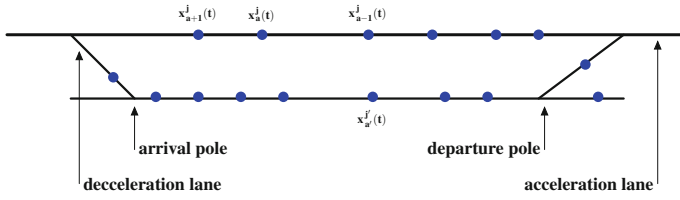**Fig. 1** Spacing-equilibrium speed fundamental diagram of sky-car motion

Fig. 2 Notations of sky-car following model

$\forall t \geq 0, \forall a \in \Lambda, \exists!(j) \in A_M$ such that,

$$\begin{cases} x_a^j(t+1) = x_a^j(t) + \delta t u_a^j(t) \\ u_a^j(t+1) = \min\left(u_a^j(t) + \delta t w_a^j(t), U_e\left(r_a^j(t)\right), u_{p_a}\left(x_a^j(t)\right)\right) \\ w_a^j(t) = f_a\left(r_a^j(t), u_a^j(t)\right). \end{cases} \quad (2)$$

Let us briefly describe how merges and diverges work in our model. Diverges are trivial. Let a be the first podcar on an upstream link (j). Let (d_1) be the next link pertaining to the mission of the podcar a, and nd_1 be the last podcar on this lane. Then the motion of the podcar a is given by Eq. 2 with $r_a^j(t)$ being the sum of the distance from a to the intersection plus the distance from the intersection to the podcar nd_1. This can be stated as: $r_a^j(t) = |x_a(t) - x_I|_{(j)} + |x_i - x_{nd_1}|_{(d_1)}$ (Fig. 2).

Let us now consider a merge with two upstream links (u_1) and (u_2), and (d) the downstream link, a_1 and a_2 the first podcars on links (u_1), (u_2) respectively, and a_d the last podcar on the downstream link. The two upstream podcars are liable to compete for passage through the intersection (I). The first issue to be solved is to determine which podcar will cross first the intersection (I). For each podcar a_i we calculate $\Delta t_i = |x_{a_i}(t) - x_I|_{(u_i)}/u_{a_i}^{u_i}(t)$, time required to reach the intersection. The velocity $u_{a_i}^{u_i}(t)$ is calculated following Eq. 2, with the distance $r_{a_i}^j(t)$ being the sum of the distance from a_i to the intersection plus the distance from the intersection to the podcar a_d. Once the order of passage is decided, it is not changed. The trajectory of the first podcar to pass is calculated by Eq. 2 with respect to the podcar a_d. Let a_1 be this podcar. The trajectory of the second podcar is calculated with respect to the podcar a_d but with an additional term forcing passage as second. This term is applied as long as the podcar a_1 has not exited link (a_1). Thus, the velocity of the podcar a_2 is $u_{a_2}^{u_2}(t+1)$:

$$u_{a_2}^{u_2}(t+1) = \min\left(u_{a_2}^{u_2}(t) + \delta t w_{a_2}^{u_2}(t), U_e\left(r_{a_2}^{u_2}(t)\right), u_{p_a}\left(x_{a_2}^{u_2}(t)\right), \alpha \frac{|x_{a_2} - x_I|_{(a_2)}}{|x_{a_1} - x_I|_{(a_1)}} u_{a_1}^{u_1}\right). \quad (3)$$

3.2 Travellers' Demand Optimisation

The following notation will be used.

- k, ℓ, m: the attributes for stations or destinations or origin points of the trips.
- $T_{m\ell}(t)$: the demand of displacement from ℓ to m: ($\ell \to m$) between the instants t and $t + \delta t$. So there is $T_{m\ell}(t)\delta t$ customers that want to travel from the station ℓ to the station m.
- $N_\ell(t)$: the number of sky-cars at the station ℓ.
- $K_\ell(t)$: the maximal capacity in term of number of travellers that can board at the station ℓ, and at the time t. The following relation holds: $N_\ell(t) * K_R = K_\ell(t)$, with K_R the residual capacity of any sky-car.
- $K_\sigma(t)$: the capacity of the sky-car σ at time t. This variable changes only at stations due to the passengers boarding in σ and the passengers exiting the σ. So K_R constrains $K_\sigma(t)$ such that $K_\sigma(t) \leqslant K_R, \forall t$.
- $S_W(\ell, t)$: the ordered set of sky-cars waiting to board passengers at station ℓ.
- $D_\ell(t)$: the demand at the station ℓ and at the time t.
- $n_{\ell m}(t)$: the number of sky-cars that want to go to the stop m from the station ℓ at time t. This number represents the total demand at ℓ to m.
- $U_\ell(\sigma, t)$: the set of achievable sky-car stations from the station ℓ.
- $\tau_{\ell m}$: the travel time from ℓ to the achievable station m.
- $v_{\ell m \sigma}$: the number of travellers from ℓ to m using the sky-car σ at the instant t. This the number of travellers that is transferring exactly from the stop ℓ to m. That is to say the performed travellers' demand by the system.
- $N_{\ell m}(t)$: the performed demand. Hence, the following holds: $N_{\ell m}(t) = \min(n_{\ell m}(t), K_{\ell m}(t))$ with $N_{\ell m}(t) = \sum\limits_{\sigma \in S(\ell,t)\ ;\ m \in U_\ell(\sigma,t)} K_\sigma(t)$.
- $\sigma \in S(\ell, t)$ means that σ is at the station ℓ at time t.
- $m \in U_\ell(\sigma, .)$ means that m is in the neighbourhood of ℓ and is easily reachable from ℓ using the sky-car σ, when departing at time t at ℓ.

At a station ℓ, the demand $D_\ell(t)$ at time t collapses in: $D_\ell(t) = \sum\limits_{m} \left\{ \left\lfloor \frac{T_{\ell m}(t)\delta t}{K_R} \right\rfloor + 1 \right\}$.

Therefore, the estimation of the travel time, from ℓ to m at time t, is suggested to follow the below optimisation problem (4):

$$\min \sum_{\sigma \in S(\ell,t)\ ;\ m \in U_\ell(\sigma,t)} v_{\ell m \sigma} * \tau_{\ell m}(\sigma, t)$$

$$\text{s.t.} \begin{cases} N_{\ell m}(t) = \sum\limits_{\sigma / m \in U_\ell(\sigma,t)} v_{\ell m \sigma}, & \forall \ell, \\ \sum\limits_{m} v_{\ell m \sigma} \leqslant K_\sigma, & \forall \sigma, \\ v_{\ell m \sigma} \in \mathbb{N}, & \forall \ell, m, \forall \sigma, \forall t. \end{cases} \tag{4}$$

The residues from ℓ to m, is $r_{\ell m}(t) = n_{\ell m}(t) - N_{\ell m}(t)$. Added to the arrival of sky-cars at time t, denoted by $a_{\ell m}(t)$, we get $n_{\ell m}(t + 1)$.

3.3 Multi-modality—Spatial Interactions with Other Modes

Let us consider a multi-modal transport system with the sky-car transit system. We assume that the whole multi-modal system is semi-computerised, that is to say there is advanced information for travellers about traffic conditions, for each network mode. For the sky-car transit system, there is dynamic allocation of podcars on stations with respect to the following:

- the known cumulative demands,
- the stocks of sky-cars at stations on the off line guideway, and
- the foreseeable demands induced by passengers travel orders for some future times.

We propose a logit model for the modal choice in general, and user paths choice. In the case of this PRT system, it is only up to the system manager to make the path choice according to the origin, the destination and the traffic state of system itself. We assume only three choices for users in our considered multi-modal system comprising only road network (by referring to private vehicles) and personal maglev network. Any OD pair could be joined with the below choices:

- mode m_1: the use of road vehicle, then parking search availability to park and parking, and pedestrian walk for attending final destination, or
- mode m_2: the use of sky-car and pedestrian walk, or
- mode m_3: the use of modes m_1 and mode m_2.

For $\forall p \in \{1, 2, 3\}$ (p being the index of the mode), and for $\forall w = (o, d)$, the Logit-based rules are reduced to:

$$\pi_{od}^p = P[choice = m_p \mid (o, d) = w \in W] = \frac{\exp\left(-\theta C_{od}^{m_p}\right)}{\sum_{p' \in \{1,2,3\}\,;\,(o,d)=w \in W}\exp\left(-\theta C_{od}^{m_{p'}}\right)} \quad (5)$$

The probability of choosing one mode p from an origin o to a destination d is set by:

$$\begin{cases} 0 \leq \pi_{od}^p \leq 1, & \forall p = 1, 2, 3 \,, \forall w = (o, d) \in W, \\ \sum_{p=1}^{3} P[choice = m_p] = 1. \end{cases} \quad (6)$$

$C_{od}^{m_p}$ is the cost of the mode m_p from origin o to destination d, cost which depends on the monetary cost, the predicted time that will be spent in the system (given by a system of information), and the search time of availability of parking-car (in case when using partially car mode), and the walking time.

4   Conclusions and Perspectives

The implementation of the model and the sky-car demand-responsive system shall show its real performance. The proposed system of equations is a queue approach with adaptive cruise control on the dynamic of sky-cars. The model proposed in this paper focussed on Lagrangian coordinates of the motion of sky-cars in the whole PRT system. We discuss about multi-modal trips that take into account the new responsive automated transport system. The relocation of sky-cars shall be addressed to respond to extra transport demands at stations where there are no available sky-cars to board passengers, and where re-routing of other sky-cars which are at rest in other locations is relevant.

References

1. Errico, F., Crainic, T.G., Malucelli, F., Nonato, M.: A survey on planning semi-flexible transit ssystem: methodological issues and a unifying framework. Transp. Res. Part C: Emerg. Technol. **36**, 324–338 (2013)
2. Gabrel, V., Murat, C., Thiele, A.: Recent advances in robust optimization: an overview. Eur. J. Oper. Res. **235**, 471–483 (2014)
3. Jin, X., Abdulrab, H., Itmi, M.: A multi-agent based model for urban demand-responsive transport system intelligent control. In: Intelligent Vehicles Symposium, 2008 IEEE, pp. 1033–1038 (2008)
4. Jin, X., Wang, D.: An intelligent model for urban demand-responsive transport system control. Intell. Inf. Technol. Appl. Workshops **2008**, 151–154 (2008)
5. Maciejewski, M.: Benchmarking minimum passenger waiting time in online taxi dispatching with exact offline optimization methods. Arch. Transport **30**(2), 67–75 (2014)
6. Maciejewski, M., Bischoff, J.: Large-scale microscopic simulation of taxi services. Procedia Comput. Sci. **52**, 358–364 (2015)
7. Margulies, R.: High-Speed, Elevated, Mass Transit Gets Real. Press Release. A NASA Space Act Company (2014)
8. Wong, R., Szeto, W., Wong, S.: A cell-based logit opportunity taxi customer-search model. Transp. Res. Part C: Emerg. Technol. **48**, 84–96 (2014)

Phenomena-Based Traffic Flow Multi-scale Modelling

Mahtab Joueiai, Hans van Lint and Serge Hoogendoorn

Abstract   The aim of multi-scale modelling is developing both theoretical and computational methods that can be used to couple microscopic, mesoscopic and coarse-level descriptions of complex traffic system, in order to describe a variety of phenomena. In multi-scale modelling approach, the modelling paradigms are switched dynamically depending on traffic condition. One important question in this approach pertains to the criteria that trigger the switching mechanism. The time and position of shifting from one modelling paradigm to the next should be chosen such that the consistency of traffic features at the interface between implemented models is ensured. This paper presents a generic simulation strategy that enables shifting paradigm from one modelling scale to the next, based on the propagation and emergence of traffic phenomena. The interface between implemented models in this approach, dynamically adapt its position regards the phenomenon of interest. The paper concludes with an illustrative example that shows the applicability of our proposed methods.

1   Introduction

Traffic models are important part of understanding and predicting the traffic condition. Traffic models and simulation are used to assess the performance of roads, networks and new control systems. Therefore, a model should be a close approximation of a real traffic system to be able to accurately predict dynamic traffic features.

Models at each level of complexity are necessarily simplified to minimise computation and to emphasise the key factors that are required to reproduce certain traffic phenomena. Different modelling paradigm are thus developed that each could predict and reproduce a certain range of phenomena. This implies that there exists no

M. Joueiai (✉) · H. van Lint · S. Hoogendoorn
Delft University of Technology, Stevinweg 1, 2628 CN Delft, The Netherlands
e-mail: m.joueiai@tudelft.nl

H. van Lint
e-mail: j.w.c.vanLint@tudelft.nl

S. Hoogendoorn
e-mail: s.p.hoogendoorn@tudelft.nl

single simulation model that is able to reproduce and predict all the phenomena of interest under all sorts of circumstances over all scales. As a result, modellers and traffic engineers need to carefully select the models that are suitable for specific applications (e.g. the evaluation of ITS). In many cases, this is not trivial, and for some applications (e.g. in large mixed urban and freeway traffic networks) even impossible.

An obvious solution is to use a combination of models that runs on different spatial and temporal scales. Such multi-scale model is able to reproduce any traffic phenomena at the desired scale. During the simulation of a multi-scale model, the abstraction level of traffic flow model is switched dynamically, depending on prevailing traffic conditions. For example, macroscopic models could be employed for fast and efficient simulation of traffic networks such as freeways, whereas microscopic models could be used to simulate and predict traffic conditions on specific points of interest such as coordinated intersections. This approach is attractive if the required simulation fidelity varies spatially. Examples of such approach can be found in [3, 10]. In these examples macro/meso and micro models are implemented on different parts of the network.

Despite the widely acknowledged need for multi-scale modelling and simulation, there is a scarcity of underpinning literature on the methodology and generic description of the process. One important question in this approach, relates to the criteria that activates the switching mechanism. The time and position of shifting the modelling paradigms should be chosen wisely to avoid inconsistency between integrated models. Furthermore, finding the appropriate modelling scale that can accurately reproduce the phenomena of interest is not a trivial task.

In this paper we first discuss the concept of choosing an appropriate level of traffic model. In Sect. 2, a discrete mechanism to switch from one modelling representation to the next is presented. This approach is based on the emergence and propagation of the traffic phenomena. Section 4 is devoted to an experimental example that demonstrates the applicability of our proposed methods. The paper concludes with the results and conclusion.

1.1 Dynamic Modelling Scale Selection

Traditionally, a model is selected by a modeller or the analyst, who chooses a model based on experience, heuristics and personal judgement, to depict events that are assumed to occur on well-defined spatial and temporal scales. However, one might argue that selecting the appropriate model for reproducing the phenomena of interest, should not only depends on modeller's experience, but it also closely relates to the degree of complexity of the phenomena and the power of the model to predict them.

The complexity of traffic phenomena is observer dependant. Suppose that the phenomena are reported by a sequence of observers observing the system at different scales. For example, one of the observers looks at traffic from 1 km above the ground. Traffic for this observer appears as a fluid with propagated waves. The variation of

density, flow and speed in this case are dependent to each other, but the observer cannot see the inter-connected relationship between individual acceleration/declaration and propagated waves. On the other hand, the observer who looks at traffic 100 m above the ground sees traffic as a collection of moving particles that are reactive to each other as well as to the traffic state. This scale dependence reflects the observer's ability to distinguish details of the system. All observers observe the same system in its entirety. Larger scale observers, however, see only redundant information.

To choose an appropriate model that can accurately reproduce a phenomenon of interest, The scale of the model should match the observation scale that phenomena's complexity. The classification of various traffic models to micro, meso and macro scales is not sufficient to understand the modelling's characteristics at each scale. Thus, we apply the modelling classification that is presented in [8]. This classification categorises the traffic models based on *behavioural law* that governs the models and *representation scale* of them.

The behavioural law scale makes a distinction between the models that their governing mathematical and computational formulation consider the individual behaviour of a driver (individual behavioural law) and the models that consider the analysis of the propagation of density or flows (collective behavioural law). The second criterion is the representation scale. It differentiates the ability of models to predict and reproduce the phenomena according to the scale at which the traffic is represented: i.e. vehicle to flow representation. With such classification it is easier to find a model that has sufficient detail to reproduce and predict a complex phenomenon.

2 Discrete Phenomena-Based Multi-scale Algorithm

In this paper, we present an algorithm to multi-scale modelling based on the notation of *event-based simulation* [9]. The central assumption in this approach is that the simulation model changes instantaneously in response to certain discrete sequence of events. The events that trigger the switching mechanism from one modelling paradigm to the next, is a set of traffic phenomena that are occurring at various temporal and spatial scales. Emergence and propagation of traffic phenomena causes the traffic states to change between *free flow*, *synchronised flow* and *jam* [5, 6].

The change of traffic state cause a discontinuity in traffic flow. This discontinuity can be tracked by following the trajectory of the interface that separates the traffic states ($\Gamma(x, t)$). The interface between traffic states is assumed to be sharp- meaning that from one time and position point to the next, the traffic state is changing from $\beta 1$ to $\beta 2$ and there is no diffuse phase between these two states. The sharp interface Γ at any given time, separates the two traffic phases $\beta 1$ and $\beta 2$ so that:

$$\beta(z) = \begin{cases} \beta 1 \text{ for } x > 0 \\ \beta 2 \text{ for } x < 0 \\ \Gamma \text{ for } x = 0 \end{cases} \tag{1}$$
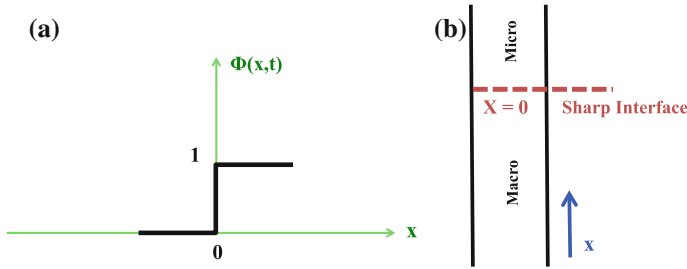
Fig. 1 One dimensional representation of phase transition and interface between phases. Phase field (**a**). Sharp interface (**b**)

In order to determine the time and position of sifting the modelling paradigms in multi-scale modelling approach, we propose to use the interface of phase transition to act as an interface between implemented models. Lets define the phase field $\phi(x) \in$ [0, 1] to approximate the sharp interface topologies. We associate $\phi = 0$ with phase $\beta 1$ and $\phi = 1$ with phase $\beta 2$. A direct description of the resulting sharp interface topology would yield that $\phi(x)$ is a step function, see Fig. 1a.

The interface of phase transition Γ and respectively the interface between implemented models, lies within the range $0 < \phi < 1$ and it is dynamically change its position regards to the propagation of the phenomenon of interest. The presented method in this part is inspired by the ideas in [2].

3 Experimental Case

To illustrate the applicability of our proposed solutions, the following experiment is provided. The road section under consideration is 13 km long, and contains a ramp metering exactly half-way. Initially, the entire road stretch is modelled with fast and efficient macroscopic LWR model. When the red light starts, a shock-wave propagates to the upstream road section. Our phenomenon of interest is the queuing and acceleration/deceleration process in the congested area.

The descriptive and explanatory information that is needed to simulate the queue and vehicle's decelerated in congestion enforce the use of a model that lies within both *individual* behavioural law scale and *vehicle* representation. We chose IDM as a microscopic model to reproduce and predict the vehicles behaviour in congestion. Therefore, we simulate the queuing and acceleration process during the ramp metering with the microscopic model and the rest of the road section with the macroscopic model.

Table 1 *IDM* parameter settings

Parametres	Quantity
Desired velocity, v_0	100 km/h
Safe time headway, T	1.6 s
Maximum acceleration, a	0.73 m/s^2
Comfortable deceleration, b	1.67 m/s^2
Acceleration exponent, δ	4
Minimum jam distance, s_0	2 m
Jam distance, s_1	0 m
Vehicle length, l	5 m

Table 2 *LWR* parameter settings

Parameters	Quantity
Critical density, ρ_{crit}	25 veh/km
Jam density, ρ_{jam}	150 veh/km
Mean speed, V_f	80 km/hr^2

As shorthand we use superscript *A* and *B* to denote variables and quantities related to the macroscopic and microscopic models respectively. Simulation time is set to 1 h which is discretised into $i = k\Delta t^A$, $k = 0, 1, 2, \ldots$ *macroscopic* time steps (e.g. $\Delta t^A = 12$ s) and $j = k\Delta t^B$ *microscopic* time step (e.g. $\Delta t^B = 1$ s). The LWR is numerically solved by *Godunov* scheme as reinterpreted for the LWR model by [1, 7]. To satisfy the *Courant-Friedrich-Levy (CFL)* condition, the network is spatially discretised to $n = 1, 2, \ldots N$ cells of each $\Delta x = 260$ m.

The IDM variable and parameters can be found in Table 1 and the LWR variables are in Table 2.

The discrete position of the interface S_i^{up} and S_i^{dn} can be determined as in [3, 4].

This interface isolates the two models such that average behaviour of models at the interface is in agreement and as a result, traffic is locally consistent along the interface.

Figure 2 shows the result of the dynamic interface due to the development of the shock-wave in 1 h simulation in which 1 ramp meter takes place. Figure 3 shows results of a 3 h simulation in which three ramp meters activate. The simulation results show that the dynamic interface ensures a correct wave propagation in multi-scale model, and, as a result, do not induce unwanted shock waves, artificial modification or oscillations of reality abstraction (network) when changing the representation.
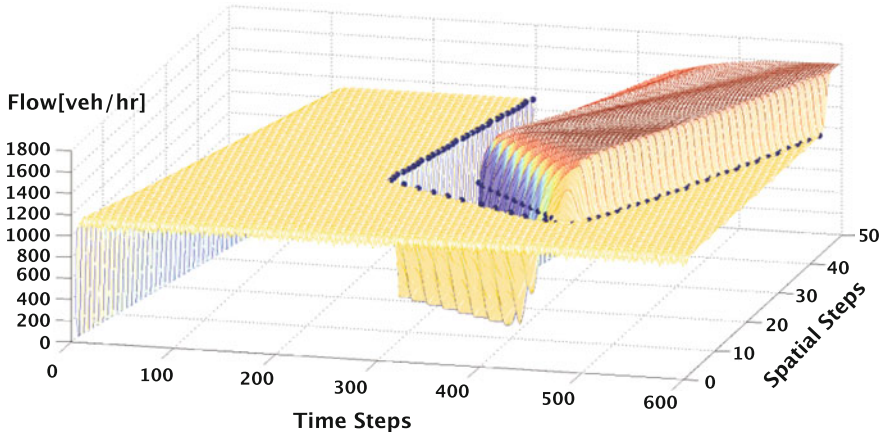
Fig. 2 Traffic flow resulting from *red phase* and dynamic interface developed by the shock-wave
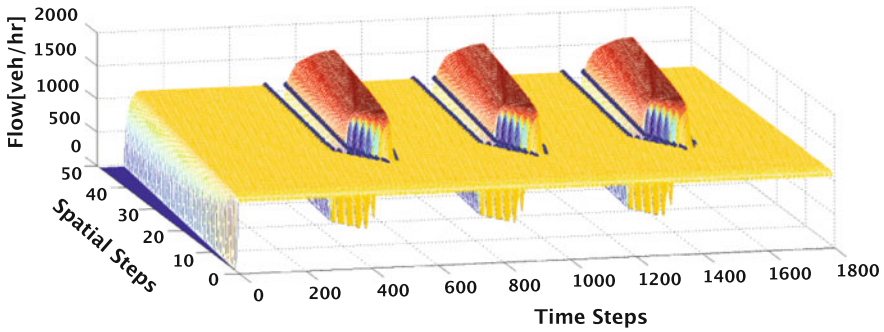

Fig. 3 *Red phases* in sequence are tracked by dynamic interface in a 3 h simulation

4   Conclusion

This article presents a new multi-scale simulation algorithm that enables the switching mechanism from one modelling paradigm to the next, depending on the prevailing the traffic condition. The presented approach is based on the emergence and propagation of traffic phenomena that are separately occurring in the traffic network. The simulation results in the example case shows that we could successfully single out the phenomenon of interest to simulate it with finer scale model. The dynamic interface between models in this example, ensured the consistency of traffic features that are passing through the interface.

   Furthermore, we provided a concept of dynamically select an appropriate modelling scale that can reproduce and predict the phenomena of interest with sufficient accuracy and degree of details. This concept can eventually help model users to systematically select the fittest model for the purpose at the hand. Also model developers

can implement the modelling selection concept that is presented in this paper to find the modelling scales that are not yet developed, but are needed.

References

1. Daganzo, C.F.: A finite difference approximation of the kinematic wave model of traffic flow. Transp. Res. Part B Methodol. **29**(4), 261–276 (1995)
2. Hildebrand, F., Miehe, C.: A regularized sharp interface model for phase transformation accounting for prescribed sharp interface kinetics. PAMM **10**(1), 673–676 (2010)
3. Joueiai, M., Leclercq, L., Van Lint, H., Hoogendoorn, S.: A multi-scale traffic flow model based on the mesoscopic LWR model. In: Transportation Research Board 94th Annual Meeting, pp. 15–5311 (2015)
4. Joueiai, M., Van Lint, H., Hoogendoorn, S.: Multiscale traffic flow modeling in mixed networks. Transp. Res. Rec. J. Transp. Res. Board **2421**, 142–150 (2014)
5. Kerner, B.S.: Experimental features of self-organization in traffic flow. Phys. Rev. Lett. **81**(17), 3797 (1998)
6. Kerner, B.S.: Phase transitions in traffic flow. In: Traffic and Granular Flow'99, pp. 253–283 (2000)
7. Lebacque, J.P.: The Godunov scheme and what it means for first order traffic flow models. In: Internaional Symposium on Transportation and Traffic Theory, pp. 647–677 (1996)
8. Lesort, J.B., Bourrel, E., Henn, V.: Various scales for traffic flow representation: some reflections. In: Traffic and Granular Flow'03, pp. 125–139. Springer (2005)
9. Maria, A.: Introduction to modeling and simulation. In: Proceedings of the 29th Conference on Winter Simulation, pp. 7–13. IEEE Computer Society (1997)
10. Poschinger, A., Kates, R., Meier, J.: The flow of data in coupled microscopic and macroscopic traffic simulation models. In: Proceedings of the 7th World Congress on Intelligent Systems (2000)

Calibrating the Local and Platoon Dynamics of Car-Following Models on the Reconstructed NGSIM Data

Valentina Kurtc and Martin Treiber

Abstract The NGSIM trajectory data are used to calibrate two car-following models—the IDM and the FVDM. We used the I80 dataset which has already been reconstructed to eliminate outliers, non-physical data, and internal and platoon inconsistencies contained in the original data. We extract from the data leader-follower pairs and platoons of up to five consecutive vehicles thereby eliminating all trajectories that are too short or contain lane changes. Four error measures based on speed and gap deviations are considered. Furthermore, we apply three calibration methods: local or direct calibration, global calibration, and platoon calibration. The last approach means that a platoon of several vehicles following a data-driven leader is simulated and compared to the observed dynamics.

1 Introduction

Nowadays, microscopic traffic data have become more available and provides information about thousands of vehicle trajectories. As a result, the problem of analysing and comparing microscopic traffic flow models with real microscopic data has become more actual. In this paper, we consider the NGSIM I80 data set for calibration. Two car-following models of similar complexity are studied—the Intelligent-Driver Model (IDM) [13] and the Full Velocity Difference Model (FVDM) [4]. We apply four error measures to investigate the robustness of these models. To compare the results with respect to these error measures, the two-sample Kolmogorov–Smirnov test is used. Finally, we compare the residual errors of the global and platoon calibration methods to estimate the ratio between inter-driver and intra-driver variations.

V. Kurtc (✉)
St. Petersburg Politechnic University, Polytechnicheskaya, 29, Saint Petersburg, Russia
e-mail: kurtsvv@gmail.com

M. Treiber
Technische Universtät Dresden, Wurzburger Str. 35, 01062 Dresden, Germany
e-mail: treiber@vwi.tu-dresden.de

2   Car-Following Models Under Investigation

Two microscopic car-following models are considered—the IDM and the FVDM. These are formulated as (coupled) ordinary differential equations and characterised by an acceleration function which depends on the actual speed $v(t)$, the approaching rate $\Delta v(t) = v - v_l$ to the leader, and the gap $s(t)$. Both considered models contain five parameters and are therefore formally equivalent in their complexity.

The IDM is defined by the acceleration function [13]

$$\dot{v}_{\text{IDM}}(v, \Delta v, s) = a \left[1 - \left(\frac{v}{v_0} \right)^4 - \left(\frac{s^*(v, \Delta v)}{s} \right)^2 \right] \tag{1}$$

This expression combines the acceleration strategy to reach a desired speed v_0 with a braking strategy that compares the actual gap s with the dynamically desired gap $s^*(v, \Delta v) = s_0 + \max(0, vT + v\,\Delta v/(2\sqrt{ab}))$. A more detailed model description can be found in [13].

The acceleration function of the FVDM model [4] is as follows

$$\dot{v}_{\text{FVDM}}(v, \Delta v, s) = \frac{v_{\text{opt}}(s) - v}{\tau} - \lambda \Delta v \tag{2}$$

The model properties are defined by the optimal velocity function $v_{\text{opt}}(s)$. In this paper we consider it as follows:

$$v_{\text{opt}}(s) = \frac{v_0}{2} \left[\tanh \left(\frac{s}{l_{int}} - \beta \right) - \tanh(-\beta) \right] \tag{3}$$

3   The Data Set

The Next Generation Simulation (NGSIM) I-80 trajectory dataset [3] is considered for calibrating. It was recorded from 4:00 to 4:15 p.m. on April 13, 2005. The monitored area is approximately 500 m length and has 6 lanes. The internal and platoon inconsistencies as well as the noise from original data measurements have already been eliminated [7]. Calculating of derived quantities was performed and a smoothing algorithm was proposed in [12]. NGSIM data contains information about 3366 vehicle trajectories, that is, for each car we have its current lane position, longitudinal coordinate of its front centre, speed, and acceleration, its length and type (motorcycle, auto or truck), ID of the immediate following and leading vehicle in the current lane. A great part of the deviations between measured and simulated trajectories can be attributed to the different driving styles, as has been shown in previous works [5]. Microscopic traffic models can easily cope with this kind of heterogeneity, because different parameter values can be attributed to each individual drivervehicle unit. To obtain these distributions of calibrated model parameters, a significant

number of trajectories have to be analysed, that is why the NGSIM trajectory data sets are considered in this work.

The consecutive trajectories used for the calibration are extracted by following procedure:

1. Consider trajectory sets of more than 30 s length because the calibration of shorter ones does not sufficiently represent the car-following model properties.
2. Filter out all active and passive lane changes. We do this, because the calibrated car-following models describe only the longitudinal dynamics.
3. Eliminate the first and last 5 s of the remaining trajectory sets to filter out some inconsistencies. It allows to exclude the influence of not longitudinal effects such as lane changes.
4. Filter out all trajectories on the right most (HOV) and left most (on-ramp) lanes.

4 Calibration Methodology

To find the optimal parameter values of a car-following model with a non-linear acceleration function such as Eqs. (1) or (2), we need to solve a non-linear optimisation problem numerically. The MATLAB optimisation toolbox is used that provides several algorithms for finding minimum of constrained non-linear multi-variable function. In this case, the interior-point algorithm was used.

4.1 Simulation Setup and Calibration Methods

We initialise the microscopic model with the empirically given speed and gap, and compute the trajectory of the following car. Then, it can be directly compared to the speeds $v^{data}(t)$ and gaps $s^{data}(t)$ provided by the empirical NGSIM data.

Three calibration methods are considered:

- Local or direct calibration: at any time instant, the model's acceleration function is calibrated directly to the observed acceleration. No simulations are needed.
- Global calibration: the simulated trajectory of a follower with its prescribed leader is compared to the empirical data.
- Platoon calibration: the dynamics of a platoon of several vehicles following each other with a single data-driven leader are compared to the whole empirical dataset.

4.2 Objective Functions

The calibration procedure aims at minimising the difference between the measured and simulated dynamic variables. Any quantity which represents aspects of the driving behaviour can serve as an objective function, such as the gap s, speed v,

speed difference Δv, or acceleration a. In the following, for global and platoon calibration the errors in the gap $s(t)$ and speed $v(t)$ are used. To assess quantitatively the error between measured and simulated data, an objective function is needed. Three types of measures are considered. The absolute error measure is given by

$$S^{abs} = \frac{\sum_{i=1}^{n}(s_i^{sim} - s_i^{data})^2}{\sum_{i=1}^{n}(s_i^{data})^2} \qquad (4)$$

while the relative error measure reads

$$S^{rel} = \frac{1}{n}\sum_{i=1}^{n}\left(\frac{s_i^{sim} - s_i^{data}}{s_i^{data}}\right)^2 \qquad (5)$$

The relative measure is more sensitive to small gaps while the absolute measure focusses on large gaps. Due to the weighting bias of these two methods, we also consider the mixed error measure having a more balanced weighting:

$$S^{mix} = \frac{\sum_{i=1}^{n}(s_i^{sim} - s_i^{data})^2/|s_i^{data}|}{\sum_{i=1}^{n}|s_i^{data}|} \qquad (6)$$

In some papers, the speed instead of the gap is used to measure the performance [2, 8, 9]. To compare the calibration results corresponding to different variables, we also consider the absolute error measure S_v^{abs} which is defined as in Eq. (4), but with the speed as the dynamic quantity.

4.3　Parameter Constraints

The IDM and the FVDM contain five parameters to identify by the calibration. To restrict the solution space for optimisation to reasonable parameter values without excluding possible solutions, box constraints are applied. For the IDM, the desired speed v_0 is restricted to the interval [5, 40] m/s, the minimum distance s_0 to [0, 10] m, the desired time gap T to [−5, 5] s, and the maximum acceleration a and the comfortable deceleration b to [0.01, 10] m/s^2. We explicitly allow negative values for T, because some trajectories represent negative time gap values. For the FVDM, the box constraints are [0, 70] m/s for the desired speed v_0, [0.05, 20] s for relaxation time τ, [0.1, 100] m for the interaction length l_{int}, [0.1, 10] for the form factor β, and [0, 3] 1/s for the sensitivity parameter λ.

5　Calibration Results

Both models have been calibrated for all trajectory pairs or platoons satisfying the filtering criteria of Sect. 3. For the local and global approach, 876 trajectory pairs were under investigation, whereas for the platoon calibration only 251 trajectory sets were

studied. For each calibration approach, optimal parameter value distributions were obtained. Distributions corresponding to different error measures were compared by means of the two-sample Kolmogorov–Smirnov test.

5.1 Global and Platoon Calibration

Figure 1 visualises the distributions of the parameter values of the IDM (first row) and the FVDM (second row) as obtained from the global calibration of all the 876 trajectory pairs with respect to the error measure based on the absolute gap differences (Eq. 4). Only estimates with residual errors below 50 % are considered.

To compare distributions obtained with four different measures for each specific model parameter the two-sample Kolmogorov–Smirnov test was used. In this case, the Kolmogorov–Smirnov statistic is

$$D_{n,n'} = \sup |F_{1,n}(x) - F_{2,n'}(x)| \tag{7}$$

where $F_{1,n}$ and $F_{2,n'}$ are the empirical distribution functions of the first and the second sample respectively. The Kolmogorov–Smirnov statistic is in the range from 0.02 (parameter s_0, relative and mixed error measures) to 0.27 (parameter b, absolute with gaps and absolute with speeds error measures) for the IDM and from 0.02 (parameter λ, absolute and mixed error measures) to 0.21 (parameter λ, relative and absolute with speeds error measures) for the FVDM.
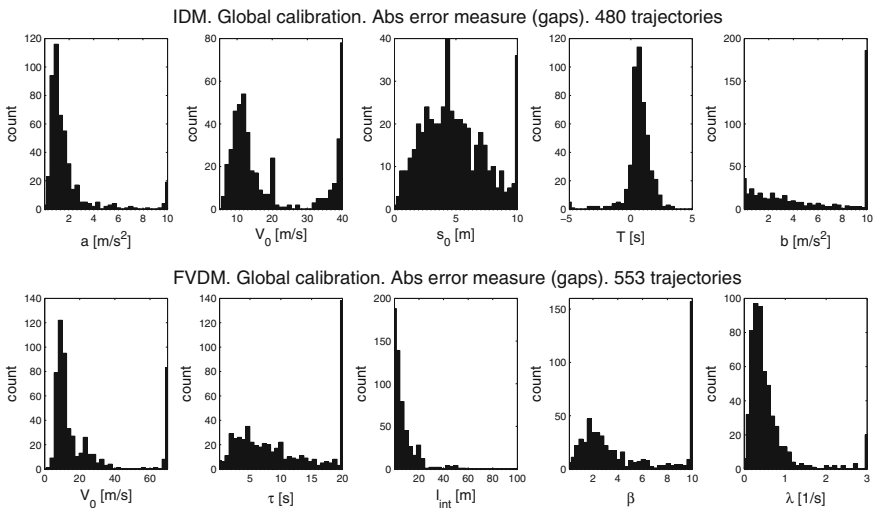
Fig. 1 Calibration results for IDM and FVDM if calibrated (global calibration) on the error measure of the absolute gap differences. Plots are histograms of the resulting parameter values
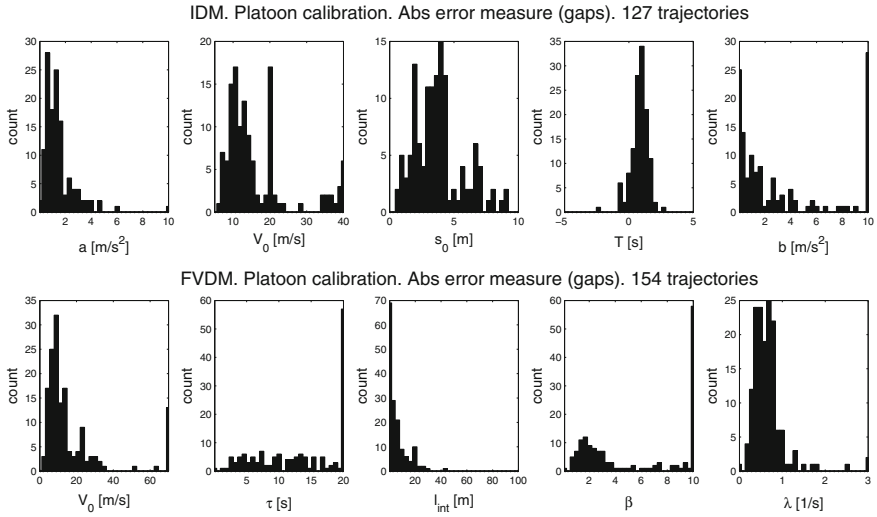
Fig. 2 Calibration results for IDM and FVDM if calibrated (platoon calibration) on the error measure of the absolute gap differences. Plots are histograms of the resulting parameter values

For the platoon approach we use trajectory sets which contain at least five vehicles following each other. In accordance with filtering rules, 251 data sets were considered for calibration. The optimisation procedure was evaluated with four error measures as well. Figure 2 presents the parameter values with respect to the error measure based on the absolute gap differences, which estimated errors are less or equal to 100 % for both models. In case of platoon calibration the Kolmogorov–Smirnov statistic is in the range from 0.05 (parameter b, relative and mixed error measures) to 0.38 (parameter b, absolute with gaps and absolute with speeds error measures) for the IDM and from 0.05 (parameter l_{int}, absolute and mixed error measures) to 0.35 (parameter l_{int} and β[1], relative and absolute with speeds error measures) for the FVDM.

Table 1 presents the obtained calibration errors. For the global approach these range from 8.3 to 12.5 %, which is lower than typical error ranges obtained in previous studies [1, 5, 10, 11]. Platoon method corresponds to higher error values, because it does not allow to distinguish between drivers. These are in the range of 12.8 to 32.4 %.

5.2 Inter-driver and Intra-driver Variations

Let us consider the absolute gap error $\varepsilon_i = s_i^{sim} - s_i^{data}$ for the specific trajectory at time t_i. Then we can calculate the variance of this error considering that the mean is equal to zero. It is well-known that variations in driving behaviour come in two

Table 1 Calibration errors for IDM and FVDM

	IDM		FVDM	
	Global	Platoon	Global	Platoon
abs_s	0.098	0.256	0.097	0.239
rel_s	0.125	0.324	0.112	0.303
mix_s	0.111	0.296	0.105	0.279
abs_v	0.086	0.131	0.083	0.128

Table 2 Inter-driver and intra-driver variation. IDM and FVDM

	IDM		FVDM	
	abs_s	abs_v	abs_s	abs_v
$Var(\varepsilon^{global}), [m^2]$	1.74	0.35	1.83	0.32
$Var(\varepsilon^{superglobal}), [m^2]$	12.01	0.57	10.42	0.54
$Var(\varepsilon_{inter}), [m^2]$	10.27	0.22	8.59	0.22
$Var(\varepsilon_{inter})/Var(\varepsilon_{intra}), [1]$	5.9	0.6	4.7	0.7

forms—inter- and intra-driver variations. In case of global approach the trajectory of one vehicle is calibrated and, thus only intra-driver variation is considered, that is, $\varepsilon^{global} = \varepsilon_{intra}$. The platoon method incorporates several driver styles simultaneously and, as a result takes into account both types of variation $\varepsilon^{platoon} = \varepsilon_{intra} + \varepsilon_{inter}$. Assuming no correlation between these two types of errors $cov(\varepsilon_{intra}, \varepsilon_{inter}) = 0$, we can derive the inter-driver variation as follows

$$Var(\varepsilon_{inter}) = Var(\varepsilon^{platoon}) - Var(\varepsilon^{global}) \tag{8}$$

Both values in the right-hand side of Eq. 8 can be directly calculated. Table 2 visualises the results.

6 Conclusion

The NGSIM trajectory data were used to calibrate two car-following models—the IDM and the FVDM. Four error measures were considered basing on speeds and distances to the leader. Three approaches were used for estimating model parameters—local, global and platoon calibration. During the global calibration the error rates of the models in comparison to the data sets for each model reach from 8.3 to 12.5 %. The global method incorporates only intra-driver variability (a non-constant driving style of human drivers), because it considers only one vehicle following its leader. On the contrary, the platoon approach exploits several drivers simultaneously and,

as a result, the inter-driver variation is incorporated as well. Calibration errors in this case are higher and were found to be between 12.8 and 32.4 %.

The parameter values distributions for the IDM represent negative time gaps T as well. Studying of the empirical trajectories with negative T shows the non-trivial driver behaviour—speed increasing and gap decreasing simultaneously. Such behaviour could be interpreted as failed lane changing.

A significant part of the deviations between measured and simulated trajectories can be attributed to the inter-driver variability [5, 6]. In this paper we estimated the ratio between inter-driver and intra-driver variations. It was found between 0.6 and 0.7 % for calibration according to speeds and from 4.7 to 5.9 % calibration with gaps. This ratio is much higher for gaps because, in congested traffic, the speed is more or less determined by the leading vehicles, while the gap can be chosen freely.

As for benchmarking of car-following models, no model considered in this study appears to be significantly better. Calibration with four objective functions and the two-sample Kolmogorov–Smirnov test demonstrates the same robustness properties of both investigated models.

References

1. Brockfeld, E., Kühne, R., Wagner, P.: Calibration and validation of microscopic traffic flow models. Transp. Res. Rec. J. Transp. Res Board **1876**, 62–70 (2004)
2. Ciuffo, B., Punzo, V.: Kriging meta-modelling in the verification of traffic micro-simulation calibration procedure. optimization algorithms and goodness of fit measures. In: TRB 90th Annual Meeting Compendium of Papers (2011)
3. FHWA, U.S.: Department of Transportation: ngsim: next generation simulation. http://www. ngsim.fhwa.dot.gov. Accessed 5 May 2007
4. Jiang, R., Wu, Q., Zhu, Z.: Full velocity difference model for a car-following theory. Phys. Rev. E **64**(1), 017101 (2001)
5. Kesting, A., Treiber, M.: Calibrating car-following models by using trajectory data: method-ological study. Transp. Res. Rec. J. Transp. Res. Board **2088**, 148–156 (2008)
6. Ossen, S., Hoogendoorn, S., Gorte, B.: Interdriver differences in car-following: a vehicle trajectory-based study. Transp. Res. Rec. J. Transp. Res. Board **1965**, 121–129 (2006)
7. Punzo, V.: A multistep procedure for vehicle trajectory reconstruction: application on the ngsim 180-1 dataset
8. Punzo, V., Ciuffo, B., Montanino, M.: May we trust results of car-following models calibration based on trajectory data? TRB 2012 Annu. Meet. (2012)
9. Punzo, V., Montanino, M., Ciuffo, B.: Do we really need to calibrate all the parameters? variance-based sensitivity analysis to simplify microscopic traffic flow models. IEEE Trans. Intell. Transp. Syst. **16**(1), 184–193 (2015)
10. Punzo, V., Simonelli, F.: Analysis and comparison of microscopic traffic flow models with real traffic microscopic data. Transp. Res. Rec. J. Transp. Res. Board **1934**, 53–63 (2005)
11. Ranjitkar, P., Nakatsuji, T., Asano, M.: Performance evaluation of microscopic traffic flow models with test track data. Transp. Res. Rec. J. Transp. Res. Board **1876**, 90–100 (2004)
12. Thiemann, C., Treiber, M., Kesting, A.: Estimating acceleration and lane-changing dynamics from next generation simulation trajectory data. Transp. Res. Rec. J. Transp. Res. Board **2088**, 90–101 (2008)
13. Treiber, M., Hennecke, A., Helbing, D.: Congested traffic states in empirical observations and microscopic simulations. Phys. Rev. E **62**(2), 1805 (2000)

Scaling from Circuit Experiment to Real Traffic Based on Optimal Velocity Model

Akihiro Nakayama, Macoto Kikuchi, Akihiro Shibata, Yuki Sugiyama, Shin-ichi Tadaki and Satoshi Yukawa

Abstract The optimal velocity   (OV) model was proposed to explain the physical mechanism of jam formation. The emergence of a traffic jam can be understood as a kind of dynamical phase transition. We confirmed the physical mechanism by two experiments. In this study, we investigate the relation between experimental results and observations of real traffic based on the OV model. In the OV model, the critical density at which a traffic jam occurs is determined by the OV function. The OV function is estimated from data of headway and velocity obtained by the experiments. Then, we propose a scaling rule of the OV function from the experiments to real traffic. Using this rule, we obtain critical density as a function of a single parameter. The obtained critical density is consistent with the observed values for highway traffic. From this result, we conclude that the jam formation in real traffic is explained by the same mechanism as the circuit experiments.

A. Nakayama (✉)
Faculty of Science and Technology, Meijo University, Nagoya, Japan
e-mail: spock@meijo-u.ac.jp

M. Kikuchi
Cybermedia Center, Osaka University, Toyonaka, Japan
e-mail: kikuchi@cmc.osaka-u.ac.jp

A. Shibata
Computing Research Center, High Energy Accelerator Research Organisation,
Ibaraki, Japan
e-mail: ashibata@post.kek.jp

Y. Sugiyama
Department of Complex Systems Science, Nagoya University, Nagoya, Japan
e-mail: sugiyama@phys.cs.is.nagoya-u.ac.jp

S. Tadaki
Department of Information Science, Saga University, Saga, Japan
e-mail: tadaki@cc.saga-u.ac.jp

S. Yukawa
Department of Earth and Space Science, Osaka University, Toyonaka, Japan
e-mail: yukawa@ess.sci.osaka-u.ac.jp

1 Introduction

The optimal velocity (OV) model was proposed to explain why a traffic jam occurs [4]. The occurrence of a traffic jam is considered to be a kind of dynamical phase transition. If the car density is low, homogeneous flow, which corresponds to free flow in real traffic, is realised. If the car density exceeds a certain critical value, the homogeneous flow becomes unstable and transits to jammed flow. In order to confirm this physical mechanism of traffic jam, we carried out two circuit experiments. In the first experiment [12], we confirmed that the traffic jam occurs without bottlenecks, that is, without any causes which can be identified. The second experiment consisted of many sessions with various car density. From the experiment, we estimated the critical density [14]. This result shows that the density is the control parameter of jam formation. As a result of two experiments, the physical mechanism of traffic jam is confirmed. However, there is a criticism that circuit experiments are unrealistic situations and the results obtained by those experiments cannot be applied to real traffic.

In this study, we investigate the relation between circuit experiments and real traffic. We first determine the parameters of the OV model in the two experiments. The experimental values are different from those for real traffic, because the maximum velocities in the circuit experiments are smaller than those in real traffic. Next, we find a relation between the parameters in the circuit experiments and real traffic, and define a scaling rule for the parameters. If the relation is established, we can predict the critical density in real traffic without additional estimation of parameters. In our method, the critical density is given by a function of a single parameter. The predicted critical density is tested against observations of real traffic.

This paper is organised as follows. In Sect. 2, we briefly review the OV model. The estimation of the model parameters is shown in Sect. 3, and the scaling relation between the experiments and real traffic is shown in Sect. 4. A summary is given in Sect. 5.

2 Review of Model

The OV model is expressed by the equations of motion

$$\frac{d^2 x_i}{dt^2} = a \left[V(x_{i+1} - x_i) - \frac{dx_i}{dt} \right], \tag{1}$$

where x_i is the position of the ith car. The parameter a is called sensitivity. The OV function $V(h)$ expresses the optimal velocity as a function of headway h. Typically, we adopt a hyperbolic tangent function as the OV function

$$V(h) = \alpha \tanh[\beta(h - h_0)] + v_0. \tag{2}$$

Sensitivity a and the OV function V are assumed to be common to all cars.

The OV model predicts that a homogeneous flow becomes unstable and transits to a jammed flow if

$$\left.\frac{dV(h)}{dh}\right|_{h=h_{\mathrm{mean}}} > \frac{1}{2}a\,, \tag{3}$$

where h_{mean} is the mean headway. Then, the critical density $\rho_c = 1/h_{\mathrm{critical}}$ can be analytically calculated from Eq. (3).

$$\rho_c = \left[\frac{1}{\beta}\cosh^{-1}\sqrt{\frac{2\alpha\beta}{a}} + h_0\right]^{-1}. \tag{4}$$

Therefore, the difference of critical density between the experiments and real traffic is reduced to the difference in the OV function.

Properties of traffic jams in the OV model are summarised as follows. When the jammed flow becomes stationary, the trajectories of all cars in the headway-velocity space are expressed by a hysteresis-like loop shown in Fig. 1 [3]. In other words, the motion of all cars becomes periodic. In most of the period, however, cars stay in the states represented by the two cusps of the loop. The lower cusp represents the state of cars inside jam clusters, and indicates the minimum headway at which cars stop. The upper cusp represents the state in which cars are running almost freely in the regions outside the jam clusters. The backward velocity of a jam cluster is given by the velocity-axis intercept of the line connecting the upper and lower cusps (Fig. 1). Here, we note that the inflection point of the hyperbolic tangent function also lies on this line.

Because the motion of all cars is periodic, each car retraces the motion of the preceding car with a certain time delay. The time delay T is equal to the time interval at which cars depart from a jam cluster one after another. Therefore, T is given by

$$T = \frac{h_{\mathrm{min}}}{v_{\mathrm{back}}}, \tag{5}$$

where h_{min} is the minimum headway and v_{back} is the backward velocity of jam clusters.
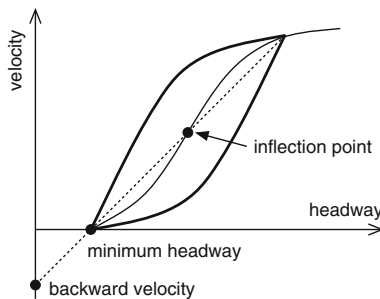
Fig. 1 Typical hysteresis-like loop. The OV function is represented by a *thin solid curve*. The *thick solid* loop represents the periodic motion of the cars. The *dashed line* connects two cusps. *Black dots* on the *line* represent the inflection point, the minimum headway and the backward velocity, respectively

It is known that a relation exists between sensitivity a and the time delay T in the framework of the OV models [1, 2, 8, 13]. The value of aT is known as $1.6 \sim 1.8$, and is insensitive to changes in the model parameters. Here, we set

$$aT = 1.8. \tag{6}$$

Then, the sensitivity is not a free parameter, and is essentially determined by the OV function through T.

3 Estimation of OV Function

In this section, we estimate the parameters in the OV functions from the experimental data. OV functions express the relation between headway and velocity. In the experiments, three types of flow, free, jammed, and stop-and-go flow are realised. Figure 2 shows relations between headway and velocity for the three types of flow. Obviously, data points cover only a part of the OV function in the cases of free and jammed flows. We can estimate the OV function in the case of stop-and-go flows.

In the estimation, we first choose five representative points to determine the OV function, and next fit a function to these points.

Two of the five points are two cusps of the loop shown in Fig. 1. The lower cusp is given by the minimum headway, which is the headway in jam clusters. To determine the minimum headway, we select data of stopped cars and average their headway. The upper cusp is found in the data sequence at the moment that stopped cars exist.

Three of the five points are determined by the distribution of data points of headway and velocity. We first obtain smooth distribution by Parzen window density estimation. In this method, we assign a Gaussian distribution for each data point and sum them over all data points. Two peaks and one saddle point of the smoothed distribution are found. Then, we can determine five representative points. Figure 3a shows the smoothed distribution and the five points. The OV function fitted to these points is obtained by the standard least square method. The estimated OV function is also shown in Fig. 3a. We observed the stop-and-go flow in four cases in the two experiments. Then, four OV functions are obtained for these cases. Figure 3b shows the OV functions for four cases.
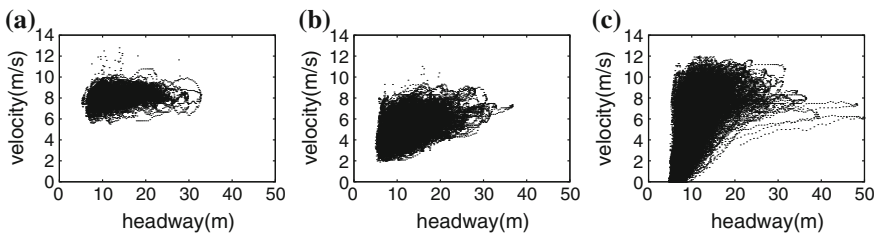
Fig. 2 Headway-velocity relations for the three types of flow: free flow (a); jammed flow (b); stop-and-go flow (c) *Dots* represent headways and velocities for all cars

(a)

(b)
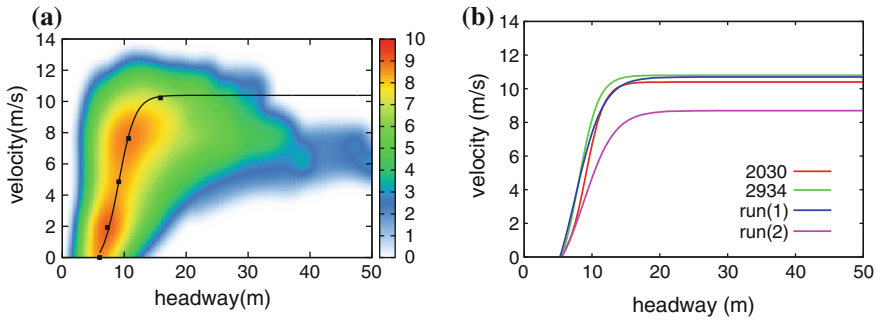
Fig. 3 OV functions. Smoothed distribution of headway and velocity. *Colours* represent the logarithm of the summation of Gaussian distributions. *Black dots* represent two peaks and a saddle point of the distribution. Two cusps are also shown by *black dots*. *Solid curve* represents the fitted OV function (**a**), OV functions are determined for four cases of stop-and-go flow. Two legends 2030 and 2934 represent session IDs in the second experiment, and run (I) and run (II) represent two sessions in the first experiment (**b**)

4 Scaling Relation

In this section, we propose a scaling rule for the OV function. The OV function (Eq. 2) has four parameters, α, β, h_0, and v_0. The scaling rule should be defined by a single scaling parameter, and therefore three relations are necessary to reduce free parameters. For this purpose, we use two observational facts.

One is a relation among inflection points for experiments and real traffic. The inflection points for real traffic can be easily identified from car following experiments on real highways [11, 16]. Figure 4 shows examples observed on Chuo, Tomei, and Tokyo metropolitan highways [11]. The inflection point is considered to be the most unstable point in the OV model, and therefore is expected to exist at the place

(a)

(b)

(c)
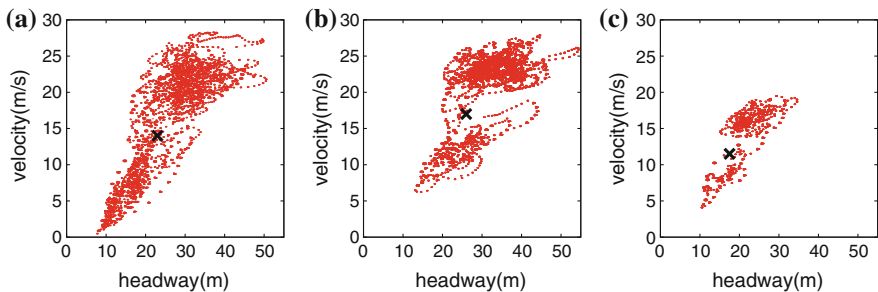
Fig. 4 An example of the car following experiment: Chuo (a); Tomei (b); Tokyo (c) *Red dots* represent the position of data points of headway and velocity. The *black cross* represents guessed inflection points

Fig. 5 *Black squares* represent inflection points from our experiments. *White and black circles* represent inflection points from Japanese highways reported in [11] and [16], respectively. *Solid line* represents the line fitted to the data
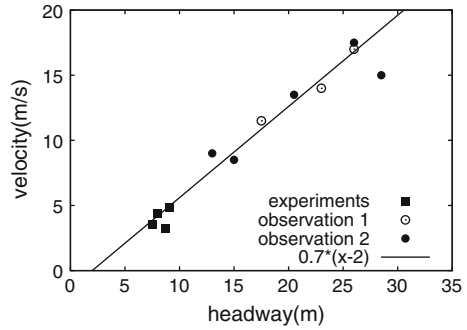
Fig. 6 Illustration of the scaling rule. *Solid curves* represent two OV functions related by the scaling rule. Each *dashed line* connects the inflection point and the point corresponding to the backward velocity
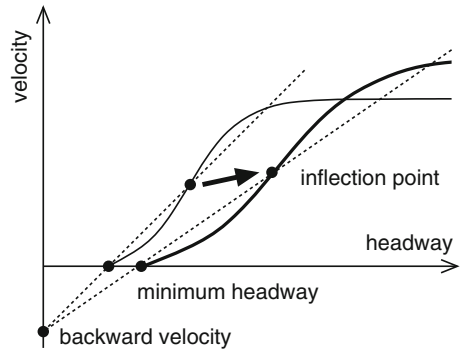
where there are no data points. The position of the inflection point for each case is estimated by eye.

Figure 5 shows inflection points observed in the experiments and on real highways. We suppose that there is a linear relation

$$v = 0.7(h - 2), \tag{7}$$

among inflection points.

The other observational fact is that the backward velocity of jam clusters is common for the experiments and real traffic. Observations on real highways show that the backward velocity is roughly 20 km/h [12, 15]. On the other hand, the backward velocity is roughly 6 m/s in our circuit experiment [14]. Obviously, both jam clusters have almost the same backward velocity.

Now, we can define a scaling rule by use of the above two facts and the property of jam in the OV model. The scaling rule is summarised as follows: (1) Inflection point lies on the line (Eq. 7), (2) Backward velocity is 6 m/s, (3) The OV function passes the point corresponding to minimum headway determined by the infection point and the backward velocity. Figure 6 shows an illustration which explains the scaling rule.

From this scaling rule, we can find relations among parameters of OV functions. Suppose two OV functions for experiments and for real traffic as
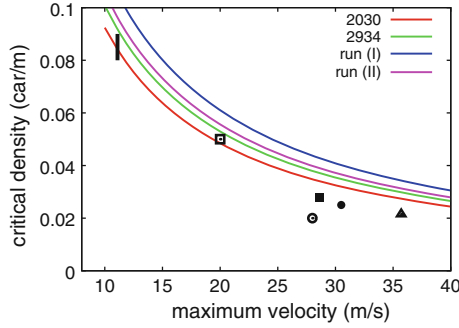
Fig. 7 Critical densities for sessions 2030, 2934, run (I), and run (II) shown in Fig. 3b. *Black solid bar* represents the range of critical density estimated in [14]. *White square*, *black square*, *white circle*, *black circle*, and *black triangle* represent the critical densities for real highways reported in [7], [5], [9], [6], and [10], respectively

$$V(h) = \alpha \tanh[\beta(h - h_0)] - v_0, \tag{8}$$

$$V'(h) = \alpha' \tanh[\beta'(h - h_0')] - v_0', \tag{9}$$

respectively. Then, the relations among parameters are given by

$$\alpha' = \frac{v_0'}{v_0}\alpha, \tag{10}$$

$$\beta' = \frac{h_0 - h_{\min}}{h_0' - h_{\min}'}\beta, \tag{11}$$

$$h_{\min}' = \frac{v_{\text{back}}}{v_0' + v_{\text{back}}}h_0' . \tag{12}$$

and Eqs. (6) and (7). Any of parameters, α', β', etc., can be used as scaling parameter. For convenience, we adopt the maximum velocity $\alpha' + v_0'$ as the scaling parameter, because it corresponds to the speed limit of a road.

Then, the critical density (Eq. 4) can be expressed by a function of the maximum velocity. Because we found four OV functions as shown in Fig. 3b, we obtain four expressions for the critical density. Figure 7 shows the profiles of critical density in the four cases and observed values on real highways [5–7, 9, 10] and the experiments [14]. The estimated critical density roughly agrees with the observed values.

5 Summary

In this study, we investigated the relation between critical densities for the circuit experiments and real traffic based on the OV model. In the OV model, the difference of critical densities is essentially determined by the difference of OV functions. For the purpose, we first estimated the OV function from the data obtained by the circuit experiments. In order to find the relation between OV functions, we used two observational facts. One is the relation among inflection points of OV functions, and

the other is the common backward velocity of jam clusters. These facts determined the scaling relations among the parameters of OV functions. As a result, we can express the critical density as a function of a scaling parameter. The agreement of estimated critical density with observed values is fair. Then, we can conclude that the jam formation in real traffic is explained by the same mechanism as in the circuit experiments.

References

1. Bando, M., Hasebe, K., Nakanishi, K., Nakayama, A.: Analysis of optimal velocity model with explicit delay. Phys. Rev. E **58**(5), 5429 (1998)
2. Bando, M., Hasebe, K., Nakanishi, K., Nakayama, A.: Delay of vehicle motion in traffic dynamics. Jpn. J. Ind. Appl. Math. **17**(2), 275–294 (2000)
3. Bando, M., Hasebe, K., Nakayama, A., Shibata, A., Sugiyama, Y.: Structure stability of congestion in traffic dynamics. Jpn. J. Ind. Appl. Math. **11**(2), 203–223 (1994)
4. Bando, M., Hasebe, K., Nakayama, A., Shibata, A., Sugiyama, Y.: Dynamical model of traffic congestion and numerical simulation. Phys. Rev. E **51**(2), 1035 (1995)
5. Hall, F.L., Allen, B.L., Gunter, M.A.: Empirical analysis of freeway flow-density relationships. Trans. Res. Part A Gen. **20**(3), 197–210 (1986)
6. Kikuchi, M., Nakayama, A., Nishinari, K., Sugiyama, Y., Tadaki, S., Yukawa, S.: Long-term traffic data from Japanese expressway. In: Traffic and Granular Flow'01, pp. 257–262. Springer (2003)
7. Koshi, M., Iwasaki, M., Ohkura, I.: Some findings and an overview on vehicular flow characteristics. In: Proceedings of the 8th International Symposium on Transportation and Traffic Flow Theory, vol. 198, pp. 403–426. University of Toronto: Toronto, Ontario (1983)
8. Nakanishi, K., Itoh, K., Igarashi, Y., Bando, M.: Solvable optimal velocity models and asymptotic trajectory. Phys. Rev. E **55**(6), 6519 (1997)
9. Neubert, L., Santen, L., Schadschneider, A., Schreckenberg, M.: Single-vehicle data of highway traffic: a statistical analysis. Phys. Rev. E **60**(6), 6480 (1999)
10. Nishinari, K.: Jamology: physics of self-driven particles and toward solution of all jams. In: Distributed Autonomous Robotic Systems 8, pp. 175–184. Springer (2009)
11. Oba, T.: An experimental study on car-following behavior. Ph.D. thesis, Thesis of Master of Engineering, University of Tokyo (1988)
12. Sugiyama, Y., Fukui, M., Kikuchi, M., Hasebe, K., Nakayama, A., Nishinari, K., Tadaki, S.I., Yukawa, S.: Traffic jams without bottlenecks experimental evidence for the physical mechanism of the formation of a jam. New J. Phys. **10**(3), 033001 (2008)
13. Sugiyama, Y.B., Yamada, H.: Simple and exactly solvable model for queue dynamics. Phys. Rev. E **55**(6), 7749 (1997)
14. Tadaki, S.I., Kikuchi, M., Fukui, M., Nakayama, A., Nishinari, K., Shibata, A., Sugiyama, Y., Yosida, T., Yukawa, S.: Phase transition in traffic jam experiment on a circuit. New J. Phys. **15**(10), 103034 (2013)
15. Wardrop, J.: Experimental speed/flow relations in a single lane. In: Proceedings of the 2nd International Symposium on the Theory of Road Traffic Flow. Ed. J. Almond OECD (1965)
16. Xing, J.: A study on the bottleneck phenomenon and car-following behavior on motorways. Ph.D. thesis, Thesis of Doctor of Engineering, University of Tokyo (1992)

Traffic Flow Optimisation at Sags by Controlling the Acceleration of Some Vehicles

Bernat Goñi-Ros, Victor L. Knoop, Kenichi Kitahama, Bart van Arem and Serge P. Hoogendoorn

Abstract Sags are bottlenecks in freeway networks. Nowadays, there is a growing interest in the development of traffic management measures for sags based on the use of in-car systems. This contribution determines the movements that individual (equipped) vehicles should make in order to minimise congestion. Specifically, we optimise the accelerations of some selected vehicles as they move along a one-lane freeway stretch with a sag, setting as objective the minimisation of total travel time. The optimisation results highlight the relevance of two traffic management strategies: (a) motivating drivers to accelerate fast along sags; and (b) limiting the inflow to sags. Also, they suggest ways to apply these strategies in practice by regulating the acceleration of vehicles equipped with in-car systems. These results prove the usefulness of the proposed method as a tool for control measure development.

1 Introduction

Sags (or sag vertical curves) are freeway sections along which the gradient increases gradually in the direction of traffic. The capacity of sags is lower than that of sections with other vertical profiles [1]; hence, traffic often becomes congested at sags in high-demand conditions [2]. For example, in Japanese intercity freeways, 60 % of traffic jams occur at sags [1]. The main cause of congestion appears to be that most drivers do

B. Goñi-Ros (✉) · V.L. Knoop · B. van Arem · S.P. Hoogendoorn
Delft University of Technology, Stevinweg 1, 2628 CN Delft, The Netherlands
e-mail: b.goniros@tudelft.nl

V.L. Knoop
e-mail: v.l.knoop@tudelft.nl

B. van Arem
e-mail: b.vanarem@tudelft.nl

S.P. Hoogendoorn
e-mail: s.p.hoogendoorn@tudelft.nl

K. Kitahama
Toyota Motor Corporation, 1200, Mishuku, Susono, Shizuoka 410-1193, Japan
e-mail: kenichi_kitahama@mail.toyota.co.jp

not accelerate enough as they move along the vertical curve [3]. Consequently, they keep longer headways than expected given their speed [4]. This leads to periodic formation of stop-and-go waves when traffic demand is sufficiently high [5]. The bottleneck is generally the end of the vertical curve [6]. In the last decades, various traffic control measures have been proposed for mitigating congestion at freeway sags. Most of these measures use variable message signs as actuators [1, 7, 8]. Recently, however, there is a growing interest in developing traffic control measures that use in-car systems as actuators [9, 10]. Although this type of measures have great potential, they are mostly in early phases of development. We argue that, at this stage, it is important to determine how equipped vehicles should move at sags in order to minimise congestion. This would lay the theoretical foundation for the development of effective traffic control applications.

The main goal of this paper is to identify the optimal acceleration behaviour of vehicles equipped with in-car systems at sags and the related effects on traffic flow, assuming low penetration rates. To this end, we optimise the accelerations of some vehicles of a traffic stream as they move along a one-lane freeway stretch with a sag, considering as objective the minimisation of total travel time. This is done for various scenarios defined by the number of controlled vehicles and their positions in the stream. By analysing the results, we identify the main strategies that vehicles equipped with in-car systems should use at sags to minimise congestion.

2   Optimisation Problem

2.1   System Elements

The system consists of a stream of n vehicles moving along a single-lane freeway stretch. Every vehicle is assigned a number i that corresponds to its position in the stream ($i = 1, 2, \ldots, n$). The set that contains all numbers i is denoted by N. A total of m vehicles are controlled vehicles. The subset of N that contains the numbers i of these vehicles is denoted by M. Each controlled vehicle is assigned a number j that corresponds to its position in relation to the other controlled vehicles ($j = 1, 2, \ldots, m$). The freeway stretch has no ramps and its vertical profile is known.

2.2   State and Control Variables

The state variables are: (a) position of all vehicles along the freeway (r_i, $\forall i$); (b) speed of all vehicles (v_i, $\forall i$); and (c) amount of freeway gradient compensated by the drivers of all vehicles ($G_{\text{com},i}$, $\forall i$). These variables are the ones needed to determine the trajectories of all vehicles in the space-time plane (see Sect. 2.3). The state at simulation time step τ is defined as follows:

$$\mathbf{x}(\tau) = \begin{bmatrix} r_1(\tau) & r_2(\tau) & \ldots & r_n(\tau) \\ v_1(\tau) & v_2(\tau) & \ldots & v_n(\tau) \\ G_{\text{com},1}(\tau) & G_{\text{com},2}(\tau) & \ldots & G_{\text{com},n}(\tau) \end{bmatrix} \tag{1}$$

The control variables are the maximum accelerations of all controlled vehicles ($u_j, \forall j$). Section 2.3 describes how u_j influences the actual vehicle acceleration. The control input at control time step κ is defined as follows:

$$\mathbf{u}(\kappa) = \begin{bmatrix} u_1(\kappa) & u_2(\kappa) & \ldots & u_m(\kappa) \end{bmatrix} \tag{2}$$

Different counters are used for simulation and control time steps (τ and κ) because the control time step length (T_c) can be assigned a different value than the simulation time step length (T_s), as long as T_c is a multiple of T_s.

2.3 State Dynamics

The position and speed of all vehicles change over time as follows:

$$r_i(\tau + 1) = r_i(\tau) + v_i(\tau) \cdot T_s + 0.5 \cdot a_i(\tau) \cdot T_s^2 \tag{3}$$

$$v_i(\tau + 1) = v_i(\tau) + a_i(\tau) \cdot T_s \tag{4}$$

In Eqs. 3 and 4, $a_i(\tau)$ denotes the acceleration of vehicle i at time step τ, which is calculated as follows. For non-controlled vehicles, $a_i(\tau)$ is equal to the acceleration given by the car-following model presented in [11] ($a_{\text{CF},i}(\tau)$). For controlled vehicles, $a_i(\tau)$ is the minimum of the control input ($u_j(\kappa)$) and $a_{\text{CF},i}(\tau)$. Therefore:

$$a_i(\tau) = \begin{cases} a_{\text{CF},i}(\tau) & \text{if } i \notin M \\ \min(u_j(\kappa), a_{\text{CF},i}(\tau)) & \text{if } i \in M \end{cases} \tag{5}$$

where i and j are the same vehicle, and κ is such that $\tau \cdot T_s \in [\kappa \cdot T_c, (\kappa + 1) \cdot T_c)$.

The car-following model has the following variables: speed, relative speed, spacing, gradient and compensated gradient (G_{com}). The gradient is dependent on the freeway location. The way G_{com} changes over time is explained in [11].

2.4 Cost Function and Optimisation Problem

The cost function (J) is defined as the total travel time of all vehicles from their initial positions to the arrival point R:

$$J(\mathbf{x}(0), \mathbf{x}(1), \ldots, \mathbf{x}(\tfrac{T}{T_s}), \mathbf{u}(0), \mathbf{u}(1), \ldots, \mathbf{u}(\tfrac{T}{T_c})) = \sum_{i=1}^{n} \left(T_s \cdot \tau_{R,i} + \Delta t_i \right) \tag{6}$$

where $\tau_{R,i}$ denotes the last simulation time step at which vehicle i is upstream of R:

$$\tau_{R,i} = \max\left(\tau \mid r_i(\tau) \leq R\right) \tag{7}$$

and Δt_i denotes the time required by vehicle i to move from its position at time step $\tau_{R,i}$ to point R, which is calculated by solving the following quadratic equation:

$$\frac{a_i(\tau_{R,i})}{2} \cdot (\Delta t_i)^2 + v_i(\tau_{R,i}) \cdot \Delta t_i + (r_i(\tau_{R,i}) - R) = 0 \tag{8}$$

The discrete-time optimisation problem, which is non-linear and non-convex, can be formulated as the following mathematical program:

Find $\mathbf{u}^*(0), \mathbf{u}^*(1), \ldots, \mathbf{u}^*(\frac{T}{T_c})$

that minimise $J(\mathbf{x}(0), \mathbf{x}(1), \ldots, \mathbf{x}(\frac{T}{T_s}), \mathbf{u}(0), \mathbf{u}(1), \ldots, \mathbf{u}(\frac{T}{T_c}))$

subject to:

$$\mathbf{x}(0) = \mathbf{x}_0 \tag{9}$$

$$\mathbf{u}(\kappa) \in \mathscr{U}, \text{ for } \kappa = 0, 1, 2, \ldots, \frac{T}{T_c} \tag{10}$$

$$\mathbf{x}(\tau + 1) = \mathbf{f}(\mathbf{x}(\tau), \mathbf{u}(\kappa)), \text{ for } \tau = 0, 1, 2, \ldots, \frac{T}{T_s} \tag{11}$$

where κ is such that $\tau \cdot T_s \in [\kappa \cdot T_c, (\kappa + 1) \cdot T_c)$.

In Eq. 9, $\mathbf{x}_0$ denotes the initial state, which is assumed known. In Eq. 10, $\mathscr{U}$ denotes the admissible control region. T is the total simulation period.

3 Experimental Set-Up

We carried out a series of optimisation experiments that entailed solving the problem presented in Sect. 2.4 (using sequential quadratic programming) for various scenarios. The goal of these experiments was to determine the optimal acceleration behaviour of controlled vehicles at sags (and the related effects on traffic flow), assuming low penetration rates and nearly-saturated traffic conditions.

Eight scenarios were defined. In all scenarios, the traffic stream contains 300 vehicles ($n = 300$). The scenarios differ in the number of controlled vehicles (m) and their positions in the stream (set M). To define the scenarios, we set the number of controlled vehicles to 0, 1, 2 or 3, and their positions to $\frac{n}{4}$, $\frac{2n}{4}$ and/or $\frac{3n}{4}$. A scenario was defined for every possible configuration of set M.

All other inputs are the same in all scenarios. The simulation time step length (T_s) is 0.5 s and the control time step length (T_c) is 8 s. The total simulation period (T) is 800 s. The freeway stretch can be divided in three consecutive sections: (a) constant-gradient downhill section; (b) sag vertical curve; and (c) constant-gradient uphill section. The sag vertical curve is 600 m long. Upstream and downstream of the sag, the freeway slope is equal to -0.5% and 2.5%, respectively.

Table 1 Values of the car-following model parameters

| Description	Value	Units
Desired speed	120	km/h
Maximum acceleration	1.4	m/s^2
Maximum comfortable deceleration	2.1	m/s^2
Net distance headway at standstill	3	m
Safe time headway	1.2	s
Congestion factor on safe time headway	1.0	Dimensionless
Sensitivity to non-compensated gradient	22	m/s^2
Maximum gradient compensation rate	0.0004	s^{-1}

Along the vertical curve, the gradient increases linearly over distance. The arrival point used to calculate travel times (R) is 3400 m downstream of the end of the sag. All vehicle-driver units are 4 m long and are assigned the same value for every parameter of the car-following model (see Table 1). At time zero, the initial speed of all vehicles is equal to the desired speed (120 km/h), the first vehicle of the stream is located on the constant-gradient downhill section (3000 m upstream of the sag), and the traffic density is the critical density of that section. Initially, the compensated gradient is equal to the actual gradient for all vehicle-driver units, hence the freeway gradient has no influence on vehicle acceleration. The set of admissible maximum acceleration values is the same for all controlled vehicles and for all control time steps: it contains all real numbers between -0.5 and 1.4 m/s^2.

4 Results

The optimisation results show that the optimal acceleration behaviour of controlled vehicles is defined by two strategies. Sections 4.1 and 4.2 describe the characteristics of these strategies and their effects on traffic flow.

4.1 Primary Strategy

The primary strategy is used by all controlled vehicles in all scenarios. It involves performing a four-phase manoeuvre in the sag area (see for example Fig. 1). The first phase (D1) begins upstream of the sag or right after entering it. During this phase, controlled vehicles decelerate moderately (at the minimum acceleration rate allowed by the controller) and their distance headway increases considerably. During the second phase (A1), which begins halfway through the vertical curve, controlled
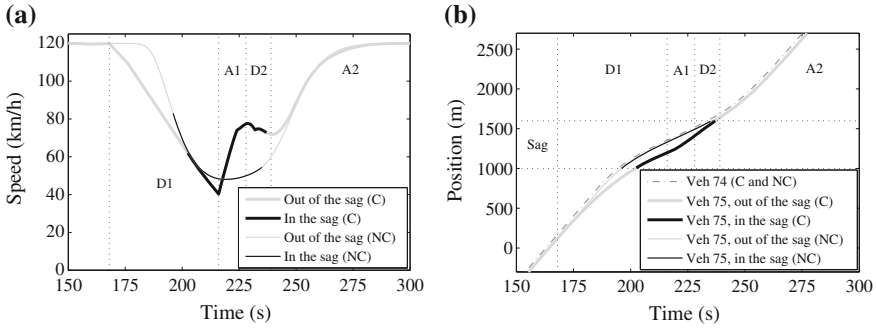
Fig. 1 Example of four-phase manoeuvre in the sag area (scenario with $M = \{75\}$). The behaviour of vehicle 75 in the control scenario (C) and the no-control scenario (NC) are shown together for comparison purposes: speed over time (vehicle 75) (**a**); position over time (vehicles 74 and 75) (**b**)
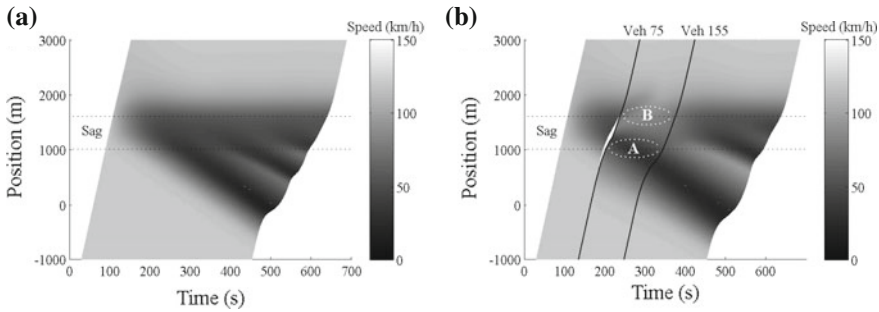
Fig. 2 Speed contour plots: no-control scenario (**a**); the scenario with $M = \{75\}$ (*A* is region of low traffic speed and limited flow; *B* is a region of high traffic speed and high flow) (**b**)

vehicles accelerate fast (with maximum acceleration rates up to 1 m/s^2 or higher) and their distance headway decreases quickly. The third phase (D2) begins on the last part of the vertical curve. In this phase, controlled vehicles decelerate slowly in order to adjust to the behaviour of the leader. Their distance headway continues to decrease because the preceding vehicle is slower. Controlled vehicles catch up with their leader at around the end of the sag. From that point on, controlled vehicles simply accelerate to the desired speed (fourth phase, A2).

In all cases, the type of manoeuvre described above has two main effects on traffic flow. Firstly, it induces the first group of vehicles located behind the controlled vehicle (up to 85 vehicles in some cases) to accelerate fast along the sag. As a result, traffic speed at the end of the vertical curve (bottleneck) increases and stays moderately high (70–90 km/h) for a particular period (2–3 min), contrary to what happens in the no-control scenario (compare Fig. 2a, b). The main consequence of this increase in traffic speed is that the flow at the bottleneck increases by up to 5 %, which leads to a decrease in total travel time. Secondly, every manoeuvre triggers a stop-and-go wave on the first part of the sag (see Fig. 2b) that temporarily limits the inflow to the vertical curve. Limiting the inflow is beneficial because it slows down the formation

(a)

(b)
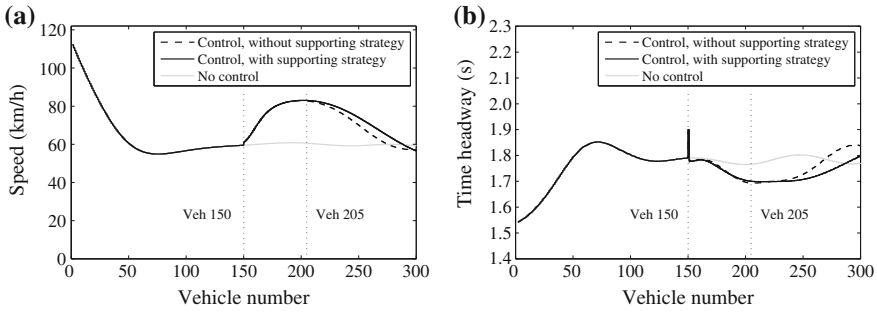
Fig. 3 Speed (**a**) and time headway (**b**) of every vehicle at the end of the sag in: (i) the no-control scenario; (ii) the control scenario with $M = \{150\}$ (including the supporting strategy); and (iii) a virtual scenario corresponding to the scenario with $M = \{150\}$ in which the supporting strategy was excluded from the solution

of congestion at the end of the sag, hence high levels of sag outflow can be maintained for a longer period of time.

4.2 Supporting Strategy

The supporting strategy is only applied by some controlled vehicles in some scenarios. It consists in performing one or more deceleration-acceleration manoeuvres upstream of the sag, catching up with the preceding vehicle before entering the vertical curve. The characteristics of these manoeuvres are very case-specific, but their overall effect on traffic flow is similar in all cases[1]. Essentially, they change the location and severity of congestion upstream of the vertical curve in such a way that the inflow to the bottleneck is slightly lower than if the supporting strategy was not applied. As a result, the primary strategy is able to produce high traffic speeds and flows at the end of the sag for a slightly longer period of time (see for example Fig. 3a, b). This causes additional total travel time savings. It is important to note, however, that in all scenarios the primary strategy is the one that contributes the most to reduce the total travel time.

5 Conclusions

The goal of this paper was to identify the main strategies that define the optimal acceleration behaviour of vehicles equipped with in-car systems at sags and their effects on traffic flow, considering as objective the minimisation of total travel time.

---

[1]The effects of the supporting strategy have been identified by comparing the scenarios in which some or all controlled vehicles use this strategy with corresponding virtual scenarios in which the supporting strategy was excluded from the solution.

To this end, we optimised the accelerations of some vehicles of a traffic stream that moves along a single-lane freeway stretch with a sag. Our findings provide valuable insight into how congestion can be reduced at sags by means of traffic control measures based on the use of in-car systems. More specifically, they highlight the relevance of motivating drivers to accelerate fast along sags and limiting the inflow to the vertical curve. In addition, they indicate ways to do that by regulating the acceleration of equipped vehicles. Our findings also prove the usefulness of the proposed optimisation method as a tool for control measure development. We conclude that this method could be used to identify effective traffic management strategies for other types of bottlenecks, possibly considering alternative control objectives.

Further research is necessary to determine whether the traffic management strategies identified in this paper would also be the most effective in other scenarios (such as scenarios with multi-lane freeways, higher penetration rates and/or lower traffic demand). In addition, further research is necessary to translate the identified strategies into implementable traffic control measures (e.g., cooperative adaptive cruise control applications).

References

1. Xing, J., Sagae, K., Muramatsu, E.: Balance lane use of traffic to mitigate motorway traffic congestion with roadside variable message signs. In: 17th ITS World Congress (2010)
2. Koshi, M., Kuwahara, M., Akahane, H.: Capacity of sags and tunnels on Japanese motorways. ITE J. **62**(5), 17–22 (1992)
3. Yoshizawa, R., Shiomi, Y., Uno, N., Iida, K., Yamaguchi, M.: Analysis of car-following behavior on sag and curve sections at intercity expressways with driving simulator. Int. J. Intell. Transp. Syst. Res. **10**(2), 56–65 (2012)
4. Koshi, M.: An interpretation of a traffic engineer on vehicular traffic flow. In: Traffic and Granular Flow'01, pp. 199–210. Springer, Berlin (2003)
5. Patire, A.D., Cassidy, M.J.: Lane changing patterns of bane and benefit: observations of an uphill expressway. Transp. Res. Part B: Methodol. **45**(4), 656–666 (2011)
6. Brilon, W., Bressler, A.: Traffic flow on freeway upgrades. Transp. Res. Rec. J. Transp. Res. Board **1883**, 112–121 (2004)
7. Goñi-Ros, B., Knoop, V.L., van Arem, B., Hoogendoorn, S.P.: Mainstream traffic flow control at sags. Transp. Res. Rec. J. Transp. Res. Board **2470**, 57–64 (2014)
8. Sato, H., Xing, J., Tanaka, S., Watauchi, T.: An automatic traffic congestion mitigation system by providing real time information on head of queue. In: 16th ITS World Congress (2009)
9. Hatakenaka, H., Hirasawa, T., Yamada, K., Yamada, H., Katayama, Y., Maeda, M.: Development of AHS for traffic congestion in sag sections. In: 13th ITS World Congress (2006)
10. Papacharalampous, A., Wang, M., Knoop, V.L., Goñi-Ros, B., Takahashi, T., Sakata, I., van Arem, B., Hoogendoorn, S.R.: Mitigating congestion at sags with adaptive cruise control systems. In: 18th IEEE International Conference on Intelligent Transportation Systems (2015)
11. Goñi-Ros, B., Knoop, V.L., Shiomi, Y., Takahashi, T., van Arem, B., Hoogendoorn, S.P.: Modeling traffic at sags. Int. J. Intell. Transp. Syst. Res. **14**(1), 64–74 (2016)

Impact of Synchronised Flow in Oversaturated City Traffic on Energy Efficiency of Conventional and Electrical Vehicles

**Peter Hemmerle, Micha Koller, Gerhard Hermanns,
Michael Schreckenberg, Hubert Rehborn and Boris S. Kerner**

Abstract In this study of city traffic, we show that empirical synchronised flow patterns, which have been revealed recently in oversaturated traffic, exhibit considerable impact on the energy efficiency of vehicles. In particular, we have found that energy consumption in oversaturated city traffic can decrease considerably when the oversaturated city traffic consists of synchronised flow patterns rather than consisting of moving queues of the classical traffic flow theory at traffic signals. Using empirical GPS data measured by navigation devices on two different road sections in Düsseldorf, Germany, we show that synchronised flow patterns and moving queues differ in their cumulated vehicle acceleration (a sum of positive speed differences along a vehicle trajectory) despite similar mean speeds. Energy efficiency in return is dependent on the cumulated vehicle acceleration. We consider both the fuel consumption of conventional vehicles with combustion engines and the energy balance of electrical vehicles.

P. Hemmerle (✉) · M. Koller · H. Rehborn
Daimler AG, RD, HPC: 059-X901, 71059 Sindelfingen, Germany
e-mail: peter.hemmerle@daimler.com

M. Koller
e-mail: micha.koller@daimler.com

H. Rehborn
e-mail: hubert.rehborn@daimler.com

G. Hermanns · M. Schreckenberg · B.S. Kerner
Physics of Transport and Traffic, University of Duisburg-Essen, Lotharstr. 1,
47057 Duisburg, Germany
e-mail: gerhard.hermanns@uni-due.de

M. Schreckenberg
e-mail: michael.schreckenberg@uni-due.de

B.S. Kerner
e-mail: boris.kerner@uni-due.de

1   Introduction

Synchronised flow is known to be one of the three traffic phases in Kerner's three-phase theory of traffic [6–10]. The three phases are:

1. Free flow.
2. Synchronised flow.
3. Wide moving jams.

Congested highway traffic is subdivided into the synchronised flow phase and the wide moving jam phase. Recently, it was predicted that synchronised flow patterns (SPs) should exist in oversaturated city traffic at traffic signals as well [13].

Real field GPS (global positioning system) data measured by navigation devices are commonly used for on-line route guidance. An analysis of such data has confirmed the existence of SPs in oversaturated city traffic [12]. It has been revealed that oversaturated city traffic after speed breakdown consists of SPs, sequences of moving queues (MQs) corresponding to the classical theory of city traffic [1–3, 15, 16, 18], and mixtures of these two spatio-temporal traffic patterns.

In this paper, we study the impact of SPs in oversaturated city traffic on the energy efficiency of vehicles. We compare SPs and MQs with regard to their cumulated vehicle acceleration, which is a sum of positive speed differences. We relate the cumulated vehicle acceleration to energy efficiency by means of macroscopic energy matrices. We address both conventional vehicles with a combustion engine and electrical vehicles. The data basis of this work are empirical anonymised GPS data from navigation devices, empirical data of fuel consumption and electrical energy measured in field trials with vehicles, and microscopic speed and acceleration data from traffic flow simulations.

2   Empirical Synchronised Flow Patterns in Oversaturated City Traffic

For the study of spatio-temporal traffic patterns in oversaturated city traffic we use anonymised GPS probe data measured by navigation devices in vehicles provided by the company TomTom. A navigation device measures the GPS locations of the vehicle at time instants t_n with a fixed time interval $\Delta T = t_{n+1} - t_n$ between GPS measurements. In on-line applications, $\Delta T = 5\,\text{s}$ is commonly used. We consider GPS probe data from two road stretches in the city of Düsseldorf, Germany: a 630 m section of Völklinger Straße and a 450 m section of Südring (see [4] for sketches of these road sections). There is a traffic signal at the downstream end of both sections and no traffic signals between their upstream and downstream ends. Measurements with stationary traffic detectors confirm that on these road stretches oversaturated traffic occurs on many days [12].
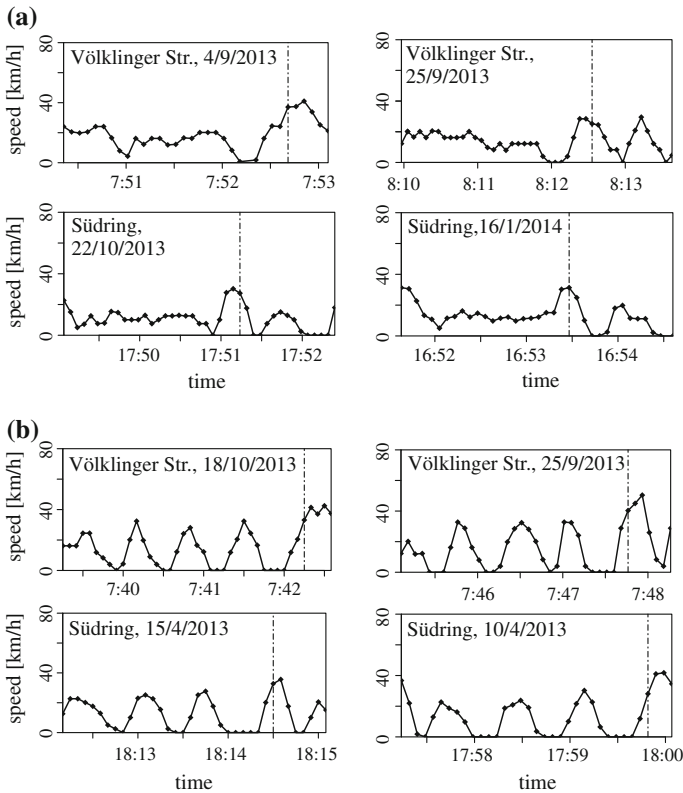
Fig. 1 Empirical examples of single-vehicle speeds from anonymised GPS probe data measured by navigation devices in vehicles on the roads Völklinger Straße and Südring in Düsseldorf, Germany. *Dash-dotted lines* indicate the time instant of the first measurement after the vehicle has passed the traffic signal and thus left the road section under consideration: synchronised flow patterns (SPs) (**a**); sequences of moving queues (MQs) [4] (**b**)

Empirical single-vehicle speeds derived from GPS data are shown in Fig. 1. In Fig. 1a, the vehicles stop no more than once at the traffic signal location before passing the signal. Before these stops, the vehicles traverse SPs: they move with a speed that is considerably lower than free flow speed, but within the SP, they do not stop, and hence there is no flow interruption. In contrast, when vehicles traverse MQs (Fig. 1b), traffic flow is interrupted as the vehicles stop several times in queues. When leaving each queue, a vehicle accelerates from speed zero and moves on to the next queue, until it eventually reaches the traffic signal location.

3   Cumulated Vehicle Acceleration

While the SPs and MQs shown in Fig. 1 have similar mean vehicle speeds, they differ considerably with regard to the acceleration behaviour of the vehicles. Obviously, both speed and acceleration affect the energy efficiency of vehicles.

   To quantitatively assess how SPs and MQs affect the energy efficiency of vehicles, we choose macroscopic parameters that can feasibly be calculated on the basis of GPS data from navigation devices and that correlate with the energy efficiency of vehicles. The mean speed per road section is such a parameter. However, in addition to the mean speed, the speed differences $v_{n+1} - v_n$ (see Fig. 2) between GPS measurements contain information about the frequency and strength of acceleration along a vehicle trajectory. The *cumulated vehicle acceleration A* per road length is a sum of positive speed differences between GPS measurements. It is defined by the formula [11]

$$A = L^{-1} \sum_{n=1}^{N-1} (v_{n+1} - v_n)\, \Theta\,(v_{n+1} - v_n - \Delta v), \tag{1}$$

where L is the road section length, $\Theta(x)$ the Heaviside function, and $\Delta v \geq 0$ is used to reduce the effect of the error resulting from speed calculations from GPS data. We use $\Delta v = 0.5$ km/h.

   The idealised and artificial speed profiles depicted in Fig. 3 give an idea of the order of magnitude of the cumulated acceleration in certain situations.

   For the empirical vehicle speeds from Fig. 1 and several additional examples of SPs and MQs from the two considered road sections, the dependency of the cumulated vehicle acceleration on the mean vehicle speed is shown in Fig. 4. Clearly, the cumulated vehicle acceleration is greater for MQs than for SPs.
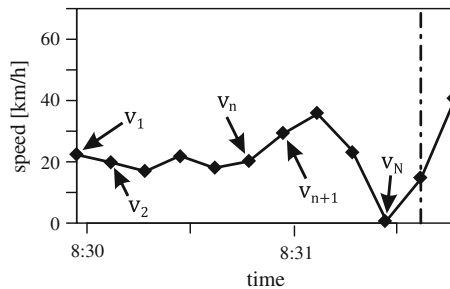

Fig. 2 Example of single-vehicle GPS data. The cumulated vehicle acceleration is calculated on the speed differences (e.g. $v_{n+1} - v_n$) between GPS measurements. The dash-dotted line indicates the time instant of the first measurement after the vehicle has left the road section under consideration [11]
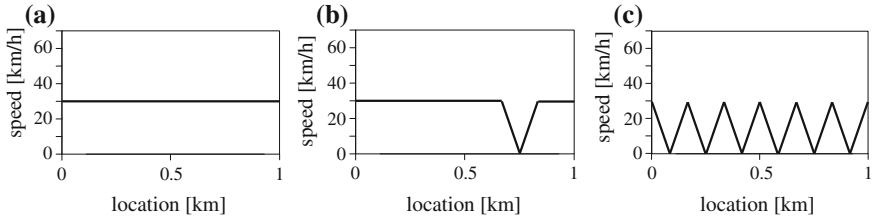
Fig. 3 Hypothetical vehicle speeds on a road of length $L = 1\,\text{km}$ with different values of the cumulated vehicle acceleration A [4]: $A = 0\,\text{h}^{-1}$ (**a**); $A = 30\,\text{h}^{-1}$ (**b**); $A = 180\,\text{h}^{-1}$ (**c**)

Fig. 4 Dependency of the cumulated vehicle acceleration A on the mean speed V for several examples of empirical synchronised flow patterns and moving queues on the examined road sections of Völklinger Straße and Südring in Düsseldorf, Germany
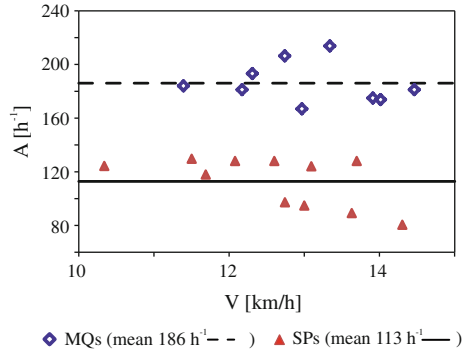

4 Energy Efficiency of Vehicles

For energy efficiency calculations, we use empirical microscopic consumption matrices. These are based on empirical CAN (Controller Area Network) bus data of speed, acceleration and fuel consumption or, respectively, electrical energy recorded from the following vehicles: a conventional medium-sized vehicle with a combustion engine [14] and a Smart electric drive. These vehicles were driven during field trials in real traffic [14]. Neither data from test bench measurements nor consumption models (compare [17]) were used.

The empirical microscopic matrices were aggregated by grouping energy values into matrix elements according to their associated speed and acceleration values. For each matrix element, the energy median was then calculated. Visualisations of the resulting energy matrices are shown in Fig. 5, where normalised energy scales are used. For the fuel consumption, which is a measure of the energy consumption of conventional vehicles, the normalised values are between 0 and 1. For the electrical vehicle, due to energy recuperation associated with regenerative braking, several energy values associated with negative acceleration are negative.

The empirical microscopic energy matrices were combined with microscopic speed and acceleration data from a traffic flow simulation of city traffic [5]. As a result, macroscopic energy matrices were calculated that can be used in energy-efficient route guidance. For the conventional vehicle, simulated trajectories were
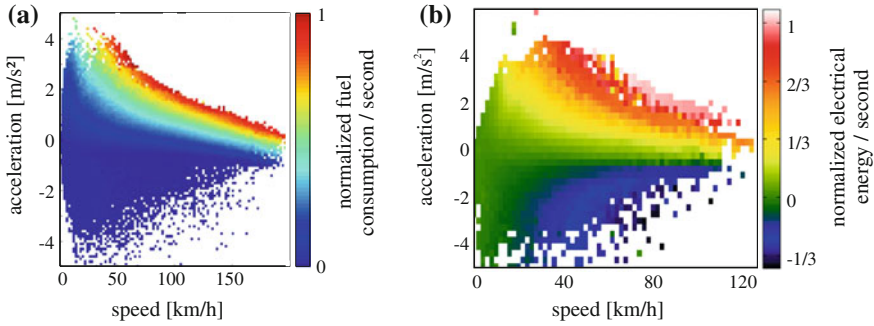
Fig. 5 Empirical microscopic consumption matrices: matrix for a conventional vehicle [14] (**a**); matrix for an electrical vehicle (**b**)

classified according to their mean speed and cumulated acceleration, and mean 'relative consumption' values were calculated for each class. The relative consumption value 1 (as well as the 'relative electrical energy' value 1) corresponds to a drive with time-independent speed 60 km/h. The resulting macroscopic consumption matrix M_C for a conventional vehicle (see Fig. 6) shows the following results [4]:

1. For mean speeds between 0 and 65 km/h, fuel consumption increases with decreasing mean speed.
2. Fuel consumption increases with increasing cumulated acceleration.

We have seen in Sect. 3 that the cumulated acceleration is greater for MQs than for SPs. This finding in combination with the above result under 2 (compare Fig. 6b) leads to the following conclusion. The fuel consumption associated with MQs is considerably greater than the fuel consumption associated with SPs.

For electrical vehicles we chose a modified approach to take account of energy recuperation associated with regenerative braking. To this end, we split the simulated trajectories into their portions with non-negative and negative acceleration for separate energy calculations, and calculated two separate macroscopic matrices: Matrix
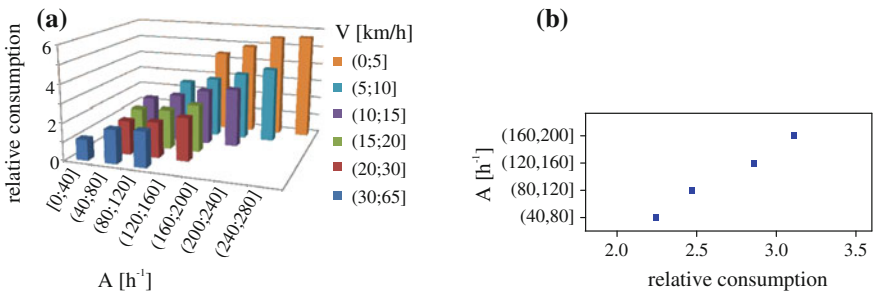
Fig. 6 Macroscopic consumption matrix M_C for a conventional vehicle with a combustion engine [4]: Mean dependency of fuel consumption on mean speed V and cumulated vehicle acceleration A (**a**) and Mean dependency of fuel consumption on the cumulated vehicle acceleration A for typical SP and MQ between 10 and 15 km/h (**b**)
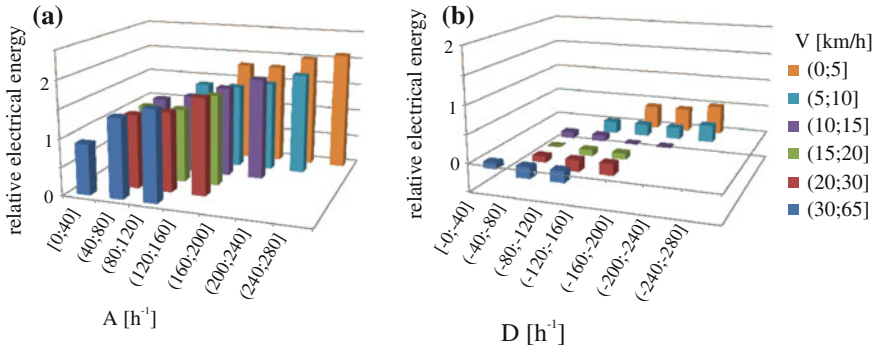
Fig. 7 Macroscopic energy matrices: Mean dependency of electrical energy on mean sped V and cumulated vehicle acceleration M_{E1} (**a**) and Mean dependency of electrical energy on mean speed V and cumulated vehicle deceleration M_{E2} for an electrical vehicle (**b**)

M_{E1} (Fig. 7a) represents the dependency of the electrical energy balance on mean speed and cumulated acceleration, matrix M_{E2} (Fig. 7b) represents the dependency of the electrical energy balance on mean speed and cumulated deceleration D which is defined in analogy to the cumulated acceleration (Eq. 1) by the formula

$$D = L^{-1} \sum_{n=1}^{N-1} (v_{n+1} - v_n)\, \Theta(-(v_{n+1} - v_n) - \Delta v). \qquad (2)$$

In M_{E2} (Fig. 7b) there are both negative entries, where the recuperation prevails ($15\,\text{km/h} \leq V \leq 65\,\text{km/h}$), and positive entries ($0\,\text{km/h} \leq V \leq 15\,\text{km/h}$), where the consumption prevails. A comparison between M_{E1} and M_{E2} shows that for all mean speeds and possible combinations of A and D, energy consumption considerably outweighs energy recuperation. M_{E1} is qualitatively similar to matrix M_C for conventional vehicles. However, for mean speeds between 0 and 20 km/h that are associated with oversaturated city traffic, the relative electrical energy consumption according to M_{E1} and M_{E2} is considerably lower than the relative fuel consumption according to M_C. This means that the impact of oversaturated traffic on energy efficiency is stronger for a conventional vehicle than for an electrical vehicle. One has to keep in mind the different sizes of the vehicles that the energy data have been measured with. However, the difference in relative energy consumption between electrical and conventional vehicles affects energy-efficient route guidance. Due to oversaturated traffic, the most energy-efficient route for conventional vehicles can be different from the most energy-efficient route for electrical vehicles.

5 Conclusions

1. Oversaturated city traffic after speed breakdown commonly consists of synchronised flow patterns (SPs), sequences of moving queues (MQs), and mixtures of these.

2. The cumulated acceleration is considerably greater for MQs than for SPs.
3. The energy consumption of vehicles increases with increasing cumulated acceleration.
4. Items 2 and 3 mean that the energy consumption of vehicles traversing MQs is considerably greater than the energy consumption of vehicles traversing SPs.
5. The impact of oversaturated city traffic on the energy efficiency of vehicles is stronger for a conventional vehicle than for an electrical vehicle.

References

1. Dion, F., Rakha, H., Kang, Y.S.: Comparison of delay estimates at under-saturated and oversaturated pre-timed signalized intersections. Transp. Res. Part B Methodol. **38**(2), 99–122 (2004)
2. Gartner, N.H., Stamatiadis, C.: Traffic networks, optimization and control of urban. In: Meyers R.A. (ed.) Encyclopedia of Complexity and System Science, pp. 9470–9500. Springer (2009)
3. Geroliminis, N., Skabardonis, A.: Identification and analysis of queue spillovers in city street networks. IEEE Trans. ITS **12**(4), 1107–1115 (2011)
4. Hemmerle, P., Koller, M., Rehborn, H., Kerner, B.S., Schreckenberg, M.: Fuel consumption in empirical synchronised flow in urban traffic. IET Intell. Transp. Syst. **10**(2), 122–129 (2016)
5. Hermanns, G., Hemmerle, P., Rehborn, H., Koller, M., Kerner, B.S., Schreckenberg, M.: Microscopic simulation of synchronized flow in oversaturated city traffic. Effect of drivers speed adaptation. Transp. Res. Rec. **2490**, 47–55 (2015)
6. Kerner, B.S.: Experimental features of self-organization in traffic flow. Phys. Rev. Lett. **88**(17), 3797 (1998)
7. Kerner, B.S.: Congested traffic flow: observations and theory. Transp. Res. Rec.: J. Transp. Res. Board **1678**, 160–167 (1999)
8. Kerner, B.S.: The physics of traffic. Phys. World **12**(8), 25–30 (1999)
9. Kerner, B.S.: The Physics of Traffic. Springer (2004)
10. Kerner, B.S.: Introduction to Modern Traffic Flow Theory and Control. Springer (2009)
11. Kerner, B.S.: Cumulated vehicle acceleration. Traffic Eng. Control **55**(4), 139–141 (2014)
12. Kerner, B.S., Hemmerle, P., Koller, M., Hermanns, G., Klenov, S.L., Rehborn, H., Schreckenberg, M.: Empirical synchronized flow in oversaturated city traffic. Phys. Rev. E **90**(3), 032810 (2014)
13. Kerner, B.S., Klenov, S.L., Hermanns, G., Hemmerle, P., Rehborn, H., Schreckenberg, M.: Synchronized flow in oversaturated city traffic. Phys. Rev. E **88**(5), 054801 (2013)
14. Koller, M.: Kraftstoffmehrverbrauch auf Basis dynamischer Verkehrslagen. Ph.D. thesis, Eberhard Karls Universität Tübingen (2015)
15. Newell, G.F.: Approximation methods for queues with application to the fixed-cycle traffic light. Siam Rev. **7**(2), 223–240 (1965)
16. Robertson, D.I.: TRANSYT: a traffic network study tool. Transport and road research laboratory report lr 253. TRL, Crowthorne (1969)
17. Treiber, M., Kesting, A.: Traffic Flow Dynamics. Data Models and Simulation. Springer, Heidelberg (2013)
18. Webster, F.V.: Traffic signal settings. Road Research Laboratory (1958). Tech. Paper No. 39

Evaluation of Air Transportation Network Resilience Using Adaptive Capacity

Suhyung Yoo and Hwasoo Yeo

Abstract Enhancing network resilience has been an important research topic for several decades with the increasing failures of critical infrastructure by disasters or terrorist attack. For critical infrastructures, such as electricity grid, water supply, and transportation, reliability to provide a stable level of service is most required. This paper proposes a resilience evaluation methodology with application to air transportation system. It is one of the major worldwide transportation modes and known as one of representative scale-free networks, which is relatively robust against random failure but vulnerable to targeted attack on hubs. This paper evaluates the air transportation network resilience using proposed adaptive capacity concept. Suggested measurements quantify the adaptive capacity, by which the capability of a network is to replace the damaged node with other redundancy of the network. Consequently, this study will help to diagnose the network resilience and contribute to planning for improvement of network resilience.

1 Introduction

Network resilience has been importantly researched for a reliable system to maintain a stable level of performance of the system. Critical infrastructures, including electricity grid, water, and transportation system, especially have direct impact on our daily life by providing a certain level of service maintaining our society. There has been noticeable disruptive events, such as the 9/11 attack in 2001, the volcano Eyjafjallajkull, Iceland eruption in 2010, and recent threats of ISIS terrorism, that are examples to show the necessity of evaluating network adaptive capacity to sustain level of service and to maintain the network resilience [5]. The word 'resilience' stems from the Latin verb 'resilio', meaning 'rebound' [10, 11]. It first emerged
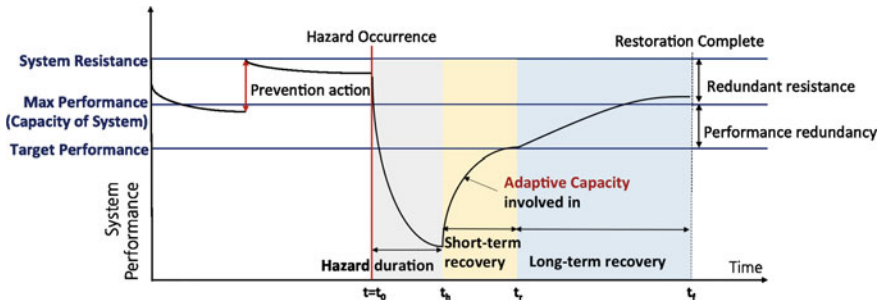
S. Yoo (✉) · H. Yeo
Department of Civil and Environment Engineering, Korea Advanced Institute
of Science and Technology, Daejeon, South Korea
e-mail: suhyung.yoo@kaist.edu

H. Yeo
e-mail: hwasoo@kaist.edu

Fig. 1 The reaction process of a system resilience before and after hazard occurrence

in ecology fields to investigate the properties of a number of different types of stability. As the term resilience has been studied and adopted in other researches, it has been mixed with other words such as risk, vulnerability, robustness reliability and flexibility. There are various definitions of resilience [8, 10–12]. This paper uses the definition of resilience, which is the characteristic of the system's ability to return to a stable state following a strong perturbation caused by failure, disaster or attack, following Holling [8]. According to [12], the resilience framework consists of three system capacities reducing systemic impact and total recovery effort. They are absorptive capacity, adaptive capacity and restorative capacity. Each capacity has a role in enhancing the system resilience and affects to different state of the response to a disruption. Figure 1 depicts this recovery process of the system resilience before and after hazard occurrence.

In this paper, the adaptive capacity composes the main idea to measure the network resilience by the ability of the system to respond to external impact on the system and to adjust its resources for recovery of the target system performance level through the short-term recovery period. At the same time, this research uses the air transportation network as an example, which is one of critical infrastructures providing the worldwide rapid transportation.

The air transportation network has been studied as one of representative scale-free networks [1, 3, 4, 7], which is composed of hub nodes with high degrees and follows a power-law distribution. In the complex network theory, most of complex systems are able to be represented as a network, in which components become nodes and the interaction between components are edges connecting two nodes. Following the research, the complex theory studies have found that a scale-free network, such as the air transportation system, is vulnerable against an attack on a hub [1, 2, 6, 7]. Consequently, the resilience of the air transportation network is required to be investigated for providing a reliable service of transportation. Thus, this paper has a purpose to identify vulnerable nodes and to quantify the network resilience in terms of the adaptive capacity.

2 Methodology

This paper regards the air transportation network as a node-based spatial scale-free network with node capacity. In other words, the network's degree follows power-law distribution (scale-free network), the nodes are located in a space equipped with a metric (spatial network), the cost of link connection is relatively low (node-based network), and each node has a capacity to function. The simulated network is a weighted, undirected graph with nodes (airports) and links (air routes). The basic idea for quantifying network resilience and measuring adaptive capacity is the ability of a network if an attacked node can be replaced by other adjacent nodes. When a performance level of a system is maintained after a disruption, the system can be regarded as resilient. We calculate the performance level by accumulating the whole airports' capacity and margin within the network. Assume that a network is in its initial stable condition, in which each node has performance redundancy under the capacity. When a disruption occurs, one node is extracted from the network, and all connected links are disabled. It alters the balance between capacity and work load (flow), causing redistribution of flows within the network. If the adjacent nodes have enough margin to absorb the redistributed flow, the network can adapt to the shock and maintain stable performance level. In other words, a substitution happens when the network has enough adaptive capacity.

The simulation will proceed to remove vertices in two ways: a random failure or a sustained attack in the network. The latter approach is closely related to the study of percolation in physics. Percolation is referred to the process that results from taking a network and removing some fraction of its vertices together with the edges connected to the vertices [9].

2.1 New Measurements for Network Resilience

This part demonstrates the network, in which each node is disabled randomly. The failed node's flow is reassigned to the closest node first, only if it has enough margin to handle the traffic.

- Degree of adaptation (k_a): the number of nodes required to absorb the shock and substitute.
- Unit cost of adaptation ($cost_{unit}$): the unit cost of each flight in terms of detoured distance.
- Total cost of adaptation ($cost_{total}$): the total cost of all traffic in terms of detoured distance.

In case of sustained attack, the simulation removes the nodes from the network one by one until all nodes are extracted. Following the sustained attack, some parts of network fail in the order of their importance. As the attacked node's flow is redistributed to other nodes, the remaining margin of the network is changed and

measured to quantify the network adaptive capacity.

$$Indicator\ of\ adaptive\ capacity = \frac{\sum_i^n Margin_k(k)}{\sum_i Margin_i} \tag{1}$$

where a network has n nodes and $Margin_k$ is ith node's margin after kth node is attacked.

- Alpha index: the fraction of nodes required to remain a certain level of remaining margin.
- Alpha zero (α_0): the fraction of nodes at which the network cannot afford to absorb the extra load.
- Adaptive capacity coefficient: the difference between adaptive capacity of the network failure under random failure and sustained attack.

$$ACC = \frac{Area\ below\ sustained\ attack\ profile}{Area\ below\ random\ failure\ profile} = \frac{\int_{\rho=0}^{1} pA_\rho}{\int_{\rho=0}^{1} rA_\rho} \tag{2}$$

where ρ is a fraction of nodes removed from 0 to 1.

This study assumes that the ideal resilient network may lose its adaptive capacity constantly as nodes are removed. However, the less resilient network fails faster and its remaining margin drops faster than the ideal one.

3   Results

This research utilises the US air transportation network to examine the measurements suggested in the last section through the simulation of a network failure and the change of its adaptive capacity.

3.1   Simulation Under a Single Failure

In this part, the adaptive capacity of a network under a single failure will be investigated. The experiment attacks a single node, redistributes the attacked node's work load to other adjacent nodes in order of closeness, and evaluates its effect on the network. The simulation runs 1000 times for random generation of weather conditions to decide each airport's capacity. So, the distribution of each measure is obtained by recursive simulations.

Table 1 shows the summary of simulation results. In the previous studies of complex network theory, a node was evaluated by its degree or weighted degree to represent the importance. If a node has high value of weight, it is thought to have high impact on the network in case of failure. The vulnerable airports are identified in the

Table 1 Summary of simulation results under a single attack, showing top 10 airports

Airport	Degree	Weighted degree	k_a	$cost_{unit}$	$cost_{total}$
ORD	203	32,378,906	3	81.92	7,676
ATL	195	45,308,685	3	171.8	19,070
IAH	173	19,528,631	3	90.51	5,341
DEN	187	25,497,348	2	136.1	8,794
DFW	187	27,100,656	2	107.6	9,892
LAX	164	32,427,115	2	27.9	1,936
LAS	163	19,923,594	2	182.6	7,339
SLC	134	9,910,493	1	241.7	7,601
MSP	206	16,282,038	1	98.94	2,968
DTW	166	15,683,787	1	79.16	2,399

The ranks are in order of the median value

order of the degree of adaptation, in Table 1. Airports ORD, ATL, and IAH require three airports to adapt to the disruption. When additional costs are ignored, the values of total cost of adaptation, which considers both the number of detours flights and their detoured distance, implies that airports ATL, DEN, and DFW are less resilient.

The left graph of Fig. 2 shows the result of the unit cost of adaptation. Top 2 (FAI, ANC) airports are located in Alaska, which is located apart from the main territory of America and has a wide area so that each airport is placed to be far each other. And
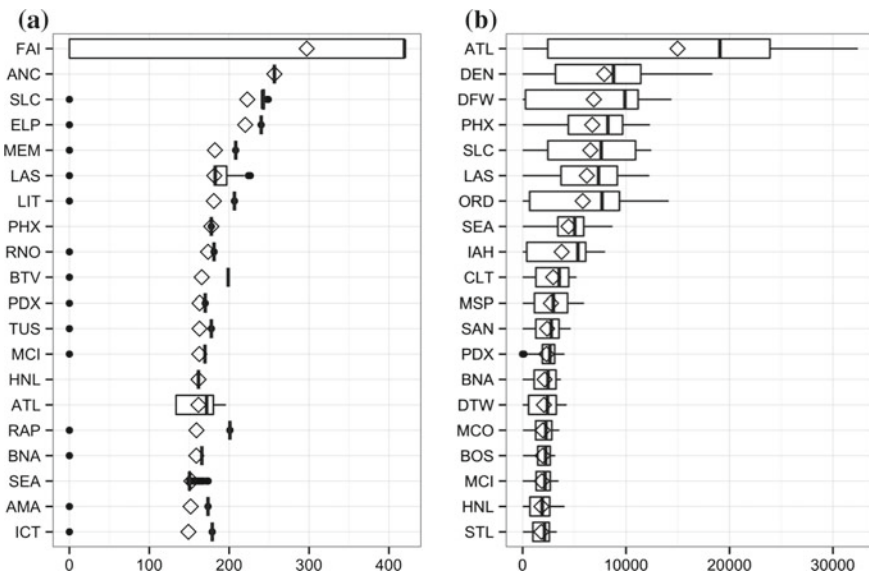
Fig. 2 Recursive simulation results in box plot. *Diamond symbol* represents its mean value: unit cost of adaptation (UC) (**a**) and total cost of adaptation (TC) (**b**)

the airports such as SLC, ELP, MEM and LIT are the mid-sized and isolated airports, although they may be the important airport in the state. Whether the airport is large or small, the presence of the alternative node with enough margin is important for adaptation.

On the other hand, the right side of Fig. 2 shows that airports ATL, DEN, and DFW are identified as the most important ones to improve their adaptive capacity. But for improving of adaptive capacity, it should be noted that the results are stochastic with responding to the disruptive circumstance. The dispersion of data is also an useful information to compare and analyse similar results. The result shows a range as shown in a box plot in Fig. 2. For instance, the airport ORD shows lower mean value of TC than airport LAS, while it has larger deviations. It means that ORD has higher uncertainty than LAS. This uncertainty requires us more careful preparedness because the cost of detour for ORD ranges from 675 miles to 9362 miles for total traffic.

3.2   Simulation Under a Sustained Attack

Next, the simulation attacks the nodes one by one until all nodes fail. When a network collapses, the indicator of adaptive capacity drops differently depending on the network topology and the types of attack. Note that the area under a profile implies the network performance. So the area between two profiles represent the difference caused by the network failure under the intended attack. By definition, as the area between two profiles is smaller and the adaptive capacity coefficient is closer to one, the network has more adaptive capacity and can be regarded as resilient under a sustained attack.

The simulation investigates the sub-network resilience of the US region. Table 2 shows the analytic result of the experiment. The US network has 0.66 value of

Table 2 Regional sub-network resilience: adaptive capacity coefficient and alpha index

Region	Adaptive capacity coefficient	$\alpha_{0.5}$	α_0
USA	0.48	0.13	0.52
Alaskan	0.88	0.36	0.86
Central	0.66	0.22	0.83
Eastern	0.51	0.16	0.40
Great Lakes	0.50	0.12	0.59
New England	0.71	0.25	0.92
Northwest Mountain	0.56	0.13	0.71
Southern	0.46	0.13	0.45
Southwest	0.48	0.16	0.55
Western Pacific	0.48	0.15	0.43
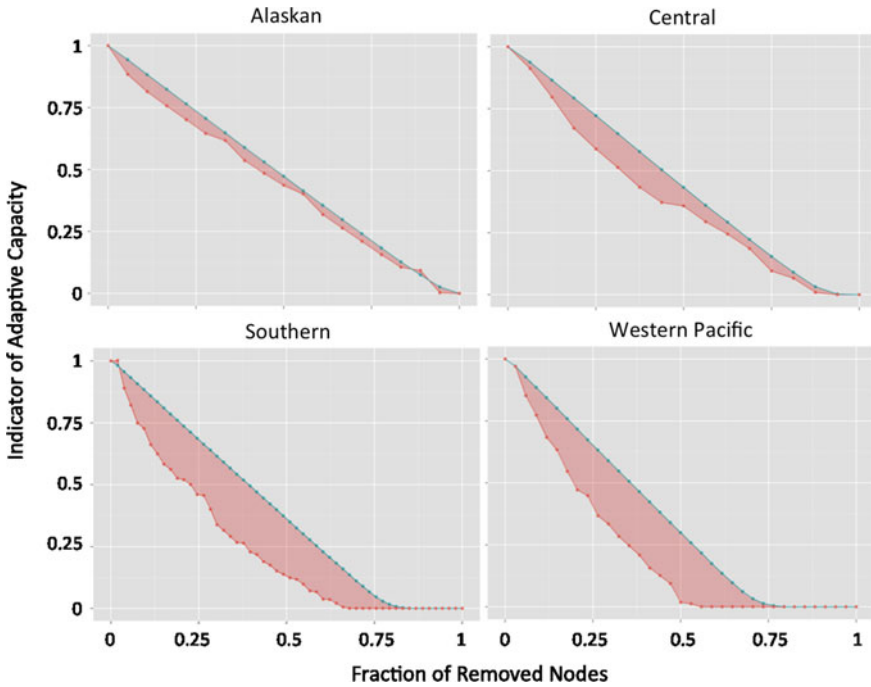
Fig. 3 Regional profile of adaptive capacity indicator (y-axis) by the fraction of removed nodes (x-axis). The *blue line* shows random failure case, and *red line* is for an intended attack case

adaptive capacity coefficient, in other words, the network can function 66 % of the network capability compared to the failure under random error. Compared to the value of US, the region Southern and Western pacific are worst resilient with less adaptive capacity coefficient. On the other hand, Alaskan, Central, and New England regions are relatively resilient. Figure 3 depicts the result of the resilient case (Alaskan, Central) and the less resilient case (Southern, Western pacific). As the line falls steeply to the bottom, the network can be thought less resilient because the relatively small fraction of nodes may cause a failure of the whole network.

4 Conclusion

This study has initiated with the need of evaluating critical infrastructure's resilience. To secure a stable level of service, the short-term emergency recovery from a disruption is needed through sufficient adaptive capacity of a system. So this paper regards the network's adaptive capacity as the system capability of self-organisation for recovery of system performance level to reflect the essential ability for resilient

infrastructure. Following the idea, the research has been conducted to simulate two types of network failure and measure the adaptive capacity with several measurements. Both the unit cost and total cost of adaptation are measured by additional distance to detour. It has demonstrated the air transportation network simulation under two types of attack, a single failure and a sustained attack.

The first part discovered the vulnerable nodes with less ability of adaptation, in terms of the number of nodes and the distance to detour. Under a single failure, the airports ATL, DEN, PHX, LAS, and SLC are identified as less resilient node. On the other hand, the airports ORD, LAX, JFK, and SFO seem to be relatively resilient in the US air transportation network. In the latter part, sustained attack is dealt with and the sub-network's resilience is evaluated by quantifying the adaptive capacity between random failure and intended attack scenarios. Compared to the average of US region, the Southern and Western pacific region are shown as relatively less resilient.

Consequently, this paper identified the vulnerable airports and sub-regions for diagnosing network resilience. Following this research, future study can develop a strategy to improve the resilience of infrastructure. For example, a projection of demand change or expanding airport capacity.

References

1. Albert, R., Barabási, A.: Statistical mechanics of complex networks. Rev. Mod. Phys. **74**, 47–98 (2002)
2. Albert, R., Jeong, H., Barabási, A.L.: Error and attack tolerance of complex networks. Nature **406**(6794), 378–382 (2000)
3. Barabási, A., Albert, R.: Emergence of scaling in random networks. Science **286**, 509–512 (1999)
4. Barrat, A., Barthélemy, M., Pastor-Satorras, R., Vespignani, A.: The architecture of complex weighted networks. Proc. Nat. Acad. Sci. U.S.A. **101**(11), 3747–3752 (2004)
5. Cox, A., Prager, F., Rose, A.: Transportation security and the role of resilience: a foundation for operational metrics. Transp. Policy **18**(2), 307–317 (2011)
6. Crucitti, P., Latora, V., Marchiori, M., Rapisarda, A.: Efficiency of scale-free networks: error and attack tolerance. Physica A **320**, 622–642 (2003)
7. Guimerà, R., Mossa, S., Turtschi, A., Amaral, L.A.N.: The worldwide air transportation network: anomalous centrality, community structure, and cities' global roles. Proc. Nat. Acad. Sci. U.S.A. **102**(22), 7794–7799 (2005)
8. Holling, C.S.: Engineering resilience versus ecological resilience. In: Engineering Within Ecological Constraints, vol. 31, p. 32 (1996)
9. Iyer, S., Killingback, T., Sundaram, B., Wang, Z.: Attack robustness and centrality of complex networks. PloS one **8**(4), e59613 (2013)
10. Reggiani, A.: Network resilience for transport security: some methodological considerations. Transp. Policy **28**, 63–68 (2013)
11. Rose, A.: Economic resilience to disaster. CARRI Research Report 8 (2009)
12. Vugrin, E.D., Warren, D.E., Ehlen, M.A., Camphouse, R.C.: A framework for assessing the resilience of infrastructure and economic systems. In: Sustainable and Resilient Critical Infrastructure Systems, pp. 77–116. Springer (2010)

Network-Wide Mesoscopic State Estimation Based on a Variational Formulation of the LWR Model and Using Lagrangian Observations

Yufei Yuan, Aurélien Duret and Hans van Lint

Abstract This paper presents a generic data assimilation framework based on a mesoscopic-LWR model formulated in Lagrangian-space coordinates and using Lagrangian observations. This is a challenging work since probe trajectories are not directly related to specific vehicle/platoon indexes in the simulation model. Therefore, we develop a method to incorporate probe information and to further estimate states. The proposed method has been validated on a homogeneous road stretch, and it provides promising results for further extension of the framework.

1 Introduction

Traffic state estimation (TSE) is crucial in dynamic traffic management. Model-based TSE relies on two components: a model-based component and a data assimilation algorithm. The same traffic flow model can be formulated in three two-dimensional coordinates regarding space x, time t and vehicle number n. Laval and Leclercq [3] have presented three equivalent variational formulations of the first-order traffic flow models, namely $N(x, t)$ model, $X(t, n)$ model, $T(n, x)$ model, respectively, under the theory of Hamilton–Jacobi partial differential equations. This paper presents a generic data assimilation framework based on a mesoscopic-LWR model formulated in vehicle number-space (Lagrangian-Space, L-S) coordinates, using Lagrangian observations. The information that we can receive from road networks is (i) probe trajectory information (Lagrangian data), and (ii) flow and speed information from loop sensors (Eulerian data). The question is how to estimate traffic state on the network from the two data sources?

Y. Yuan (✉) · H. van Lint
Delft University of Technology, Stevinweg 1, 2628CN Delft, The Netherlands
e-mail: y.yuan@tudelft.nl

H. van Lint
e-mail: j.w.c.vanlint@tudelft.nl

A. Duret
LICIT, IFSTTAR-ENTPE, 69675, Bron Cedex, France
e-mail: aurelien.duret@ifsttar.fr

Duret et al. [2] have proposed an assimilation framework to incorporate loop detector data into the mesoscopic-LWR model. With this LS-LWR formulation, cell boundaries have to be located at network discontinuities. Thus, it requires no intermediate nodes within a homogeneous road stretch, and this would improve computational efficiency. Moreover, cell boundaries also have to be defined at loop sensor locations to assimilate those Eulerian observations.

In this work, we will focus on incorporating Lagrangian observations into the data assimilation framework. This is a challenging work, since probe trajectories are not directly related to specific vehicle/platoon indexes in the simulation model. Therefore, we need to first estimate the best possible vehicle index of a selected trajectory via a data assimilation procedure. The traffic information from this trajectory will be further used to update model states.

2   Lagrangian-Space Formulation of the LWR Model

This section first presents a mesoscopic formulation of the LWR model as the process model in the estimation framework. The LWR model is formulated in vehicle platoon and space (n, x) coordinates. We apply a variational formulation of the T-model. The numerical solution to the Hamilton–Jacobi formulation, under the assumption of a triangular fundamental relation with the free-flow speed v_m, the maximum wave speed w and the jam density k_x, reads as follows:

$$T(n, x) = max(T(n, x - \Delta x) + \frac{\Delta x}{v_m}, T(n - \Delta n, x - \frac{\Delta n}{k_x}) + \frac{\Delta n}{wk_x}) \qquad (1)$$

This indicates traffic flow is divided into vehicle platoons of certain size Δn, and road stretch is discretised into spatial cells of certain length Δx. The state in this formulation is the passage time $T(n, x)$ of vehicle platoons at cell boundaries. This state is always determined by the maximum of two uncorrelated terms: the demand (arrival) time and the supply time. For an elaborate description we refer to [3].

3   Methodology

The mesoscopic-LWR assimilation framework proposed in [2] allows to incorporate loop data along the spatial dimension. Alternatively, information can also be observed along the vehicle number dimension. The Lagrangian type observation allows more accurate estimates and provides additional state information that is not available from loop data.

3.1 Data Assimilation with Lagrangian Data

In this paper, we focus on incorporating Lagrangian observations. First, we will look at how to deal with a single data source from probe vehicles. The main idea is to derive general (internal) boundary conditions along probe trajectories (n fixed). At these probe boundaries, we know the observed information (position x and time t) and can estimate probe vehicle indices (namely n_p^a) based on the variational principles. That is, the 'observation' information is compared to the model 'background' information to deliver 'analysis' states of vehicle indices. Next, the indexing probes would act as internal boundaries, directly provide the analysis states, in supply times at its upstream boundary and arrivals times at its downstream boundary. Finally, the passage times of influencing vehicles can serve as arrival/supply time constraints to further update traffic states in the simulation model.

Data assimilation is progressing with a sequential framework. Let us consider an observation period P during which time positions from probes have been collected. Three steps are identified to transform time position information from probes into traffic conditions at surrounding boundaries.

3.1.1 Step 1. Estimation of Probe Index

Let us consider the trajectory of a probe p from which several (at least two) intermediate time positions, denoted $t_{p,i}^o$ and $x_{p,i}^o$, have been observed during the period P. According to the variational principle, a ('analysis') probe index $n_{p,i}^a$ can be estimated from its 'observed' time position ($t_{p,i}^o$ and $x_{p,i}^o$) and from the 'background' state (b-state) at its downstream boundary (x_{down}) and upstream boundary (x_{up}). Let n_u and n_w be the indexes at upstream and downstream boundaries, as illustrated in Fig. 1a.

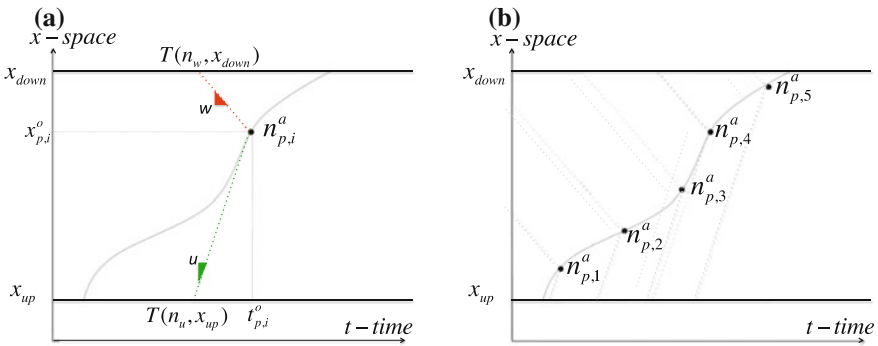$$n_{p,i}^a = min(n_{u,up}, n_{w,down} + k_x(x_{down} - x_{p,i}^o)) \qquad (2)$$

Fig. 1 Estimation of (analysis) probe index of trajectory: one point (**a**); several points (**b**)

subject to $T(n_u, x_{up}) = t^o_{p,i} - \frac{x^o_{p,i} - x_{up}}{u}$, $T(n_w, x_{down}) = t^o_{p,i} - \frac{x_{down} - x^o_{p,i}}{w}$. Here, $n^a_{p,i}$ denotes the analysis probe index, i denotes the index of measurement of each probe trajectory p.

Then, we could estimate the most possible vehicle index that corresponds to this probe trajectory (a-state, n^a_p) as the simple average of vehicle index $n^a_{p,i}$ at each point i, see Fig. 1b. As a first approximation, we consider the average:

$$n^a_p = (\overline{n^a_{p,i}}), i \in p \tag{3}$$

3.1.2 Step 2. Estimation of Arrival and Supply Times (Analysis a-state)

According to the shockwave theory, time position information of the probe vehicle will be propagated in two directions: downstream with the free-flow speed u in arrival time and upstream with the congested wave speed w in supply time. Consequently, information from probe vehicles will only be used to update the arrival/supply times at surrounding boundaries over the period P. Then, the model will confront new arrivals and supplies to improve traffic states at cell boundaries. Note on the arrival and supply times:

- Arrival times
  It should be noted that the influencing probe vehicles are located in a time window with a length P that moves with a speed u between x_{up} and x_{down}, as in Fig. 2. Within the area, the dynamics of each probe provides information of its own upcoming arrival times. The *latest* observed time position information of the probe vehicle p, denoted by $t^o_{p,end}$ and $x^o_{p,end}$, respectively, will be used to update its arrival time at the downstream boundary following:

$$t^a_{a,n^a_p} = t^o_{p,end} + \frac{x_{down} - x^o_{p,end}}{u} \tag{4}$$
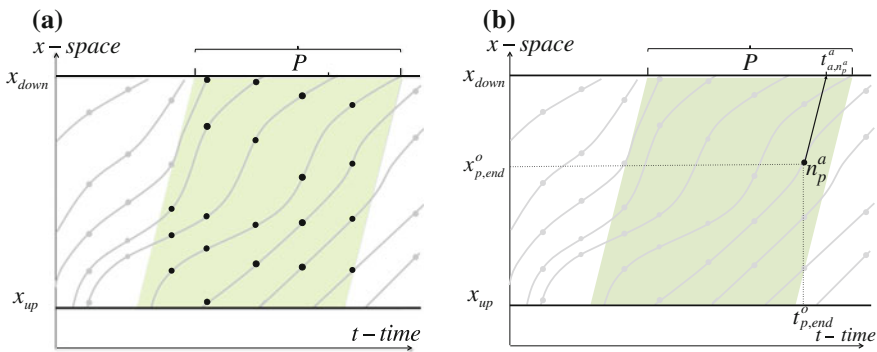
Fig. 2 Arrival time estimation for influencing vehicles: determination of observed traffic state and influencing vehicles (**a**); estimation of arrival time from a probe (**b**)

Here, the subscript 'a' is for 'arrival' and the superscript 'a' is for 'analysis'.

- Supply times

  Similarly, the influencing probe vehicles are located in a time window with a length P that moves with a speed w between x_{up} and x_{down}, as illustrated in Fig. 3. Within the area, probe trajectories provide information related to the supply times of their followers. Based on the variational principle, we show that

$$t^a_{s,n^a_p+k_x(x^o_{p,i}-x_{up})} = t^o_{p,i} + \frac{x^o_{p,i} - x_{up}}{w}, \forall i \in p \tag{5}$$

Here, the subscript 's' is for 'supply' and the superscript 'a' is for 'analysis'. The probe vehicle n^a_p sends as many supply times as time positions observed along its trajectory. To go further, one can interpolate linearly the trajectory of the probe to obtain supply times for a continuous set of followers influenced by the probe vehicle n^a_p, denoted by $S(n^a_p)$:

$$S(n^a_p) = \{n^a_p + k_x(x^o_{p,start} - x_{up}) : n^a_p + k_x(x^o_{p,end} - x_{up})\} \tag{6}$$

Note that the vehicle index n may be influenced by several probe trajectories. The final supply time, denoted $\widehat{t}^a_{s,n}$, will be calculated by averaging all the supply times that contribute to the current vehicle index. To do so, for each vehicle index n, we will build the list $L(n)$ of probe vehicles that send supply times $\{t^a_{s,L(n)}\}$

$$\widehat{t}^a_{s,n} = \{\overline{t^a_{s,L(n)}}\}, n \in L(n) \tag{7}$$

In this step, the analysis state of supply/arrival times is directly obtained from the estimated internal probe boundaries. Even if the current procedure does not present a proper analysis step, we cannot say that we fully trust the observations from probe trajectories. We do not use a 'conventional' assimilation technique to find the best compromise between observations and backgrounds. Here, the philosophy is to combine both observations from probes $(x - t)$ and background
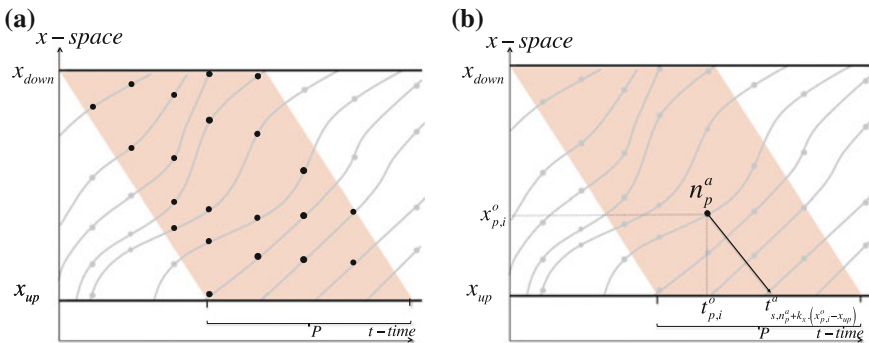
Fig. 3 Supply time estimation for influencing vehicles: determination of observed traffic state and influencing vehicles (**a**); estimation of supply time from a probe (**b**)

$(T(n, x)$ at boundaries) to estimate the most likely state $(n - x - t)$ of probes. This is Step 1. However, the resulting analysis states cannot be directly used to update the model, because it can only be updated at its cell boundaries. Consequently, we have proposed a procedure that transforms the analysis state $(n - x - t)$ into boundary conditions at the models cell boundaries. This is handled in Steps 2 and 3. Note that if analysis states present some inconsistencies, certain methods (e.g. the Kalman filter) could also be proposed to find the best compromise between the inconsistent analysis states.

3.1.3   Step 3. Update of the Model and CFL Condition

During the observation period P, the analysis state serves as supply/arrival time constraints to overwrite the background supply/arrival times for the influencing vehicles. Next, the simulation model will calculate the most possible states based on the maximum between supply and arrival (see Eq. 1).

The update procedure requires to respect the CFL condition [1], which to ensure the numerical stability. Let ΔT denote the duration of the observation period P. If ΔT is larger than ΔT^{CFL} that is the minimum time for information to travel across two node boundaries (boundary distance divided by free-flow speed), the update has to be processed step by step restricted by the time step ΔT^{CFL}.

3.2   Comparison of Data Assimilation Using Eulerian and Lagrangian Data

The difference from the methodology in [2] for loop data is that the 'analysis' arrival/supply information is used to determine the new boundary conditions for influencing vehicles, instead of updating model states (passage times) directly. The main contribution of this work is to develop a method (outlined in Steps 1–3) that considers probe data, and further the fusion between these two data sources. The data assimilation with Lagrangian data is developed under a consistent structure as the one with loop data. Therefore, the two data assimilation frameworks can support each other.

## 4   Model Validation with Experiments

The next step is to validate the proposed data assimilation framework. We have built a Mesoscopic Simulation Platform. This platform has been used to validate the data assimilation framework with only loop data, in a synthetic case and a realistic large-scale network. For now, we will consider additional probe data for model validation.

First, the validation at a local scale is performed on a homogeneous road stretch of 4 km in length. The fundamental diagram is bilinear, with three parameters: $v_m = 30$ m/s, $w = 5$ m/s and $k_x = 0.17$ veh/m.

The ground truth is generated with the same LS-LWR model, but with a finer cell resolution, with the complete vehicle trajectories. The result returns the passage time of every single vehicle with a space frequency $dx = 1/k_x = 5.9$ m. The probe data have then been generated by identifying probe vehicles with a random selection of a subset of 5 % of vehicles and an interpolation of probe trajectories every 30 s. Here, the demand–supply scenario is defined as follows. The simulation duration is set to 1 hour. The demand at the entry is constant (0.25 vps). The supply at the position $x = 3.5$ km has been modified to simulate an incident (for instance an accident), which decreases the capacity between $t = 15$ min and $t = 45$ min. Congestion is rapidly triggered, propagates backward and then resolves before the end of the simulation. The vehicle trajectories and their respective travel times are illustrated in Fig. 4.

Then, the LS-LWR model has been run with a low space resolution ($dx = 1$ km) as it would have been implemented for a real-time monitoring purpose. The same parameters have been considered, but the model does not know that an incident occurs: it ignores its location and capacity. First, the model has run (without the assimilation procedure) and the results returns a free-flowing on the network. Then the model has run considering probe data (red circle in Fig. 4a) and the proposed assimilation procedure. The global results with 5 % probes are illustrated in Fig. 5.

The LS-LWR model returns passage time, consequently the travel times are convenient to illustrate the performance of the model. In Fig. 5c the overall shape of the estimated travel times is similar to the travel times returned by the ground truth. It clearly demonstrates the ability of the model to adjust its traffic states accordingly. Focusing on partial travel time along the stretch of road, one can observe that the travel times between the *entry* and 3 km is perfectly estimated. This demonstrates the ability of the method to estimate and propagate supply information backward. However, between 3 km and the *exit*, travel times globally fit the ground truth, but they also show regular dropout. This phenomenon can be explain as follows. The incident occurs between these two points. Consequently, the assimilation procedure here is used to update both arrival times downstream (*exit*) and supply time (3 km). However, it has been noticed that only arrival times of probe vehicles are properly analysed during the assimilation procedure, which explains that travel times regu-
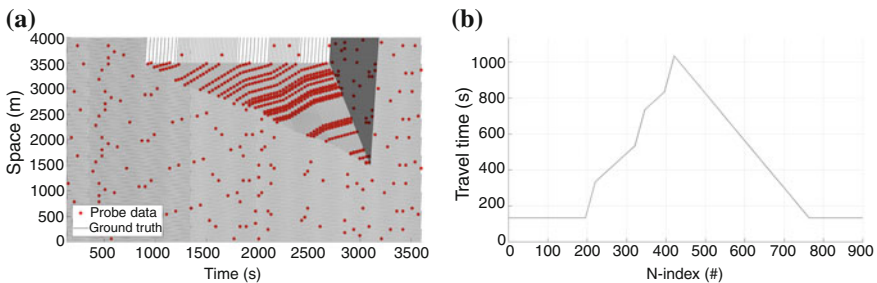
Fig. 4 Ground truth data: trajectories and probe data (**a**); travel times (**b**)

(a)   **(b)**   **(c)**
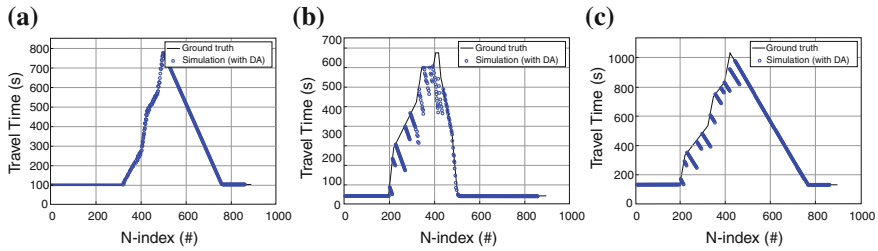
Fig. 5 Results: estimated travel times: between *entry* and 3 km (**a**); between 3 km and *exit* (**b**); between *entry* and *exit* (**c**)

larly meet the ground truth every time a probe vehicle is observed. On the contrary, the travel times gradually dropout from the ground truth when no probe vehicle is observed. It is expected that this phenomenon is mitigated as the rate of probe vehicle increases.

Based on the proposed assimilation procedure, the experiment succeeds to reconstruct traffic states over the whole spatiotemporal domain based on a limited amount of probe data. Overall, the method fulfils the expectations of state estimation. The main contribution of the probes is to capture the information between spatial boundaries and further propagate it downstream and upstream, and thus to update traffic states by means of arrival/supply time constraints.

5   Conclusion and Future Work

This paper has proposed a generic network-wide mesoscopic state estimation framework based on variational-formulated LWR model in Lagrangian-space coordinates, to incorporate Lagrangian observations. The experiment has demonstrated the validity of the proposed method. Future research includes, (i) to validate the framework in a more general case, a realistic large-scale network; (ii) to test both Lagrangian and Eulerian observations (data fusion) in a consistent and coherent data assimilation framework; (iii) to apply specific data assimilation techniques to account for model and observation reliability.

References

1. Courant, R., Friedrichs, K., Levy, H.: On the partial difference equations of mathematical physics. IBM J. Res. Dev. **11**(2), 215–234 (1967)
2. Duret, A., Leclercq, L., El Faouzi, N.E.: Data assimilation based on a mesoscopic-LWR modeling framework and loop detector data: methodology and application on a large-scale network. In: Proceedings of the Transportation Research Board 95th Annual meeting. Transportation Research Board, Washington, D.C. (2016)
3. Laval, J., Leclercq, L.: The Hamilton–Jacobi partial differential equation and the three representations of traffic flow. Transp. Res. Part B Methodol. **52**, 17–30 (2013)

Route Choice Behaviour in a Three Roads Scenario

Dominik Wegerle and Michael Schreckenberg

Abstract We present results of three simple three roads scenarios, which were simulated with an extended Nagel–Schreckenberg CA model. We studied how the global travel times of cars could be optimised by simple routing or distribution strategies. Besides the well-known methods as shortest path, travel times and equal distribution we tested alternating loads and present two strategies based on a remaining road capacity. The strategies were applied only to 25 % of the cars, whereas the remaining cars and trucks were distributed over the three roads as a fixed proportional load. The first scenario contains three different road lengths of 20, 22 and 24 km length and the fixed load is evenly distributed. In the second scenario, all three roads have a length of 20 km, but the fixed load is distributed unequally. The third scenario combines the different road length with an unequally distributed load.

1 Introduction

This research was part of the project DiNav—Dynamics in Navigation [7], to improve the efficient usage of road networks and to lower travel times. Former studies [6] as well as recent results [1–3] also based on the Nagel–Schreckenberg CA model [5] have led us to the idea to investigate simple routing or distribution strategies on a more complex three roads scenario. In this case, more complex means simulating with two vehicle classes on three roads each with two lanes and overtaking rules for cars. In addition, this study presents two routing strategies based on the maximum vehicle flow capacity, which was derived as well from the simulation.

D. Wegerle (✉) · M. Schreckenberg
Physics of Transport and Traffic, University of Duisburg-Essen,
47057 Duisburg, Germany
e-mail: dominik.wegerle@uni-due.de

M. Schreckenberg
e-mail: michael.schreckenberg@uni-due.de

2 Simulation

For the simulations we used an extended Nagel–Schreckenberg CA model [5] with two vehicle classes: cars and trucks. Cars have a length of one cell equivalent to 7.5 m and a maximum velocity of five cells per second equivalent to 135 km/h. Trucks have a length of two cells equivalent to 15 m and a maximum velocity of three cells per second equivalent to 81 km/h. Furthermore, we simulated roads with two lanes and asymmetric lane change rules for cars only, according to [4]. Trucks can only use the right lane. The vehicular traffic was split into three fractions. Ten percent of the traffic flow was considered to be trucks. The remaining cars were split into a fixed load (75 % cars) and an additional load (25 % cars). Only this additional load of 25 % of the cars are affected by the routing strategies. The other cars and trucks are distributed by fixed ratios. For the whole network, we wanted a desired traffic flow of 6480 vehicles per hour. The outcome of this are 648 trucks per hour and 4374 cars per hour as the fixed load and 1458 cars per hour as the additional load. We simulated a period of thirteen hours. Every simulation started with empty roads. Each simulation was repeated one hundred times.

2.1 Global Topology

We presume that the three roads connect one source with one destination. Even though the three roads share the same destination, we assume that there is an infinite outlet capacity. These roads may have different length or not, but share the same characteristics. Each of the three roads has the same bottleneck structure to reduce the flow capacity towards the end. The bottleneck is implemented as a speed limit with two cells per second as maximum velocity. The bottlenecks are about 200 m long and start at 90 % of each roads length.

2.2 Routing/Distributing Strategies

In this three road scenarios we tested eight routing, respectively, distribution strategies. However, at first, we simulated each scenario without the additional load to determine the travel times under free flow conditions. Besides, we want to be assured that this empty road system is under saturated and behave stable. The investigated methods can be grouped into three categories. The first two methods, shortest path and equal distribution, are static methods. Followed by two cyclical approaches, which can be categorised as dynamic. The last group of methods are dynamic and responsive methods with feedback strategies. In the following, we will describe the applied methods in more detail.

Shortest Path The shortest path algorithm routes the whole additional load to the shortest of the three roads. In the scenarios with different road length this would be road A. It is easily predictable that this will lead to an over saturated system and to a breakdown in the vehicular flow. We will look at the results here nevertheless.

Equal Distribution Here, the additional load is split evenly by one third. This method is independent of road or scenario differences.

Alternating Roads Rather than splitting the load evenly, this method will route the respective cars cyclical on the roads. Each minute the extra load will be directed to another road.

Travel Time This is the first method with a feedback strategy, assuming that the travel time of each vehicle can be measured. It prefers the road with the shortest mean travel time. Those travel times are measured from all cars, which left the road within the last minute. Each minute the mean travel times are recomputed for each road. In case the current mean travel time could not be calculated, the mean travel time under free flow conditions will be used instead.

Travel Time Additional Load In this case the mean travel times on a road are calculated only from cars of the additional traffic load. This is based on the assumption that only cars which can be influenced in their routing decisions are able to send travel times to a central service. Again without current travel time information, the free flow value acts as substitute.

Remaining Road Capacities We came up with the idea to use a remaining road capacity as feedback strategy. Therefore we identified the flow capacity for the roads in our scenarios. This was done by simulations a single road with the same road and traffic characteristics. However, in this special test case, we started with a low traffic flow which was then increased in small steps over time. The result of one of those simulations is shown in Fig. 1. This simulations indicate that a flow of 40 veh/min is the appropriate maximum capacity for the roads used in our simulations. The actual traffic flow is measured with a virtual loop detector at the beginning of each road and aggregated over 1 min. The remaining road capacities are calculated for each road by subtracting the current flows from the maximum road capacity. Negative

Fig. 1 Simulating one road with slowly increasing vehicle flow (*red*) to determine maximum road capacity. With flow up to 40 vehicles per minute the travel times (*black*) increases proportional, but above travel times become unstable and rise exponentially. In the end the whole system collapses
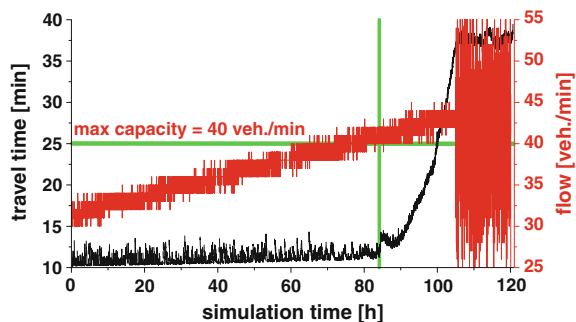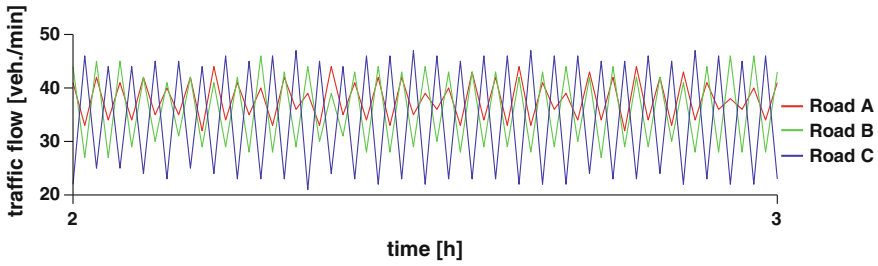
Fig. 2 Resulting traffic flow per minute within scenario II and the remaining road capacity strategy
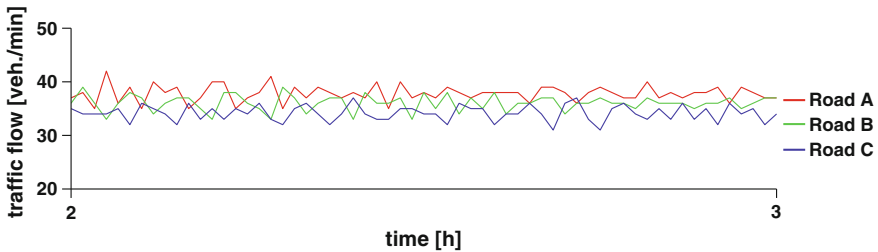

Fig. 3 Resulting traffic flow per minute within scenario II and the mean remaining road capacity strategy

remaining capacities are neglected. These results are then standardised to generate a distribution formula for the additional load. Figure 2 shows that this method induces a high fluctuation in the traffic flows.

Mean Remaining Road Capacity To enhance the former method the mean remaining capacities over 3 min generate the adapted distribution formula. This last method leads to more stable traffic flows as shown in Fig. 3.

3 Scenarios and Results

The three scenarios differ regarding to the road length and the distribution ratios for the fixed load. Below, each scenario is explained and the respective results are discussed. To calculate the mean travel time for each method and scenario the first and last half an hour of all simulations were discarded. To compare the distribution strategies in each scenario the results are presented in tables. The first table lists the distribution strategies in their tested order and shows the average road use for each road and strategy. The second table lists the travel times for all cars and for cars of the additional load. The strategies are in order of the increasing average overall travel time.

3.1 Scenario I

In the first scenario the three roads have different length. Road A has a length of 20 km with the bottleneck between 18.0 and 18.2 km. Road B is 10 % longer, therefore has a length of 22 km with the bottleneck between 19.8 and 20.0 km. Road C is the longest with 24 km length (20 % longer than road A) and has the bottleneck between 21.6 and 21.8 km. The fixed load is equally distributed. This results in a desired vehicle flow of 1458 cars and 216 trucks per hour on each road (Table 1).

We can summarise that all methods were able to reach the desired vehicular flow rates, besides the shortest path algorithm, which could only reach about 62 % of the additional vehicular flow. In this scenario, all strategies which utilised the roads more or less equal achieve an average global travel time about six to eight percent above free flow conditions, as Table 2 shows. Both strategies considering the travel times shift the additional load from road C to road A and perform less in reference to the average travel times.

3.2 Scenario II

The second scenario has three roads with the same length. Roads A, B and C have the length of 20 km with the bottleneck between 18.0 and 18.2 km. But in contrast to scenario I, the fixed load is now distributed uneven. The desired fixed vehicle flow on road A is raised by 20 % to 1750 cars and 259 trucks per hour. That is 40 % of the fixed traffic load. Road B remains at a third of the fixed load with the vehicle flow of 1458 cars and 216 trucks per hour. The main vehicle flow on road C is lowered by 20 % to 1166 cars and 173 trucks per hour equal to 26.67 % of the fixed load. The shortest path algorithm was excluded here, because of the missing difference in road length (Tables 3, 4, 5 and 6).

In this scenario with symmetric roads, but asymmetric fixed traffic loads the performance of strategies with an even distribution dropped. Now, the capacity driven

Table 1 Distribution of the additional load on the three roads in scenario I

Strategy	Road A (%)	Road B (%)	Road C (%)
No additional load	0.00	0.00	0.00
Shortest path	100.00	0.00	0.00
Equal distributed	33.33	33.33	33.33
Alternating roads	33.30	33.30	33.41
Travel time	42.15	36.45	21.40
Travel time additional load	42.02	36.80	21.17
Remaining capacity	33.28	33.19	33.52
Mean remaining capacity	33.33	33.34	33.33

Table 2 Simulation results of the mean travel times in scenario I

Strategy	Mean travel time all cars (min)	Percentage (%)	Mean travel time additional load (min)	Percentage (%)
No additional load	11.018	100.00	NA	NA
Equal distributed	11.708	106.26	11.737	100.10
Mean remaining capacity	11.711	106.29	11.725	100.00
Remaining capacity	11.769	106.81	11.835	100.94
Alternating Roads	11.857	107.61	11.948	101.90
Travel time additional load	12.818	116.34	13.427	114.51
Travel time	13.137	119.23	13.912	118.65
Shortest path	23.386	212.25	37.900	323.23

Table 3 Distribution of the additional load on the three roads in scenario II

Strategy	Road A (%)	Road B (%)	Road C (%)
No additional load	0.00	0.00	0.00
Equal distributed	33.33	33.33	33.33
Alternating roads	33.34	33.29	33.37
Travel time	16.39	35.49	48.13
Travel time additional load	18.25	37.36	44.39
Remaining capacity	17.78	34.34	47.88
Mean remaining capacity	18.29	33.33	48.38

Table 4 Simulation results of the mean travel times in scenario II

Strategy	Mean travel time all cars (min)	Percentage (%)	Mean travel time additional load (min)	Percentage (%)
No additional load	10.129	100.00	NA	NA
Mean remaining capacity	10.671	105.35	10.623	100.00
Remaining capacity	10.728	105.91	10.733	101.04
Travel time additional load	11.617	114.70	12.172	114.59
Travel time	11.747	115.98	12.405	116.78
Equal distributed	12.056	119.02	11.853	111.57
Alternating roads	12.159	120.04	12.026	113.20

Table 5 Distribution of the additional load on the three roads in scenario III

Strategy	Road A (%)	Road B (%)	Road C (%)
No additional load	0.00	0.00	0.00
Shortest path	100.00	0.00	0.00
Equal distributed	33.33	33.33	33.33
Alternating roads	33.31	33.29	33.40
Travel time	30.15	32.94	36.29
Travel time additional load	36.78	31.46	31.76
Remaining capacity	17.89	34.21	47.90
Mean remaining capacity	18.36	33.33	48.31

Table 6 Simulation results of the mean travel times in scenario III

Strategy	Mean travel time all cars (min)	Percentage (%)	Mean travel time additional load (min)	Percentage (%)
No additional load	10.972	100.00	NA	NA
Mean remaining capacity	11.681	106.46	11.974	100.00
Remaining capacity	11.739	106.99	12.085	100.93
Equally distributed	12.948	118.01	12.847	107.29
Alternating roads	13.095	119.35	13.059	109.06
Travel time	13.351	121.68	13.461	112.42
Travel time additional load	16.152	147.21	16.615	138.76
Shortest path	23.777	216.70	37.071	309.60

strategies distributed the additional load in average similar to the methods with the travel time feedback but beat them when the average travel time is concerned. Distributing the additional flow even over the three roads results in a steady rise of travel times on road A, which then dominates the average global travel time. All strategies were able to reach the desired vehicular flow rates.

3.3 Scenario III

The third scenario is a combination of the former two. We simulated the three roads scenario with the different road length (20, 22 and 24 km) and the shifted distribution (40, 33.33 and 26.67 %) of the fixed traffic load. Again the simulation results are combined within the following tables.

Again all the algorithms except shortest path, were able to reach the desired
vehicular flow rates. The shortest path method could reach just about 39 % of the
additional vehicular flow. The capacity based strategies head the table of the average
travel times again, even though a significant load shift towards the longest road C is
observed. In addition the travel time strategy with the feedback of only cars of the
additional load lead here as well to an over saturated road A which results in a poor
performance of the average travel time. We observe that the values for the average
distribution is contrary to the results considering the travel times of all cars.

4 Conclusion and Outlook

All three chosen scenarios show that a distributing or routing strategy which takes the
actual traffic flow and the flow capacity of a road into account can improve the average
travel time in a road network. Averaging this method over 3 m stabilises the traffic
flow and increases the performance. Both strategies work especially well in systems
with asymmetric basic loads. In further studies we want to compare these methods
with even more feedback strategies. Also, it is interesting to investigate networks
with shorter road length and how these methods perform under time variant dynamic
vehicular traffic flows. The same applies for studies with different ratios between the
fixed and the additional traffic load.

References

1. Chen, B., Xie, Y., Tong, W., Dong, C., Shi, D., Wang, B.: A comprehensive study of advanced information feedbacks in real-time intelligent traffic systems. Phys. A Stat. Mech. Appl. **391**(8), 2730–2739 (2012)
2. Dong, C., Ma, X., Wang, B.: Effects of vehicle number feedback in multi-route intelligent traffic systems. Int. J. Mod. Phys. C **21**(08), 1081–1093 (2010)
3. Dong, C., Ma, X., Wang, B., Sun, X.: Effects of prediction feedback in multi-route intelligent traffic systems. Phys. A Stat. Mech. Appl. **389**(16), 3274–3281 (2010)
4. Knospe, W., Santen, L., Schadschneider, A., Schreckenberg, M.: Disorder effects in cellular automata for two-lane traffic. Phys. A Stat. Mech. Appl. **265**(3–4), 614–633 (1999)
5. Nagel, K., Schreckenberg, M.: A cellular automaton model for freeway traffic. J. Phys. I **2**(12) (1992)
6. Wahle, J., Bazzan, A.L.C., Klügl, F., Schreckenberg, M.: Decision dynamics in a traffic scenario. Phys. A Stat. Mech. Appl. **287**(3–4), 669–681 (2000)
7. Wegerle, D., Schreckenberg, M., Schönharting, J., Wolter, S., Wessely, A., Schäfer, R.P., Witte, N., Lorkowski, S.: EffizienzCluster Logistik Ruhr, DiNav—Dynamics in navigation. In: Clausen, U., ten Hompel, M., Klumpp, M. (eds.) Efficiency and Logistics. Lecture Notes in Logistics, pp. 93–98. Springer, Berlin (2013)

Traffic Phase Dependent Fuel Consumption

**Micha Koller, Peter Hemmerle, Hubert Rehborn, Boris Kerner
and Stefan Kaufmann**

Abstract Fuel consumption is one of the key cost factors relevant for the movement of vehicles. In times of increasing traffic congestion on both freeways and urban road sections the question arises how the fuel consumption is influenced by congestions congestion occurring in many sections of the road network. Congested traffic states are defined based on Kerner's three-phase traffic theory [1, 2]. The article presents the probability functions of traffic breakdowns for road sections: the probability curve as function of the traffic flow rate is an increasing function of the flow rate and similar for both freeway an urban sections with traffic signals [4]. Therefore, the recognition of traffic breakdowns and the determination of the emerging traffic state is crucial for the prediction of the additional fuel consumption. By investigating empirical field data from vehicles driving on a specific freeway section statistical analysis reveals the additional fuel consumption factors for the two different congested states in comparison to free flow.

1   Introduction

Currently, the deviation of emission and pollution measurements on test benches from measurements in real traffic is discussed in public. Beside vehicle emissions also the fuel consumption is part of this discussion. Automobile manufacturers in Europe

M. Koller (✉) · P. Hemmerle · H. Rehborn
Daimler AG, RD/U, HPC: 059-X830, 71063 Stuttgart, Germany
e-mail: micha.koller@daimler.com

P. Hemmerle
e-mail: peter.hemmerle@daimler.com

H. Rehborn
e-mail: hubert.rehborn@daimler.com

B. Kerner
University of Duisburg-Essen, Lotharstr. 1, 47057 Duisburg, Germany
e-mail: boris.kerner@uni-due.de

S. Kaufmann
IT-Designers GmbH, Entennest 2, 73730 Esslingen am Neckar, Germany
e-mail: stefan.kaufmann@stz-softwaretechnik.de

apply the New European Driving Cycle to calculate their vehicle consumptions. Empirical data show that speed profiles of vehicles driving through congested traffic can be distinctly more complex than it is covered in the New European Driving Cycle. This can be one reason for the differences between measurements in real traffic and driving cycle measurements.

In the literature there are many theories and simulations about increased fuel consumption caused by congested traffic. However, literature which provides an empirical evidence for increased fuel consumption is hardly available.

Empirically the existence of two different phases of congested traffic is verified. The dependence between the increased fuel consumption and the traffic phases is unknown but important for the development of future driving assistance systems, automatic driving and traffic management.

Within this article we clarify how severely congested traffic affects the fuel consumption. Based on empirical data we discuss the dependency between the increased fuel consumption and traffic phases. Additionally, we explain that the increased fuel consumption has a probabilistic nature.

2   Kerner's Three-Phase Traffic Theory

Kerner's three-phase traffic theory describes in addition to free traffic flow (F) two phases of congested traffic: synchronised flow (S) and wide moving jam (J).

As example we consider highway section with a bottleneck caused by on-ramp (Fig. 1a). The empirical data from 23 June 1998 measured on the A5 near Frankfurt, Germany gives an empirical example of the traffic phases (Fig. 1b).
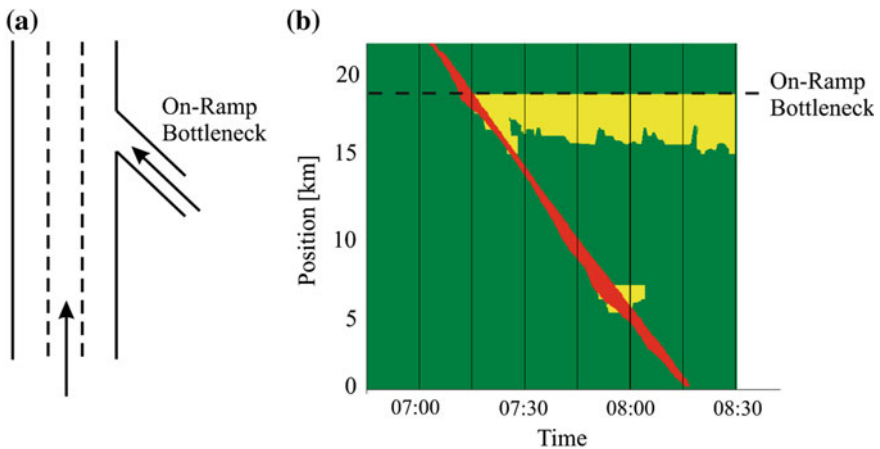
Fig. 1 Empirical example of a traffic situation [1]: schematic three-lane highway with on-ramp bottleneck (**a**); reconstructed spatiotemporal traffic phases (**b**)
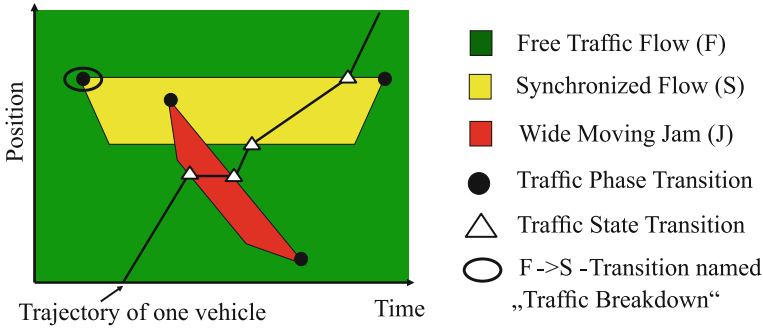
Fig. 2 Schematic illustration of traffic phase transitions and traffic state transitions

The wide moving jam phase is characterised by its constantly moving downstream front as it can be seen in the example as red marked area.

The synchronised flow phase is shown as yellow area. The downstream front of the traffic phase synchronised flow is fixed at the location of the on-ramp bottleneck.

Congested traffic occurs if a traffic phase transition from free traffic flow to synchronised flow happens (F→S phase transition). This is also named traffic breakdown and is marked by the black ellipse in Fig. 2. This example visualises a spontaneous F→S traffic phase transition. Other traffic phase transitions are indicated as black points in the time space diagram. Within synchronised flow a wide moving jam can emerge in another phase transition. The black line in Fig. 2 indicates the trajectory of one vehicle passing this traffic pattern. When a vehicle enters a new traffic phase, we call this a traffic state transition. First the vehicle passes through free traffic flow till there is a traffic state transition at the time the vehicle enters the wide moving jam. Traffic state transitions of the example vehicle are represented by white triangles.

3 Probabilistic Traffic Breakdown Curves

Considering traffic breakdowns on highways spontaneous F→S traffic phase transitions have a probabilistic nature as it is theoretically described in [2]:

$$P_{\text{theoretical}}^{F \to S} = \frac{1}{1 + e^{\alpha(q_p - q_{sum})}} \tag{1}$$

The parameters α, q_p and q_{sum} depend on the specific bottleneck. We analysed empirical data measured over three years by stationary detectors located on highways. The empirical probability of spontaneous F→S traffic phase transition can be described as:

$$P_{empirical}^{F \to S} = \frac{h_{F \to S}(q_i, q_i + \Delta q_i)}{h_F(q_i, q_i + \Delta q_i)} \tag{2}$$
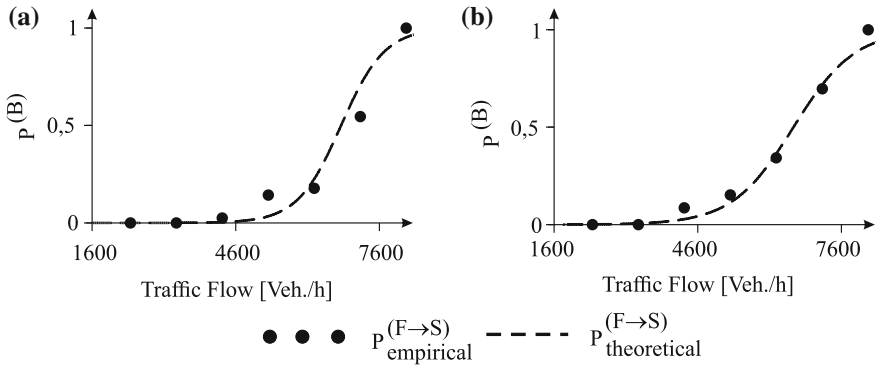
Fig. 3 Theoretical and empirical probability for spontaneous $F \rightarrow S$ traffic phase transitions: on-Ramp bottleneck (**a**); off-Ramp bottleneck (**b**)

The frequency of traffic breakdowns observed in the flow interval $(q_i, q_i + \Delta q_i)$ is divided by the frequency of the occurrence of flow rates in the same interval before the traffic breakdown.

Our results (Fig. 3) show that the theoretically predicted probability (black line) is similar to the empirically measured (black points) probability for spontaneous F→S traffic phase transitions. This is valid for both on-ramp (Fig. 3) and off-ramp bottlenecks (Fig. 3) on highways: traffic breakdowns can be found in broad range of traffic flow between 3840 and 8640 veh/h.

The three-phase traffic theory also explains traffic breakdowns on urban roads with traffic signals. In this case a traffic breakdown occurs if the state of the traffic signal switches from undersaturation to oversaturation. Theoretically, the probability of traffic breakdown is described as [3]:

$$P^{B_{LSA}}_{\text{theoretical}} = \frac{1}{1 + e^{\beta(q_p - \bar{q}_{in})}} \quad (3)$$

The parameters β, q_p and $\bar{q}_{in}$ depend on the specific traffic signal.

Data measured by a stationary detector located in Düsseldorf on the Völklinger Straße were used to determine the empirical probability for a traffic breakdown which is:

$$P^{B_{LSA}}_{\text{empirical}} = \frac{h_{B_{LSA}}(q_i, q_i + \Delta q_i)}{h_F(q_i, q_i + \Delta q_i)} \quad (4)$$

The comparison (Fig. 4) shows that the probability for empirically found traffic breakdowns on urban roads with traffic signals follows the theoretical probability.

The program of this traffic signal changes during the day. During the morning hours between 6:30 a.m. and 11 a.m. (Fig. 4a) traffic breakdowns occur at traffic flows between 1680 and 2640 veh/h. In the evening between 6:00 p.m. and 8:30 p.m. (Fig. 4b) traffic breakdowns occur already at traffic flows between 960 and 1920
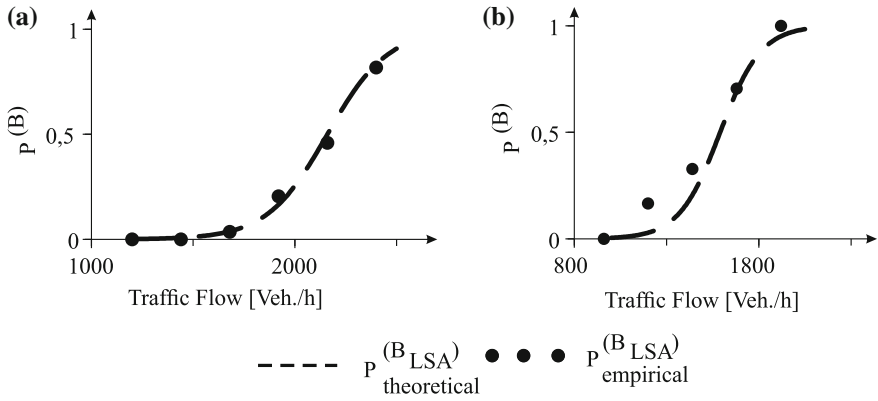
Fig. 4 Theoretical and empirical probability for traffic breakdowns on a urban road [5]: Völklinger Str., morning (**a**); Völklinger Str., evening (**b**)

veh/h which is caused by a shorter duration of the green phase of the traffic signal compared with the morning program. This probability function also shows that on urban roads traffic breakdown can occur in a broad range of traffic flow.

The analysis of the empirical data shows that traffic breakdown has a probabilistic nature both at highway bottlenecks and urban traffic signals. In the following we will show that the increased consumption is dependent on the traffic phase and therefore also has a probabilistic nature.

4 Microscopic Vehicle Measurements

We analysed empirical measurements which were recorded in vehicles driving through real traffic situation on a public highway. A space-time diagram of an exemplary traffic situation on the observed highway (Fig. 5) shows vehicle trajectories as black lines. The slope of the lines indicates the velocity. Considering Trajectory 1 (Fig. 5) the vehicle drives within the free flow phase first. Then a rapid deceleration follows as the vehicle experiences a traffic state transition form free flow to wide moving jam.

Detailed empirical measurements of the vehicle labelled as Trajectory 1 during this traffic state transition are shown in Fig. 6. The velocity (Fig. 6a) decreases from over 100 to 0 km/h. Beside strong decelerations up to 3 m/s^2 also acceleration up to 3 m/s^2 were measured (Fig. 6b). The consumption was determined per time (Fig. 6c) and per distance (Fig. 6d). During the deceleration the vehicle consumptions per time is in average higher than during the vehicle standstill in the second half of the diagram (Fig. 6c). Reversed to that the fuel consumption per distance is low during the deceleration and goes up to infinity if the vehicle standstill (Fig. 6d).
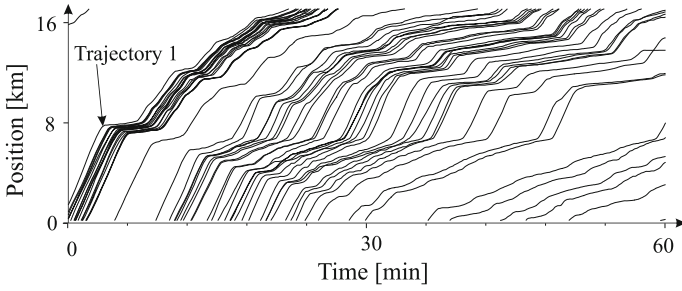
Fig. 5 Exemplary microscopic vehicle trajectories [5]

Fig. 6 Measurements during a traffic state transition from free traffic flow to wide moving jam [5]: Velocity (**a**); Acceleration (**b**); consumption per time (**c**); consumption per distance (**d**)
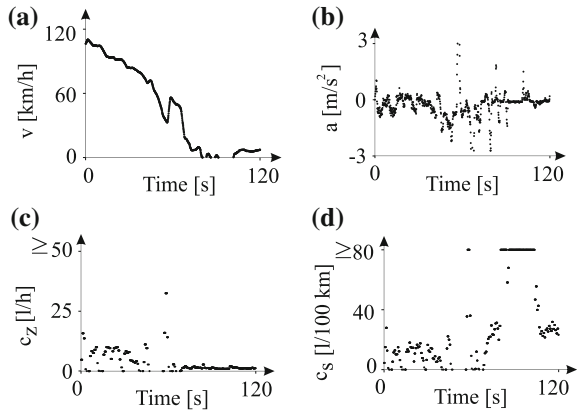

5 Empirical Fuel Consumption

In total, we examine vehicle trajectories with a length of approximately 5444 km, 5.6 million velocity and 3.6 million consumption measurements. The empirical velocity data is used to reconstruct the traffic phases by applying the in-vehicle traffic state detection [6]. After that, the consumption data can be assigned to the three traffic phases.

The vehicles drove 130 h in free traffic flow, 52 h in the phase of synchronised flow and 13 h in the phase of wide moving jam. The distribution of all consumption measurements per traffic phase is shown in Fig. 7 as boxplot. This means that the black box covers 50 % of all measurements and the anchors indicate the minimum and maximum consumption value.

The fuel consumption during congested traffic can be much higher than in free flow. The fuel consumption is dependent on the traffic phase. In the phase of wide moving jam much higher fuel consumption can be found than in the phase of synchronised traffic.

Fig. 7 Boxplots of the consumption distribution per traffic phase: C_F free traffic flow, C_S synchronised flow and C_J wide moving jam [5]
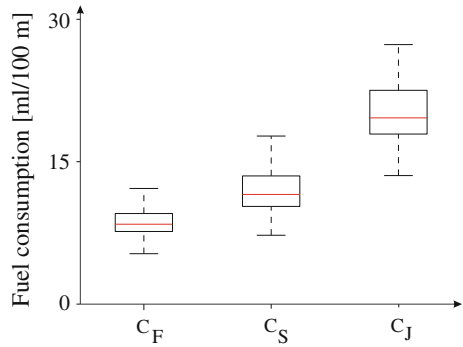
Table 1 Average increased fuel consumption per traffic phase

Traffic phase	Arithmetic average consumption	Increased consumption
Free traffic flow	$\bar{C}_F = 8.73\,\frac{l}{100\ km}$	$MV_{AB,F} = 1$
Synchronised flow	$\bar{C}_S = 12.43\,\frac{l}{100\ km}$	$MV_{AB,S} = \frac{\bar{C}_S}{\bar{C}_F} = 1.42$
Wide moving jam	$\bar{C}_J = 20.41\,\frac{l}{100\ km}$	$MV_{AB,F} = \frac{\bar{C}_J}{\bar{C}_F} = 2.34$

The red line indicates the median that is very close to the arithmetic mean which is listed in Table 1. Based on that an average increased consumption per traffic phase is determined and listed in the last column of Table 1.

6 Increased Fuel Consumption for a Typical Traffic Situation

On average a wide moving jam has a length of 1023 m [6]. Often wide moving jams propagate for more than one hour across the highway. This is chosen as typical traffic situation for which we quantify the increased fuel consumption (Fig. 8).

Vehicle V1 drives only trough free traffic flow and vehicle V2 has to pass a wide moving jam with the length of 1023 m. Based on the average consumption values the vehicle fuel consumption is C_F within the traffic phase of free traffic flow and C_J within the traffic of wide moving jams. Vehicle V1 consumes $C_{V1} = 1023\ m \cdot \bar{C}_F = 89.31$ ml and vehicle V2 consumes $C_{V1} = 1023\ m \cdot \bar{C}_J = 208.79$ ml.

A typical wide moving jam increase the fuel consumption of a single vehicle by $C_{V2} - C_{V1} = 119$ ml. On a three-lane highway a flow rate of 6000 veh/h can be assumed. Thus, the collective increased fuel consumption for this typical traffic situation is 6000 veh/h · 119 ml = 714 l/h.

Fig. 8 Typical traffic
situation: wide moving jam
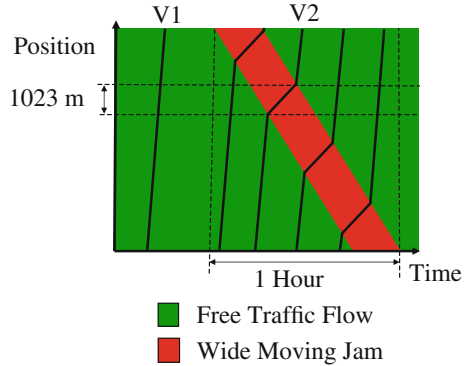
7 Conclusions

- Empirical microscopic data show that fuel consumption in congested traffic can be significantly higher than in free flow.
- In congested traffic, fuel consumption can depend considerably on whether the synchronised flow phase or wide moving jam phase of congested traffic is realised.
- At the same average speed in congested traffic, fuel consumption can be considerably smaller in the synchronised flow phase than in the wide moving jam phase.
- The empirical evidence of the dependence of fuel consumption on the traffic phase can be used for the development of new driver assistance systems and traffic control strategies.

References

1. Kerner, B.S.: The Physics of Traffic. Springer, Berlin (2004)
2. Kerner, B.S.: Introduction to Modern Traffic Flow Theory and Control. Springer, Berlin (2009)
3. Kerner, B.S.: Physics of traffic gridlock in a city. Phys. Rev. E **84**, 045102(R) (2011)
4. Kerner, B.S., Hemmerle, P., Koller, M., Hermanns, G., Klenov, S.L., Rehborn, H., Schreckenberg, M.: Empirical synchronized flow in oversaturated city traffic. Phys. Rev. E **90**, 032810 (2014)
5. Koller, M.: Kraftstoffmehrverbrauch auf Basis dynamischer Verkehrslagen. Ph.D. thesis. Eberhard Karls Universität Tübingen (2015)
6. Palmer, J.: Fahrzeugautonome und verteilte Erkennung räumlich-zeitlicher Verkehrsmuster zur Nutzung in Fahrerassistenzsystemen. Ph.D. thesis. Eberhard Karls Universität Tübingen (2011)

Examining Perimeter Gating Control of Urban Traffic Networks with Locally Adaptive Traffic Signals

Mehdi Keyvan-Ekbatani, Xueyu Gao, Vikash V. Gayah and Victor L. Knoop

Abstract Traditionally, urban traffic is controlled by traffic lights. Recent findings of the Macroscopic or Network Fundamental Diagram (MFD or NFD) have led to the development of novel traffic control strategies that can be applied at a network-wide level. One pertinent example is perimeter flow control (also known as gating or metering), which limits the rate at which vehicles are allowed to enter an urban region. This paper studies to which extent a combination of adaptive traffic control and gating improves the traffic flow. To this end, combinations of gating and traffic signal timing tested implemented in a microsimulation. It is found that gating is much more effective than adaptive signal timing for high traffic loads. Adaptive signal timing can improve the network performance by increasing the maximum flow and increasing the critical accumulation, i.e. the number of vehicles inside a protected network for which the performance is maximised. The latter helps to reduce queuing outside the protected network.

1 Introduction

The objective of urban traffic control (UTC) has traditionally been to implement signal timings that minimise the total vehicular delay in the network. UTC systems constitute a scientific field with long-lasting, extensive research and development activities. Widely applied UTC strategies like SCATS (Sydney Coordinated Adaptive Traffic System) [7], despite being applicable to large-scale networks, are not

M. Keyvan-Ekbatani (✉) · V.L. Knoop
Delft University of Technology, Stevinweg 1, 2628 CN Delft, The Netherlands
e-mail: m.ekbatani@tudelft.nl

V.L. Knoop
e-mail: v.l.knoop@tudelft.nl

X. Gao · V.V. Gayah
Pennsylvania State University, University Park, State College, USA
e-mail: xug103@psu.edu

V.V. Gayah
e-mail: gayah@engr.psu.edu

very efficient when the traffic network is saturated or over-saturated. On the other hand, traffic-responsive strategies like OPAC [1], which are more advanced, apply optimization algorithms with exponential increase of complexity. Because of this complexity, these do not permit a practical central network-wide application. In fact, Gayah et al. [2] showed that in an extremely congested network, typical adaptive traffic signal control schemes might have little to no effect on the network due to downstream congestion and queue spill-back. Moreover, the aforementioned methods may allow too much traffic to enter into the part of the network to be protected from over-saturation and only act after the congestion starts occurring. This might be an important reason that most of the existing adaptive traffic control strategies do not operate efficiently in highly congested urban road networks.

Assuming a constant length of the trip in a network, one can also show that the outflow of the network (i.e., rate vehicles reach their destination) is maximised if the accumulation is at the critical accumulation. For accumulations less than the critical value, the relationship between outflow and accumulation is increasing. The relationship between these two macroscopic traffic values at the network level is called Macroscopic or Network Fundamental Diagram (MFD or NFD). Geroliminis and Daganzo [3] verified the existence of the NFD using the data of downtown Yokohama in Japan. The notion of NFD is still under thorough investigation in various aspects, but it can be applied as a basis for development of urban signal control strategies. As details of individual links are not required to describe the real-time traffic state at the network level, NFD is useful to introduce elegant control concepts that can maintain the accumulation at the capacity level.

The control idea derived from the aforementioned approach is to hold vehicles back upstream of a 'protected network (PN)' such that the accumulation does not exceed the critical value in order to maximise the outflow. This control strategy is called gating or perimeter control. This concept has already been utilised to numerous efficient perimeter flow control policies in homogeneous networks (see [4] for single region, and [6] for multiple concentric regions).

As discussed in [5], the scatter and hysteresis in the NFD might be decreased slightly by applying only gating or perimeter control strategy, since the PN will operate at the capacity level and possible gridlocks are avoided as much as possible. considering the fact that the PN utilises the fixed-time signal control plan, the network may still experience heterogeneity in distribution of congestion. To the best of our knowledge, for a more homogeneous distribution of the density in PN, none of the existing gating strategies consider an adaptive traffic control. Up to now, these two (control) schemes (i.e. adaptive traffic control and gating control) have only been implemented separately in the studies. This paper tries to fill this gap and integrate the gating concept at the boundary of the PN with the traffic-responsive adaptive signal control strategy inside the PN. Two different adaptive traffic signal strategies are considered with the feedback-based gating strategy developed in [4]: (1) a simple volume-based strategy and (2) a modified version of the SCATS algorithm. To this end, we set up six different control scenarios in the microscopic simulation environment AIMSUN. The control scenarios are as follows: (1) fixed control, (2) modified SCATS [8], (3) volume-based strategy [2], (4) only-gating, (5) gating plus modified

SCATS, (6) gating plus volume-based strategy. Two overall performance indexes (i.e., average delay (s/km) and maximum virtual queue (veh)) have been utilised to evaluate the efficiency of the tested scenarios. The study shows that application of adaptive traffic signal control in PN increases the critical accumulation in NFD and consequently leads to shorter virtual queue sizes (i.e. vehicles waiting to enter the network) during the gating time.

The remainder of this paper is set up as follows: Sect. 2 presents the control strategies (i.e. gating and adaptive control). Section 3 discusses the simulation set-up and the test-bed description. Section 4 illustrates a comparative appraisal of the six simulated scenarios. Finally, summary and conclusions are included in the last section.

2 Control Strategies

Four different control strategies are implemented in this study. As a base-line we applied the fix-time control. Two different adaptive control strategies are used within the PN: (1) volume-based strategy; (2) modified SCATS and the recently developed feedback-based gating control strategy [5].

2.1 Adaptive Traffic-Responsive Strategies

In this paper, two different adaptive traffic-responsive strategies (adopted from previous efforts) were considered. The goal of both strategies was to provide more green time to the approach(es) with more traffic. Offsets between adjacent signals were not modified by either strategy. In the first strategy, a fixed cycle length was adopted for each signal that was then divided among competing approaches every cycle. A simple proportional algorithm was used to allocate the available green time at each intersection based on traffic volume measured at upstream detectors on each approach. In this algorithm, the green time to a subject approach i is determined as follows:

$$g_i(t) = (C - L) \frac{v_i(t - 1)}{\sum_i v_i(t - 1)} \tag{1}$$

where $g_i(t)$ is the green time allocated to approach i during cycle t, C is the fixed cycle length, L is the lost time for vehicle movement (usually due to and directly proportional to the number of phase changes) and $v_i(t - 1)$ is the volume observed on approach i during cycle $t - 1$. All available green time was allocated in this way. Thus, it is possible that some approaches received zero green time if no vehicles were queued at the approach. This strategy was called the 'volume-based' strategy. In this paper, a fixed cycle length of 90 s was used for all adaptive traffic signals.

The second strategy is a simplified version of the realistic SCATS, which is currently applied in many cities throughout the world. This strategy was adopted from [8] where it was used to assess the impacts of adaptive signal control on the NFD using simulation. In this strategy, both the green time and total cycle lengths are variable and adjusted based on volume data obtained from upstream loop detectors. As described in [8], an appropriate cycle length is first select based on the volume ratio observed during the previous cycle. This cycle length is designed to maintain a volume ratio between 0.85 to 0.95 during the next cycle and is selected based on the following rules:

$$C(t) = \begin{cases} STOPPER & \text{if } C(t) = \text{MIN}, R(t-1) > 0.4 \\ MIN & \text{if } C(t) = \text{STOPPER}, R(t-1) < 0.2 \\ \min\{C(t-1) + \text{STEP}, \text{MAX}\} & \text{if } R(t-1) > 0.95 \\ \max\{C(t-1) - \text{STEP}, \text{STOPPER}\} & \text{if } R(t-1) < 0.85 \\ C(t-1) & \text{otherwise} \end{cases} \tag{2}$$

where MIN and MAX are the minimum and maximum cycle lengths, respectively, STOPPER is an intermediate cycle length that allows for sharp increases in cycle length due to sharp increases in traffic demands, and $R(t-1)$ represents the volume ratio at a given intersection during cycle $t-1$. The cycle length is allocated among the competing approaches based on the vehicle demand on each approach. The following equation is used to allocate this green time:

$$g(t) = (C(t) - L - G_{\min}) \frac{d_i(t-1)}{\sum_i d_i(t-1)} + g_{i,\min} \tag{3}$$

where $G_{\min}$ is the minimum green time allocated to each approach, and $g_{i,\min}$ is the vehicle demand on approach i. For this paper, the following values were used for the adaptive signals with SCATS: MIN $= 42$ s, MAX $= 132$ s, STOPPER $= 66$ s, STEP $= 6$ s, $g_{i,\min} = 6$ s.

2.2 Feedback-Based Gating Control

Keyvan-Ekbatani et al. [4] developed a control design model and an appropriate feedback controller for the described gating task. Given the derived model structure (4), the following proportional-integral-type (PI) feedback controller is appropriate:

$$q_g(k) = q_g(k-1) - K_p[TTS(k) - TTS(k-1)] + K_I\left[\widehat{TTS} - TTS(k)\right] \tag{4}$$

TTS is the Total Time Spent, $\widehat{TTS}$ is desired set-point (critical accumulation in NFD, see [4]), q_g is the gated flow ordered by the controller, K_P and K_I are the proportional and integral gains, respectively. The flow calculated by the regulator (5) must be

constrained by pre-specified minimum and maximum values to account for operational constraints. Proper controller parameters may be derived by the methodology presented in [6] or manual fine tuning.

3 Simulation Set-up and Scenario Description

A greater part of Chania urban network in Greece is modelled in the microscopic simulator AIMSUN. Since the objective was to test our proposed control strategies on a network with realistic features but not completely identical, we manipulated the number of traffic lights in the PN. Figure 1 demonstrates the location of the eight gated links (shown by the black arrow and violet circle) and the traffic lights controlled with fix-time and adaptive (i.e. modified SCATS and volume-based) traffic control signal plan (shown by violet squares) within the protected network. In the middle of every link inside the red border line, a loop detector has been installed, and the related measurements are collected every cycle (90 s in the case of the fixed cycle lengths). The utilised 4-h trapezoidal demand profile simulates traffic conditions similar to the real traffic conditions (mimicking the peak and off peak period).

The following control scenarios (including gating and no-gating) are simulated in this study:

1. (no-gating) The traffic lights in the PN (indicated by square and circle) are controlled applying fix-time control signal plan.
2. (no-gating) 'Volume-based' traffic-responsive control strategy is implemented to control all the traffic lights within PN.
3. (no-gating) Adaptive traffic control strategy 'modified SCATS' is used for controlling the signalised junctions within PN.

Fig. 1 Part of Chania urban network modelled in AIMSUN; PN is indicated by *bold red line*

4. Gating at the perimeter and fix-time control inside PN.
5. Gating at the border and 'volume-based' for the rest of the traffic lights in the PN.
6. Gating at the boundary and 'modified SCATS' within PN.

We use 15 different replications (i.e. simulation runs) for each investigated scenario and then calculated the average value of the 15 runs for each performance index (the average vehicle delay (s/km) and maximum queue length (veh)) in order to compare different control strategies.

4   Simulation Results

Figure 2a displays the NFD (*TTD* vs. *TTS*; *TTD* is Total Travelled Distance) for the Chania PN (assuming that all links are detector-equipped) for the first 2 h of the employed scenarios 1, 2 and 3, i.e. the loading period of the network, and the congestion is created; 15 different replications (shown by empty dots in the plot) were carried out. Utilising Eq. (1–3), the *TTD* and *TTS* of the PN are estimated every 90 (cycle time of all the fixed traffic lights in the network). For a better clarification of the PN traffic state, a moving-average curve for the scattered NFD of each scenario has been shown with different colour. An interesting finding at this stage of the study is the fact that using adaptive traffic control lead to higher critical accumulation (750 vehicles for the green and the blue curve). The shifted $\widehat{TTS}$ value in the case of adaptive traffic control signal plan might be extremely beneficial since it allows more vehicles into the PN during gating. This might help to reduce the gated queue size at the boundary of protected network and reduce the negative impact of the growing queues upstream of the gated junctions. To illustrate better the advantageous effect of the gating strategy on the traffic flow throughput (i.e. *TTD*) in the PN, the NFDs for scenarios 4, 5 and 6 are shown in Fig. 3b. Obviously, the feedback controller has perfectly performed and maintained the *TTS* or the vehicle accumulation in the PN
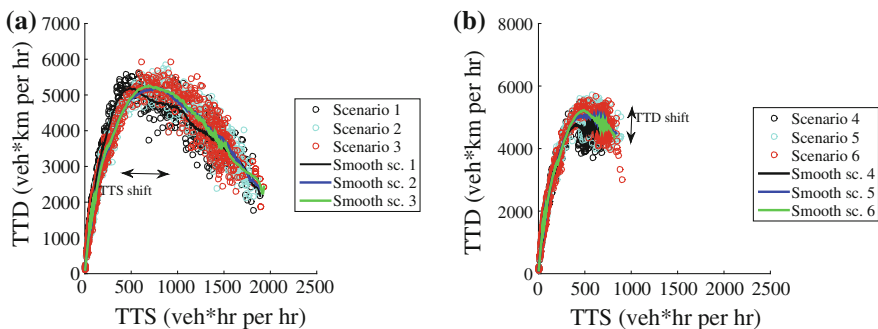
Fig. 2 NFD for the first 2 h. No-gating scenarios (scenario 1, 2, and 3) (**a**); gating scenarios (scenario 4, 5 and 6) (**b**)

Table 1 Average values of performance indexes for different control scenarios (over 15 replications)

Performance index	Scenario 1	Scenario 2	Scenario 3	Scenario 4	Scenario 5	Scenario 6
Delay (sec/km)	389	294	351	203	193	203
Max. virtual queue (veh)	728	696	702	965	808	888
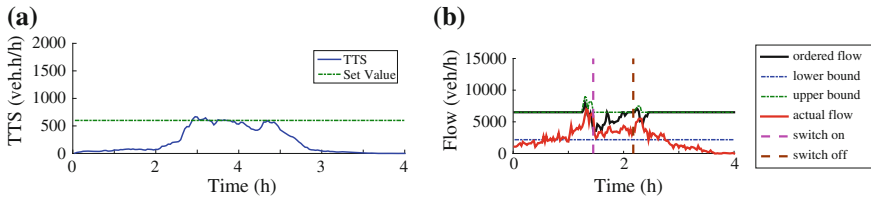
Fig. 3 Results for scenario 4: *TTS* versus time (**a**); flow versus time (**b**)

close to the critical value of the corresponding scenario (in a region of *TTS* 700 to 750 veh) and consequently kept the network throughput at the maximum level during the peak period. The *TTD* for the gating scenarios plus adaptive control has higher value compared to the gating plus fix-time.

Table 1 summarises the average simulation results for the six different scenarios (over 15 runs each) studied in this research. In the no-gating case, the adaptive traffic control strategies lead to an improved mobility (lower average delay) compared to the fix-time signal plan. Under gating, the average delay improved significantly compared to the no-gating scenarios.

Figure 3 illustrates the controller action during the simulation for scenario 4. Concentrating on Fig. 3a, the controller managed perfectly to maintain the TTS close to the set-value (shown by the green horizontal dashed line). Similar results are obtained for scenarios 5 and 6. The red line in Fig. 3b shows the actual flow crossing the stop bar at the gated junction and entering the PN. There is a gap between the actual flow and the flow ordered by the controller (red and black lines). This could be due to the flow distribution policy, which in this case is only based on the saturation flows of the gated links. In an on-going work, a queue management policy will be implemented at the gated junctions in order to reduce the chance of wasting green times due to blockages downstream or lack of demand at the gated links.

5 Conclusions

In this paper, we examined the joint implementation of two unique urban traffic control strategies: perimeter gating of a protected network and adaptive traffic signal control. The former limits vehicle entries into a protected network to maximise

throughput within the protected region. The latter modifies signal timings at individual intersections in response to real-time traffic fluctuations. Here, we have showed that the combination of these two strategies can be even more beneficial. The adaptive signal control strategies help to provide more efficient NFDs in which more vehicles can be accommodated within the protected network with higher overall throughputs. The gating strategy makes use of these higher accumulations and throughputs, which results in fewer vehicles queuing at the boundaries of the protected network during the implementation of gating. Overall, the results find that the combination of gating and adaptive signal control results in lower network delays, shorter boundary queues (on average).

References

1. Gartner, N.H.: OPAC: a demand-responsive strategy for traffic signal control. 906 (1983)
2. Gayah, V.V., Gao, X.S., Nagle, A.S.: On the impacts of locally adaptive signal control on urban network stability and the macroscopic fundamental diagram. Transp. Res. Part B: Methodol. **70**, 255–268 (2014)
3. Geroliminis, N., Daganzo, C.F.: Existence of urban-scale macroscopic fundamental diagrams: some experimental findings. Transp. Res. Part B: Methodol. **42**(9), 759–770 (2008)
4. Keyvan-Ekbatani, M., Kouvelas, A., Papamichail, I., Papageorgiou, M.: Exploiting the fundamental diagram of urban networks for feedback-based gating. Transp. Res. Part B: Methodol. **46**(10), 1393–1403 (2012)
5. Keyvan-Ekbatani, M., Papageorgiou, M., Knoop, V.L.: Controller design for gating traffic control in presence of time-delay in urban road networks. Transp. Res. Part C: Emerg. Technol. **59**, 308–322 (2015)
6. Keyvan-Ekbatani, M., Yildirimoglu, M., Geroliminis, N., Papageorgiou, M.: Multiple concentric gating traffic control in large-scale urban networks. IEEE Trans. Intell. Transp. Syst. **16**(4), 2141–2154 (2015)
7. Lowrie, P.: Scats: the sydney coordinated adaptive traffic systemprinciples, methodology, algorithms. In: IEE International Conference on Road Traffic Signalling, pp. 67–70
8. Zhang, L., Garoni, T.M., de Gier, J.: A comparative study of macroscopic fundamental diagrams of arterial road networks governed by adaptive traffic signal systems. Transp. Res. Part B: Methodol. **49**, 1–23 (2013)

A Comparison of Tram Priority at Signalised Intersections in Melbourne

Lele Zhang, Timothy Garoni and Somayeh Shiri

Abstract We study tram priority at signalised intersections using a stochastic cellular automaton model for multi-modal traffic flow. We simulate realistic traffic signal systems, which include signal linking and adaptive cycle lengths and split plans, with different levels of tram priority. We find that tram priority can improve service performance in terms of both average travel time and travel time variability. We consider two main types of tram priority, which we refer to as full and partial priority. Full tram priority is able to guarantee service quality even when traffic is saturated, however, it results in significant costs to other road users. Partial tram priority significantly reduces tram delays while having limited impact on other traffic, and therefore achieves a better result in terms of the overall network performance. We also study variations in which the tram priority is only enforced when trams are running behind schedule, and we find that those variations retain almost all of the benefit for tram operations, but with reduced negative impact on the network.

1 Introduction

To promote use of public transport, which is a key means of alleviating congestion in urban transport networks, it is important for public transport to run reliably. One useful tool is to provide transit priority at signalised intersections. Transit signal priority (TSP) has been used in practice since the 1970s. Several studies on TSP have been undertaken previously, either via analysing empirical data [1, 4] or using simulation methods [2, 5–7].

Most of these studies focus on bus signal priority, and very few concern trams. Compared to buses, trams operating in mixed traffic have much higher impact on other road users, and vice versa. In addition, studies on bus priority cannot be directly adapted to the case of trams due to the following reasons: trams block the entire link

L. Zhang (✉) · T. Garoni · S. Shiri
School of Mathematical Science, Monash University, Melbourne, VIC 3800, Australia
e-mail: lele.zhang@monash.edu

T. Garoni
e-mail: tim.garoni@monash.edu

S. Shiri
e-mail: somayeh.shiri@monash.edu

587

when they stop, trams cannot change lane and it is comparatively difficult for early trams to stay on schedule.

Simulation studies of TSP have typically been limited to small-scale networks. [6] studied the impact of active bus priority under various traffic conditions on a 4-lane route. [2] also considered a 4-lane mixed traffic environment. [5] evaluated the heuristic algorithm, which deals with multiple requests of priority, on a 2-intersection arterial. [7] tested the advanced TSP control method on one intersection. These studies were all confined to the question of bus priority. Furthermore, all of them, except [2], in which the signal system used was not specified, are confined to the study of fixed cycle signal systems, which are rarely used in practice nowadays.

In this paper we utilise a multi-modal stochastic cellular automaton (CA) model on a 8×8 square grid governed by SCATS (Sydney Coordinated Adaptive Traffic System), to study four tram priority schemes currently used, or being considered, in Melbourne, Australia. The schemes all belong to *active* priority [4], which is to say that the signal control system starts priority strategies when the trams are detected at prescribed locations. The scenarios can be divided into two groups: *full* (or *absolute*) and *partial* priority. The former signals start the priority phase immediately after detecting a tram and keep the phase running until the tram traverses the approaching intersection while the latter group has less disruptive priority tactics, which include a clearance phase and a green extension. For both signals, we consider two variants: *conditional* and *unconditional* priority. The former is active only when trams are behind schedule. Unconditional partial priority is currently employed in Melbourne.

2 Multi-modal Traffic Model

The multi-modal CA model used in our simulations extends the NetNaSch uni-modal traffic model, (see [3] for a comprehensive description), to include multi-modal traffic and complex vehicular behaviours. In this paper, we focus on two vehicle classes of *private vehicles* (or *cars*) and *trams*. In the studied network, illustrated in Fig. 1a, each alternating east-west route is a tram route. For each tram link there are two lanes, of which the right lane is a car-tram mixed lane, whereas for a non-tram link there are two lanes plus an additional right-turning lane.

Each lane is discretised into a number of cells, each of 7.5 m long. Each vehicle can occupy z cells, $z = 1, 2, \ldots$, and take speed $v = 0, 1, \ldots, v_{max}$, depending on local traffic conditions. In our simulations, we set $z = 1$ and $v_{max} = 3$ for private vehicles, and set $z = 3$, and $v_{max} = 2$ for trams. The length of each link and each right-turning lane were set to 750 and 90 m, respectively. The model includes *boundary links* as a means of inputting and outputting vehicles, but does not consider them part of the network for the purposes of measuring observables (see [3] for more details).

In our model, for each tram link there are three stops being located kerbside, one stop every 250 m. In our simulations, the probability that a tram loads/unloads passengers at stop s was set to 1 if s was an intersection stop and 0.5 otherwise. When a tram stops to load/unload passengers, traffic in the left-hand lane must come to a stop in order to give way to passengers.

Fig. 1 The network used. Illustration of an 8 by 8 square-lattice network studied in our simulations (**a**). All links carry bidirectional traffic. Boundary links are treated as ramps (buffering zones) for inputting and outputting vehicles. Signal phases. Phases E and F are only used at tram nodes (**b**)
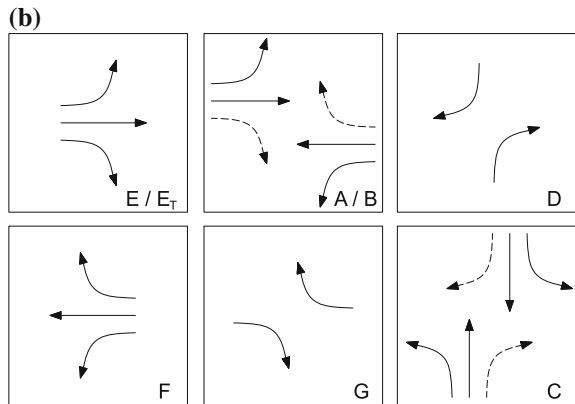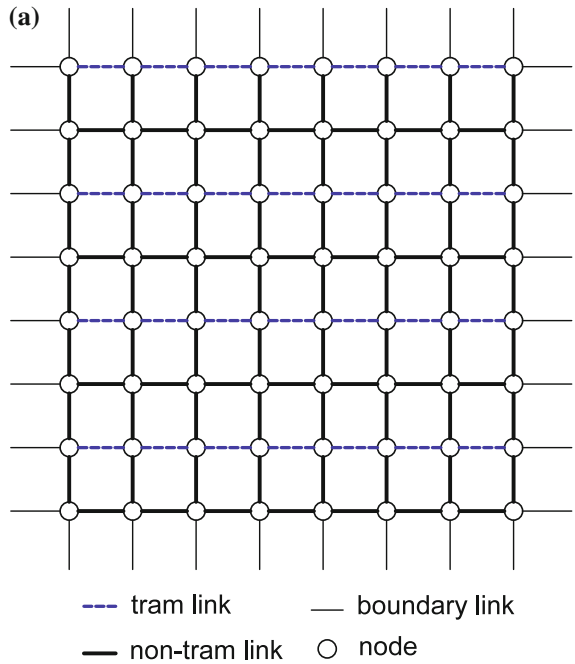
In this paper we consider open boundary conditions. At each time step, vehicles enter a boundary inlink with a prescribed inflow rate and exit via a boundary outlink with a prescribed outflow rate. We simulated the network over a 4 h period, and measured the last 3 h, considering the first hour as a burn-in period. We applied two orthogonal peak directions: eastbound and southbound.

The inflow rate for cars follows a typical AM-peak profile, and is higher in the second and the third hours than the other hours. The inflow rates in the peak directions are about twice as large as those in the counter-peak directions during the peak hours. For tram inlinks, the inflow rates of vehicles are only 50 % of those for the non-tram inlinks in the same direction. The outflow rates have similar profiles to the inflow

rates. We consider two scenarios: over-saturated (OS) and unsaturated (US). Link density in OS scenario can reach higher than that of US scenario when the network is running close to capacity. Trams are inserted into the network on the boundary inlinks periodically at deterministic times. Every hour 12 trams are scheduled on each tram route in the peak direction, and 9 trams in the counter-peak direction.

In our simulations, at each non-tram node (tram node), each link was assigned with a probability 0.85 (0.9) of continuing straight ahead, a probability 0.06 (0.04) of turning into a non-peak-direction link, and a probability 0.09 (0.06) of turning into a peak-direction link. For trams, turning decisions are deterministic as they need to follow routes. As shown in Fig. 1b, each node in the network was assigned with a set of phases, depending on the signal system discussed in the next section.

To evaluate the different priority systems, we use throughputs as the total number of cars (trams) that have traversed the network in a duration of simulation time. We further compare aggregated travel time per car (tram), defined by the mean total travel time spend in the network by those cars (trams), for different priorities. In addition, we evaluate aggregated travel time per car (tram) variability to measure the extent to which the travel time varies from tram (car) to tram (car) on a particular day. By considering occupancy numbers for both trams and cars, we further evaluate the throughput of people and travel time per person. In our simulations, we assumed that the number of occupants that each car carries is identical, that is, 1.2 [8]. Moreover, we assumed that the occupancy of trams operating in the same direction is the same. Namely, 80 if the tram runs in the peak direction and otherwise 20.

For each distinct choice of traffic signal systems and boundary conditions, we performed 100 independent simulations, in order to estimate the expected values of the quantities defined in the last subsection. We used one standard error to set the error bars.

3   Traffic Signal Systems

The SCATS traffic signal system uses knowledge of the recent state of traffic to choose appropriate values of three key signal parameters: cycle length, split time, and linking offset. At each intersection it can adaptively adjust both the total cycle length, and the fraction (*split*) of the cycle given to each particular phase. In addition, it can coordinate (*link*) the traffic signals of several consecutive nodes along a predetermined route in a subsystem by introducing *offsets* between the starting times of specific phases, thereby creating a green wave (see [9] for details). In our simulations, on non-tram nodes, whose inlinks are all non-tram links, we apply SCATS model with signal linking from east to west and phases A, D, C and G in Fig. 1b.

For tram nodes, we consider five variants of SCATS with/without tram priority: $\mathbb{NT}$ which is SCATS with no tram priority, $\mathbb{PU}$ which is SCATS with partial and unconditional tram priority, $\mathbb{PC}$ which is SCATS with partial and conditional tram priority, $\mathbb{AU}$ which is SCATS with absolute and unconditional tram priority, and $\mathbb{AC}$ which is SCATS with absolute and conditional tram priority. We do not apply linking along tram routes since the tram priority phase and tram loading/unloading renders

the linking inefficient. Therefore, tram nodes choose their own cycle lengths and split plans according to their local traffic conditions, independent of their neighbours.

$\mathbb{NT}$ assigns 20 % of the cycle length to either phase E or F. The purpose of phases E and F is primarily to clear right-turning cars in the east-west direction. When a tram passes a mid-link detector, a priority process is called provided that no one is already running. When the tram has passed the middle-link detector but not the end-link one, $\mathbb{PU}$ runs phase E_T, and when it has passed the end-link detector but has not traversed the intersection, $\mathbb{PU}$ runs phase B. $\mathbb{PU}$ is a partial priority system in the sense that the time for running priority phases E_T and B is limited, not more than 20 % per cycle. When the tram priority process is triggered, $\mathbb{AU}$ starts phase E_T *immediately* and keeps running it indefinitely until the tram that triggered the process has traversed the intersection. $\mathbb{PC}$ and $\mathbb{AC}$ are conditional variants of $\mathbb{PU}$ and $\mathbb{AU}$, respectively. In these cases, tram priority processes can be called only if tram detectors detect a late tram.

4 Simulation Results

4.1 Tram Performance

Figure 2b, d, f compare the tram performance for various signal schemes under OS scenario. Note that the results under US are mostly similar to that of OS. As expected, tram priority reduces the average tram travel time in the eastbound direction, when compared to the no priority system $\mathbb{NT}$. It is also unsurprising that the $\mathbb{AU}$ scheme produces the largest improvements, saving about 56 % eastbound travel time. The average travel times under the $\mathbb{PU}$ system lie in-between the results of $\mathbb{NT}$ and $\mathbb{AU}$. The performance of eastbound trams is improved whilst westbound trams does not suffer significant delays. In terms of throughputs, the priority systems produce essentially the same results. $\mathbb{NT}$ results in a marginally lower eastbound throughput than other systems.

Bus priority only produces significant delay savings at high levels of saturation [6]. By contrast, tram priority achieves great savings in both US and OS scenarios. This is because trams are more likely to be affected by cars, especially right-turning ones. Since trams cannot change lane, a single right-turning car, which has to give way to opposite traffic on the mixed traffic lane during phase A (or B) could block the tram for an entire phase and cause a significant delay. For $\mathbb{NT}$, the large delay in eastbound tram travel times is due to insufficient running time for phase E (or E_T).

In addition to improve travel times and throughputs, tram priority significantly reduces eastbound travel time variability. The absolute priority systems provide the best result in the eastbound direction and the worst result in the westbound direction.

4.2 Private Vehicle Performance

Figure 2b, d, e, f show the mean travel time of cars travelling along different approaches under OS scenario. The tram performance under US scenario is similar, albeit less significant. For the west-east direction, we separate cars that have
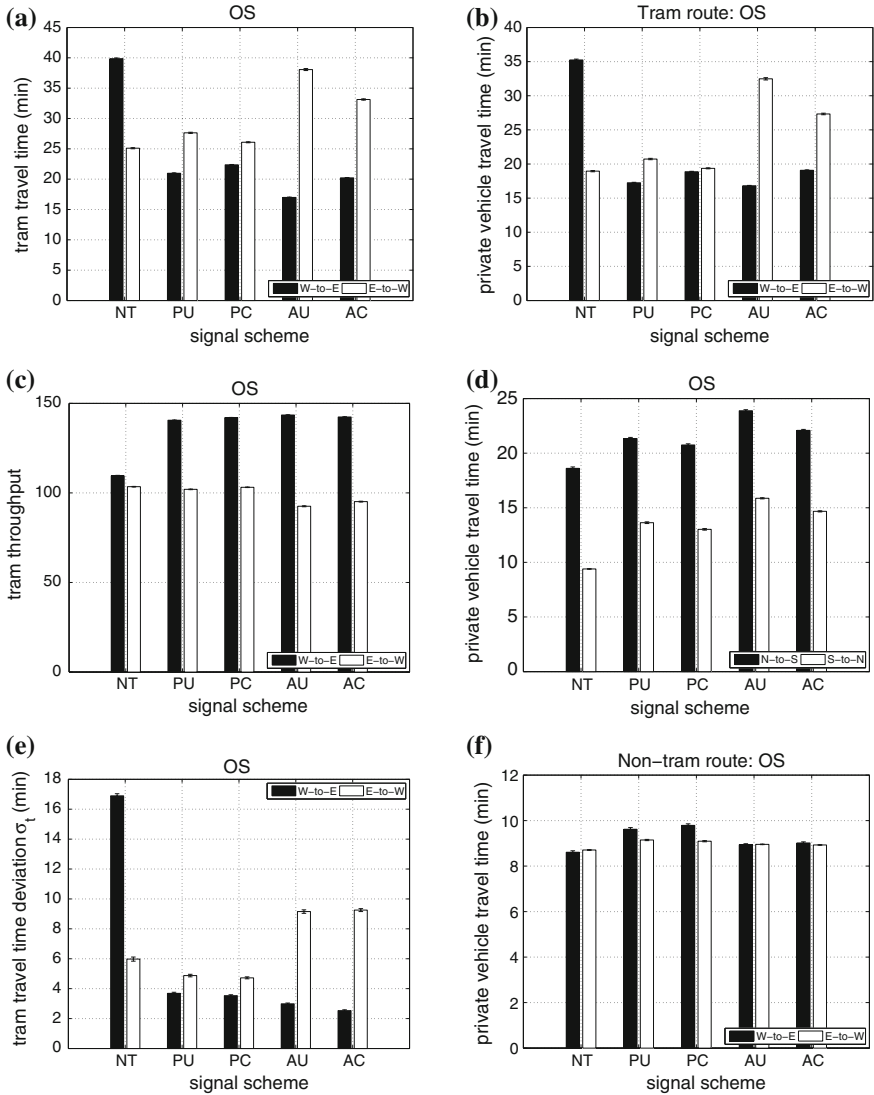
Fig. 2 *Left* Tram performance (OS). *Right* Mean car travel times (OS). Error bars corresponding to one standard deviation are shown but are usually too small to observe: mean tram travel time (**a**); W–E tram routes (**b**); mean tram throughput for all routes (**c**); N–S routes (**d**); tram travel time variability (**e**); W–E non-tram routes (**f**)

travelled along non-tram routes from those along tram routes. We remark that a car is considered to travel along a tram route only if it traverses the whole route without turning into other links. Similar definitions are used for cars travelling in different directions.

Although the inflow rate of cars on tram routes is much less than that on non-tram routes, the car travel time along tram routes is much longer, which is partly due
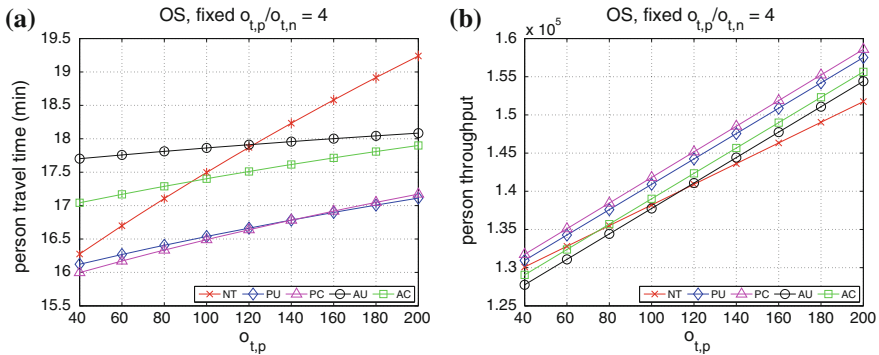
Fig. 3 Person performance (OS). $o_{t,p}/o_{t,n} = 4$ and $o_{t,p} = 40, 60, \ldots, 200$. Error bars corresponding to one standard deviation are shown but are usually smaller than the symbol size of the data point: mean person travel time (**a**); mean person throughput (**b**)

to trams and partly due to right-turning cars at nodes. Right-turning cars result in capacity drops at tram nodes, since there are no exclusive right-turning lanes on tram routes and such vehicles are required to give way to opposing traffic during phases A and B and so hinder other straight-going vehicles behind them.

As expected, when tram priority process is active, regardless of the scheme used, both southbound and northbound travel times increase. The higher the priority imposed, the more the north-south traffic gets penalised. Even though the $\mathbb{AU}$ and $\mathbb{AC}$ schemes penalise all three non-priority directions, they penalise the north-south traffic more than $\mathbb{PU}$ and $\mathbb{PC}$ do. This is because SCATS uses adaptive split plans.

Interestingly, we observe from Fig. 2f that in the OS case tram priority can penalise the traffic in parallel non-tram routes. Perhaps surprisingly, the penalty generated by $\mathbb{PU}$ and $\mathbb{PC}$ is larger than that by $\mathbb{AU}$ and $\mathbb{AC}$. This arises because absolute tram priority results in larger decreases in both the north-south flow and the amount of traffic turning into the east-west direction, which therefore induces an effective *gating* of the west-east non-tram routes.

4.3 Person Performance

We pinned the car occupancy o_c and the ratio $o_{t,p}/o_{t,n}$ of tram occupancy in the peak and counter-peak directions, and studied people travel time and throughput as a measure of network performance with various $o_{t,p}$, shown in Fig. 3.

$\mathbb{AU}$ provides the worst result in the US case and for $o_{t,p} \geq 120$ in the OS case, whereas $\mathbb{PC}$ always provides the best result. $\mathbb{PU}$ and $\mathbb{PC}$ obtain the smallest travel times for all reasonable values of tram occupancy. The travel time curve for $\mathbb{NT}$ intersects with $\mathbb{AC}$ and $\mathbb{AU}$ at $o_{t,p} = 100$ and $o_{t,p} = 120$ separately. This implies that although the absolute tram priority schemes bring relatively large penalties to other road users, compared to no priority scheme, they provide better overall network efficiency in terms of person travel times when tram occupancy is sufficiently high.

5 Conclusion

We have utilised a multi-modal traffic model to study a variety of tram priority schemes in a mixed traffic environment on a square- lattice network. In particular we have studied the adaptive traffic signal system SCATS with a number of tram priority scenarios, using a morning-peak traffic profile and two orthogonal peak directions. We have considered two scenarios with low and high levels of saturation.

Regardless of the traffic condition, the absolute tram priority results in the best tram service in the priority direction at the expense of delaying other traffic in the non-priority directions. With respect to the overall person performance, the partial priority gives the best result. The savings for priority-direction traffic derived from the absolute priority is negated by the costs imposed on opposing traffic, unless trams have extremely high occupancy. For both the absolute priority and the partial priority, the conditional version achieve almost the same level of improvement of service as the unconditional version but with reduced impact on other traffic. Therefore, the partial conditional priority system appears worth trialling. In the case that the absolute tram priority is necessary, e.g. in order to keep tram service on time regardless of the traffic condition, the absolute conditional priority should be implemented, rather than the absolute unconditional.

The analysis of tram priority presented in this paper is just a first attempt at using the multi-modal traffic simulation model on large-scale networks. Future work will extend the study of the tram priority to two directions: both peak and counter-peak for all the priority schemes. This is challenging since counter-peak-direction tram priority may disadvantage peak-direction trams.

References

1. Currie, G., Goh, K., Sarvi, M.: An analytical approach to measuring the impacts of transit priority. In: 92nd Annual Meeting of the Transportation Research Board. Washington, DC (2013)
2. Currie, G., Sarvi, M., Young, B.: A new approach to evaluating on-road public transport priority projects: balancing the demand for limited road-space. Transportation **34** (2007)
3. de Gier, J., Garoni, T., Rojas, O.: Traffic flow on realistic road networks with adaptive traffic lights. J. Stat. Mech. Theory Exp. **4** (2011)
4. Furth, P., Muller, T.: Conditional bus priority at signalized intersections. Transp. Res. Rec. **1731** (2000)
5. He, Q., Head, K.L., Ding, J.: Heuristic algorithm for priority traffic signal control. In: Transportation Research Board 90th Annual Meeting, vol. 2259 (2011)
6. Jepson, D., Ferreira, L.: Assessing travel time impacts of measures to enhance bus operations. part 2: study methodology and main findings. Road Transp. Res. **9** (2000)
7. Lee, J., Shalaby, A., Greenough, J., Bowie, M., Hung, S.: Advanced transit signal priority control with online microsimulation-based transit prediction model. In: Transportation Research Board 84th Annual Meeting, vol. 1925 (2005)
8. VicRoads: Traffic monitor 2011–2012. Technical report (2013)
9. Zhang, L., de Gier, J., Garoni, T.: A comparative study of macroscopic fundamental diagrams of arterial road networks governed by adaptive traffic signal systems. Transp. Res. Part B **49** (2013)

Part III
Other

Boarding of Finite-Size Passengers to an Airplane

Jevgenijs Kaupužs, Reinhard Mahnke and Hans Weber

Abstract An airplane boarding model, introduced earlier by Hemmer and Frette, is considered. In this model, N passengers have reserved seats, but enter the airplane in arbitrary order. Here we focus on the blocking relations between passengers. The total boarding time is equal to the longest blocking sequence, represented by a line, connecting points of the two-dimensional q versus r scatter plot. Here, $q = i/N$ and $r = j/N$, i and j being sequential numbers of passengers in the queue and their seat numbers, respectively. Such blocking sequences have been studied theoretically by Bachmat. We have developed an algorithm for numerical simulation of the longest blocking sequences, and have compared the results with analytical predictions for $N \to \infty$.

1 Introduction

The growing need for mobility through the world shows no sign of slowing down. Like the vehicular traffic, also the air traffic is a very important part of the global transportation network [9]. A distinguishing feature of air traffic is that a significant part of the total transportation time is related to the boarding of an airplane. Here, we study an airplane boarding model, introduced in 2012 by Frette and Hemmer [8]. Following this paper, there has been a spurt of activity regarding airplane boarding, resulting in five papers in Physical Review E [3–6, 8] in roughly 16 months. This problem has been also later discussed during the Traffic and Granular Flow confer-

J. Kaupužs (✉)
Institute of Mathematical Sciences and Information Technologies,
University of Liepaja, Liepaja 3401, Latvia
e-mail: kaupuzs@latnet.lv

R. Mahnke
Institute of Physics, Rostock University, 18051 Rostock, Germany
e-mail: reinhard.mahnke@uni-rostock.de

H. Weber
Department of Physics, Luleå University of Technology, 97187 Luleå, Sweden
e-mail: Hans.Weber@ltu.se

ence in 2013 [11]. In the model considered by Frette and Hemmer [8], N passengers have reserved seats, but enter the airplane in arbitrary order. Besides, there is only a single isle of rows and only one seat in each row. Each passenger occupies a place equal to the distance between rows. In this model, a passenger requires one time step to place carry-on luggage and get seated, the time for walking along the isle being neglected. However, a passenger must wait for a possibility to move forwards to his/her seat if the motion is blocked by other passengers. The number of seats is equal to the number of passengers in this model. In [4], the same process has been considered with more than one seat per row. It has been also discussed what happens if only some fraction p of the passengers occupies the seats. In a series of works [2, 4, 5, 8], a non-random ordering of passengers has been also considered. One of the basic quantities of interest is the boarding time t_b of an airplane. All these papers deal with a numerical estimation of the mean boarding time $\langle t_b \rangle$, stating that it is more ore less well consistent with the power law $\langle t_b \rangle = cN^\alpha$. Estimates $\alpha = 0.69 \pm 0.01$ and $c = 0.95 \pm 0.02$ have been obtained in [8] from the data with a small number of passengers, $2 < N < 16$.

Later on, it has risen an interesting discussion [4–6] about the value of the exponent α, describing the asymptotic power law at $N \to \infty$. It has been found that the numerical estimates converge to a remarkably different from 0.69 value $\alpha = 1/2$ for large N. In particular, $\alpha = 0.5001 \pm 0.0001$ has been found in [6] from the Monte Carlo simulation data up to $N = 2^{16}$. In fact, $\alpha = 1/2$ is exactly the analytical value reported earlier in [1]. As explained in [4], the $\propto N^{1/2}$ asymptotic behaviour follows from the mathematical theorem reported already in [7, 10]. In [1], the proportionality coefficient $c = 4 - 2\ln 2 \approx 2.6137$ has been also found. A similar value 2.6092 ± 0.0002 has been numerically obtained in [6] (see Fig. 1 in [6]). Corrections to scaling have been considered in [6], as well as in [1]. Numerical estimation in [6] suggests that correction-to-scaling exponent θ in $\langle t_b \rangle = cN^\alpha \left(1 + \mathcal{O}\left(N^{-\theta}\right)\right)$ is approximately 1/3. It has been also numerically found there that the variance of t_b scales with a similar exponent $\gamma \approx 1/3$. In [11], some analytical arguments have been provided, suggesting that the scaling relation $\gamma = 1 - 2\theta$ holds. It has been found in [11] that the numerically estimated exponents γ and θ very accurately satisfy this scaling relation, whereas the consistency with the value 1/3 is not perfect, allowing a possibility that $\theta < 1/3$ holds in reality. Probably, even larger than $N = 2^{16}$ system should be simulated to obtain a reliable numerical estimate of this exponent. In [1] it has been argued that $\alpha - \theta$ is larger than 1/6, i.e. $\theta < 1/3$. The question about the precise values of θ and γ is interesting and merits further investigation.

2 Blocking Sequences

In our current study, we use the following definitions of the blocking sequences.

(i) Suppose passenger A takes his/her seat at the nth time step. We say that passenger A has been blocked by passenger B, if B is the closest passenger in front of A among those ones, which took seat at the $(n-1)$th time step.

(ii) We depict this blocking relation by drawing an arrow from B to A in the scatter plot (number in queue versus seat number). Nodes and arrows, pointing in certain flow direction, represent a blocking sequence. Its length is equal to the number of nodes. By definition, unconnected nodes are blocking sequences of length 1.

By these definitions, the longest blocking sequences have the length t_b, where t_b is the boarding time. They can be easily deciphered starting from the passengers who get seated at the last time step. The number of such sequences is equal to the number of these passengers.

3 Point-Like Passengers

Let us denote by i_A and i_B the sequential numbers of passengers A and B in the queue. By the definition, we always have $i_B < i_A$ if B is blocking A (i.e. B enters airplane first). In a model with point-like passengers, passenger A can be blocked by passenger B only if $j_B < j_A$, where j_A and j_B are the seat numbers of passengers A and B, respectively. It means that blocking sequences are increasing sequences with arrows always pointing upwards.

However, an arbitrary increasing sequence is not necessarily a blocking sequence we defined here. In our blocking sequence, the seating time increases just by one time step $\Delta t = 1$ when moving forwards by one node along the sequence. To the contrary, we can have $\Delta t \geq 1$ for an arbitrary increasing sequence. The maximum possible length thus is t_b, which corresponds to the case, where the increment of seating time is always $\Delta t = 1$. In such a way, we have $\Omega_{bl} \subset \Omega_{incr}$, where Ω_{bl} is the set of longest blocking sequences and Ω_{incr} is the set of longest increasing sequences. In general, Ω_{incr} contains more elements than Ω_{bl} owing to the fact that many passengers can get their seats simultaneously. However, since all sequences of Ω_{bl} and Ω_{incr} have the same (and maximal possible) length t_b, these sequences are equivalent and look similar for a large system. Namely, it is expected that they follow a certain line inside the unit square for normalised quantities $q = i/N$ and $r = j/N$ at $N \to \infty$, where N is the number of passengers. For point-like cars, this line is known to be the diagonal.

4 Finite-Size Passengers

In the model introduced by Hemmer and Frette passengers are not point-like. They occupy space, which is equal to the distance between seats. For finite-size passengers, $j_B < j_A$ does not necessarily hold, since the blocking can occur via passengers staying between A and B. In the asymptotic limit $N \to \infty$, the condition $j_B < j_A$ (for $i_B < i_A$) is replaced by

$$dr > -dq \, k\alpha(q, r) \tag{1}$$

for $dq > 0$. Here $k = bu/w$, where u is the passenger width, w is the distance between successive rows (in our case seats), b is the number of passengers per row (in our case $b = 1$) and $\alpha(q, r) = \int_r^1 p(q, z)dz$ with $p(q, r)$ being the probability distribution in $q - r$ plane ($p(q, r) \equiv 1$ for random queue).

In the asymptotic case, the longest sequences obeying the causal relation (Eq. 1) have the length t_b. (We can conclude it, considering seating times as in the case of point-like passengers). Denoting this set of sequences by Ω, we have $\Omega_{bl} \subset \Omega$, since the blocking sequences satisfy Eq. 1 at $N \to \infty$ and also have the length t_b.

According to [1–3], it is expected that the sequences of set Ω follow a certain line in the $q - r$ plane. Since $\Omega_{bl} \subset \Omega$, it has to be true also for the set of longest blocking sequences Ω_{bl}. This line L is obtained by maximising the line integral,

$$\int_L ds \to \max ,\tag{2}$$

with the conditions that the integration path (line L) goes from $(0, 0)$ to $(1, 1)$ and belongs to the unit square. Besides, the measure is given by

$$(ds)^2 = 4D^2 \, p(q, r) \left[dqdr + k\alpha(q, r)(dq)^2 \right],\tag{3}$$

called the Lorentz metric. In fact, one finds that $D = 1$.

By solving the variational problem one finds [1] that L is given by the geodesic line

$$r(q) = C_1 e^{kq} + C_2 e^{2kq} + 1\tag{4}$$

for $k < \ln 2$ with coefficients C_1 and C_2 determined from the conditions that $r(0) = 0$ and $r(1) = 1$. For $k > \ln 2$, this line does not fit inside the unit square and therefore the path L goes along the border $r = 0$ up to some point $q = q_0$ and then follows the geodesic (Eq. 4) from $(q_0, 0)$ to $(1, 1)$ [1]. Besides, q_0 is such that the geodesic line is tangent to the border $r = 0$ at this point [1]. In such a way, for $k \geq \ln 2$ one finds

$$r(q) = 0 \qquad\qquad : \quad 0 \leq q \leq q_0(k) ,\tag{5}$$
$$r(q) = -4e^{k(q-1)} + 4e^{2k(q-1)} + 1 \quad : \quad q_0(k) \leq q \leq 1 ,\tag{6}$$

where $q_0(k) = 1 - \ln 2/k$. The resulting curve for $k = 1$ is shown in Fig. 1 by a solid line. The mean boarding time $t_b = d(k)\sqrt{N}$ has been reported in [1], where

$$d(k) = 2\sqrt{\frac{e^k - 1}{k}} \qquad\qquad : \quad k \leq \ln 2 ,\tag{7}$$
$$d(k) = 2\sqrt{k} + 2(1 - \ln 2)/\sqrt{k} \quad : \quad k > \ln 2 ,\tag{8}$$

It corresponds to the length of the $r(q)$ curve in the Lorentz geometry, where distances are measured according to the metric (Eq. 3).

5 Simulation Results and Analysis

In order to test the above discussed theoretical predictions, Monte Carlo simulations of the boarding process have been performed in the simple model with $k = 1$, outlined in the beginning of this section. The longest blocking sequences have been determined according to the definitions given in Sect. 2. These sequences, extracted from three different simulation runs with $N = 10^7$ passengers (left), as well as from one simulation run with $N = 10^8$ passengers (right) are shown in Fig. 1.

As we can see, the amplitude of random deviations from the theoretical asymptotic curve is still rather large for $N = 10^7$. These deviations are remarkably smaller for $N = 10^8$. It confirms the expected convergence to the analytical solution (Eqs. 5–6) at $N \to \infty$.

It is interesting to note that the fluctuations around the geodesic within $q_0(k) \leq q \leq 1$ are remarkably larger in magnitude than those within $0 \leq q \leq q_0(k)$, where the theoretical curve follows the lower border of the $q - r$ square. On the other hand, the fluctuations in the latter region have larger influence on the total boarding time. Indeed, the geodesic maximises the boarding time and, therefore, a small deviation from it in the form of $\delta \cdot f(q)$, where $\delta \to 0$, produces a deviation of order $\mathscr{O}\left(\delta^2\right)$ in the boarding time t_b. To the contrary, such a deviation from the lower border of the $q - r$ square produces a fluctuation of order $\mathscr{O}(\delta)$ in t_b.

In fact, there is a phase transition in the behaviour of the boarding process at $k = \ln 2$, if the parameter k is varied. In the case of point-like passengers, $k \to 0$, the geodesic is just the diagonal $q = r$. Moreover, the deviations of longest blocking sequences from the diagonal is described by the Tracy–Widom distribution, yielding the correction-to-scaling exponent $\theta = 1/3$, which remains valid for $k < \ln 2$. This exponent has to be changed to a smaller value at $k > \ln 2$ due to the fluctuations in the longest blocking sequences (seen in Fig. 1) within $0 \leq q \leq q_0(k)$ [1], which emerge as soon as k exceeds the critical value $\ln 2$.
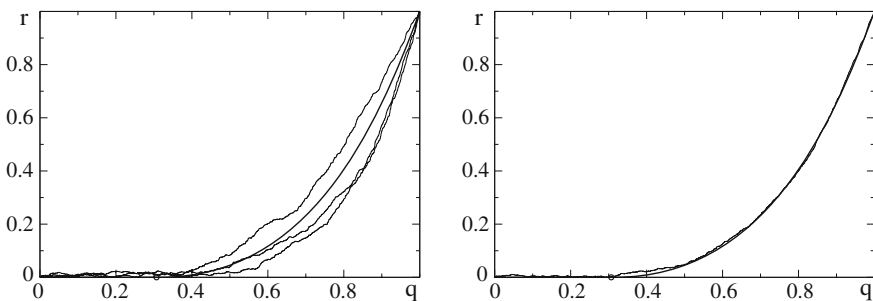
Fig. 1 The analytical *curve* representing the longest blocking sequences in the asymptotic limit $N \to \infty$ at $k = 1$, given by Eqs. 5–6. The point of departure from border $q_0 = 1 - \ln 2 = 0.30685\ldots$ is marked by a *circle*. The fluctuating *curves* represent the longest blocking sequences, extracted from 3 different simulation runs with $N = 10^7$ passengers (*left*) and from one simulation run with 10^8 passengers (*right*)

In view of this fact, it is important to refine our previous estimations of the exponent θ in [6]. As already mentioned in Sect. 1, the number of passengers $N = 2^{16} = 65536$, considered in [6], might be still too small for an accurate estimation of the exponent θ. Indeed, even at $N = 10^7$ the deviations from the theoretical asymptotic behaviour in Fig. 1 are rather large. A numerical estimation of θ from the data for much larger number of passengers (e. g., $N = 10^9$) is a challenge for further simulations, which eventually should be based on a faster algorithm of finding longest blocking sequences.

While the scaling of the mean boarding time $\langle t_b \rangle$ is described by the exponent $\alpha = 1/2$, its variance $\mathrm{var}(t_b) = \langle t_b^2 \rangle - \langle t_b \rangle^2$ is described by another exponent γ, i.e. $\mathrm{var}(t_b) \propto N^\gamma$ holds at $N \to \infty$. An idea has been proposed in [11], that the exponents γ and θ obey the scaling relation

$$\gamma = 1 - 2\theta . \tag{9}$$

Here, we propose a way, which is different from that one in [11], to obtain such a scaling relation. First we note that the variance can be written as

$$\mathrm{var}(t_b) = \left\langle (t_b - \langle t_b \rangle)^2 \right\rangle . \tag{10}$$

Furthermore, the typical values of t_b are smaller than the theoretical asymptotic mean value $\langle t_b \rangle^{as} = d(k)\sqrt{N}$, where $d(k)$ is given by Eqs. 7–8. It is consistent with the fact that $\langle t_b \rangle^{as}$ corresponds to the blocking curve of maximal length (according to the Lorenz metric), so that fluctuations, illustrated in Fig. 1, typically lead to a smaller value of t_b. On the other hand, t_b can be quite close to $\langle t_b \rangle^{as}$. It can be seen from the probability distribution for boarding times $P(t_b)$, illustrated in Fig. 2.

The probability distribution is shifted below $\langle t_b \rangle^{as}$ in such a way that $\langle t_b \rangle^{as} - \langle t_b \rangle$ is comparable with the width of the distribution. It implies that $| t_b - \langle t_b \rangle |$ is comparable with $\langle t_b \rangle^{as} - \langle t_b \rangle$ for typical random realisations of the boarding process. Moreover, $\langle t_b \rangle^{as} - \langle t_b \rangle$ scales asymptotically as $\propto N^{\alpha - \theta}$ according to $\langle t_b \rangle = cN^\alpha \left(1 + \mathcal{O}\left(N^{-\theta} \right) \right)$ at $N \to \infty$. Hence, typical values of $(t_b - \langle t_b \rangle)^2$ in Eq. 10
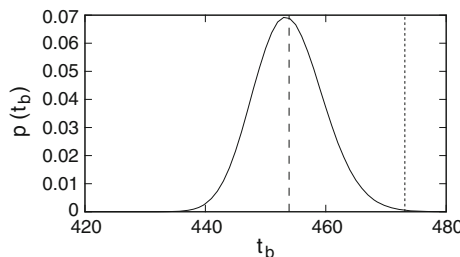
Fig. 2 The probability distribution $P(t_b)$ of the boarding time t_b for the model with $N = 2^{15}$ passengers. The mean boarding time $\langle t_b \rangle = 453.91$ (*dashed line*) and the asymptotic mean boarding time $\langle t_b \rangle^{as} = 473.13$ (*dotted line*), corresponding to Eqs. 7–8, are indicated by *vertical straight lines*

are comparable with $N^{2(\alpha-\theta)}$ for any large enough N. Consequently, var(t_b) scales as $\propto N^{2(\alpha-\theta)}$ at $N \to \infty$, i.e. the scaling relation

$$\gamma = 2(\alpha - \theta) \tag{11}$$

holds according to this consideration. Since we have $\alpha = 1/2$, the scaling relation (Eq. 11) reduces to (Eq. 9). The actual consideration is sufficiently general, so that this scaling relation is expected to hold both at $k \leq \ln 2$ and $k > \ln 2$.

6 Concluding Remarks

In the current study, a simple airplane boarding model, introduced earlier by Frette and Hemmer, has been investigated from different new aspects. In particular, we have focused on the study of blocking relations between the passengers and longest blocking sequences via Monte Carlo simulations and analysis with an aim to test the known theoretical results. We have tackled an important question about the phase transition in the behaviour of the boarding process in a generalised model at a certain value of the control parameter k. It is related to some change in the correction-to-scaling exponent θ. Furthermore, we have provided new arguments for the existence of certain universal scaling relation (Eq. 9 or 11) between the exponents, describing the power-law behaviour of the model. Fluctuations in the longest blocking sequences, discussed throughout the paper, allow us to put these phenomena in a general framework of stochastic transport in complex systems [12, 13].

References

1. Bachmat, E., Berend, D., Sapir, L., Skiena, S., Stolyarov, N.: Analysis of airplane boarding via space-time geometry and random matrix theory, submitted. J. Phys. A: Math. Theor. **39**, L453–459 (2006)
2. Bachmat, E., Berend, D., Sapir, L., Skiena, S., Stolyarov, N.: Analysis of airplane boarding times. Oper. Res. **57**(2), 499–513 (2009)
3. Bachmat, E., Khachaturov, V., Kuperman, R.: Optimal back-to-front airplane boarding. Phys. Rev. E **87**(6), 062805 (2013)
4. Baek, Y., Ha, M., Jeong, H.: Impact of sequential disorder on the scaling behavior of airplane boarding time. Phys. Rev. E **87**(5), 052803 (2013)
5. Bernstein, N.: Comment on Time needed to board an airplane: a power law and the structure behind it. Phys. Rev. E **86**(1), 023101 (2012)
6. Brics, M., Kaupužs, J., Mahnke, R.: Scaling behavior of an airplane-boarding model. Phys. Rev. E **87**(4), 042117 (2013)

7. Deuschel, J.D., Zeitouni, O.: Limiting curves for iid records. Ann. Probab. pp. 852–878 (1995)
8. Frette, V., Hemmer, P.C.: Time needed to board an airplane: a power law and the structure behind it. Phys. Rev. E **85**(1), 011130 (2012)
9. Jaehn, F., Neumann, S.: Airplane boarding. Eur. J. Oper. Res. **244**(2), 339–359 (2015)
10. Kerov, C., Vershik, A.: Asymptotics of the plancherel measure of the symmetric group and the limiting form of young tableaux. Soviet Math. Dokl **18**, 527–531 (1977)
11. Mahnke, R., Kaupužs, J., Brics, M.: Air traffic, boarding and scaling exponents. In: Traffic and Granular Flow'13, pp. 305–314. Springer (2015)
12. Mahnke, R., Kaupuzs, J., Lubashevsky, I.: Physics of Stochastic Processes: How Randomness Acts in Time. Wiley (2009)
13. Schadschneider, A., Chowdhury, D., Nishinari, K.: Stochastic Transport in Complex Systems: from Molecules to Vehicles. Elsevier (2010)

Collective Dynamics and Motility of Soft Elliptical Particles

Ruben van Drongelen and Timon Idema

Abstract Swarming behaviour is abundant in nature. Over many different length scales, in for example herds, flocking birds and swimming bacteria, roughly identical individuals interact locally to achieve group behaviour. The similarities between these examples suggests the existence of a general underlying principle. We propose here a local interaction model for self-propelling, elliptical particles that results in collective motion. Any particle interacts with its neighbours only, experiences noise on its orientation and pushes inwards if it is in the outer layer of the group. Initially, alignment between particles is the result of steric repulsion. We observe two types of group behaviour. The first type is a migrating group, where particles in the bulk are aligned over large length scales, but do not rearrange. The second type has very little net motion. The elliptical particles form smaller regions of aligned and antialigned particles, effectively cancelling the net motion of the group. Finally, we compare the group behaviour of elliptical particles to circular ones and investigate the importance of polar alignment. We conclude that polar alignment is a requirement for large-scale collective dynamics, like collective migration and rotation.

1 Introduction

Many organisms do not just live by themselves. They live in groups. Such groups consist of hundreds to hundreds of thousands of roughly identical individuals. Examples range over many length scales: herds of mammals, flocks of birds [2] and schools of fish [1, 11], insects [3], and amoebae [9, 12] and bacteria [4]. In all cases, the collective behaviour of the group is the result of interactions between individuals that are close together. Especially on the smallest scale, clusters can reach packing fractions approaching unity. As a general rule, individuals have little knowledge about the dynamics of the group. Still, the behaviour of the group as a whole is obviously important to every individual in it. Therefore, we want to understand how rules between neighbouring individuals govern the group behaviour.

R. van Drongelen · T. Idema (✉)
Delft University of Technology, Van der Maasweg 9, 2629 HZ Delft, The Netherlands
e-mail: R.vanDrongelen@tudelft.nl

T. Idema
e-mail: T.Idema@tudelft.nl

Swarming dynamics are a highly nonlinear result of specific local interactions, as can be seen by simulating group dynamics based on simple rules for individuals. For example, the well-known Vicsek model describes a flock of birds as a collection of self-propelled point particles with fixed speed, an interaction that aligns an individual's direction of flight to the velocity of its neighbours, and orientational noise [13, 14]. To prevent the swarm from falling apart, Vicsek et al. originally used unrealistic periodic boundary conditions. Variations of the Vicsek model add a long-range attraction potential or confine the particles by a fixed boundary [5, 7]. Recently, we showed that a system can provide its own boundary by imposing a local outsiders-want-in rule [6]. Particles on the boundary will turn towards the group and push inwards, until they are part of the bulk again. In that work we focussed on circular particles. Here we extend our results by investigating the effect of anisotropy on the local alignment, and ultimately, the group dynamics.

We model collective dynamics of elliptical particles in viscous environments. In the model, particles repel each other if they overlap, propel themselves along their major axis, experience noise on this direction and push themselves inwards if they are on the outside. All of these are local interactions. We find that the resulting clusters are either collectively aligned without internal dynamics, or dynamic with only local alignment and no net motion. These results are in contrast with our earlier work on circular particles with polar alignment, which do exhibit global collective dynamics. We also carry out two types of control simulations to investigate if polar alignment, or the geometry of the particles, is responsible for collectively dynamic systems. Our results show that clusters perform collective migration and rotation once we add a polar alignment rule, whereas clusters of circular particles with a two-way alignment will always break up. Indeed, for birds and fish, polar alignment is a clearly visible feature. Cells of the social amoebae *Dictyostelium discoideum* align their velocities and the resulting cluster exhibits collective migration, as well as rotation [15]. The *Myxococcus xanthus* bacteria align through steric interactions, and use velocity reversals to achieve collective migration [10, 16]. In contrast, large groups of whirligig beetles, that align in an apolar way, exhibit no net motion.

2 Model

We consider N identical, self-propelling ellipses with aspect ratio $\gamma = 2 : 1$ and minor axis σ_0. We denote the position of the centre of ellipse i by $\mathbf{r}_i$ and its orientation by ψ_i, such that ψ_i is the angle between the major axis and the positive $\hat{\mathbf{x}}$-axis. Particles propel themselves along their major axis. They are subjected to a viscous drag. We consider the overdamped limit where particles have negligible inertia. Since they mostly move along the direction of self-propulsion, we can approximate our equations of motion from the expressions for the linear and angular drag on disks, reported in Landau and Lifshitz [8]. The drag force and torque on particle i are given by

$$\mathbf{F}_i = \frac{16}{3}\eta\sigma_0\mathbf{v}_i \equiv \zeta\,\mathbf{v}_i \quad \text{and} \quad T_i = \pi\eta_R\gamma\sigma_0^2\omega_i \equiv \mu\omega_i. \tag{1}$$

In these definitions for ζ and μ, η and η_R are the translational and rotational viscosities, and $\mathbf{v}_i$ and ω_i are the linear and angular velocity of particle i.

Overlapping particles experience a soft, harmonic, repulsive force, which we model by a modified Gay–Berne potential. The potential, in accordance with the work of Zeravcic et al. [17] on the jamming of soft ellipsoidal particles, is given by

$$V(r_{ij}, \sigma_{ij}) = \begin{cases} \frac{1}{2}k\left(\sigma_{ij} - r_{ij}\right)^2 & \text{for } r_{ij} \leq \sigma_{ij} \\ 0 & \text{for } r_{ij} > \sigma_{ij} \end{cases}, \tag{2}$$

where k is the spring constant, and $r_{ij} = |\mathbf{r}_j - \mathbf{r}_i|$ is the distance between the centres of ellipse i and j. The range parameter σ_{ij} indicates how much two particles overlap. This parameter depends on the relative position of particle i to j, $\mathbf{r}_{ij}$, and their respective orientations ψ_i and ψ_j. The range parameter is defined by

$$\sigma_{ij} = \sigma_0 \left[1 - \frac{\chi}{2}\left(\frac{(\hat{\mathbf{r}}_{ij}\cdot\hat{\mathbf{u}}_i + \hat{\mathbf{r}}_{ij}\cdot\hat{\mathbf{u}}_j)^2}{1 + \chi\hat{\mathbf{u}}_i\cdot\hat{\mathbf{u}}_j} + \frac{(\hat{\mathbf{r}}_{ij}\cdot\hat{\mathbf{u}}_i - \hat{\mathbf{r}}_{ij}\cdot\hat{\mathbf{u}}_j)^2}{1 - \chi\hat{\mathbf{u}}_i\cdot\hat{\mathbf{u}}_j}\right)\right]^{-1/2}. \tag{3}$$

The vector $\hat{\mathbf{u}}_i = \cos(\psi_i)\hat{\mathbf{x}} + \sin(\psi_i)\hat{\mathbf{y}}$ corresponds to the major axis of ellipse i, and $\hat{\mathbf{r}}_{ij}$ is the unit vector pointing from i to j. The dimensionless parameter $\chi = \frac{\gamma^2-1}{\gamma^2+1}$ depends on the aspect ratio γ of the particles. In general, the corresponding force is not along $\hat{\mathbf{r}}_{ij}$ (see Fig. 1a). Consequently, there is also a torque that leads to local alignment. The force and torque on particle i are the total derivatives of the potential:

$$\mathbf{F}_i = -\frac{\mathrm{d}}{\mathrm{d}r_{ij}}V(r_{ij}, \sigma_{ij})\hat{\mathbf{r}}_{ij} \quad \text{and} \quad T_i = -\frac{\mathrm{d}}{\mathrm{d}\psi_i}V(r_{ij}, \sigma_{ij}). \tag{4}$$

Following Vicsek et al. [13], we model self-propelled particles with a constant self-propulsion force and noise on the direction. These interactions are described by

$$\mathbf{F}_i = F_{\text{self}}\hat{\mathbf{u}}_i \quad \text{and} \quad T_i = T_{\text{noise}}\xi_i, \tag{5}$$
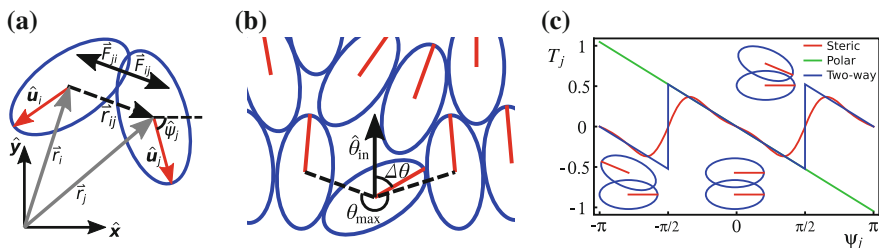
Fig. 1 Schematic view of the forces. The repulsive force between particles i and j causes torques on both particles (**a**). Explanation of the outsiders-want-in rule. The particle at the *bottom* identifies itself as a boundary particle by measuring the maximum angular separation between any pair of consecutive neighbours. If this angle exceeds the critical value θ_c, the particle turns inwards and exerts an additional force to squeeze in (**b**). The torque exerted on particle j as a function of its orientation for different alignment rules. The steric alignment torque when particle j is located directly above i with orientation $\psi_i = 0$, is shown in *red*. The torques resulting from the polar alignment rule and the two-way alignment rule are in *green* and *blue*, respectively (**c**)

with F_{self} and T_{noise} the strength of self-propulsion and noise, respectively, and ξ_i is a random number drawn from the set $\{-1, 1\}$ at each time step. Finally, we use a local boundary term to prevent the system of particles from falling apart. This eliminates the necessity of a geometrical confinement or attraction between particles on either short or long range. To find out if a particle is on the boundary, it measures the largest angle between consecutive neighbours, $\theta_{max,i}$ (see also Fig. 1b). If this angle is larger than the critical value θ_c, this particle will exert an extra force and torque to return to the cluster. The additional force and torque are

$$\mathbf{F}_i = \left(\theta_{max,i} - \theta_c\right) F_{in}\hat{\mathbf{u}}_i, \qquad \text{and} \qquad T_i = T_{in}\Delta\theta_i, \tag{6}$$

respectively. Again, the strength of these interactions are F_{in} for the force and T_{in} for the torque. The torque is proportional to $\Delta\theta_i$, the angle between the orientation $\hat{\boldsymbol{\psi}}_i$ and the inward direction defined by the exterior bisector of angle $\theta_{max,i}$.

We make our variables dimensionless for the purpose of our computer simulation. We fix the length scale by imposing $\sigma_0 = 1$. The characteristic time scale for repulsion is given by $\tau = \zeta/k$. We set the time scale and force scale with $\tau = k = 1$ and denote the duration of one simulation step by Δt. Every other interaction X in our model also has a characteristic time scale τ_X. The strength of the other interactions X will be denoted by $\lambda_X = \tau/\tau_X$. Hence we have (i) for the noise, $\lambda_n = \zeta T_{noise}^2 \Delta t/(2k\mu^2)$, (ii) for the additional inwards force, $\lambda_F = 2F_{in}/(k\sigma_0)$, (iii) for the additional inwards torque, $\lambda_T = \zeta T_{in}/(k\mu)$, and (iv) for the self-propulsion $\lambda_s = 2F_{self}/(k\sigma_0)$. Furthermore we fixed $\mu = 1$, $\theta_c = 0.9\pi$, $\lambda_F = 0.16$ and $\lambda_T = 0.1$.

The model described above consists of finite self-propelled particles with repulsive overlapping interactions. We apply a local boundary term, where particles on the boundary of the cluster push inwards, to keep the cluster together. Both the finite size and the local boundary rule are different from those of the Vicsek model. Finally, in contrast with the Vicsek model, any alignment in the system is the result of steric interactions between the anisotropic particles, instead of being hard-coded into the model. Consequently, ours is the simplest possible model for generating collective behaviour without confinement and long-range interactions.

3   Results and Discussion

The ellipses are self-propelling agents, which makes them polar particles, even though the potential is periodic in the angles ψ_i and ψ_j with a period of π instead of 2π. Therefore, we use the order parameter $\phi = \frac{1}{N}\left|\sum_i \hat{\mathbf{u}}_i\right|$, identical to the Vicsek order parameter, to classify the different types of behaviour that we observe.

3.1   Steady State Behaviour of Elliptical Particles

We investigated the effect of self-propulsion strength and orientational noise on the behaviour of the cluster. We found two distinct types of behaviour, which we will label
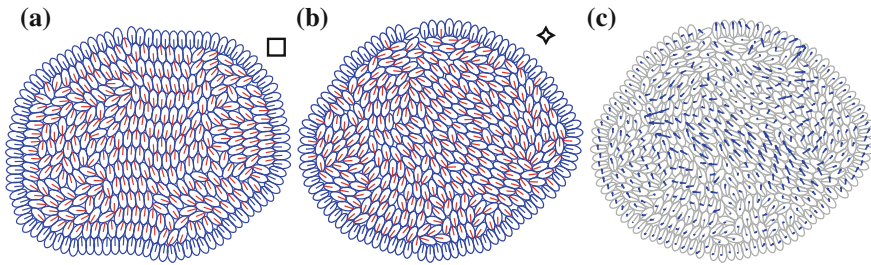
Fig. 2 Typical snapshots. Jammed configuration (**a**). Random configuration (**b**). Overlay of the velocity field of the random configuration shown in **b** (**c**)
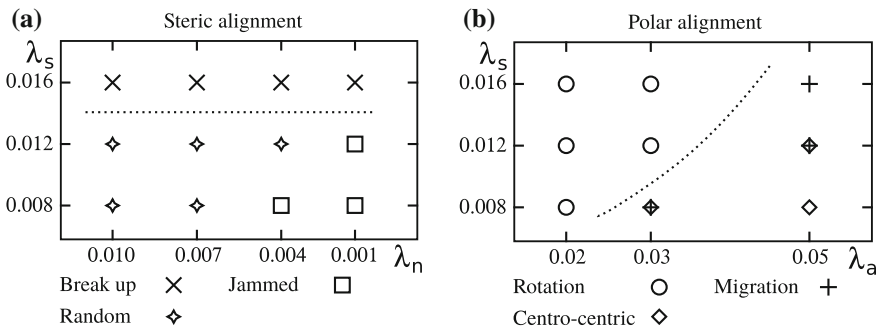
Fig. 3 State diagrams. On the *vertical axis* we increase the self-propulsion speed of the particles, and on the *horizontal axis* we increase the effective alignment between them. We drew *dashed lines* between states that are topologically different. The symbols are shown in Fig. 2 for steric alignment and Fig. 4 for polar alignment, with their phenotypes. Elliptical particles that align through steric repulsion (**a**). Elliptical particles with the polar alignment rule introduced in Sect. 3.3 (**b**)

'jammed' and 'random'. In the jammed state, particles do not rearrange (see Fig. 2a). The order parameter ϕ is constant in time for periods longer than 5 % of the total simulation length and the trajectory of the average position of all particles consists of straight lines or arcs of constant curvature. In the random state the particles swim in small streams contained inside a ring constituted of inward facing boundary particles (see Fig. 2b, c). Particles enter the boundary where the streams hit the boundary. Once they are classified as boundary particles, they turn around and remain part of the boundary until they find a spot where they can enter the bulk again. We observe no global alignment and the value of the order parameter is very low. In short, this state has a mixing dynamics with alignment on short length scales. As a result, the centre of mass of the entire cluster exhibits no net motion.

Not surprisingly, the jammed state occurs when the orientational noise on the particles is low (see Fig. 3a). Introducing increasingly more noise at low or intermediate self-propulsion speeds gradually leads to the random state. For these states to be stable, the self-propulsion speed cannot be too high. A high self-propulsion speed always leads to break-ups into multiple small clusters.

3.2   *Motility of Clusters of Circular Versus Elliptical Particles*

In earlier work [6], we found that clusters of circular particles with a polar alignment rule exhibit four main types of behaviour: clusters that break up (type 1), jammed clusters with strong alignment (type 2), dynamical clusters where particles rotate collectively around a common centre (type 3), and dynamical clusters that migrate collectively (type 4). For the last type, the local alignment results in a global preference for the orientation of the particles. This direction corresponds to the direction of movement of the cluster, which performs a random walk over time.

3.3   *Effects of Polar Alignment and Shape on Collective Dynamics*

In contrast to polar circular particles, that display dynamic, collective behaviour of rotating and migrating clusters, we find that clusters of elliptical particles do not achieve global, collective behaviour. This drastic change can only be caused by two factors. First, the geometry of the particles changes the way the particles can arrange in a cluster. Second, we also disposed of the polar alignment rule. After all, the Gay–Berne potential aligns our particles as well, eliminating the need to put alignment in the system as a separate rule. However, this potential also antialigns the particles. To determine which effect is responsible for collective behaviour, we tested two different scenarios. In the first, we replaced the steric alignment interaction with a polar alignment rule. Consider for example orientations of i and j that differ by an angle ψ_{ij}, such that $\hat{\mathbf{u}}_i \cdot \hat{\mathbf{u}}_j = \cos(\psi_{ij})$, then the torque on particle i is $T_i = T_{\text{align}} \psi_{ij}$. The amplitude of this interaction is T_{align} and we set the strength of the alignment interaction with $\lambda_a = \zeta T_{\text{align}}/(k\mu)$. The second scenario we tested has a two-way alignment, similar to the torque which resulted from the modified Gay–Berne potential, but now for circular particles. For ellipses, the torque depends in a very non-trivial way on the positions of both particles and their orientations. It is impossible to generalise the steric alignment to a two-way alignment for circles. Instead, we choose an alignment torque analogous to the polar alignment rule, but with two stable states, aligned and antialigned. In Fig. 1c, we plot the torque exerted on particle j as a function of its orientation ψ_j. The two-way alignment torque is a good approximation to the steric alignment torque for elliptical particles when particle j is located exactly to the side of particle i. In both cases we fixed $\lambda_n = 0.003$, $\lambda_F = 0.06$, and $\lambda_T = 0.3$ in simulations.

   The results of the first scenario are shown in Figs. 3b and 4. We retrieve many of the observed types of behaviour we saw for circles when we reinstate the polar alignment. We find a collective migration state (see Fig. 4b) and a collective rotation state (see Fig. 4c). For collective migration, the location of the orientational defect dictates the movement. When the defect is near the centre of the cluster, the movement will be very slow. In Fig. 4a, we see that the order parameter for this case is $\phi \approx 0$. We call this specific type of behaviour centro-centric. This state is different from a jammed state
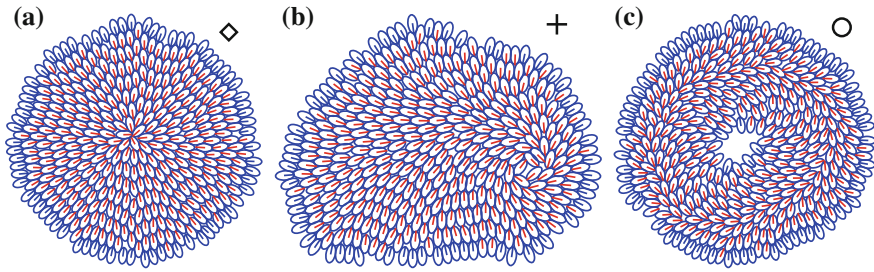
Fig. 4 Typical snapshots of the simulation for ellipses with polar alignment. Alignment towards the centre (**a**). Collective migration (**b**). Rotation (**c**)

because we still observe rearrangements and small variations in the order parameter. For higher speeds the defect moves to the edge. At the highest self-propulsion speed we simulated, a small rotation centre forms in the place of the defect. The collective movement is still in the direction of this rotation centre and is ultimately responsible for a random walk of the cluster. In all cases, the order parameter is significantly lower ($\phi \lesssim 0.3$) than it was for circles ($\phi > 0.3$). Consequently, the absolute speed of the cluster is lower as well.

In agreement with clusters of circular particles, clusters of elliptical particles will rotate for low values of the alignment parameter (see Figs. 3b and 4c). There is a clear difference between rotating and migrating clusters phenotypically. The distinction between centro-centric and actual migration is not as clear. Rather than a sharp boundary between the two types of behaviour, we observe a gradual change, where the order parameter monotonically increases with the alignment and the self-propulsion parameter, λ_a and λ_s, respectively. Compared to steric alignment, the cluster can still break up, but only for large λ_s (not shown in the state diagram). Similarly, the polar alignment system will jam only for large λ_a.

Surprisingly, the two-way alignment rule applied to circular particles (scenario 2) made the steady state behaviour unstable. In all cases, the cluster broke up into multiple clusters. There are two reasons why circular particles with two-way alignment are different from elliptical particles with a steric two-way alignment. First, steric alignment still allows for alignment mismatches. For very little overlap, the exerted torque will also be small. The anisotropic nature of the particles will create overlap with other particles until all torques are balanced. The result will look like Fig. 2a, b, where we observe mismatches that are stable. Circular particles do not create overlap when they rotate, and will therefore always align. Second, the two-way alignment also makes particles turn towards the boundary. If there are more particles pushing out towards the boundary than boundary particles pushing in, the boundary will be pushed out. This will cause the cluster to break up.

4 Conclusion

Anisotropic particles do not automatically swarm with an outsiders-want-in rule. Without polar alignment clusters will break up easily. In addition, for low self-

propulsion speeds the particles may be jammed into a configuration with a long correlation length for alignment, or they only align locally such that the net movement of the cluster effectively averages out. Clusters collectively migrate or rotate when particles align their self-propulsion direction. The elongated shape of the particles decreases the value of the order parameter compared to migrating clusters of circular particles. Consequently, clusters of elliptical particles do not move quite as fast as their circular counterparts. Our model suggests that locally interacting organisms in viscous environments, i.e. unicellular organisms and cells, need to communicate their orientation to collectively move.

References

1. Calovi, D.S., Lopez, U., Ngo, S., Sire, C., Chaté, H., Theraulaz, G.: Swarming, schooling, milling: phase diagram of a data-driven fish school model. New J. Phys. **16**(1), 015026 (2014)
2. Cavagna, A., Del Castello, L., Dey, S., Giardina, I., Melillo, S., Parisi, L., Viale, M.: Short-range interactions versus long-range correlations in bird flocks. Phys. Rev. E **92**(1), 012705 (2015)
3. Collett, M., Despland, E., Simpson, S.J., Krakauer, D.C.: Spatial scales of desert locust gregarization. Proc. Natl. Acad. Sci. **95**(22), 13052–13055 (1998)
4. Czirók, A., Ben-Jacob, E., Cohen, I., Vicsek, T.: Formation of complex bacterial colonies via self-generated vortices. Phys. Rev. E **54**(2), 1791 (1996)
5. Czirók, A., Vicsek, T.: Collective behavior of interacting self-propelled particles. Phys. A Stat. Mech. Appl. **281**(1), 17–29 (2000)
6. van Drongelen, R., Pal, A., Goodrich, C.P., Idema, T.: Collective dynamics of soft active particles. Phys. Rev. E **91**(3), 032706 (2015)
7. Henkes, S., Fily, Y., Marchetti, M.C.: Active jamming: self-propelled soft particles at high density. Phys. Rev. E **84**(4), 040301 (2011)
8. Landau, L., Lifshitz, E.: Fluid Mechanics, vol. 6 (1987). Course of Theoretical Physics, pp. 227–229
9. Rappel, W.J., Nicol, A., Sarkissian, A., Levine, H., Loomis, W.F.: Self-organized vortex state in two-dimensional dictyostelium dynamics. Phys. Rev. Lett. **83**(6), 1247 (1999)
10. Thutupalli, S., Sun, M., Bunyak, F., Palaniappan, K., Shaevitz, J.W.: Directional reversals enable myxococcus xanthus cells to produce collective one-dimensional streams during fruiting-body formation. J. R. Soc. Interface **12**(109), 20150049 (2015)
11. Tunstrøm, K., Katz, Y., Ioannou, C.C., Huepe, C., Lutz, M.J., Couzin, I.D.: Collective states, multistability and transitional behavior in schooling fish. PLoS Comput. Biol. **9**(2), e1002915 (2013)
12. Vasiev, B., Siegert, F., Weller, C.J.: A hydrodynamic model for dictyostelium discoideum mound formation. J. Theor. Biol. **184**(4), 441–450 (1997)
13. Vicsek, T., Czirók, A., Ben-Jacob, E., Cohen, I., Shochet, O.: Novel type of phase transition in a system of self-driven particles. Phys. Rev. Lett. **75**(6), 1226 (1995)
14. Vicsek, T., Zafeiris, A.: Collective motion. Phys. Rep. **517**(3), 71–140 (2012)
15. Weijer, C.J.: Dictyostelium morphogenesis. Curr. Opin. Genet. Dev. **14**(4), 392–398 (2004)
16. Wu, Y., Kaiser, A.D., Jiang, Y., Alber, M.S.: Periodic reversal of direction allows myxobacteria to swarm. Proc. Natl. Acad. Sci. **106**(4), 1222–1227 (2009)
17. Zeravcic, Z., Xu, N., Liu, A., Nagel, S., van Saarloos, W.: Excitations of ellipsoid packings near jamming. EPL (Europhys. Lett.) **87**(2), 26001 (2009)

Capacity Estimation Method of a Waterway Intersection

Xavier Bellsolà Olba, Winnie Daamen, Tiedo Vellinga and Serge P. Hoogendoorn

Abstract The growth of maritime transportation leads to more crowded and intensively used waterways. This research presents a method to estimate the capacity of a waterway intersection. An analogy between roads and waterways is used and the conflict technique is applied to a waterway intersection. The flows in each direction and their conflicting movements lead to the capacity calculation. Data analysis provides insight into vessel behaviour in an intersection. Moreover, the value of the method has been proven with a case study. This is a generic method that can be applied in any waterway intersection based on the conflicts between the different sailing directions in the intersection and the flow shares inferred from empirical data or predictions. Its application can improve traffic management strategies or traffic rules in waterway intersections.

1 Introduction

Maritime transportation is growing and waterways have to handle larger vessels and greater traffic flows. Thus, waterway intersections become intensively used and more crowded for navigation. Port authorities are concerned about the maximum vessel traffic flow that their network and intersections can accommodate, so the central question in this research is: *"How can we determine the capacity of a waterway intersection?"*. Although extensive research to assess risks in ports and waterways has already been performed, there is no existing method to estimate the capacity of waterway intersections.

X. Bellsolà Olba (✉) · W. Daamen · T. Vellinga · S.P. Hoogendoorn
Delft University of Technology, Stevinweg 1, 2628 CN Delft, The Netherlands
e-mail: x.bellsolaolba@tudelft.nl

W. Daamen
e-mail: w.daamen@tudelft.nl

T. Vellinga
e-mail: t.vellinga@tudelft.nl

S.P. Hoogendoorn
e-mail: s.p.hoogendoorn@tudelft.nl

The capacity definition for a waterway intersection, which is different from a whole port, has been recently discussed [1]. This definition, similar to the previously used capacity definition for approach channels [8], considers the capacity as: *"the maximum flow to be handled by a given cross section or location satisfying the requirements on navigation and safety level"*. The number of ships passing the intersection through cross sections in each direction can be compared to the current situation, and it gives insight into the level of utilisation of the intersection.

The objective of this research is to develop a method to estimate the capacity of any waterway intersection. A feasible analogy with road traffic at intersections is used to develop the method. Moreover, Automatic Identification System (AIS) data from an intersection in the Port of Rotterdam is used to validate the method, with a real case study.

The paper starts with a literature review on road intersection theories (Sect. 2). Based on the previous section, a capacity estimation method is developed (Sect. 3). Section 4 presents the Automatic Identification System (AIS) used in vessels. Insights from the AIS data analysis are presented in Sect. 5. The results are presented (Sect. 6) and the document ends with conclusions.

2 Literature Review

Only few research on marine traffic congestion of a whole port has been performed [2, 11]. However, the capacity of an intersection is not influenced by the waiting times or service times that form the basis of these methodologies. As previously introduced, its capacity is determined by the maximum flow that can be sustained by the infrastructure.

Previous research on unsignalised road intersections presented two methods, the gap-acceptance theory [10] and the conflict technique [3]. The first one is based on the definition of a minimum critical gap between vehicles. The driver of the vehicle without priority will accept the gap between vehicles to enter the intersection if the offered gap is larger than his critical gap. However, this method has some drawbacks [4]. The determination of the critical gap is difficult and its estimation is a source of uncertainty. Moreover, this theory will not work well if drivers do not comply with the rules of priority. The second method simplifies the intersection capacity analysis, considering the different flows in each direction and the interaction between them. A total of 28 movements are allowed in a road intersection (vehicles, pedestrians and bicycles) and the conflicting movements can be identified with a conflict matrix. The probability that the intersection is not blocked can be calculated and the capacity of the road intersection is obtained.

3 Capacity Estimation Method

Waterway intersections are similar to unsignalised road intersections, but due to the drawbacks, introduced in the previous section, the gap-acceptance theory is not considered. An analogy between road and maritime traffic, using conflict technique,

is considered as the base to develop a capacity estimation method for waterway intersections.

There are several differences between roads and waterways, as vessels adapt their speed and they do not break or stop in or upstream of an intersection. Moreover, in this approach, all vessels are assumed to have the same priority, no right way priority as in roads, and there is only one waterway user type with high variety in vessel types, with a total of 12 movements. If a vessel is occupying the intersection, no other vessel is allowed to enter. In reality specific vessels might have priority over all the rest, just being allowed to sail alone. Since this situation would reduce the resulting capacity, no specific priorities are considered.

The method is built considering the existence of a minimum safety time clearance to be kept by one vessel from its predecessor, that can be defined as *safe headway* (h_s). Previous research considered the safe vessel braking distance (d_s) as 4 times the vessel length [5, 6]. For sailing in confined waters, d_s is considered to be 3 times the vessel length. Using the vessel safe distance $(d_{s,i})$ and the corresponding speed (v_i), the safe headway for each individual ship $(h_{s,n})$ can be calculated as follows:

$$h_{s,n} = d_{s,i}/(v_i \times 60) \qquad (1)$$

The probability that stream i occupies the intersection $(P_{s,i})$ can be obtained multiplying the maximum traffic volume in stream i (q_i) and the time that a vessel occupies the intersection $(t_{s,i})$ (see Eq. (1)). $t_{s,i}$ is obtained considering an average speed for all ships and the specific distance to cover by each direction inside the intersection.

$$P_{s,i} = q_i \times t_{s,i} \qquad (2)$$

A conflict matrix identifying all movements that, according to the clearance time, cannot occur simultaneously, is used to define the conflict factor between two streams (A_{ij}) (0 if no conflict or 1 if conflict). Then, the probability of conflict (P_c) can be calculated as the sum of the probability of occupying the intersection by stream i, multiplied by the sum of probabilities that another stream occupies the intersection times A_{ij}:

$$P_c = \sum_i \left(P_{s,i} \times \sum_{j \neq i} P_{s,j} \times A_{ij} \right) \qquad (3)$$

The method assumes no overtaking between ships in the intersection. Thus, the mean value of all $h_{s,i}$ can be used to calculate the maximum flow in one direction (q_{1D}):

$$q_{1D} = 1/(h_{s,mean} \times 60) \qquad (4)$$

Finally, the capacity of the intersection (C) can be calculated as follows:

$$C = [1 + (1 - P_c)] \times q_{1D} \qquad (5)$$

4 Automatic Identification System (AIS)

The Automatic Identification System (AIS) was developed by The International Association of Marine Aids to Navigation and Lighthouse Authorities (IALA). AIS is an autonomous and continuous broadcast system, operating in the VHF maritime mobile band [7]. AIS allows automatic exchange of shipboard information from the vessel sensors, including static, dynamic and voyage related data between one vessel and another and between a vessel and the shore stations (see Fig. 1). AIS tracking devices are compulsory since December 1, 2014. The requirement applies to both commercial and recreational navigation on the Rhine canal with a ship of 20 metres or more and also for small professional vessels operating with their own drive [9].

The principal functions of AIS, indicated by IALA [7], are

- Information exchange between vessels within VHF range of each other, increasing situational awareness and safety.
- Information exchange between a vessel and a shore station, such as a Vessel Traffic Service (VTS), to improve traffic management in congested waterways.
- Automatic reporting in areas of mandatory and voluntary reporting.

The most relevant information included in the AIS messages is summarised in Fig. 1. In this table, the information obtained from radar data is also shown.

AIS has different practical applications, such as collision avoidance, vessel traffic services (VTS), maritime security, aids to navigation, search and rescue or accident investigation. Thus, the use of AIS or radar data for research provides the opportunity to develop statistical analysis of accidents, vessel behaviour, etc., which can be performed under different circumstances, including weather, time of the day or year, among others.

Information	AIS	Radar
MMSI number	X	
Length [m]	X	X
Breadth [m]	X	X
Longitude (X coord.)	X	X
Latitude (Y coord.)	X	X
Speed	X	X
Heading	X	X
Course over ground	X	
Draught	X	X
Date / Time	X	X
Vessel type	X	
Navigational status	X	
Track number		X
...		
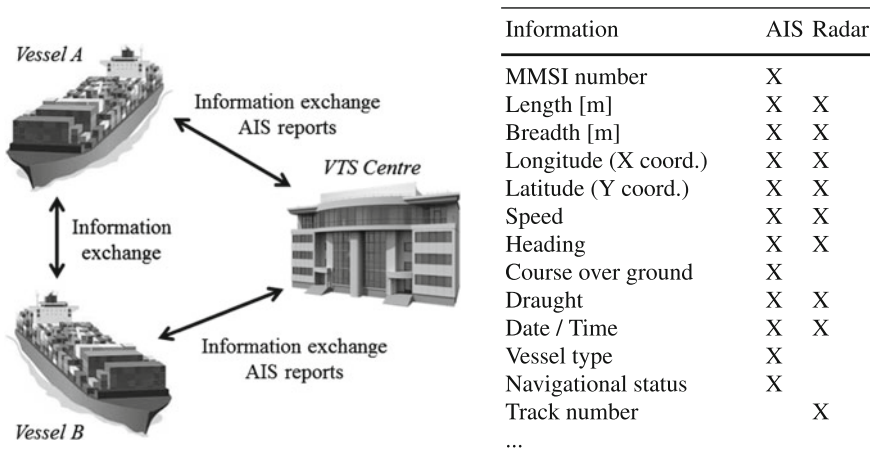
Fig. 1 Details on AIS system (*left*) and AIS and radar information (*right*)

5 Dataset and Research Area

A dataset from the T junction between two waterways, Oude Maas and Hartelkanaal (see Fig. 2), which was provided by the Port of Rotterdam Authority, is used in this research. The chosen intersection is one of the busiest in the Port of Rotterdam.

The dataset contains 7 days of information of both AIS and radar data. The Port of Rotterdam has radar stations all along their waterways, which is really useful in this case since not all the inland vessels are AIS-equipped. The total amount of ships just from AIS data would be underestimated. The dataset contains all the signals with Radar data, but only 62 % of these signals have AIS details. For this reason, the radar data has been used for the analysis. The differences in the dynamic variables (speed, latitude, longitude, etc.) are minimum between AIS and radar data. In specific cases there are large differences that might be due to problems with the AIS or the radar signal. As introduced in the previous section, Fig. 1 shows the differences in content between AIS and radar data.

The minimum interval between consecutive signals from a vessel is 5 s, for both AIS and radar, and the dataset has almost half a million messages recorded from 5209 different vessels. These vessels might make repeated visits during the period in different days or times of the day. Each record consists of a coordinate point in the area and the tracks are obtained by joining each of these points for each vessel.

From the whole dataset, almost 70 % of the messages are from moored vessels, which leaves 3395 vessel individual tracks. 66 % of these trips have a whole track going from one of the entrances of the intersection to another one (see Fig. 3a). The rest of the data are partial tracks with few signals and do not provide enough information for their analysis.

Correlations between vessel dimensions and their speeds or headways might be expected in vessel navigation in a port. However, the data revealed that no corre-

Fig. 2 Research area (Port of Rotterdam)
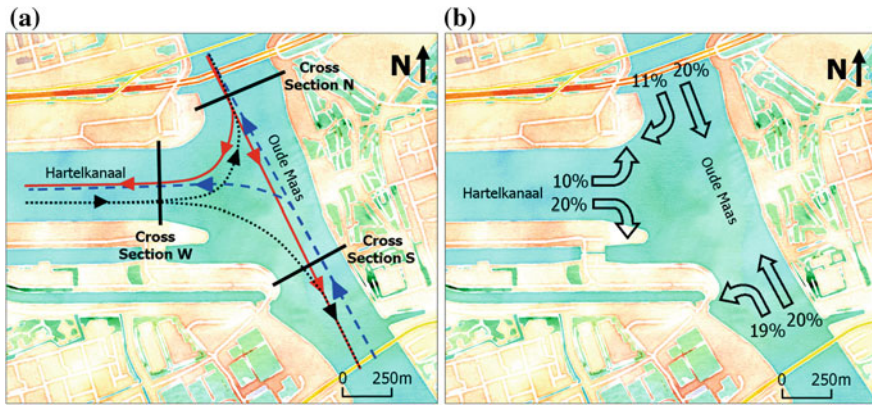
Fig. 3 Waterways intersection map: vessel paths (**a**); traffic shares (**b**)

lation exists between speed or headway (passing time interval with respect to the predecessor) and length or breadth of the vessels. The assumption in the estimation method, previously introduced, which considered an average speed for all vessels to calculate the intersection occupation time, can be accepted.

6 Case Study Results

In order to validate the applicability of the estimation method presented in Sect. 3, it has been applied in the research intersection and the results are presented in this section.

First, the safe headway is calculated for each vessel ($h_{s,i}$) and it is compared to the actual one (h_i). More than 95 % of h_i are higher than $h_{s,i}$, and some of the lower ones occur due to overtaking situations. Based on this, the authors consider h_s to be a suitable variable to calculate the vessel flow.

The method assumes a unique speed for all vessels to calculate $h_{s,i}$. Due to the heterogeneous traffic flow and their variety of speeds, even during peak times, the flow is considered to be heterogeneous. Hence, a vessel speed of 8 knots is used, based on the average speed results from the data, to calculate $h_{s,i}$. Then, $h_{s,mean}$ is obtained as the average of all the individual $h_{s,i}$, which is equal to 1.20 min. By using $h_{s,mean}$ in Eq. (4), q_{1D} equals 49.9 vessels per hour (ves/h). This value is based on the assumption of regular vessel arrivals, but in reality the arrival is mostly stochastic and uncontrolled. However, in case of considering stochastic arrivals, q_{1D} would result in a lower value and the resulting capacity would be underestimated. Figure 3a shows the possible movements from each direction. This helps to identify the conflicting movements between directions and to build a conflict matrix for this intersection (see Table 1). The traffic shares for each direction, obtained from the dataset, are shown in Fig. 3b.

Table 1 Conflict matrix

Direction	NS	NW	SN	SW	WN	WS
NS		1	0	1	1	1
NW			0	1	0	0
SN				1	1	0
SW					1	0
WN						1
WS						

The time that a vessel is occupying the intersection is calculated based on the following conditions. The intersection length is defined for each direction, according to Fig. 3a, and the space occupied from a conflicting vessel is considered to be half of this length. Since no differences in speed regarding the direction exist, a speed of 8 knots is considered to calculate $t_{s,i}$. Considering this occupation time and the different shares per direction, the flows and conflict probabilities for each direction are obtained (see Table 2). P_c is obtained from the sum of all $P_{c,i}$ and equals 0.59. Finally, the resulting capacity of the studied intersection (C) is 70.2 ves/h.

In order to assess the validity of the capacity obtained, it can be compared with the maximum observed vessel flow, which can be calculated from empirical data using a 6 min interval of time. For this interval, there are several maximum flows of 6 vessels, except one peak of 7, but this can be considered an outlier result due to the interval boundaries. With that, the maximum flow is 70 ves/h. This result is close to the value obtained with the estimation method and suggests the feasibility of the method.

Another indicator to assess the reliability of the obtained result is the total number of vessels that can be found at the same time instant inside the research area. The dataset reveals that, for the week of data, the maximum amount of vessels present is 10 and the estimation method results in 10.9 vessels, on average. Based on experts opinion from the Port of Rotterdam Authority, the peak times in this intersection might not allow more vessels at the same time, which proves that the estimated capacity is a useful threshold.

Table 2 Probability of conflict per direction

Direction	Share (%)	q [ves/h]	$t_{s,i}$ [min]	$P_{s,i}$	$P_{c,i}$
NS	20	10.1	1.52	0.26	0.15
NW	11	5.6	0.74	0.07	0.03
SN	20	10.0	1.52	0.25	0.08
SW	19	9.2	1.41	0.21	0.15
WN	10	5.0	1.38	0.11	0.10
WS	20	10.1	1.16	0.20	0.07

7   Conclusion

A generic method to estimate waterway intersection capacity has been developed. The background of this method is the conflict technique, previously developed for road traffic. An analogy between road and waterway traffic helps to develop the method that identifies the conflicting interactions between vessel movements that occur in an intersection. The result of the method provides the maximum amount of vessels passing the intersection in a time period, e.g. an hour, assuming that we have a perfect and independent arrival of vessels.

The case study shows that the current maximum vessel flow is almost the same as the capacity calculated with the method, which proves the validity of the method. Hence, the estimated value can be used to assess and improve current traffic management strategies or some traffic rules, looking for a traffic optimisation in the intersection.

In future work, the capacity of other port intersections will be estimated in order to assure the usefulness of the method and its generic applicability. Weather conditions as current or wind effects will also be considered in further research.

References

1. Bellsolà Olba, X., Daamen, W., Vellinga, T., Hoogendoorn, S.P.: An approach to port network capacity. In: International Workshop on Nautical Traffic Models, IWNTM 2014, Wuhan, China, pp. 104–113 (2014)
2. Bellsolà Olba, X., Daamen, W., Vellinga, T., Hoogendoorn, S.P.: Estimating port network traffic capacity. Sci. J. Marit. Univ. Szczec. **42**(114), 45–53 (2015)
3. Brilon, W., Miltner, T.: Capacity at intersections without traffic signals. Trans. Res. Rec. J. Trans. Res. Board **1920**, 32–40 (2005)
4. Brilon, W., Wu, N.: Capacity at unsignalized intersections derived by conflict technique. Trans. Res. Rec. J. Trans. Res. Board **1776**, 82–90 (2001)
5. Fujii, Y., Tanaka, K.: Traffic capacity. J. Navig. **24**(4), 543–552 (1971)
6. Goodwin, E.M.: A statistical study of ship domains. J. Navig. **28**(03), 328 (1975)
7. International Association of Maritime Aids to Navigation and Lighthouse Authorities (IALA): Guidelines on Automatic Identification System (AIS) (2004)
8. PIANC: Harbour approach channels design guidelines (2014)
9. Rijkswaterstaat: Traffic information: AIS (2015)
10. Troutbeck, R.J., Brilon, W.: Unsignalized intersection theory. In: Traffic-flow theory. Transportation Research Board Special Report 165 (1997)
11. Yeo, G.T., Roe, M., Soak, S.M.: Evaluation of the marine traffic congestion of north harbor in busan port. J. Waterw. Port Coast. Ocean Eng. **133**(2), 87–93 (2007)

Granular Flow to a Blast Iron Ore Furnace: Influence of Particle Size Distribution on Segregation of a Mixture

Dingena Schott, Wouter Vreeburg, Carmen Molhoek and Gabriel Lodewijks

Abstract The infeed ofThe material in a blast furnace isThe composed of a mixtureThe of three different materials: sinter, iron ore pellets and coke. They are each very different in shape, size and mechanical properties and likely this promotes segregation, an unwanted effect. However up till now it is not clear to what extent the Particle Size Distribution (PSD) of each of the three components affects the homogeneity. This work aims to assess the influence of particle size distributions of the individual components on the homogeneity of the infeed material by Discrete Element Model (DEM) Simulations. It can be concluded that modelling the PSD of the individual components is not required to model the tendency to segregate of the mixture of iron ore pellets, sinter and coke. Representing each of the materials by its mean particle size d50 reduces the number of particles and simulation time drastically without compromising the simulation results of the used material models.

1 Introduction

In the steel making process raw materials such as ores and additives are fed into a blast furnace. For an optimum performance of a blast furnace the homogeneity of the infeed material is important to ensure constant chemical reactions. This means that segregation is an unwanted effect.

A schematic of a blast furnace of Tata Steel is shown in Fig. 1. In the stockhouse a mixture of three materials (sinter, pellets and coke) is charged into a skip hoist, which is elevated and emptied into one of the top bins. From the top bins the mixture

D. Schott (✉) · W. Vreeburg · C. Molhoek · G. Lodewijks
Department of Maritime and Transport Technology, Delft University of Technology,
Mekelweg 2, Delft, The Netherlands
e-mail: D.L.Schott@tudelft.nl

W. Vreeburg
e-mail: W.P.J.Vreeburg@student.tudelft.nl

C. Molhoek
e-mail: C.P.Molhoek@student.tudelft.nl

G. Lodewijks
e-mail: G.Lodewijks@tudelft.nl
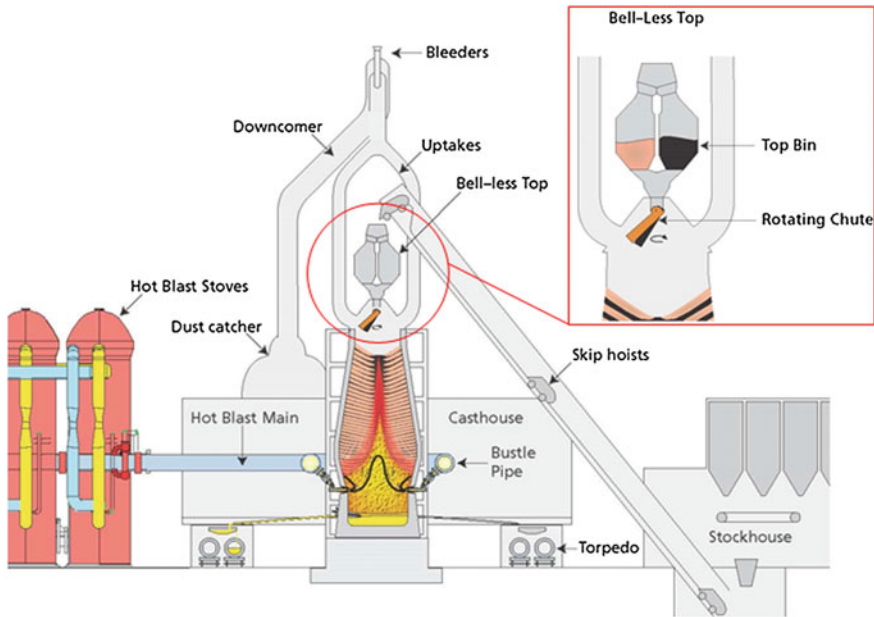
Fig. 1 Schematic for feeding the blast furnace for steel making (*source* Tata Steel)

is fed into the furnace with a rotating chute, to equally spread the materials in the oven as much as possible. It is generally known and well described in literature (e.g. [5]) that segregation is likely to occur when a mixture of different sized components with different densities is in movement.

Here, segregation can occur at several process steps such as during hoisting of the skips (vibratory segregation), feeding of the top bins and blast furnace (trajectory segregation and percolation segregation). The three different materials (sinter, pellets and coke) are very different in shape, size and mechanical properties and likely to promote segregation. However, up to now it is not clear to what extent the Particle Size Distribution (PSD) of each of the three products affects the homogeneity.

Therefore, this work aims to assess the influence of Particle Size Distributions of the individual components on the homogeneity of the infeed material. For this purpose a Discrete Element Model was built as it allows to model individual particles with different properties representing different materials. After calibration of the material properties for each individual material the effect of the PSD on segregation is assessed.

2   Material Properties

The materials that are used in this research are sinter, iron ore pellets and coke. As can be seen from Fig. 2, the surface roughness of the materials is different as well as the shape. The mean particle sizes, the PSD and densities differ as well. The

Fig. 2 The materials: sinter [1] (**a**); Iron ore pellets [6] (**b**); Coke [2] (**c**)

Table 1 Averaged measured angle of repose (95 % confidence interval)

	Sinter	Pellets	Coke	Mix
No. of tests	5	5	7	4
Angle of repose	21.8	20.1	25.0	18.4

mean particle diameter (d50) is 12.8 mm for sinter, 11.1 mm for iron ore pellets and 22.1 mm for coke.

The angle of repose (AoR) of each of the materials was tested with a laboratory set-up. The test was also performed on the mix of material that is fed in the blast furnace with a ratio of sinter:pellets:coke of 10:20:1 ton. For every material a number of tests were performed to achieve an interval that contains, within a 95 % confidence interval, the true mean (Table 1).

3 Discrete Element Method (DEM) Model

A model of the laboratory set-up was made to simulate the performed laboratory tests and to calibrate the materials.

3.1 Particle Modelling

To model the particle–particle interaction and the particle–geometry interaction the Hertz-Mindlin contact model with RVD was used in EDEM®Academic 2.6.1.

For sinter and coke particles an irregular shape is chosen (Fig. 3), while iron ore pellets were modelled as a sphere as they are roughly spherical in reality. Due to the use of irregular shaped particles the rolling friction does not play an important role in simulations and can be eliminated in the calibration simulations for sinter and coke. The maximum diameter of these particles is set equal to their respective d50.

The particle properties were chosen based on used values in previous research, available documentation and based on experience of the authors. The sliding friction coefficient is calibrated using a laboratory test set-up described in the next section.

Fig. 3 Shapes of the
particles: irregular particle
shape for coke and
sinter (**a**); spherical particle
representing iron ore pellets
(**b**)
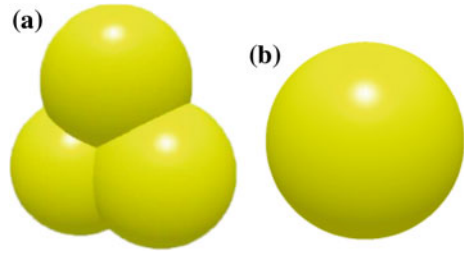
3.2 Test Set-Up

The laboratory tests were performed in a hard plastic cylinder, with a circular hole
in the flat bottom where the material is flows through after two doors blocking the
funnel are opened at high speed and the material drops in another cylindrical box
(Fig. 4). The linear rotation speed (30 rad/s), its duration (0.1 s) and total rotation
(3 rad) are chosen such that the material is first settled before the doors open at 0.8 s.
The total simulation time was 4 s. The Poisson ratio of the set-up was chosen as
0.3, the shear modulus 70 GPa and the material density as 1500 kg/m^3. Based on
experience, these properties have negligible influence on the results.

Calibration was performed by measuring the angle of repose of the individual
materials and the mixture in the lower bin, both in the laboratory set-up and in the
simulation package EDEM®Academic 2.6.1 (Fig. 4). The mixture is created with
the ratio 20:10:1 for iron ore pellets, sinter and coke on a mass basis, as in practice.

The final sliding friction coefficients were 0.45 (iron ore pellets), 0.3 (sinter), 0.2
(coke) and 0.1 (mixture, interaction between components). For these values good
matches between the angle of repose found in experiments (Table 1) and simulations
with a percent error <3 % were obtained.

Fig. 4 Experimental set-up
with example calibration
results (*right*). DEM model
of the experimental set-up
for determining the angle of
repose (**a**), sinter (**b**), coke
(**c**), iron ore pellets (**d**),
mixture (**e**)
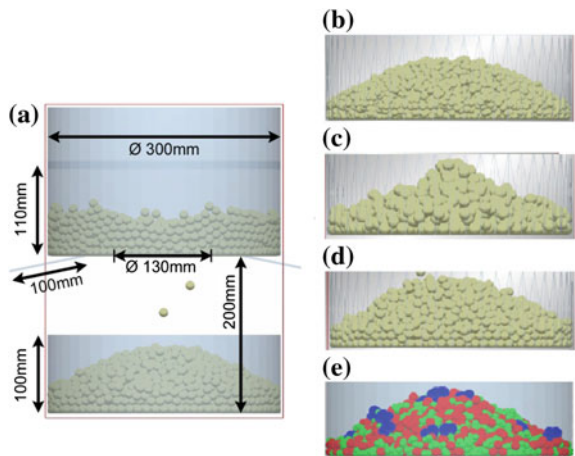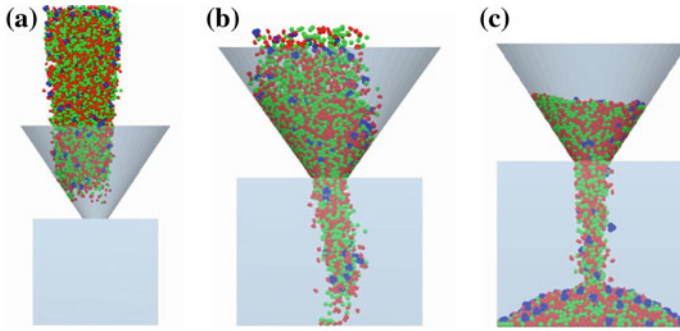
Fig. 5 Segregation test set-up Asymmetric filling of the cone (**a**); start of flow towards receiving box (**b**); cone build up in receiving box (**c**)

4 Segregation Test Set-Up

The set-up for testing the difference in segregation of the mixture with and without PSD consists of a rectangular box and a cone (Fig. 5). The materials enter the cone asymmetric to create movement and to promote segregation. The dimensions of the box are 500 × 150 × 400 mm (width × depth × height). The simulated time is 3 s.

Both mixes (with and without PSD) are created with the ratio sinter, iron ore pellets and coke as 10:20:1.

4.1 Material Mix—Without PSD

The simulations without PSD have 6 kg of sinter, 12 kg of iron ore pellets and 0.6 kg of coke as the total created mass in EDEM. The particles were modelled according to the mean particle size as specified in Table 1. The total number of generated particles was 7000 and computational time of these simulations without PSD was around 20 min.

4.2 Material Mix—with PSD

The given particle size distributions contained a PSD of 6–8 intervals. Using the whole range of particle size in the simulations will lead to unacceptable long computational times. The cause is mainly the simulation grid size which relates to the smallest particle size. To keep the computation times acceptable the PSD were converted to 4 sizes of the material for all three materials while the d50 was kept the same.

In addition, to decrease the computational time further, the amount of material was limited to 5 kg of sinter, 10 kg of pellets and 0.5 kg of coke. The total number of generated particles was 22500, and the computational time of the simulations with PSD rose from 20 min to 10–12 h. As said this rise is caused by the smallest particle size and the number of particles in the simulation.

4.3 Analysis Method

Existing mixing indices focus mostly on binary mixtures [3] and triangular diagrams [4] are generally used for determining chemical components and not for a weight based prescribed mixing ratio as is the case within this work. Therefore, a custom made approach was developed to analyse the results.

The receiving box is equipped with a grid of $8 \times 3 \times 7$ (width $\times$ depth $\times$ height) bins (Fig. 6). From these bins the composition of the mixture was extracted and compared with the initial mixing ratio of 10:20:1. The figure illustrates percolation segregation: the largest particles (coke) will remain on top of the slope whilst the smaller particles fill the voids while moving down the slope.

The masses in each bin are exported to Excel2010. When dividing the mass of sinter, iron ore and coke by the mass of coke in that particular box, the ratio of the materials in that box is obtained. When dividing these obtained ratios by the ratio in which the material enters the simulation (10:20:1), it can be seen which material is over populating the bin, which material is not or if the mixture is good. For example: when an end-ratio of 1:1:1 is obtained, the mixture is perfect. When an end-ratio of 2:1:1 is obtained there is twice as much sinter in that bin.

It is also possible to obtain a ratio of for example 10:10:1, indicating there is 10 times as much iron ore and 10 times as much sinter. There is no overpopulation from one material, only a low presence of another. In this research it is chosen to treat this too as a 'good' mixture.

When there is no coke present in a bin, the amount of iron ore is divided by sinter and multiplied by 10. For sinter the other way around: sinter / iron ore $\times$ 20. This
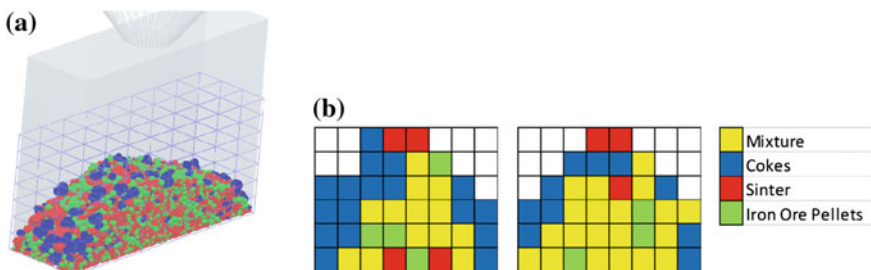
Fig. 6 Receiving box after settlement of materials: grid bins in receiving box for analysing purposes (**a**); examples of results, showing mixture or predominant components (**b**)

gives the ratio compared to each other. When only one material is present, the ratio will be for example 0:1:0.

If the mixture is within the set limit of the prescribed mixture ratio the bin colours yellow, otherwise it shows which material dominates the bin (Fig. 6 right). This was done for each of the 3 slices in depth direction and each simulation was repeated 4 times. From the visualisation the percentage of bins with dominant presence of materials was calculated. In absence of a definition for 'good mixture' two definitions were used for the ratio sinter, iron ore pellets and coke: (1) a wide range 5..20:10..40:1 and (2) narrow range 8..12:16..24:1.

5 Results

The results of modelling a mixture of coke, sinter and iron ore with or without their respective particle size distributions is shown in Figs. 7 and 8. The figures show the mean values of 12 data points with their 95 % confidence intervals for two different 'good mixture' definitions.

When using the narrow range definition there seems to be an effect of including the PSD when looking at the mixture (first bars), as the average of the 12 data points is 9 % lower. However looking at the dominance of individual components this is not significant as the confidence intervals overlap.

As expected a wider range for the definition of 'good mixture' leads to a higher percentage of bins in which the mixture can be called 'good'. This is because it is more unlikely for an individual component to dominate a cell. The average values of the mixture modelled with and without PSD differ 9 %, however the confidence intervals do overlap, and a significant effect of modelling the PSD cannot be shown.

It can be concluded that, with the given model, the results of modelling the individual components with PSD are not significantly different from modelling without PSD, i.e. mono sized particles with their respective d50.

Fig. 7 Percentage of bins with predominant presence of materials as a result of modelling with and without PSD, for the narrow 'good mixture' definition
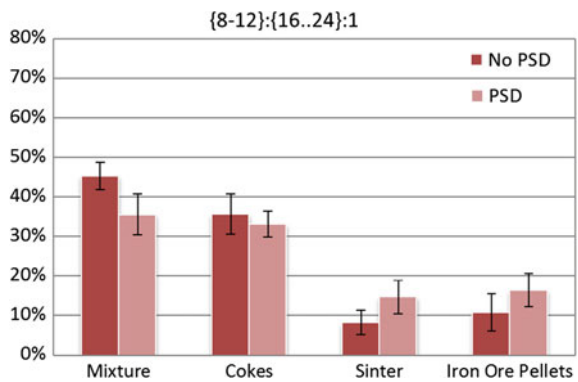
Fig. 8 Percentage of bins with predominant presence of materials as a result of modelling with and without PSD, for the wide 'good mixture' definition
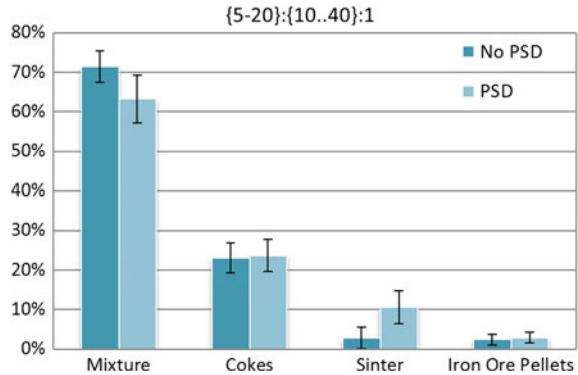
6 Conclusion

Modelling the PSD of the individual components is not required to model the tendency to segregate of the mixture of iron ore pellets, sinter and coke. Representing each of the materials by its mean particle size d50 reduces the number of particles and simulation time drastically without compromising the simulation results of the used material models.

Further work should include (1) recalibration of the material model with PSD, and then analyse the effect once more, (2) studying the effect of the full range of PSD, including the smallest real size particles, (3) studying the effect of the domain size and (4) influence of wall material parameters. To be sure the DEM model accurately represents segregation of this mixture in practice validation is required. However this model can be used for a first investigation of the material behaviour, settlement and segregation in a blast furnace.

References

1. DK Recycling und Roheisen: Sintering Plant, http://www.dk-duisburg.de/en/prozess/sinteranlage.html (2015). Accessed 12 Mar 2015
2. Hua-An Group: Metallurgical Coke, http://www.sinohuaan.com/profiles.html (2015). Accessed 12 Mar 2015
3. Rhodes, M.: Introduction to Particle Technology. Wiley (1998)
4. Rousseau, R.: Handbook of Separation Process Technology. Wiley (1987)
5. Schulze, D.: Powders and Bulk Solids. Springer (2008)
6. Wikimedia Commons: Category: Iron Ore Pellets, https://commons.wikimedia.org/wiki/Category:Iron_ore_pellets (2015). Accessed 12 Mar 2015

Two-Channel Partially Coupled Exclusion Process with Mutually Interactive Langmuir Kinetics

Arvind Kumar Gupta

Abstract In this work, we investigate an open system comprised of two-parallel TASEP under partially asymmetric coupling conditions incorporating the mutual interaction with the surrounding environment through Langmuir Kinetics in both the channels. Motivated by the recent finding on clustering of motor proteins on microtubules, the attachment and detachment rates are assumed to be dependent on the state of the neighbouring sites. Under the mean-field assumption, the hydrodynamic equations representing the evolution of particle density is studied and steady-state phase diagrams are obtained. The effect of mutually interactive Langmuir Kinetics (MILK) on the phase diagram is discussed for two different situations. For symmetric MILK, the topological structure of the phase diagram remains preserved; while for the antisymmetric MILK, significant changes are observed in the qualitative nature of phase diagram. Monte Carlo simulations are performed to validate the theoretical findings.

1 Introduction

Recently, non-equilibrium systems involving particles movement in a preferred direction [12] have been comprehensively studied because of very rich dynamical and steady-state behaviour [3]. In last few decades, the collective dynamics of intracellular transport is studied by a paradigmatic model namely totally asymmetric simple exclusion process (TASEP) [7], in which particles follow hard-core exclusion principle with certain preassigned rules. A two-channel open TASEP has been found to describe some complex non-equilibrium phenomena [10].

An important class of TASEP with particle attachment and detachment in bulk (Langmuir Kinetics), having applications in intracellular transport [6], has gained much attention. Single-channel TASEP coupled with LK [8] has been studied comprehensively, which shows significantly different dynamics in comparison to TASEP

A.K. Gupta (✉)
Department of Mathematics, Indian Institute of Technology Ropar,
Rupnagar 140001, India
e-mail: akgupta@iitrpr.ac.in

without LK. The outcomes of competition between boundary and bulk dynamics result in features such as phase coexistence and localisation of shocks etc.

Recent experimental studies, also supported by simulation results, have shown that motor proteins such as kinesin-1 interact with each other through short range weak attractions [11]. To understand the important role of weakly interactive motor proteins [1], two distinct methods viz. mean-field and modified cluster mean-field approach [2] have been used with and without LK, respectively. Lately, Vuijk et al. [13] has studied one-dimensional TASEP coupled to mutually interactive LK (MILK) while hopping rates were kept unaffected.

There are various multi-channel transport processes such as vehicular traffic and motor proteins [6]. In literature, two-lane TASEP with [4, 5] and without LK [10] have been studied thoroughly, but the important aspect of mutual interaction is not considered so far. The aim of this work is to explore the consequences of MILK on two-channel asymmetrically coupled TASEP, in which particles can shift between both the channels with unequal rates. The role of symmetry of interaction in LK on the stationary dynamics of the system is explored.

2 Model Description

We define an open system of two identical and parallel 1-D lattice channels with N sites, represented by A and B. Particles are inserted into the system under hard-core exclusion principle which move unidirectionally to the right (Fig. 1).

The state of any site is defined by a discrete occupation number $\tau_{i,j}$ ($i = 1, 2, \ldots, N$); $j = (A, B)$ which is either one (occupied site) or zero (vacant). At site $i = 1$, a particle can enter into the system with rate α if $\tau_{1,j} = 0$ while at site $i = L$, a particle can leave the system with rate β provided $\tau_{L,j} = 1$. In the bulk ($1 < i < N$) if $\tau_{i,j} = 0$, a particle attaches to the site with attachment rate $\gamma^\ell \omega_a$. On the other hand if $\tau_{i,j} = 1$, then particle firstly tries to leave the system with detachment rate
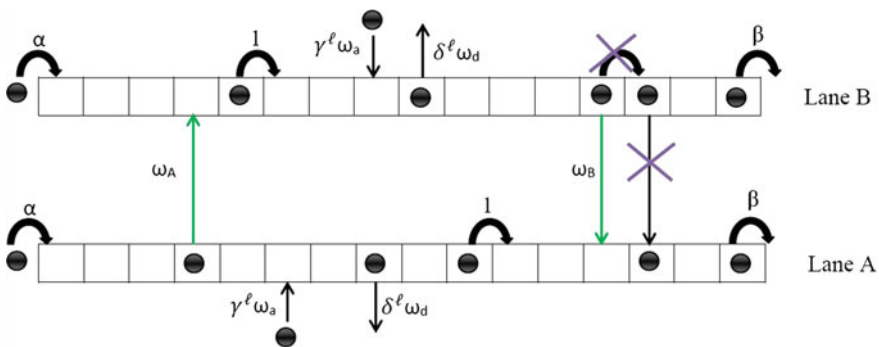
Fig. 1 Schematic diagram of the model. *Crossed arrows* indicate the forbidden transitions
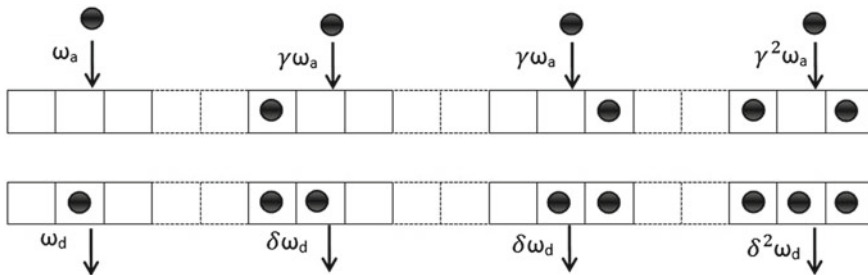
Fig. 2 Schematic diagram of mutually interactive Langmuir Kinetics (MILK)

$\delta^\ell \omega_d$. If fails to do so then it moves to the next site provided $\tau_{i+1,j} = 0$. However, if forward movement is also not possible then particle in channel A (lane B) shifts to lane B (lane A) with rate $\omega_A (\omega_B)$. The modified LK dynamics at site (i, j) depend on the state of nearest-neighbouring sites as shown in Fig. 2. Here, the parameter ℓ is a non-negative integer which represents the strength of the modifying factors of attachment/detachment rates.

The temporal evolution of bulk particle densities $(1 < i < N)$ in both the channels $(j = A, B)$ is given by the following master equation:

$$
\begin{aligned}
\frac{d\langle \tau_{i,j} \rangle}{dt} &= \langle \tau_{i-1,j}(1 - \tau_{i,j}) \rangle - \langle \tau_{i,j}(1 - \tau_{i+1,j}) \rangle + \omega_a \langle (1 - \tau_{i-1,j})(1 - \tau_{i,j})(1 - \tau_{i+1,j}) \rangle \\
&+ \gamma \omega_a \langle (1 - \tau_{i,j})[(1 - \tau_{i+1,j})\tau_{i-1,j} + (1 - \tau_{i-1,j})\tau_{i+1,j}] \rangle \\
&+ \gamma^2 \omega_a \langle \tau_{i-1,j}(1 - \tau_{i,j})\tau_{i+1,j} \rangle - \omega_d \langle \tau_{i,j}(1 - \tau_{i-1,j})(1 - \tau_{i+1,j}) \rangle \\
&- \delta \omega_d \langle \tau_{i,j}((1 - \tau_{i-1,j})\tau_{i+1,j} + (1 - \tau_{i+1,j})\tau_{i-1,j}) \rangle \\
&- \delta^2 \omega_d \langle \tau_{i-1,j}\tau_{i,j}\tau_{i+1,j} \rangle \mp \omega_A \langle \tau_{i,A}\tau_{i+1,A}(1 - \tau_{i,B}) \rangle \\
&\pm \omega_B \langle \tau_{i,B}\tau_{i+1,B}(1 - \tau_{i,A}) \rangle.
\end{aligned}
\tag{1}
$$

where $\langle ... \rangle$ denotes the statistical average and last two terms on right hand side take negative (positive) and positive (negative) sign for channel $A(B)$. At boundaries $(i = 1, N)$, particle densities evolve as:

$$
\begin{aligned}
\frac{d\langle \tau_{1,j} \rangle}{dt} &= \alpha \langle (1 - \tau_{1,j}) \rangle - \langle \tau_{1,j}(1 - \tau_{2,j}) \rangle \\
\frac{d\langle \tau_{N,j} \rangle}{dt} &= \langle \tau_{N-1,j}(1 - \tau_{N,j}) \rangle - \beta \langle \tau_{N,j} \rangle.
\end{aligned}
\tag{2}
$$

Firstly, we factorise correlations using mean-field approximation and then find the continuum limit of model by coarse-graining the lattice with lattice constant $\epsilon = 1/N$ and rescaling the time $t' = t/N$. To observe competing interplay between boundary and bulk dynamics, we define $\Omega_a = \omega_a N$, $\Omega_d = \omega_d N$, $\Omega_A = \omega_A N$ and $\Omega_B = \omega_B N$. For a larger system size (i.e. $N >> 1$), we replace the discrete number $\tau_{i,j}$ by a continuous variable $\rho(x, t) \in [0, 1]$ with $x = i/N$ and get the following system for average densities after ignoring subscript i.

$$\frac{\partial}{\partial t'}\begin{bmatrix}\rho_A \\ \rho_B\end{bmatrix} + \frac{\partial}{\partial x}\begin{bmatrix}-\frac{\epsilon}{2}\frac{\partial \rho_A}{\partial x} + \rho_A(1-\rho_A) \\ -\frac{\epsilon}{2}\frac{\partial \rho_B}{\partial x} + \rho_B(1-\rho_B)\end{bmatrix} =$$
$$\begin{bmatrix}\Omega_a(1-\rho_A)(1+\rho_A(\delta-1))^2 - \Omega_d\rho_A(1+\rho_A(\gamma-1))^2 \\ -\Omega_A\rho_A^2(1-\rho_B) + \Omega_B\rho_B^2(1-\rho_A) \\ \Omega_a(1-\rho_B)(1+\rho_B(\delta-1))^2 - \Omega_d\rho_B(1+\rho_B(\gamma-1))^2 \\ +\Omega_A\rho_A^2(1-\rho_B) - \Omega_B\rho_B^2(1-\rho_A).\end{bmatrix} \quad (3)$$

Here, ρ_A and ρ_B represent the average density in channel A and channel B, respectively, while the right hand side denotes the non-conservative terms formed by the combination of lane changing transitions and MILK.

3 Phase Diagrams and Density Profiles

To examine the effect of MILK on the steady-state properties, we derive phase diagrams for two different cases by using the approach proposed in [5] restricting to a special choice $\Omega_a = \Omega_d$. Firstly, in the symmetric case, attachment and detachment rates are enhanced or reduced simultaneously and its effect on the phase diagram is examined. The second case deals with the antisymmetric LK rates in which if attachment rate is enhanced (reduced) then the detachment rate is reduced (enhanced) by the same factor. The fully asymmetric coupling between the channels makes the steady-state dynamics non-trivial in contrast to a symmetrically coupled two-channel TASEP with LK which is similar to two independent single-channel TASEP with LK [5]. MCS are performed to validate the results obtained from continuum mean-field equations. To minimise the boundary effects, a lattice of size $L = 1000$ is used and the simulations are carried out for 10^{10} time steps. Additionally, to ensure the occurrence of a steady state, the first 5 % steps are ignored and the densities are computed by taking time averages over an interval of $10L$.

3.1 Case 1: Symmetric MILK

In the case of symmetric modified LK, we choose $\gamma = \delta = 1 + \theta$. Based on the configuration of neighbouring sites, both attachment and detachment rates are modified symmetrically. Since $\theta \leq -1$ leads to negative rates, we restrict to the case $\theta > -1$. For $\theta = -1$, the well examined case of Ref. [4] can be retrieved. θ represents the strength of the mutual interaction due to LK dynamics and $\theta > 0$ enhances the LK dynamics provided the neighbouring sites are occupied and vice versa. Figures 3a–d show the phase diagrams for different values of θ. Clearly, six distinct stationary phases exist, viz. (LD, LD), (LD, S), (LD, HD), (S, S), (S, HD), and (HD, HD) for $\theta = 0$ (see Fig. 3a). As θ increases, the number of phases reduces form six to five with a quick (slow) disappearance (shrinkage) of (HD, HD) ((LD, LD)) phase; while
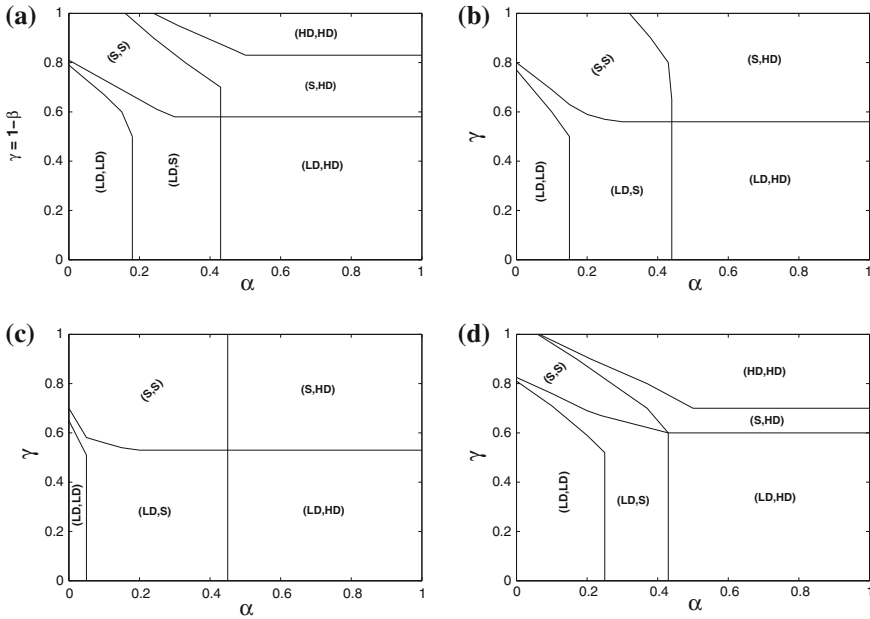
Fig. 3 Phase diagrams for $\Omega_A = 0.8$, $\Omega_B = 0.2$ and $\Omega_d = 0.2$ (a); $\theta = 0$ (b); $\theta = 0.5$ (c); $\theta = 2.0$ (d); $\theta = -0.5$. LD, HD and S denote Low Density, High Density and Shock phase, respectively

$\theta < 0$ keeps the topology of the phase diagram intact. This is due to the higher probability of occupied neighbouring sites for higher θ which leads to more detachments (attachments) in HD (LD) phase. The density profiles of different phases obtained from continuum mean-field equations are found to be in good agreement with MCS (except near the boundary layer due to the finite size effect) as shown in Fig. 4 with $\theta = 2.0$. Importantly, the density profiles in both the channels, regardless of the phase, approach to Langmuir isotherm as θ increases and ultimately we get i.e. $\rho_A = \rho_B = 1/2$ as $\theta \to \infty$.

3.2 Case 2: Antisymmetric MILK

In the previous case, we studied the effect of modified LK rates in which MI enhanced or reduced simultaneously the LK dynamics. This is in contrast to the attractive interaction seen in kinesins-1 in an in vitro experiment [11]. In this case, the proposed model is analysed to understand the coordination mechanism under the existence of attractive interactions. The LK rates are modified in an antisymmetric manner where the attachment (detachment) rate is enhanced (reduced) and vice versa. To do so, we set $\gamma = 1 + \phi$ and $\delta = 1 - \phi$ where $\phi \in [-1, 1]$ is a constant. Here, positive
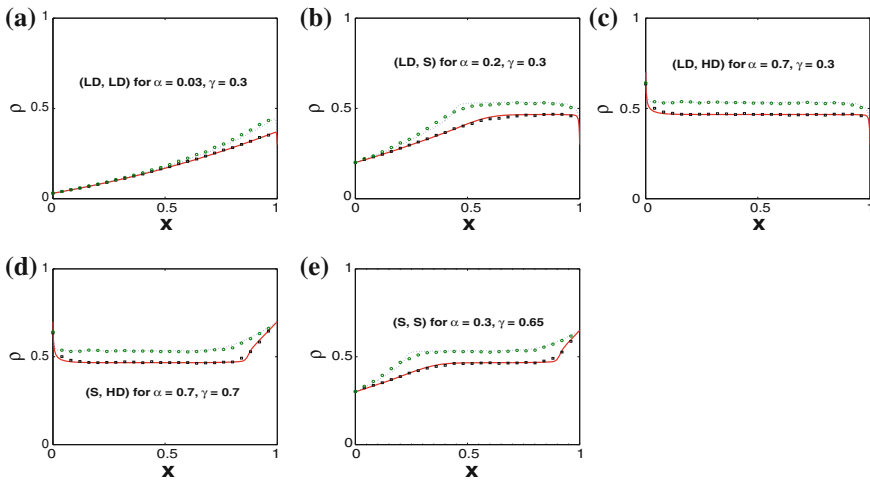
Fig. 4 Density profiles for $\theta = 2$ corresponding to the phase diagram in Fig. 3c. The *solid* (*dashed*) *lines* in *red* (*blue*) *colour* are the continuum mean-field density profiles of channel A (B). The curves marked with *squares* (*circles*) are the result of MCS for channel A (B)

(negative) values of ϕ represents the attractive (repulsive) interaction of the LK dynamic.

Firstly, the role of attractive interactions on the phase diagram is investigated by increasing the value of ϕ. For $\phi = 0$, the system reduces to the one studied in [4] with six distinct phases (see Fig. 3a). A small increase in the value of ϕ preserves the topological structure of the phase diagram with only slight shifting in the phase boundaries. The (LD, LD) phase shrinks and the (HD, HD) phase expands as there are more attachment with increasing ϕ. At $\phi = 0.5$, the topology of the phase diagram changes significantly (see Fig. 5a). Interestingly, no new phase emerges and the phase diagram consists of five phase having the same characteristics as that of $\phi = 0$. The (HD, HD) phase captures majority of the region in the phase diagram while the (LD, HD) phase disappears completely. In Fig. 6a the density profiles for different phases
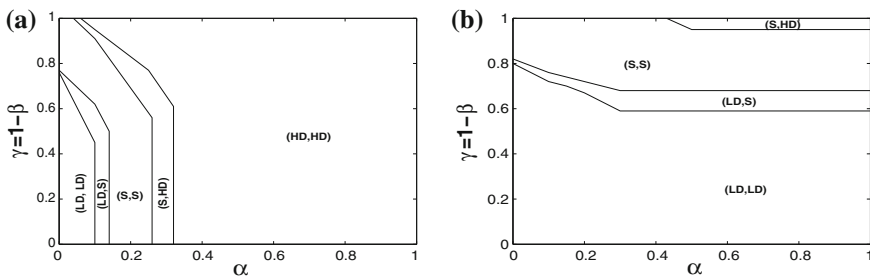
Fig. 5 Phase diagrams for $\Omega_A = 0.8$, $\Omega_B = 0.2$ and $\Omega_d = 0.2$: $\phi = 0.5$ (**a**) and $\phi = -0.5$ (**b**)
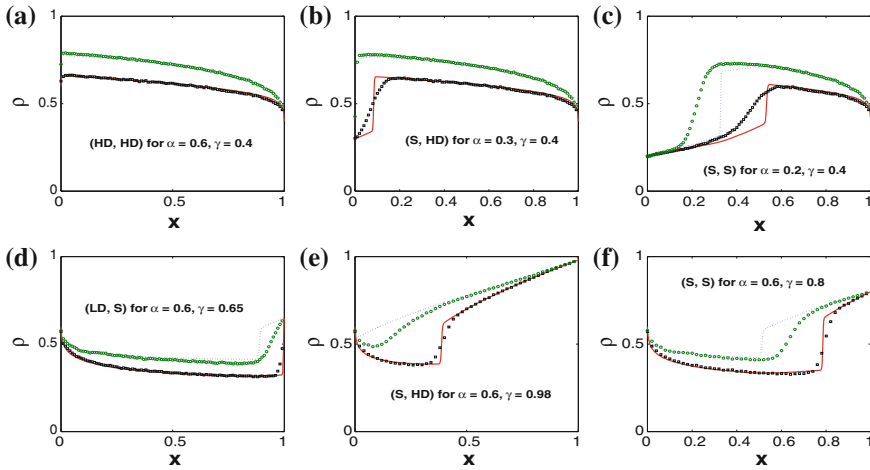
Fig. 6 Density profiles in various phases corresponding to the phase diagram in Fig. 5: $\phi = 0.5$ (**a–c**); $\phi = -0.5$ (**d–e**)

from continuum mean field along with the Monte Carlo simulation results are shown corresponding to the phase diagram in Fig. 5a.

Lastly, the case of negative ϕ is explored in Fig. 5b. Contrary to the case $\phi > 0$, as values of ϕ decreases, (LD, LD) phase enlarges and covers a major portion of the phase diagram for $\phi = -0.5$. Mainly, there are only four different stationary phases (also present for $\phi = 0$) in the phase diagram; while the topological structure of the phase diagram is quite different as compared to the one for $\phi = 0$. In general, there is a good agreement between the analytical and simulation results except some discrepancies for antisymmetric LK dynamics. There may be two reasons for such discrepancies, the finite lattice size or the mean-field approximation. As reported in Ref. [9] that the correlation due to mutual interactions (as in KLS model) may lead to some mismatch in the results obtained from mean-field approximation with Monte Carlo simulations.

4 Conclusion

We investigated a partially coupled two-channel TASEP model with MILK in both the channels by modifying LK dynamics based on the configuration of nearest-neighbouring sites. The steady-state properties of the system are examined using a mean-field approximation in the continuum limit. Under the symmetric LK dynamics in which both attachment and detachment rates increase or decrease simultaneously, the topology of the phase diagram remains qualitatively similar to the one obtained in the case of without mutual interaction. The only changes in the structure of the

phase diagram found are the gradual shifting of the phase boundaries and the shrinkage/expansion of various phases. The results of continuum mean-field equations are validated with the Monte Carlo simulation. On varying the mutual interaction between particles in antisymmetric case, we obtain a very rich phase diagram in which topology of the phase diagram changes significantly as compared to the symmetric case.

References

1. Celis-Garza, D., Teimouri, H., Kolomeisky, A.B.: Correlations and symmetry of interactions influence collective dynamics of molecular motors. J. Stat. Mech. Theory Exp. **2015**(4), P04013 (2015)
2. Chandel, S., Chaudhuri, A., Muhuri, S.: Collective transport of weakly interacting molecular motors with langmuir kinetics. EPL (Europhys. Lett.) **110**(1), 18002 (2015)
3. Chowdhury, D.: Stochastic mechano-chemical kinetics of molecular motors: a multidisciplinary enterprise from a physicists perspective. Phys. Rep. **529**(1), 1–197 (2013)
4. Dhiman, I., Gupta, A.K.: Effect of coupling strength on a two-lane partially asymmetric coupled totally asymmetric simple exclusion process with langmuir kinetics. Phys. Rev. E **90**(1), 012114 (2014)
5. Gupta, A.K., Dhiman, I.: Asymmetric coupling in two-lane simple exclusion processes with langmuir kinetics: Phase diagrams and boundary layers. Phys. Rev. E **89**(2), 022131 (2014)
6. Howard, J.: Mechanics of Motor Proteins and the Cytoskeleton. Sinauer Associates, Sunderland, MA (2001)
7. Parmeggiani, A., Franosch, T., Frey, E.: Phase coexistence in driven one-dimensional transport. Phys. Rev. Lett. **90**(8), 086601 (2003)
8. Parmeggiani, A., Franosch, T., Frey, E.: Totally asymmetric simple exclusion process with langmuir kinetics. Phys. Rev. E **70**(4), 046101 (2004)
9. Popkov, V., Rákos, A., Willmann, R.D., Kolomeisky, A.B., Schütz, G.M.: Localization of shocks in driven diffusive systems without particle number conservation. Phys. Rev. E **67**(6), 066117 (2003)
10. Pronina, E., Kolomeisky, A.B.: Two-channel totally asymmetric simple exclusion processes. J. Phys. A Math. Gen. **37**(42), 9907 (2004)
11. Roos, W.H., Campàs, O., Montel, F., Woehlke, G., Spatz, J.P., Bassereau, P., Cappello, G.: Dynamic kinesin-1 clustering on microtubules due to mutually attractive interactions. Phys. Biol. **5**(4), 046004 (2008)
12. Schmittmann, B., Zia, R.: Driven diffusive systems. An introduction and recent developments. Phys. Rep. **301**(1), 45–64 (1998)
13. Vuijk, H., Rens, R., Vahabi, M., MacKintosh, F., Sharma, A.: Driven diffusive systems with mutually interactive langmuir kinetics. Phys. Rev. E **91**(3), 032143 (2015)

Author Index